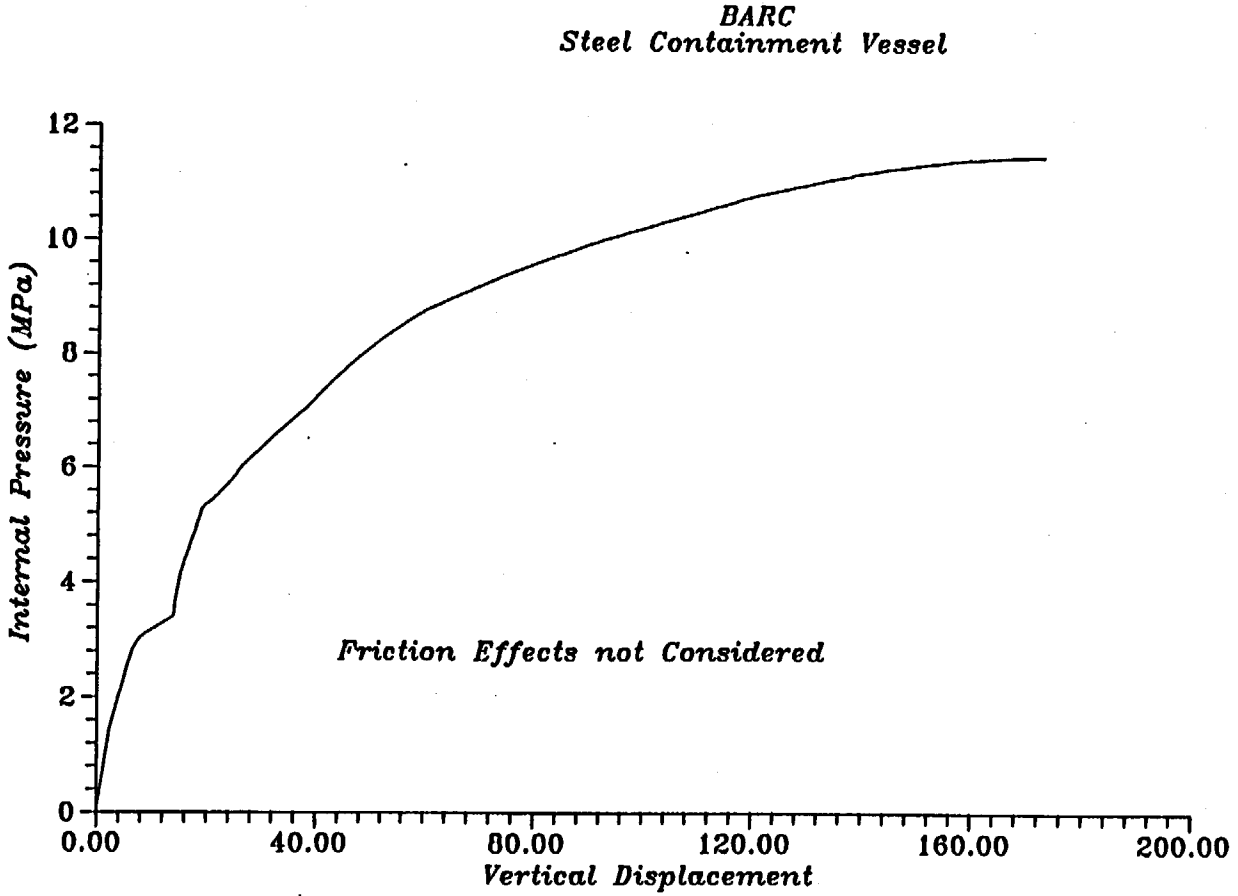

Fig.No.33 Plot of Load v/s. Displacement at ID.No.35

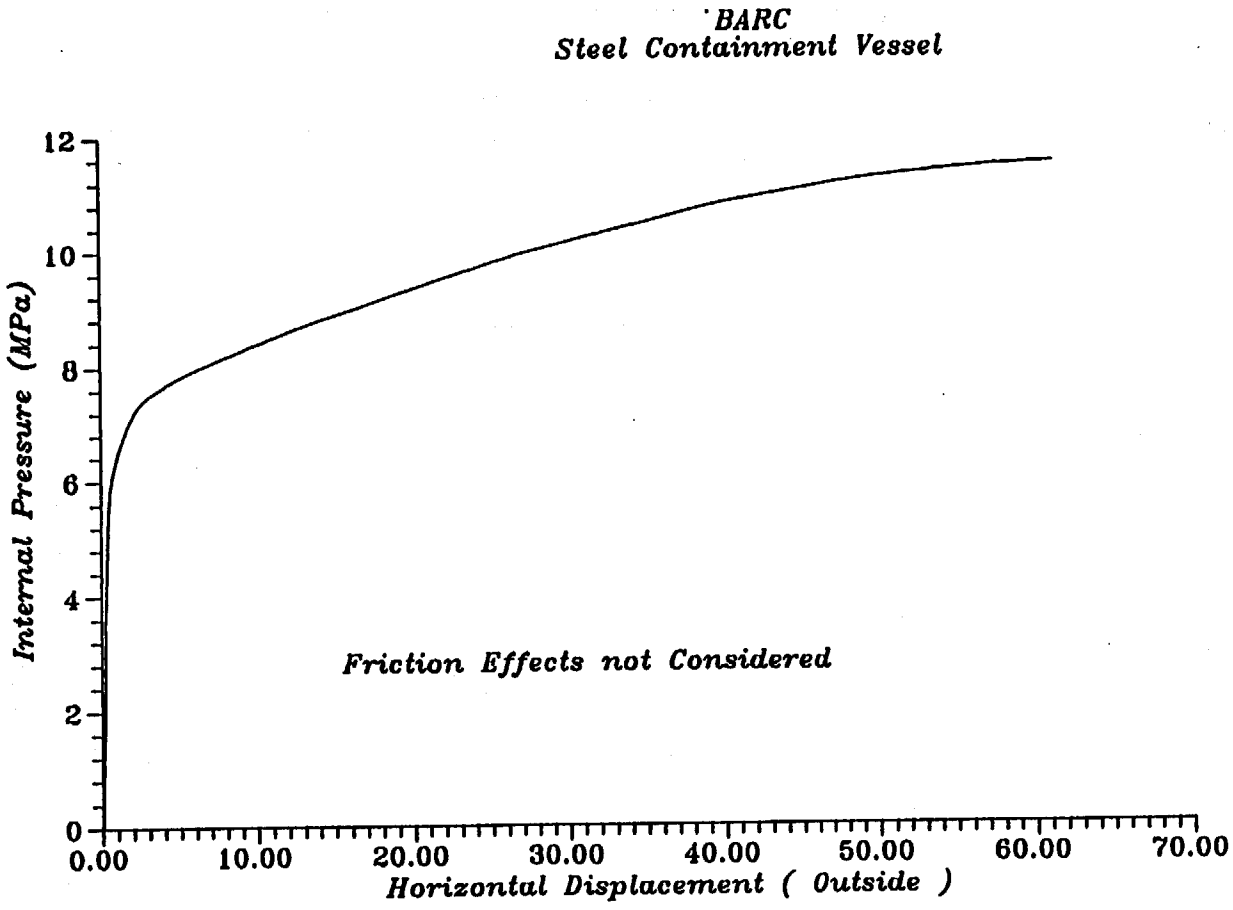

Fig.No.89 Plot of Load v/s. Displacement at ID.No.36

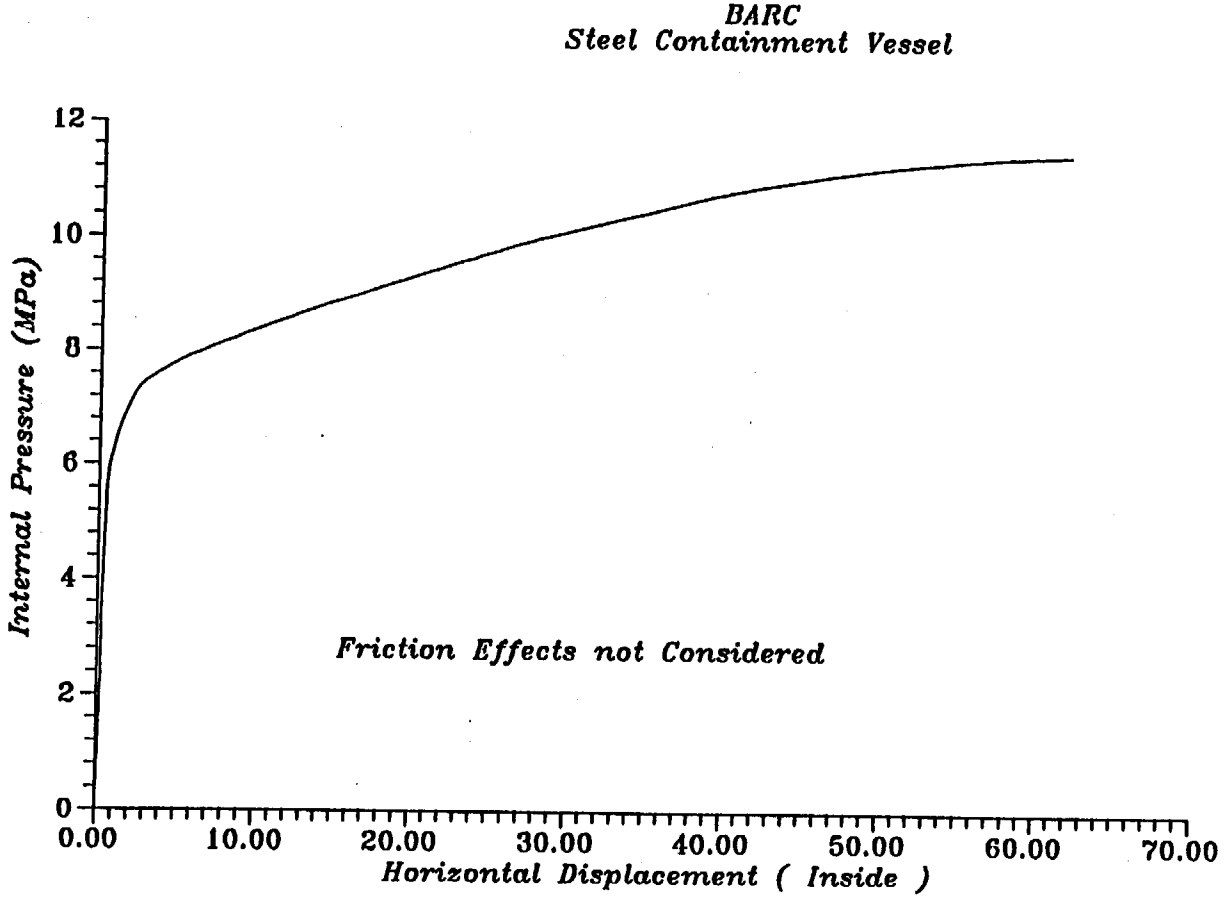

Fig.No.9o Plot of Load v/s. Displacement at ID.No.36

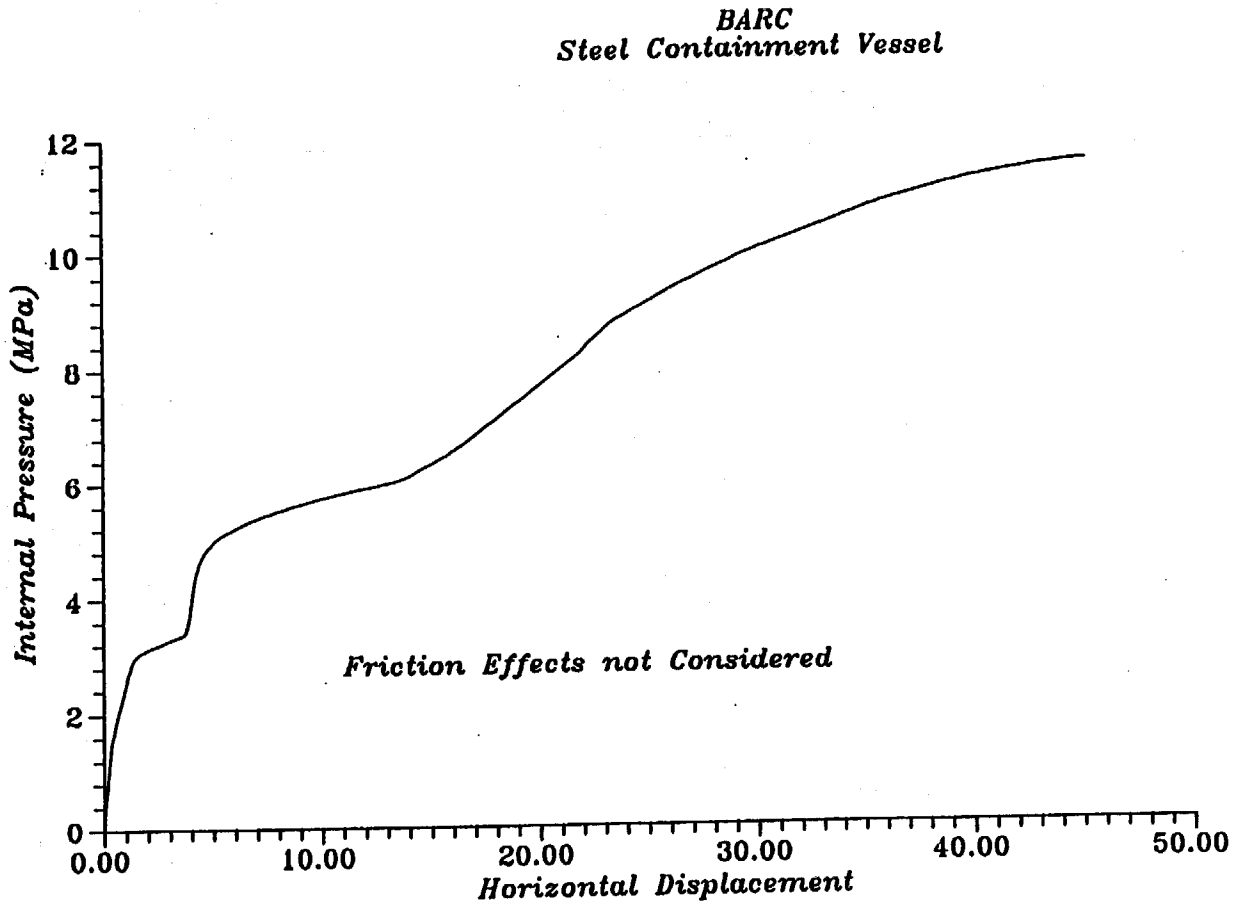

Fig.No.9i Plot of Load v/s. Displacement at ID.No.37

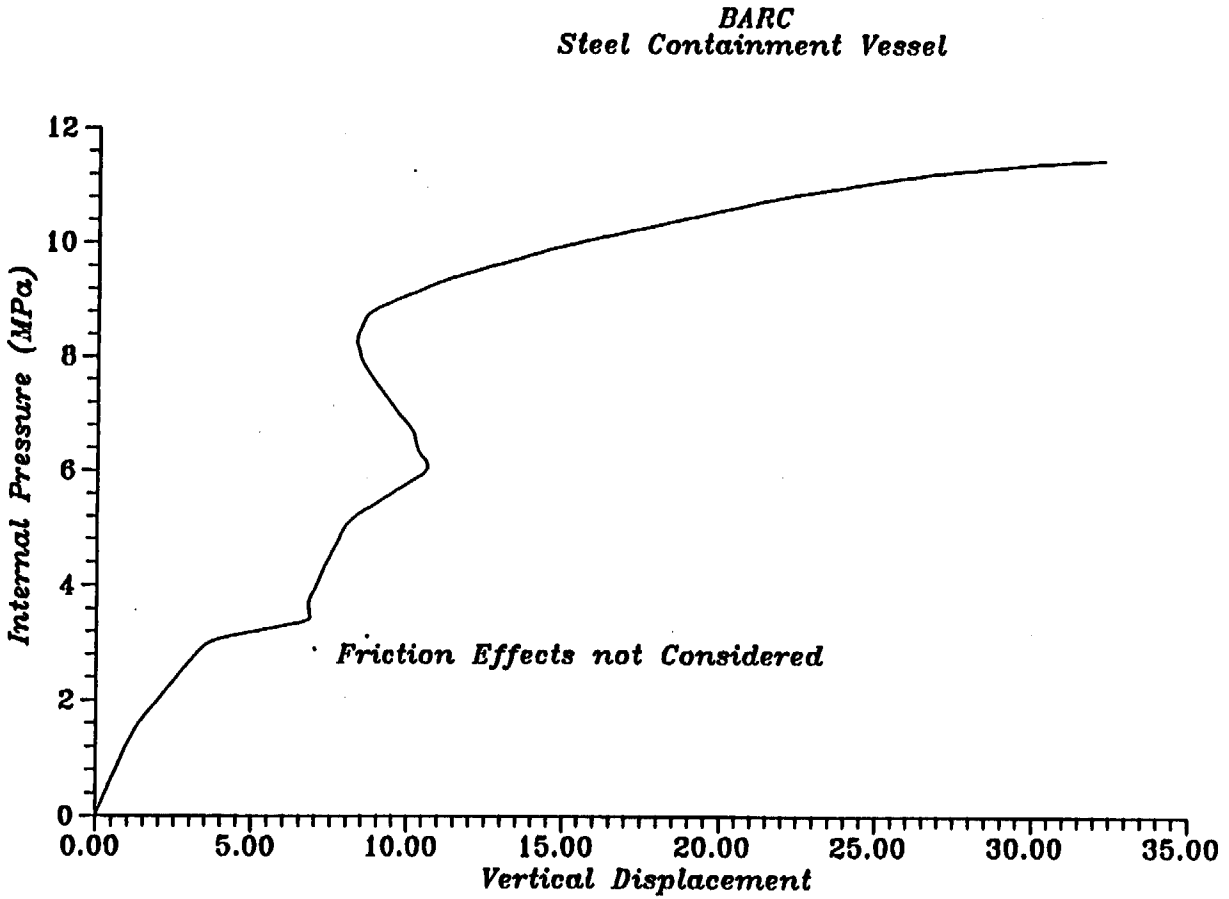

Fig.No.92 Plot of Load v/s. Displacement at ID.No.38

Appendix E-3.2

Bhabha Atomic Research Centre

India

PRETEST REPORT ON THE ANALYSIS OF STEEL CONTAINMENT MODEL (USING COMPUTER CODES TABS/NISA)

By

B.K.Dutta , P.Swami Prasad & H.S.Kushwaha
Reactor Safety Division, Bhabha Atomic Research Centre
Trombay, Mumbai 400085

MODELLING ASPECTS

The steel containment vessel along with the contact structure is an axisymmetric structure, but than the presence of instrumentation hatch. Due to the presence of hatch, one needs to model the structure either by 3-D finite elements or by using shell bending elements. However, considering the presence of all types of nonlinearities in the structure (geometrical, material and contact nonlinearities) , one needs to have very small load increments in transient calculations for monotonic iterative convergence. However, a 3-D model, with all types of static nonlinearities in the structure and very small load increments, requires enormous computational time. Due to limited computer resources, it was felt that to complete the present analysis within a specified time, it would be prudent to model the structure by using 2-D axisymmetric elements. This in turn means, we are neglecting the effect of hatch. Assuming the effect of hatch will be confined to a limited domain, analysis results are valid for the regions away from the hatch. However, in our standard plot set, we have not provided the plots which are near to the hatch area (i.e. plot ID 1 to 6 and 39).

In the present axisymmetric model, we have used 8-noded isoparametric elements. There are three divisions along the thickness of the containment. There are 180 elements in the top head, 101 elements in the flange and top cylindrical region, 24 elements in knuckle region, 199 elements in the spherical shell, 426 elements in conical shell and 168 elements in lower cylindrical shell. There are in all 1098 elements and 4041 nodes in the containment model. The contact structure is also modelled with the 2-D axisymmetric elements. There is one division in the thickness direction. There are 264 elements and 1323 nodes in the contact-structure model.

All the elements in the complete model are well shaped and the maximum aspect ratio is below 5. Beside symmetric boundary condition on the vertical plane, the bottom of the model is fixed to simulate its welding on the top surface of the ring support girder. The mesh used in the present analysis for different zones are shown in figures 1a to 1c.

The model geometry is modified, as much as possible, to match with the as-built data prescribed in Enclosure-3 of the SNL letter No. SO-95-099 dated Dec.1, 1995. For this purpose, coordinates of the nodes on the outer surface of the containment were modified to suit the measured average thickness profile. Similarly, gap between the containment model outer surface and the inner surface of the contact structure was adjusted to match the measured average values. This gap varies from 15 mm near the top of the knuckle to 23 mm at the end of spherical shell. The average gap in the conical shell is around 23.5 mm.

DESCRIPTION OF THE USE OF NUPEC TENSILE DATA

In our model, the different tensile test data were used for different zones of the containment. Average values of Engineering Stress-Strain data were calculated using four sets of data provided for every zone (Table 4 to 15 of SNL letter dated July 10, 1995). The plots of these data as used in our analysis for different zones are shown in figures 2a to 2c. As we have used Total-Lagrangian formulations for considering material and geometrical nonlinearities, Engineering Stress-Strain data has been used instead of True Stress-Strain.

FAILURE MODEL

As in our analysis only material flow is considered as per one dimensional stress-strain material curve, failure model (i.e. collapse pressure) purely depends upon the attainment of maximum equivalent plastic strain. We have computed average equivalent plastic strain over the thickness of the containment model at various cross sections. The collapse pressure is determined, when the average plastic strain exceeds the maximum equivalent plastic strain in stress-strain material curve. In the present analysis, weakest cross section has come out to be the junction between knuckle and the top head.

MODELLING OF CONTACT BETWEEN SCV AND CS

The contact between the SCV and CS and its progress at different elevations are important considerations in the present analysis. The contact between the SCV and CS at different regions is established once the perpendicular gap between the outer surface of SCV and the inner surface of CS is zero while increasing the internal pressure. Necessary Gap elements are employed to consider this effect in the present analysis. The Gap elements model the transfer of forces in the normal and tangential directions at those regions of the SCV and CS which are making contact . The tangential forces depend upon the friction factor between the surfaces. Due to the absence of any realistic friction factor value, no attempt has been made in the present analysis to consider this effect.

SAMPLE RESULTS

We have incorporated with this report some sample results obtained through our analysis. Figure 3a shows the progress of deformations of the top head along with the top cylinder and knuckle. This figure demonstrates the large vertical deformation of the crown before the attainment of collapse pressure. Figure 3b shows horizontal displacement of a point with the increase in internal pressure. The point is on the outer surface of the top head at an elevation 10 cm above the junction between top head and top cylinder. This history shows that, this point initially deforms inward upto a pressure of 12 MPa and then starts deforming rapidly in the outward direction with the further increase in pressure. Figure 3c shows the contours of equivalent plastic strain at an internal pressure 11.5 MPa near the junction between the top head and the knuckle.

A DISCUSSION ON THE POTENTIAL FOR BUCKLING OF HEAD REGION

In the present axisymmetric model, it is not possible to obtain the buckling modes, which are essentially asymmetric. However, possibility of inplane axisymmetric buckling can be checked through the present analysis. A plot of horizontal displacement of a point 10 cm above the junction between the top head and the top cylinder (i.e. Fig. 3b) , shows snap through type of deformation behaviour of this point. This may indicate possibility of a buckling of this region at higher pressure.

OCCURRENCE OF FIRST YIELD OF SCV AND FIRST CONTACT BETWEEN SCV AND CS

It is seen from the present analysis that first point of the SCV which experiences yielding is on the inner surface of this SCV at an elevation 3360 mm at a pressure 2.0 MPa. Similarly the first point at which contact is established with CS is a junction point between knuckle and top spherical shell at an elevation 3375 mm at an internal pressure of 3.5 MPa.

DISCUSSION ON EXPECTED PATTERN OF CONTACT PROPAGATION

The contact between SCV and CS establishes at multiple points during the pressurisation of SCV. These points lie at various regions of the SCV. In figure 4a the SCV is divided into seven regions to facilitate this illustration. The following Table identifies different regions designated from A to G and the elevation and the pressure at which first contact is established in each of these regions. Figure 4b shows the propagation of these contacts as a function of internal pressure.

REFERENCES

1. NISA II , Numerically Integrated Elements for System Analysis, Ver 92.0
2. TABS - Finite Element Code for Thermo Plastic Analyis of Bending Structures, by B.K.Dutta, H.S.Kushwaha.

Region	*Description of Region*		*First Contact in the Corresponding Region*	
	Location From	*Location To*	*At Elev. (mm)*	*At Pres. (MPa)*
A	Bottom (Z = 500 mm)	Lower stiffener (Z = 921 mm)	820	9.3
B	Lower stiffener (Z = 921 mm)	Material change interface (Z = 1579 mm)	1380	6.1
C	Material change interface (Z = 1579 mm)	Middle stiffener (Z = 2079 mm)	1820	4.5
D	Middle stiffener (Z = 2079 mm)	Weld line in the upper conical shell (Z = 2275 mm)	2195	5.7
E	Weld line in the upper conical shell (Z = 2275 mm)	Junction at spherical shell and upper conical shell (Z = 2694 mm)	2370	4.34
F	Junction at spherical shell and upper conical shell (Z = 2694 mm)	Upper stiffener (Z = 2893 mm)	2760	8.1
G	Upper stiffener (Z = 2893 mm)	Junction at knuckle and spherical head (Z = 3377 mm)	3245	6.5

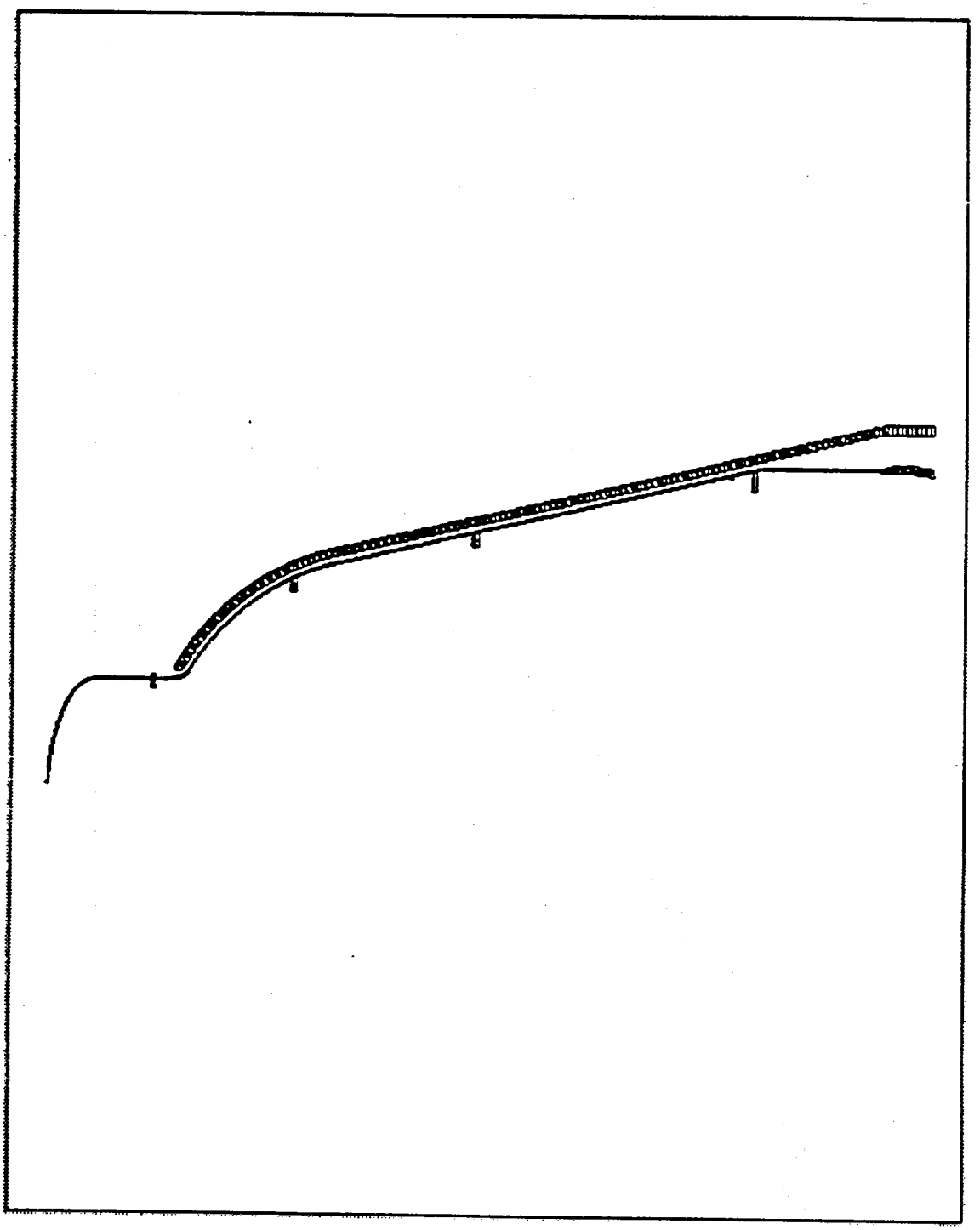

FIGURE 1a FINITE ELEMENT PLOT OF STEEL CONTAINMENT VESSEL AND CONTACT STRC.

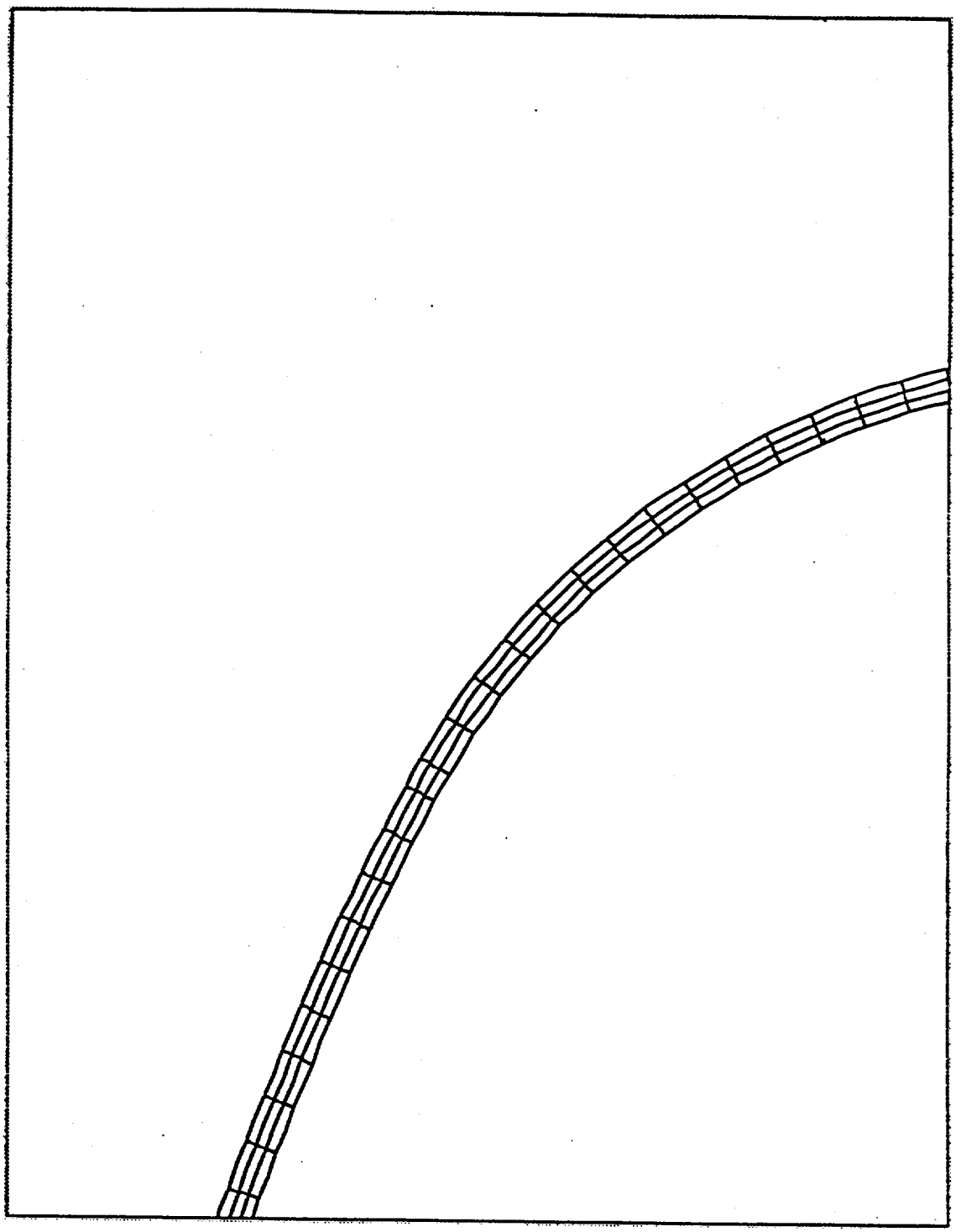

FIGURE 1b FINITE ELEMENT PLOT IN THE TOP HEAD REGION OF SCV

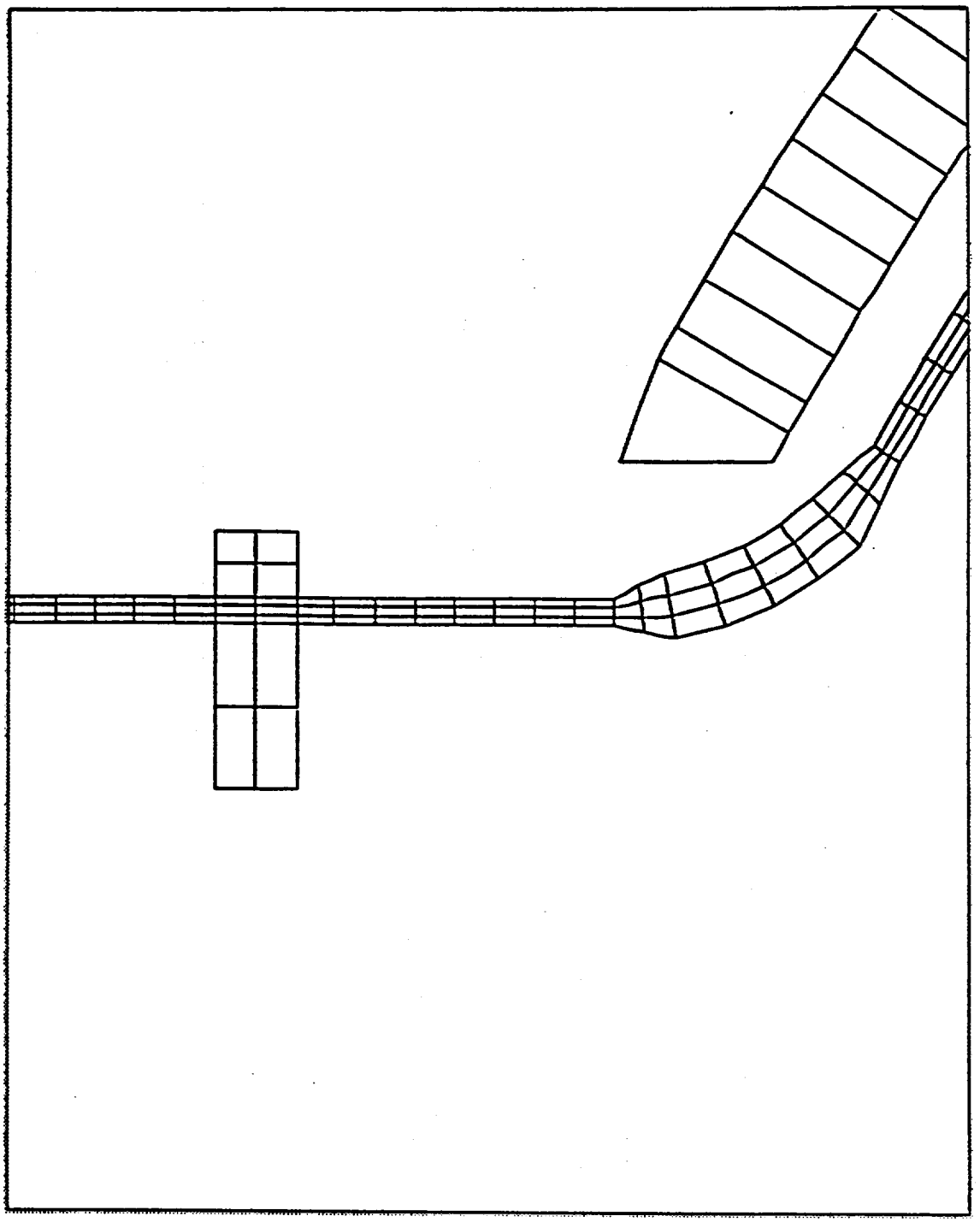

FIGURE 1C8 FINITE ELEMENT PLOT IN THE KNUCKLE REGION OF SCV

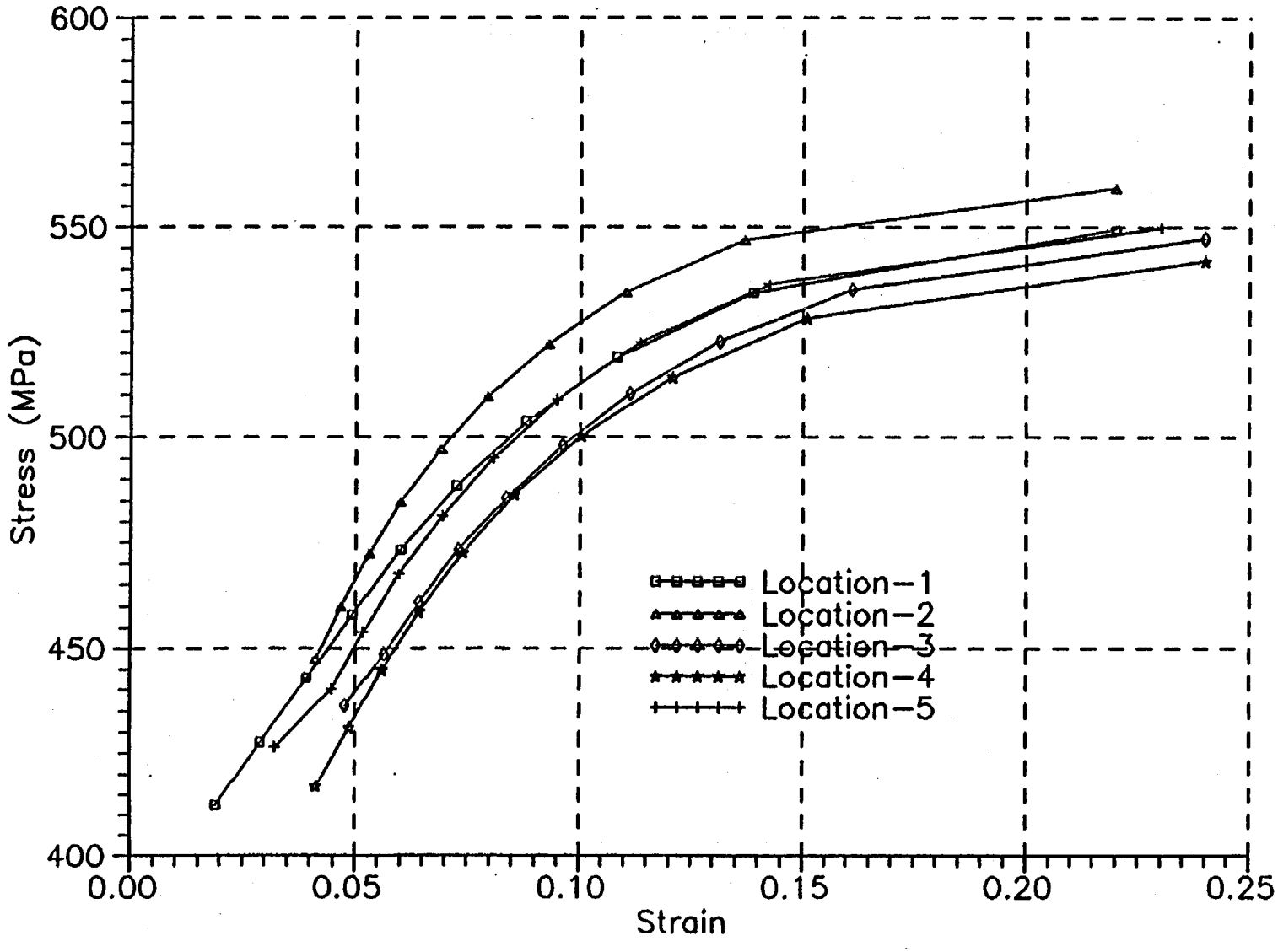

Fig.2a Stress – Strain Curves for Locations 1–5 Used in the Present Analysis

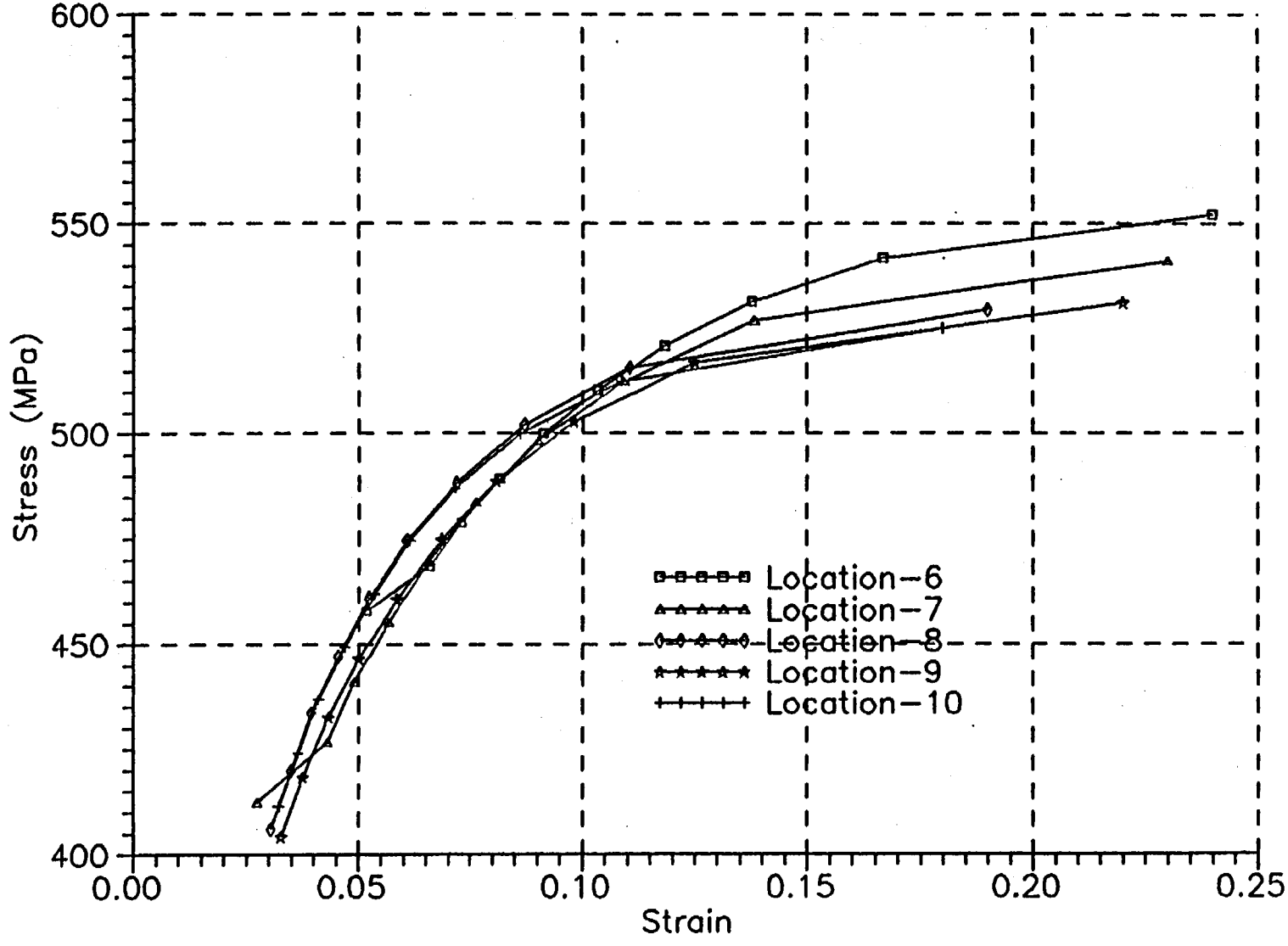

Fig.2b Stress – Strain Curves for Locations 6–10 Used in the Present Analysis

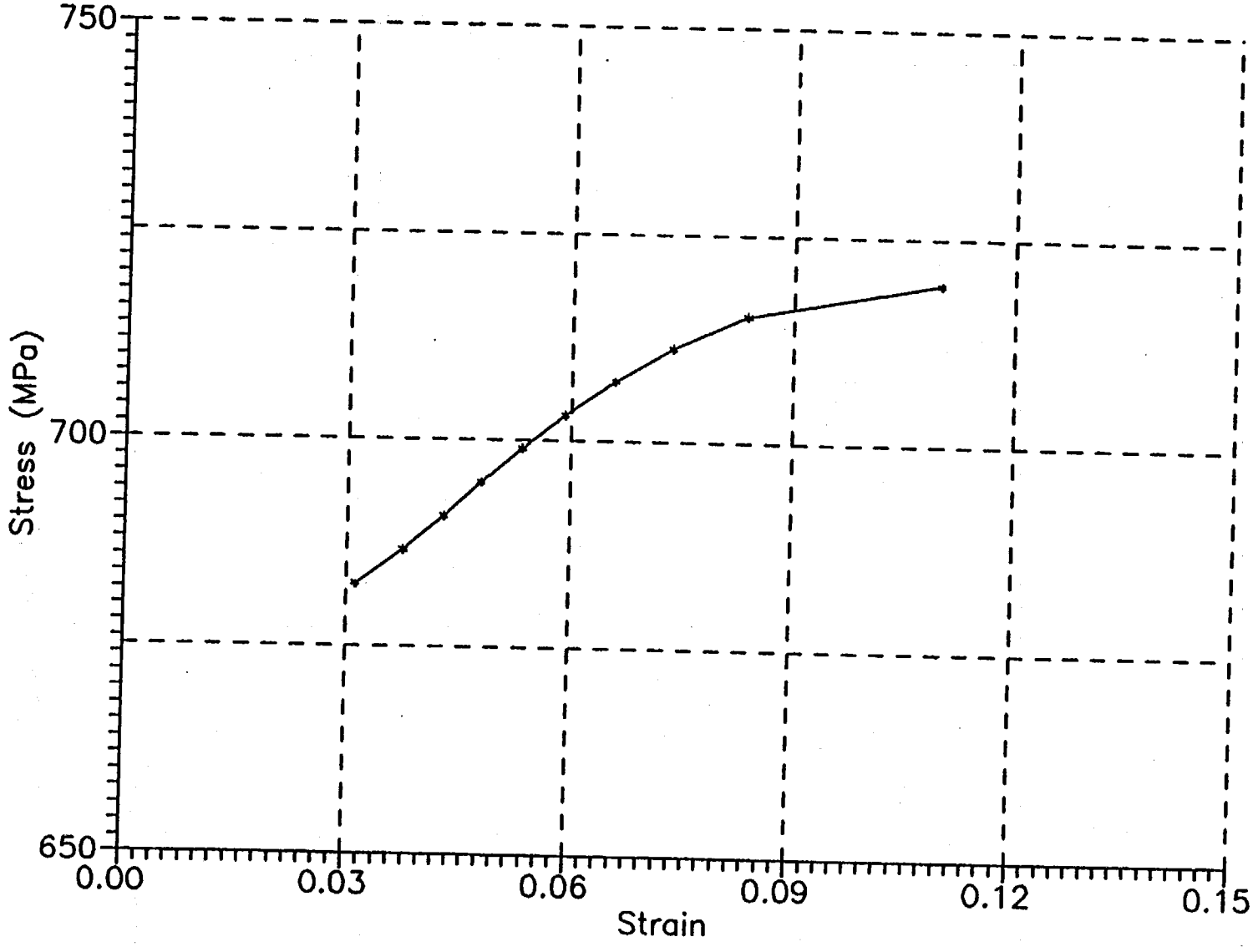

Fig.2c Stress – Strain Curve for Location–11 Used in the Present Analysis

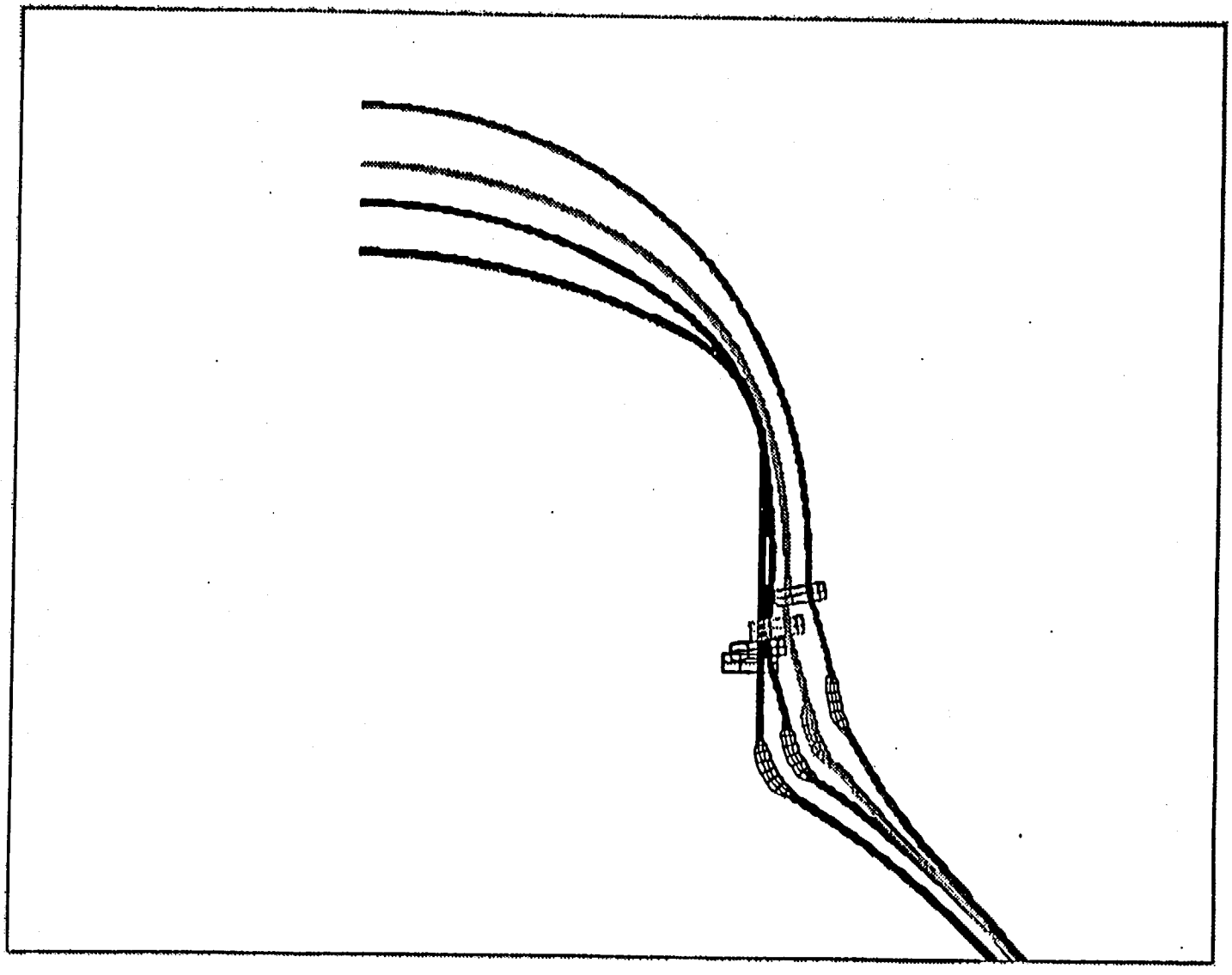

FIG.3A PROGRESS OF DEFORMATION OF SCV HEAD WITH PRESSURE

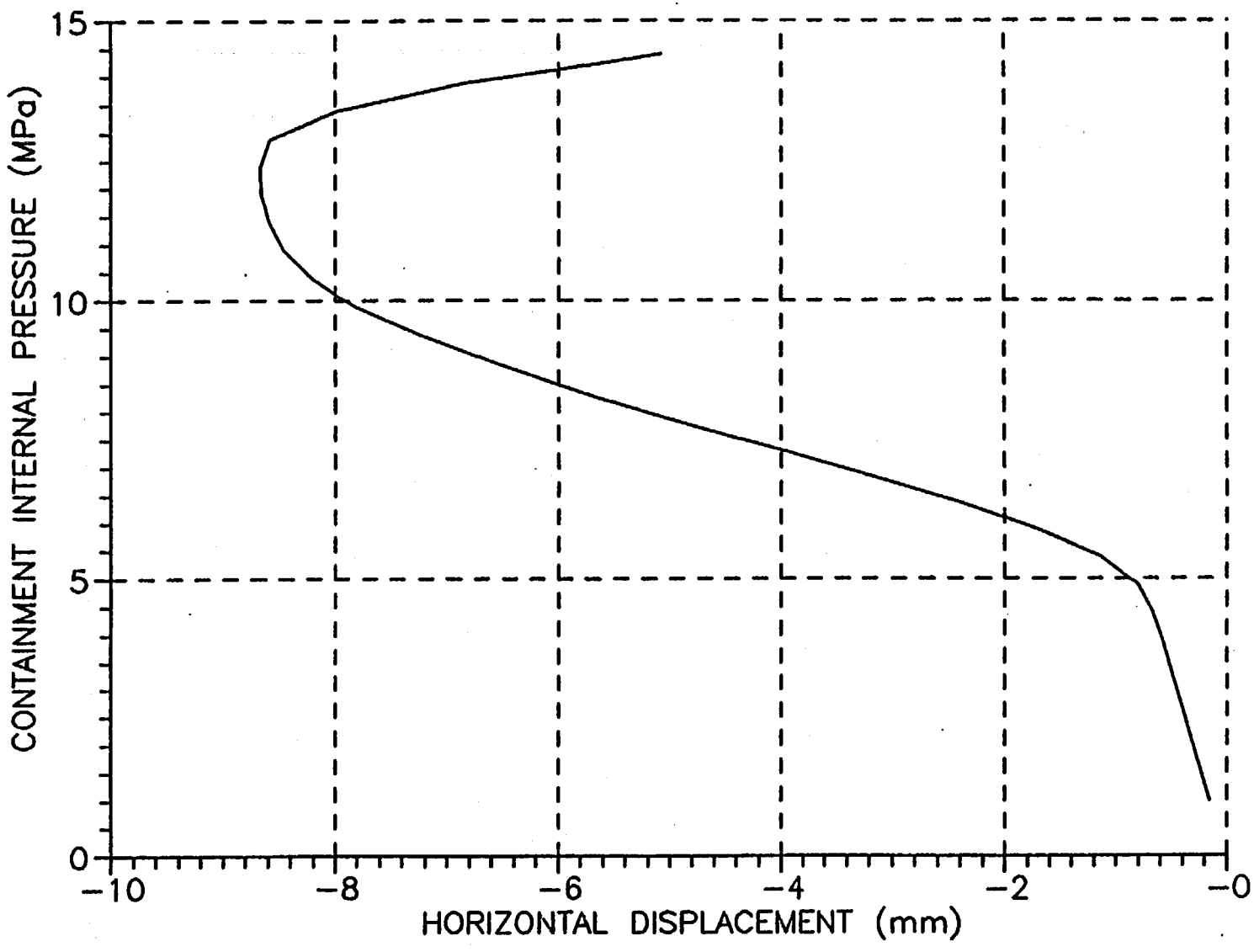

Fig.3b Plot of Horizontal Displacement of a point on Top head Outside at elevation of 3842 mm

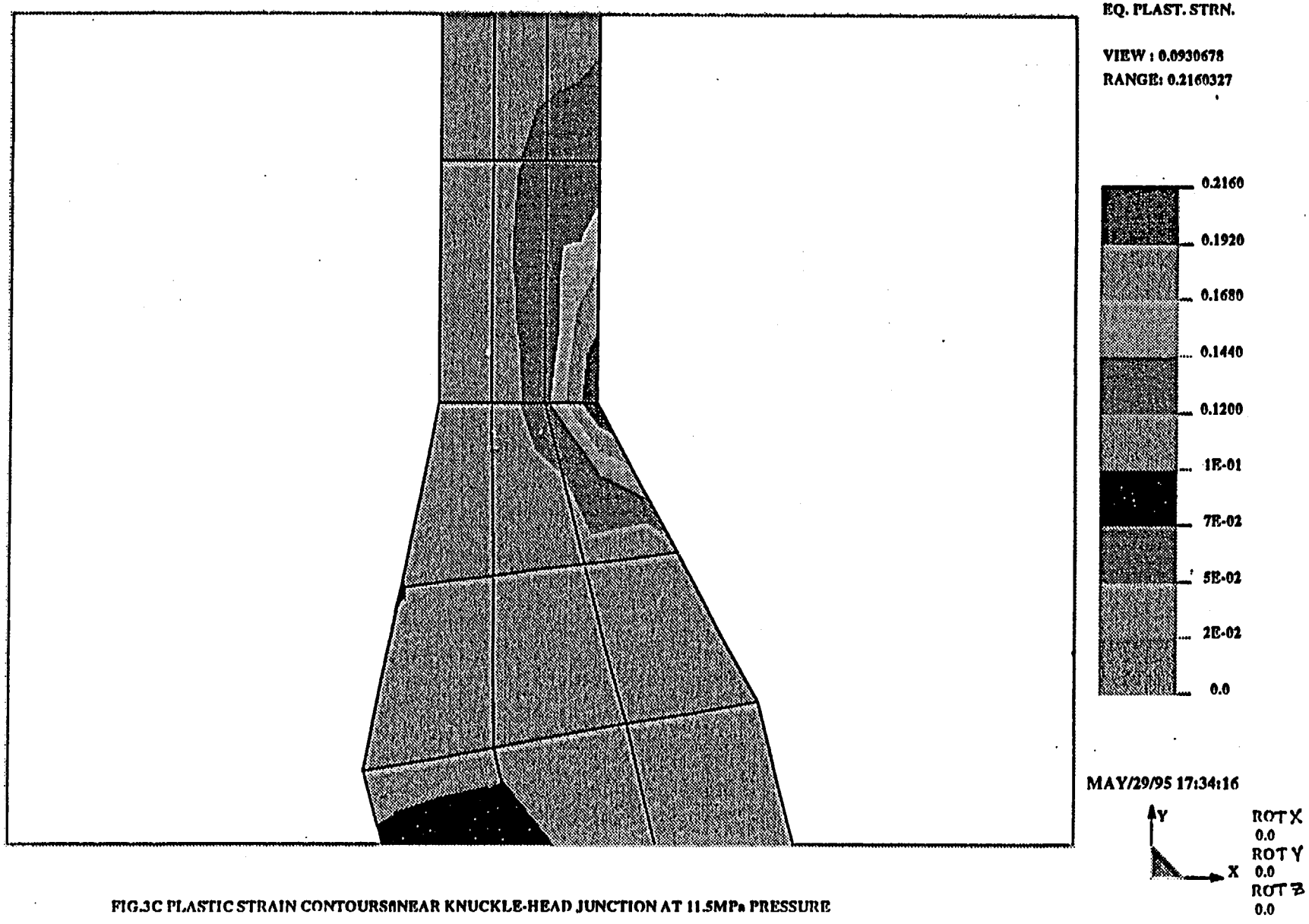

FIG.3C PLASTIC STRAIN CONTOURSNEAR KNUCKLE-HEAD JUNCTION AT 11.5MPa PRESSURE

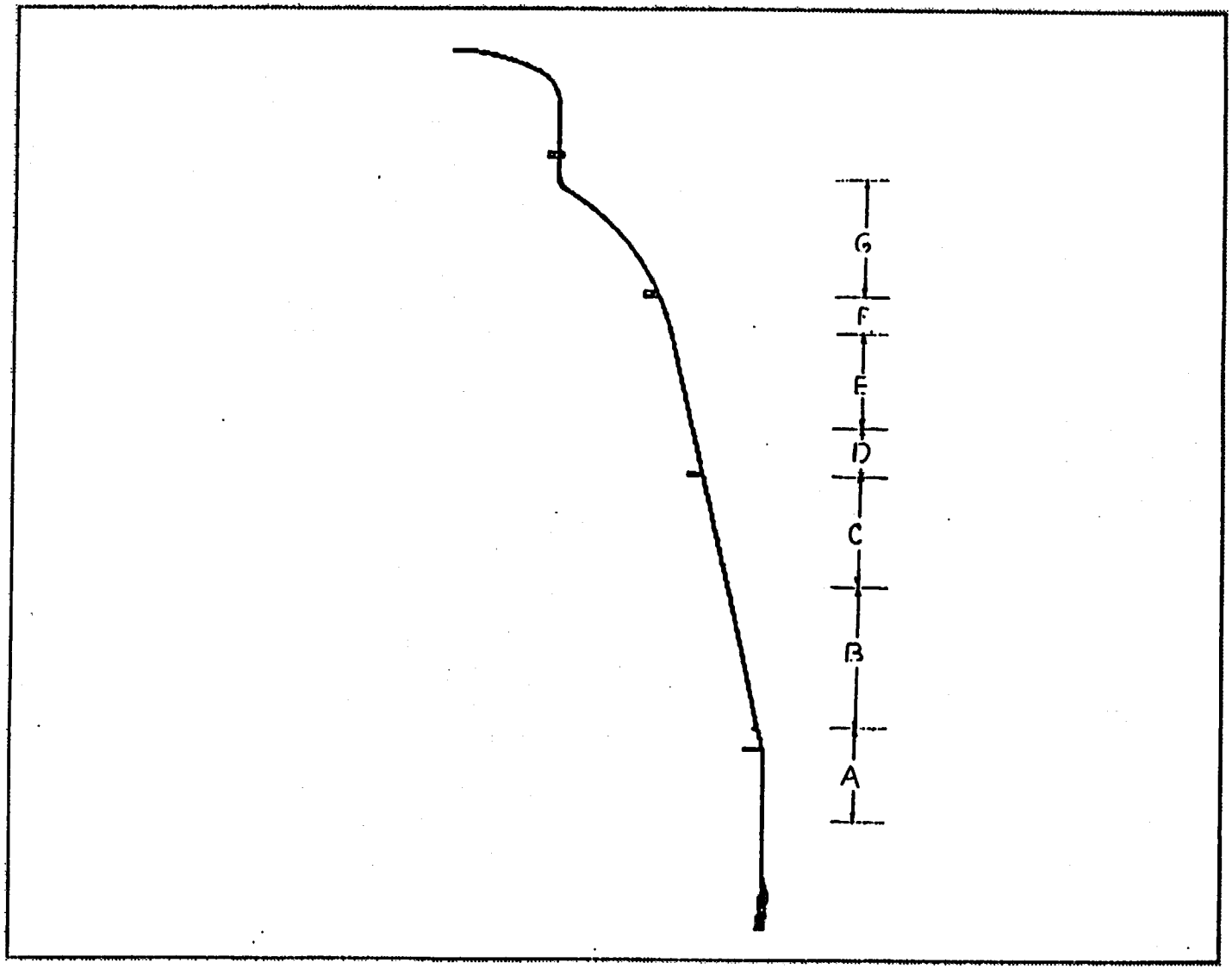

FIGURE 4a IDENTIFICATION OF REGIONS IN SCV TO ILLUSTRATE PROGRESS OF CONTACT

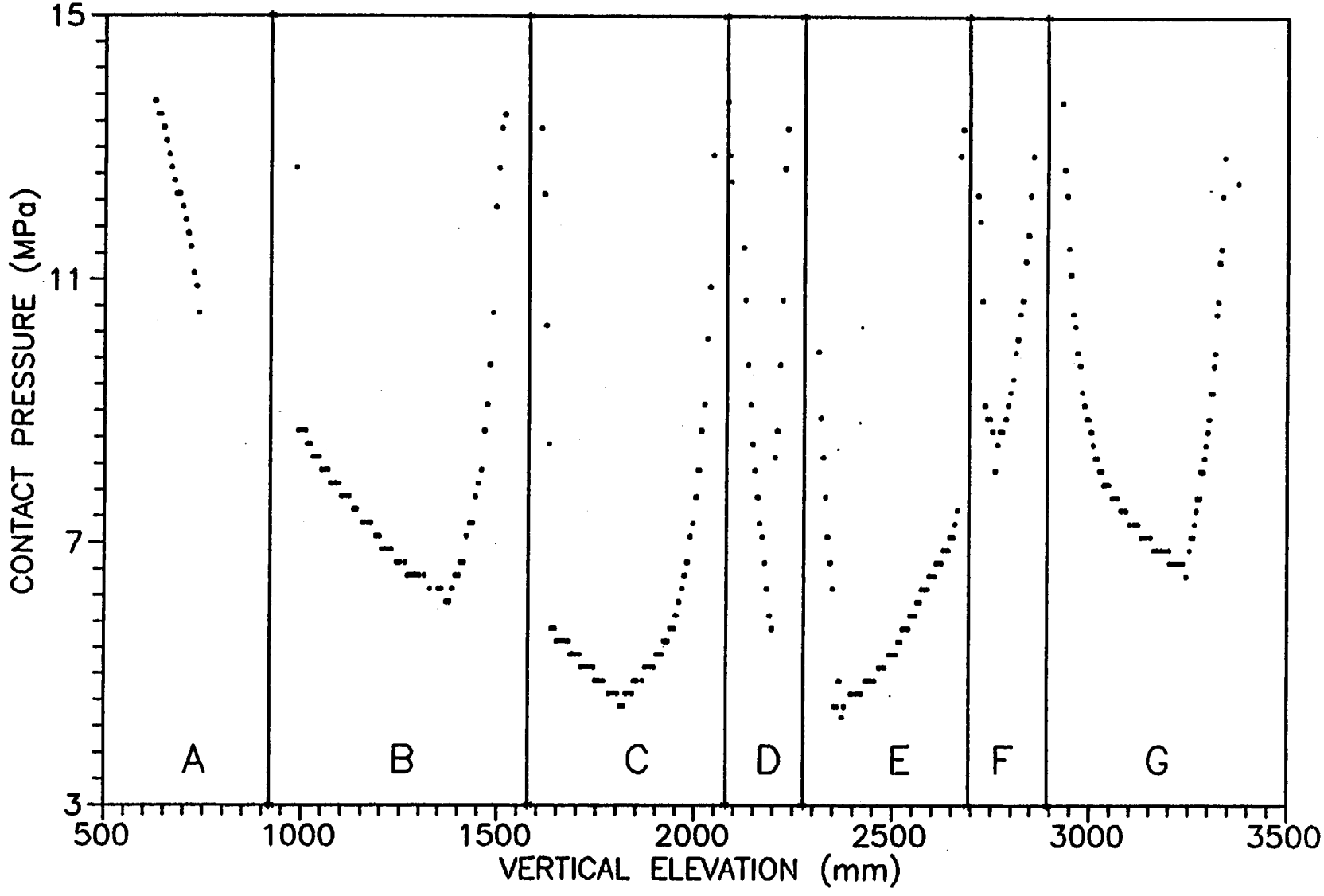

Fig.4b Progress of Contact of SCV and CS with Pressure

Appendix - A

Standard Output Plots

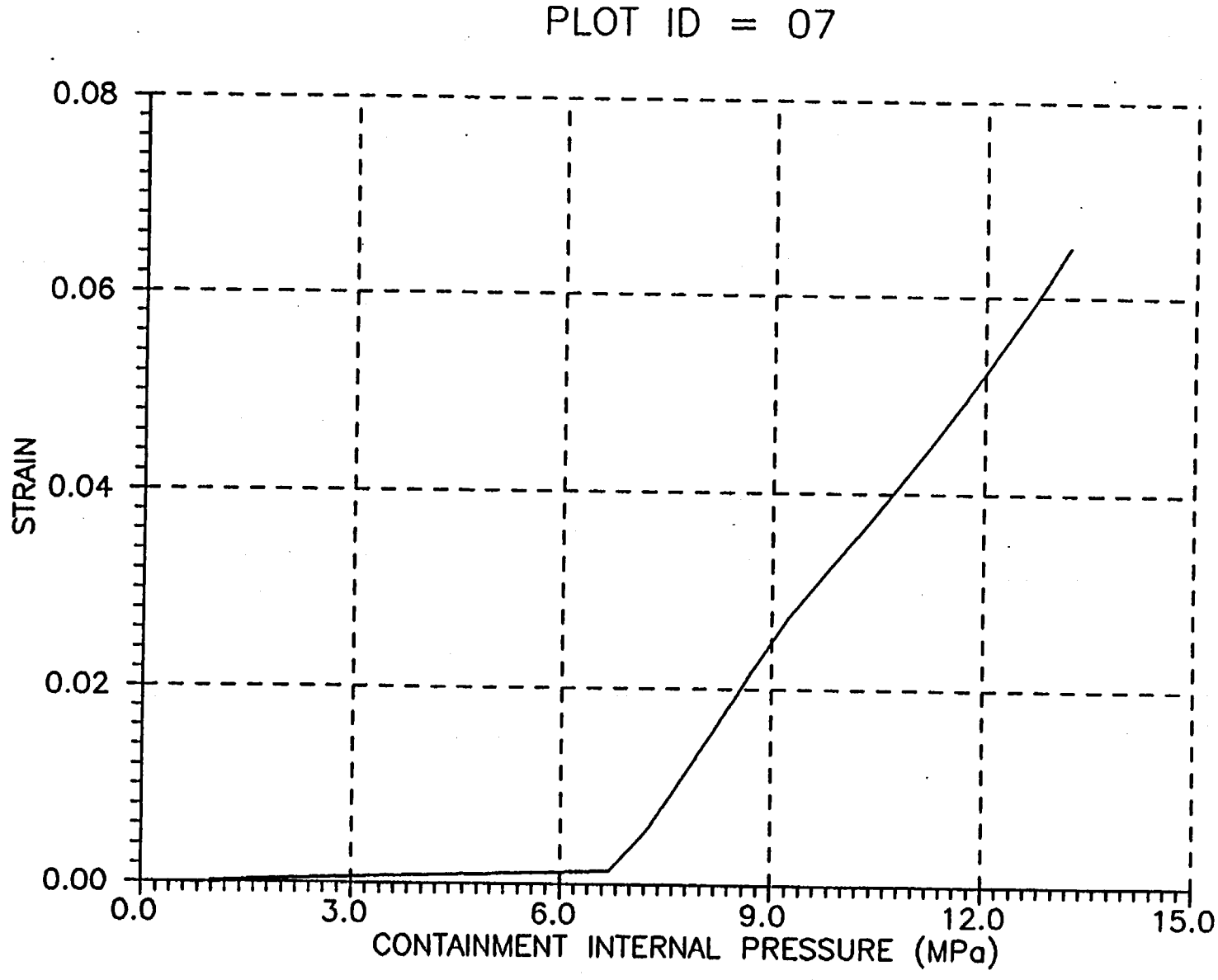

Plot of Maximum Principal Strain at top of the Containment

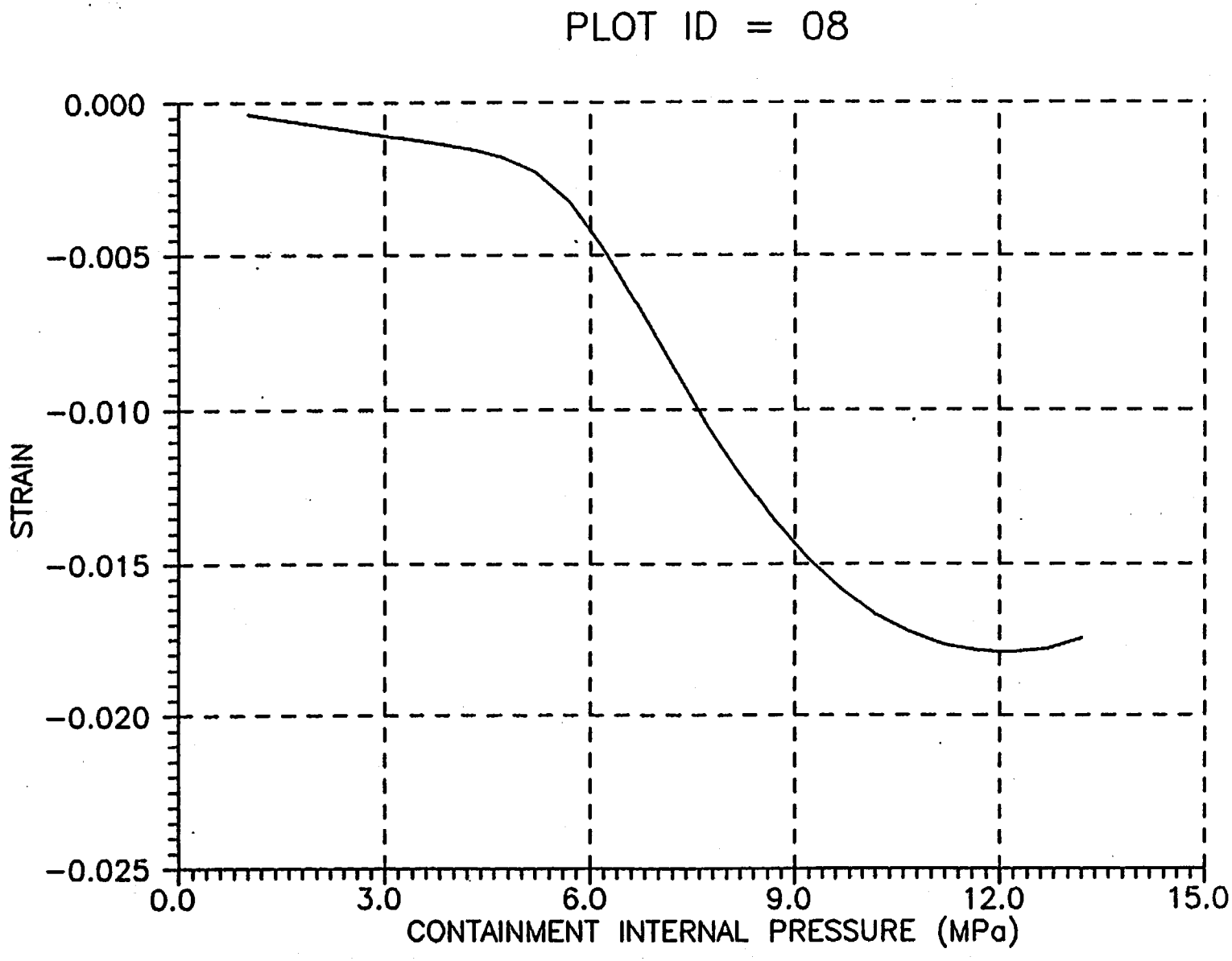

Plot of External Hoop Strain at 0.48 m from top

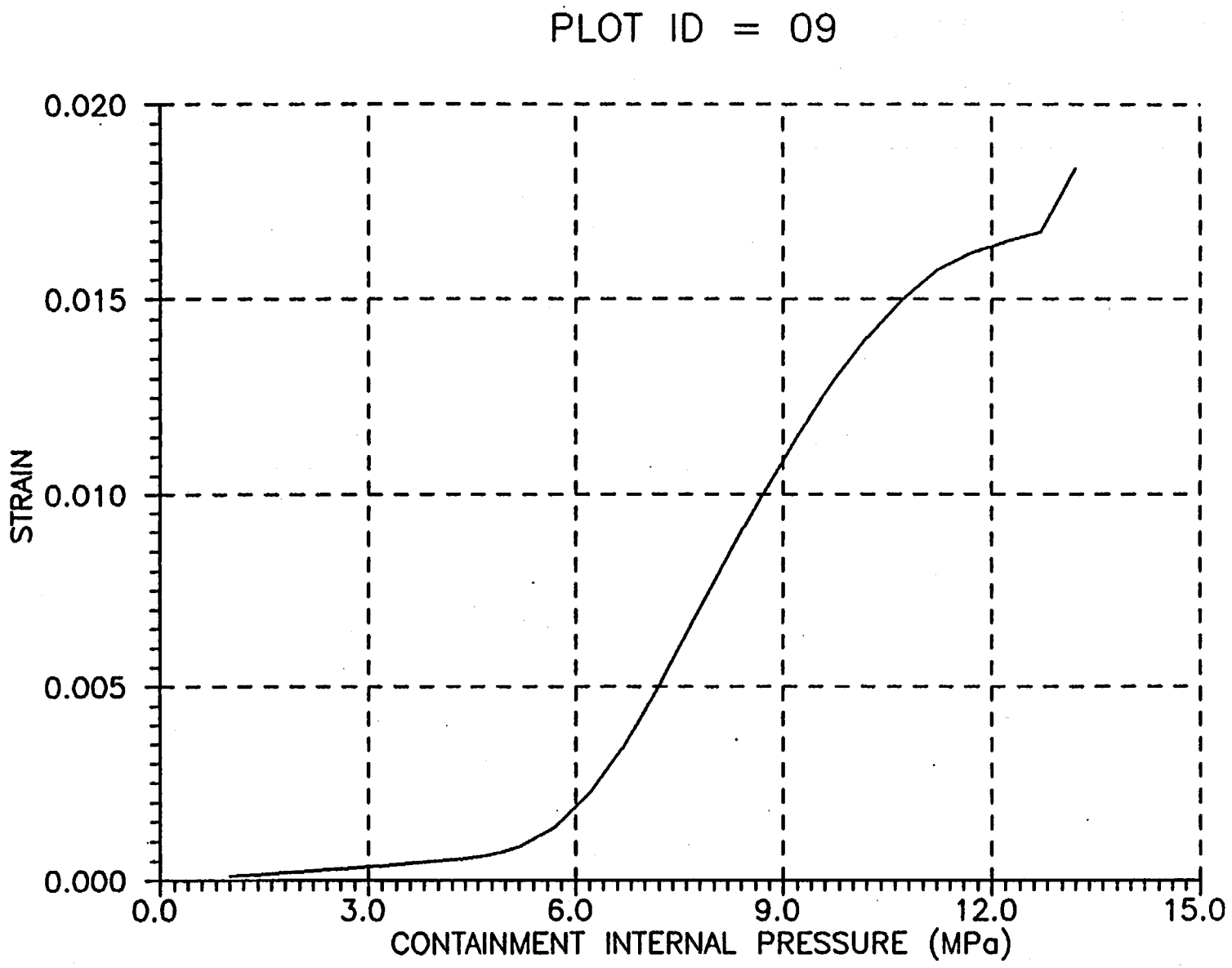

Plot of External Meridional Strain at 0.48 m from top

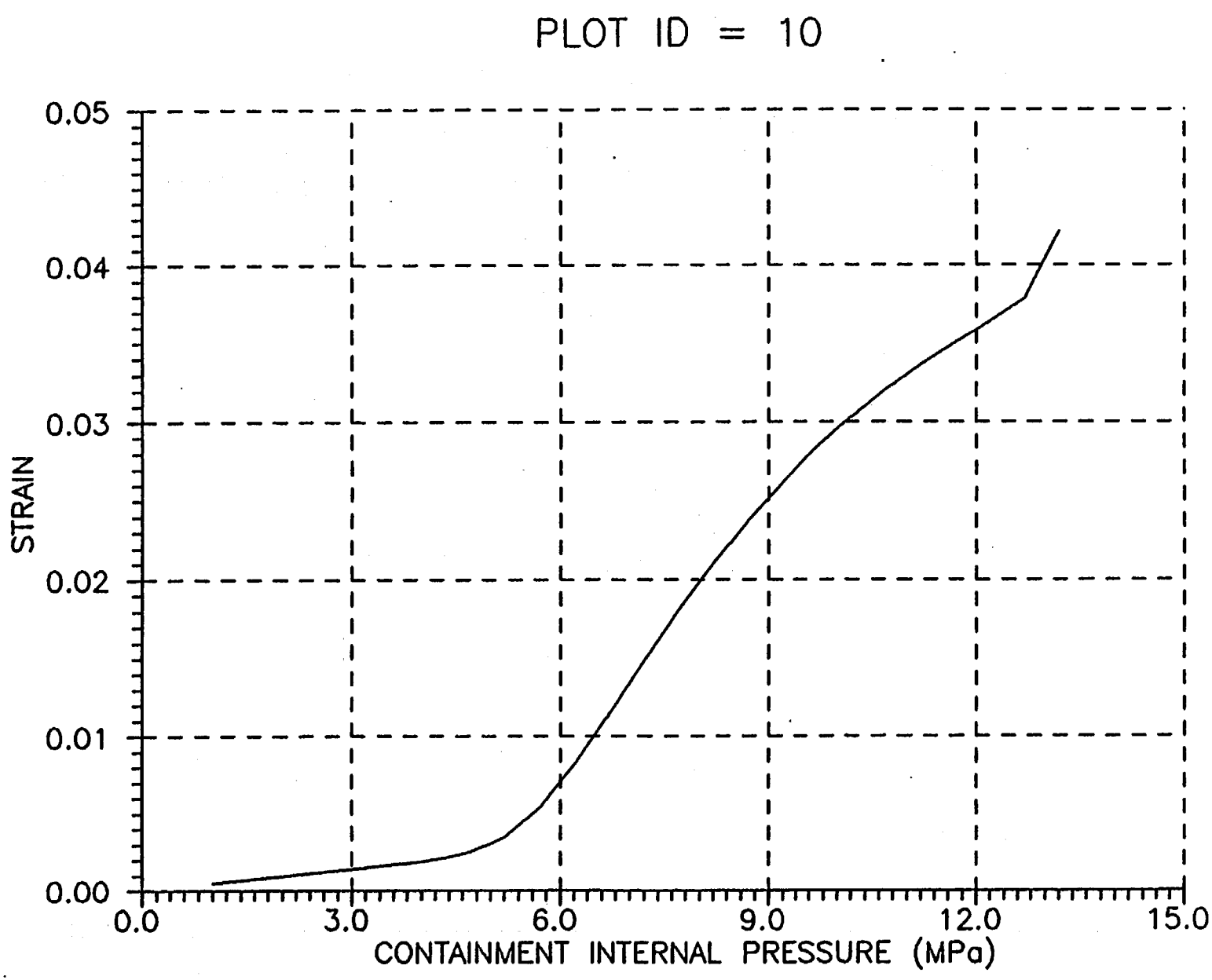

Plot of Internal Meridional Strain at 0.48 m from top

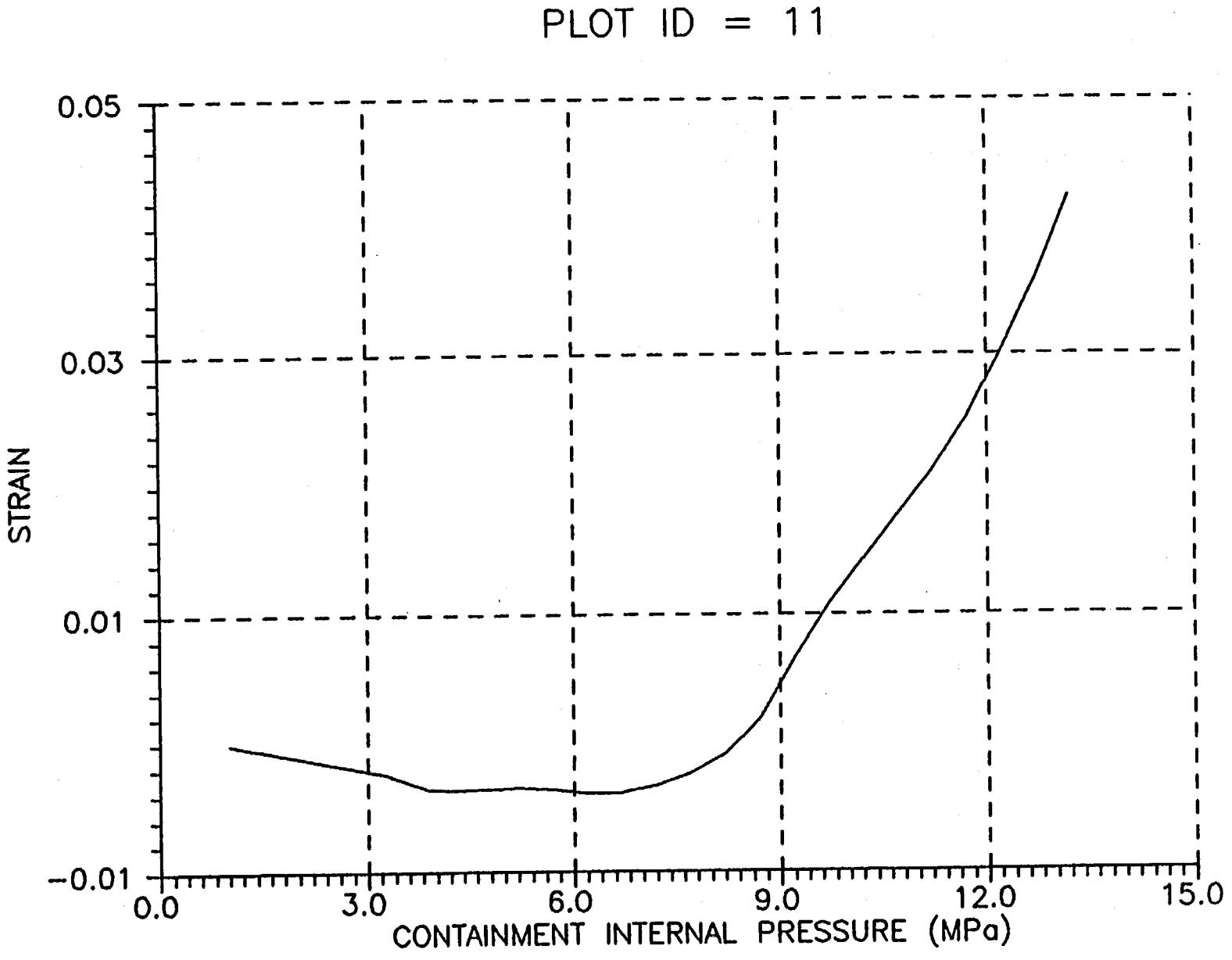

Plot of External Meridional Strain at Z = 3.47 m

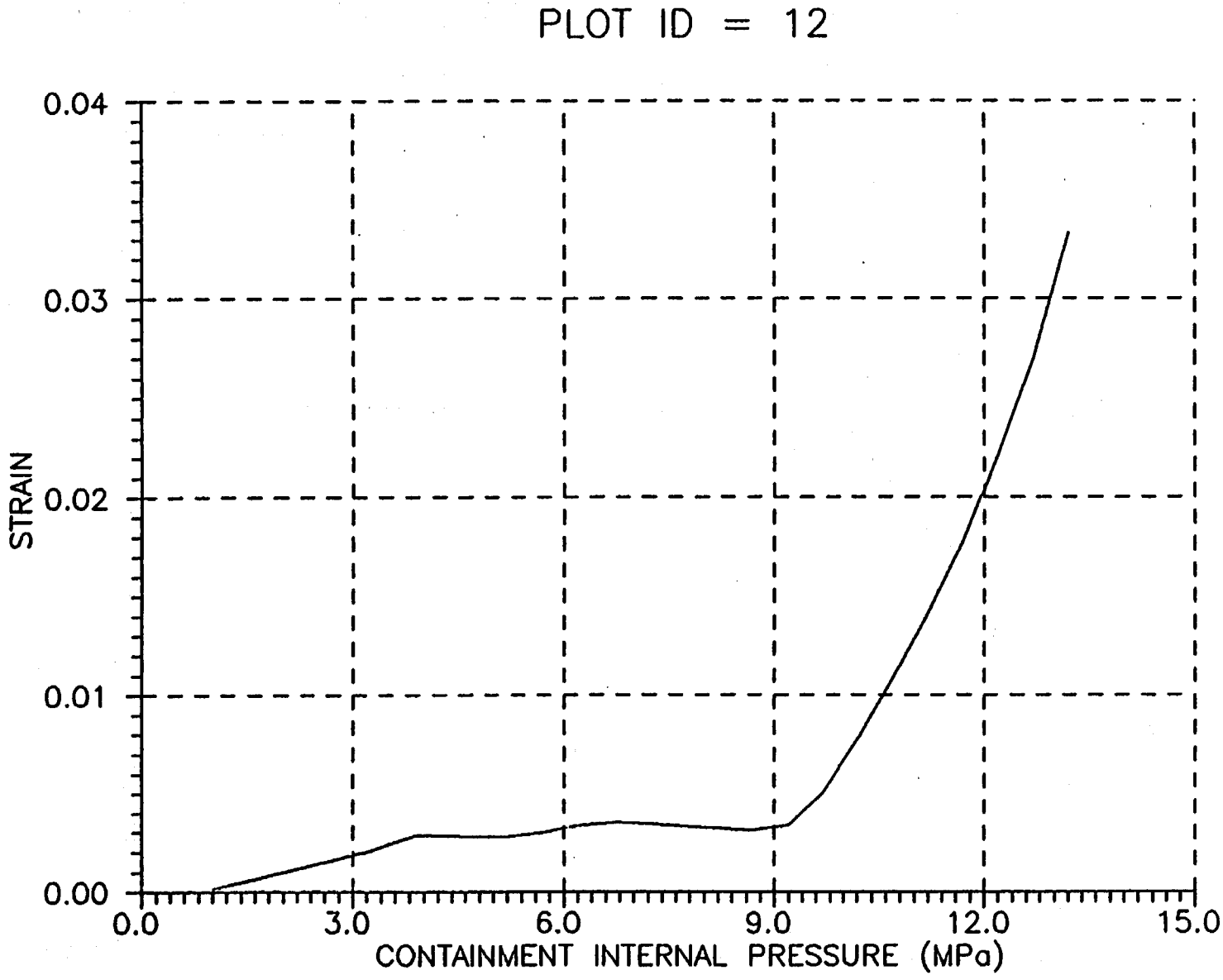

Plot of Internal Meridional Strain at Z = 3.47 m

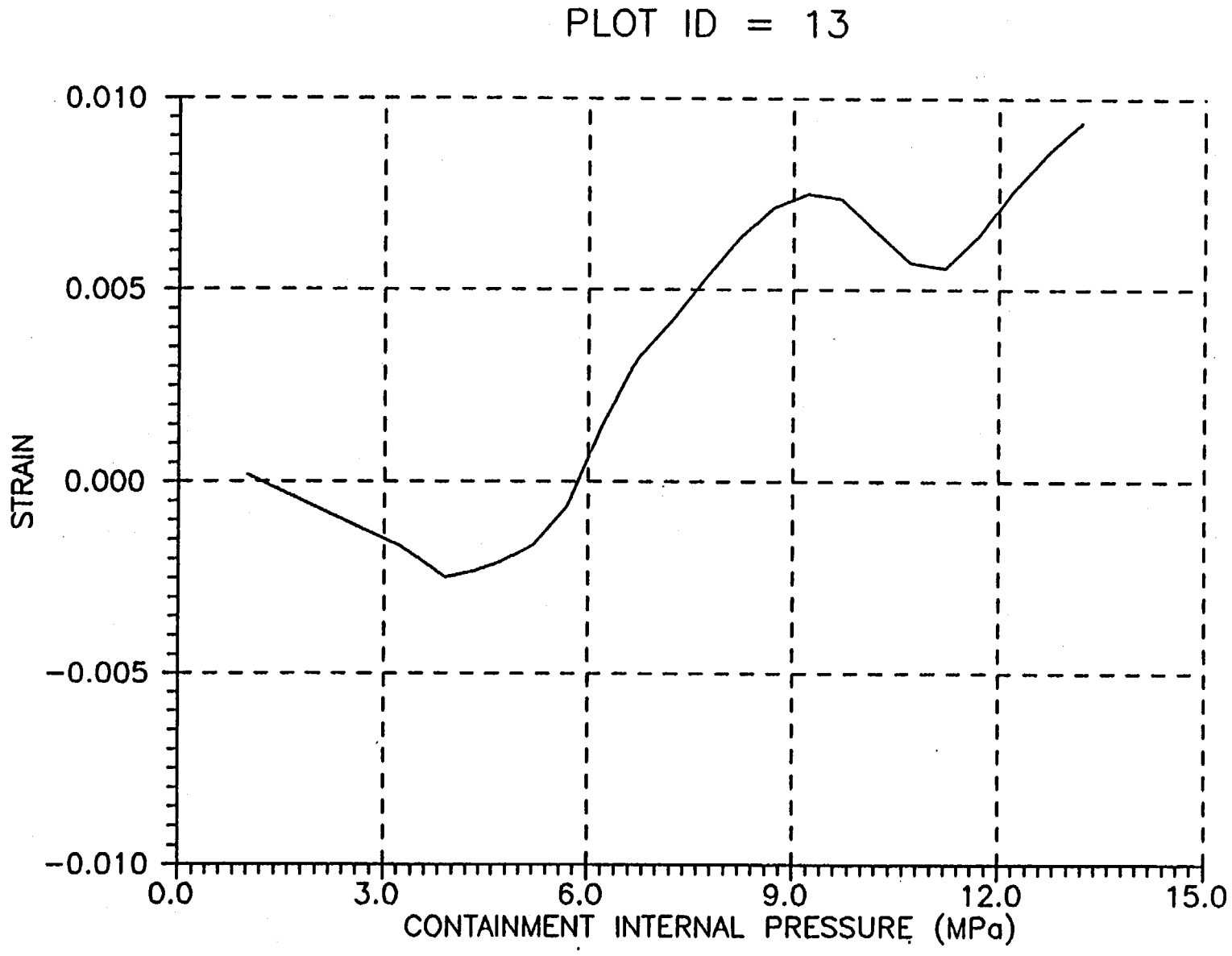

Plot of External Meridional Strain at Z = 3.32 m

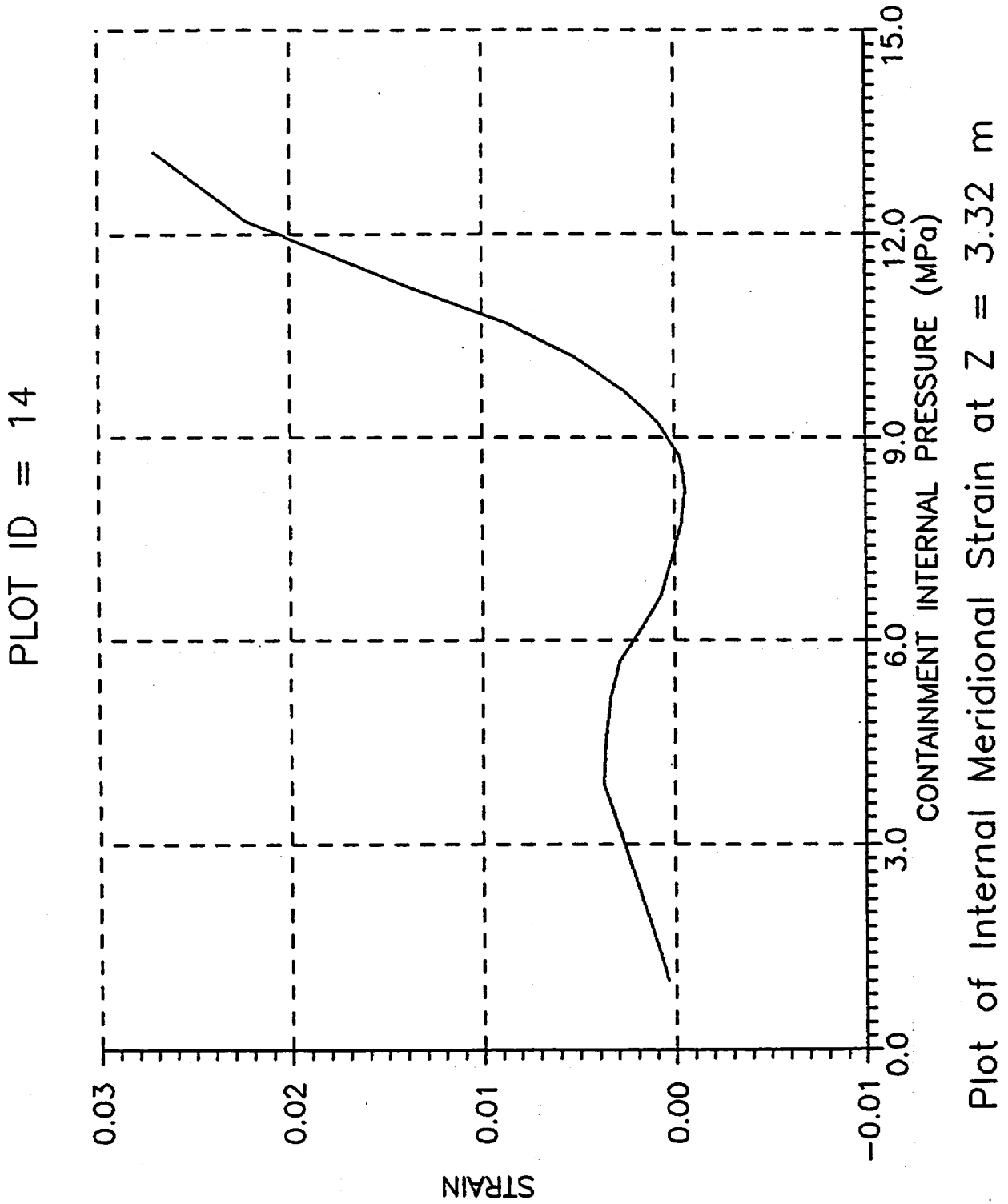
PLOT ID = 14
Plot of Internal Meridional Strain at Z = 3.32 m
STRAIN
0.03
0.02
0.01
0.00
-0.01
0.0
3.0
6.0
9.0
12.0
15.0
CONTAINMENT INTERNAL PRESSURE (MPa)

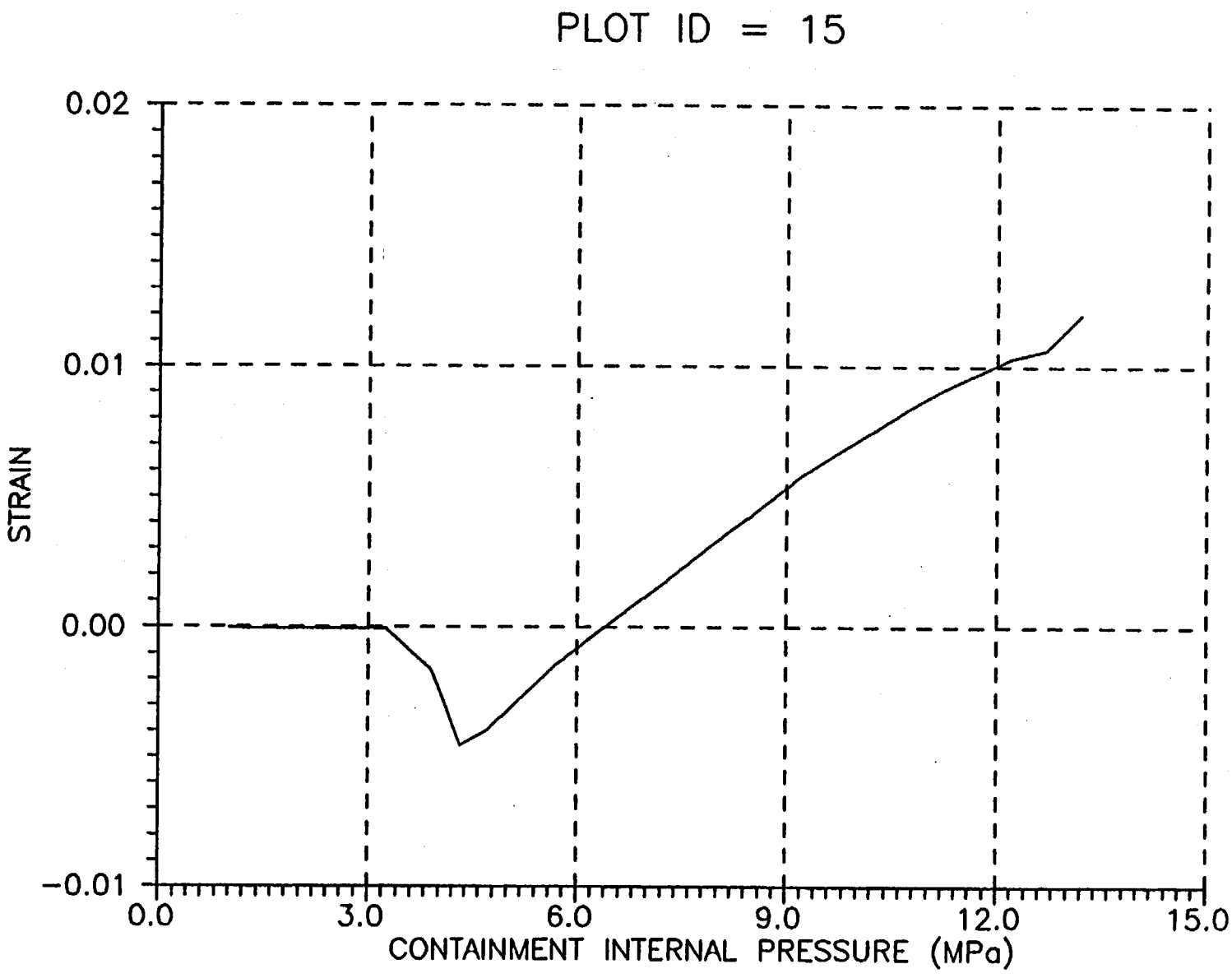

Plot of External Meridional Strain at Z = 2.10 m

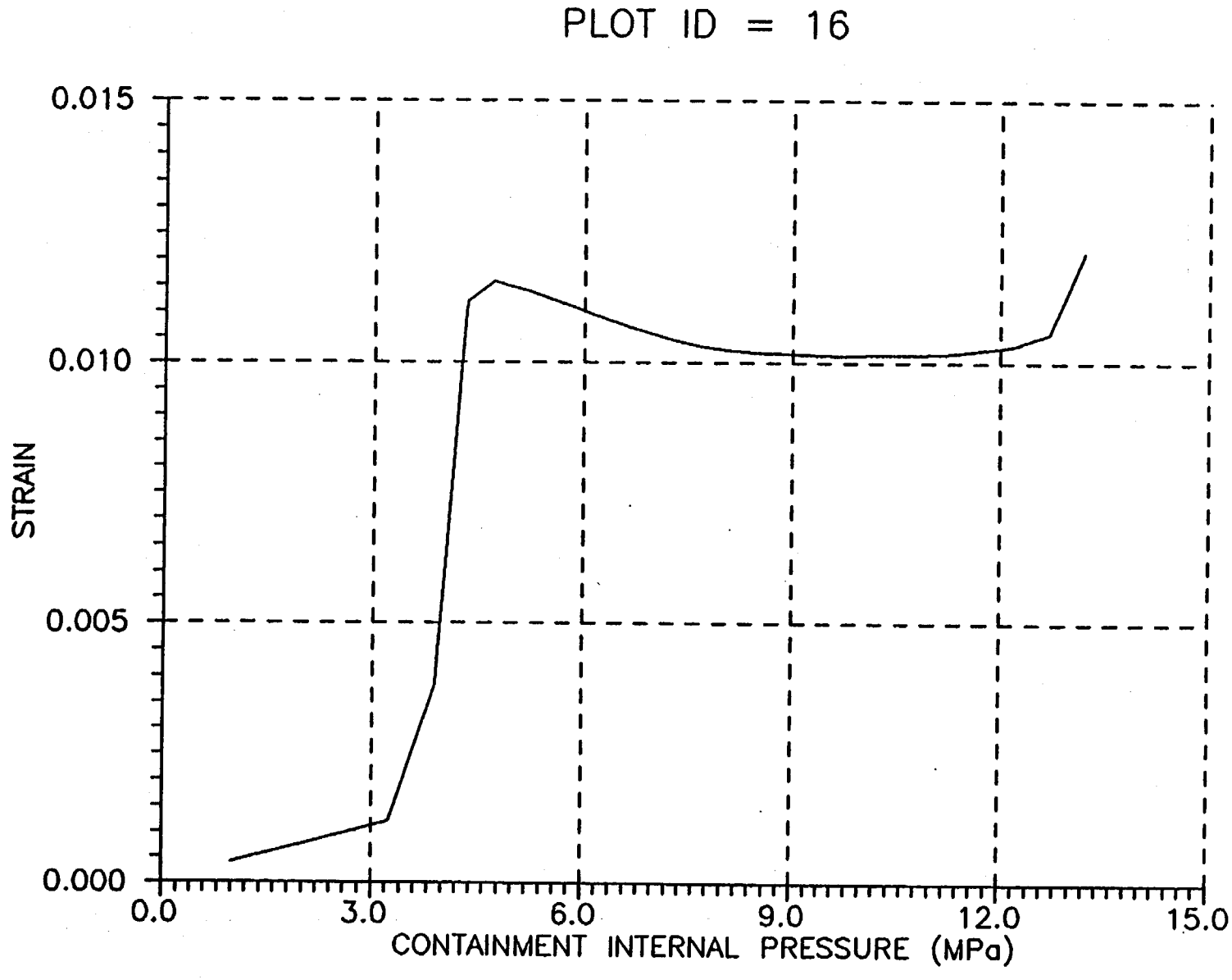

Plot of Internal Meridional Strain at Z = 2.10 m

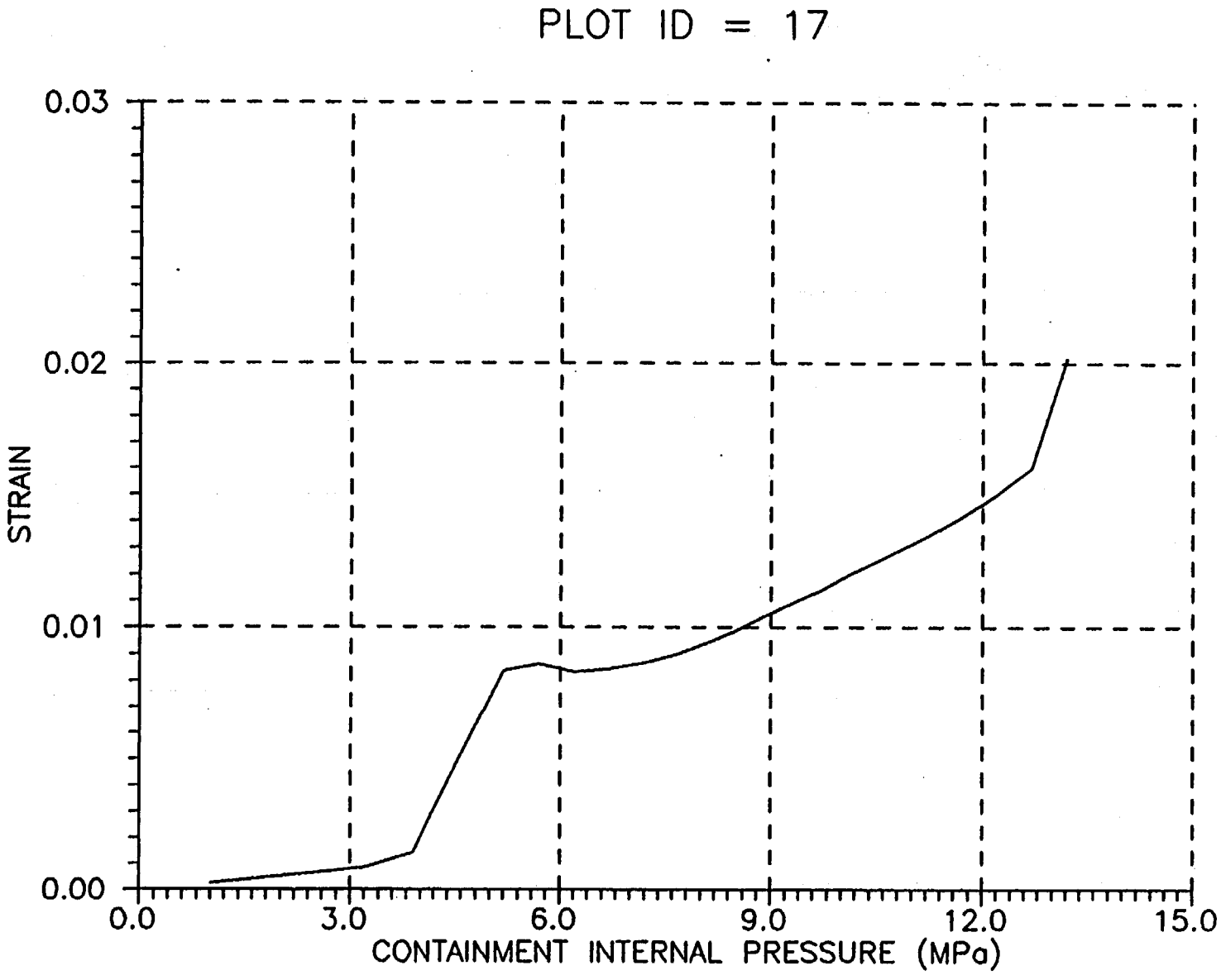

Plot of External Meridional Strain at Z = 1.60 m

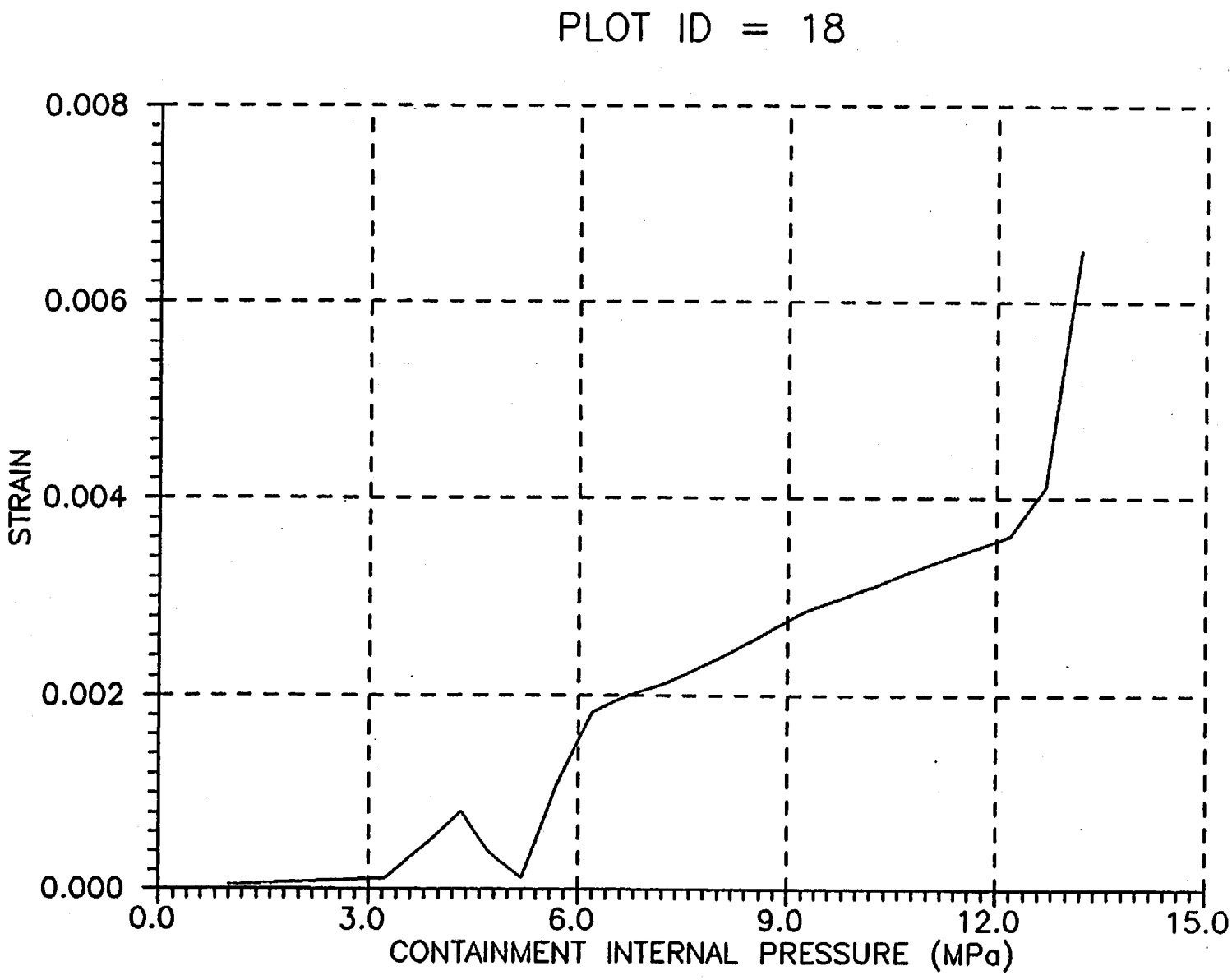

Plot of Internal Meridional Strain at Z = 1.60 m

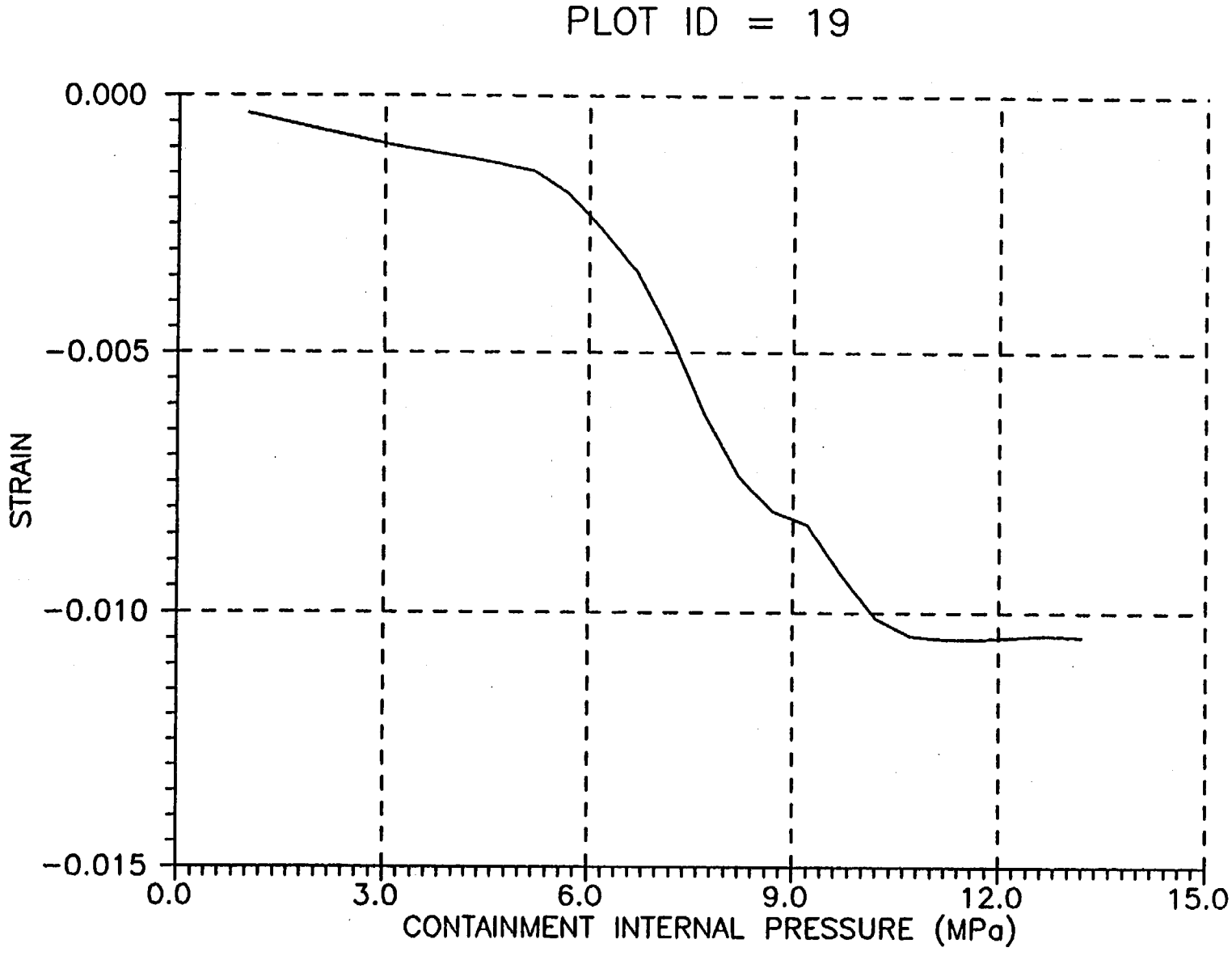

Plot of External Meridional Strain at Z = 0.80 m

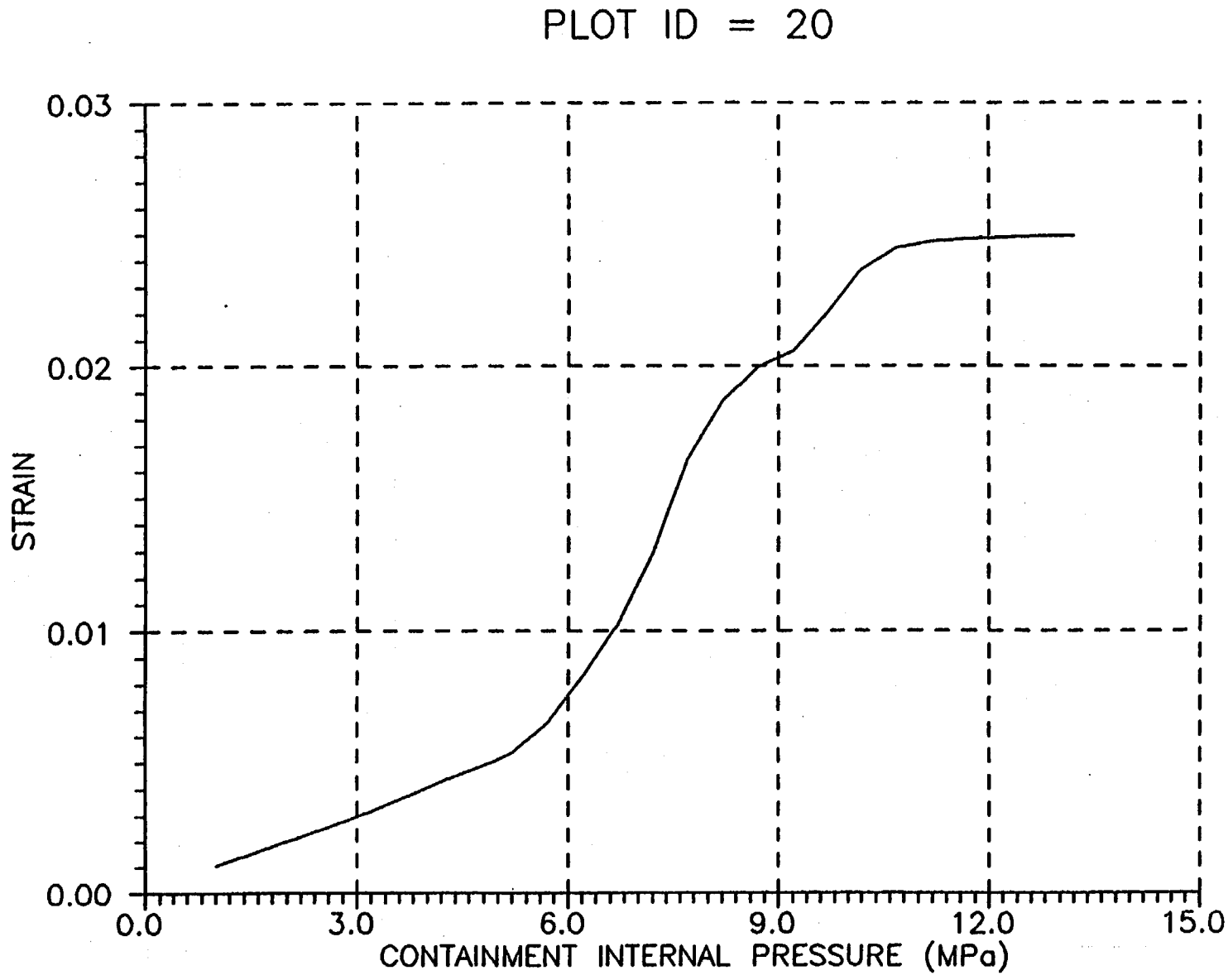

Plot of Internal Meridional Strain at Z = 0.80 m

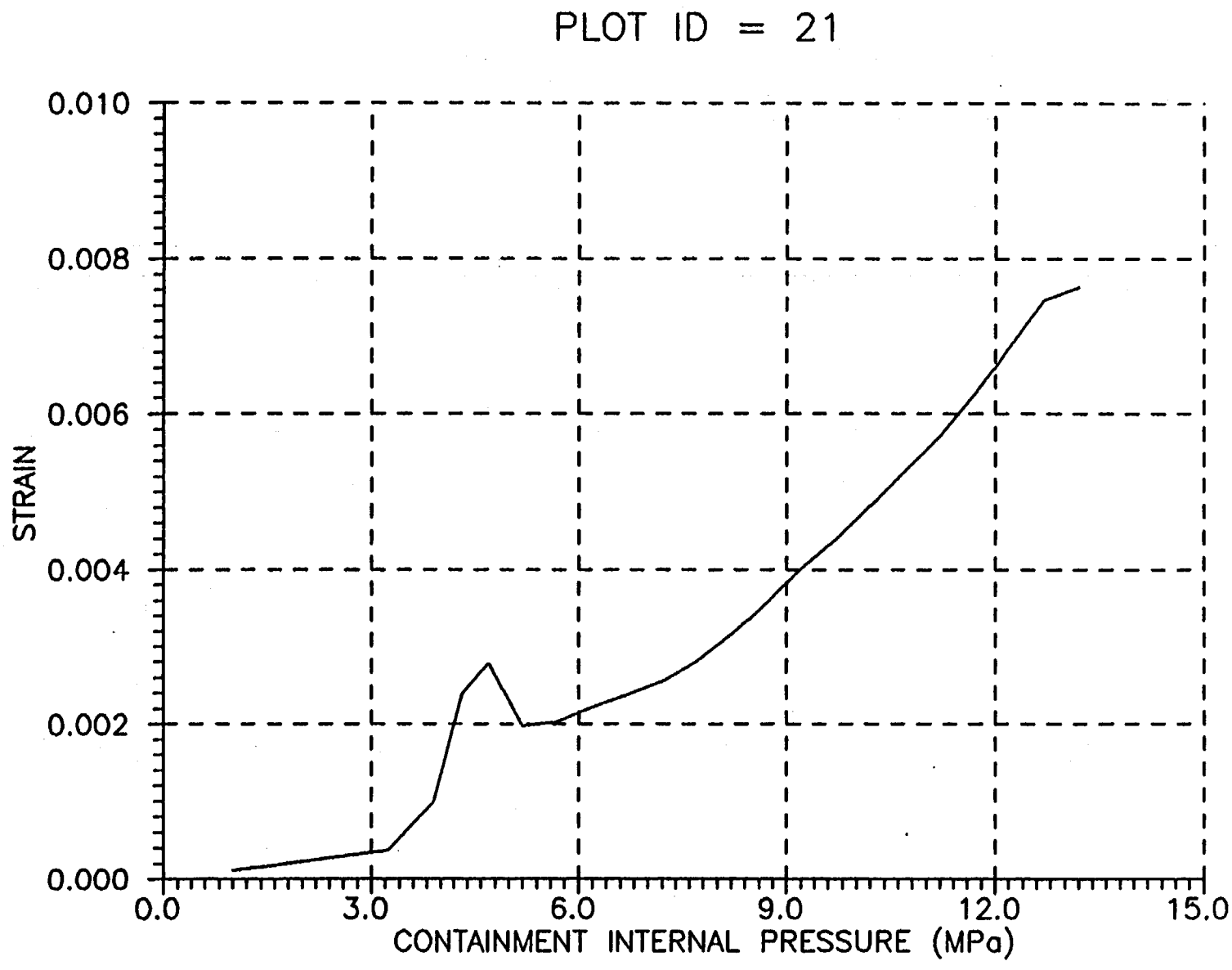

Plot of External Meridional Strain at Z = 2.49 m

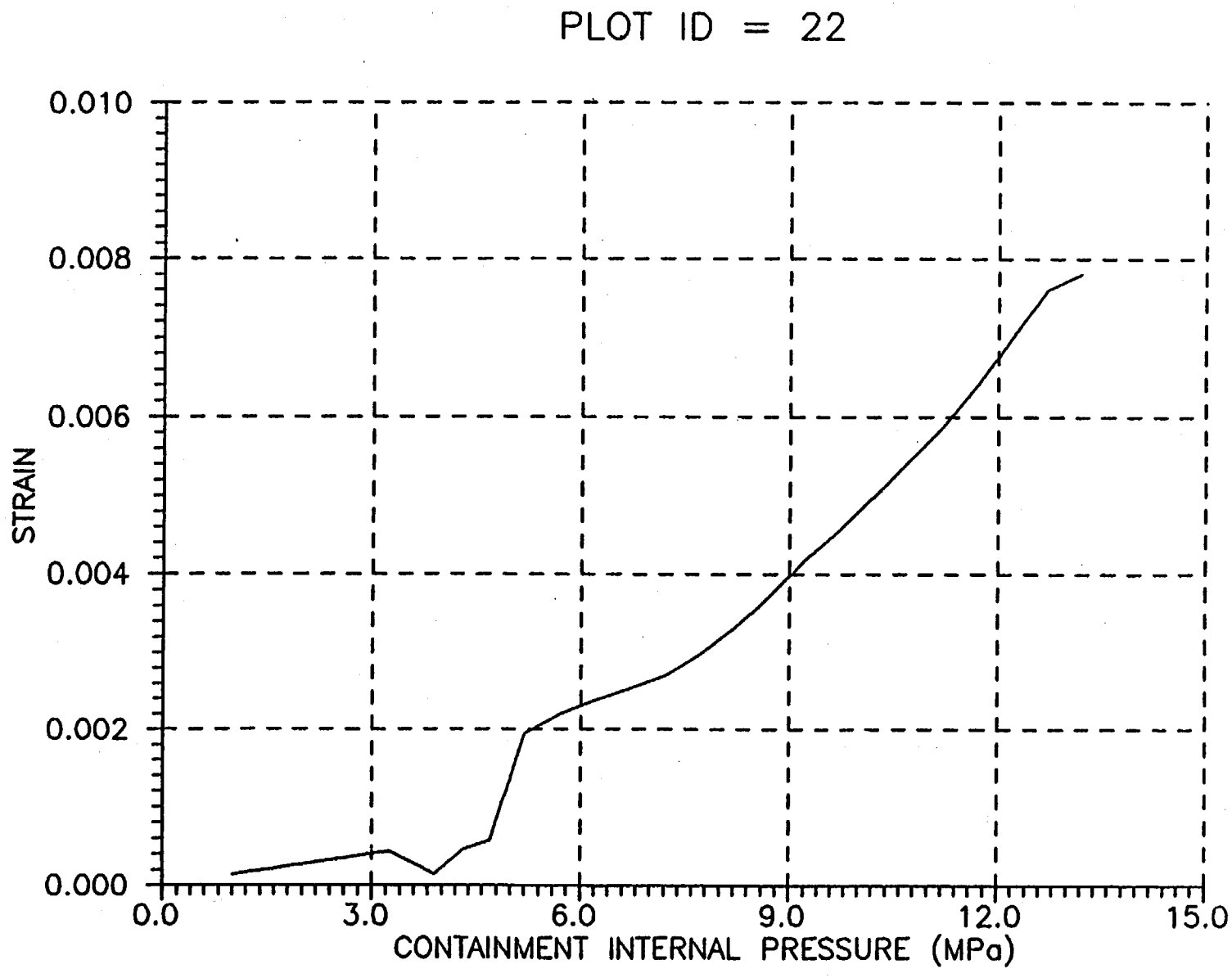

Plot of Internal Meridional Strain at Z = 2.49 m

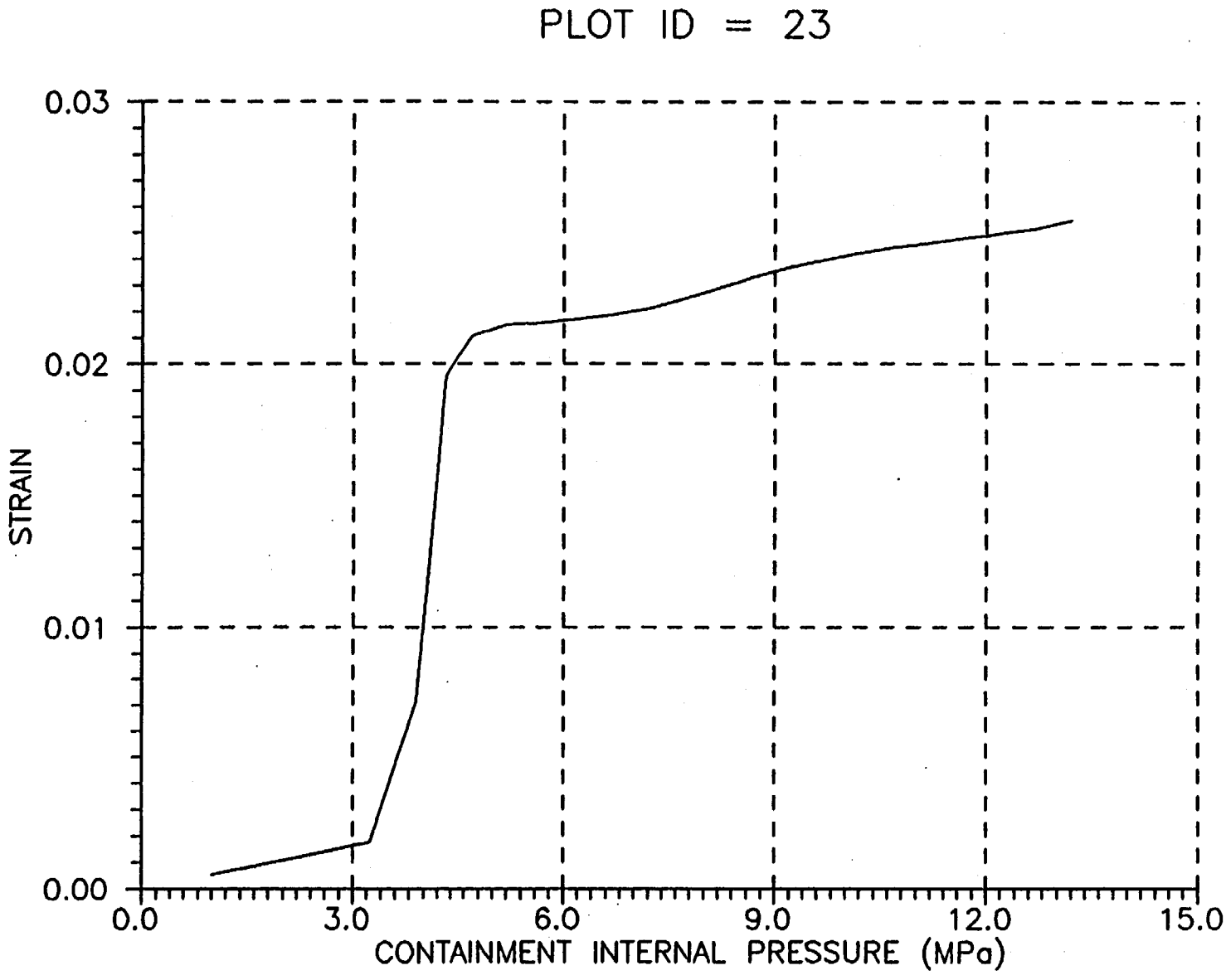

Plot of External Hoop Strain at Z = 2.49 m

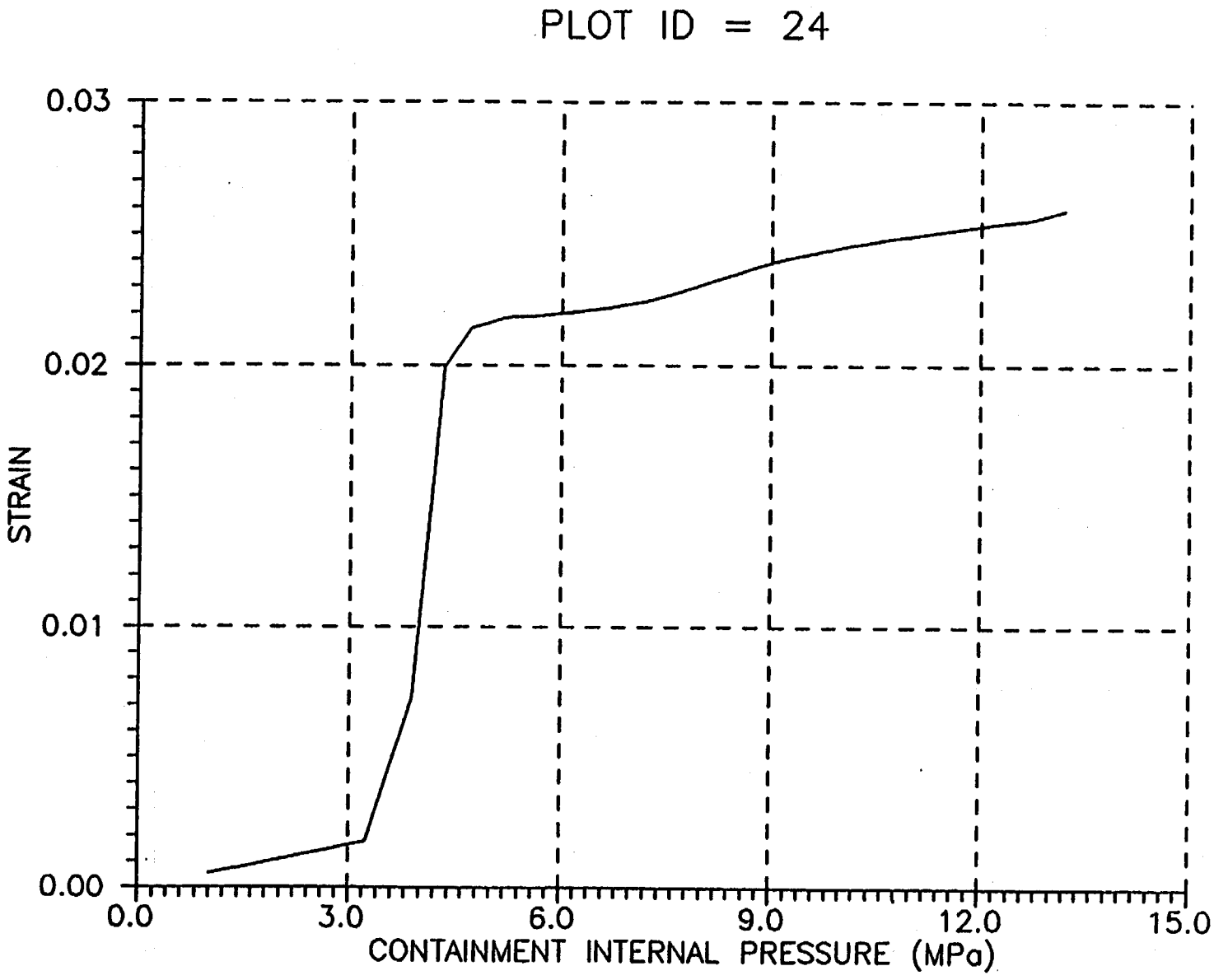

Plot of Internal Hoop Strain at Z = 2.49 m

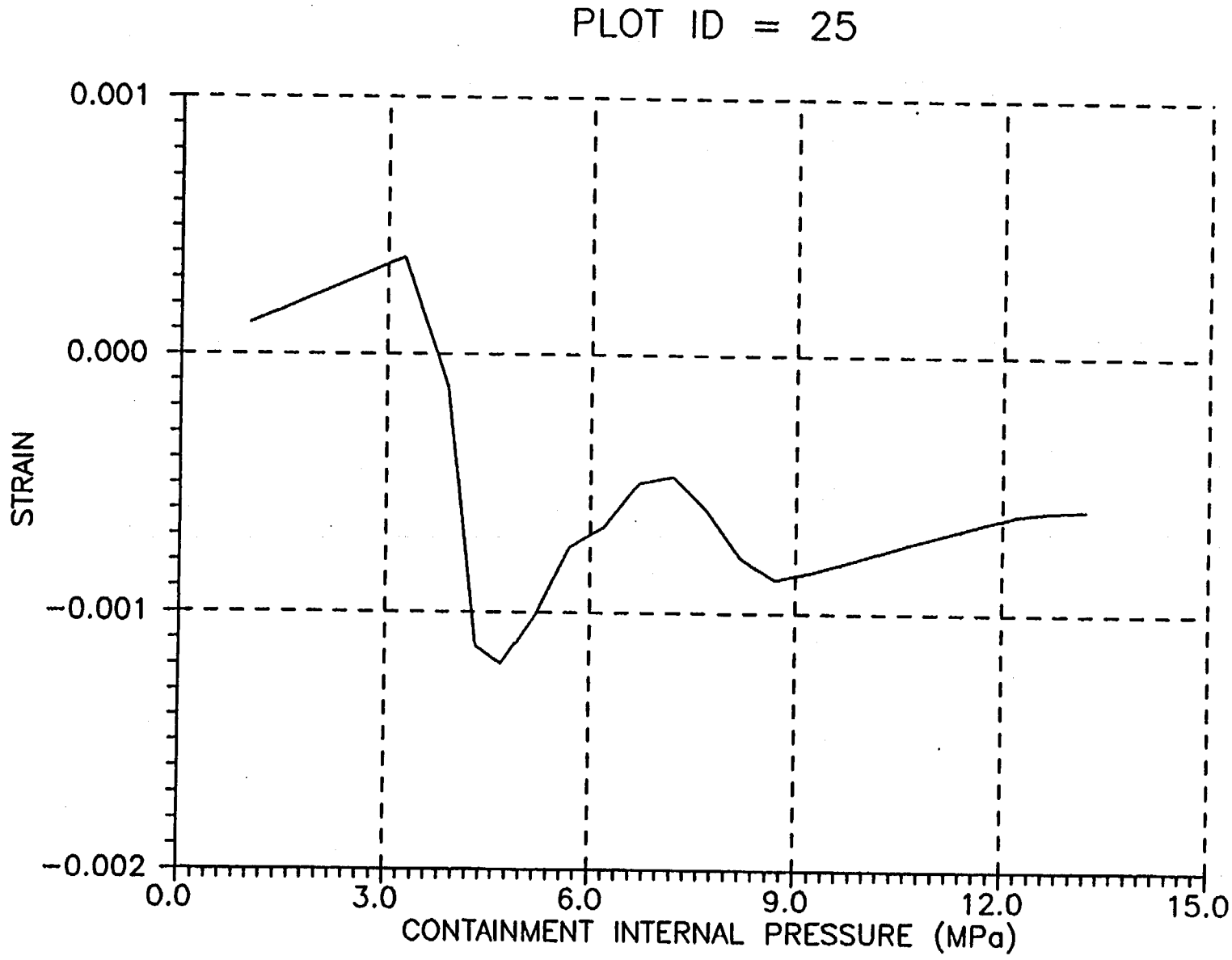

Plot of External Meridional Strain at Z = 1.45 m

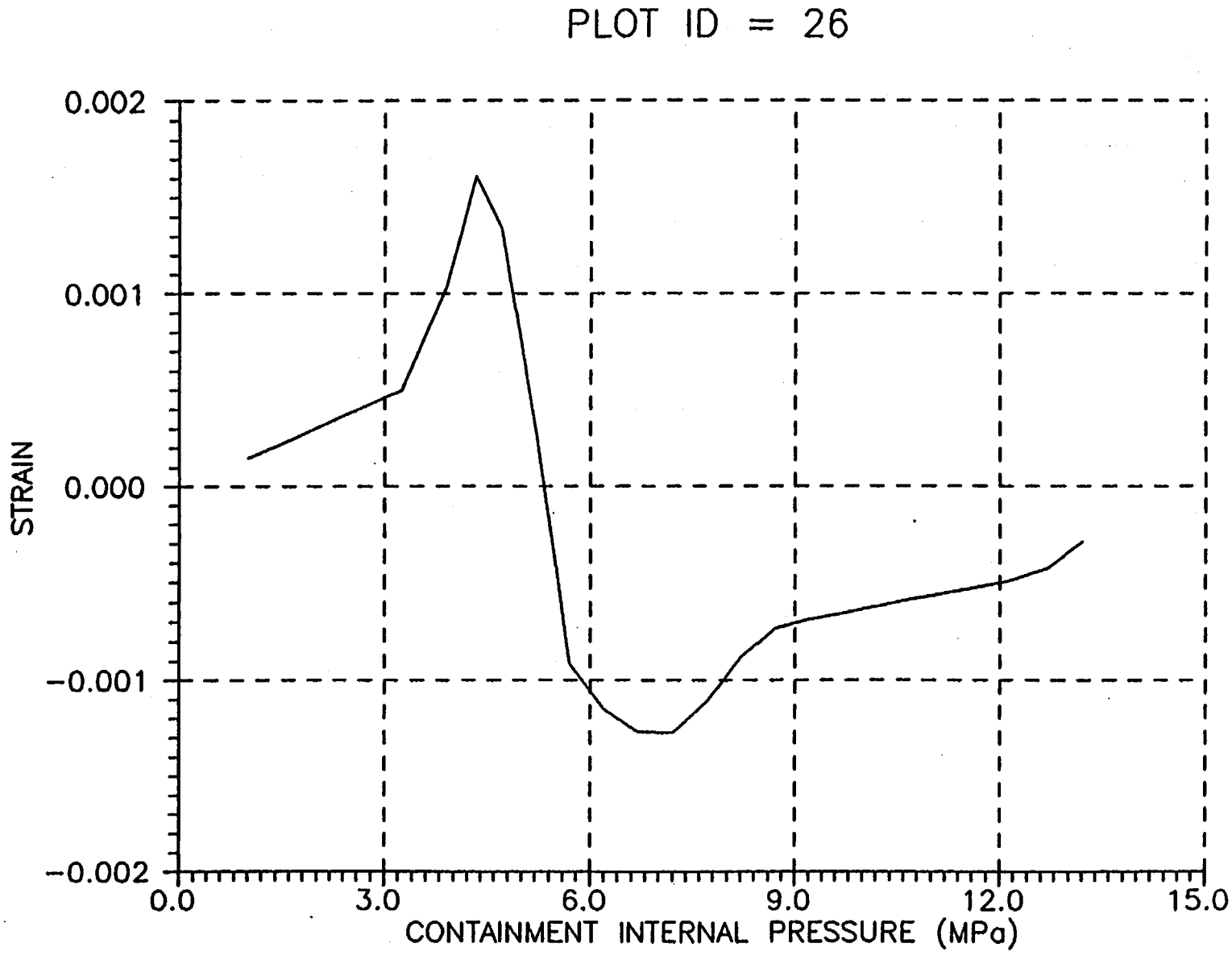

Plot of Internal Meridional Strain at Z = 1.45 m

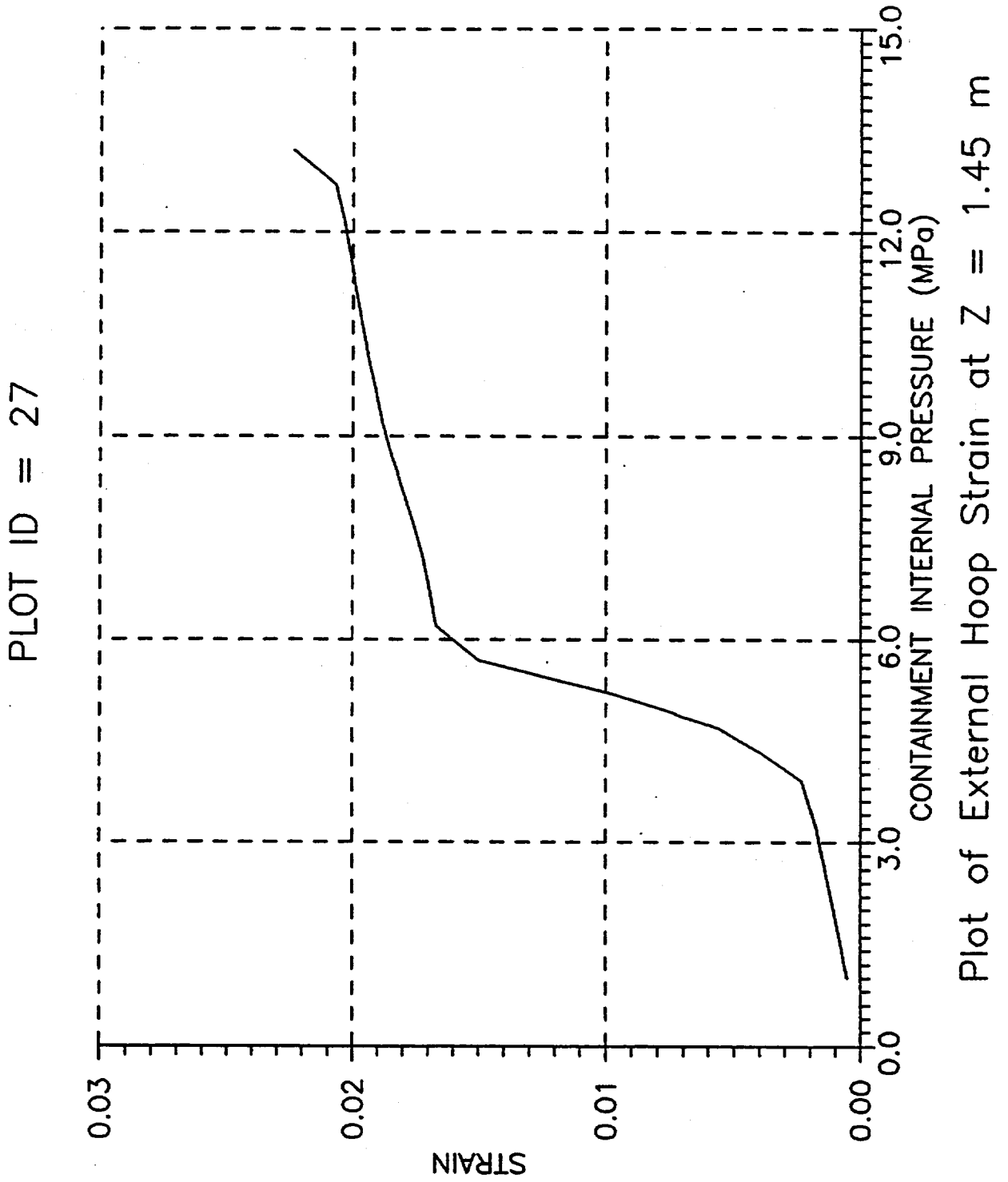
PLOT ID = 27
Plot of External Hoop Strain at Z = 1.45 m
STRAIN
0.03
0.02
0.01
0.00
0.0
3.0
6.0
9.0
12.0
15.0
CONTAINMENT INTERNAL PRESSURE (MPa)

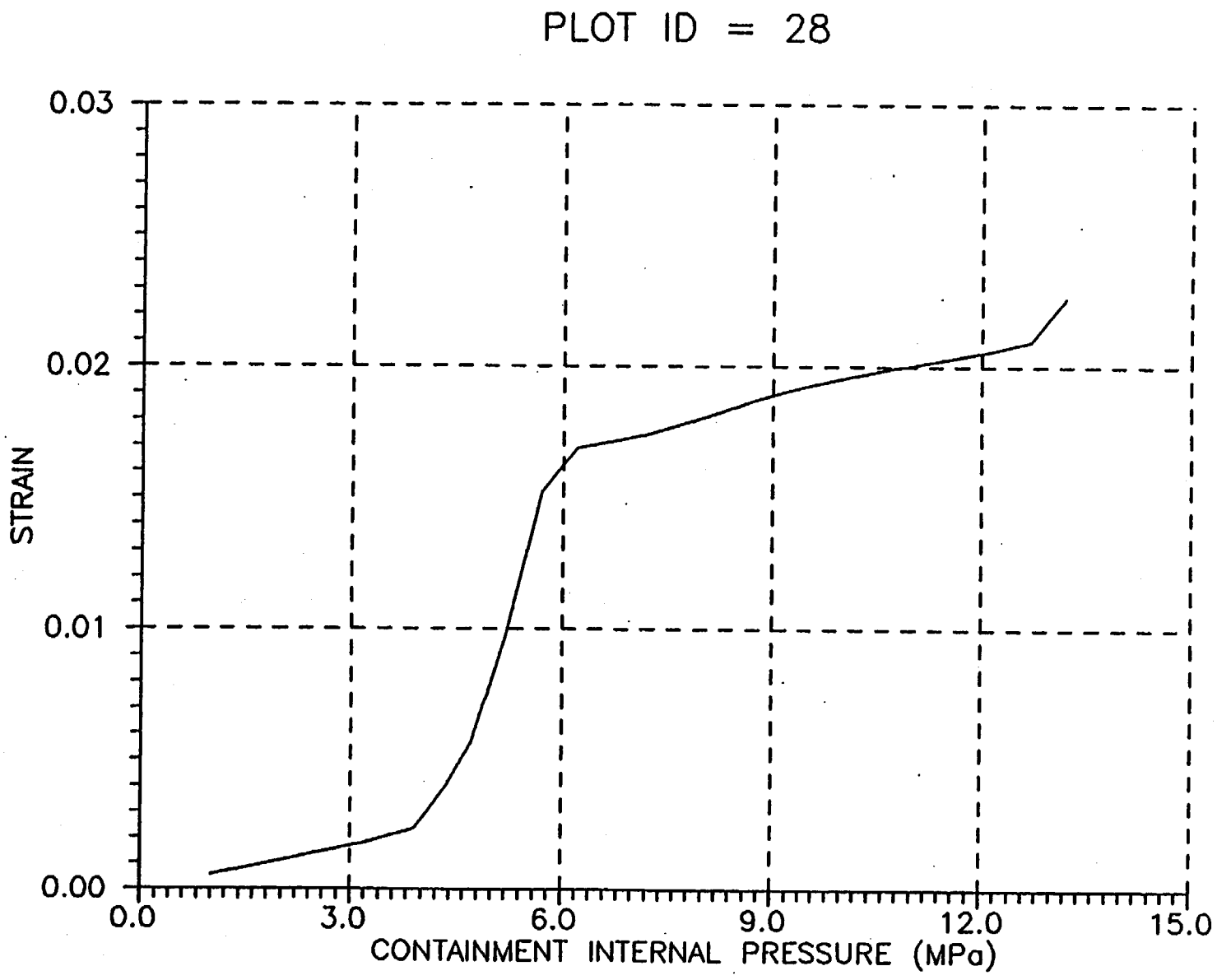

Plot of Internal Hoop Strain at Z = 1.45 m

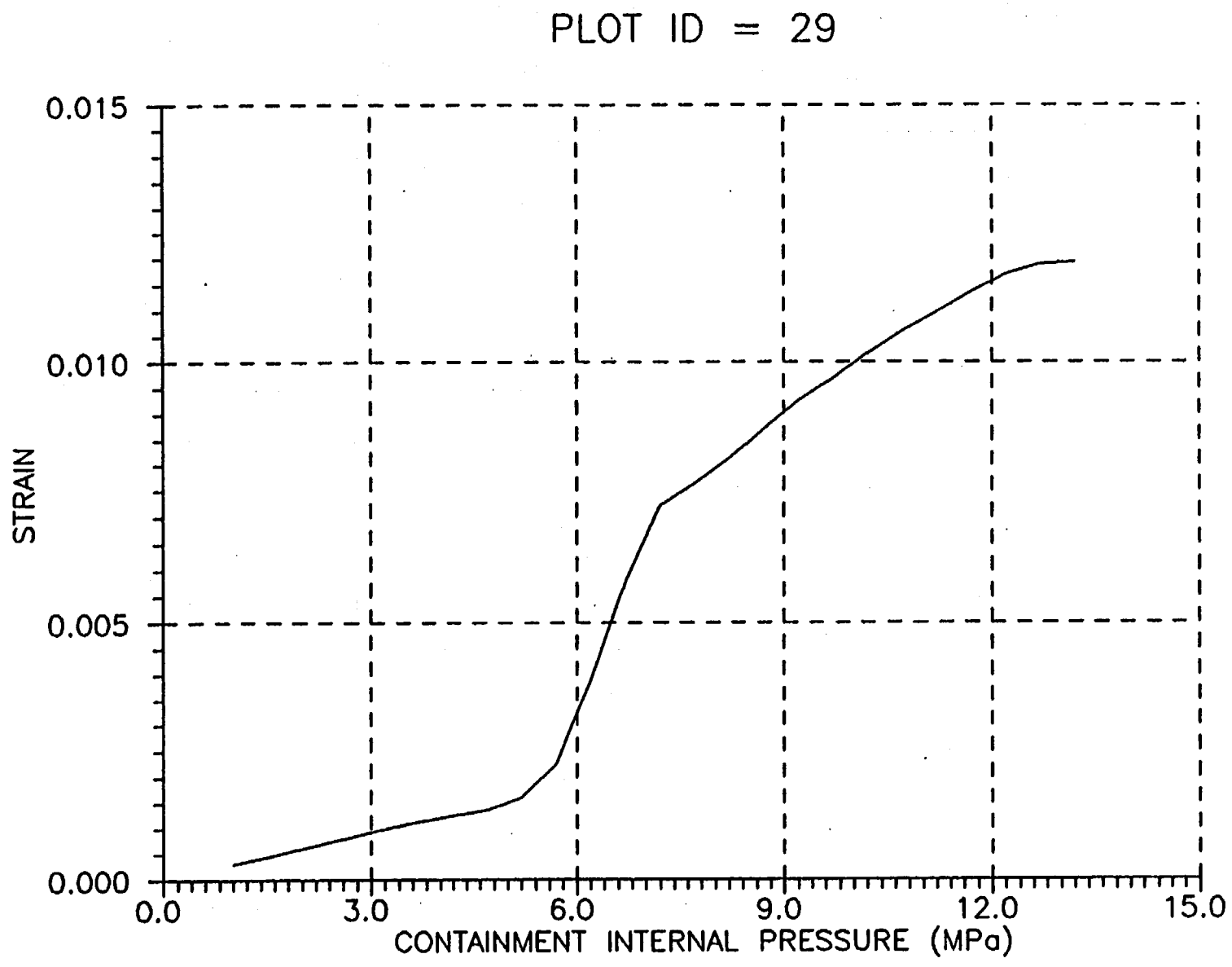

Plot of Internal Meridional Strain at Z = 3.13 m

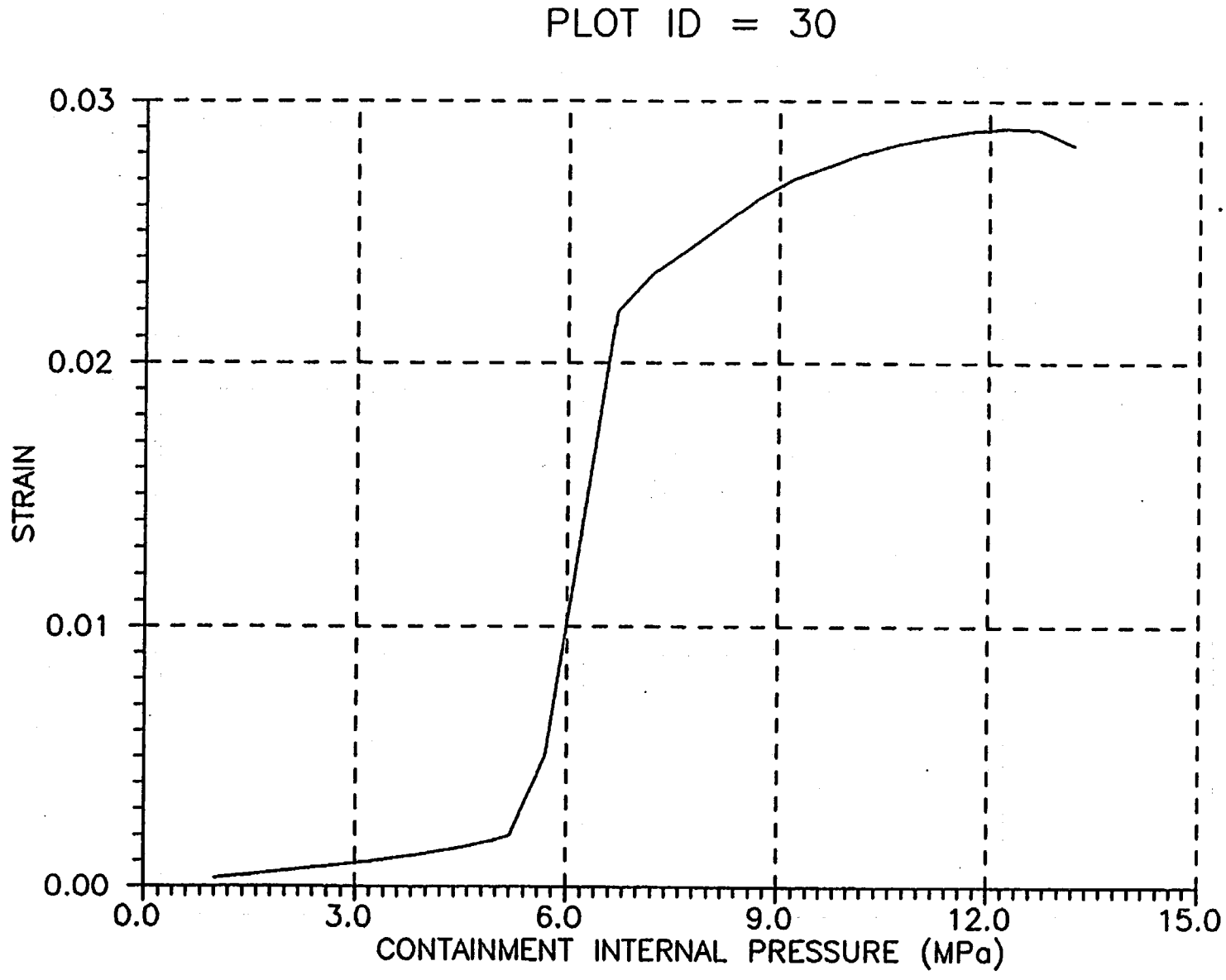

Plot of Internal Hoop Strain at Z = 3.13 m

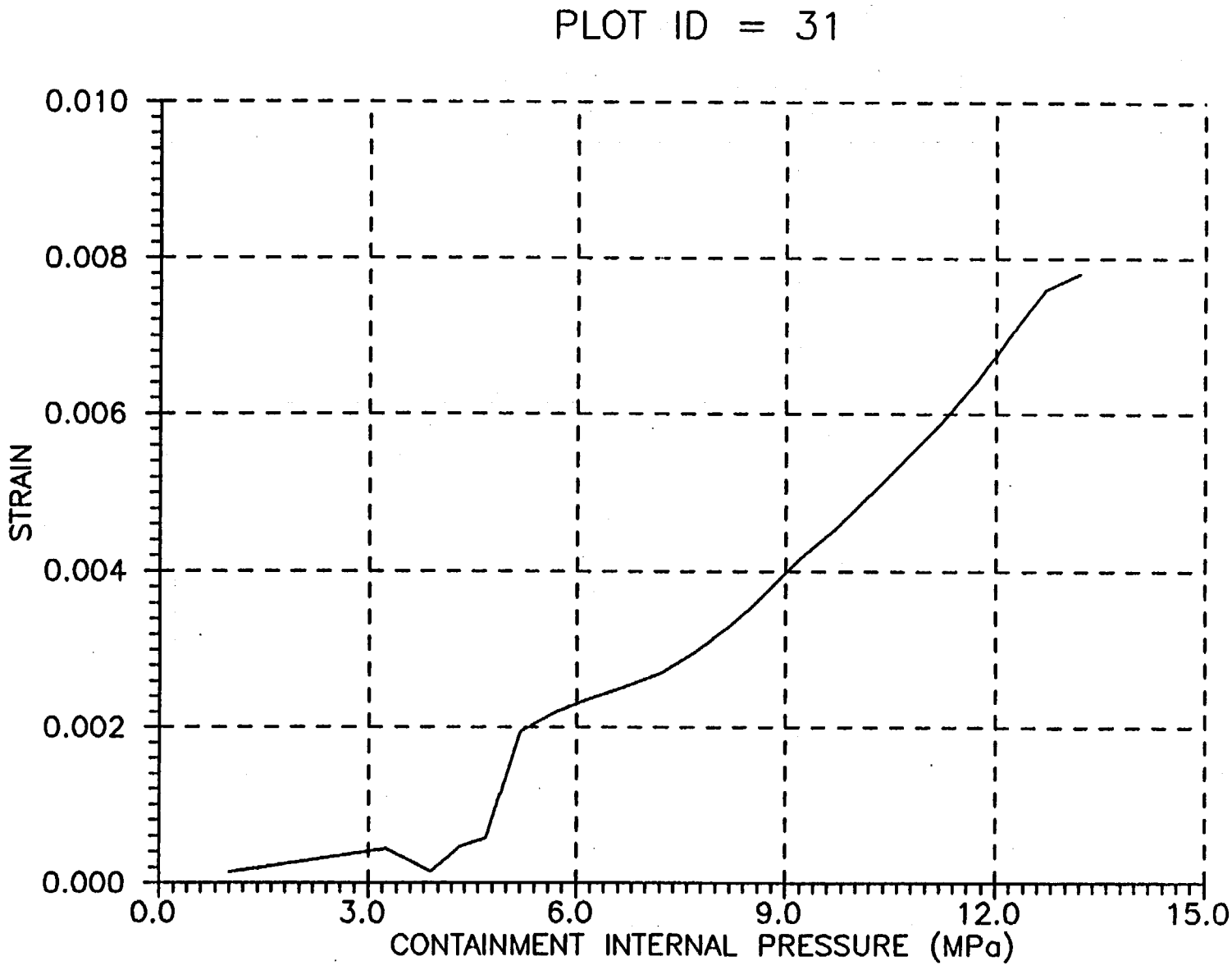

Plot of Internal Meridional Strain at Z = 2.49 m

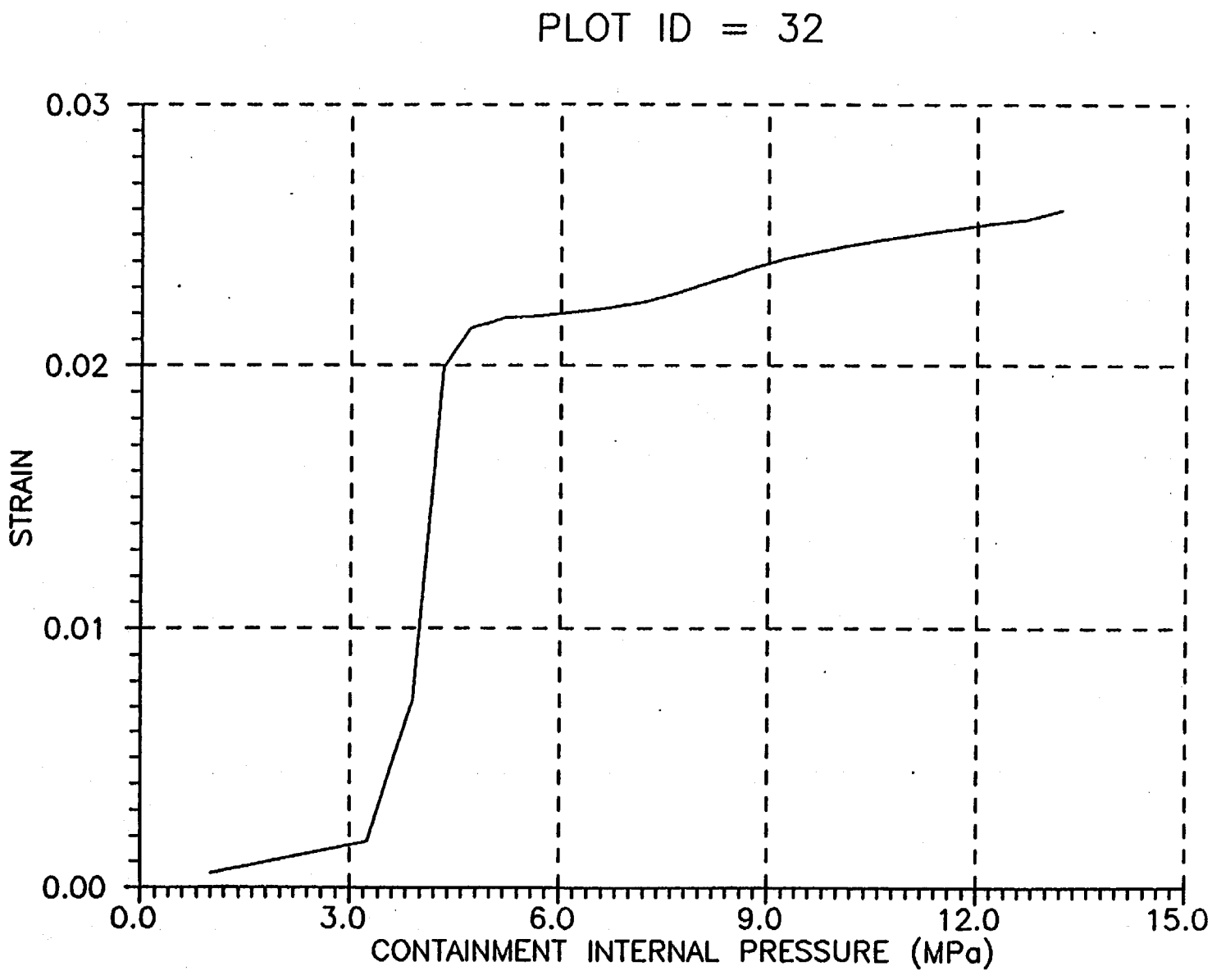

Plot of Internal Hoop Strain at Z = 2.49 m

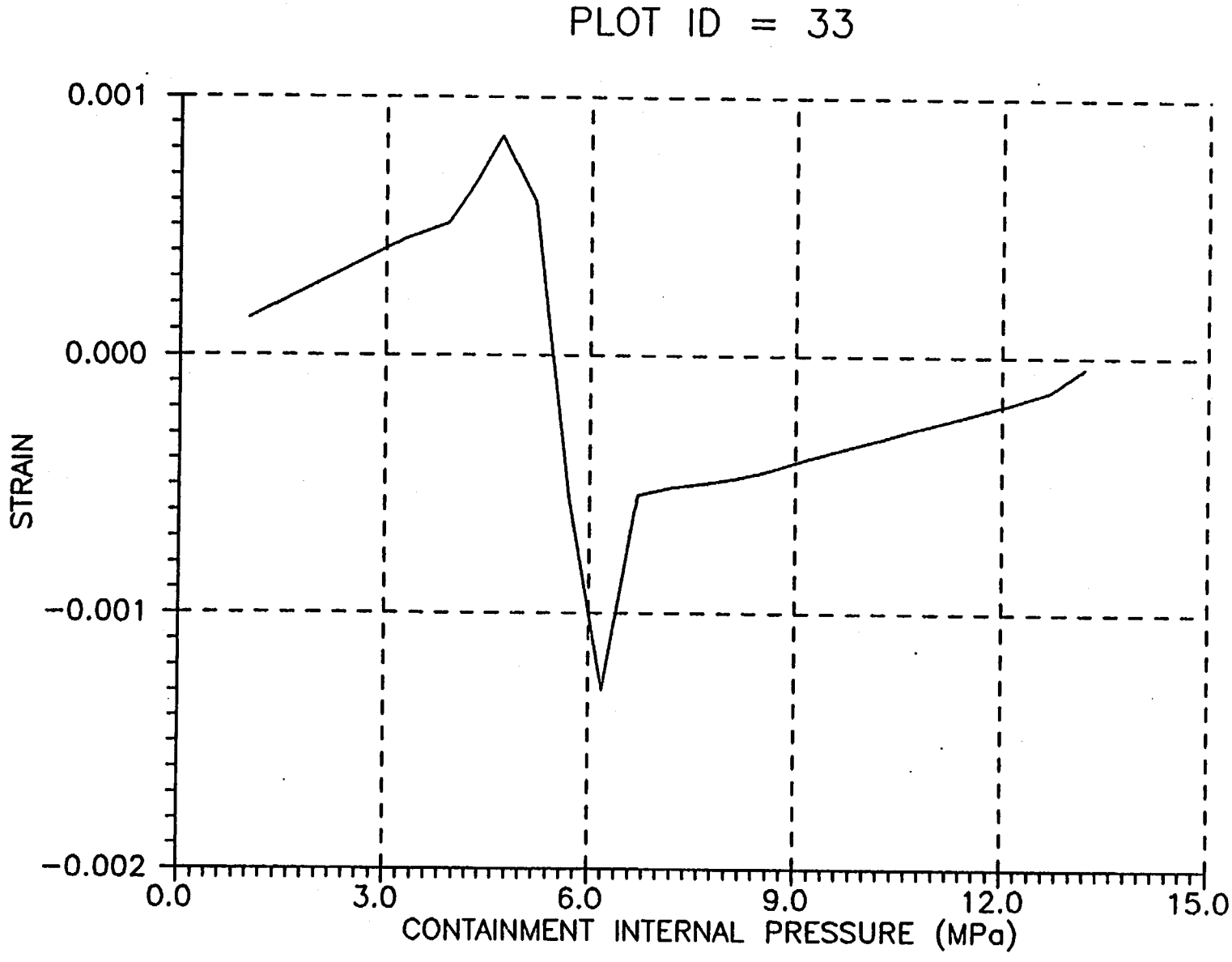

Plot of Internal Meridional Strain at Z = 1.25 m

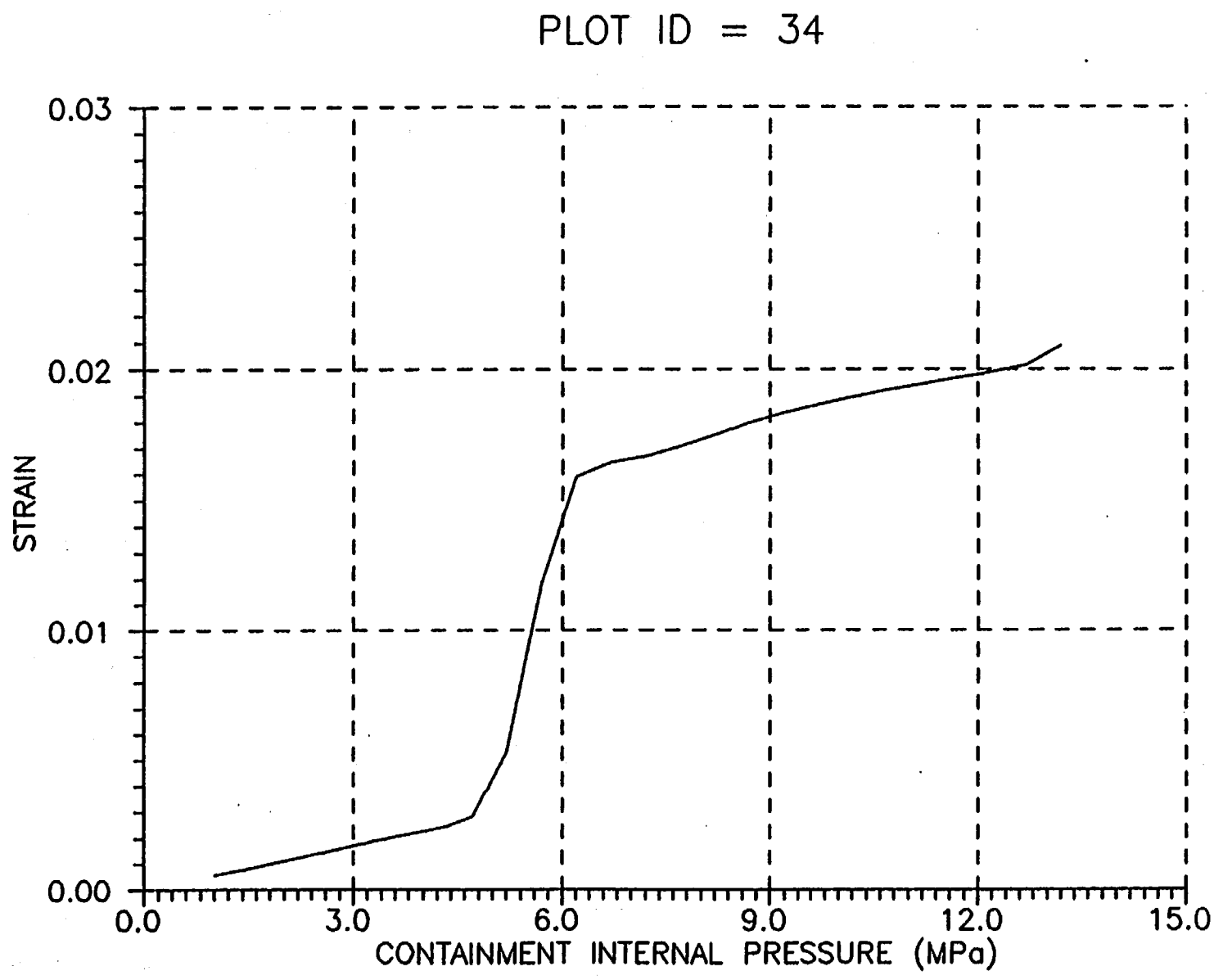

Plot of Internal Hoop Strain at Z = 1.25 m

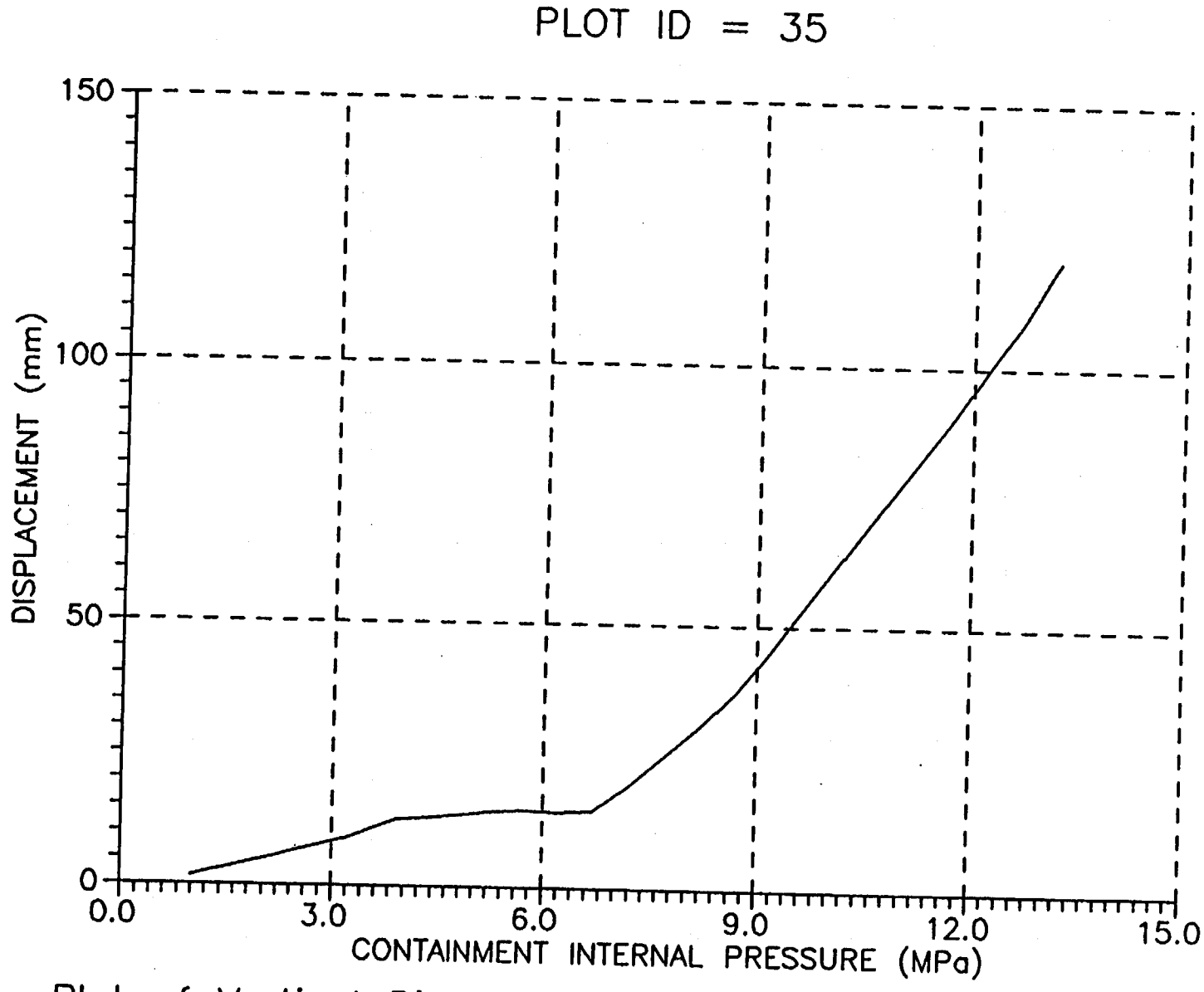

Plot of Vertical Displacement at top of the containment

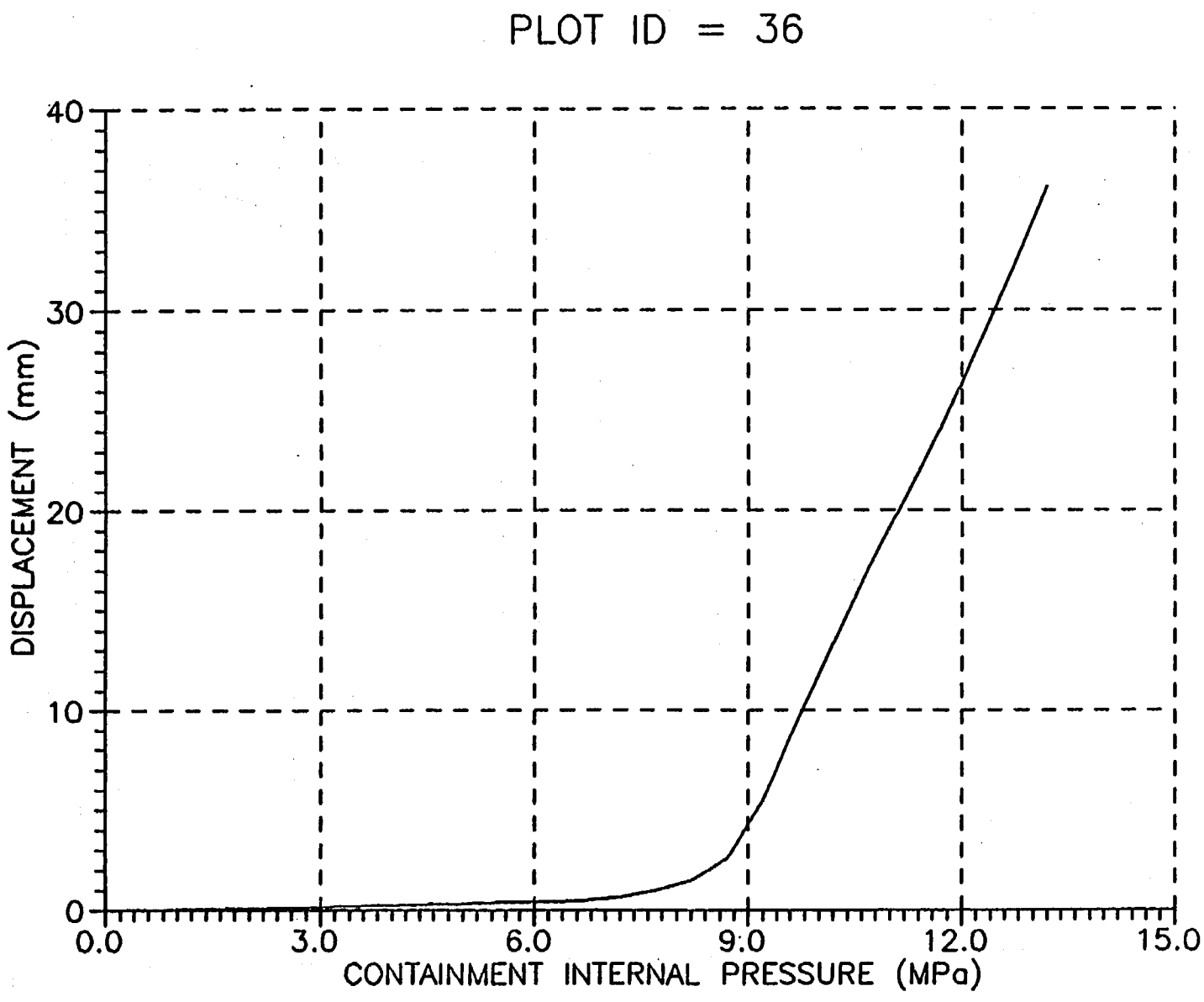

Plot of Horizontal Displacement at Z = 3.57 m

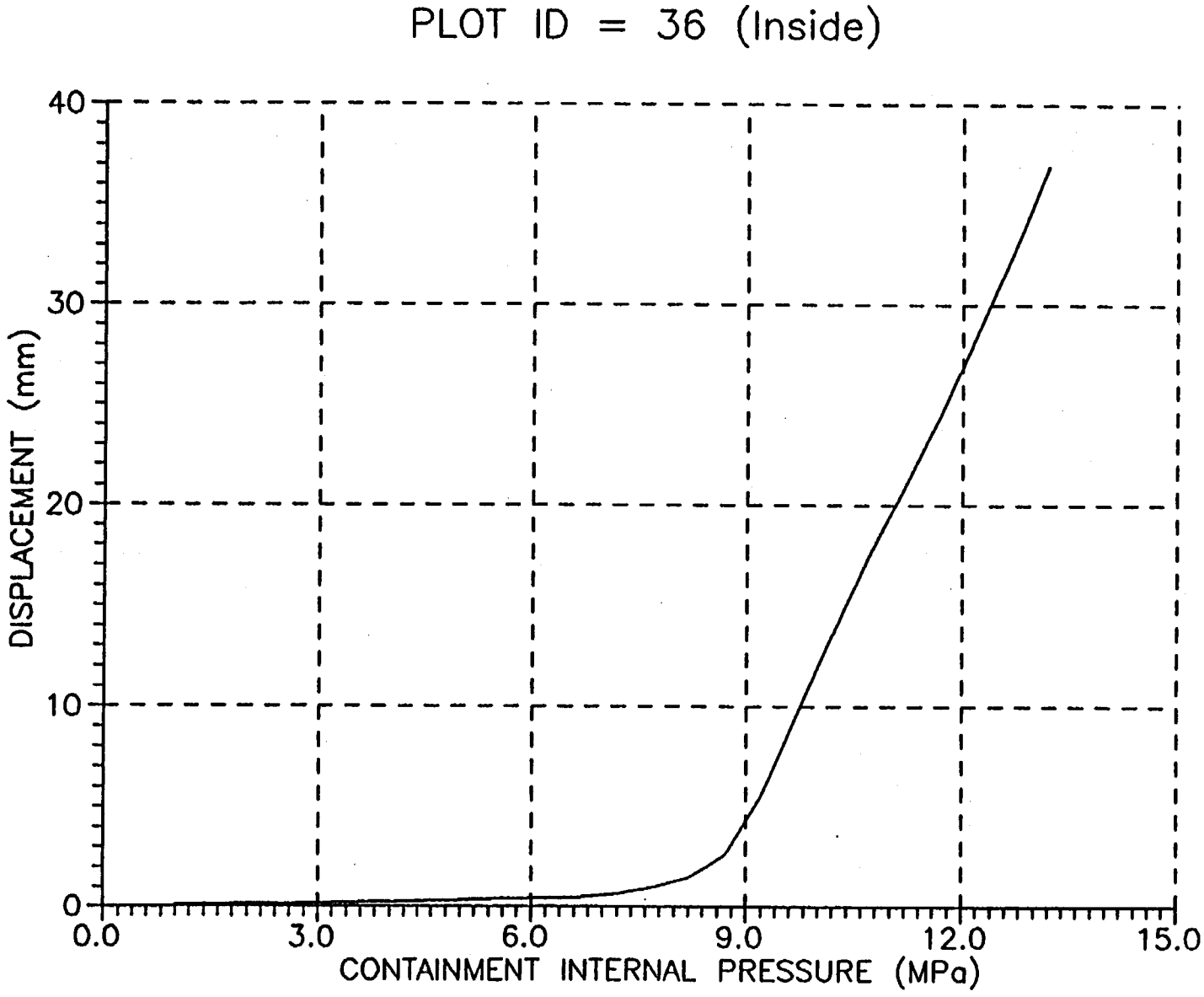

Plot of Horizontal Displacement at Z = 3.57 m

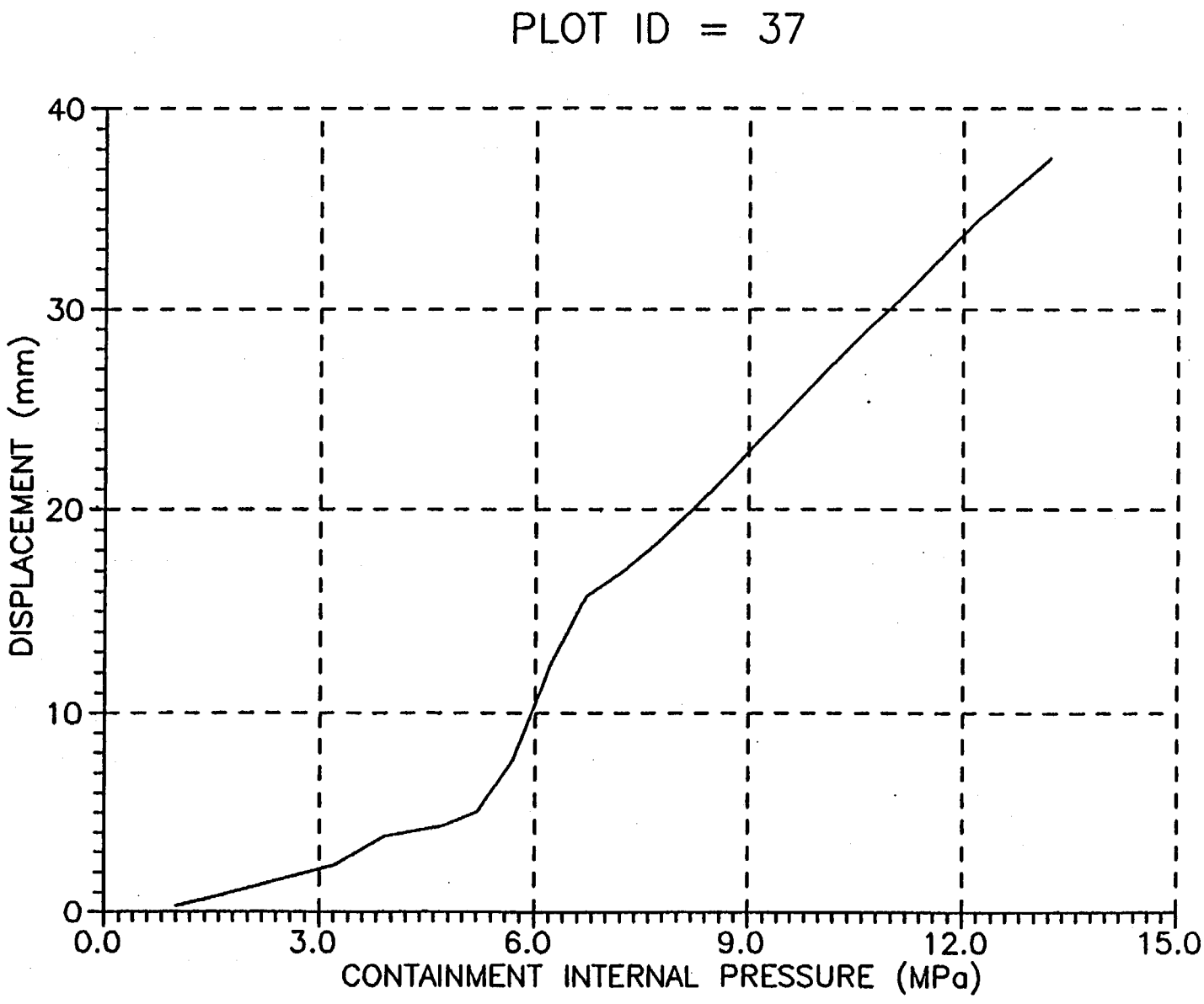

Plot of Horizontal Displacement at Z = 3.32 m

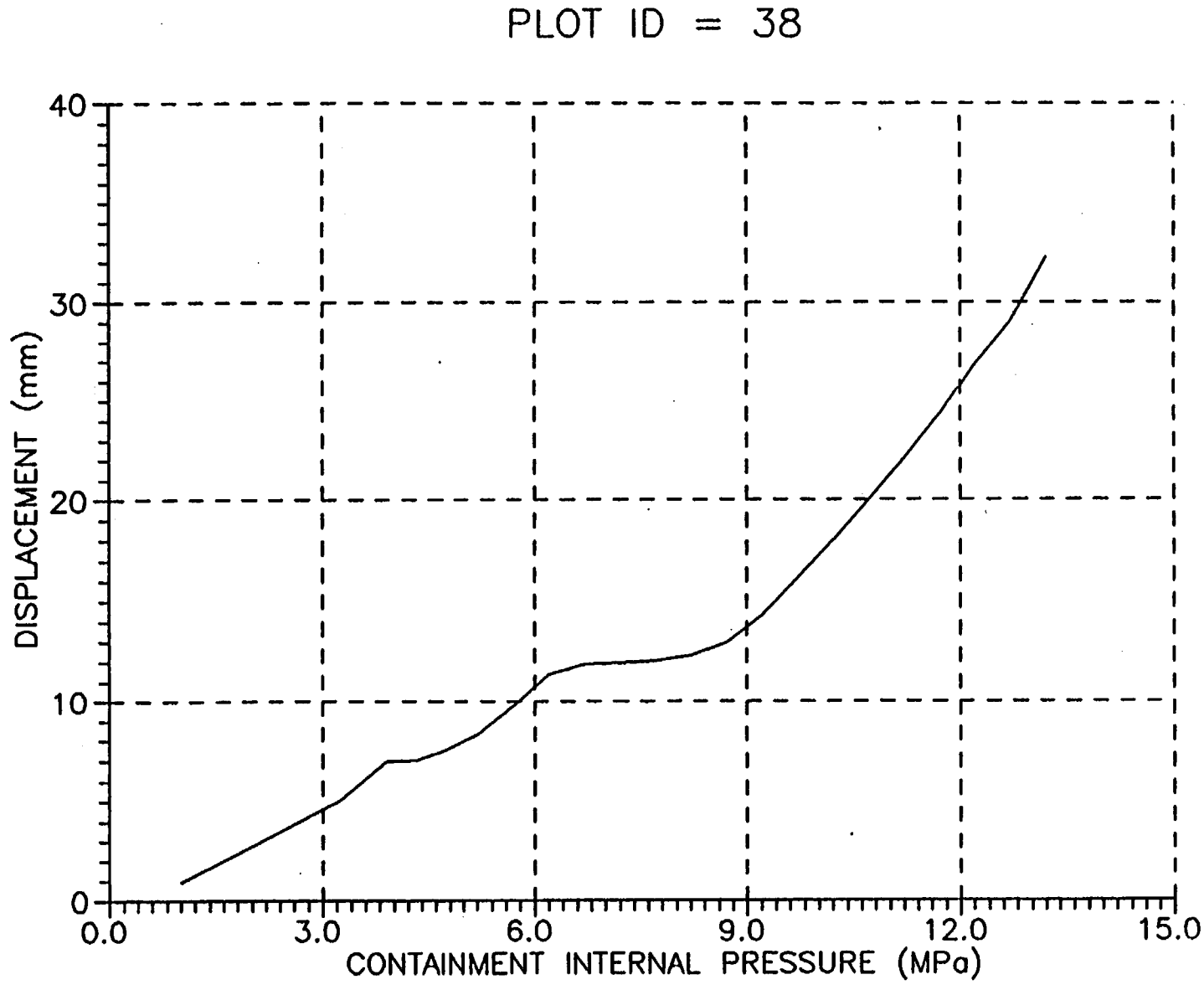

Plot of Vertical Displacement at Z = 3.32 m

Appendix E-4

General Dynamics Electric Boat Division

U.S.

ELECTRIC BOAT CORPORATION
A GENERAL DYNAMICS COMPANY

Enclosure (1) to:
415:TFT/603039/3.8

Report on Pre-Test Evaluation of the Steel Containment Vessel

Electric Boat Corporation

June 3, 1996

ELECTRIC BOAT CORPORATION
A GENERAL DYNAMICS COMPANY

NUPEC/USNRC STEEL CONTAINMENT VESSEL ROUND ROBIN ANALYSIS PROGRAM

ELECTRIC BOAT CORPORATION PRE-TEST EVALUATION OF THE STEEL CONTAINMENT VESSEL

K. ARPIN

A. BEACHAM

W. MCCORMICK

REVIEWED BY

J. MINICUCCI

May 1996

ABSTRACT: This report documents Electric Boat Corporation's pre-test evaluation of a steel containment vessel (SCV) as part of a research program sponsored by The Nuclear Power Engineering Corporation of Tokyo, Japan and the U.S. Nuclear Regulatory Commission. This program includes an internal pressurized test to failure of a model of a steel containment vessel enclosed by a steel contact structure. Round Robin pre-test and post-test analyses are being coordinated by Sandia National Laboratories. Electric Boat Corporation employed a series of finite element models in the pre-test evaluation of the SCV. Material and geometric nonlinear analyses were performed using the ABAQUS/Standard Implicit Finite Element Program. Results of this evaluation include displacement and strain predictions for the SCV which will be compared to test data following the completion of the model test series.

Table of Contents

Nomenclature:

c	clearance
CAX8R	ABAQUS 8-node biquadratic, reduced integration axisymmetric solid element
CAX6	ABAQUS 6-node quadratic, axisymmetric solid element
CS	contact structure
E	Young's modulus
F_f	allowable elastic slip fraction
l_i	characteristic contact surface face dimension
MPC	ABAQUS multi point constraint
NRC	U.S. Nuclear Regulatory Commission
NUPEC	Nuclear Power Engineering Corporation
P	pressure
PEEQ	ABAQUS equivalent plastic strain, total accumulation of plastic strain
P_o	contact pressure at zero clearance
S3R	ABAQUS 3-node triangular thin or thick shell, finite membrane strain element
S4R	ABAQUS 4-node doubly curved thin or thick shell, reduced integration, hourglass control, finite membrane strain element
SAX2	ABAQUS 3-node thin or thick quadratic axisymmetric shell element
SCV	steel containment vessel
SNL	Sandia National Laboratories
ε_e	engineering strain
ε_t	true strain
ε_{tp}	true plastic strain
θ_G	model global theta angle
μ	coefficient of friction
σ_e	engineering stress
σ_t	true stress
σ_y	yield stress, 0.2% offset

1.0 Purpose :

The purpose of this section is to describe the pretest analysis efforts performed by Electric Boat Corporation in the evaluation of the Steel Containment Vessel (SCV) and Contact Structure (CS) as defined in References (1-3). Results of this evaluation include displacement and strain predictions on the SCV which will be compared to test data following the completion of the model test series.

2.0 Background :

This work is part of a multi-national analysis effort in the evaluation of the Steel Containment Vessel (SCV) and its interaction with a Contact Structure (CS). The SCV will be internally pressurized resulting in an expansion of the vessel and subsequent contact between the SCV and the CS. The pressurization will continue until failure of the SCV. Figure 2.0.1 shows a simple schematic of the test configuration.

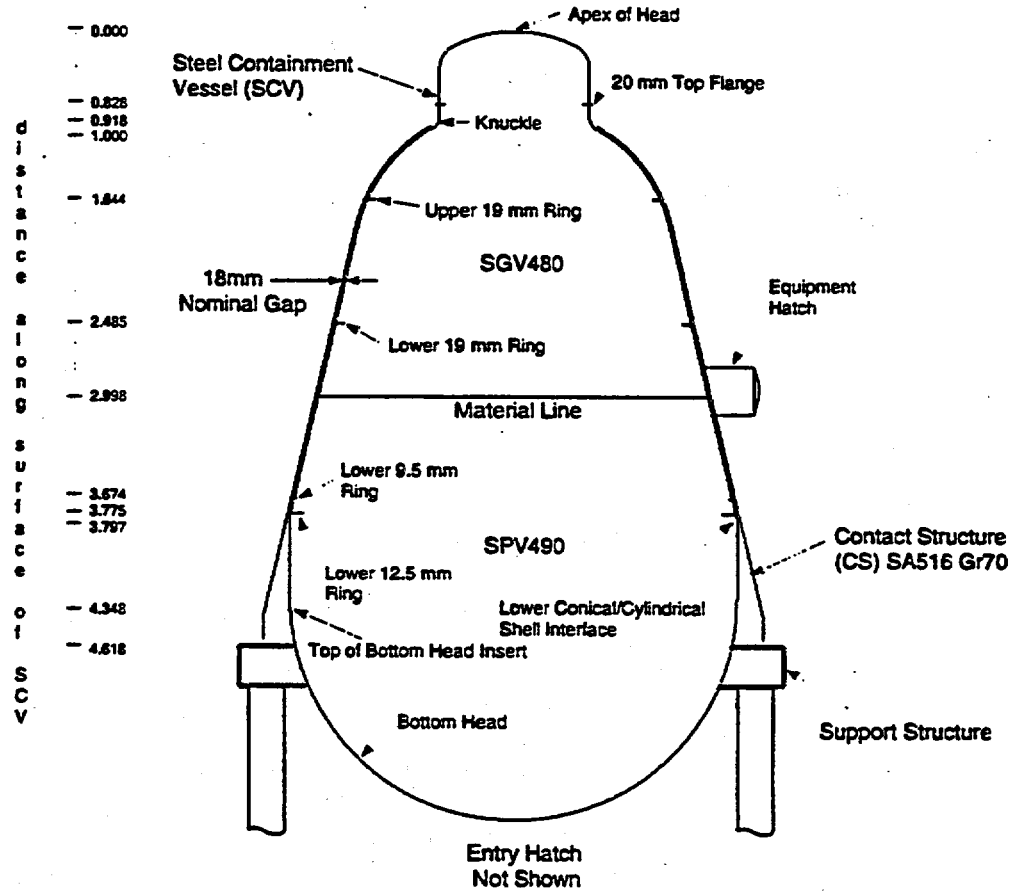

Figure 2.0.1
SCV and CS in Test Configuration

The Nuclear Power Engineering Corporation (NUPEC) of Tokyo, Japan and the U.S. Nuclear Regulatory Commission (NRC) funded all construction and test activities with Sandia National Laboratories (SNL) coordinating the "Round Robin" activities.

3.0 Material Data :

The SCV is constructed of SGV480 and SPV490 Japanese steel. The upper portion of the SCV is SGV480 Steel and the lower portion is constructed of SPV490 steel. The equipment hatch reinforcement plate is also constructed of SPV490 steel with the remaining equipment hatch made of SGV480. The CS is entirely SA516 Gr70 steel.

Elastic material data for the Japanese steels was supplied in Reference (2). An average Young's Modulus (E) of 209,850 Mpa (30.436 ksi) was used for the SGV480 steel and an average Young's Modulus of 215,750 Mpa (31.292 ksi) was used for the SPV490 steel in all the analyses. A nominal design value of 206,844 Mpa (30.000 ksi) was assumed for the CS. A Poisson's ratio of 0.3 was assumed for all the steels.

Tensile test data was supplied in Reference (1) for both the SGV480 and SPV490 steels. Four samples of engineering stress-strain data at twelve distinct locations relating to various material and thickness changes on the SCV were supplied. The engineering stress-strain was converted into true stress and strain up to the ultimate engineering stress using the following relations.

$$\varepsilon_t = \ln(1+\varepsilon_e) \qquad \text{Equation (3.0.1)}$$

$$\sigma_t = \sigma_e(1+\varepsilon_e) \qquad \text{Equation (3.0.2)}$$

This was necessary since true stress, true plastic strain data is required in the ABAQUS finite element program. Reference (4). To obtain only the plastic portion of the strain data, the elastic portion of the strain was subtracted from the total strain using the relationship below.

$$\varepsilon_{tp} = \varepsilon_t - \sigma_t/E \qquad \text{Equation (3.0.3)}$$

A least squares approach was utilized to determine the mean curve which would be used in subsequent nonlinear analyses. The true stress, true plastic strain data was fit with a variable knot B-spline least squares approximation (Reference 5). An interface program to the Reference (5) routines was developed and utilized to obtain the twelve mean material curves which would be used in all the nonlinear analyses. In operation, the test data from the four samples is read from an input file, sorted and the user prompted for the order of the spline (quadratic, cubic...), the number of B-spline coefficients and an initial guess at the internal knot locations. The program then determines the best placement of the knots which will minimize the error in a least squares sense. Experience has shown that the use of lower order splines and a minimum number of coefficients results in the best fit without unrealistic oscillation of the splines, caused from the test data spread. Once a good fit is obtained, the splines are evaluated and a piece-wise linear true stress, true plastic strain curve calculated. The range of the material curve was limited to the ultimate engineering stress limit due to the limitations of Equations 3.0.1 and 3.0.2. This limit could well be exceeded during the numerical simulations. To extend the range of the curve, the tangent slope of the curve's end point was extrapolated well beyond the ultimate limit. This approximation is consistent with true stress,true strain material behavior of most metals and should not be significant since the majority of the SCV response will be below the ultimate limit. Figures 3.0.1 and 3.0.2 show examples of this data fit for both the SGV480 and SPV490 steels. Location identifications from Reference (1) are shown in the figures for cross reference purposes. Table 3.0.1 presents the maximum, minimum and average true ultimate strain of the samples supplied.

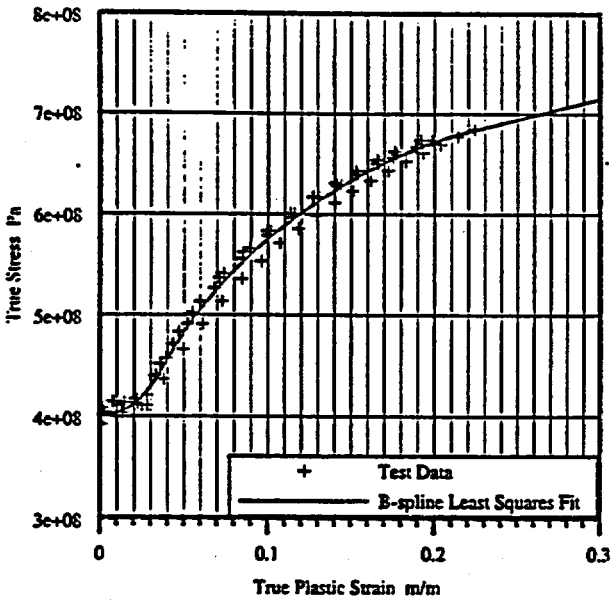

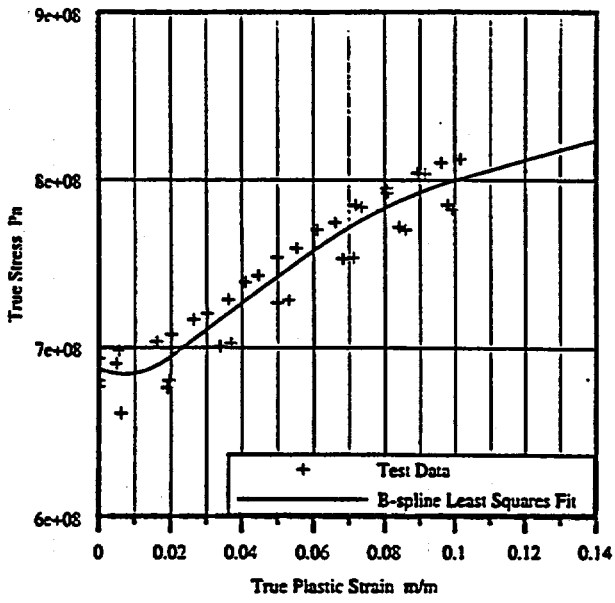

Figure 3.0.1 and Figure 3.0.2 - True Stress True Plastic Strain Data Fit
SGV480 Steel 8.5 mm Thick Conical Shell 2 Location 5
SPV490 Steel 9.0 mm Thick Cylindrical & Conical Shell Location 11

No inelastic material properties were supplied for the SA516 steel used to construct the CS. The CS was designed to remain virtually elastic for the majority of the loading sequence. At higher internal pressure, the CS does, however, experience inelastic straining starting at the top of the CS near the SCV knuckle and proceeding throughout the structure at very high pressures. The SCV will most likely fail before general yielding of the CS can be achieved but for simulation purposes, an approximate material curve was sought. A literature search failed to produce a minimum material curve for SA516 Gr70 steel, however, a material curve for ASTM A36 steel was located. ASTM A36 is similar to SA516 steel but of lower strength. The SA516 Gr70 curve, therefore, was based on the minimum material properties specified in Reference (2) and the general behavior of ASTM A36 steel. While a rough approximation, this still represents an improvement in the simulation over treating the CS as an elastic structure. If deemed necessary, post test analyses may use CS material data supplied by SNL after the test series.

Location	Material	Thickness (mm)	Max. ε_{tu} (%)	Min. ε_{tu} (%)	Avg. ε_{tu} (%)
1 Top Head Shell	SGV480	6.0	20.226	19.703	19.961
2 Top Head	SGV480	6.0	20.581	19.480	19.944
3 Conical Shell 3	SGV480	7.5	21.512	20.563	21.055
4 Spherical Shell	SGV480	8.0	24.468	18.795	21.616
5 Conical Shell 2	SGV480	8.5	22.707	19.518	20.489
6 Reinforcement Ring	SGV480	9.5	22.379	20.190	21.698
7 Reinforcement Ring	SGV480	12.5	21.365	19.954	20.589
8 Reinforcement Ring	SGV480	19.0	18.064	17.502	17.827
9 Flange, Hatch Cover	SGV480	20.0	20.811	17.344	19.272
10 Knuckle	SGV480	16.5	16.643	16.423	16.573
11 Cyl. & Conical Shell	SPV490	9.0	10.540	9.998	10.245
12 Hatch Reinforcement	SPV490	17.5	9.611	8.423	8.934

Table 3.0.1
True Ultimate Strain Values from Four Sample Lots

4.0 Finite Element Model Description :

Electric Boat Corporation has developed a series of finite element models in the evaluation of the SCV and CS. Axisymmetric shell models were utilized to evaluate general free field response away from the equipment hatch and transition regions as well as to perform various parametric evaluations. To obtain detailed response in the transition regions located around stiffener locations and the knuckle region, solid axisymmetric models were used. A quarter symmetry shell model and subsequently refined submodels were used to obtain response data near the equipment hatch sleeve. All models were evaluated with and without friction in defining the interaction between the SCV and the CS. Geometric and material nonlinearities were included in all the evaluations.

4.1 Axisymmetric Shell Models :

A series of axisymmetric shell models was developed in order to perform parametric evaluations on variations in the as-built test configuration as well as to evaluate several numerical solution alternatives available in the ABAQUS finite element program. As-built conditions of the SCV and CS were supplied by SNL in Reference (3) and include radius. gap and thickness values which were specified at elevations on the SCV and at circumferential increments around the shell (either 45 or 90 degree increments). In order to evaluate the geometric variation around the circumference, an average value was determined. For example, a mean as-built thickness was determined by averaging the eight samples taken around the SCV circumference. If multiple plate thickness measurements were taken for a given design plate thickness, these were also averaged. To evaluate the effects of plate thickness variations, an additional analysis was performed which utilized the minimum plate thickness specified around the circumference. Table 4.1.1 presents the mean and minimum plate thicknesses which were used in the axisymmetric shell models. The material location identifiers of Reference (1) and thickness labels of Reference (3) are used in the table for cross referencing purposes.

Design Thickness (mm)	Material Location Id	Thickness Label	Minimum Thickness (mm)	Mean Thickness (mm)
6.0	1	T18, T19	6.1	6.8
6.0	2	T21	6.7	6.8
7.5	3	T11,T12,T13	7.2	7.8
8.0	4	T14,T15	7.6	7.9
8.5	5	T7, T8, T9	8.2	8.7
9.5	6	T6	9.6	9.9
12.5	7	T5	13.1	13.3
19.0	8	T10	19.2	19.5
19.0	8	T16	19.8	19.9
20.0	9	T20	20.2	20.7
16.5	10	T17	16.2	16.8
9.0	11	T1-T4	8.8	9.48
17.5	12	T22	17.6	18.0
20.0	9	T23	20.2	20.7
20.0	9	T24	20.3	20.4

Table 4.1.1 - SCV Minimum and Mean As Built Plate Thicknesses

In areas of significant thickness transition such as the knuckle region and lower head area, variable thickness finite elements were used by defining the shell thickness at nodal locations. In this way, the smooth transition from one plate thickness to another was accurately modelled. The thickness values of the CS were taken from the gap size measurement supplied in Reference (3). Again, the values (four at 90 degree increments) were averaged around the circumference. These mean values were then averaged into two sections, one for the spherical shell of the CS and one for the conical section of the CS. Minimum values were also determined for each section as shown in Table 4.1.2.

Design Thickness (mm)	CS Section	Minimum Thickness (mm)	Mean Thickness (mm)
38.1	Spherical	43.36	44.33
38.1	Conical	37.01	42.50

Table 4.1.2 - CS Minimum and Mean As Built Plate Thicknesses

The gap distance values at four circumferential points at eighteen separate elevations along the CS were supplied in Reference (3). The four circumferential values per elevation were averaged as shown in Table 4.1.3. The location identifiers from Reference (3) are used in the table for cross reference purposes. For a worst case evaluation on gap distance sensitivity, approximate minimum, mean and maximum gap values were determined by evaluating measurement hole numbers 5 through 18. These locations correspond to points at which a nominal design gap of 18 mm was desired. The CS model was then constructed such that the normal gap clearance from the SCV was 17.0 mm for the minimum gap model, 21.0 mm for the mean gap model and 24.0 mm for the maximum gap model. Note that the actual gap was specified since ABAQUS/Standard, the implicit numerical solver in the family of ABAQUS codes. does not account for the thickness of the shell in the contact algorithm.

Hole #	Average Gap (mm)	Hole #	Average Gap (mm)	Hole #	Average Gap (mm)
2	133.03	8	22.52	14	22.86
3	101.69	9	23.32	15	21.45
4	71.92	10	22.99	16	19.16
5	19.76	11	23.08	17	17.98
6	20.58	12	22.43	18	16.64
7	20.88	13	21.86	19	25.91

Table 4.1.3 - Average Gap Distances

The out of roundness values supplied in Reference (3) were not used since it is believed that as the SCV exceeds the yield limit of the material, the vessel will naturally conform to a cylindrical / spherical shape. Therefore, the SCV geometry, except for plate thicknesses, was based on the design drawings supplied with Reference (1). An average design half thickness value of 3.75 mm was added to all the inside radial dimensions supplied in the drawing to obtain an approximate mid-radius value.

Several axisymmetric models were developed based on the permutations of model geometry and include (1) a mean thickness, mean gap model, (2) a mean thickness, minimum gap model, (3) a mean thickness, maximum gap model and (4) a mean gap, minimum thickness model. Figure 4.1.1 shows the mean gap model which is representative of all the axisymmetric models.

The model shown in Figure 4.1.1 is truncated at the intersection with the support structure. The support structure, as shown in Figure 2.0.1, was assumed to provide fixity at this point. In addition, the lower head is present only to complete the pressure boundary and is not part of this evaluation. SNL has taken efforts to insure that failure will not occur in this area.

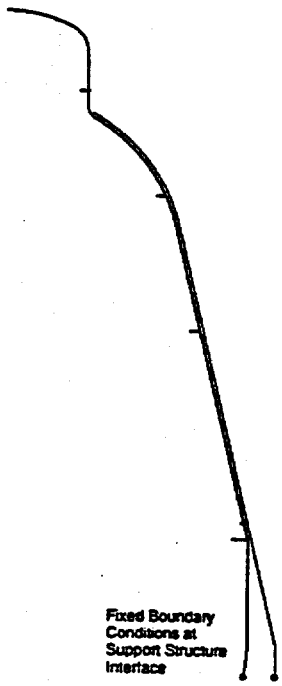

Figure 4.1.1
SCV and CS Axisymmetric Shell Model - Mean Gap

The finite element model was constructed of 248 ABAQUS SAX2 elements which are three-node thin or thick quadratic axisymmetric shell elements. The element allows transverse shear but becomes a discrete Kirchoff thin shell as the thickness decreases. Two-point integration of a quadratic interpolation function is used for the element's stiffness matrix and three-point integration of a quadratic interpolation function is used for the distribution of loads. The element also has the ability to account for reduction of thickness due to stretching parallel to its mid-surface. A full discussion of the element's theory is given in Reference (6).

The contact definition between the SCV and the CS is simply defined in ABAQUS by creating surface definitions which specify the elements or nodes associated with a given surface. The surfaces that may contact are then paired in a master-slave relationship and properties of the interaction, such as friction, defined. Contact is enforced in the algorithm by ensuring that the slave surface (SCV) must conform to the master surface (CS). That is, that nodes on the slave surface cannot penetrate the master surface, but master nodes can penetrate the slave surface. Obviously, penetration of the slave surface by the master surface nodes is to be minimized and this is accomplished through mesh refinement and the use of matching meshes between the paired surfaces. Care was taken to use matching meshes on the SCV and CS by a normal projection of the SCV mesh on to the CS. Mesh refinement studies were also performed to assure a convergent solution.

There are two solutions available in defining the sliding behavior of contact surfaces with nonlinear geometry. A finite sliding solution may be utilized which permits arbitrary separation, sliding and rotation of the surfaces, or small sliding may be used, in which arbitrarily large rotation of the surfaces are allowed, but it is assumed that a slave node will interact with only the same local area of the master surface. The computational savings that the small sliding solutions possess can be substantial, particularly for three dimensional interaction problems. For the axisymmetric

shell models. the savings were insignificant. however the results from both solution methods were nearly identical. This information was used to reduce the computational expense in performing the three dimensional general shell analyses.

The contact behavior may also be modified in a variety of ways. Two methods which are pertinent to this evaluation are the default hard contact model and the softened contact model. Figure 4.1.2a illustrates the contact definition of the hard contact model. When the surfaces are in contact, any pressure stress can be transmitted between the contacting surfaces.

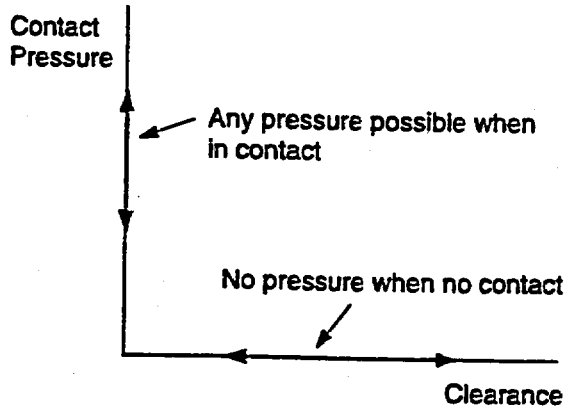

Figure 4.1.2a Hard Contact Model

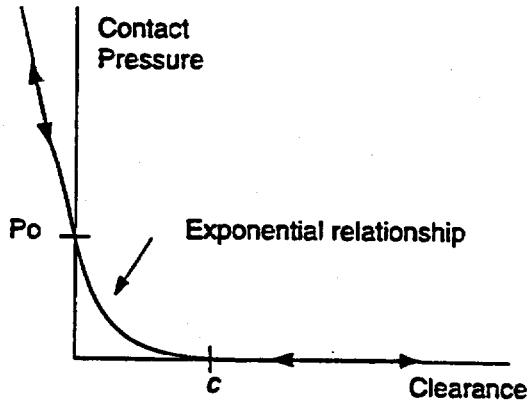

Figure 4.1.2b Softened Contact Model

This particular method had convergence problems for several of the parametric models which were evaluated. The softened contact model, as shown in Figure 4.1.2b, is useful when there is a thin, relatively soft coating on one or both of the surfaces. Per Reference (2), the SCV has four independent layers of primer or paint with a total paint thickness ranging from 3 mm to 5 mm. Contact occurs in this model when the gap distance decreases to a value of c. The pressure transmitted between the surfaces then increases exponentially with further approach. Values of $c = .001$ meters and $P_o = 1.6 \times 10^7$ Pa were used which resulted in a maximum over-closure of approximately 1.7 mm. This result is entirely plausible since compression of the paint to this level is reasonable. In addition, the variation of results between the hard and softened contact models is well within the variability in the as-built gap data. The softened contact model also removed the convergence difficulties experienced with the hard contact model and reduced the number of equilibrium iterations required in the overall solution.

Classical Coulomb theory was used to define the frictional contact between the SCV and CS. The default. stiffness method was used to implement the friction theory. This method permits some relative motion when the interface should be sticking. The amount of slip permitted is controlled through the specification of an allowable elastic slip distance. The larger the slip distance, the more rapid the rate of convergence at the expense of solution accuracy. In practice, the program scans the contact surfaces and calculates "a characteristic contact surface face dimension," l_i. The allowable slip distance is then kept below a small fraction F_f of l_i. The default value of $F_f = 0.005$ was used in all analyses. The axisymmetric model was evaluated with a coefficient of friction, $\mu = 0.0$ (no friction), $\mu = 0.4$ (steel on steel in air, Reference (7)) and $\mu = 0.2$ (steel on steel lubricated, Reference (8)) to assess the effects of friction on the response of the SCV. In one of the parametric evaluations, the CS is assumed to be linearly elastic. For this case, an extension of the standard Coulomb model which permits the specification of a shear stress limit was used. With this model, regardless of the magnitude of the normal pressure stress, sliding will occur if the magnitude of the shear stress reaches the value of the specified limit. The shear stress limit was set to the minimum yield value of SA516 Gr70 steel (262.0×10^6 Pa).

Internal pressure was incrementally applied to the inside surfaces of the SCV based on the automatic load stepping procedure available in ABAQUS. By default, this pressure is applied normally to the surface regardless of the rotation of the surface.

4.2 Quarter Symmetry Shell Model:

The SCV can be ideally represented with a half symmetry model if variations in circumferential dimensions are averaged. If the effects of the equipment hatch are localized, a quarter symmetry model may be used, which effectively models a duplicate penetration on the opposite side of the SCV. In order to reduce the model complexity and analysis cost, a quarter symmetry model was constructed and the free field results compared to an axisymmetric model (no hatch modelled). Excellent agreement between the two models was present. These findings substantiate the assumption that the effect of the hatch is localized and the benefits of a half symmetry model would be negligible.

The quarter symmetry shell model, shown in Figure 4.2.1, was therefore used to evaluate the response near the equipment hatch. The model is based on the same properties as the mean axisymmetric models. Mean as-built thickness data (See Table 4.1.1 and Table 4.1.2) was used as well as a mean as-built gap of 21 mm (as compared to the nominal gap of 18 mm). No variation in thickness or gap was supplied around the circumference of the model. The as-built gap data around the hatch was significantly larger than the data supplied away from the hatch. This is most likely attributed to distortions in the shell structure due to extensive welding in the area. The mean gap around the equipment hatch was therefore increased to 25.7 mm based on data supplied in Reference (3). The gap size transition is located at the SPV490 hatch reinforcement plate to conical shell interface. Variable thickness shell elements were used at this transition to model the thickness transition from the thin conical shell to the thick reinforcement plate. Variable thickness shell elements were also used at the knuckle and lower shell sections similar to the axisymmetric models. The radial separation between the hatch cylinder and the CS was set at an average 25.5 mm as shown in Reference (3). The finite element model is constructed of 4724 ABAQUS S3R and S4R thin or thick, reduced integration, finite membrane strain elements. Default hourglass stiffness values were used to control the spurious modes which may occur in lower order reduced integration elements. The finite membrane strain elements allow thickness change (thinning of the element) and permit transverse shear stress output. Reference (6) presents a detailed discussion on the formulation of the S3R and S4R elements. Higher order elements such as 8-noded quadratic shell elements were not utilized since they do not account for shell thinning, which was shown to have a significant effect on results at higher internal pressures. The contact interaction between the SCV and CS utilized the small sliding solution, previously discussed, with the softened contact model shown in Figure 4.1.2b. The model was evaluated with a coefficient of friction of $\mu = 0.0$ (no friction) and $\mu = 0.4$ (steel on steel in air, Reference (7)) as was done for the axisymmetric models.

In order to perform a more refined analysis around the equipment hatch, a submodel was constructed which effectively quadrupled the number of finite elements around the hatch vicinity. Figure 4.2.2 shows the refined submodel which was evaluated using the submodelling options available in the ABAQUS computer program. With this analysis option, the model shown in Figure 4.2.1 is defined as the global model. Edge displacements are then automatically interpolated from the global model onto the submodel. All other symmetric boundary conditions, pressure loads and contact definitions were applied to the submodel, as was done for the global model. In applying the edge displacements, only the translational values were applied to the perimeter elements since the interpolation scheme used in ABAQUS is inappropriate for shell rotations which are not linearly related. Rotations are therefore applied by the coupling action of the two driven nodes of a particular perimeter element. Comparison of results in the free field between the global model and submodel show very similar results. A detailed discussion of this submodel analysis option can be found in Reference (4).

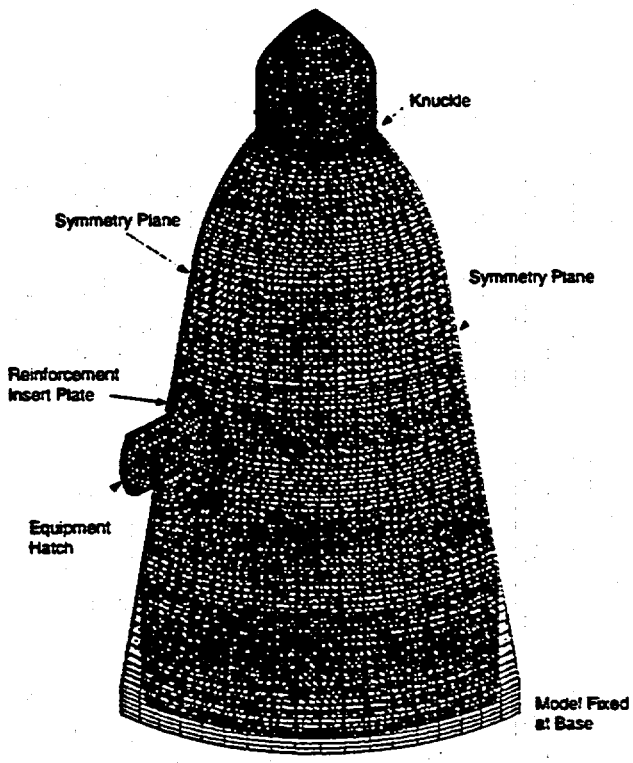

Figure 4.2.1
Quarter Symmetry Shell Model of the SCV and CS
(CS Shown in Phantom)

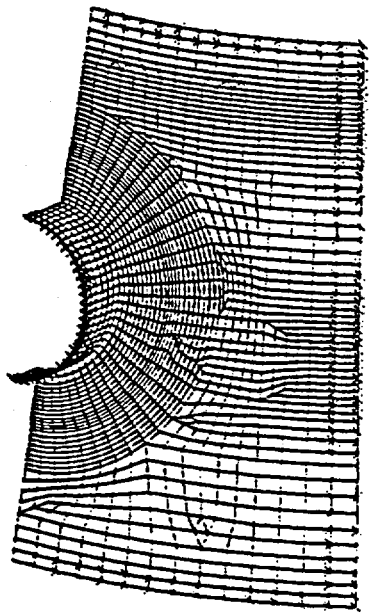

Figure 4.2.2 Submodel of Equipment Hatch Area
CS Removed for Clarity - X Marks Location of Driven Edge Displacements

4.3 Axisymmetric Solid Models

Three axisymmetric solid models were developed to evaluate, in detail, the localized response around several of the transition areas. These transition areas are characterized as locations around vessel stiffeners or significant changes in shell geometry which result in substantial strain concentrations. The axisymmetric models previously discussed do not possess the model detail necessary to accurately capture the steep strain gradients near these transitions. In addition, several of the required response locations are near the transition regions and it was necessary to verify that the strain gage locations were far enough from the severe strain gradient such that simple axisymmetric shell models could be used. All models were based on mean as-built thicknesses (Table 4.1.1) and mean gap data (gap = 21.0 mm). The contact interaction between the SCV and CS utilized the finite sliding solution, previously discussed, with the softened contact model shown in Figure 4.1.2b. The models were evaluated with a coefficient of friction, $\mu = 0.0$ (no friction), $\mu = 0.4$ (steel on steel in air, Reference (7)) as was done for the axisymmetric shell models.

Each solid model was primarily constructed using CAX8R 8-node biquadratic, reduced integration axisymmetric solid elements. Six-node quadratic CAX6 elements were used in mesh transition areas. These elements were selected over lower order elements due to their superior performance under bending loads. A detailed description of the axisymmetric solid element formulation can be found in Reference (6). Based on comparative studies to axisymmetric shell models, a minimum of four elements through the shell's thickness was used in order to accurately capture the through-thickness nonlinear strain distribution associated with the bending response.

The first section modelled encompasses the region from the top head to just above the upper 19 mm reinforcing ring of the spherical shell. In order to evaluate the effects of variations in the contact point between the SCV and the CS at the knuckle, two models were created. For the first model, the opening at the top of the CS was governed by the design height of the CS above the support structure and the assumed 21 mm mean gap. This modelling choice resulted in a relatively large open space at the top of the contact structure with contact between the SCV and CS occurring at the bottom of the knuckle. This model is shown in Figure 4.3.1. For the second model, the CS was extended such that the open space was equal to the mean value from Reference (3) from Hole #19 or 25.91 mm. This results in contact in the thicker section of the knuckle. A close-up detail of the knuckle region of this model is shown in Figure 4.3.2. Each model consists of axisymmetric shell elements in the head area which transition to axisymmetric solid elements at the top head cylindrical shell. Multipoint Constraint Equations (MPC's) were used at the shell / solid model interface to insure continuity. Twenty SAX2 quadratic axisymmetric shell elements were used in the head area while 2494 and 2654 quadratic axisymmetric solid elements were used for the remainder of the model for the first and second models respectively. Base motion data derived from the axisymmetric shell model was applied to the lower boundary of the spherical shell. MPC's were again used to apply the single node shell response data to the multiple node solid model.

The second section modelled, shown in Figure 4.3.3, is of the lower 19 mm reinforcement ring just above the elevation of the top of the equipment hatch. The model was constructed of 1974 CAX8R elements. Base motion data derived from the axisymmetric shell model was applied to the upper and lower portions of this model.

The third section, shown in Figure 4.3.4, models the intersection of the SPV490 conical shell with the SPV490 cylindrical shell. Two reinforcement rings are located just above the intersection. The model was constructed of 1472 CAX8R elements. Base motion data derived from the axisymmetric shell model was applied to the upper and lower portions of the model.

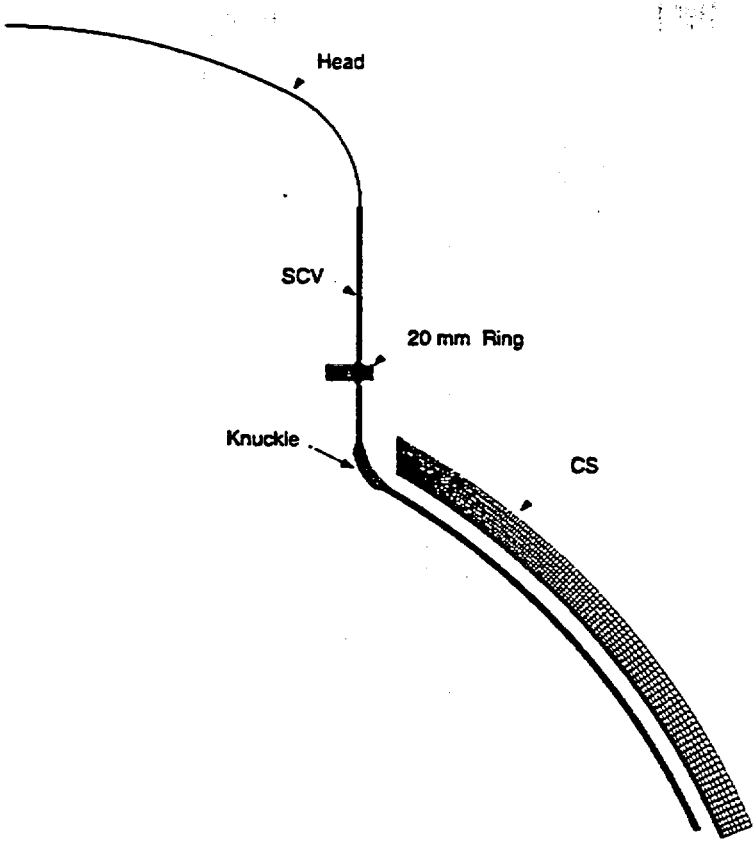

Figure 4.3.1 - Axisymmetric Solid Model Knuckle Region

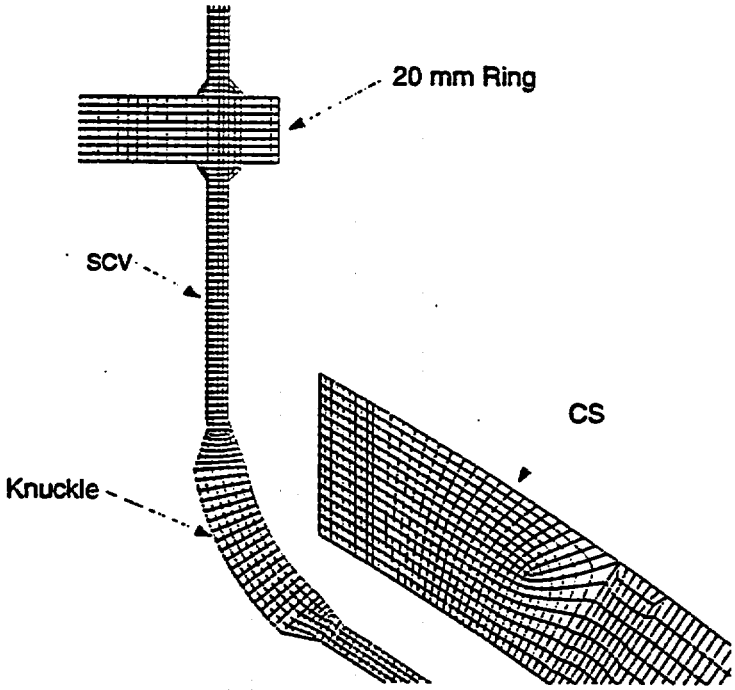

Figure 4.3.2 Axisymmetric Solid Model Knuckle Region Detailed View Based on Average Gap Distance of Reference (3) Hole 19 Measurements

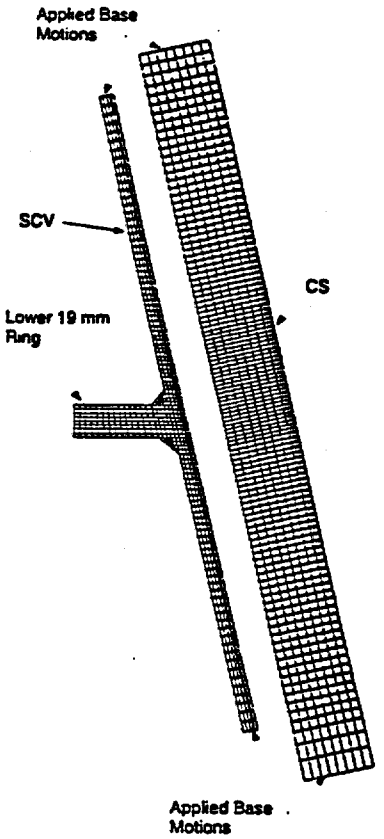

Figure 4.3.3 Axisymmetric Solid Model Lower 19 mm Reinforcement Ring

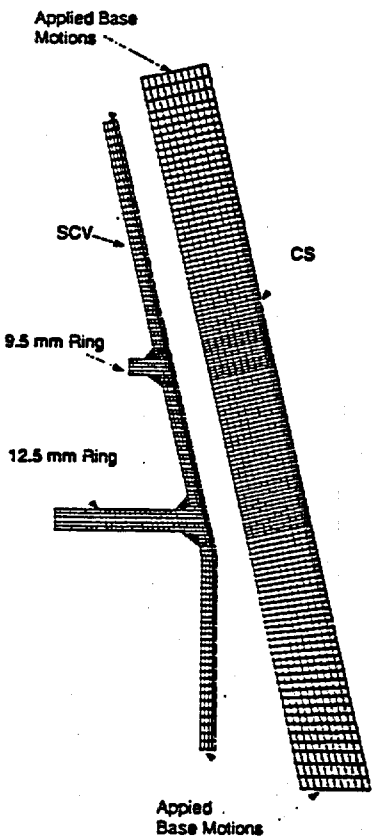

Figure 4.3.4 Axisymmetric Solid Model Conical Shell Cylindrical Shell Interface

5.0 Parametric Investigation - Axisymmetric Shell Models :

Axisymmetric shell models were used to economically evaluate a variety of model parameters from model geometry to analytical solution strategies. Table 5.01 lists the major features of the models evaluated.

Model No.	Gap (mm)	Thickness	Sliding	Contact	Friction	CS
1	21	Mean	Finite	Hard	0.40	Inelastic
2	21	Mean	Finite	Hard	0.40	Elastic
3	21	Mean	Finite	Hard	0.00	Inelastic
4	21	Mean	Finite	Softened	0.00	Inelastic
5	21	Mean	Finite	Softened	0.40	Inelastic
6	21	Minimum	Finite	Hard	0.40	Inelastic
7	17	Mean	Finite	Softened	0.40	Inelastic
8	21	Mean	Small	Hard	0.40	Inelastic
9	24	Mean	Finite	Softened	0.40	Inelastic
10	21	Mean	Finite	Softened	0.20	Inelastic

Table 5.0.1 Axisymmetric Shell Model Parametric Evaluation Reference Index

Selected plots are presented here to illustrate the variation in response that can be expected due to variation in the SCV and CS geometry including plate thickness and gap measurement as well as unknowns such as contact friction between the SCV and CS. It is believed that these evaluations represent bounding cases with respect to the variable which is being perturbed (i.e. gap size, plate thickness, frictional constant) but not necessarily a solution for a worst case analysis with respect to failure. Since the major purpose of this effort is to predict response behavior, mean property finite element models are more appropriate. The parametric evaluations will be used to aid in the assessment of the overall accuracy of the mean solution. Numerical perturbations were also evaluated to assess the effects of finite sliding versus small sliding solutions, hard versus softened contact interaction and the effect of the use of inelastic material properties on the CS.

Figure 5.0.1 shows the effect of gap distance on hoop strain for two internal pressure levels. As expected, the gap distance has the most dramatic effect on response only in the contact region. The graph was developed by plotting nodal averaged hoop strains as a function of relative distance along the SCV surface for a selected pressure level. Table 5.0.2 presents an index table of relative distance along the SCV for key areas of interest for use with the figures presented in this report. Automatic load stepping, in which ABAQUS controls the incremental increase in load based on the previous load increment convergence rate, was used in all analyses. Therefore, discrete pressure values across the various analyses performed are not exactly equal.

Figure 5.0.2 illustrates the effect of plate thickness on the response of the SCV. The portions of the SCV above the upper 19 mm ring, which are not in full contact with the CS at this pressure, show the most significant change in response. The load sharing nature of the thicker CS tends to mitigate the effects of the thickness variations in the shell plating below the 19 mm ring where uniform contact is achieved at a lower pressure.

SGV480 Material	Location	Apex of Head	Top 20 mm Ring	Top of Knuckle	Bottom of Knuckle	Upper 19 mm Ring	Lower 19 mm Ring
	Distance Along SCV (meters)	0.00	0.828	0.918	1.00	1.644	2.485
SPV490 Material	Location	SGV480/ SPV490 Material Interface	Lower 9.5 mm Ring	Lower 12.5 mm Ring	Lower Conical Shell/Lower Cylindrical Shell Interface	Top of Bottom Head Insert	Support Structure
	Distance Along SCV (meters)	2.998	3.674	3.775	3.797	4.348	4.618

Table 5.0.2 Relative Distance along SCV for Key Areas

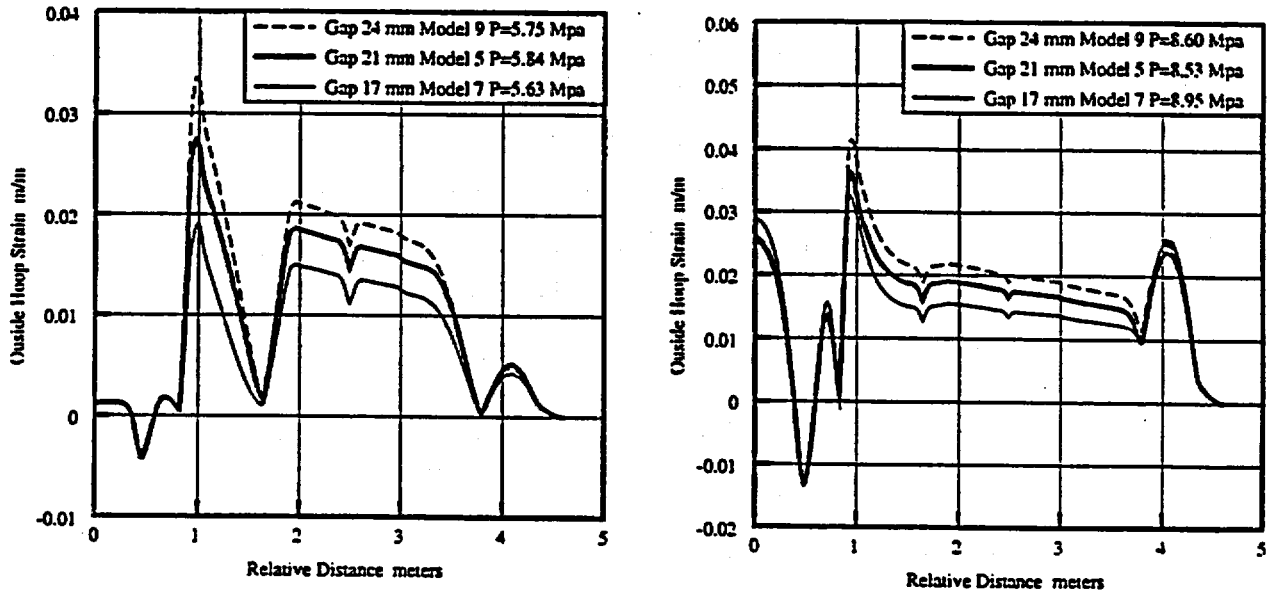

Figure 5.0.1 Gap Parametric Results
Outside Hoop Strains versus Relative Distance Along SCV

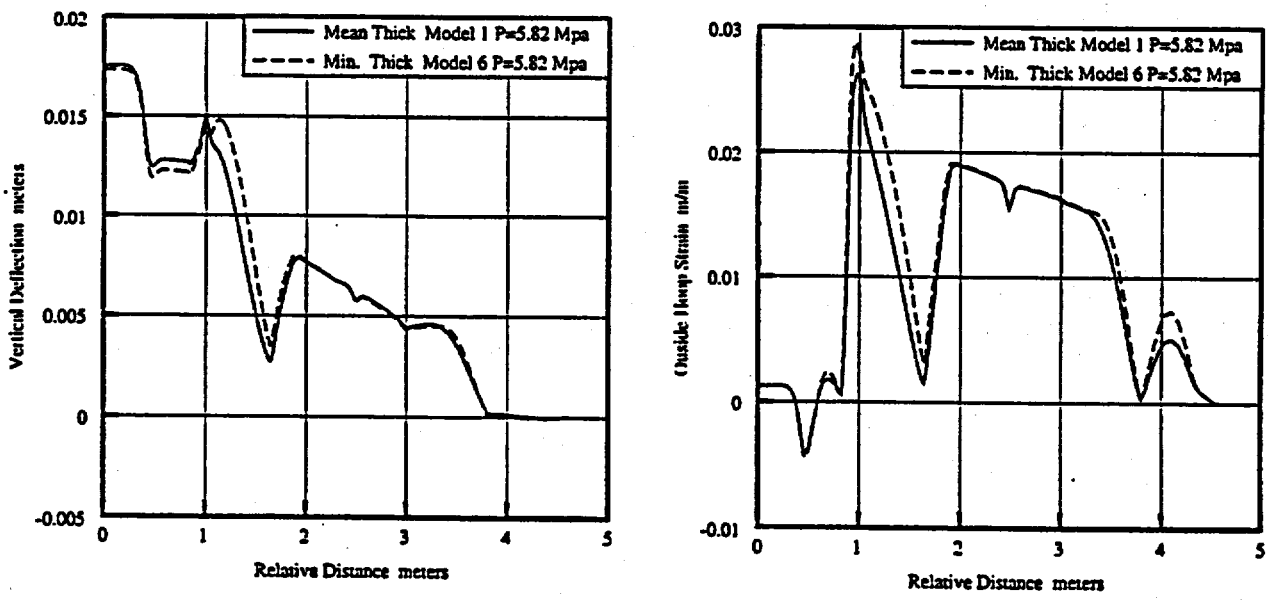

Figure 5.0.2 Thickness Parametric Results
Vertical Displacement and Outside Hoop Strain versus Relative Distance Along SCV

Figure 5.0.3 shows the effects of friction on the displacement and strain response of the SCV. The mean thickness, mean gap models were evaluated with coefficient of friction values of $\mu = 0.0$ (no friction), $\mu = 0.4$ (steel on steel in air, Reference (7)) and $\mu = 0.2$ (steel on steel lubricated, Reference (8)). With no friction, the SCV not only has positive vertical deflections due the pressure on the top head surface, but also some negative vertical motion due to bulging of the lower SPV490 cylindrical shell into the larger gap at the base of the CS. Frictional forces effectively negate the downward effective pressure. A comparison of the two evaluations which utilized frictional values shows very similar response. It is therefore believed the the actual response of the tested vessel will tend toward results which assume some level of friction. The level of friction, as long as reasonable, should only have minor effects on the general response of the SCV.

Figure 5.0.4 shows some selected results from the parametric evaluation of analysis assumptions. The comparison of hard contact results with the results of a softened contact model show very similar response. The use of the softened contact model was used to solve convergence problems in some of the analytical evaluations as well as, in a general sense, model the compression of the three to five millimeter thick SCV painted surface. The comparison of a finite sliding solution to the more economical small sliding solution also shows nearly identical results. This information was used in the quarter symmetry shell model and associated submodel to reduce computational costs.

At approximately 8.5 Mpa (1200 psi) the SCV shell response tends to show some deviations from the inelastic versus elastic treatment of the CS. At approximately 11.2 Mpa (1600 psi) the effect of the inelastic behavior of the top portion of the CS is significant. The material properties used for the CS are only an approximation and represent a lower bound to the strength of the SA516 Gr70 steel. If pressures in the SCV exceed 8.0 to 9.0 Mpa before failure, it will be necessary to obtain more exact material behavior for the CS for the post test evaluation.

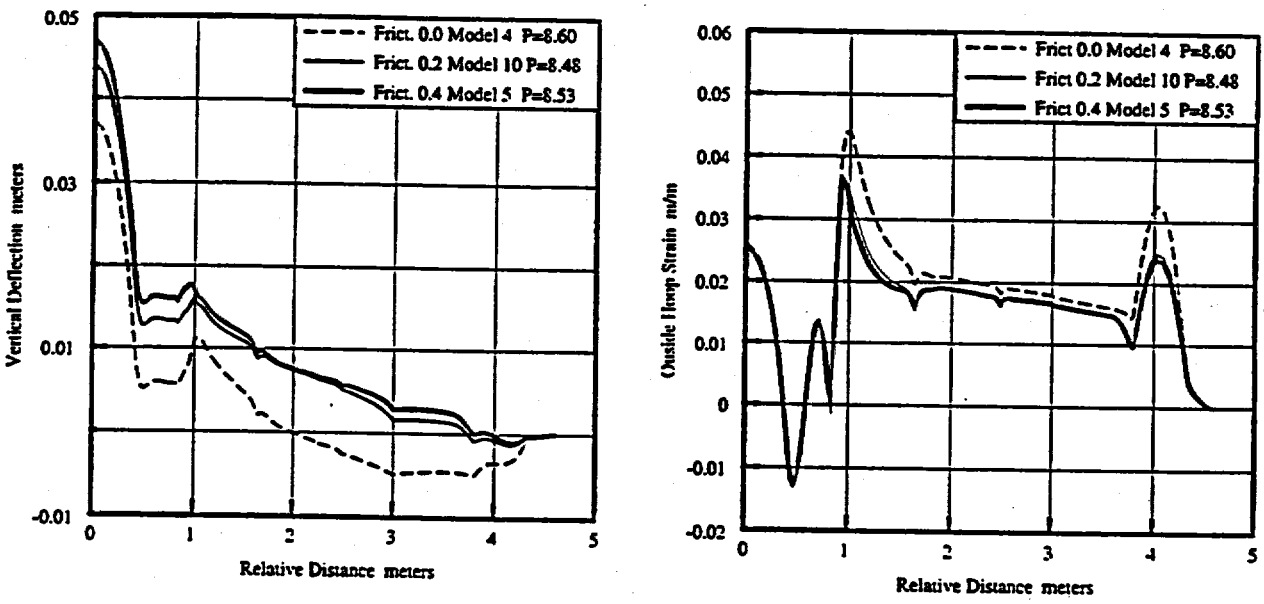

Figure 5.0.3 Coefficient of Friction Parametric Results
Vertical Displacement and Outside Hoop Strain versus Relative Distance Along SCV

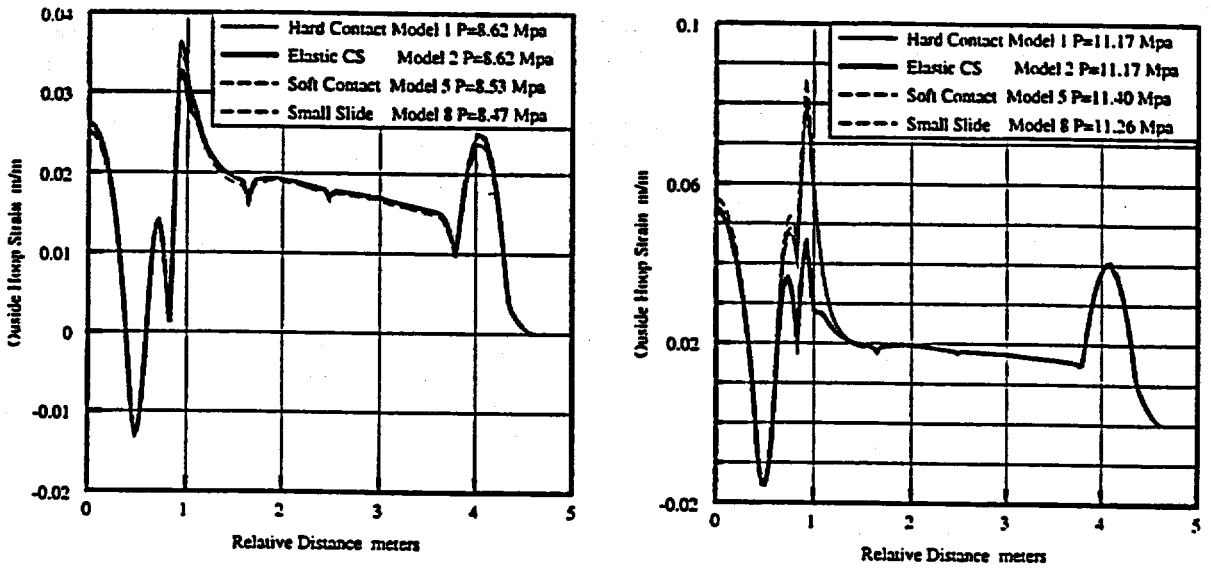

Figure 5.0.4 Analysis Assumptions Parametric Results
Outside Hoop Strains versus Relative Distance Along SCV

6.0 Quarter Symmetry Shell Model Analysis Results :

The quarter symmetry (modelled from a global theta angle, θ_G, of 0.0 degrees to 90 degrees) shell model shown in Figure 4.2.1 was evaluated assuming a coefficient of friction of 0.0 and 0.4. Results for the friction evaluation are presented in this section. The model was loaded with an internal pressure load which was incrementally increased until a convergent solution could no longer be obtained for a specified minimum load increment. A minimum load increment value of 1400 Pa (0.2 psi) was used for all analyses. Maximum pressures achieved in the simulations for the frictionless and friction models were 13.51 Mpa (1959 psi) and 13.57 Mpa (1968 psi) respectively. This is consistent with the axisymmetric models evaluated. No material failure algorithm was used in any of the analyses, so these pressures do not represent a failure condition but merely the level of pressure in which a stable solution could be found for the specified default equilibrium tolerances. Figure 6.0.1 shows a displaced fringe contour plot of the SCV with friction for the hoop component of strain at an internal pressure of 8.60 Mpa (1250 psi). The effects of the equipment hatch on the uniform strain field are readily apparent.

Hoop strain versus relative distance along the SCV at a model global theta angle, θ_G, of 45 degrees (free field) from the shell model are compared to the axisymmetric results in Figure 6.0.2 for two pressure load levels. As can be seen, free field strain results away from the equipment hatch are very similar to the axisymmetric shell model. This validates the use of the economical mean parameter axisymmetric shell model results for the required free field result predictions locations.

The contact propagation for the friction model is show in Figure 6.0.3 by plotting the gap distance versus relative distance along the SCV for various discrete pressure levels. The X-axis distance is taken relative to the lower portion of the knuckle. The path along the SCV was taken at a model global theta angle, θ_G, of 45 degrees (free field) and 90 degrees (center of equipment hatch). The gap of approximately 21 mm and 25 mm around the equipment hatch is shown in the first incremental increase in pressure. The gap distance below the lower reinforcement rings then increases dramatically based on the CS geometry. First contact takes place in the lower knuckle region at an approximate pressure of 3.5 Mpa (500 psi). The next area of contact is in the center of the upper conical shell section (conical shell 3) at a pressure of approximately 3.9 Mpa (550 psi). Contact spreads throughout the conical section and then to the spherical shell. The reinforcement rings are clearly visible in the contact plots as local peaks in the gap distance.

Results from the submodel (Figure 4.2.2) of the hatch area are consistent with those of the quarter symmetry model but with a higher level of resolution in the steep strain gradient areas of the model.

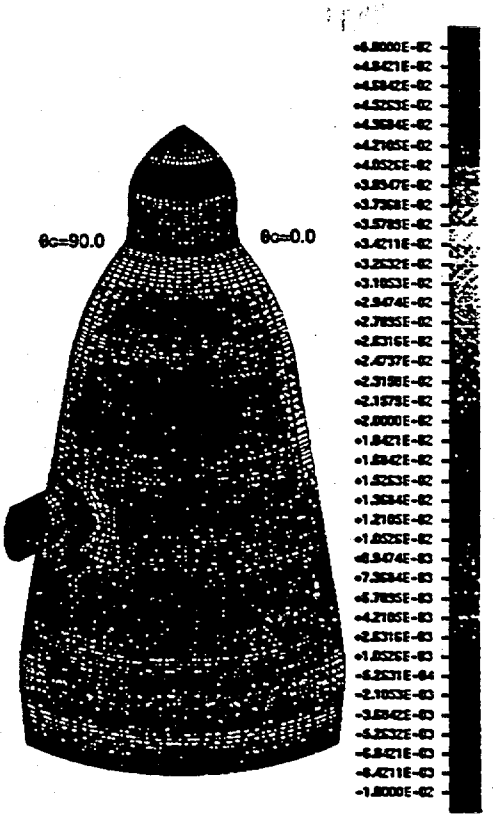

Figure 6.0.1
Deformed Fringe Contour Plot of the SCV
Outside Hoop Strain - Pressure = 8.60 Mpa (1250 psi) Deformed Scale = 1.0

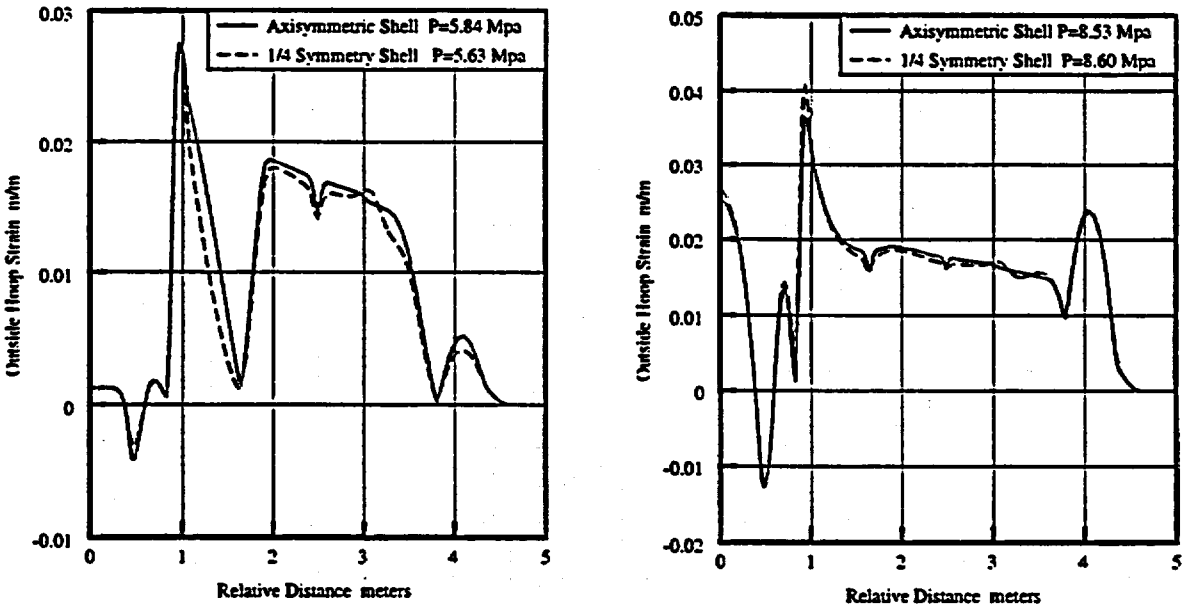

Figure 6.0.2 Comparison of Hoop Strains
Axisymmetric Shell Model Versus Quarter Symmetry Shell Model at θ_G=45 Degrees

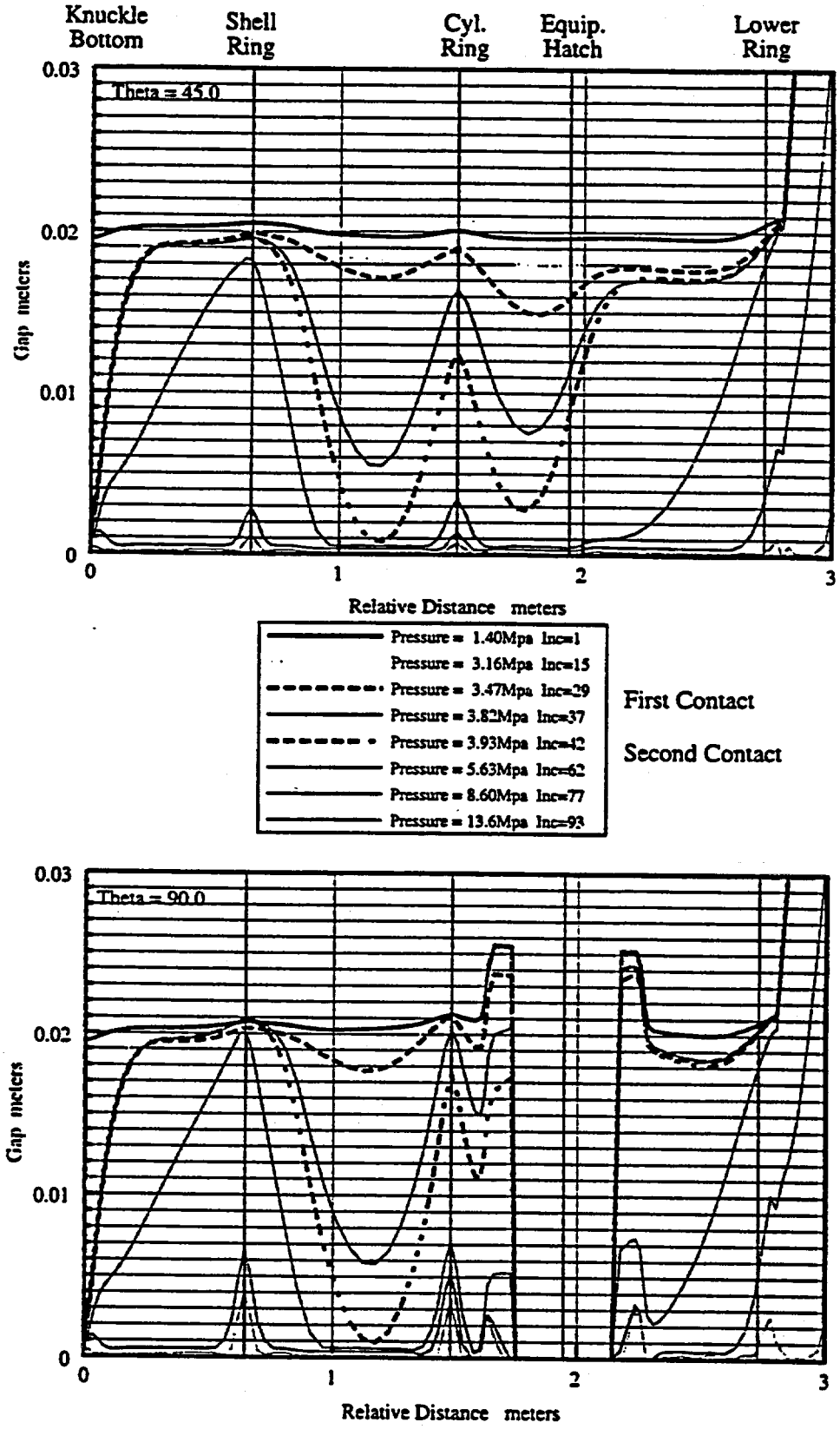

Figure 6.0.3 Quarter Symmetry Shell Model
Contact Propagation at θ_G = 45.0 and 90.0 Degrees

7.0 Axisymmetric Solid Model Results :

The axisymmetric solid models were evaluated with coefficient of friction values of 0.0 and 0.4. Responses from the friction model were compared to results from the mean property axisymmetric shell model.

Hoop strain and inside equivalent plastic strain (PEEQ) versus relative distance along the SCV (measured from the apex of the top head) were plotted at a selected pressure for the models of the top head/knuckle region for a coefficient of friction of 0.4. These strains are shown in Figure 7.0.1. Strains from the mean property axisymmetric shell model are shown on the same plot. Note that the discrete pressure values plotted are not identical for all models due to the automatic load stepping scheme used by ABAQUS. The response comparisons show generally good correlation between the axisymmetric solid models and the axisymmetric shell models. The more detailed and refined solid models more accurately capture the strain gradients. Since the axisymmetric solid models included the fillet welds and the thickness of the reinforcement ring, the peak PEEQ strains at these stiffeners vary in magnitude and move from the ring centerline in the shell model to the weld toes in the solid models. Comparisons between the axisymmetric solid models show the sensitivity of the strains in the knuckle region to the contact structure geometry. Horizontal and vertical displacements versus relative distance along the SCV are shown in Figure 7.0.2. This plot shows the sensitivity of the head and knuckle displacements to the contact structure geometry. The mean CS opening configuration is considered more representative of the actual test condition. The first modelling configuration will be used to aid in the assessment of the overall sensitivity of the knuckle response behavior. A deformed shape of the mean opening model at a pressure of 5.68 Mpa is shown in Figure 7.0.3. Note that the appearance of the penetration of the SCV into the CS is from the softened contact model. which in a general sense, approximates the compression of the SCV painted surface. The mean opening model was also evaluated assuming no friction between the SCV and CS. A solution for this model without friction could not be obtained beyond 5.85 Mpa due to solution convergence problems in the contact algorithm.

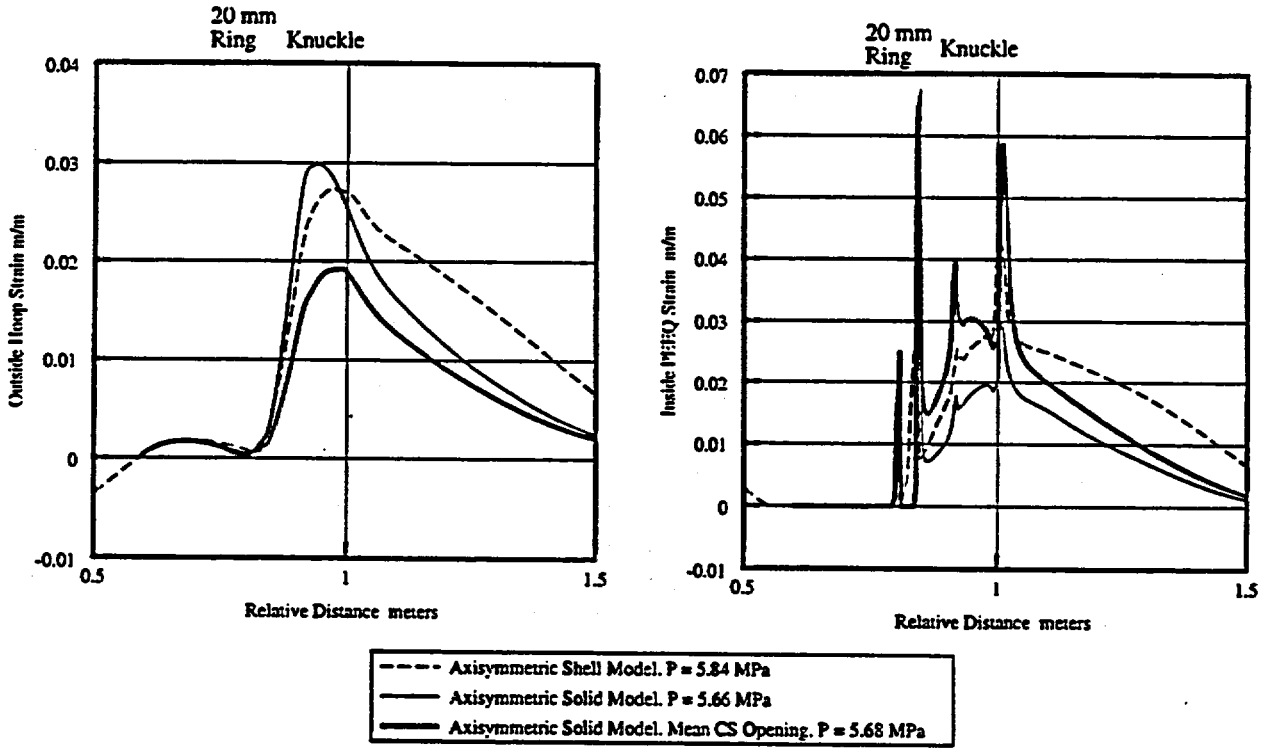

Figure 7.0.1
Knuckle Region Outside Hoop Strain and Inside PEEQ Strain versus Relative Distance Along SCV

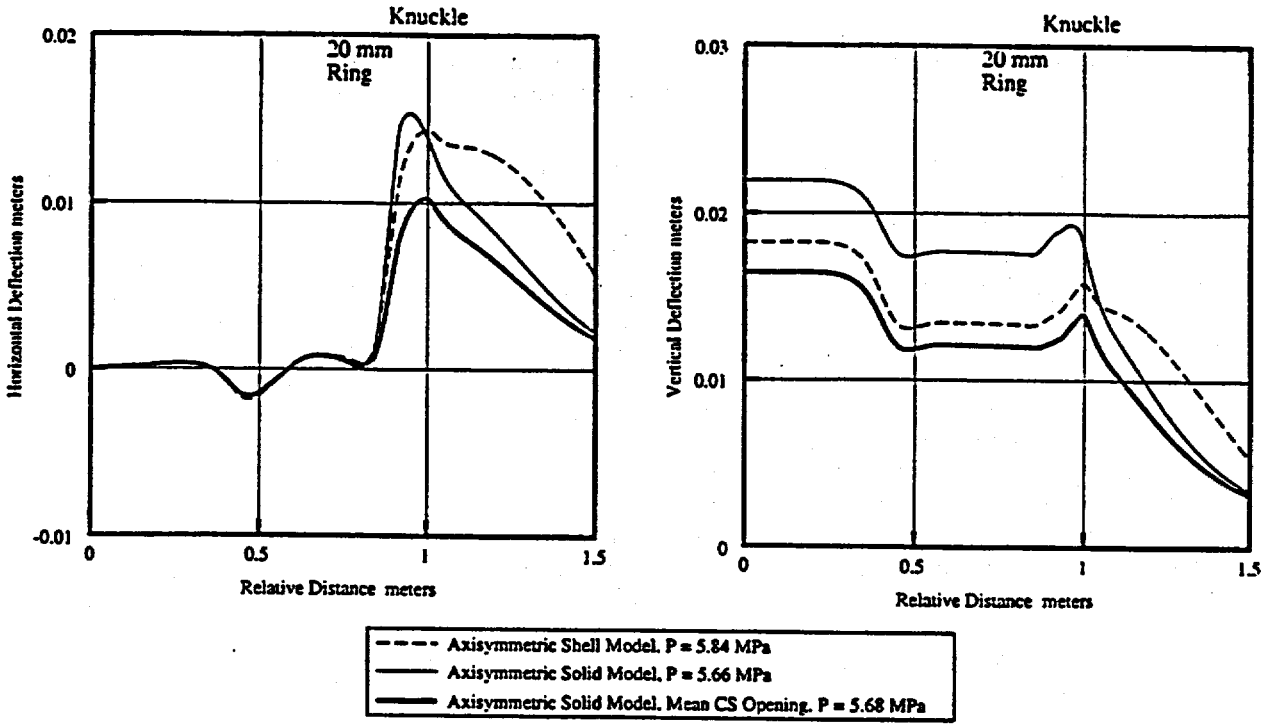

Figure 7.0.2 Knuckle Region Contact Effects
Horizontal and Vertical Deflection versus Relative Distance Along SCV

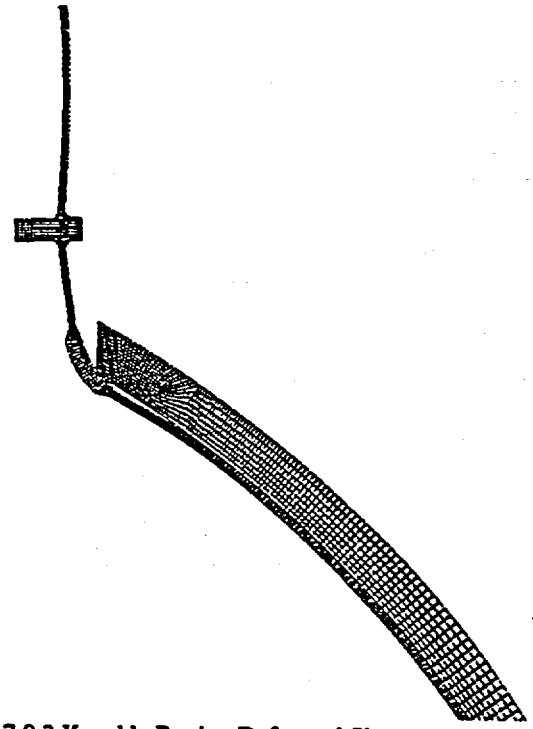

Figure 7.0.3 Knuckle Region Deformed Shape
Pressure = 5.68 Mpa (824 psi) Scale = 1.0
(overclosure at knuckle due to softened contact model)

Hoop strain and inside PEEQ strain versus relative distance along the SCV for a coefficient of friction of 0.4 were plotted at a selected pressure for the model of the lower 19 mm reinforcement ring just above the equipment hatch in Figure 7.0.4. Similar plots for the model of the intersection of the SPV490 conical and cylindrical shells are shown in Figure 7.0.5. The response comparisons show good correlation between the solid and shell models. Some variation is shown at the ring stiffeners due to the added detail and mesh refinement of the solid models. Differences in PEEQ strains at the solid model boundaries are due to the MPC's used to apply the base motion data and clearly do not affect model response away from the boundaries.

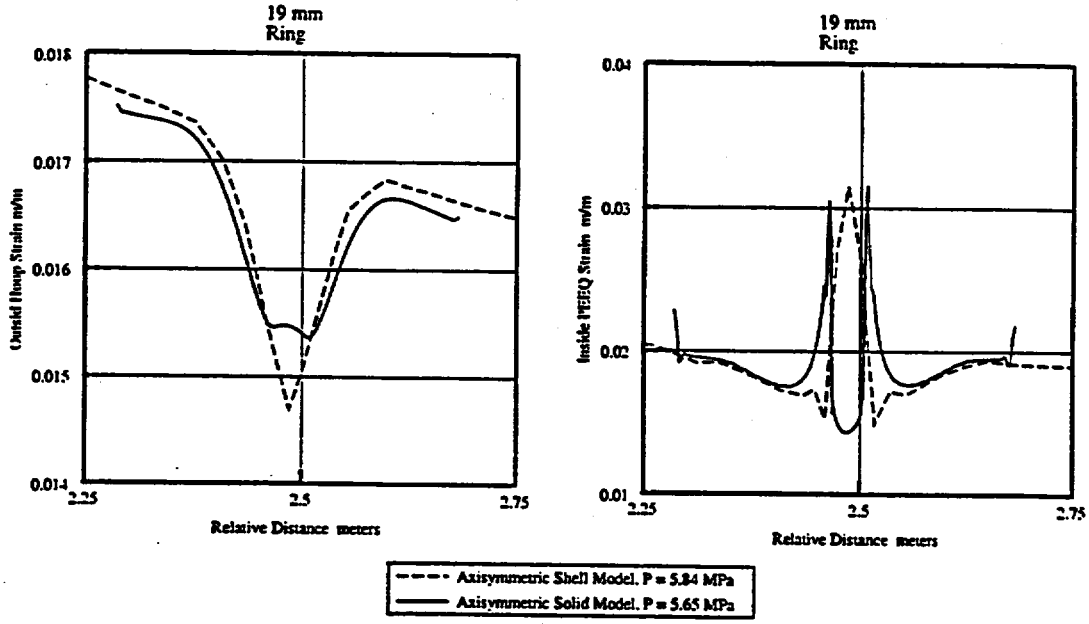

Figure 7.0.4 Lower 19 mm Reinforcement Ring
Outside Hoop Strain and Inside PEEQ Strain versus Distance Along SCV

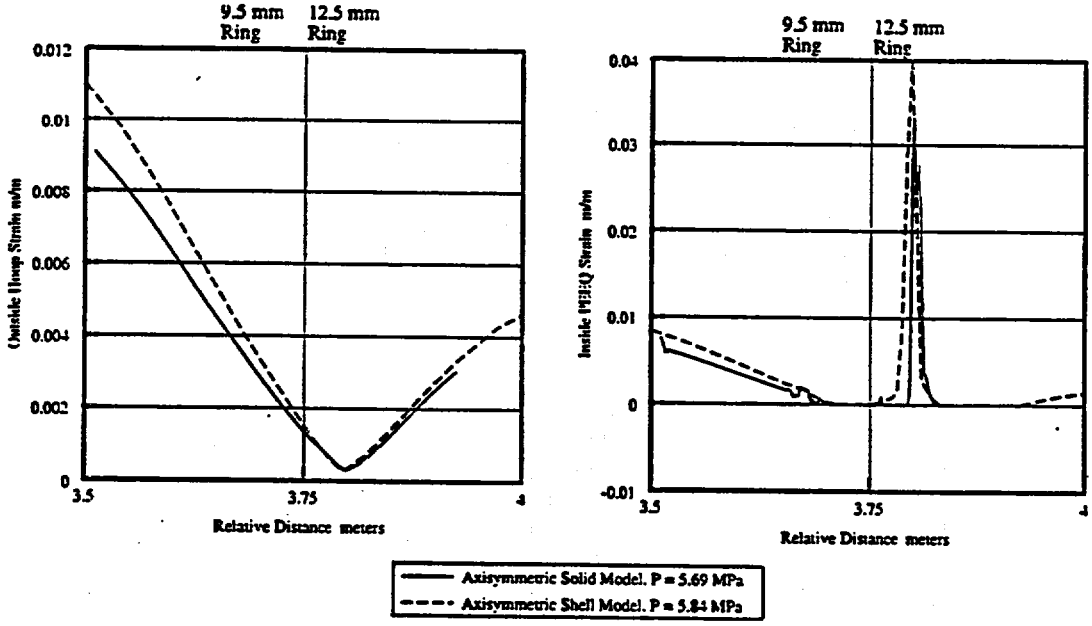

Figure 7.0.5 SPV490 Conical/Cylindrical Shell Interface
Outside Hoop Strain and Inside PEEQ Strain versus Distance Along SCV

8.0 Head Buckling Evaluation :

As the SCV is internally pressurized, compressive hoop strains increase in the lower head region and hence there is a possibility for buckling to occur prior to a material failure of the structure. The buckling response of a spherical shell is also known to be sensitive to imperfections in geometry. Since the type of imperfections are unknown, a typical assumption is that the imperfection in the geometry be defined by the lowest buckling eigenvalues of the structure. This is believed to be the most critical prestressed shape the structure could possess and therefore the most conservative. The maximum compressive hoop strain is at the center of the 166.7 mm radius in the lower head area on the inside surface. Figure 8.0.1, derived from the mean property axisymmetric model (Table 5.0.1 Model No. 5) shows the inside hoop strain as a function of internal pressure. The strain increases up to a pressure of 11 Mpa (1600 psi) and then decreases as the top head is deformed into a purely spherical shape.

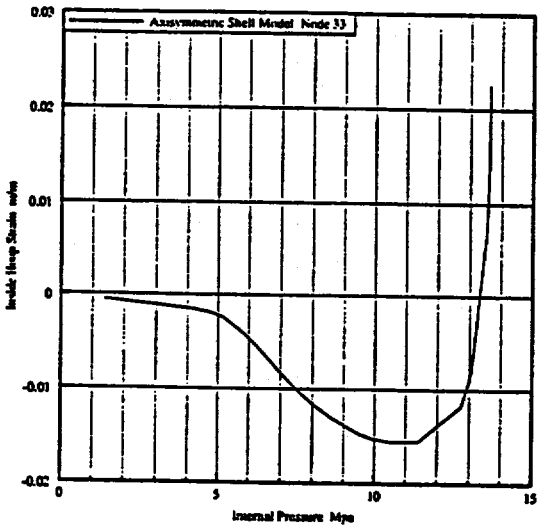

Figure 8.0.1
Maximum Compressive Hoop Strain - Mean Axisymmetric Model 5

To determine the pertinent eigenvector shape or imperfection for the inelastic buckling analysis, a three dimensional shell model of the area on the head which is in compression was developed. Only this portion was modelled, since the goal was to extract the lowest eigenvalue and associated eigenvector in the area under compression. Additions to the model would have caused this lowest buckling mode to shift to more flexible portions of the structure as investigations have proven. Figure 8.0.2 shows the shell model used in the eigenvalue buckling analysis. For these evaluations, design thickness values were used which are below the minimum as-built thicknesses. Boundary conditions are at the top and bottom edges of the shell, solely in the meridian direction. A uniform external pressure load was applied to the shell surface and the lowest buckling mode shape extracted. The mode is a fourteen wave asymmetric shape which is consistent with the results presented in Reference (9).

The mode shape amplitude, by default, was normalized to a maximum value of one. A scaling factor of 0.003 or 50 percent of the head shell thickness was then applied to the displacement response using the Reference (10) program to obtain the perturbed mesh shape. This level of imperfection is believed to be a conservative estimate of any actual as-built geometry. Figure 8.0.3 shows the perturbed mesh model of the head area which is comprised of 2592 three or four noded finite strain elements (S3R, S4R). Pinned boundary conditions at the lower cylinder edge supply stability for the solution. The evaluation was performed up to a pressure of 12.87 Mpa (1870 psi) with no true instabilities reported by the numerical solver nor any instabilities in the displacement response. It is very unlikely that the SCV will be able to obtain such a pressure without a material failure occurring somewhere in the structure due to the high strains that are present. Based on these analyses, the head area has a minimum potential to experience a buckling failure.

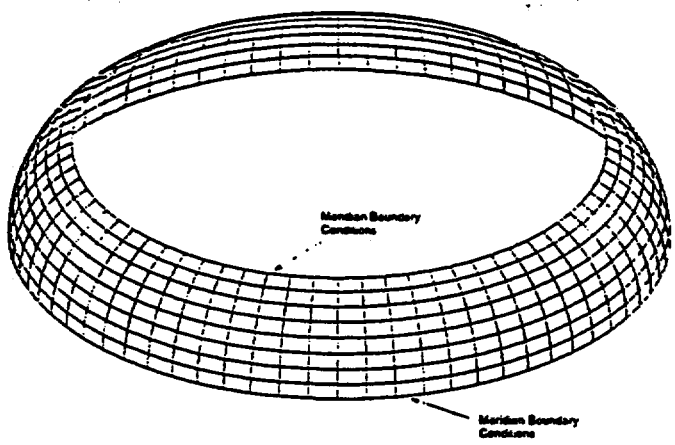

Figure 8.0.2
Eigenvalue Buckling Shell Model of Compression Head Area

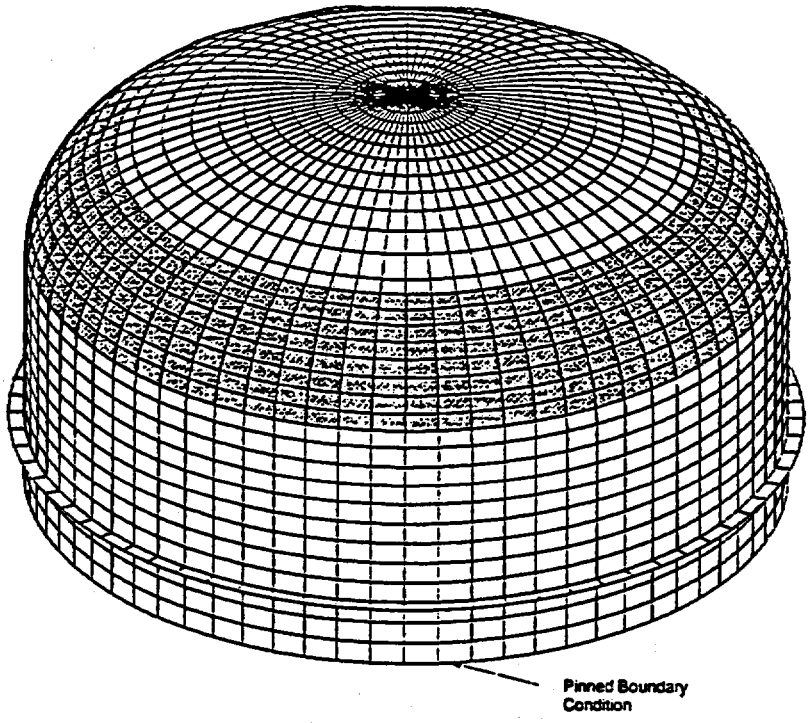

Figure 8.0.3
Inelastic Buckling Shell Model with Perturbed Mesh (Shown in Gray)

9.0 SCV Standard Output Discussion :

In Reference (1), SNL requested all participants to supply response predictions at 39 sensor locations for comparison to test results. The requested data consists of vertical and horizontal displacement response, as well as meridian, hoop and maximum principle strain results. The locations supplied in Reference (1), Table 16 were based on design drawings of the SCV. Notes were provided to relate the gage locations to adjacent stiffeners, welds, the knuckle, the hatch sleeve, etc. In Reference (11), the sensor locations were updated and four additional sensors were added. However, the updated locations were based on the as-bulit elevations for the SCV and the notes supplying relative locations were not updated. The new locations for sensors 11-39 were given as elevations in the global axis system, but the as-built elevations for critical locations such as the knuckle, reinforcement rings, weld joints, etc. were not supplied. The gage location with respect to the adjacent stiffener, weld joint, or knuckle is the critical parameter. Based on the above discussion and conversations with SNL, the relative locations from the Reference (1), Table 16 notes were maintained with the exception of gages 1-10. The locations for these gages were based on the local hatch or head coordinate systems. Since the updated locations were shifted significantly from the Reference (1) locations, and since the locations were based on local coordinate systems, the updated data was used. The as-built data was also used for locations 40-43 since these gages were not supplied in Reference (1). Since the gage locations were estimated, differences, particularly in the transition regions, in the point to point comparisons to the test data are expected.

Results for both the friction (μ= 0.4) and non-friction evaluations are included in the Appendix A Standard Output portion of this report. Mean model geometry, based on the as-built data supplied in Reference (3), was used in all the evaluations. Mean thickness (except for the locally thinned submodel as noted), gap, elastic modulus and plastic strain behavior values were used consistently throughout the various simulations. The softened contact model, previously discussed, was also used exclusively to mitigate solution convergence difficulties.

Table 9.0.1 lists the finite element models which were used for each Plot ID requested. In general, the axisymmetric shell models were used to evaluate free field response data, the axisymmetric solid models were used to evaluate transition areas around stiffener locations or rapid thickness changes and the quarter symmetry shell model and associated submodel of the hatch area were used to evaluate response points in the hatch vicinity.

Category	Plot ID	Output Quantity	Numerical Model	Category	Plot ID	Output Quantity	Numerical Model
Equip. Hatch Area	1	max. prin. strain	3-D shell submodel	Free Field	21	ext. merid.strain	axisymmetric shell
Equip. Hatch Area	2	max. prin. strain	3-D shell submodel	Free Field	22	int. merid.strain	axisymmetric shell
Equip. Hatch Area	3	ext. merid.strain	3-D shell submodel	Free Field	23	ext. hoop strain	axisymmetric shell
Equip. Hatch Area	4	int. merid.strain	3-D shell submodel	Free Field	24	int. hoop strain	axisymmetric shell
Equip. Hatch Area	5	ext. hoop strain	3-D shell submodel*	Free Field	25	ext. merid.strain	3-D shell model
Equip. Hatch Area	6	int. hoop strain	3-D shell submodel*	Free Field	26	int. merid.strain	3-D shell model
Top Head	7	max. prin. strain	axisymmetric shell	Free Field	27	ext. hoop strain	3-D shell model
Top Head	8	ext. hoop strain	axisymmetric shell	Free Field	28	int. hoop strain	3-D shell model
Top Head	9	ext. merid.strain	axisymmetric shell	Free Field	29	int. merid.strain	axisymmetric solid
Top Head	10	int. merid.strain	axisymmetric shell	Free Field	30	int. hoop strain	axisymmetric solid
Transition Regions	11	ext. merid.strain	axisymmetric solid	Free Field	31	int. merid.strain	axisymmetric shell
Transition Regions	12	int. merid.strain	axisymmetric solid	Free Field	32	int. hoop strain	axisymmetric shell
Transition Regions	13	ext. merid.strain	axisymmetric solid	Free Field	33	int. merid.strain	axisymmetric shell
Transition Regions	14	int. merid.strain	axisymmetric solid	Free Field	34	int. hoop strain	axisymmetric shell
Transition Regions	15	ext. merid.strain	axisymmetric solid	Displacements	35	vertical	axisymmetric shell
Transition Regions	16	int. merid.strain	axisymmetric solid	Displacements	36	horizontal	axisymmetric solid
Transition Regions	17	ext. merid.strain	axisymmetric shell	Displacements	37	horizontal	axisymmetric solid
Transition Regions	18	int. merid.strain	axisymmetric shell	Displacements	38	vertical	axisymmetric solid
Transition Regions	19	ext. merid.strain	axisymmetric solid	Displacements	39	horizontal	3-D shell model
Transition Regions	20	int. merid.strain	axisymmetric solid	Equip. Hatch Area	40	int. merid.strain	3-D shell submodel *
				Equip. Hatch Area	41	int. hoop strain	3-D shell submodel *
				Equip. Hatch Area	42	int. merid.strain	3-D shell submodel *
				Equip. Hatch Area	43	int. hoop strain	3-D shell submodel *

Table 9.0.1 Standard Output Model Identification
(* locally thinned shell submodel).

10.0 Key Results (First Yield, First Contact, Critical Areas)

This section discuses the predicted results associated with certain key events that occur during the pressurization of the SCV, as well as the identification of highly strained areas on the SCV.

The SCV has a design pressure of 0.78 Mpa (113 psi) based on the design pressure of the full scale steel containment vessel from which the SCV is based. To determine the first yield pressure and location, all analytical models previously presented were reviewed to identify the critical areas of the SCV. The first yield pressure is based on a Von-Mises stress intensity as compared to the minimum yield limit stress specified in Reference (2) for the SGV480 (σ_y=265.0 Mpa) and SPV490 (σ_y=490.0 Mpa) steels. As tested material properties were not used for this evaluation, therefore the estimates of yield pressure are conservative due to the use of minimum yield stress values. First yield pressure occurs at a pressure of 1.0 Mpa (145 psi) as determined by the mean gap opening axisymmetric solid model of the knuckle region (Figure 4.1.2). The maximum Von-Mises stress occurs at the bottom of the knuckle on the outside surface. Yielding also occurs at a slightly higher pressure of 1.3 Mpa (190 psi) where the material interface weld intersects the hatch reinforcement ring. This evaluation is from the mean thickness shell submodel of the equipment hatch area (Figure 4.2.2). Local thinning of the plate, as defined in the as-built conditions of Reference (3), may reduce this first yield pressure to as low as 1.1 Mpa (160 psi).

First contact between the SCV and the CS occurs in the knuckle region at a pressure of 3.2 Mpa (470 psi) as determined from the mean gap opening axisymmetric solid model. This model is the best average estimate of the as-built conditions of the SCV and CS and therefore these results represent an average estimate and not a minimum estimate of the first contact pressure. The less refined, quarter symmetry shell model (Figure 4.2.1) first contact prediction was approximately 3.5 Mpa (500 psi). This small difference in results (~6.0 %) can also be attributed to the different load increments which were used in each of the respective analyses. The propagation of contact, as the internal pressure is increased, is further discussed and illustrated in Section 6.0.

There are a number of critical areas in the SCV which are possible locations of failure. No material failure algorithm is readily available in the ABAQUS/Standard Finite Element Program which was used throughout this pretest evaluation. Since the loading is quasi-static, and the SCV is a complex welded structure, it is believed that such an automatic material failure model is unnecessary. Instead, the material minimum ultimate strain limit, which represents a material's point of ductile instability (necking), was chosen as an appropriate starting point for an assessment of a critical failure pressure. This ultimate limit would be subsequently reduced by a factor based on variations in analytical results derived from parametric investigations. A numerical technique which was originally intended for an objective comparison of time history data (Reference (12)) was used to derive average reduction factors for differences in response prediction over the SCV surface. For example, a comparison of mean gap versus maximum gap results data (Figure 5.0.1) results in an average difference of approximately 10.0% along the surface of the SCV. A reasonable reduction factor for the ultimate strain value for this parametric variation would therefore be 1.10. Similarly, reductions for thickness and friction variation would be approximately 1.10 and 1.02. The thickness reduction factor does not include the local thinning around the equipment hatch reinforcement plate since this detail was not modelled in the axisymmetric evaluations. The local thinning around the hatch was evaluated separately by a shell submodel with minimum plate thickness near the equipment hatch reinforcement plate. The friction reduction factor was derived from a comparison of the $\mu = 0.4$ and $\mu = 0.2$ evaluations since a zero friction case is improbable.

Additional reductions in the ultimate strain value would be based on unknowns in the as-built structural details such as quality of construction, weld defects and surface flaws. A mean reduction factor of 1.10 was used in Reference (13) to account for these types of unknowns and will be used here as well. Further reductions due to material variability were not performed since mean as-tested material properties were used in the numerical simulation, but minimum ultimate strain limits were used in the evaluation of the peak equivalent plastic strains. The analytical models, in varying degrees, capture the critical geometric characteristics of the SCV and CS. Since the more refined models are used in assessing the peak plastic strains, no reductions were performed for the level of analysis detail.

A review of plots which depict maximum equivalent plastic strains versus internal pressure would be prudent to insure that relatively stable behavior is also present at the reduced ultimate strain limit. Figure 10.0.1 illustrates the rapid increases in strain which can occur with a relatively small increase in pressure. This result was taken from the mean shell submodel,

Figure 4.2.2, near the material interface line and hatch reinforcement plate area. Figures 10.0.2 through 10.0.4 show critical areas of equivalent plastic strain concentration in the knuckle region, the intersection of the cylinder and conical shell and the equipment hatch area. Note that the appearance of the penetration of the SCV into the CS, as shown in Figure 10.0.2, is from the softened contact model, which in a general sense, approximates the compression of the SCV painted surface. Based on these evaluations, the equipment hatch area appears to be the most susceptible to failure due to the lower ultimate strain limit of SPV490 steel as well as the significant hoop strains which are present. In addition, Reference (3) identified local thinning of the SPV490 and SGV480 steel plate in the vicinity of the equipment hatch. To address the effects of the plate thinning, a shell submodel with the minimum plate thickness measured for the respective materials was developed. The thickness of several elements was reduced to 7.4 mm (9.0 mm design thickness) for the SPV490 steel and 7.6 mm (8.5 mm design thickness) for the SGV480 steel.

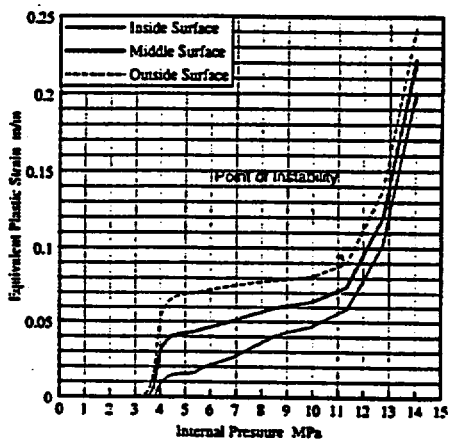

Figure 10.0.1 Representative Equivalent Plastic Strain History
Mean Shell Submodel - Friction = 0.4 - SPV490 Material

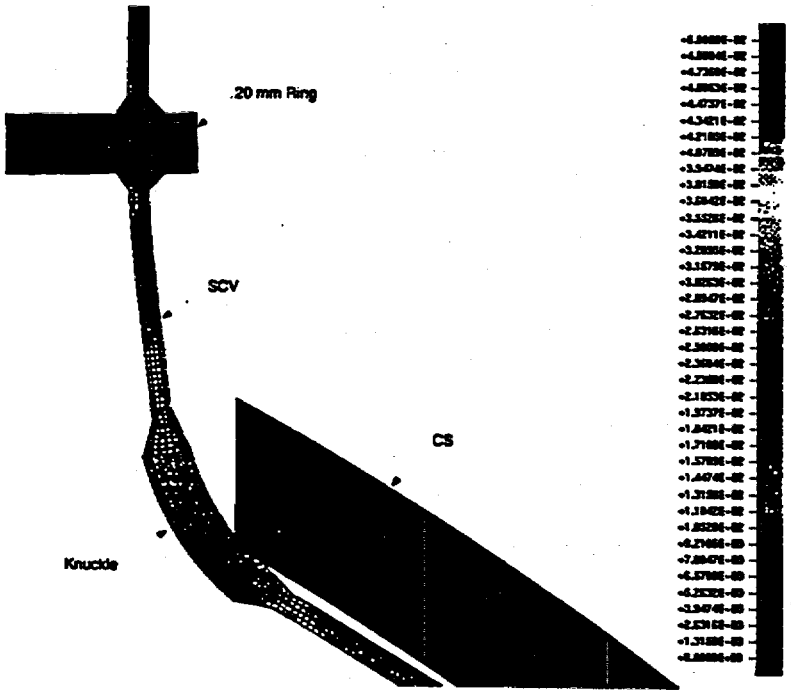

Figure 10.0.2 Deformed Fringe Contour Plot of the Mean Model Knuckle Region
PEEQ Strain - P = 6.97 Mpa (1010 psi) - Deformed Scale = 1.0

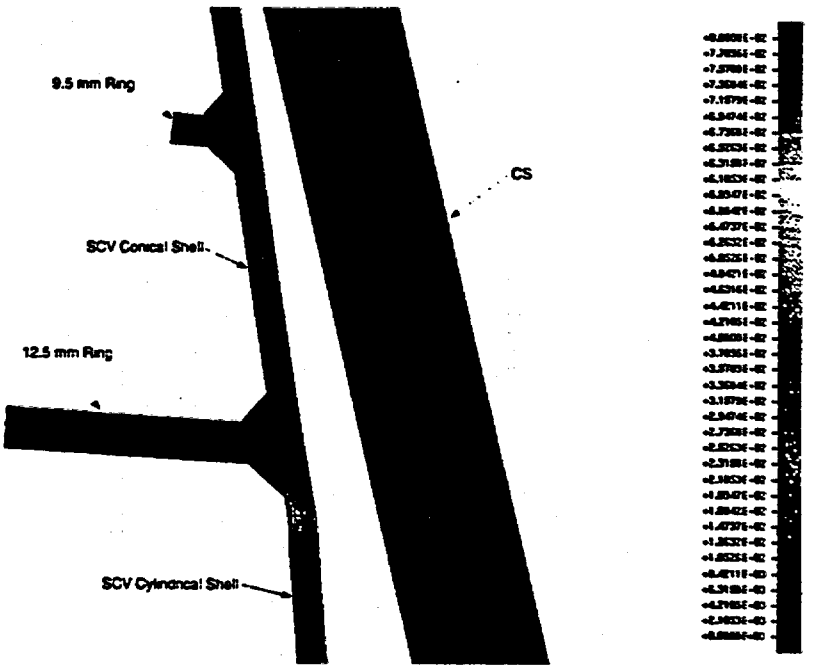

Figure 10.0.3 Deformed Fringe Contour Plot of the Mean Model Conical/Cylindrical Shell Interface
PEEQ Strain - P = 6.90 Mpa (1000 psi) - Deformed Scale = 1.0

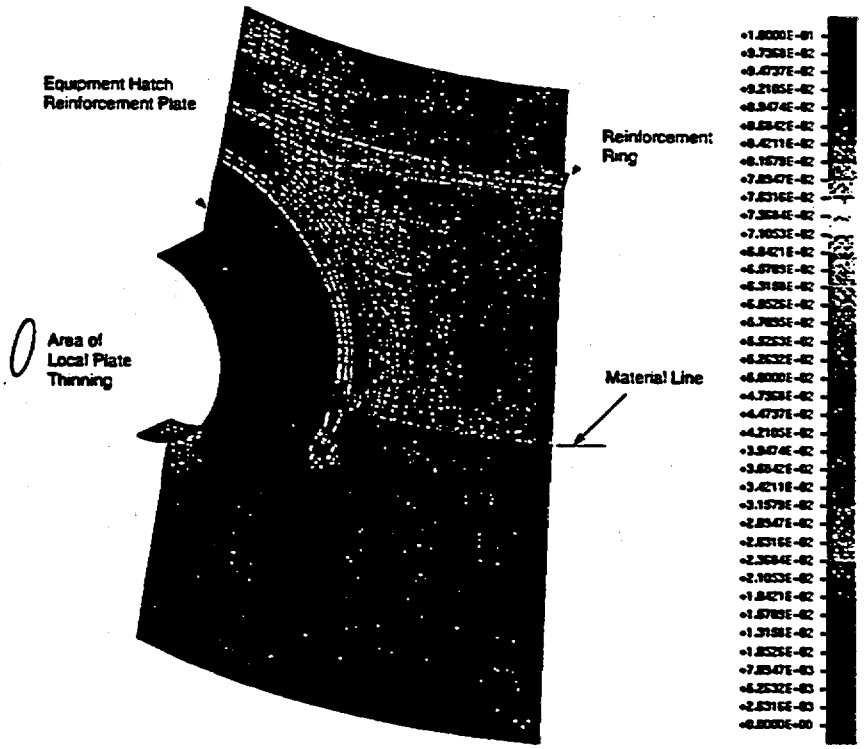

Figure 10.0.4 Deformed Fringe Contour Plot of the Locally Thinned SCV Submodel of the Equipment Hatch Area
PEEQ Strain - P = 6.90 Mpa (1000 psi) - Deformed Scale = 1.0

The local plate thinning had a significant effect on the concentrated equivalent plastic strains. While the model conservatively utilized the minimum thickness value for the thinned area, it does show the sensitivity of this area to the as-built conditions. Figure 10.0.5 shows a comparison of equivalent plastic strains (PEEQ) between the mean thickness shell submodel and the locally thinned shell model for the SPV490 material in the locally thinned area identified in Figure 10.0.4.

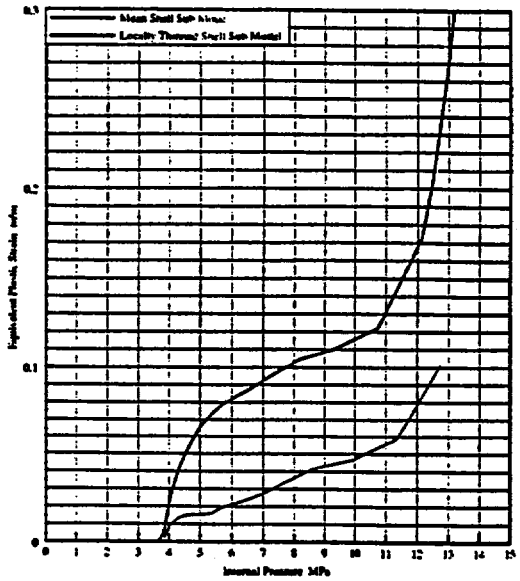

Figure 10.0.5 Comparison of Mean Thickness Shell Model to Locally Thinned Shell Model
Equivalent Plastic Strain versus Internal Pressure
SPV490 Material - Inside Surface

11.0 Conclusions

The response predictions at the standard output locations represent mean value data and therefore may be either conservative or unconservative as compared to the test response data. This is particularly true for the evaluations which include friction which are considered to be more representative of actual test conditions. The parametric evaluations which were performed using variations in gap distance, plate thickness and contact location illustrate the level of deviation between predicted response and test data which can be expected.

Section 10.0 presented several critical areas in which failure of the SCV could initiate. This does not, however, preclude failure in other areas of the SCV which may be caused by unknown as-built conditions such as poor weld penetration. The maximum pressure level prediction for which there is a high conficence (>95%) that there is a low probability of failure (<1%). as requested in Reference (1), is submitted under separate cover to insure anonymity.

References:

(1) Sandia National Laboratories Submittal.10 July 1995.

(2) Sandia National Laboratories Submittal, 21 September 1995.

(3) Sandia National Laboratories Submittal, 20 February 1996, SO-96-012.

(4) ABAQUS/Standard User's Manual, Hibbitt. Karlsson & Sorenson, Inc. Version 5.5, 1995.

(5) Math/Library User's Manual, IMSL, Version 1.0. April 1987.

(6) ABAQUS Theory Manual. Hibbitt, Karlsson & Sorenson, Inc, Version 5.5, 1995.

(7) Avallone. E.A. and Theodore Baumeister III. Marks' Standard Handbook for Mechanical Engineers, 9th Ed., McGraw-Hill, Inc., New York, 1978.

(8) ASTM D217. "Molykote Specialty Lubricants".

(9) Wu. M.T. and Shun Cheng, "Nonlinear Asymmetric Buckling of Truncated Spherical Shells," Journal of Applied Mechanics, pp. 651-660, September 1970.

(10) ABAQUS Verification Manual, Hibbitt, Karlsson & Sorenson, Inc, Version 5.5, 1995.

(11) Sandia National Laboratories Submittal, 9 May 1996, SO-96-041.

(12) Geers, Thomas L., "An Objective Error Measure for the Comparison of Calculated and Measured Transient Response Histories," The Shock and Vibration Bulletin, Bulletin 54, Part2, June 1984.

(13) Sammataro. R.F., W.R. Solonick, and N.W. Edwards, "Acceptance Criteria for Steel Containments Under Severe Accident Loads," ASME Codes and Standards in a Global Environment. PVP-Vol. 259, 1993.

Enclosure (2) to:
415:TFT/603039/3.8

Appendix A Standard Output Plots

Electric Boat Corporation

June 3, 1996

APPENDIX A

STANDARD OUTPUT

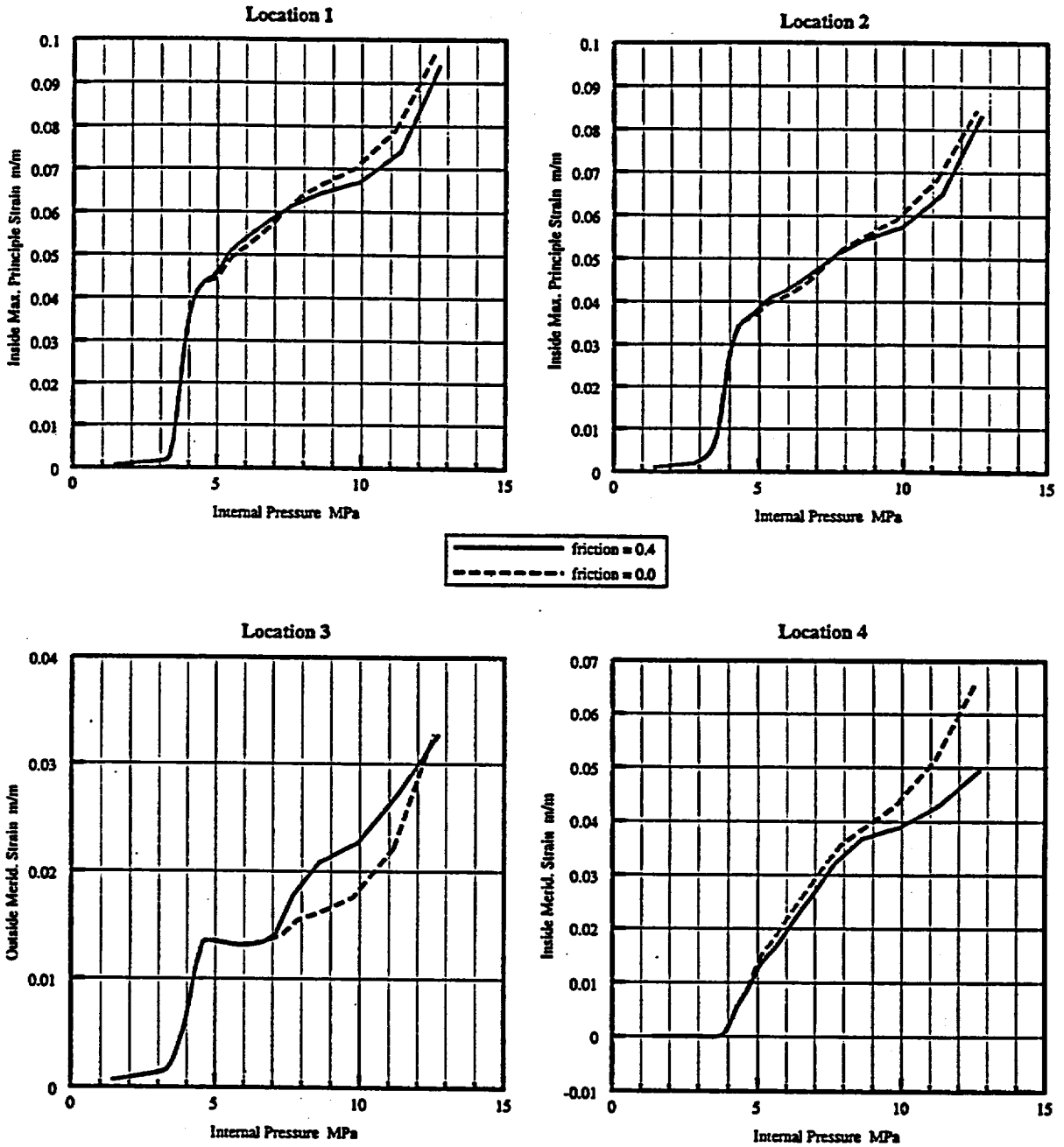
Location 1
Inside Max. Principle Strain m/m
0.1
0.09
0.08
0.07
0.06
0.05
0.04
0.03
0.02
0.01
0
0
5
10
15
Internal Pressure MPa
Location 2
Inside Max. Principle Strain m/m
0.1
0.09
0.08
0.07
0.06
0.05
0.04
0.03
0.02
0.01
0
0
5
10
15
Internal Pressure MPa
friction = 0.4
friction = 0.0
Location 3
Outside Meridl. Strain m/m
0.04
0.03
0.02
0.01
0
0
5
10
15
Internal Pressure MPa
Location 4
Inside Meridl. Strain m/m
0.07
0.06
0.05
0.04
0.03
0.02
0.01
0
-0.01
0
5
10
15
Internal Pressure MPa

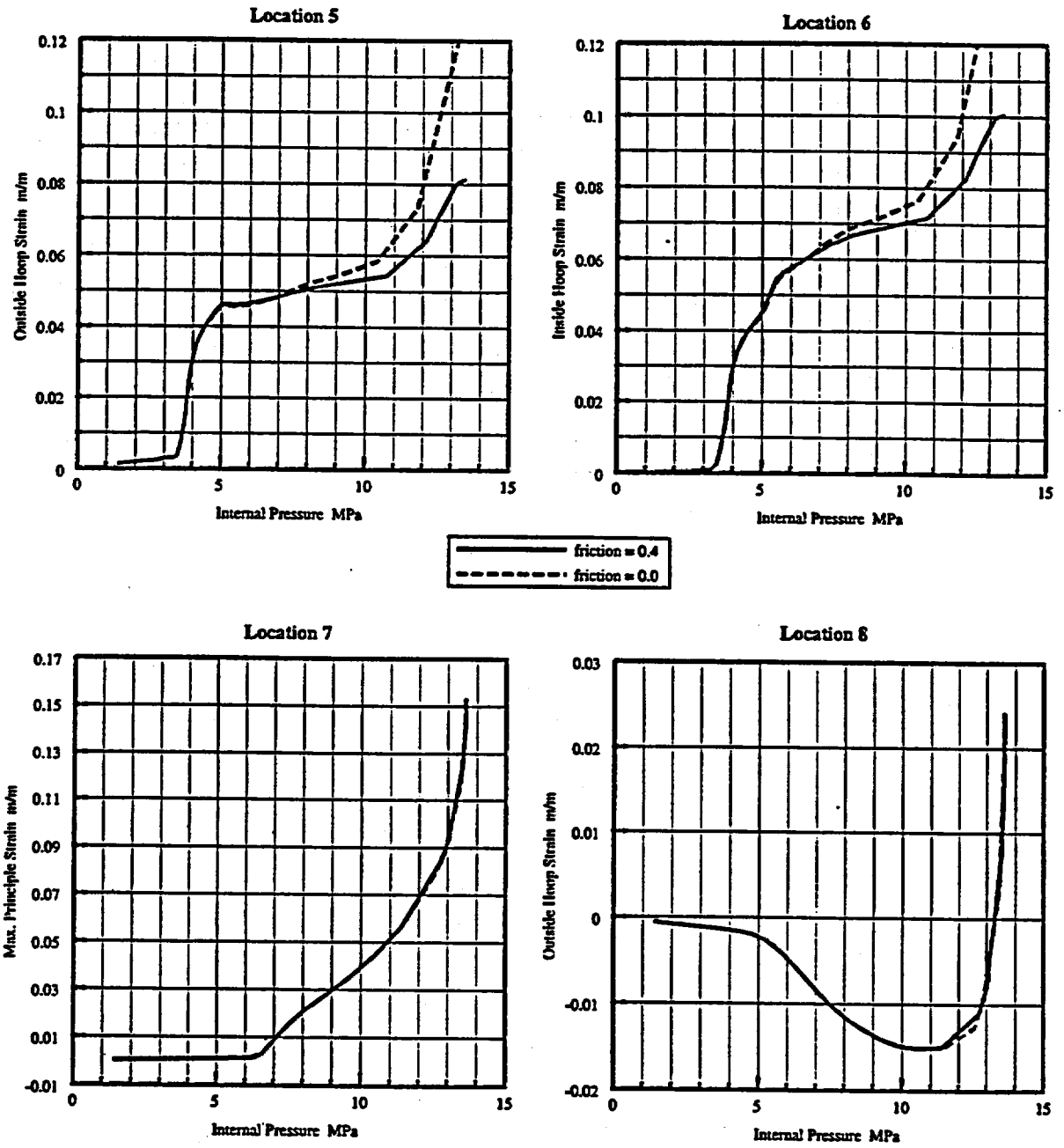
Location 5
Outside Hoop Strain m/m
0.12
0.1
0.08
0.06
0.04
0.02
0
0
5
10
15
Internal Pressure MPa
Location 6
Inside Hoop Strain m/m
0.12
0.1
0.08
0.06
0.04
0.02
0
0
5
10
15
Internal Pressure MPa
friction = 0.4
friction = 0.0
Location 7
Max. Principle Strain m/m
0.17
0.15
0.13
0.11
0.09
0.07
0.05
0.03
0.01
-0.01
0
5
10
15
Internal Pressure MPa
Location 8
Outside Hoop Strain m/m
0.03
0.02
0.01
0
-0.01
-0.02
0
5
10
15
Internal Pressure MPa

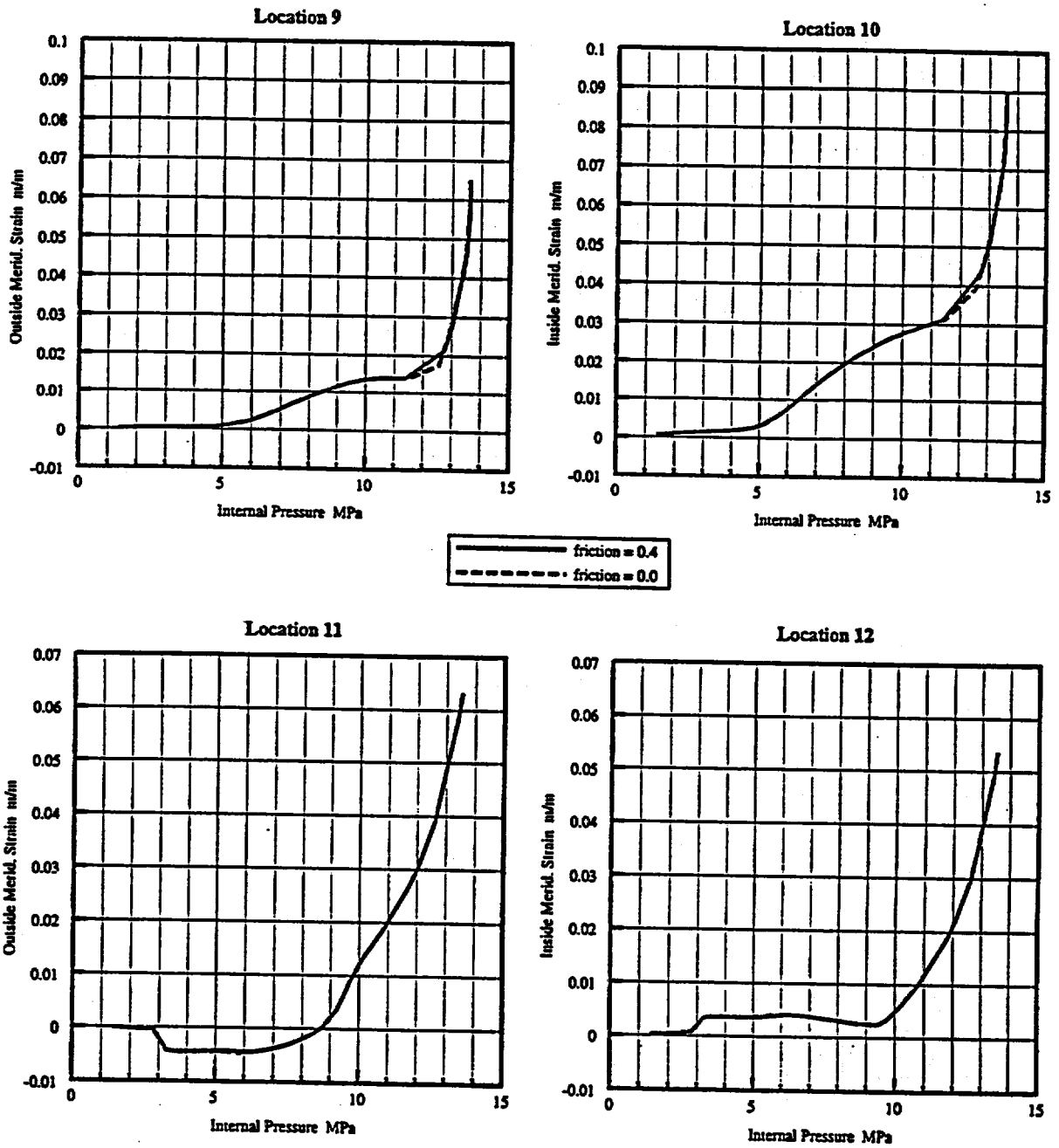
Location 9
Outside Merid. Strain m/m
0.1
0.09
0.08
0.07
0.06
0.05
0.04
0.03
0.02
0.01
0
-0.01
0
5
10
15
Internal Pressure MPa
Location 10
Inside Merid. Strain m/m
0.1
0.09
0.08
0.07
0.06
0.05
0.04
0.03
0.02
0.01
0
-0.01
0
5
10
15
Internal Pressure MPa
friction = 0.4
friction = 0.0
Location 11
Outside Merid. Strain m/m
0.07
0.06
0.05
0.04
0.03
0.02
0.01
0
-0.01
0
5
10
15
Internal Pressure MPa
Location 12
Inside Merid. Strain m/m
0.07
0.06
0.05
0.04
0.03
0.02
0.01
0
-0.01
0
5
10
15
Internal Pressure MPa

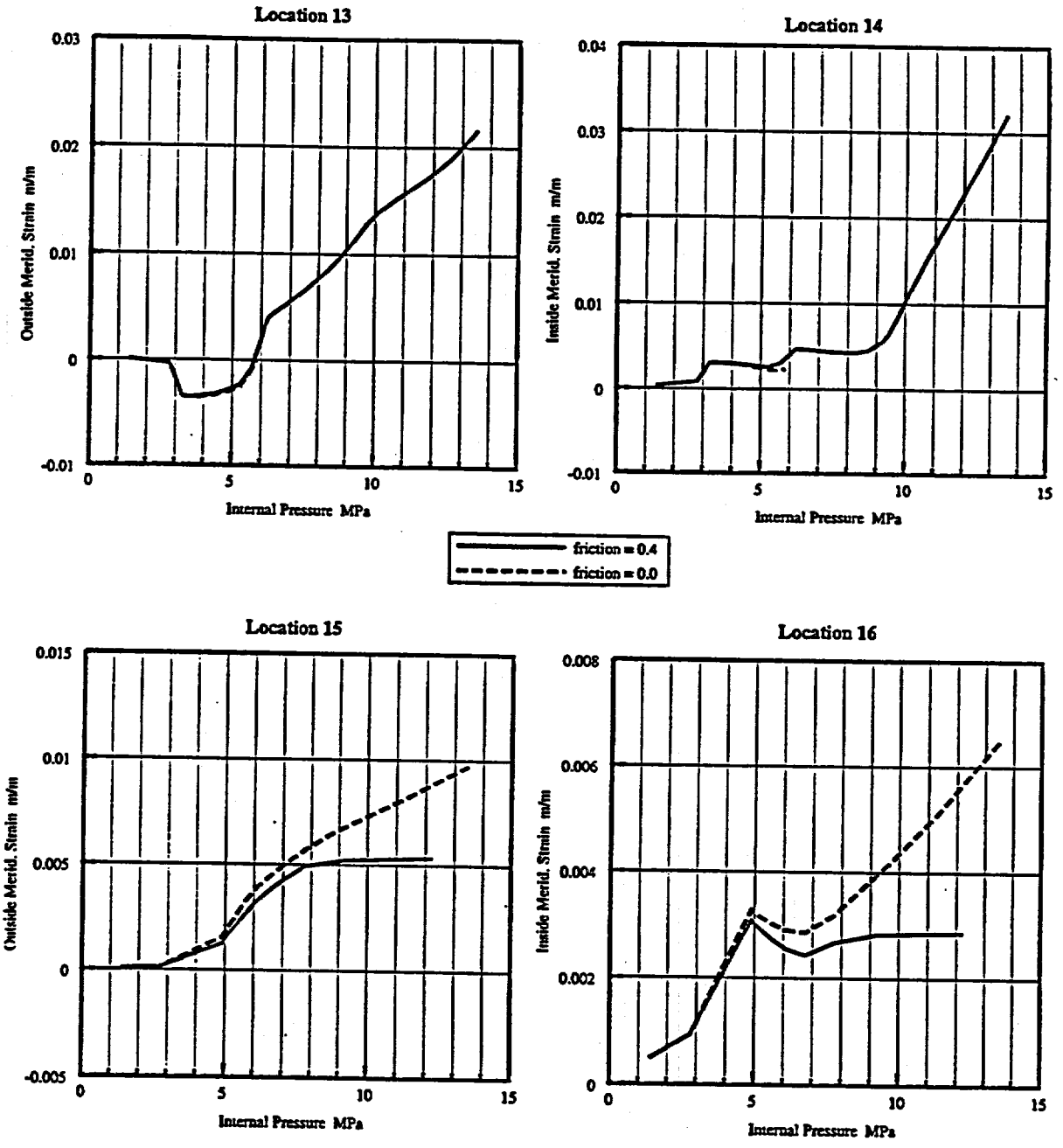
Location 13
Outside Meridl. Strain m/m
0.03
0.02
0.01
0
-0.01
0
5
10
15
Internal Pressure MPa
Location 14
Inside Meridl. Strain m/m
0.04
0.03
0.02
0.01
0
-0.01
0
5
10
15
Internal Pressure MPa
friction = 0.4
friction = 0.0
Location 15
Outside Meridl. Strain m/m
0.015
0.01
0.005
0
-0.005
0
5
10
15
Internal Pressure MPa
Location 16
Inside Meridl. Strain m/m
0.008
0.006
0.004
0.002
0
0
5
10
15
Internal Pressure MPa

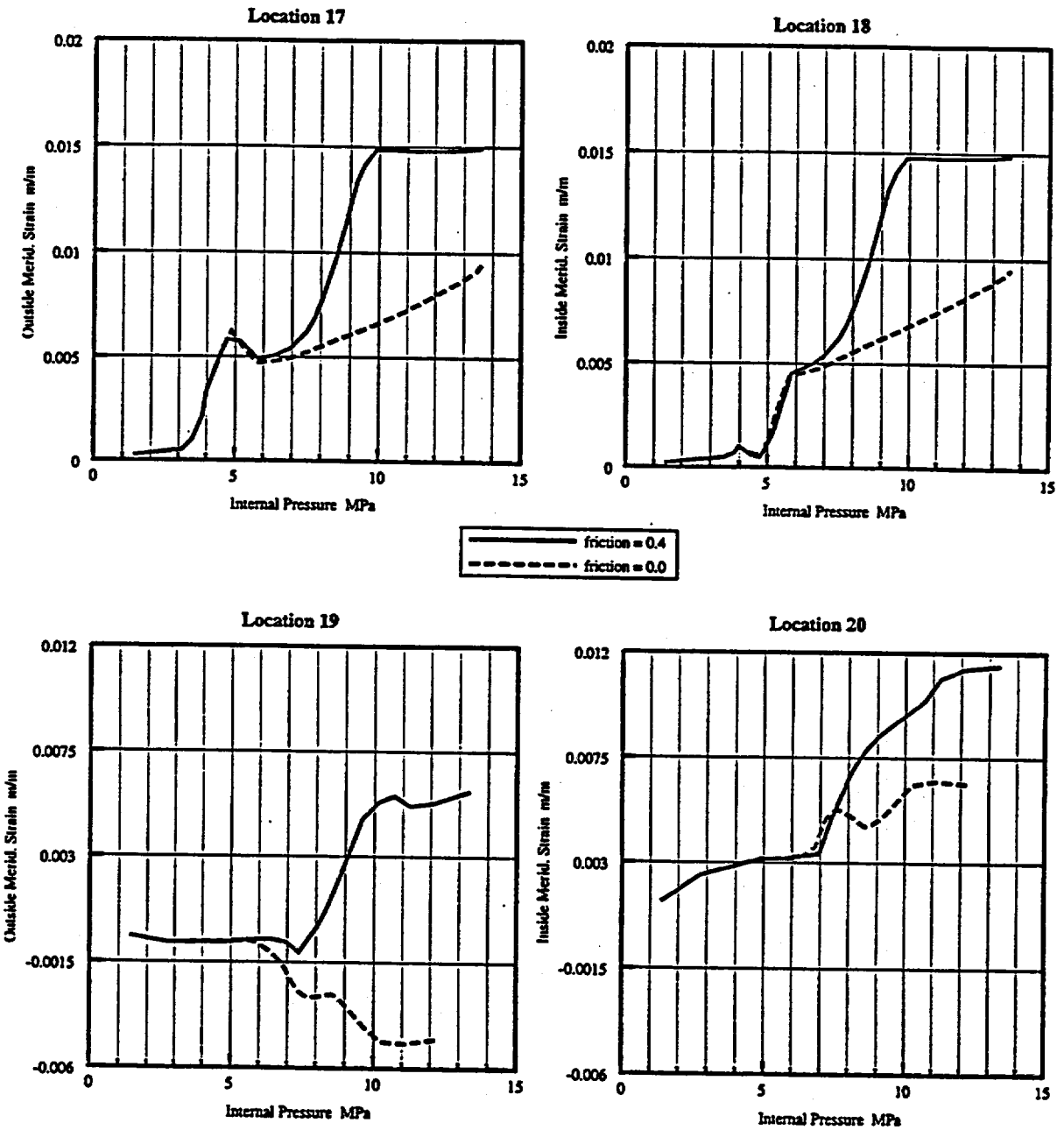
Location 17
Location 18
Location 19
Location 20
Outside Meridl. Strain m/m
Inside Meridl. Strain m/m
Internal Pressure MPa
friction = 0.4
friction = 0.0
0.02
0.015
0.01
0.005
0
0.012
0.0075
0.003
-0.0015
-0.006
5
10
15

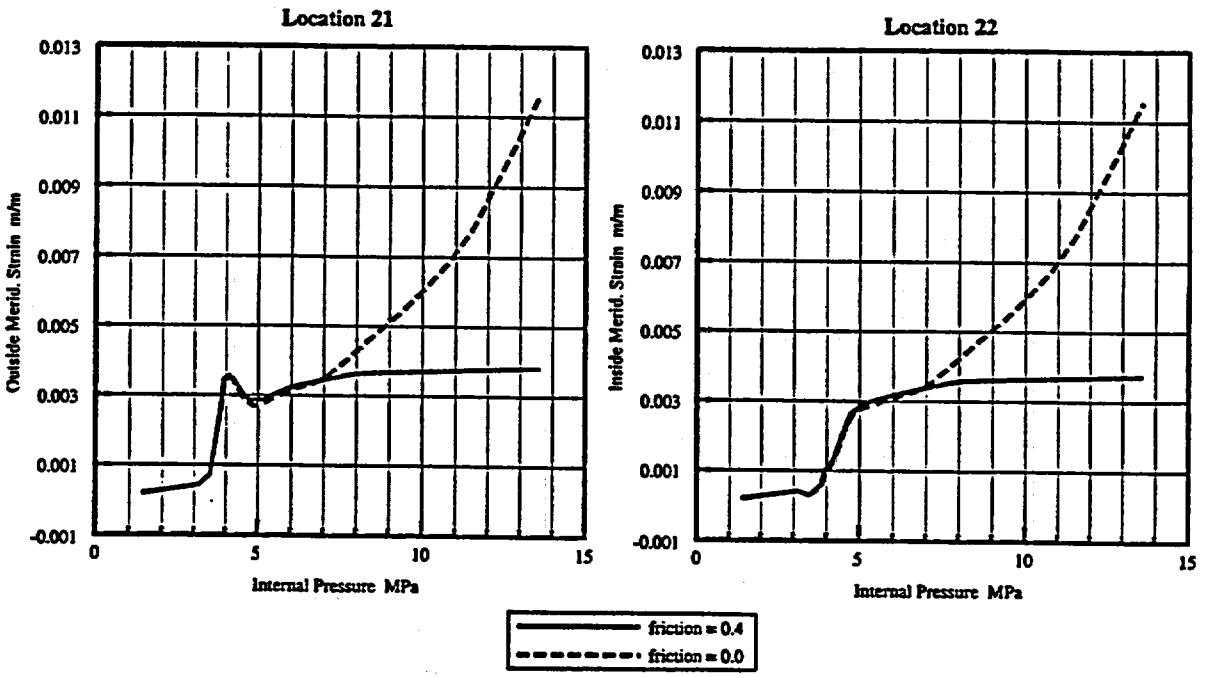
Location 21
Outside Meridional Strain m/m
0.013
0.011
0.009
0.007
0.005
0.003
0.001
-0.001
0
5
10
15
Internal Pressure MPa
Location 22
Inside Meridional Strain m/m
0.013
0.011
0.009
0.007
0.005
0.003
0.001
-0.001
0
5
10
15
Internal Pressure MPa
friction = 0.4
friction = 0.0

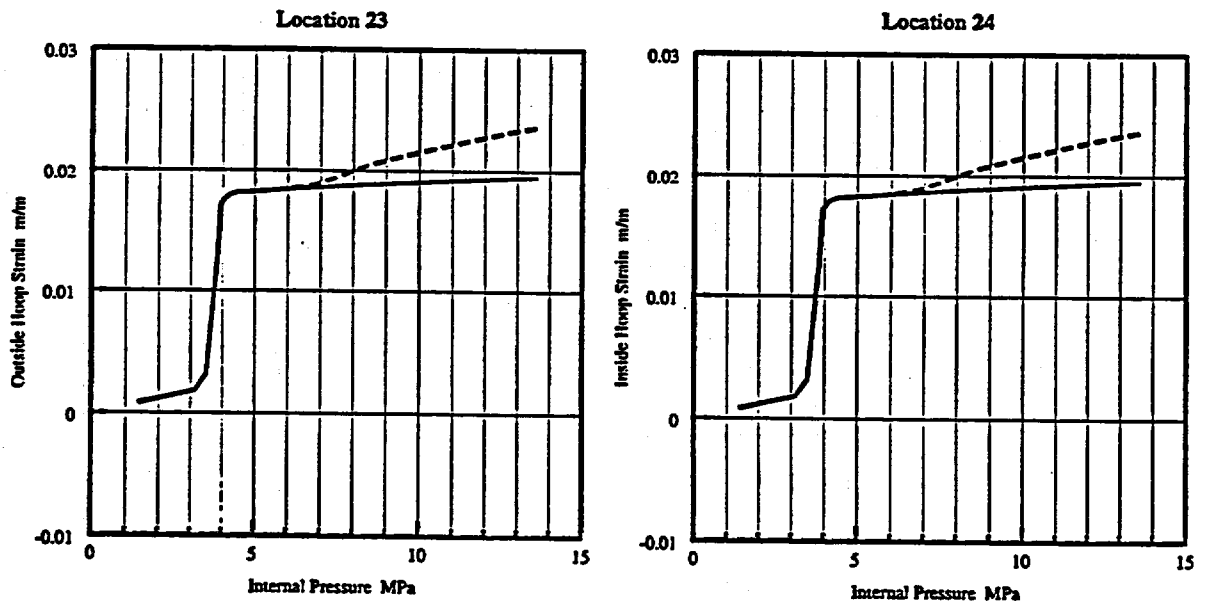
Location 23
Outside Hoop Strain m/m
0.03
0.02
0.01
0
-0.01
0
5
10
15
Internal Pressure MPa
Location 24
Inside Hoop Strain m/m
0.03
0.02
0.01
0
-0.01
0
5
10
15
Internal Pressure MPa

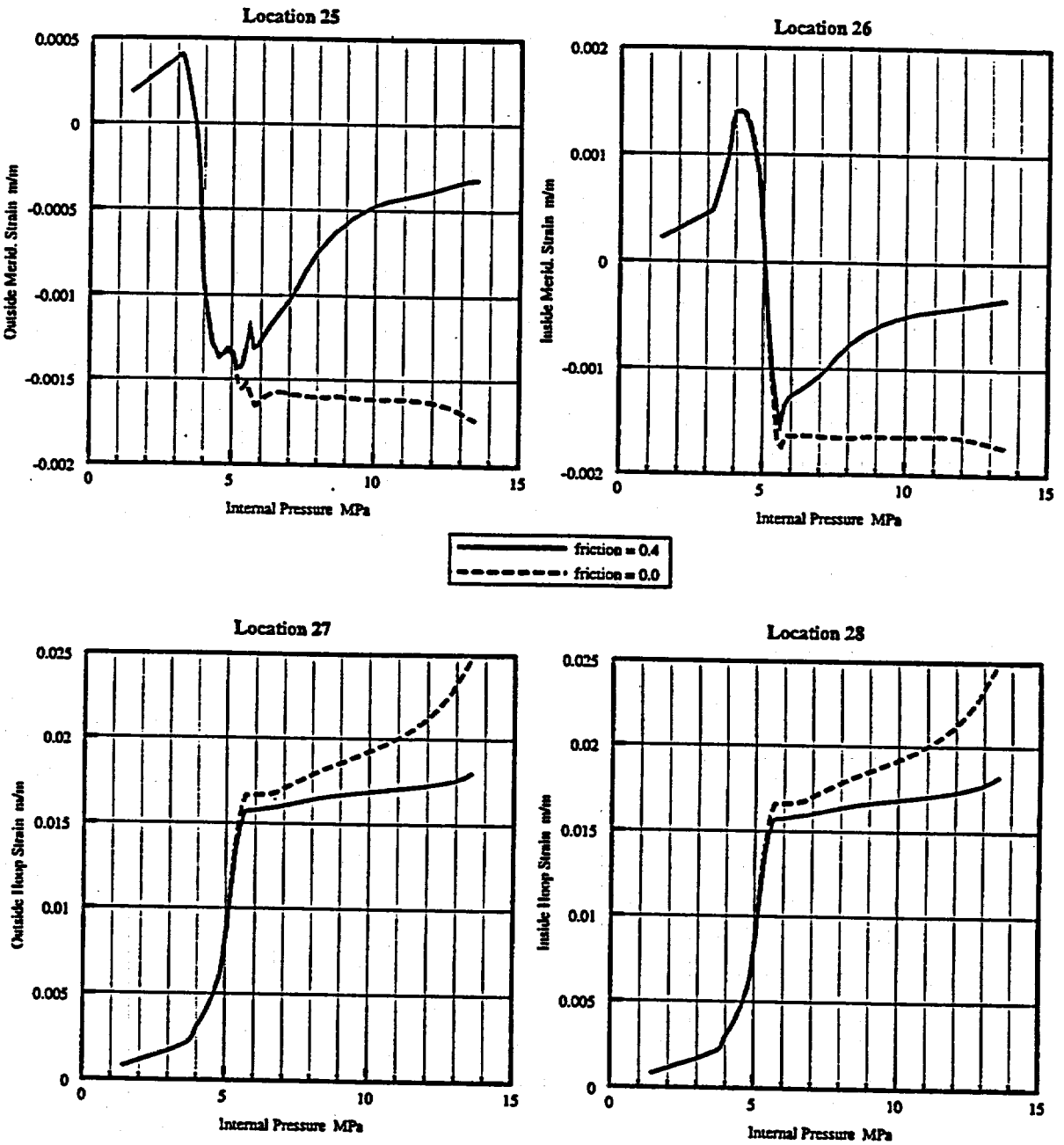
Location 25
Outside Meridl. Strain m/m
0.0005
0
-0.0005
-0.001
-0.0015
-0.002
0
5
10
15
Internal Pressure MPa
Location 26
Inside Meridl. Strain m/m
0.002
0.001
0
-0.001
-0.002
0
5
10
15
Internal Pressure MPa
friction = 0.4
friction = 0.0
Location 27
Outside Hoop Strain m/m
0.025
0.02
0.015
0.01
0.005
0
0
5
10
15
Internal Pressure MPa
Location 28
Inside Hoop Strain m/m
0.025
0.02
0.015
0.01
0.005
0
0
5
10
15
Internal Pressure MPa

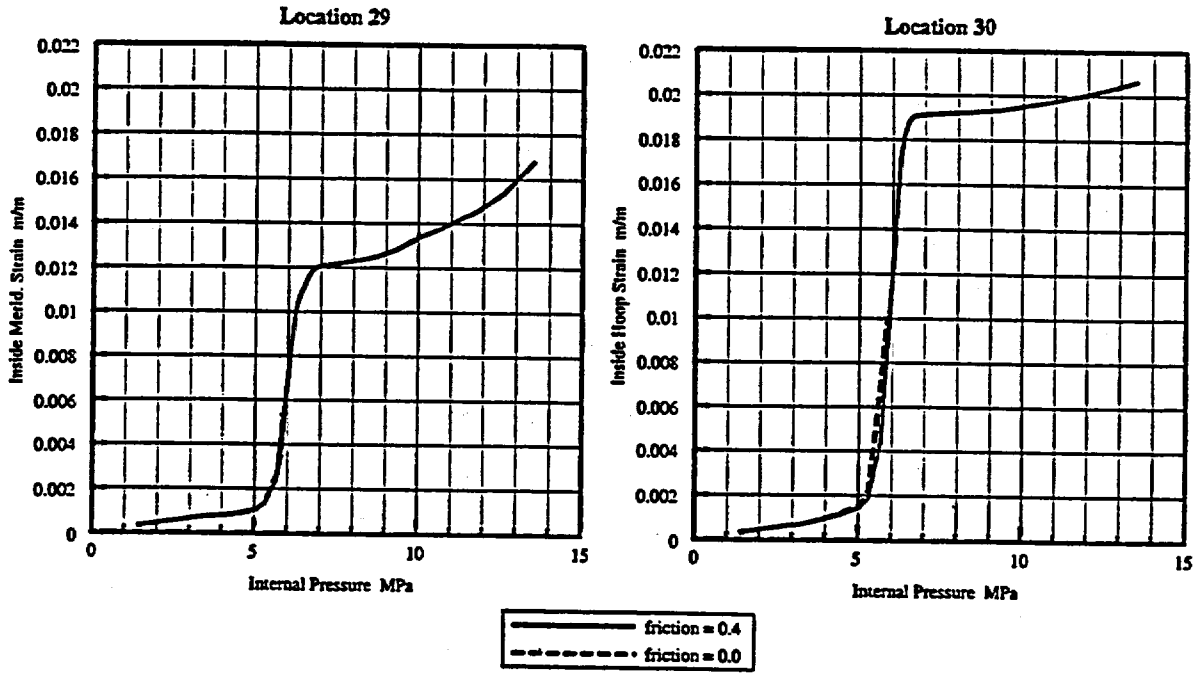
Location 29
Inside Merid. Strain m/m
0.022
0.02
0.018
0.016
0.014
0.012
0.01
0.008
0.006
0.004
0.002
0
0
5
10
15
Internal Pressure MPa
Location 30
Inside Hoop Strain m/m
0.022
0.02
0.018
0.016
0.014
0.012
0.01
0.008
0.006
0.004
0.002
0
0
5
10
15
Internal Pressure MPa
friction = 0.4
friction = 0.0
Location 31
Inside Merid. Strain m/m
0.013
0.011
0.009
0.007
0.005
0.003
0.001
-0.001
0
5
10
15
Internal Pressure MPa
Location 32
Inside Hoop Strain m/m
0.03
0.025
0.02
0.015
0.01
0.005
0
0
5
10
15
Internal Pressure MPa

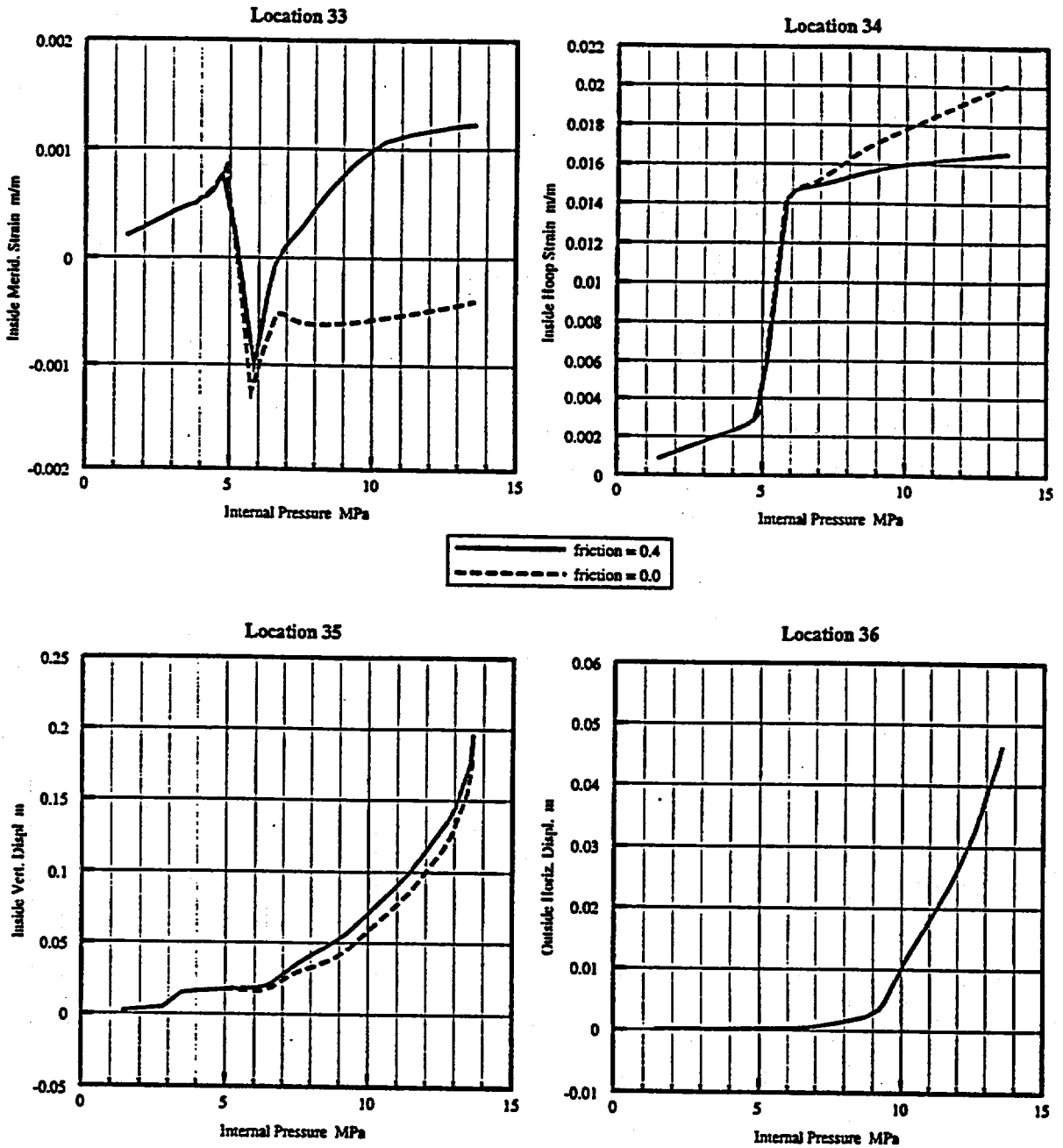
Location 33
Inside Merid. Strain m/m
0.002
0.001
0
-0.001
-0.002
0
5
10
15
Internal Pressure MPa
Location 34
Inside Hoop Strain m/m
0.022
0.02
0.018
0.016
0.014
0.012
0.01
0.008
0.006
0.004
0.002
0
0
5
10
15
Internal Pressure MPa
friction = 0.4
friction = 0.0
Location 35
Inside Vert. Displ. m
0.25
0.2
0.15
0.1
0.05
0
-0.05
0
5
10
15
Internal Pressure MPa
Location 36
Outside Horiz. Displ. m
0.06
0.05
0.04
0.03
0.02
0.01
0
-0.01
0
5
10
15
Internal Pressure MPa

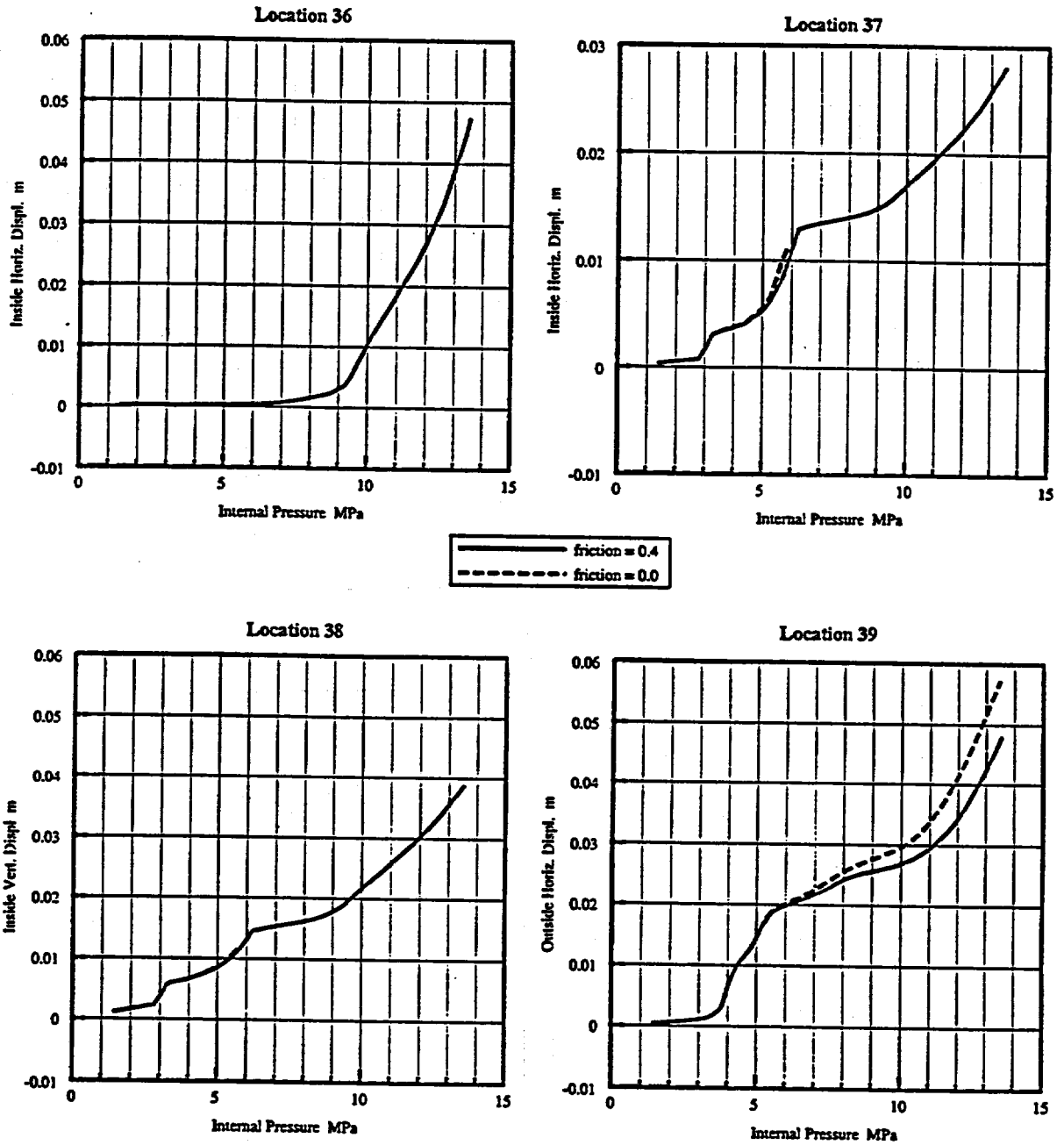
Location 36
Inside Horiz. Displ. m
0.06
0.05
0.04
0.03
0.02
0.01
0
-0.01
0
5
10
15
Internal Pressure MPa
Location 37
Inside Horiz. Displ. m
0.03
0.02
0.01
0
-0.01
0
5
10
15
Internal Pressure MPa
friction = 0.4
friction = 0.0
Location 38
Inside Vert. Displ. m
0.06
0.05
0.04
0.03
0.02
0.01
0
-0.01
0
5
10
15
Internal Pressure MPa
Location 39
Outside Horiz. Displ. m
0.06
0.05
0.04
0.03
0.02
0.01
0
-0.01
0
5
10
15
Internal Pressure MPa

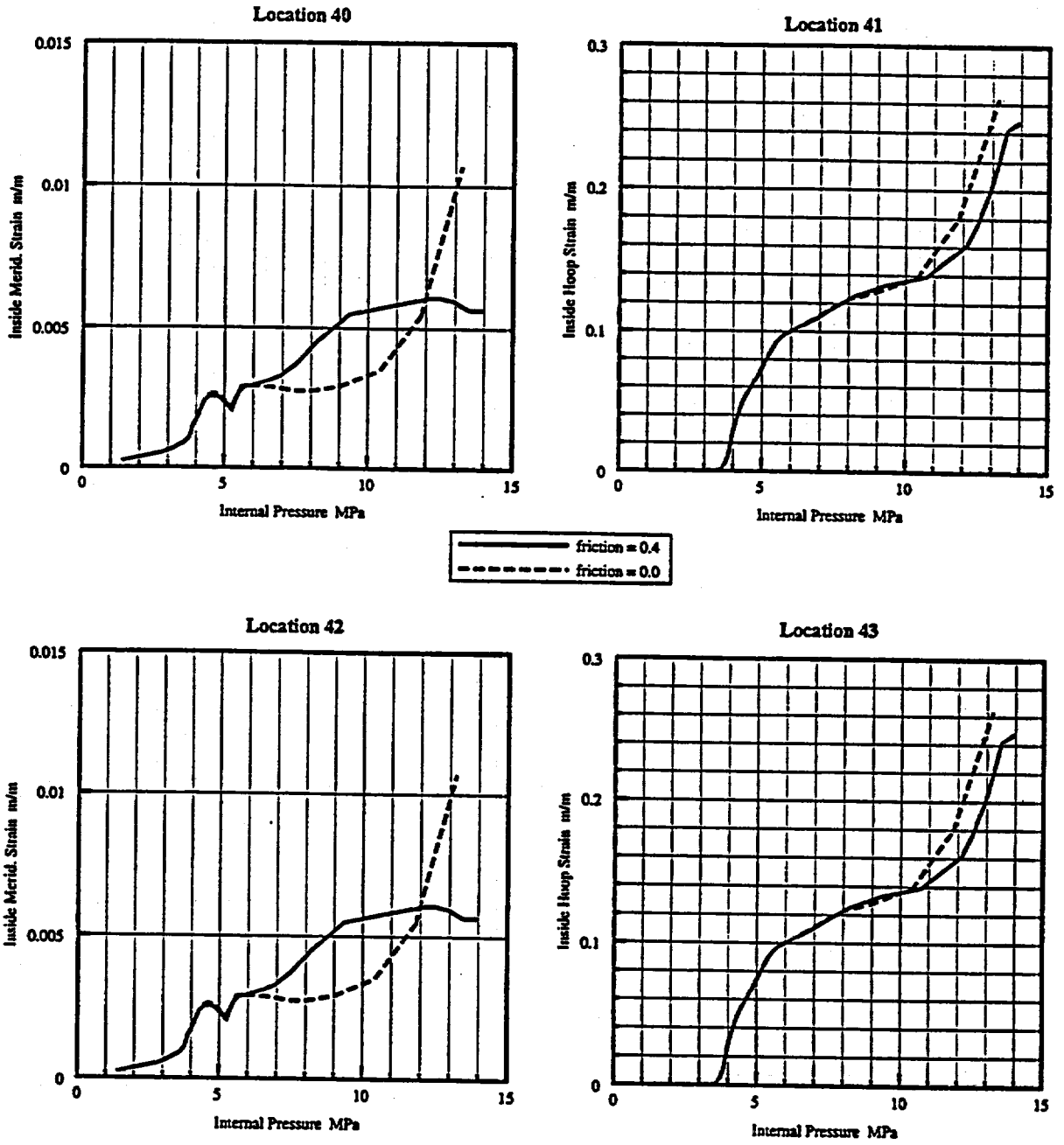
Location 40
Inside Merid. Strain m/m
0.015
0.01
0.005
0
0
5
10
15
Internal Pressure MPa
Location 41
Inside Hoop Strain m/m
0.3
0.2
0.1
0
0
5
10
15
Internal Pressure MPa
friction = 0.4
friction = 0.0
Location 42
Inside Merid. Strain m/m
0.015
0.01
0.005
0
0
5
10
15
Internal Pressure MPa
Location 43
Inside Hoop Strain m/m
0.3
0.2
0.1
0
0
5
10
15
Internal Pressure MPa

Enclosure (3) to:
415:TFT/603039/3.8

Electric Boat Corporation Low Probability of Failure Pressure Prediction

Electric Boat Corporation

June 3, 1996

Low Probability of Failure Pressure Prediction:

Reference (1) requested each participating organization to state what maximum pressure the SCV would obtain prior to failure. This prediction is to be defined such that there is a high confidence (>95%) that there is a low probability of failure (<1%) of the SCV.

As discussed in Section 10.0 of the pre-test report, Electric Boat Corporation proposed the use of the minimum ultimate strain reduced by a series of reduction factors to account for variation and unknowns in the as-tested SCV as the method for determining a suitable maximum pressure. The equipment hatch area below the material interface line was identified as a possible location for failure initiation. This location represents a critical area due to (1) the use of the lower ultimate strain limit SPV490 steel as compared to SGV480 steel, (2) strain concentrations caused from the reinforcement plate and material interface line, (3) possible weld defects, and (4) local plate thinning during construction of the SCV.

The locally thinned shell submodel of the equipment hatch region was found to possess the controlling strains of all the simulations performed. The appropriate reduction factors for this evaluation include the 1.10 factor for gap variation, the 1.02 factor for friction variation, and the 1.10 factor for as-built structural details. Combining these factors results in a total reduction factor of 1.23. Dividing the appropriate minimum ultimate strain for SPV490 steel (ε_{umin}=10.0%, Reference (1)) results in the following "failure" limit strain.

$$\varepsilon_f = \varepsilon_{umin}/1.23 = 8.0\%$$

The maximum pressure was determined by allowing the peak equivalent plastic strain to obtain this failure limit value through the thickness of the shell. This results in a maximum pressure of 4.7 Mpa (680 psi) or approximately 6 times the design pressure. Due to the use of minimum as-built plate thickness in the evaluation, minimum ultimate strain values with suitable reduction factors, and detailed modelling of the critical areas of the SCV, Electric Boat Corporation considers this pressure to define a low probability of failure value.

Appendix E-5

Japan Atomic Energy Research Institute

Japan

Pre-test Analysis of SCV Test by JAERI with ABAQUS

SUGIMOTO, Jun and NIIYAMA, Kenji*

Japan Atomic Energy Research Institute
Tokai-mura, Ibaraki-ken, 319-11 Japan

*Mitsubishi Research Institute, Inc.
Otemachi 2-3-6, Chiyda-ku, Tokyo 100 Japan

1. Introduction

Containment Model Tests to investigate a failure of the containment vessel has been initiated as a joint research program among Nuclear Power Engineering Corporation(NUPEC), U.S. Nuclear Regulatory Commission(NRC)and Sandia National Laboratories(SNL). For the effective pre-and post test analysis of these tests, a Round Robin analytical activities have been organized.

Since JAERI has done the post-test analysis of SNL's 1/6 scale RCCV test before[1][2], JAERI expressed the intention to participate in the Round Robin analysis with ABAQUS code[3]. The present paper describes the results of the pre-test analysis by JAERI for Steel Containment Vessel(SCV) test.

2. FEM Modeling with ABAQUS

(1) FEM mesh

A finite element code for non-linear problems, ABAQUS, was used to analyze the behavior of SCV and Contact Structure (CS). Both SCV and CS are modeled with shell elements. Most parts are modeled with 4-node shell elements. The top of the top head and hatch cover are modeled with 3-node shell elements. The total number of integration points in element section is five. Figures 1 and 2 show the FEM mesh of SCV and CS. The FEM Model is 180-degree symmetric, and modeled between 270 and 90 degree directions in the global coordinate system. The part lower than the upper surface of the ring support, i.e. $z < 0$ in the global coordinate system, is not modeled in the present FEM scheme, because the bottom head is much thicker than the rest of the system and the deformation of this part is expected to be negligible.

scheme, because the bottom head is much thicker than the rest of the system and the deformation of this part is expected to be negligible.

(2) Boundary conditions and contact modeling

The bottom of the model($z = 0$) is completely fixed. Symmetric conditions are used as the boundary condition on the plane of the symmetry. Nodes of SCV model are located on the inner surface of the vessel to set clearance between SCV and CS. Contact between SCV and CS is modeled with small-sliding interface element. Contact model with friction coefficient 0 between SCV and CS are calculated.

(3) Material properties

The SCV is made of two materials, SGV480 and SPV490, welded into one body. NUPEC conducted tensile tests of the material pieces cut from SCV. The results of the tensile tests were used for the material properties. The tri-linear curve was used to model stress-strain relation of the materials. Young's moduli were measured by NUPEC. The hardening coefficients for two materials were evaluated by the least squares method using tensile tests data after yielding point. After stress reaches tensile strength, the hardening coefficient was set to zero. The tensile test data at loc-11 was not used to evaluate hardening coefficient because Young's modulus is much different from that measured by NUPEC. Evaluated material properties are presented in Table 1. Figures 3 and 4 show the stress-strain relation, measured in tensile tests, used in the present analysis for SGV480 and SPV490, respectively. Material property of the CS made of SA516-70 is also presented in Table 1. The CS is assumed to be elastic in the present analysis because it is much thicker than the SCV.

3. Calculated Results

The internal pressure was loaded to the FEM model described above, and stress, strain, displacements and contact condition are calculated as a function of pressure.

(1) Distribution of Plastic Strain

Equivalent plastic strains are observed during the analysis. First yielding are seen around knuckle and in top head at pressure of 2.80 MPa. As pressure increases, it gives maximum value at just besides the hatch reinforcing plate. At pressure about 9 MPa,

the value at apex of top head overtakes that around hatch reinforcing plate. Figures 5 and 6 show distribution of equivalent plastic strain at pressure of 9.00 MPa in top head and around hatch reinforcing plate, respectively. They reach about 10 % at this pressure level. Over this pressure level, plastic strain in top head increase rapidly, though that around hatch reinforcing plate does slowly. Distribution of equivalent plastic strain at pressure of 10.81 MPa in top head and around hatch reinforcing plate are shown in figs. 7 and 8. Finally, calculation was terminated because of numerical instability due to yielding in top head region at pressure of 11.81 MPa.

(2) Contacts between SCV and CS

Contacts between SCV and CS are observed first at pressure of 4.00 MPa in upper and middle conical shells and around knuckle. Section of SCV and CS in 0 degree of global coordinate system at this pressure is shown in fig. 9. Contacts area propagate in conical shells as pressure increase. Figure 10 shows section at pressure of 7.63 MPa. In this figure, most of spherical and conical shells contact to with CS. Only in lower conical shell, area of contacts increases slowly. Section at pressure of 10.81 MPa is shown in fig. 11.

(3) Standard Outputs

Standard output #35 is shown in fig. 12. It is vertical displacement at apex of top head. The increasing rate get small around pressure of 3 MPa, because of contact between SCV and CS. Finally just under pressure at which analysis terminated, it increase rapidly because of plastic deformation in top head.

Standard output #36 is shown in fig. 13. It is horizontal displacement in upper cylindrical shell. Around this standard output point, SCV is free from CS. The increasing rate changes much around pressure of 7 MPa. This results shows that plastic deformation in top head region is getting larger over this pressure level.

Standard outputs #5 and #6 are shown in fig. 14. They are hoop strains just besides hatch reinforcing plate. They are observed on inner and external surface of the vessel at same location, respectively. Plastic strain is maximum around this point under pressure of 9 MPa. A rapid increase is seen around pressure of 4 MPa. SCV begin to contact to CS and contacts area is propagating around this pressure level. Once SCV contact to CS, these strain increase slowly until the end of the analysis.

Standard output #7 is shown in fig. 15. It is maximum principal strain at apex of top head. Increasing rate is very small in the beginning of loading and quickly get large at pressure of 5.45 MPa. The strain reaches to 12 % at the end of loading.

4. Discussions

Failure mode of SCV is discussed in this section.

Plastic strain gives maximum value around hatch reinforcing plate, and local failure is likely to occur at material or thickness change interface around this location. But, we have no failure model included in this analysis. Hence structural failure mode is mainly discussed.

In this analysis, calculation is terminated because of numerical instability due to large plastic deformation in top head. In this point of view, failure mode is expected to be rapture in top head. No structural failure is seen around hatch, though plastic strain is large in this region. The pressure at which rapture will occur in top head is 10.81 MPa. It is detected because standard output of strains in top head show sudden behavior change at this pressure. We can hardly detect confidence pressure at which SCV is expected to be free from rapture in top head. We can say that deformation will be small under pressure of 6 MPa, from standard output #7 and #36.

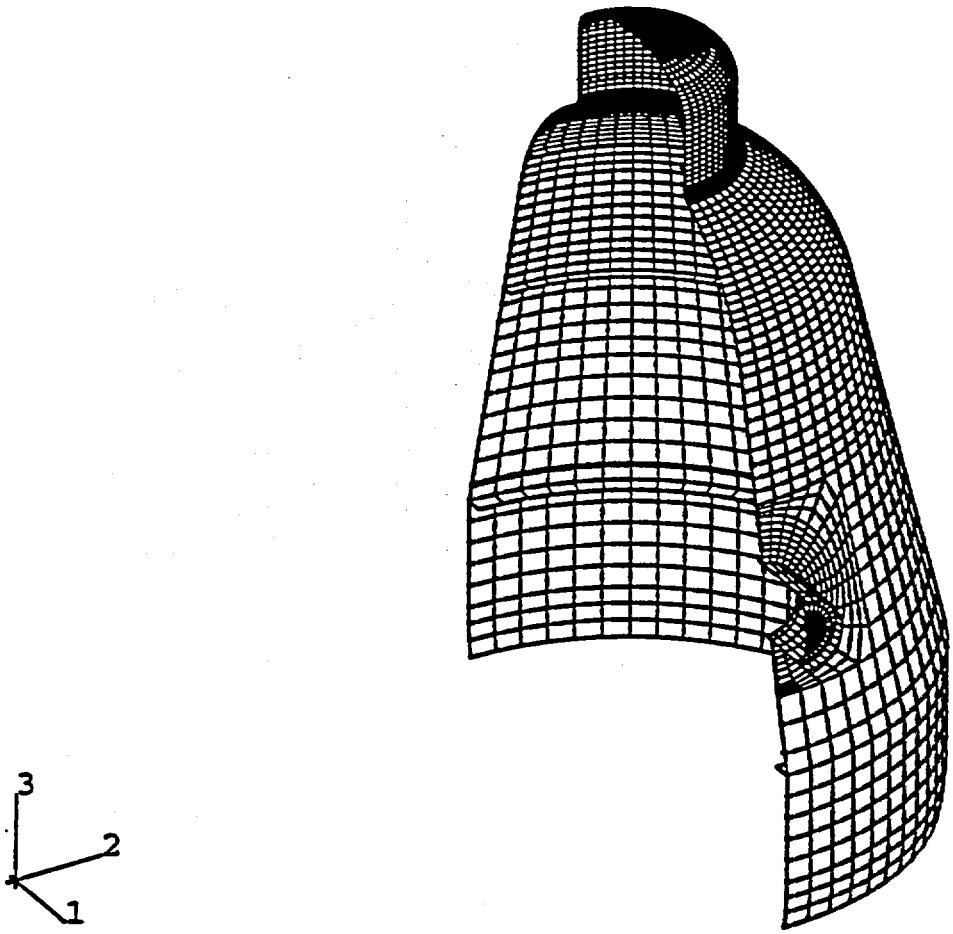

Fig. 1 FEM mesh for the Steel Containment Vessel (SCV)

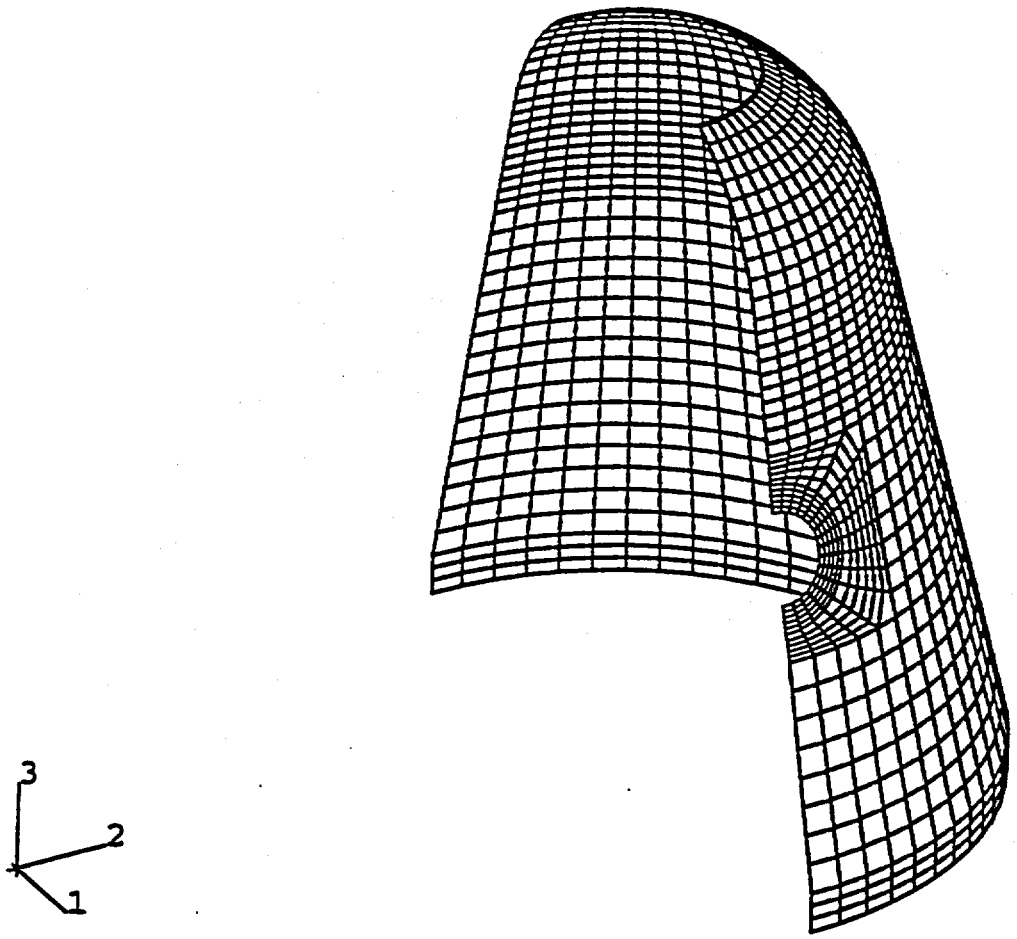

Fig. 2 FEM mesh for Contact Structure (CS)

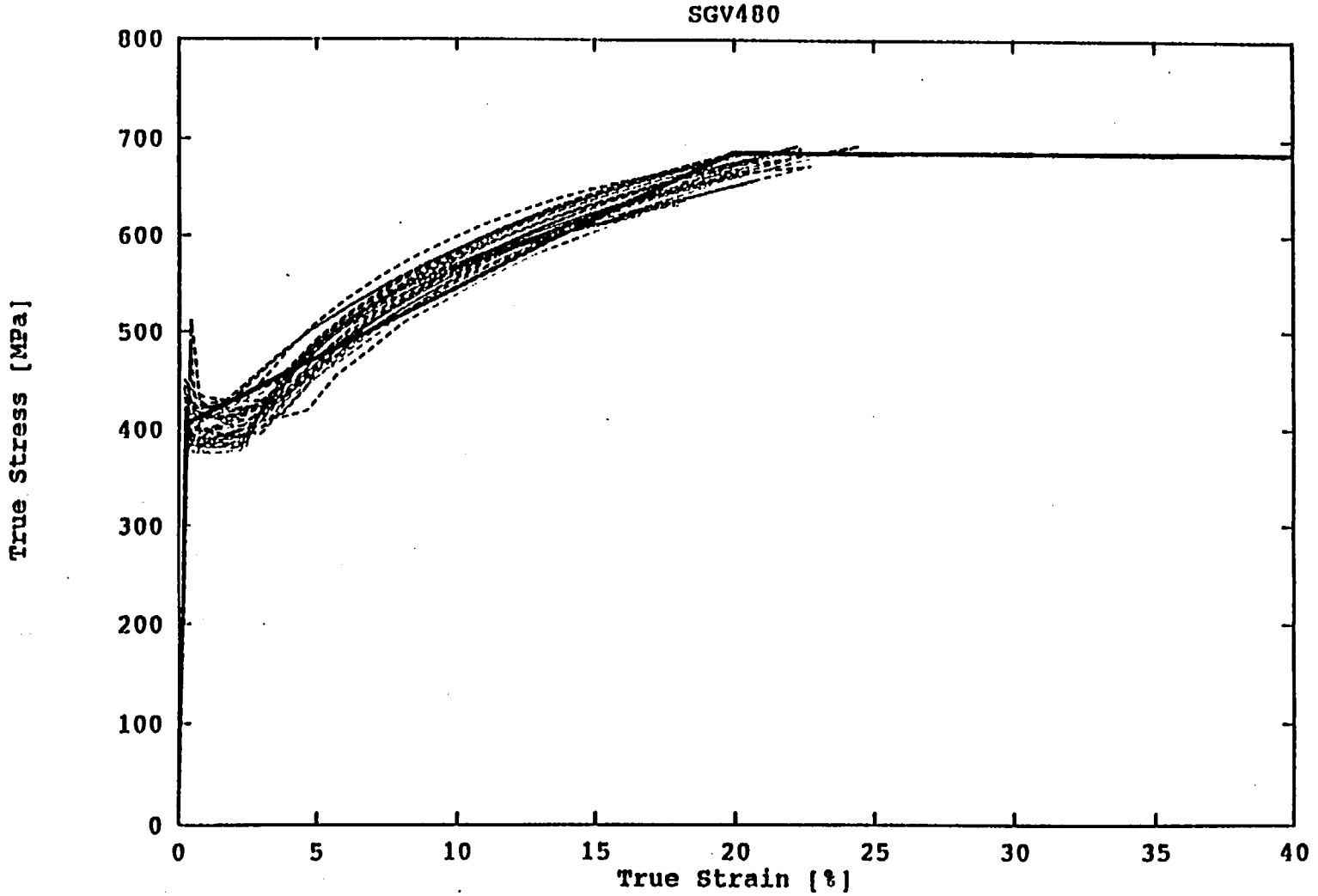

Fig. 3 Evaluated stress-strain relation
and experimental data in loc-1 thru 10 (SGV480)

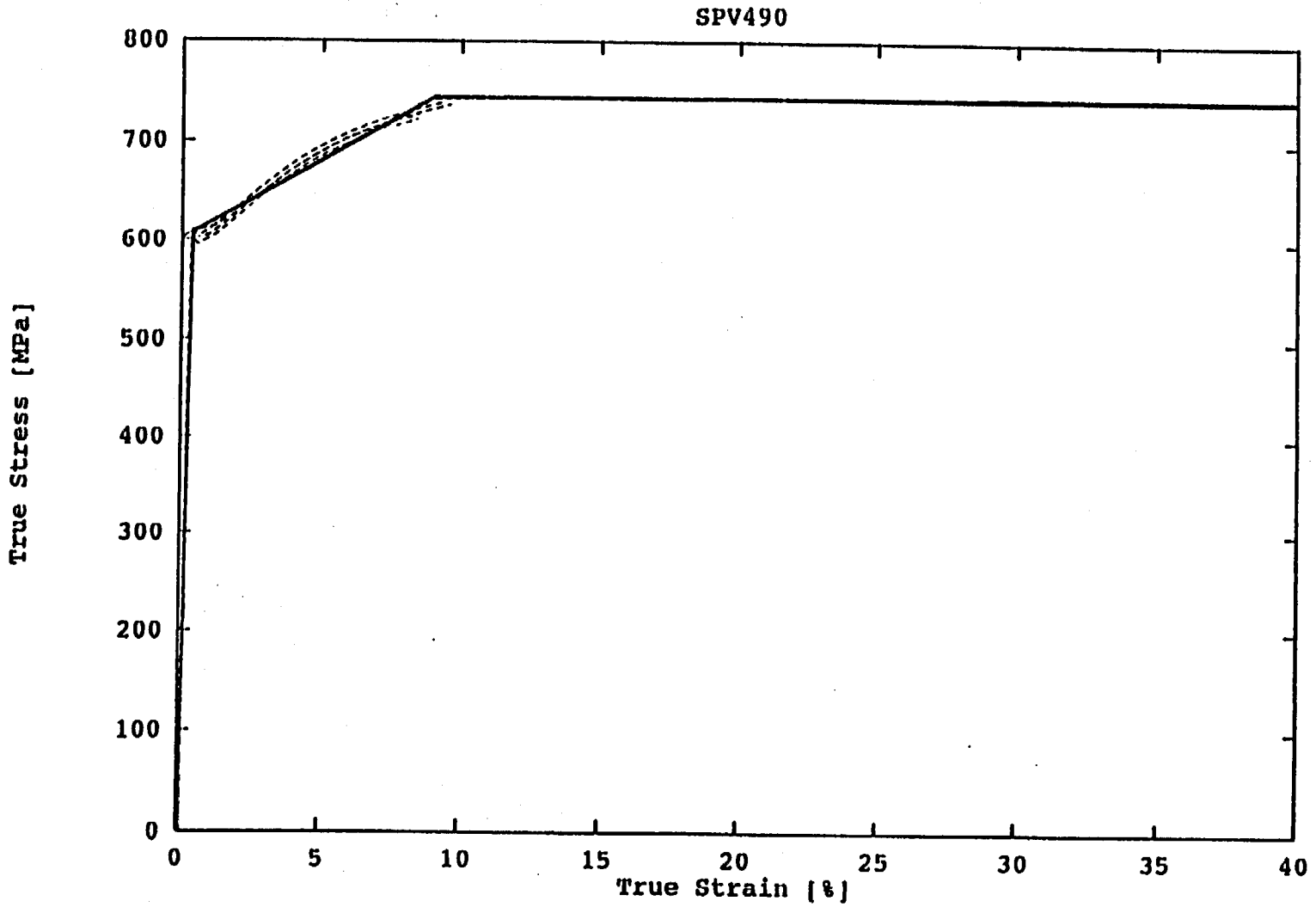

Fig. 4 Evaluated stress-strain relation and experimental data in loc-12 (SPV490)

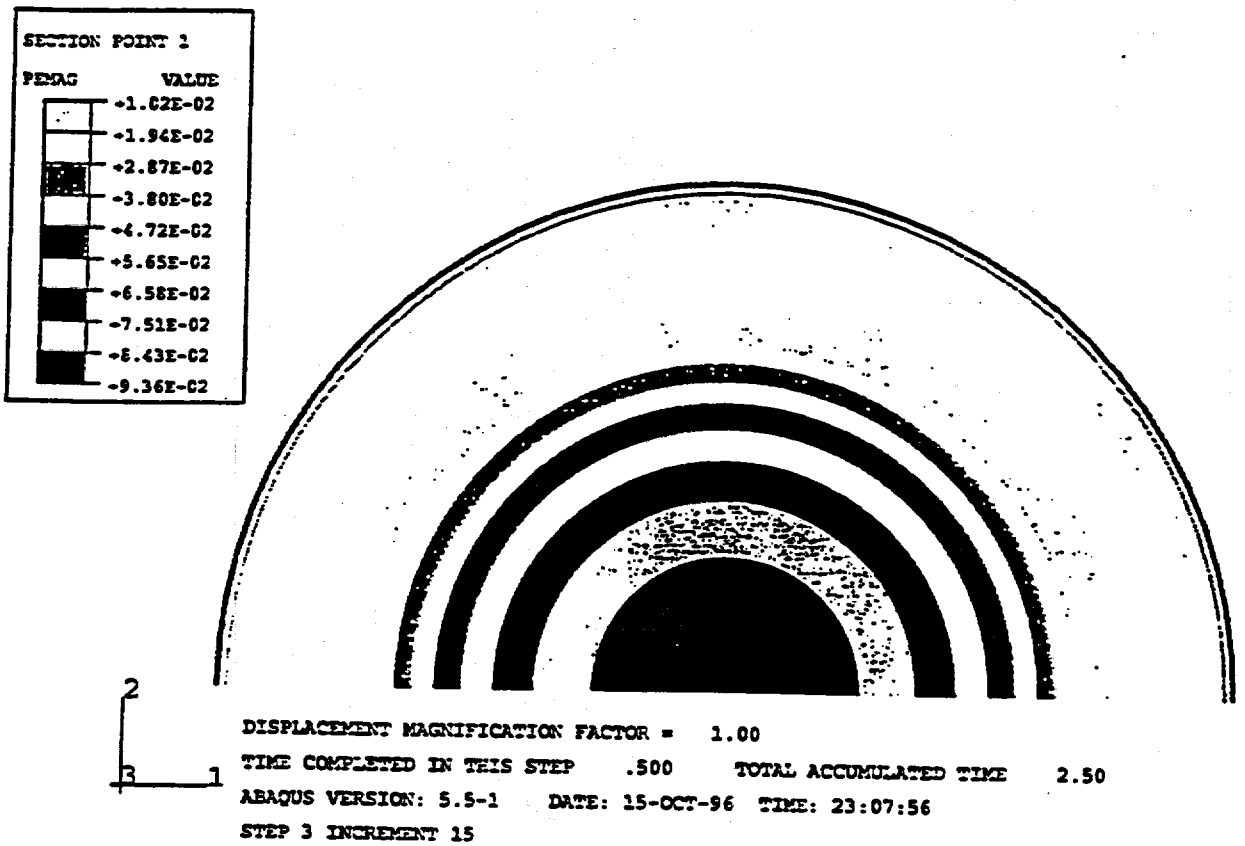

Fig. 5 Distribution of equivalent plastic strain at pressure of 9.00 MPa in top head

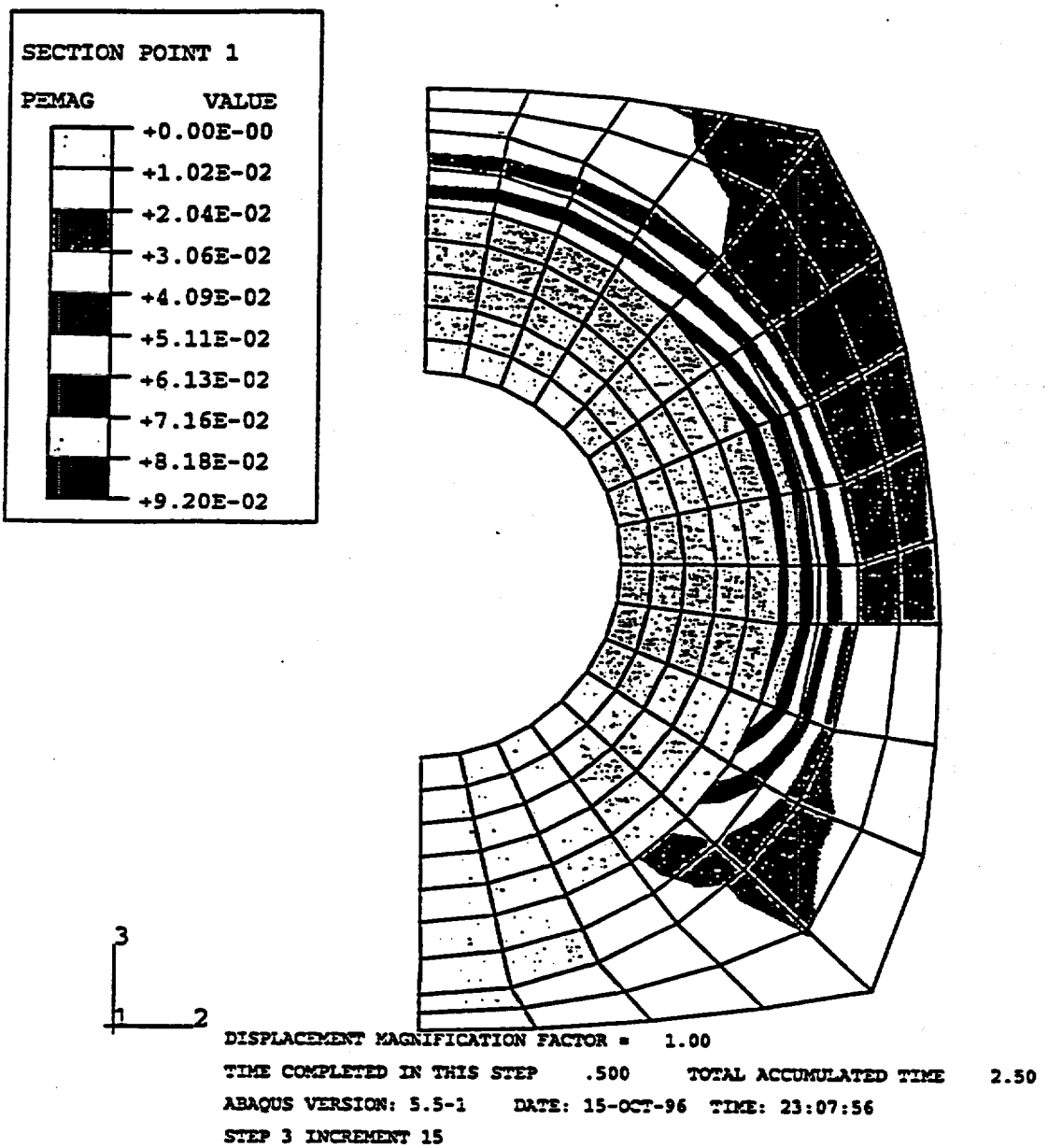

Fig. 6 Distribution of equivalent plastic strain at pressure of 9.00 MPa around hatch reinforcing plate

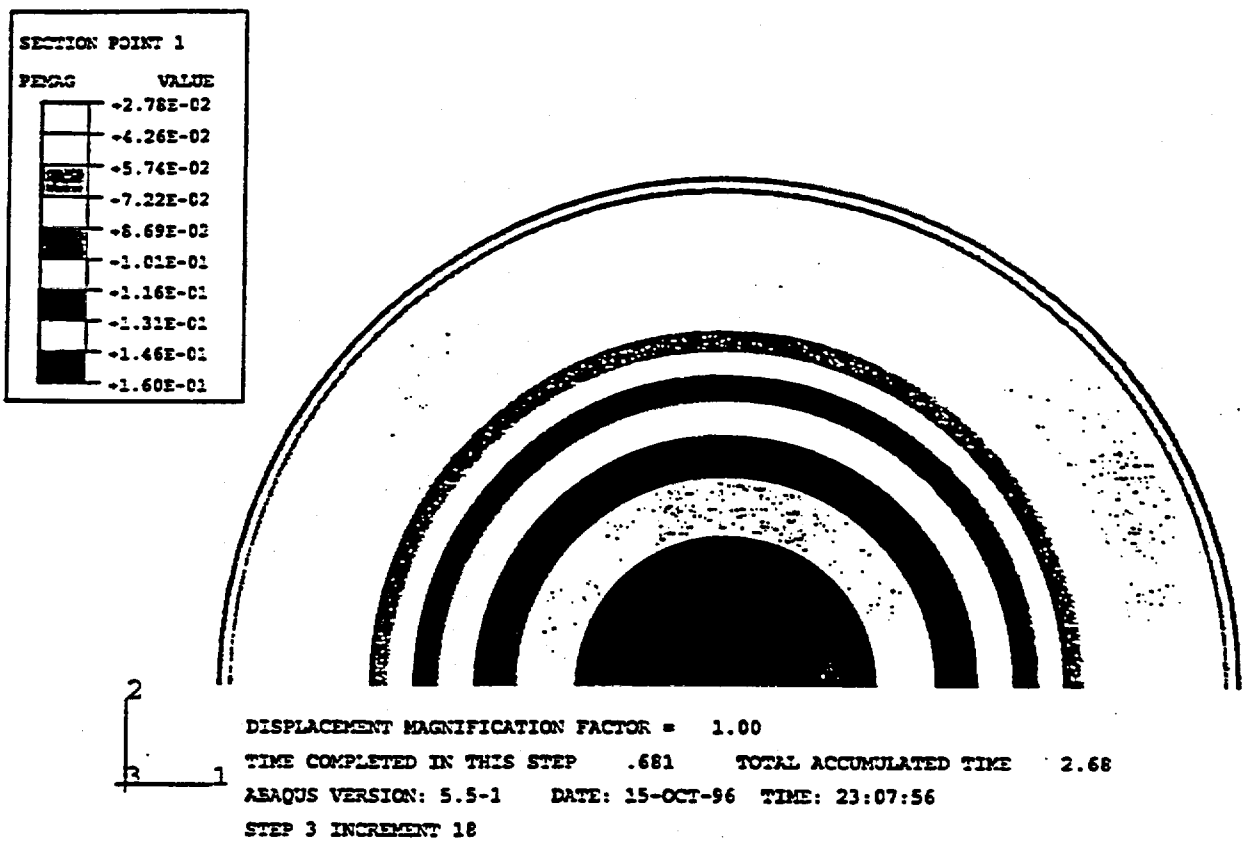

Fig. 7 Distribution of equivalent plastic strain at pressure of 10.81 MPa in top head

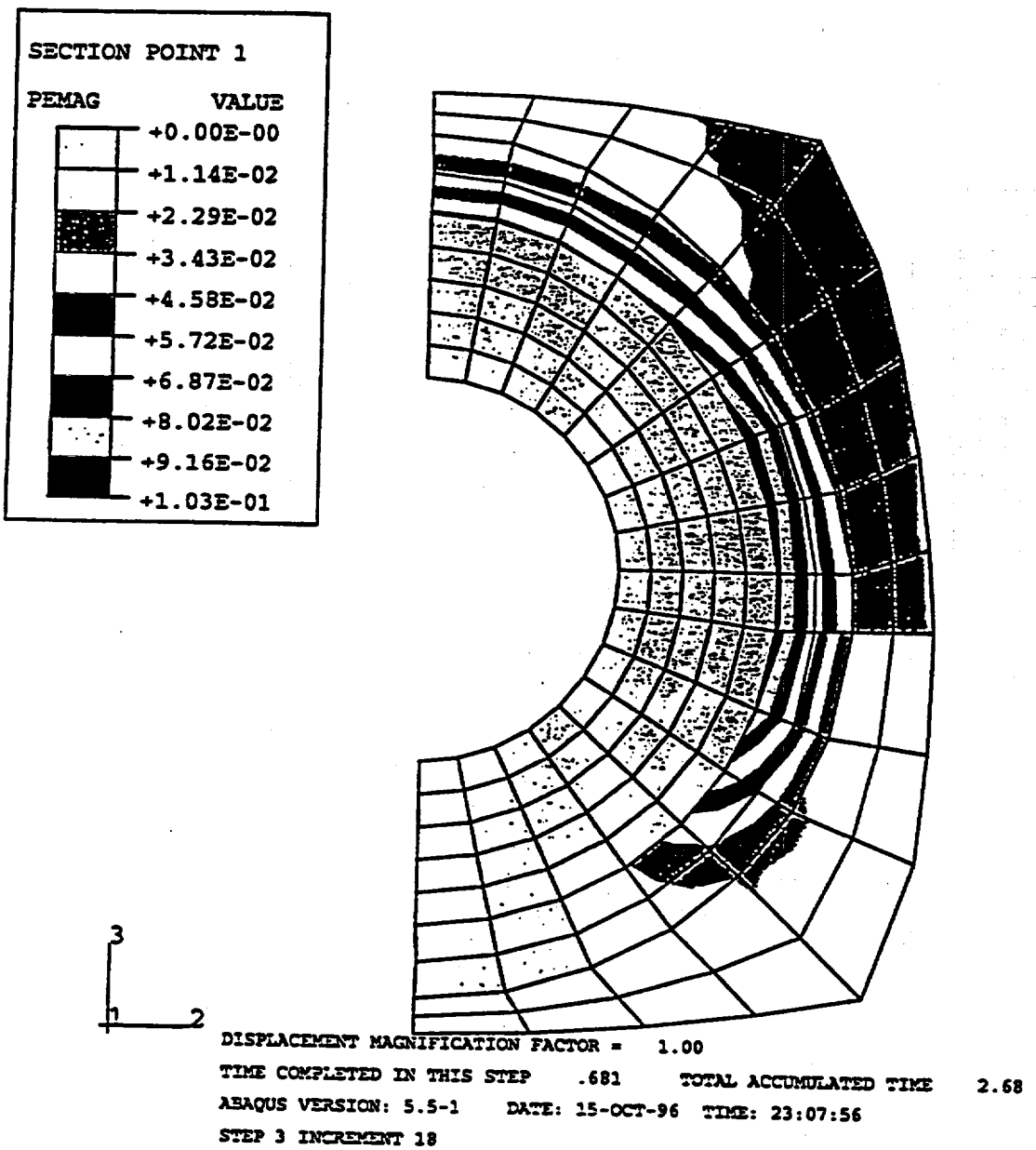

Fig. 8 Distribution of equivalent plastic strain at pressure of 10.81 MPa around hatch reinforcing plate

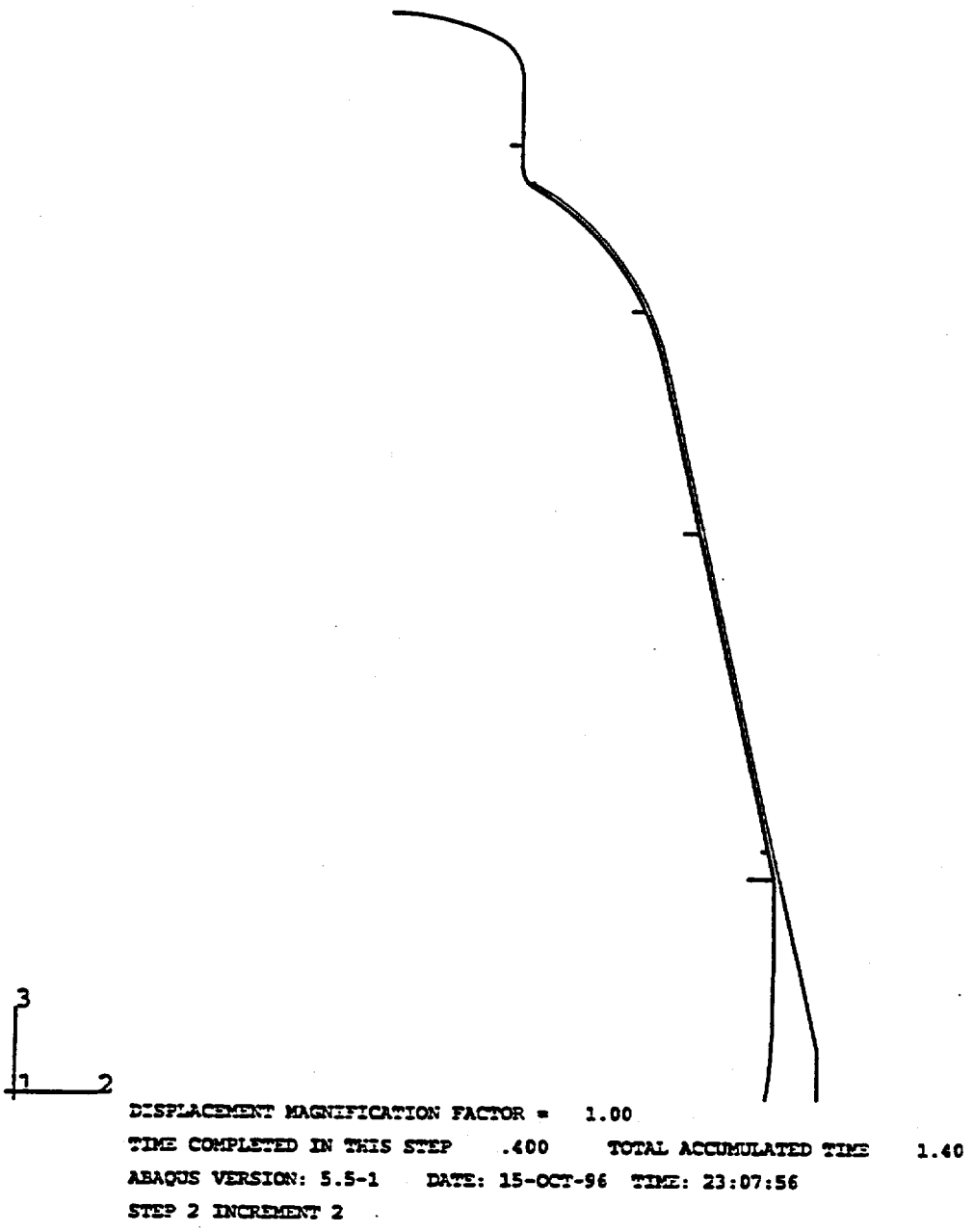

Fig. 9 Section of SCV and CS
in 0 degree of global coordinate system at pressure of 4.00

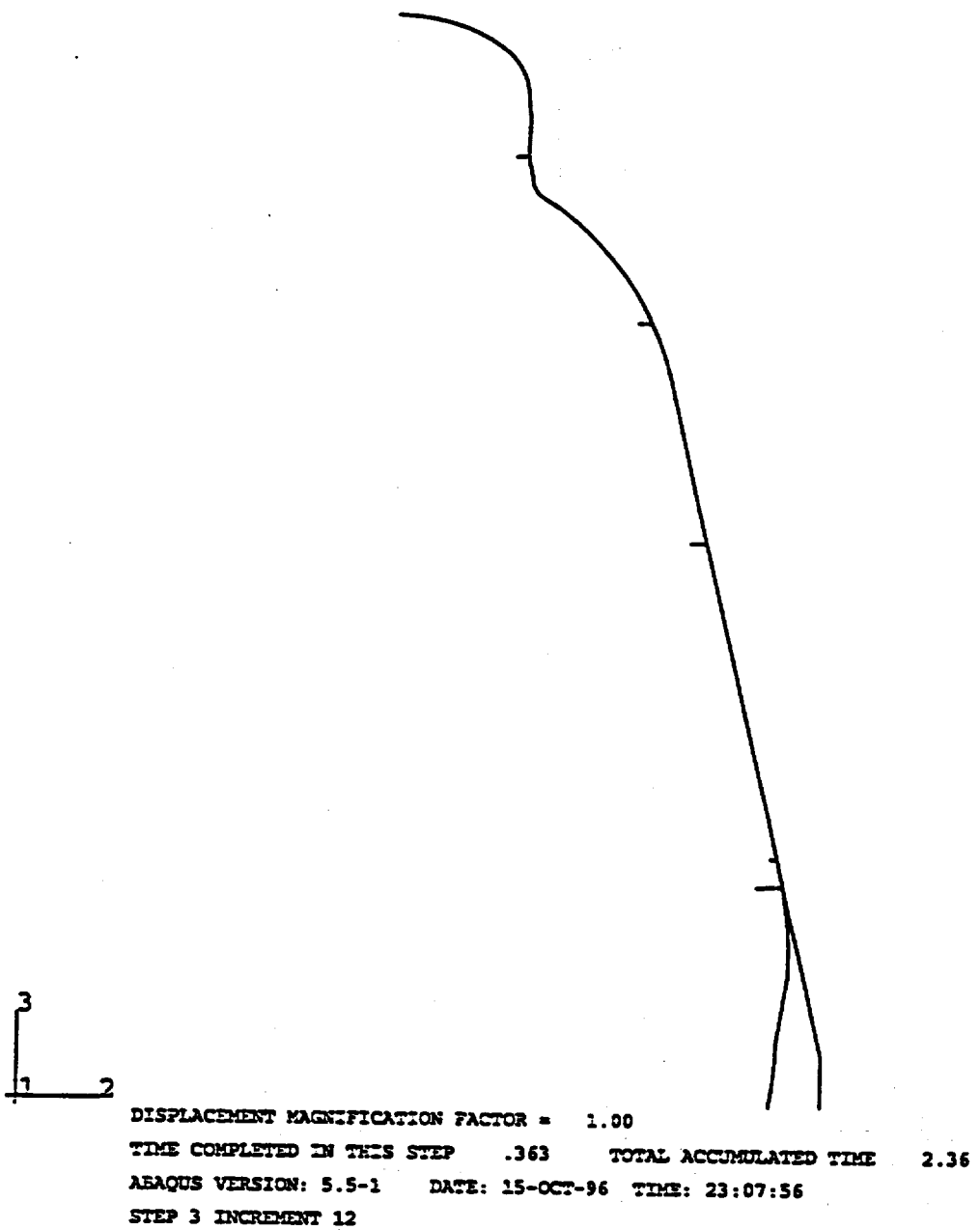

Fig. 10 Section of SCV and CS
in 0 degree of global coordinate system at pressure of 7.63

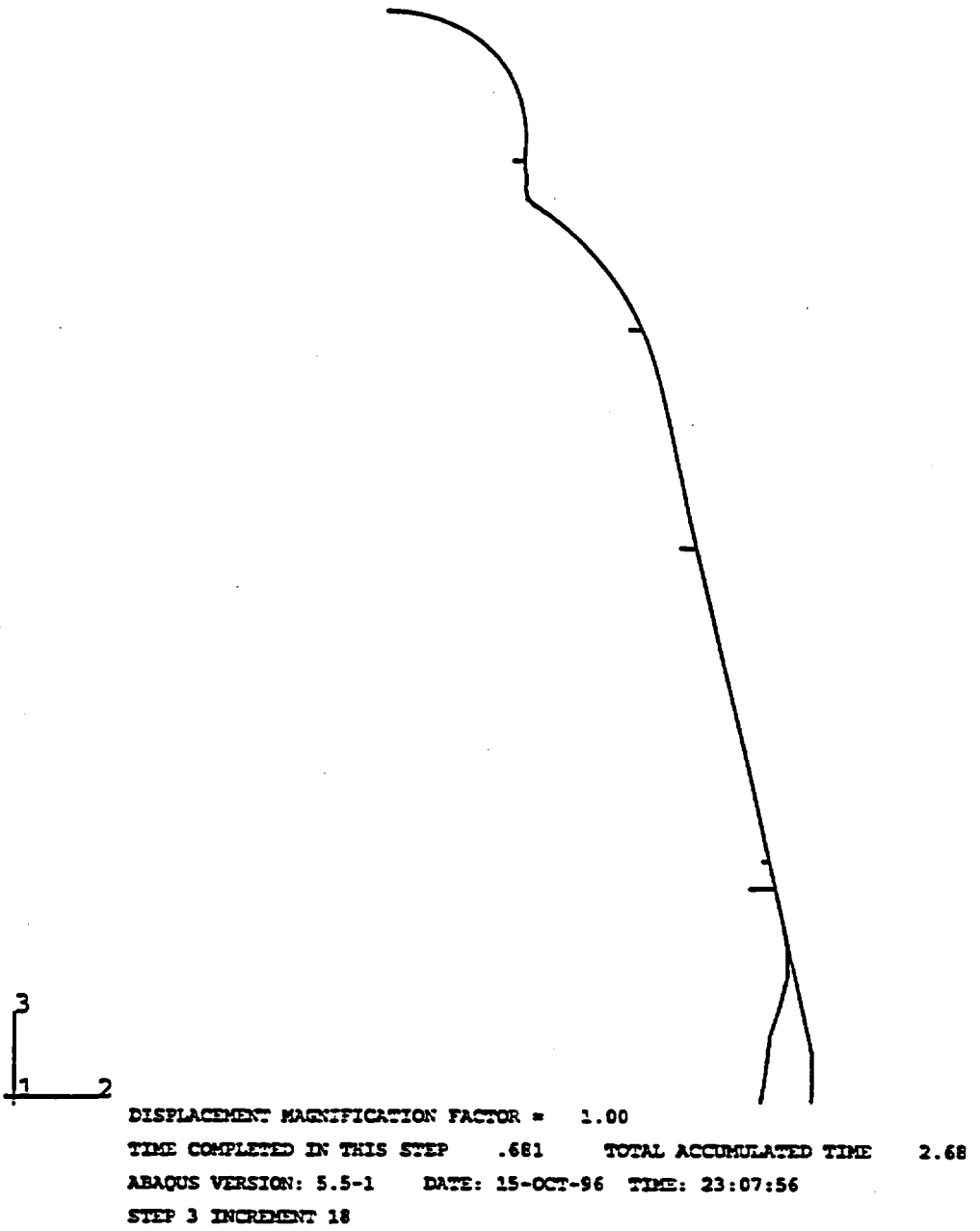

Fig. 11 Section of SCV and CS
in 0 degree of global coordinate system at pressure of 10.81

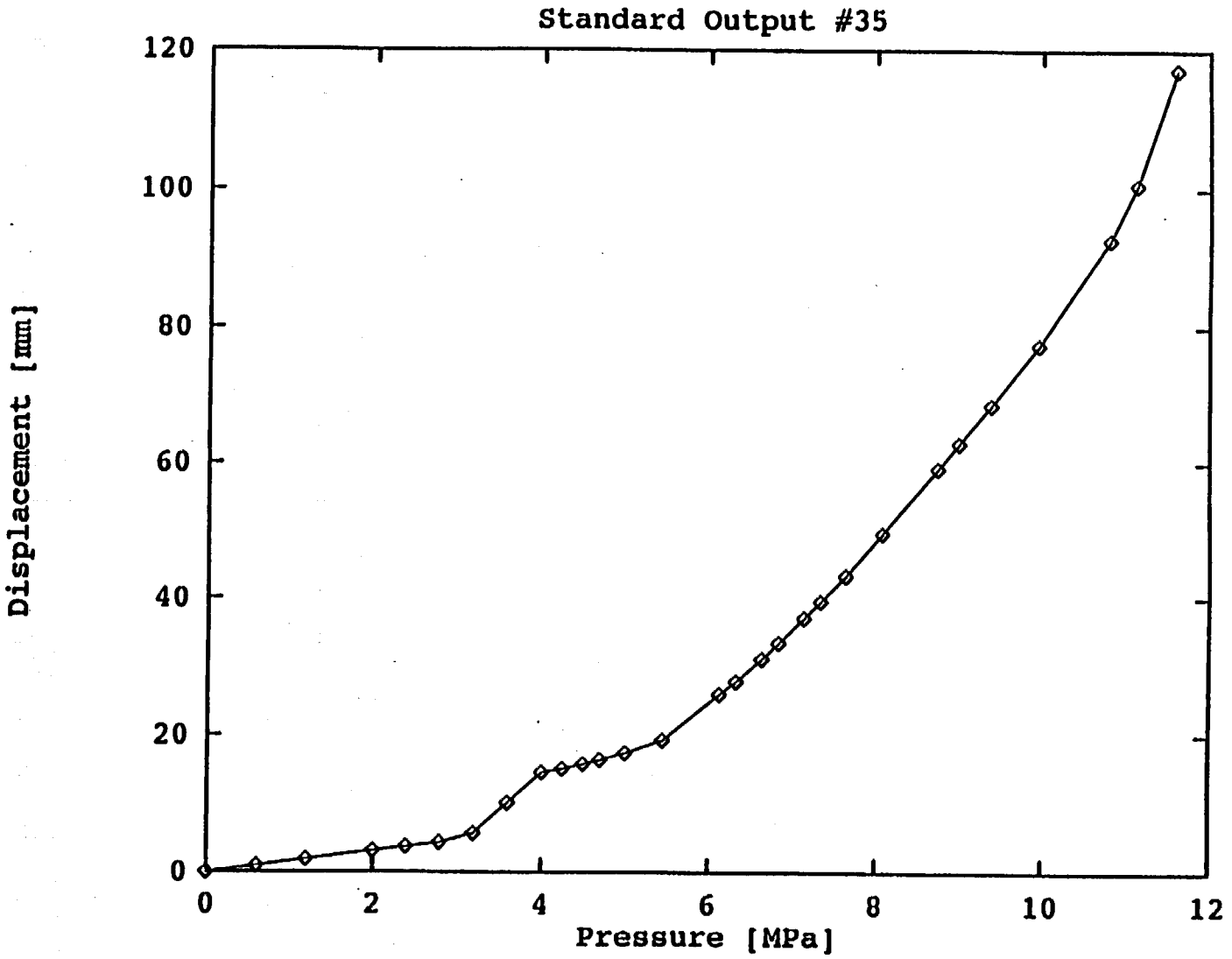

Fig. 12 Standard output #35 ;
vertical displacement at apex of top head.

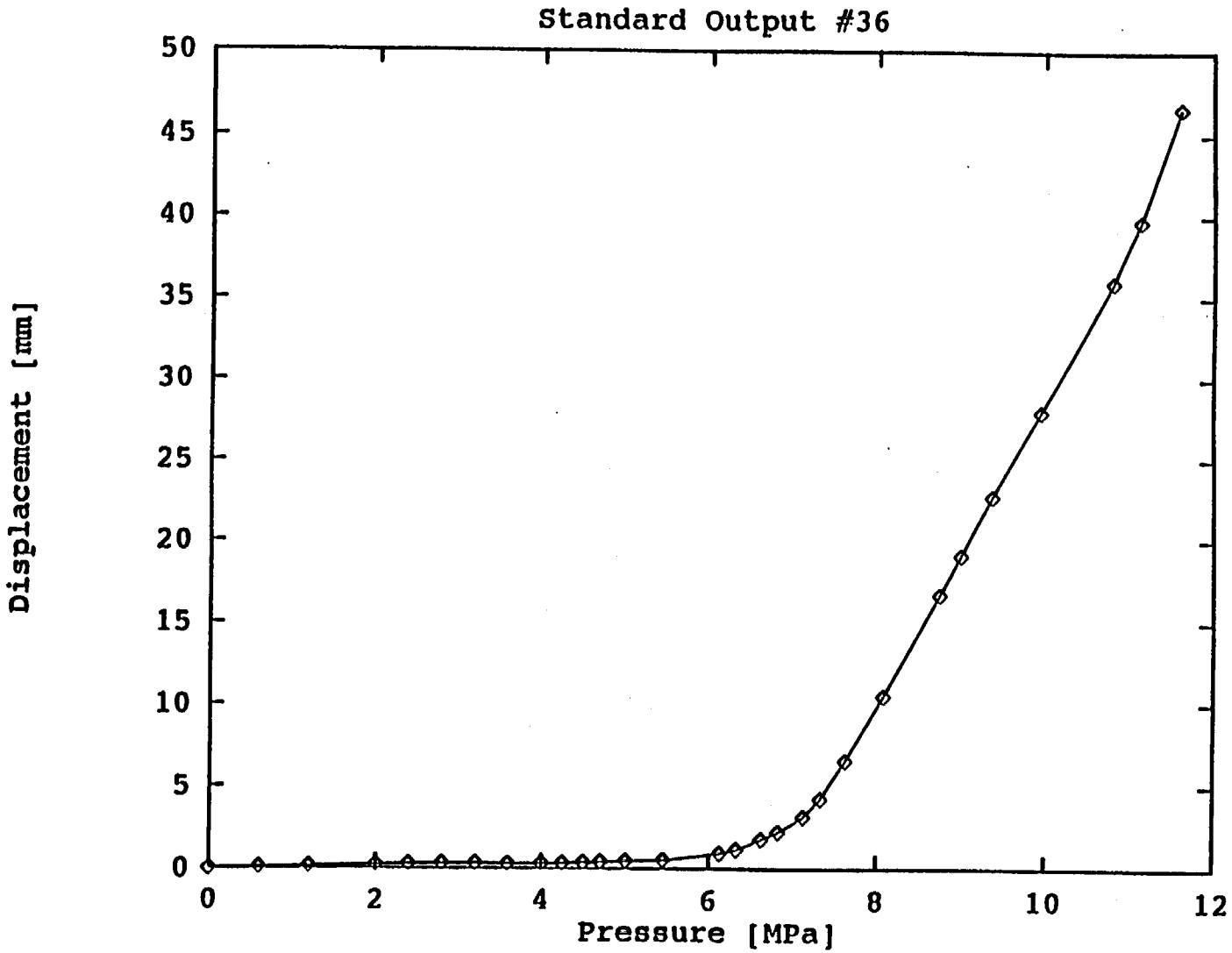

Fig. 13 Standard output #36 ;
horizontal displacement in upper cylindrical shell.

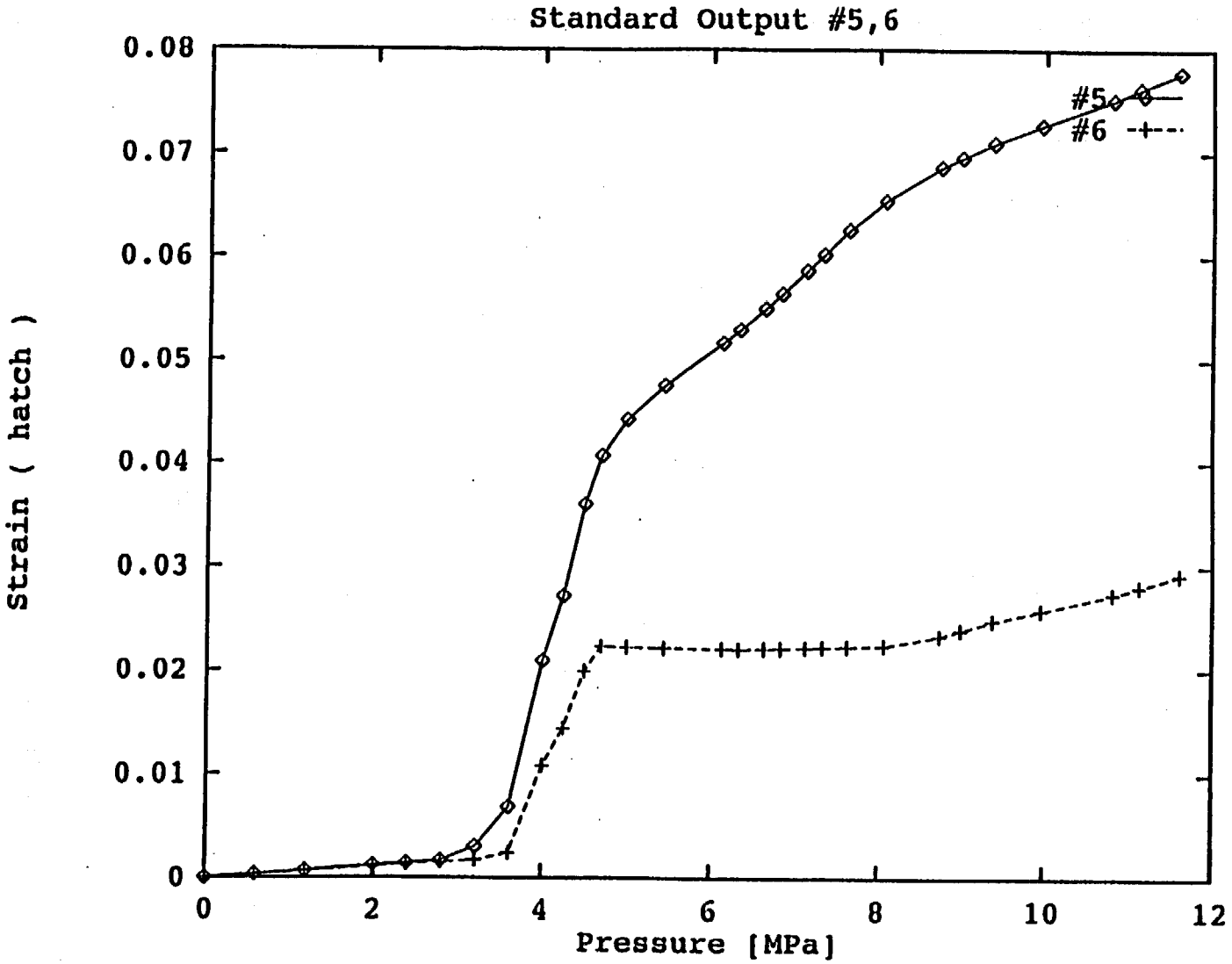

Fig. 14 Standard outputs #5 and #6 ;
hoop strains just besides hatch reinforcing plate

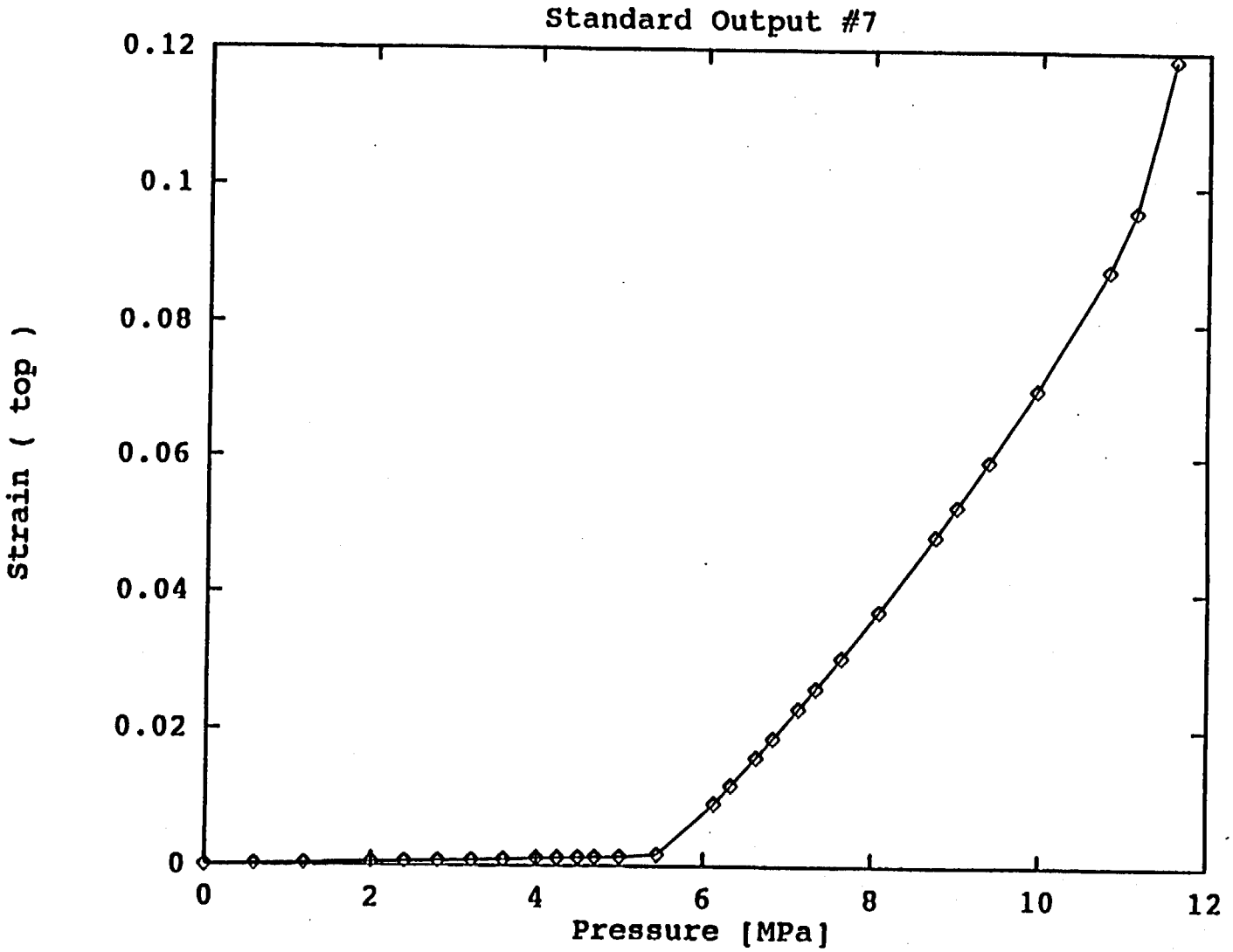

Fig. 15 Standard output #7 ;
maximum principal strain at apex of top head.

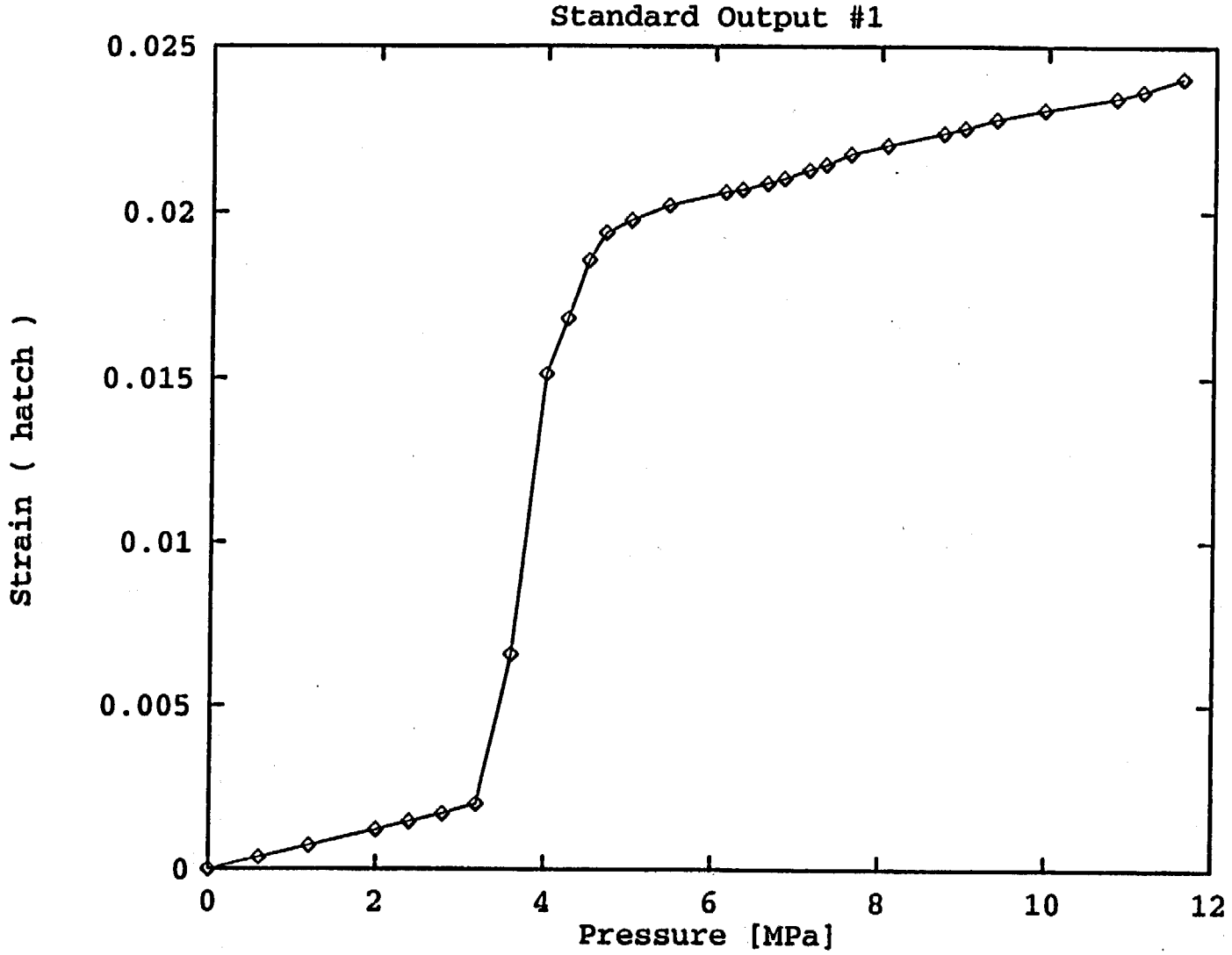
Standard Output #1
Strain (hatch)
0.025
0.02
0.015
0.01
0.005
0
0
2
4
6
8
10
12
Pressure [MPa]

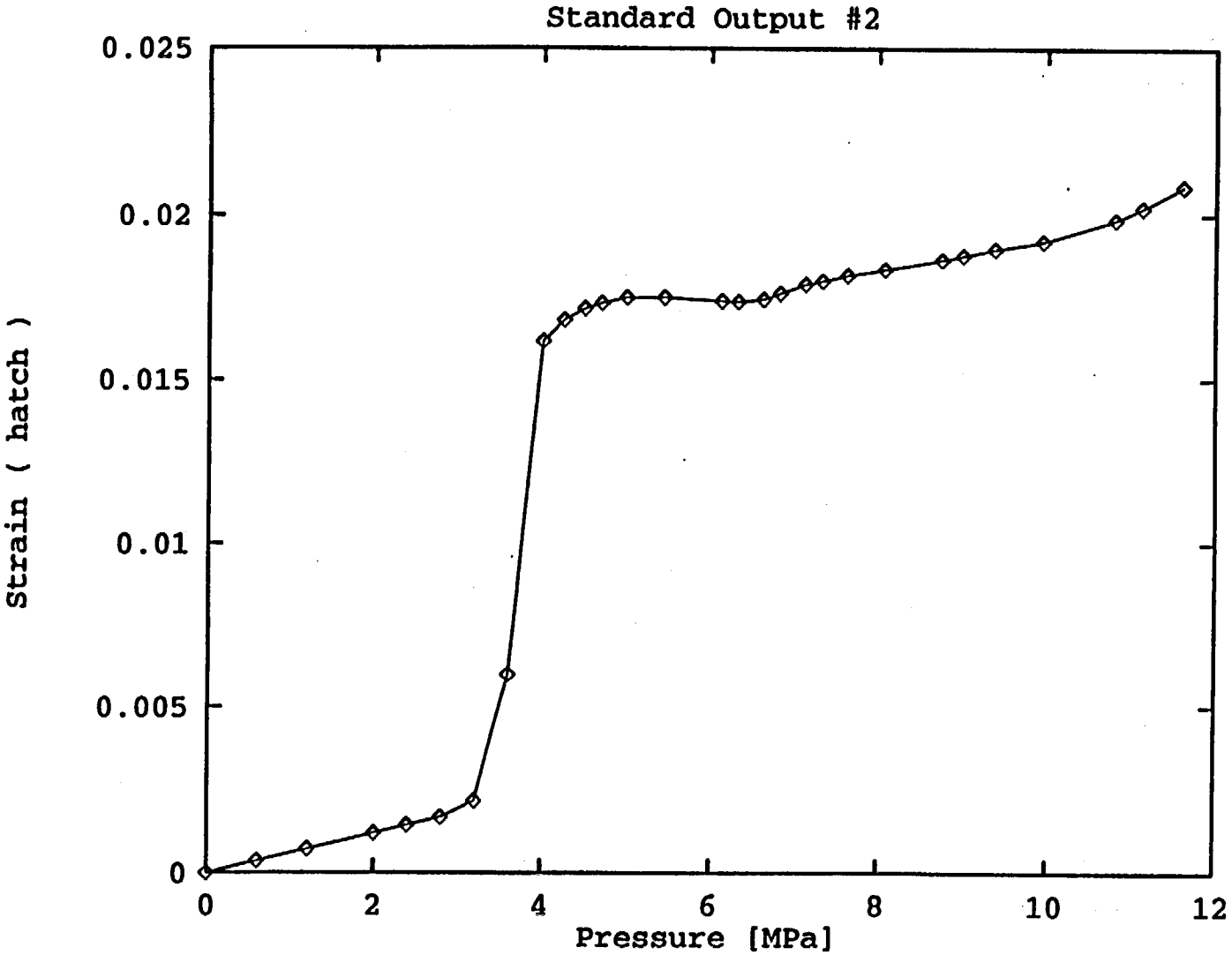
Standard Output #2
0.025
0.02
0.015
0.01
0.005
0
Strain (hatch)
0
2
4
6
8
10
12
Pressure [MPa]

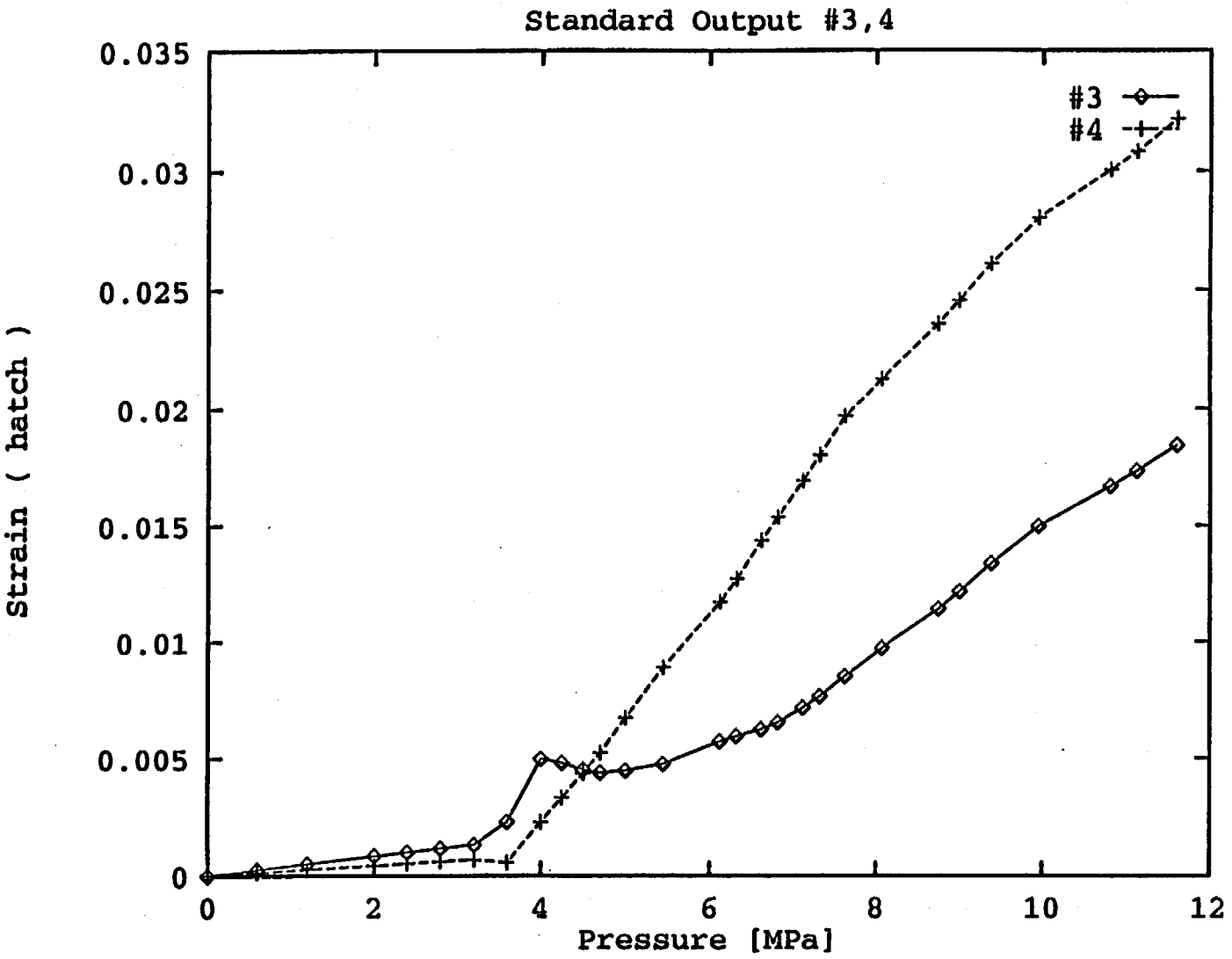
Standard Output #3,4
#3
#4
Strain (hatch)
Pressure [MPa]
0.035
0.03
0.025
0.02
0.015
0.01
0.005
0
0
2
4
6
8
10
12

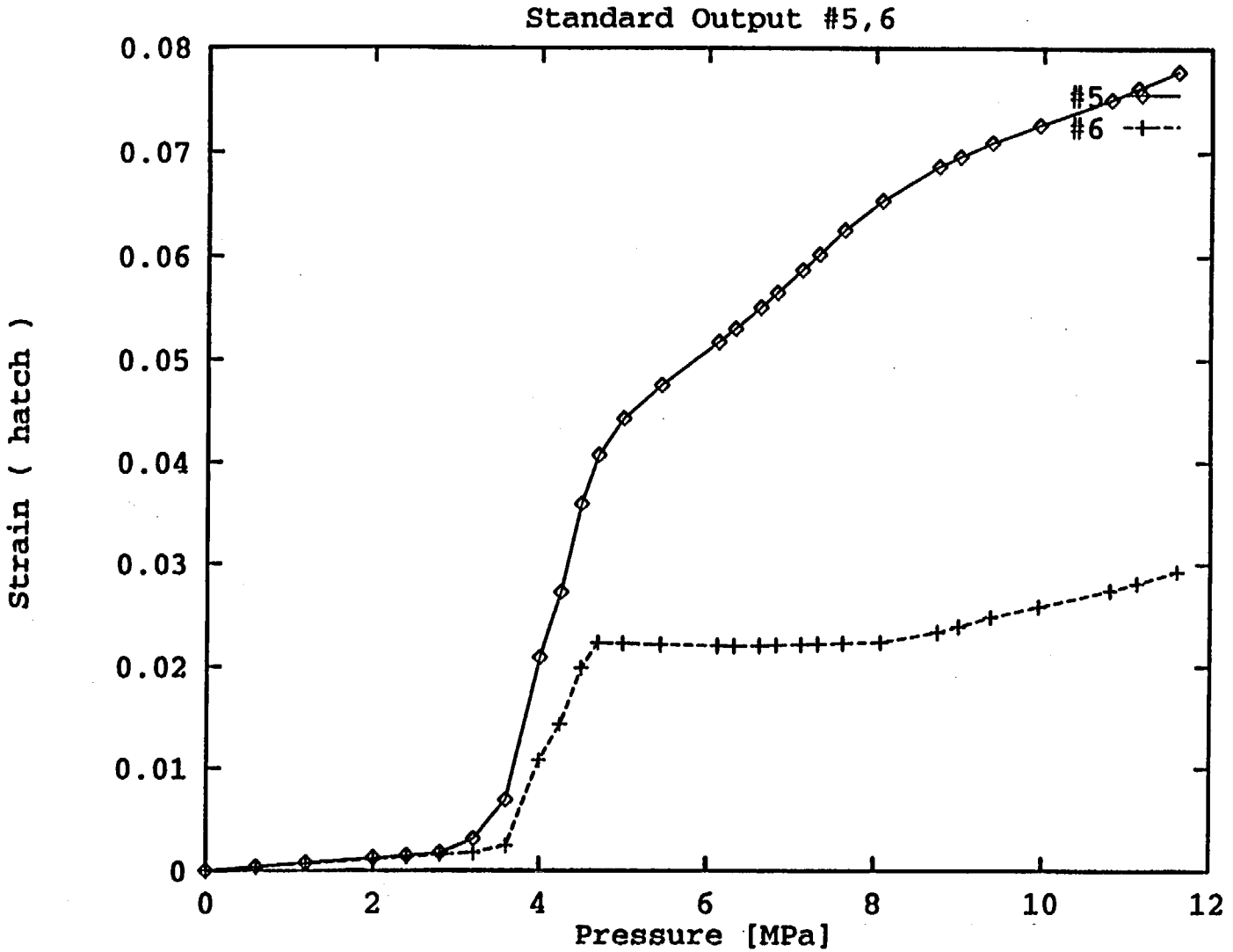
Standard Output #5,6
Strain (hatch)
Pressure [MPa]
#5
#6
0.08
0.07
0.06
0.05
0.04
0.03
0.02
0.01
0
0
2
4
6
8
10
12

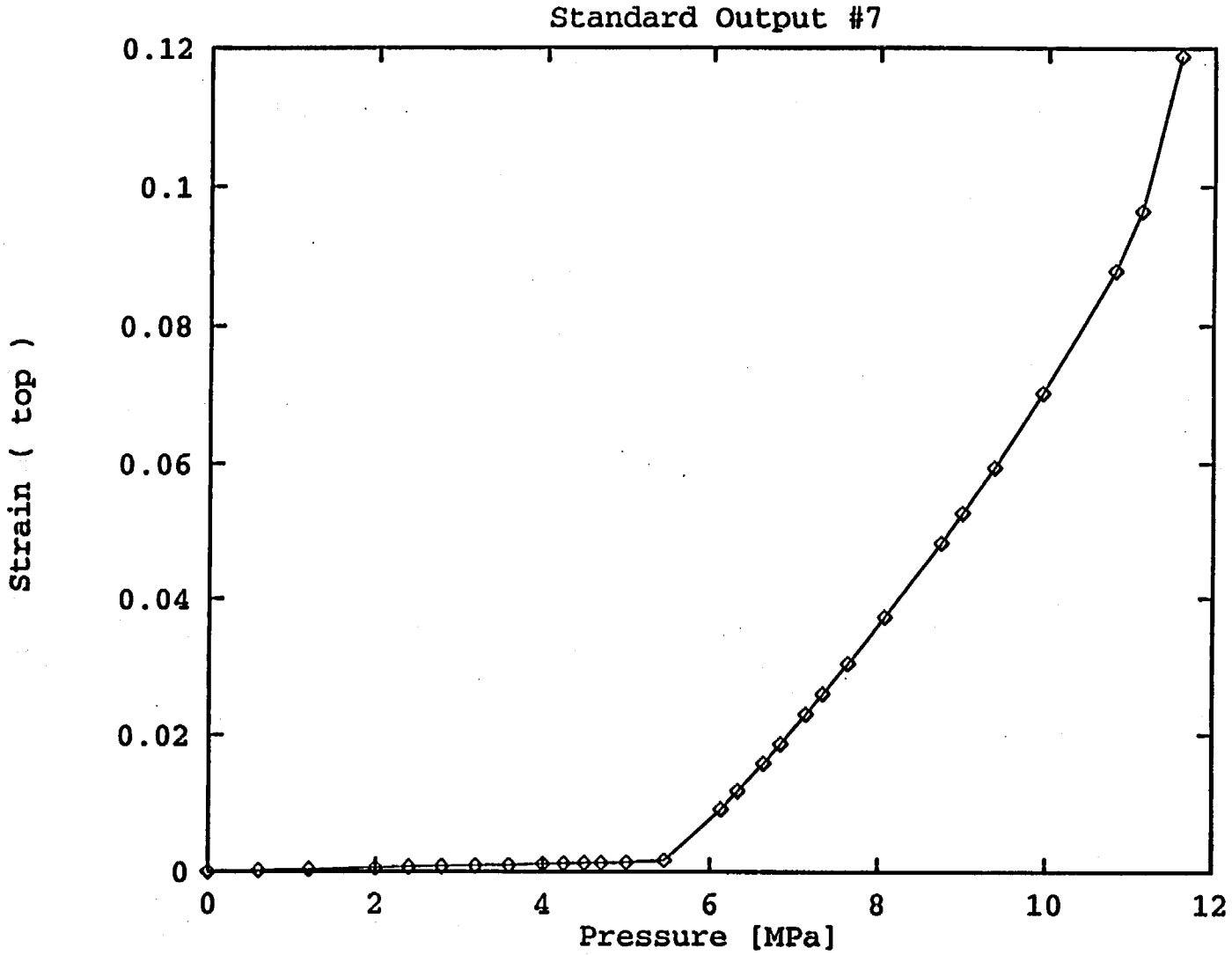
Standard Output #7
Strain (top)
0.12
0.1
0.08
0.06
0.04
0.02
0
0
2
4
6
8
10
12
Pressure [MPa]

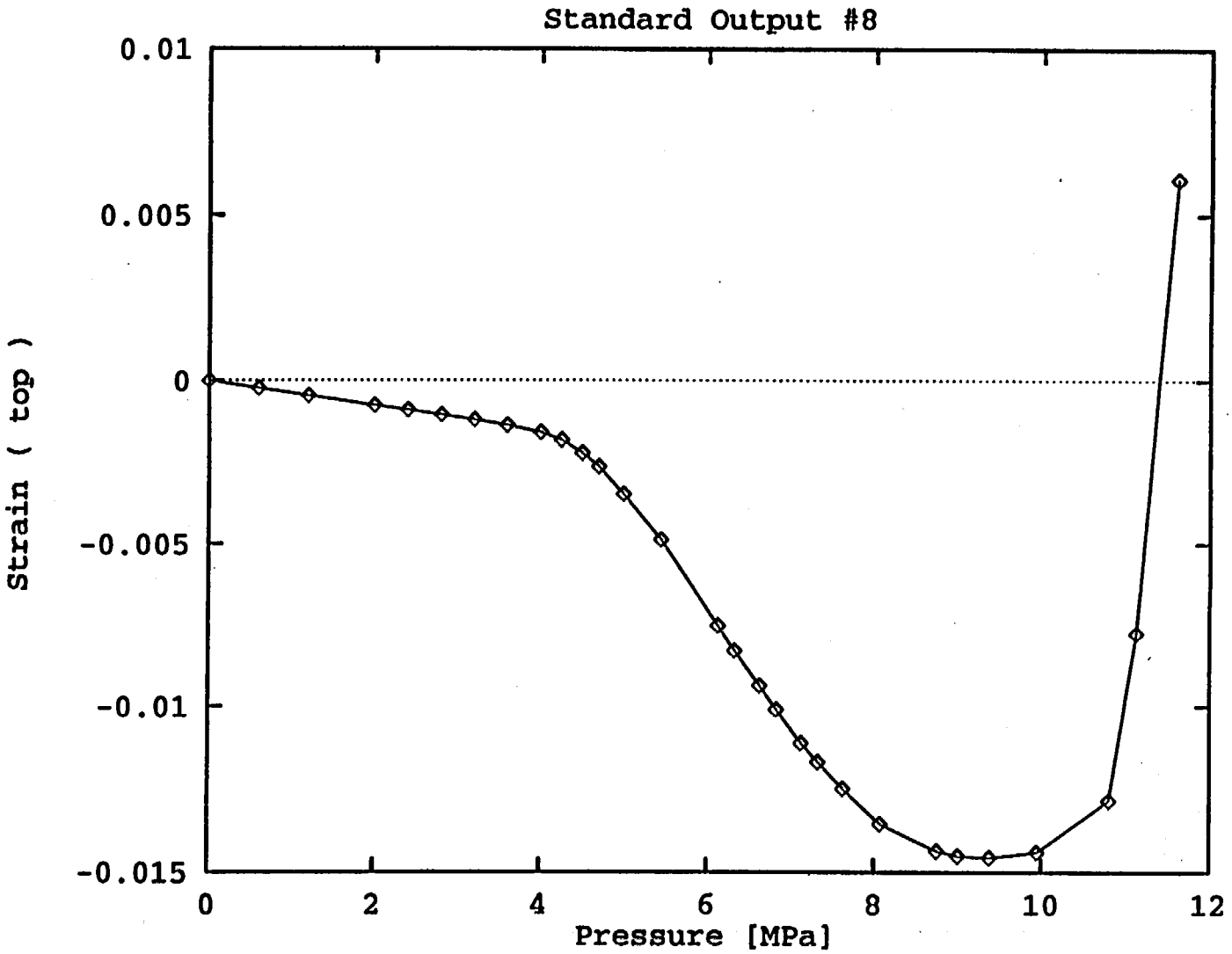
Standard Output #8
0.01
0.005
0
-0.005
-0.01
-0.015
Strain (top)
0
2
4
6
8
10
12
Pressure [MPa]

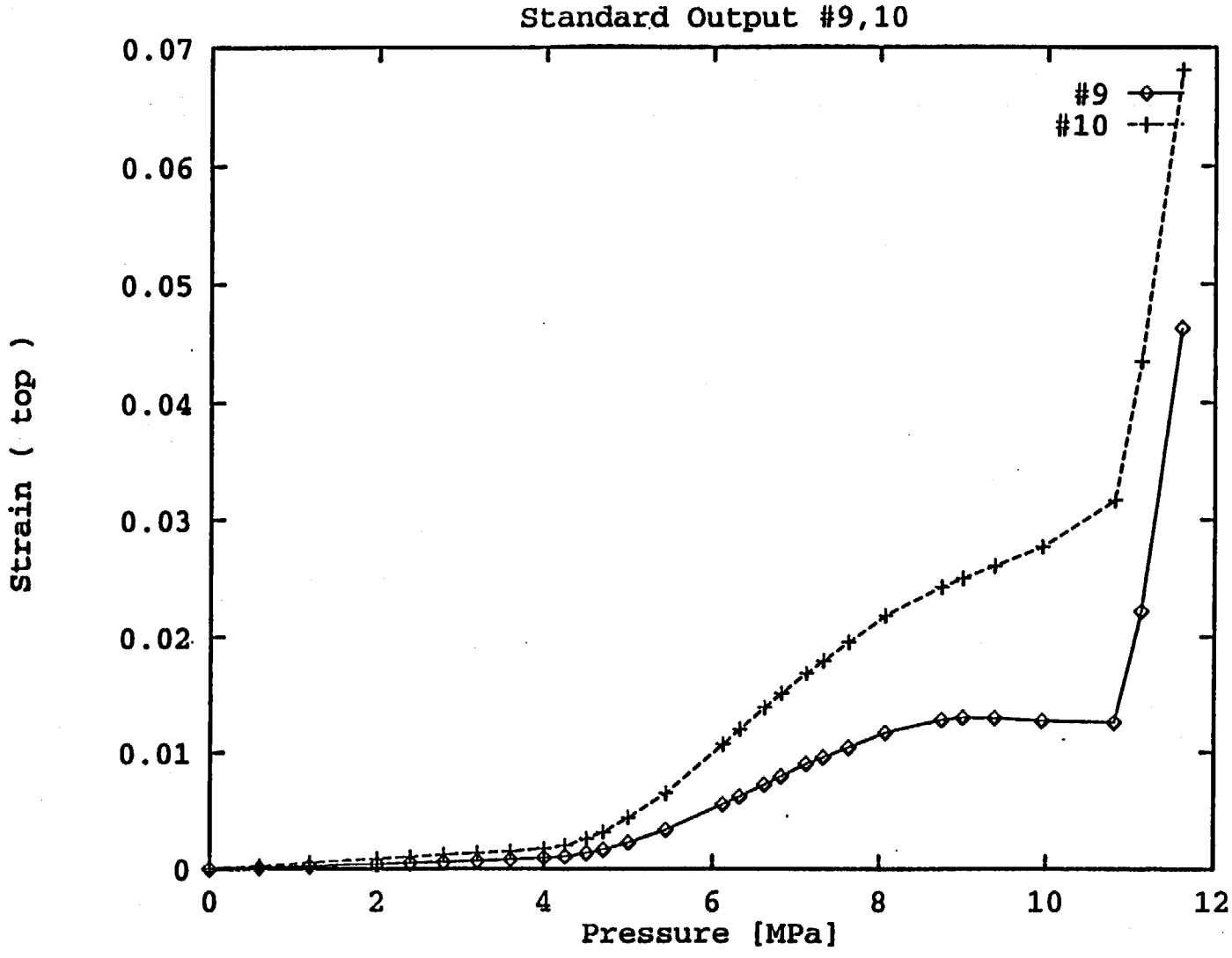
Standard Output #9,10
Strain (top)
Pressure [MPa]
#9
#10
0.07
0.06
0.05
0.04
0.03
0.02
0.01
0
0
2
4
6
8
10
12

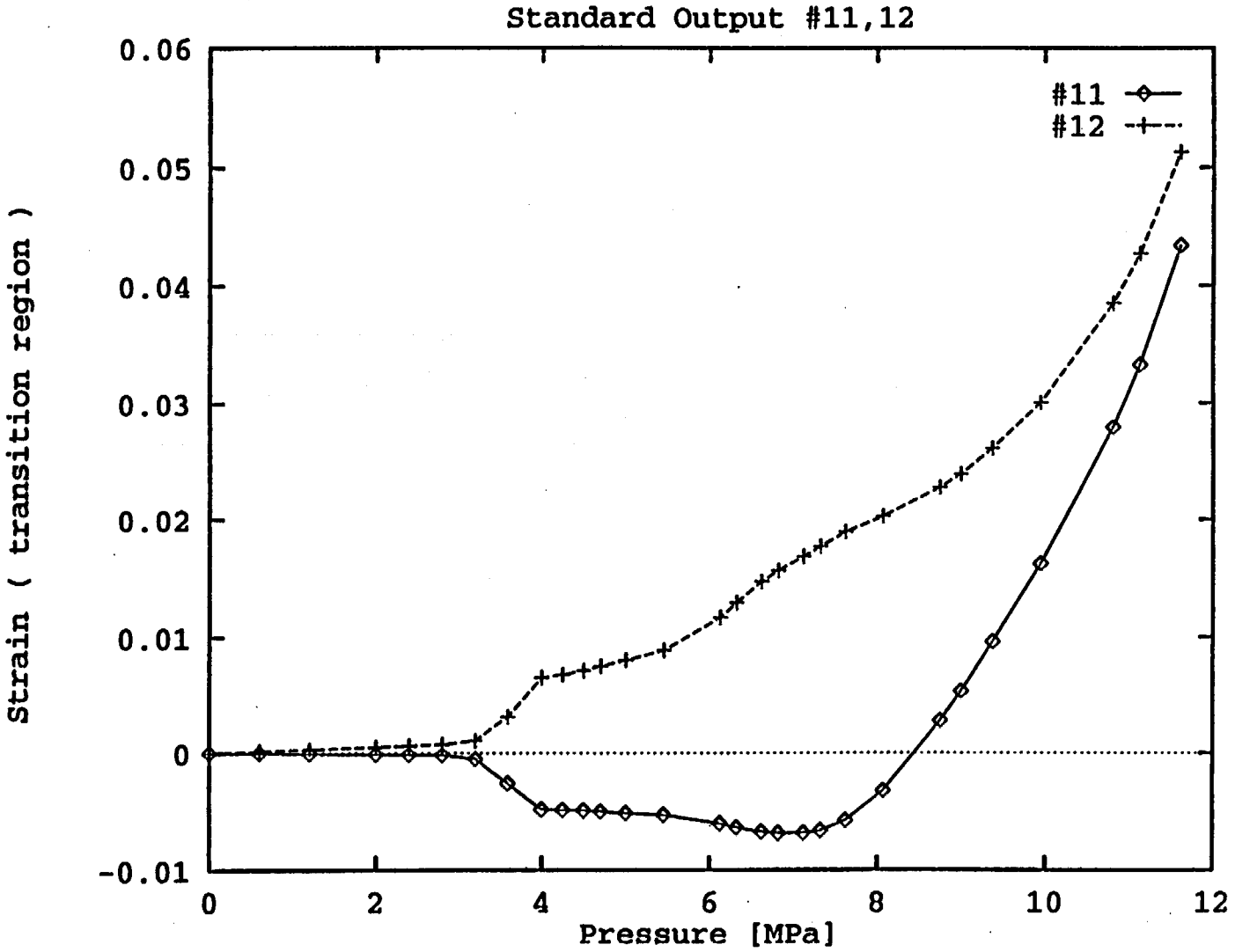
Standard Output #11,12
#11
#12
Strain (transition region)
Pressure [MPa]
0.06
0.05
0.04
0.03
0.02
0.01
0
-0.01
0
2
4
6
8
10
12

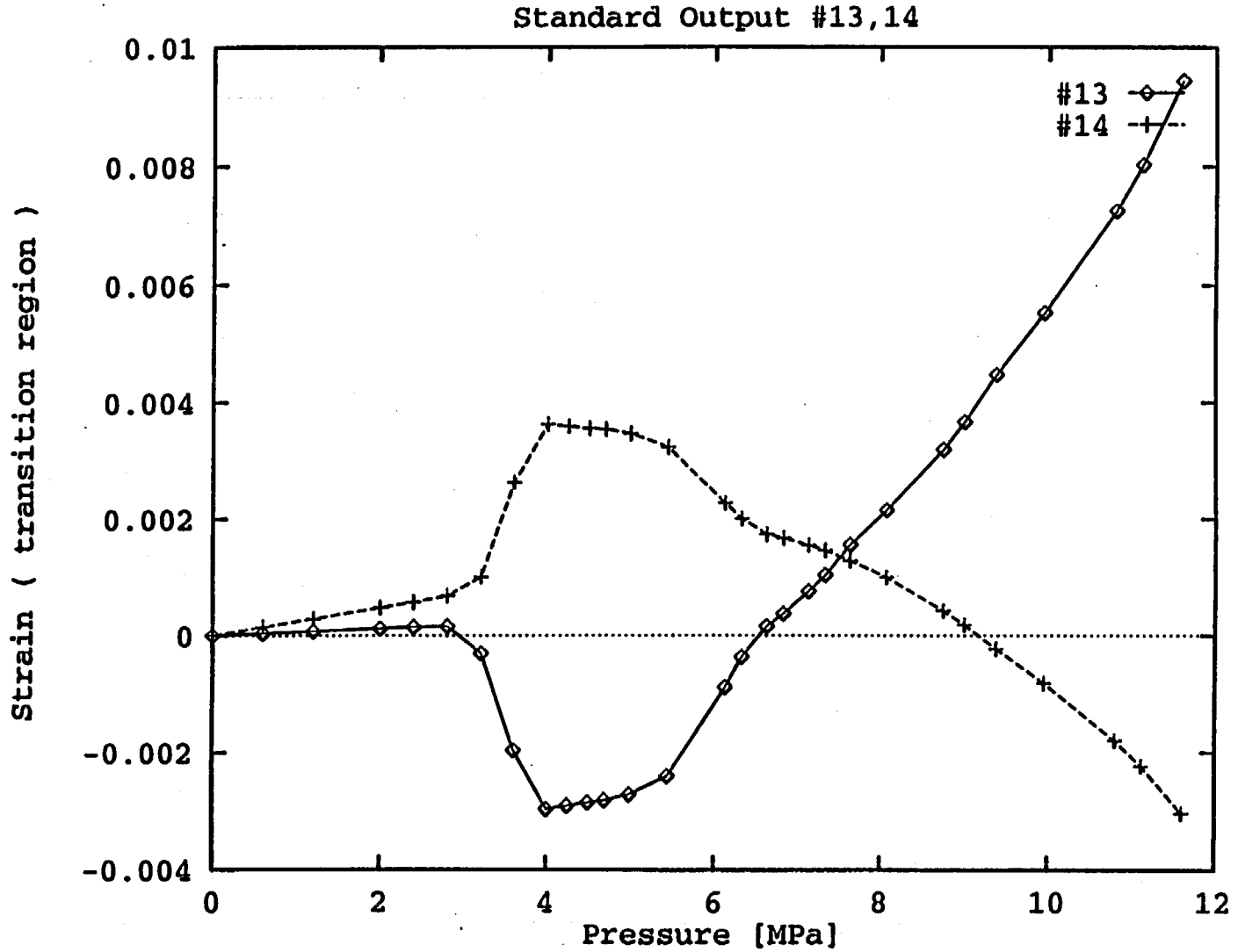
Standard Output #13,14
#13
#14
Strain (transition region)
Pressure [MPa]
0.01
0.008
0.006
0.004
0.002
0
-0.002
-0.004
0
2
4
6
8
10
12

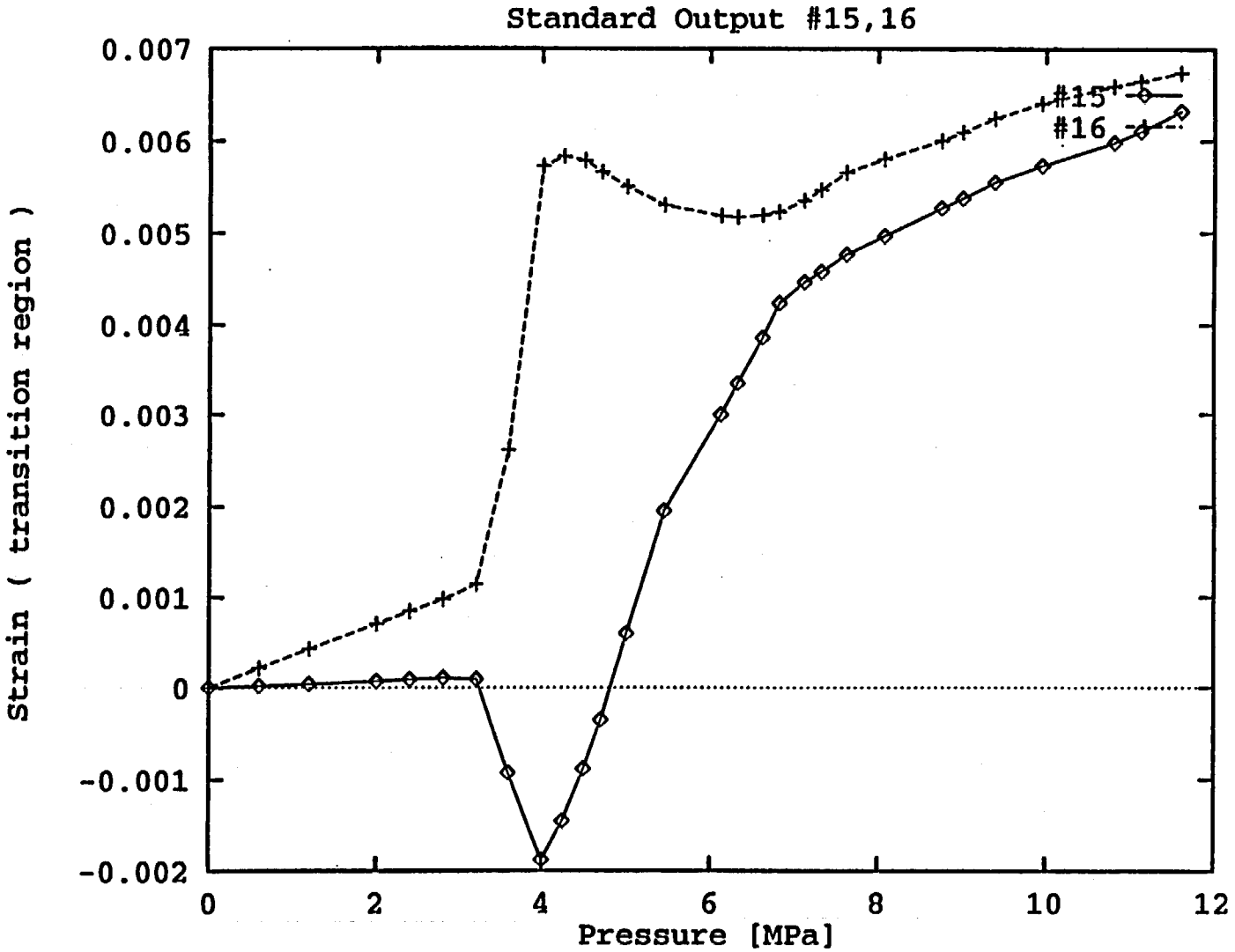
Standard Output #15,16
Strain (transition region)
Pressure [MPa]
#15
#16
0.007
0.006
0.005
0.004
0.003
0.002
0.001
0
-0.001
-0.002
0
2
4
6
8
10
12

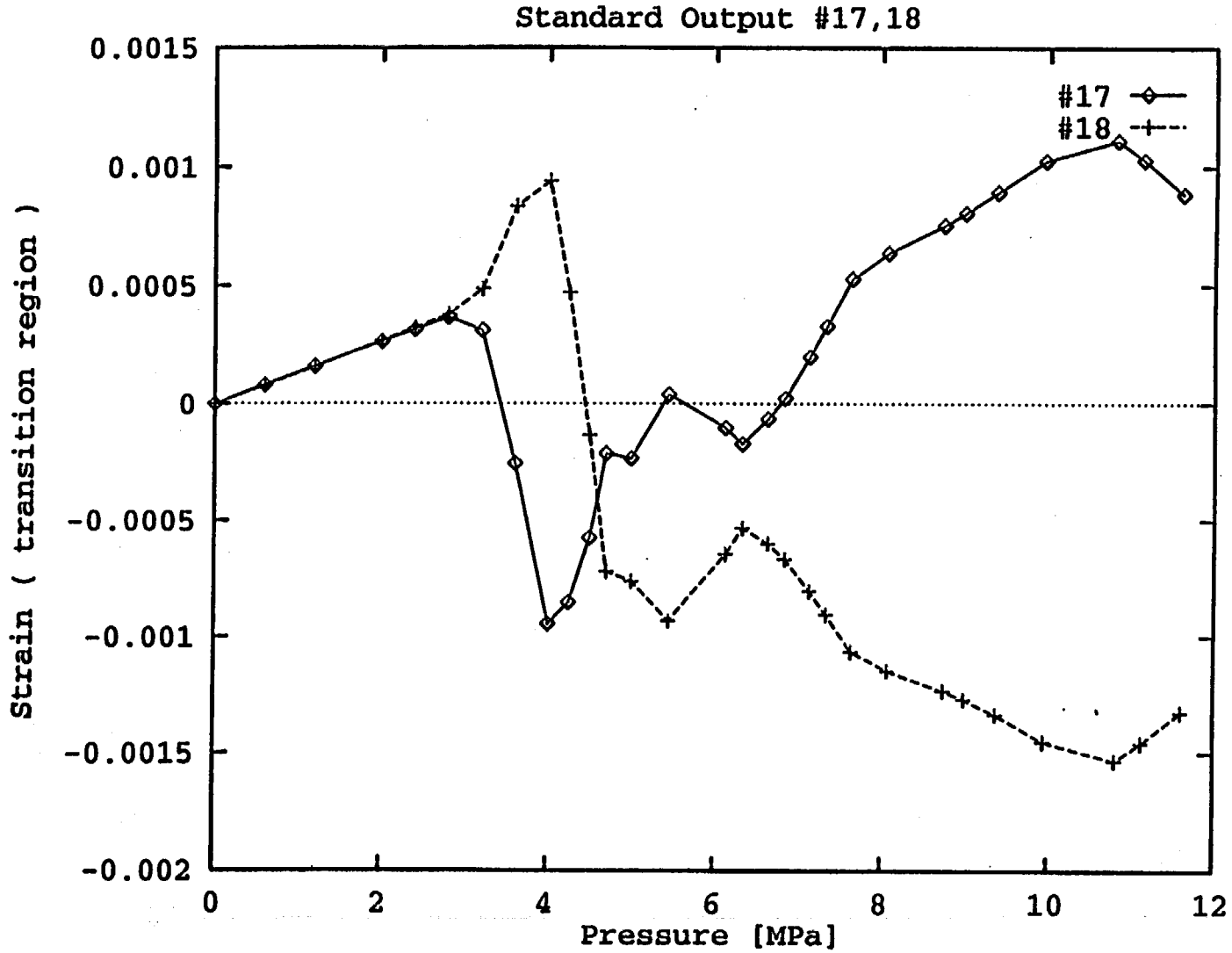
Standard Output #17,18
#17
#18
Strain (transition region)
Pressure [MPa]
0.0015
0.001
0.0005
0
-0.0005
-0.001
-0.0015
-0.002
0
2
4
6
8
10
12

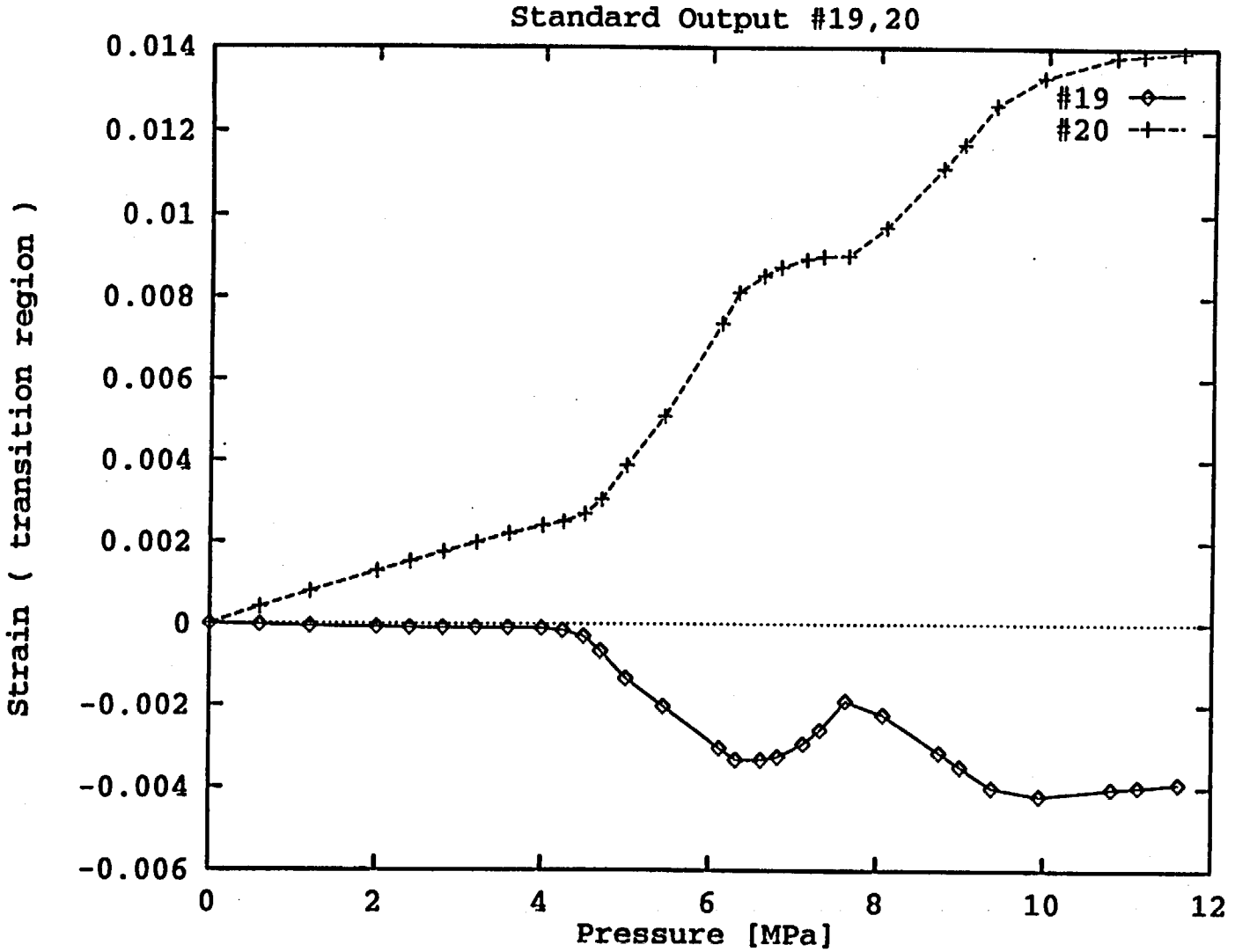
Standard Output #19,20
Strain (transition region)
Pressure [MPa]
#19
#20
0.014
0.012
0.01
0.008
0.006
0.004
0.002
0
-0.002
-0.004
-0.006
0
2
4
6
8
10
12

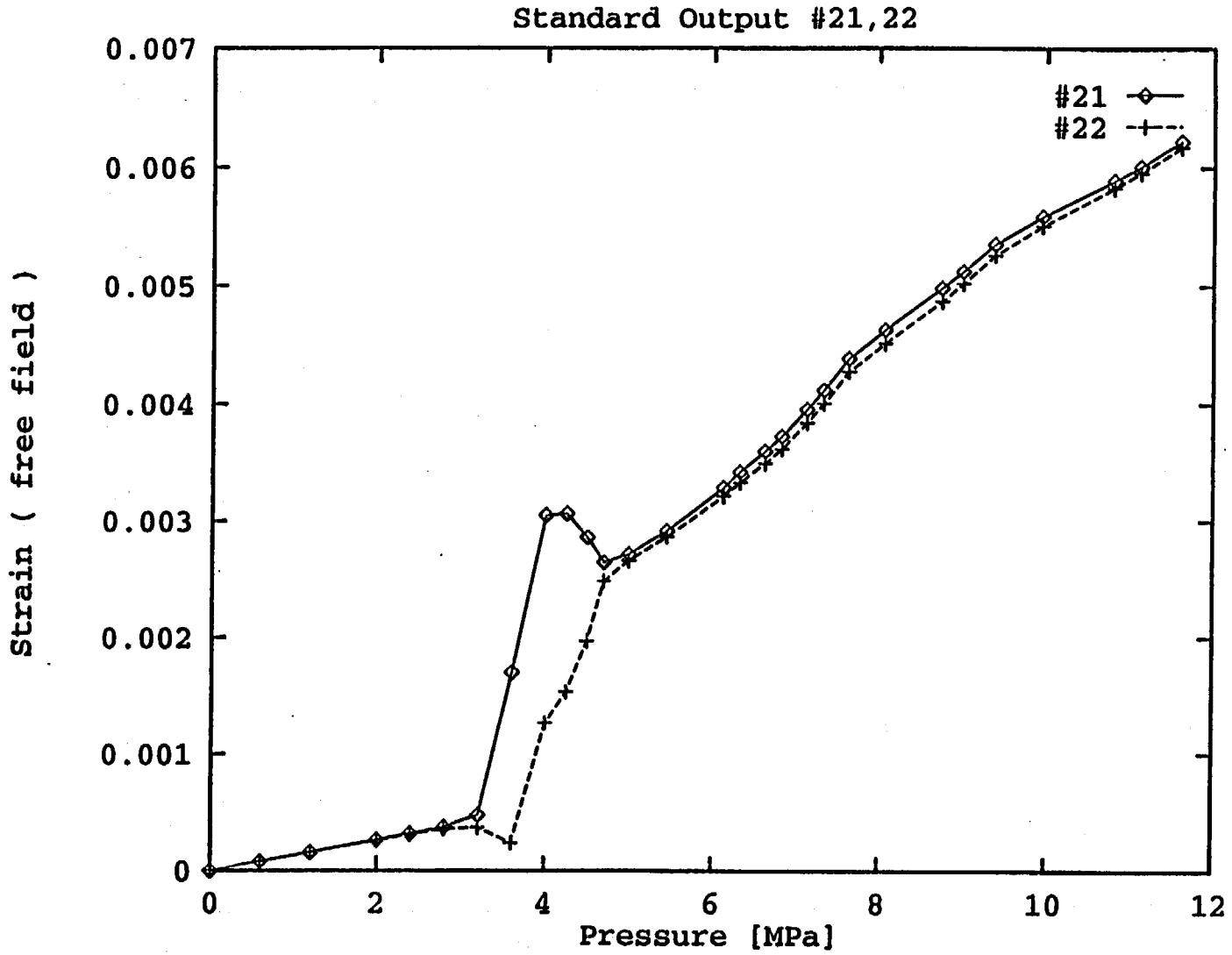
Standard Output #21,22
#21
#22
Strain (free field)
Pressure [MPa]
0.007
0.006
0.005
0.004
0.003
0.002
0.001
0
0
2
4
6
8
10
12

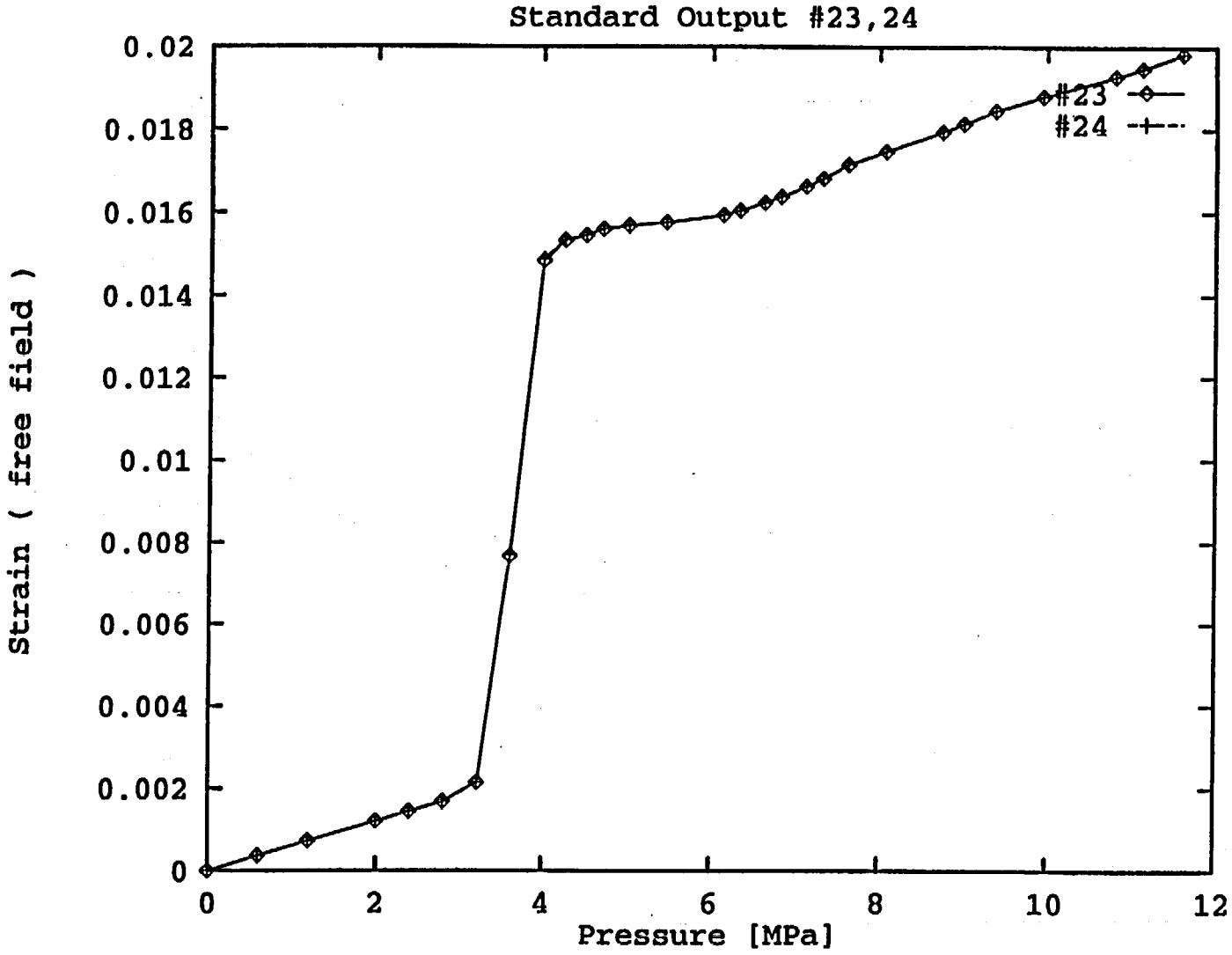
Standard Output #23,24
Strain (free field)
Pressure [MPa]
#23
#24
0.02
0.018
0.016
0.014
0.012
0.01
0.008
0.006
0.004
0.002
0
0
2
4
6
8
10
12

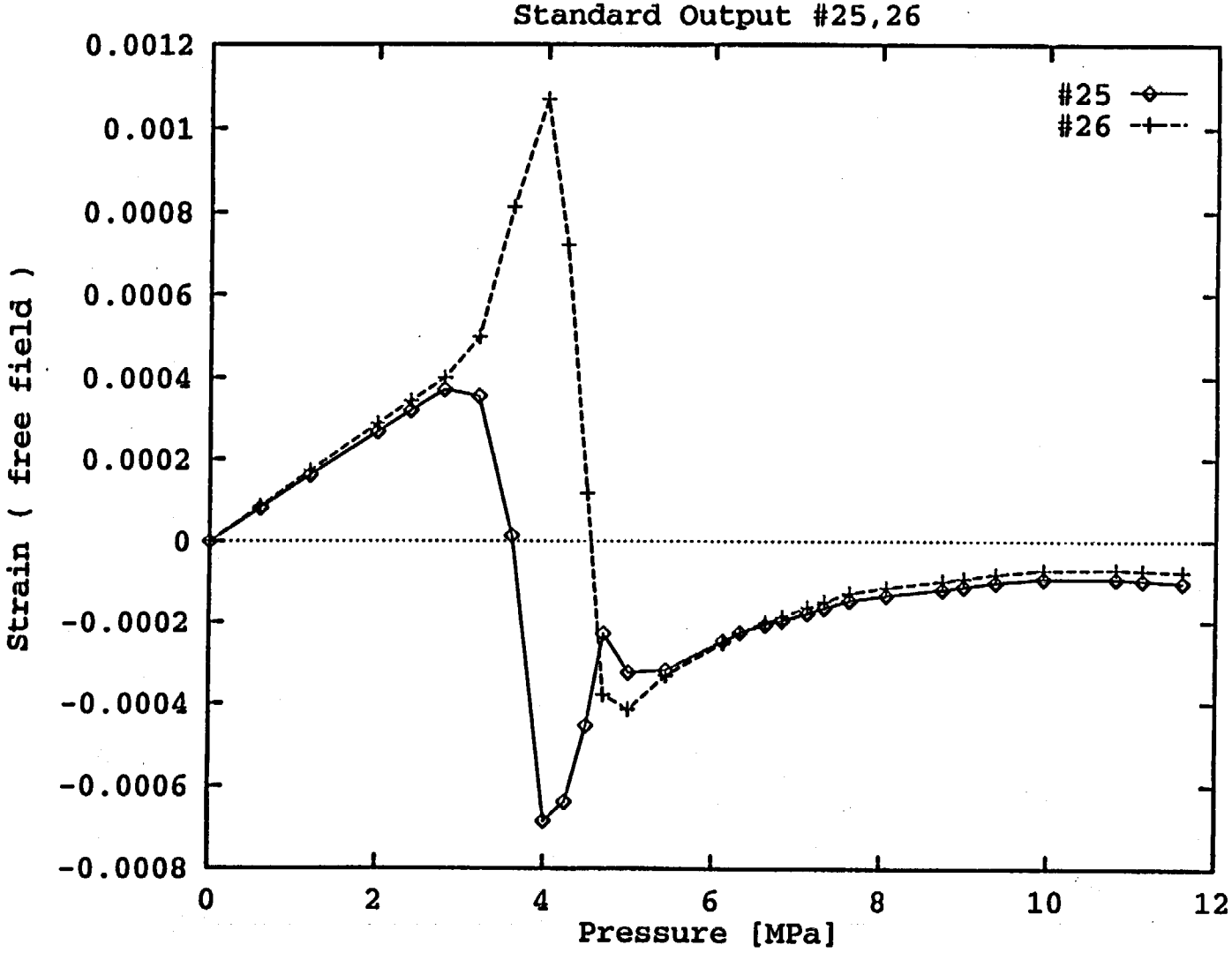
Standard Output #25,26
#25
#26
Strain (free field)
0.0012
0.001
0.0008
0.0006
0.0004
0.0002
0
-0.0002
-0.0004
-0.0006
-0.0008
0
2
4
6
8
10
12
Pressure [MPa]

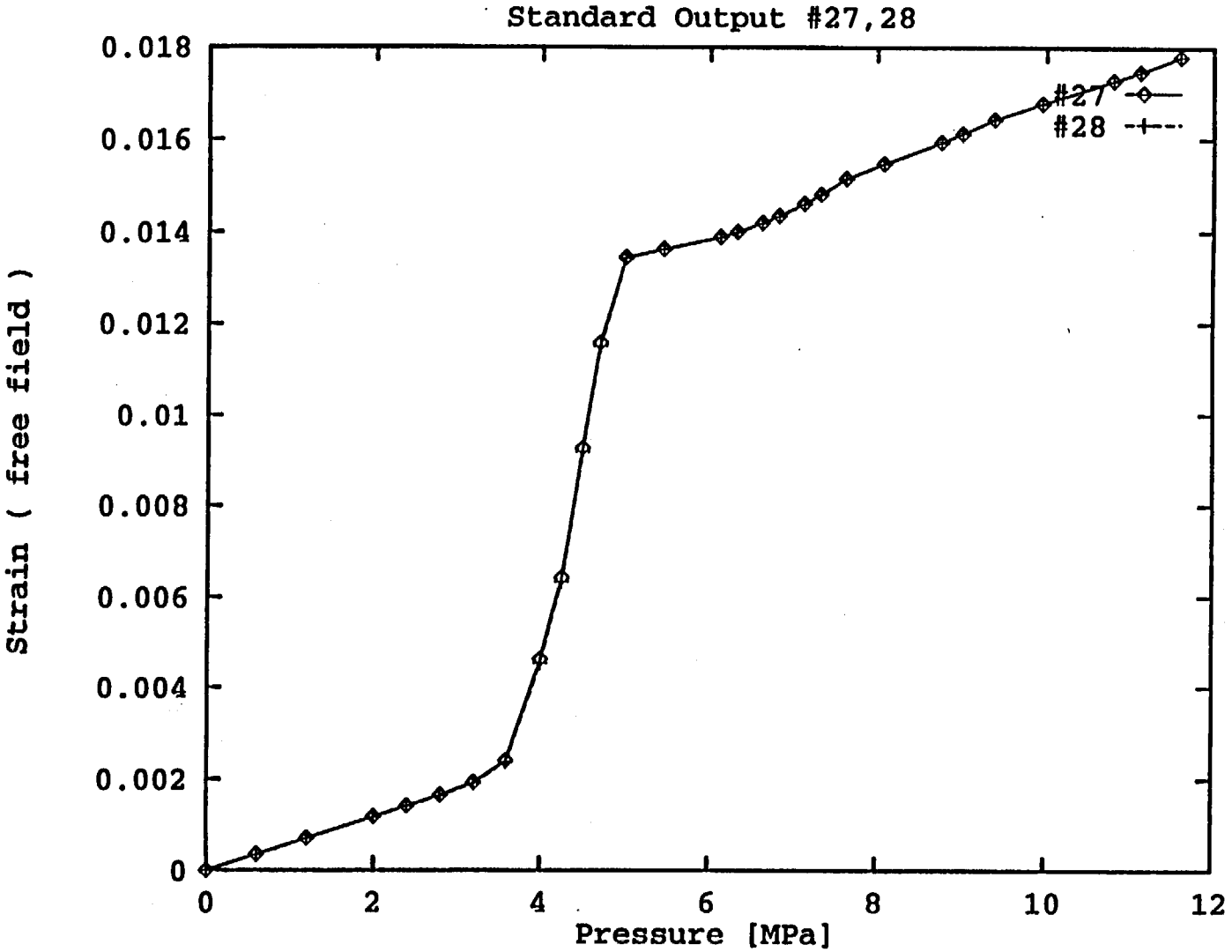
Standard Output #27,28
Strain (free field)
0.018
0.016
0.014
0.012
0.01
0.008
0.006
0.004
0.002
0
0
2
4
6
8
10
12
Pressure [MPa]
#27
#28

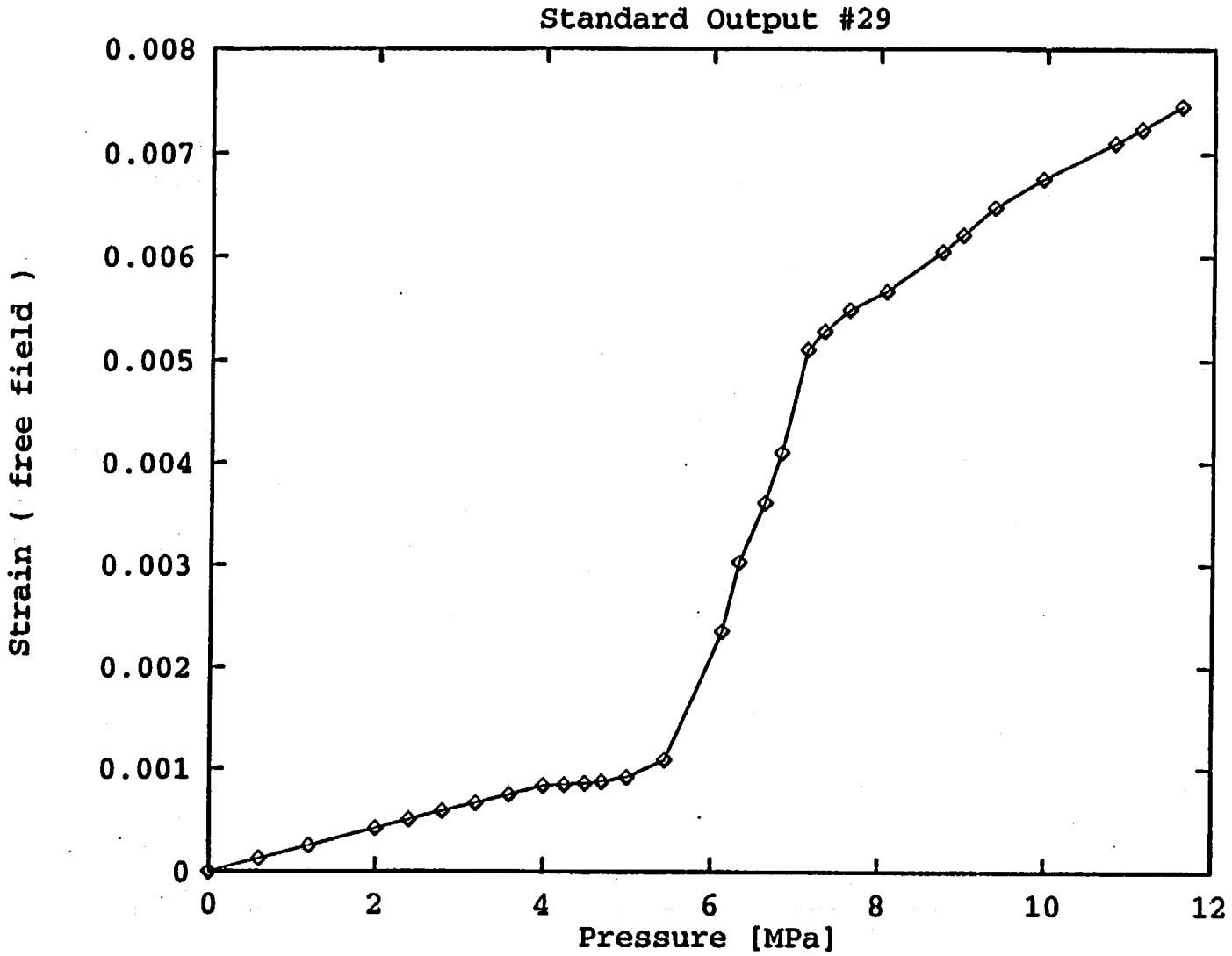
Standard Output #29
Strain (free field)
0.008
0.007
0.006
0.005
0.004
0.003
0.002
0.001
0
0
2
4
6
8
10
12
Pressure [MPa]

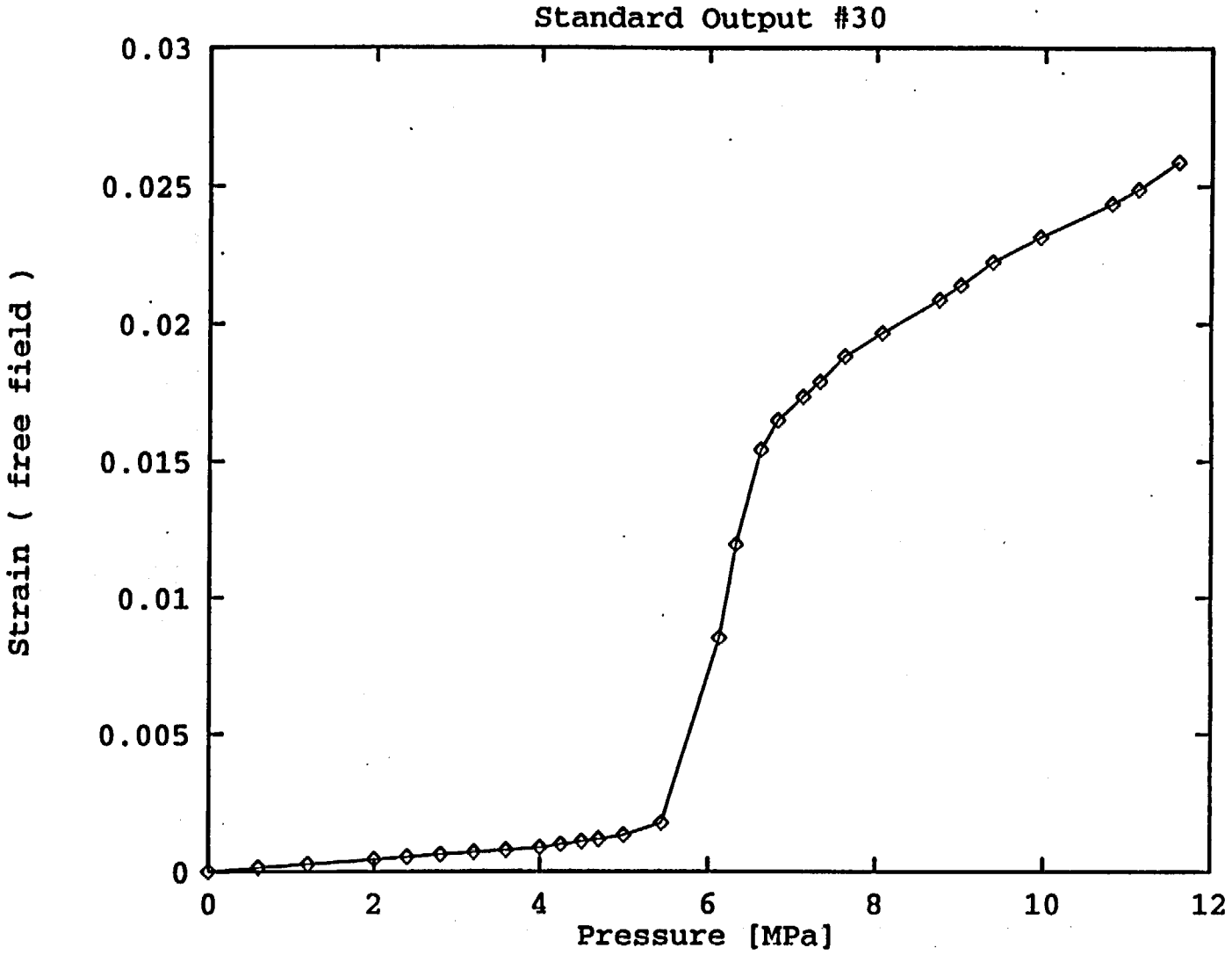
Standard Output #30
Strain (free field)
0.03
0.025
0.02
0.015
0.01
0.005
0
0
2
4
6
8
10
12
Pressure [MPa]

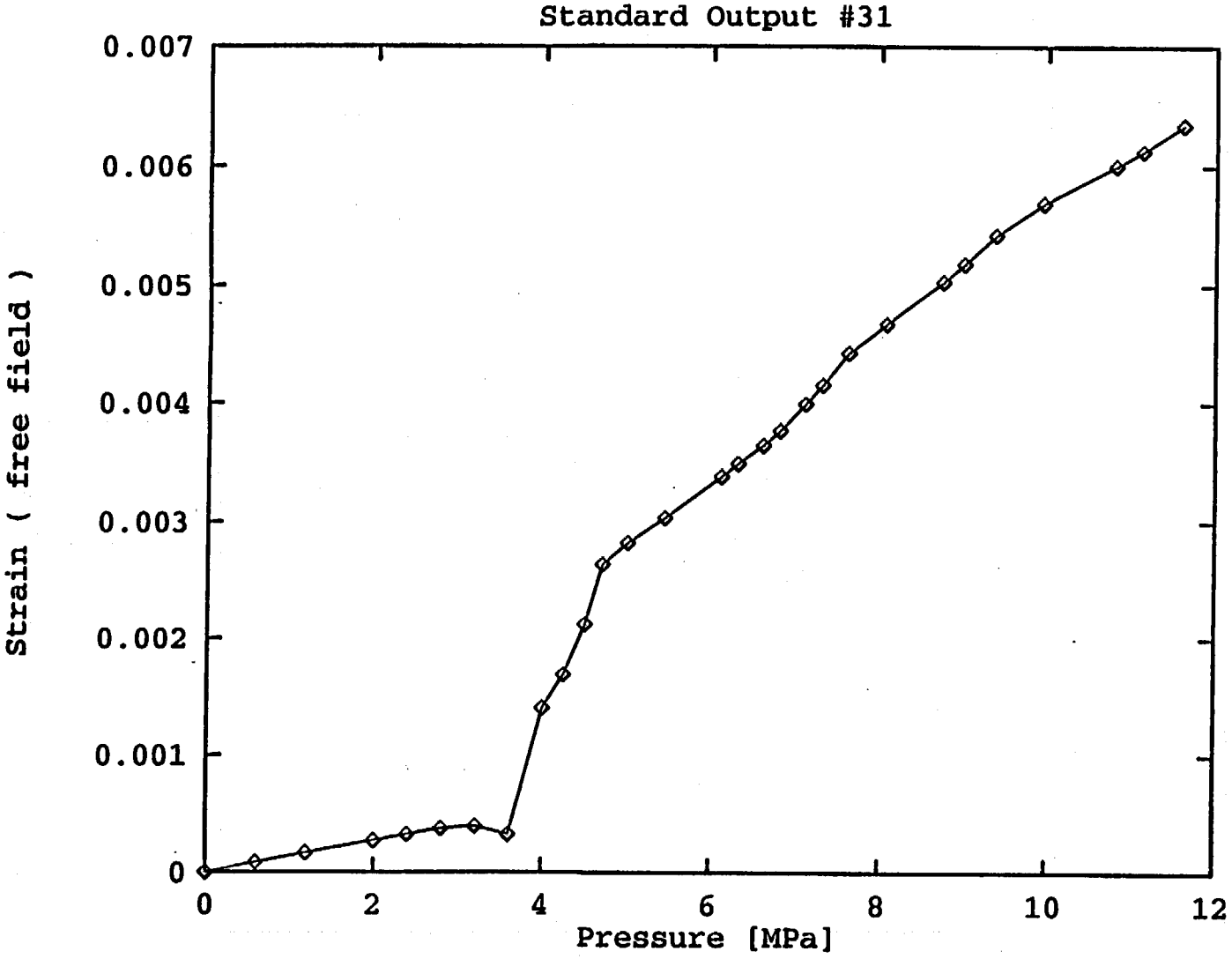
Standard Output #31
Strain (free field)
0.007
0.006
0.005
0.004
0.003
0.002
0.001
0
0
2
4
6
8
10
12
Pressure [MPa]

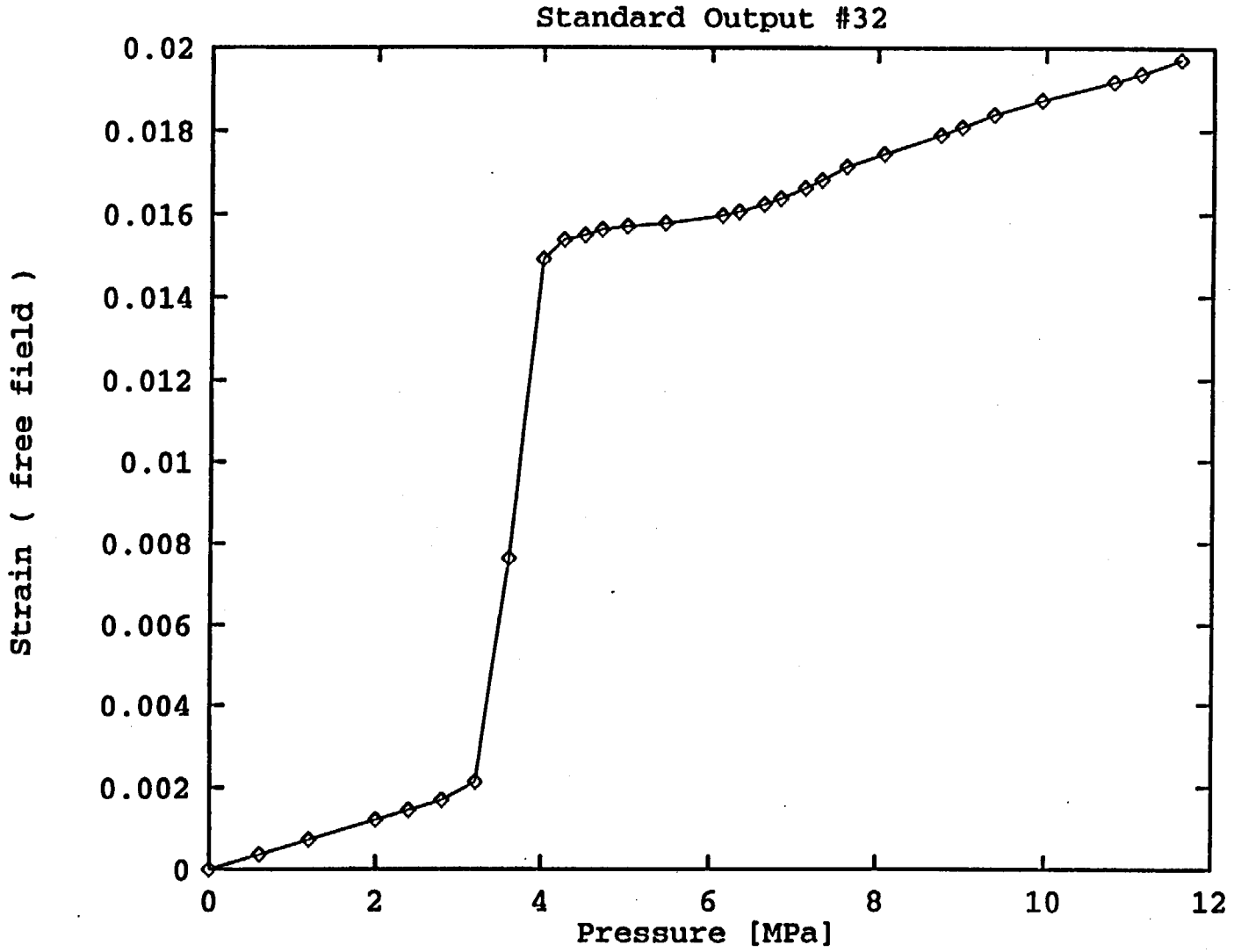
Standard Output #32
Strain (free field)
0.02
0.018
0.016
0.014
0.012
0.01
0.008
0.006
0.004
0.002
0
0
2
4
6
8
10
12
Pressure [MPa]

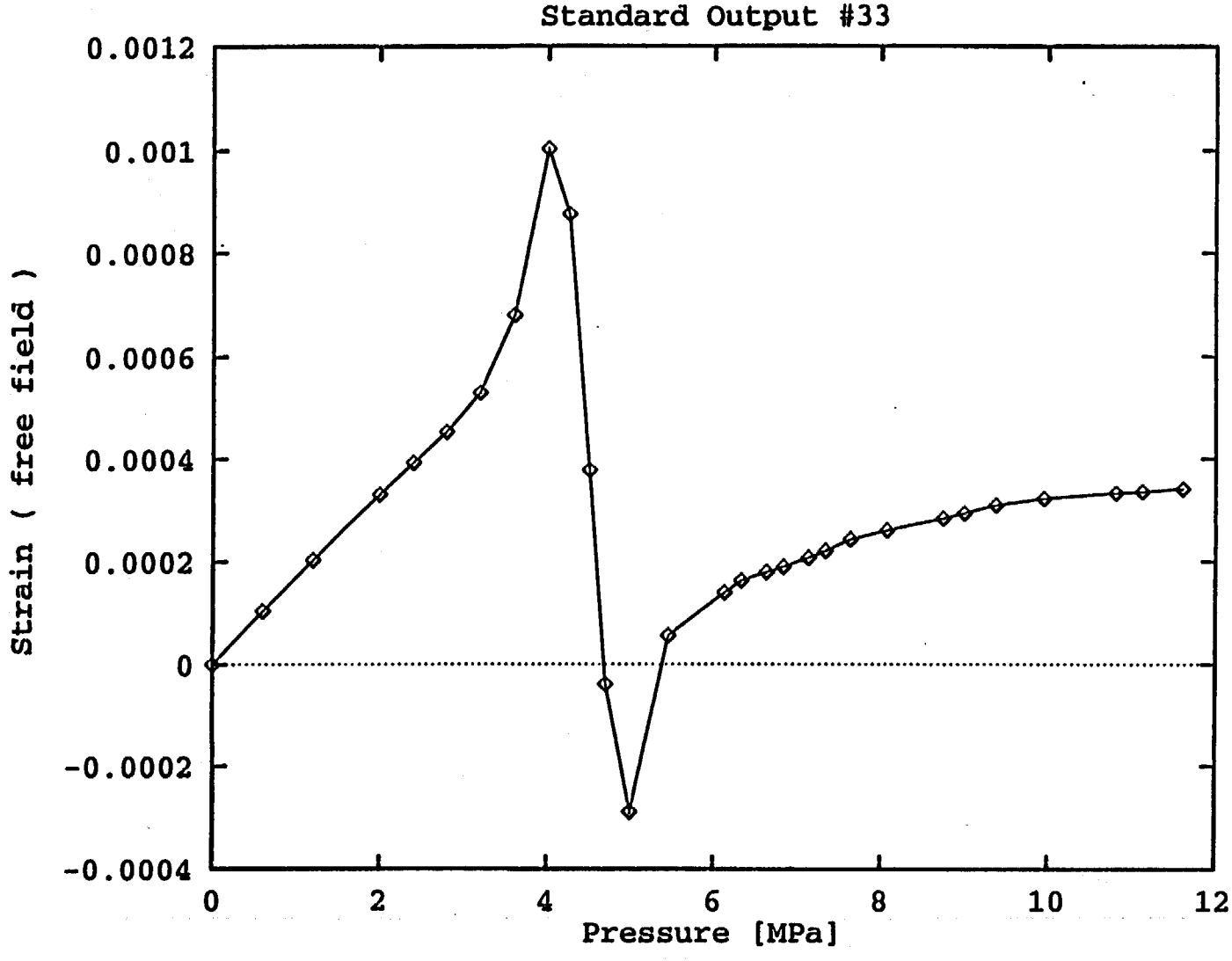
Standard Output #33
Strain (free field)
0.0012
0.001
0.0008
0.0006
0.0004
0.0002
0
-0.0002
-0.0004
0
2
4
6
8
10
12
Pressure [MPa]

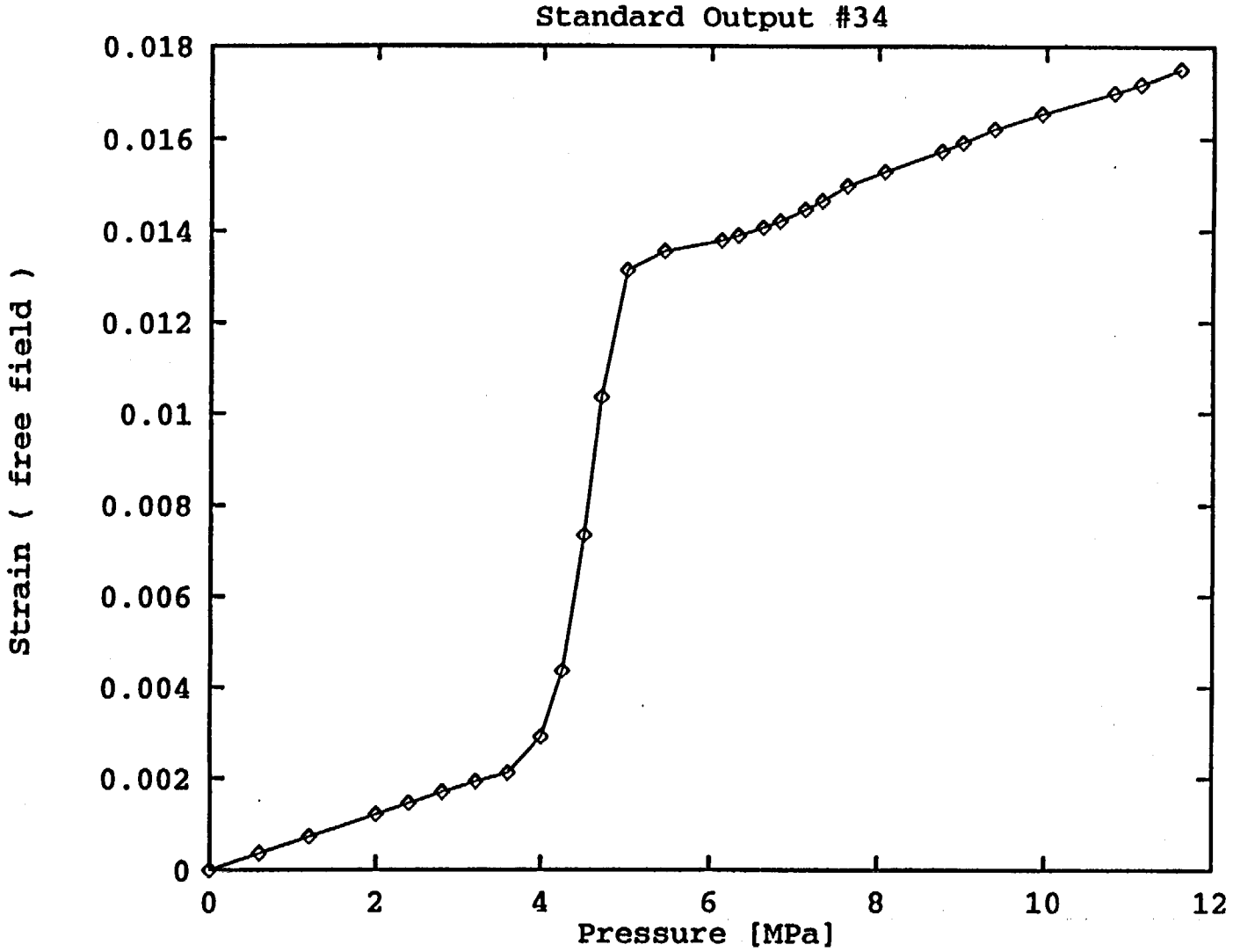
Standard Output #34
Strain (free field)
0.018
0.016
0.014
0.012
0.01
0.008
0.006
0.004
0.002
0
0
2
4
6
8
10
12
Pressure [MPa]

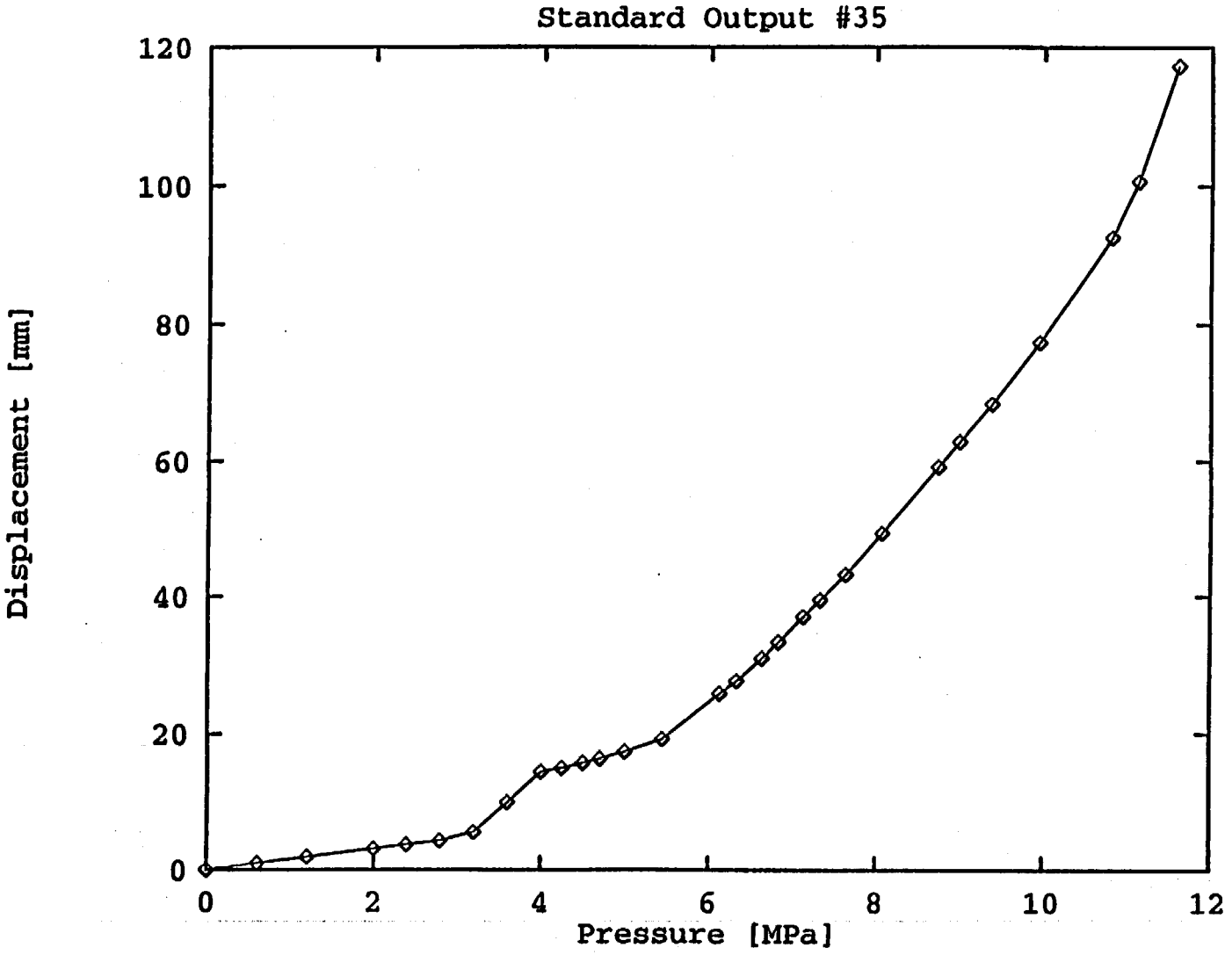
Standard Output #35
Displacement [mm]
120
100
80
60
40
20
0
0
2
4
6
8
10
12
Pressure [MPa]

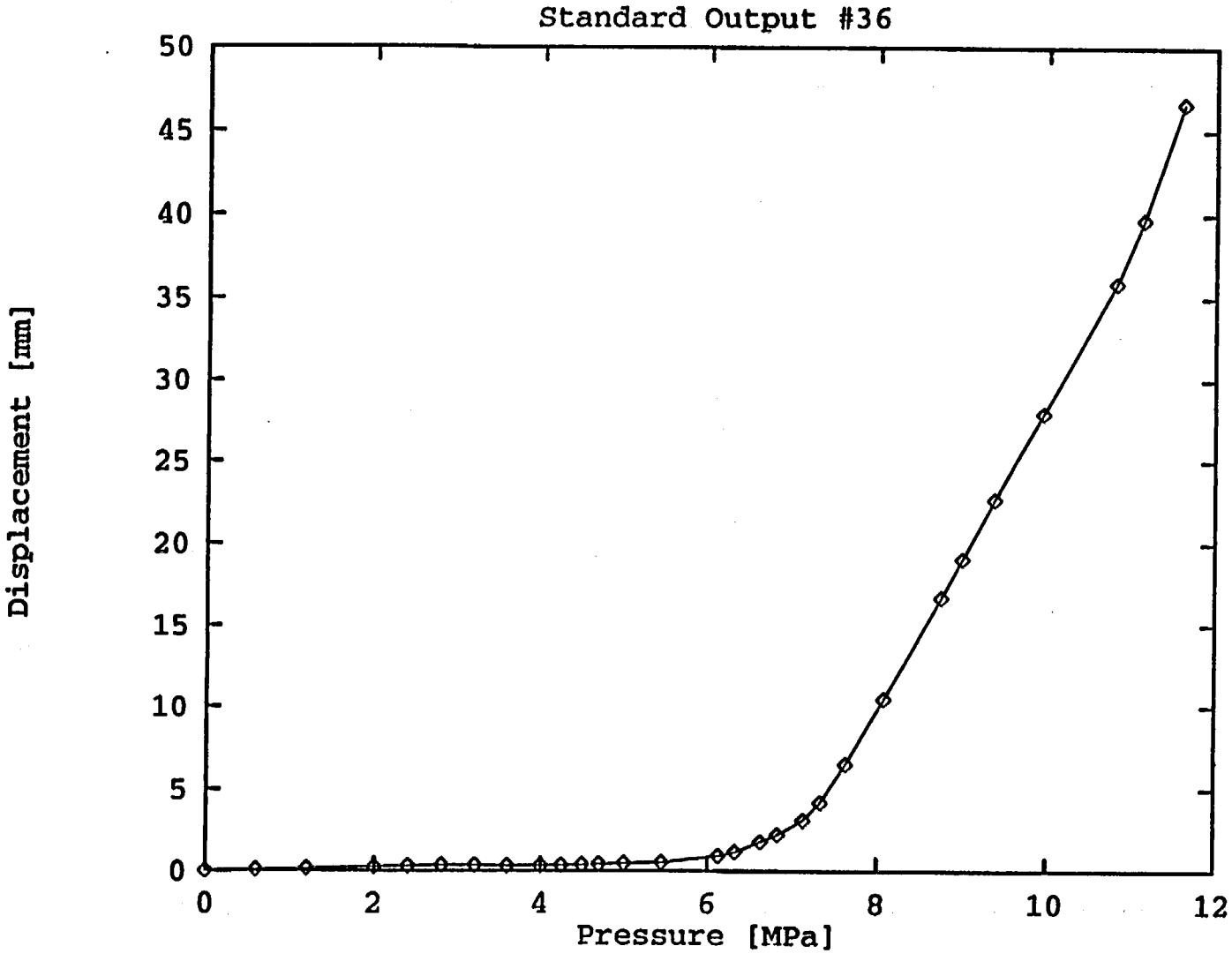
Standard Output #36
Displacement [mm]
Pressure [MPa]
0
5
10
15
20
25
30
35
40
45
50
0
2
4
6
8
10
12

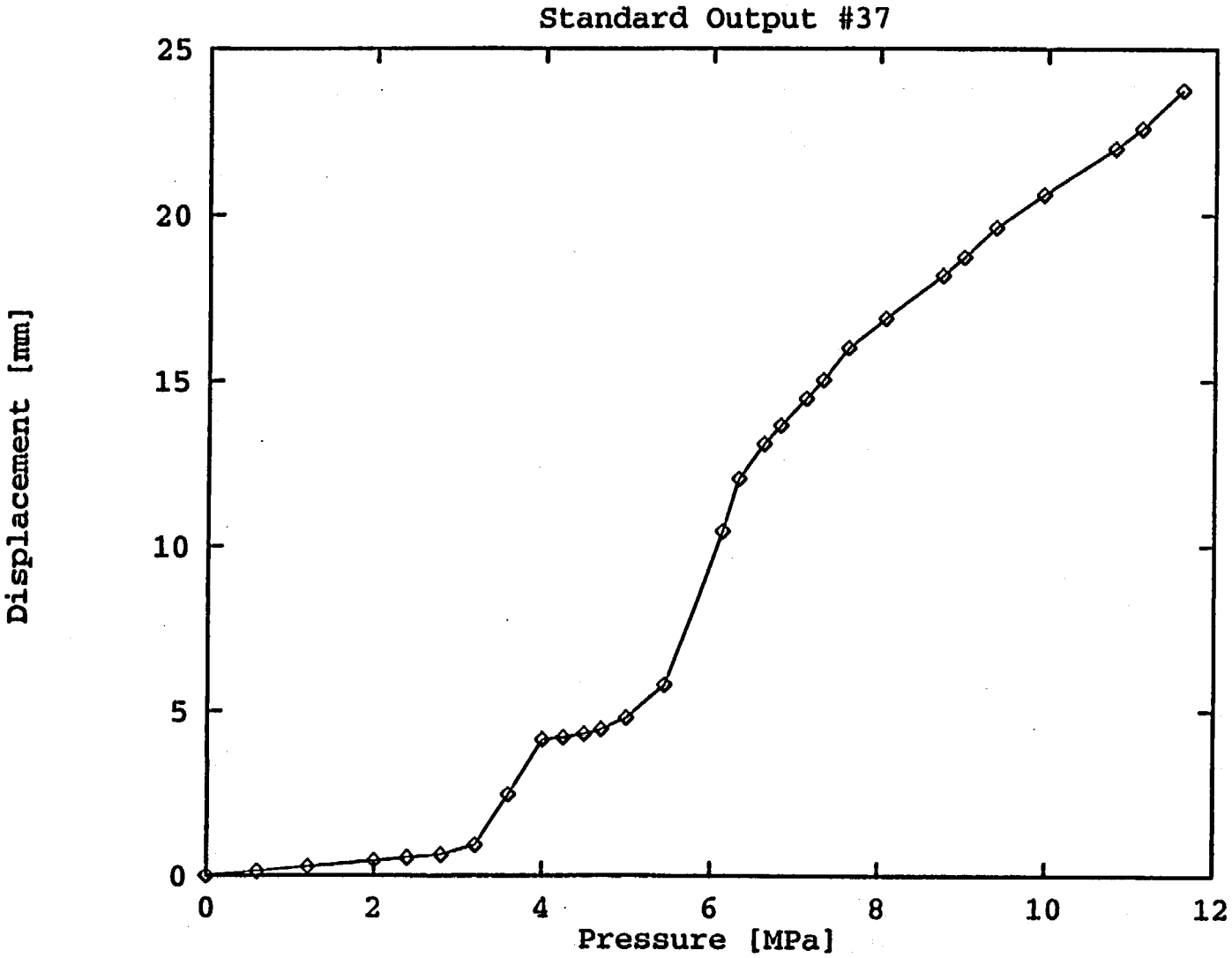
Standard Output #37
Displacement [mm]
Pressure [MPa]
0
5
10
15
20
25
0
2
4
6
8
10
12

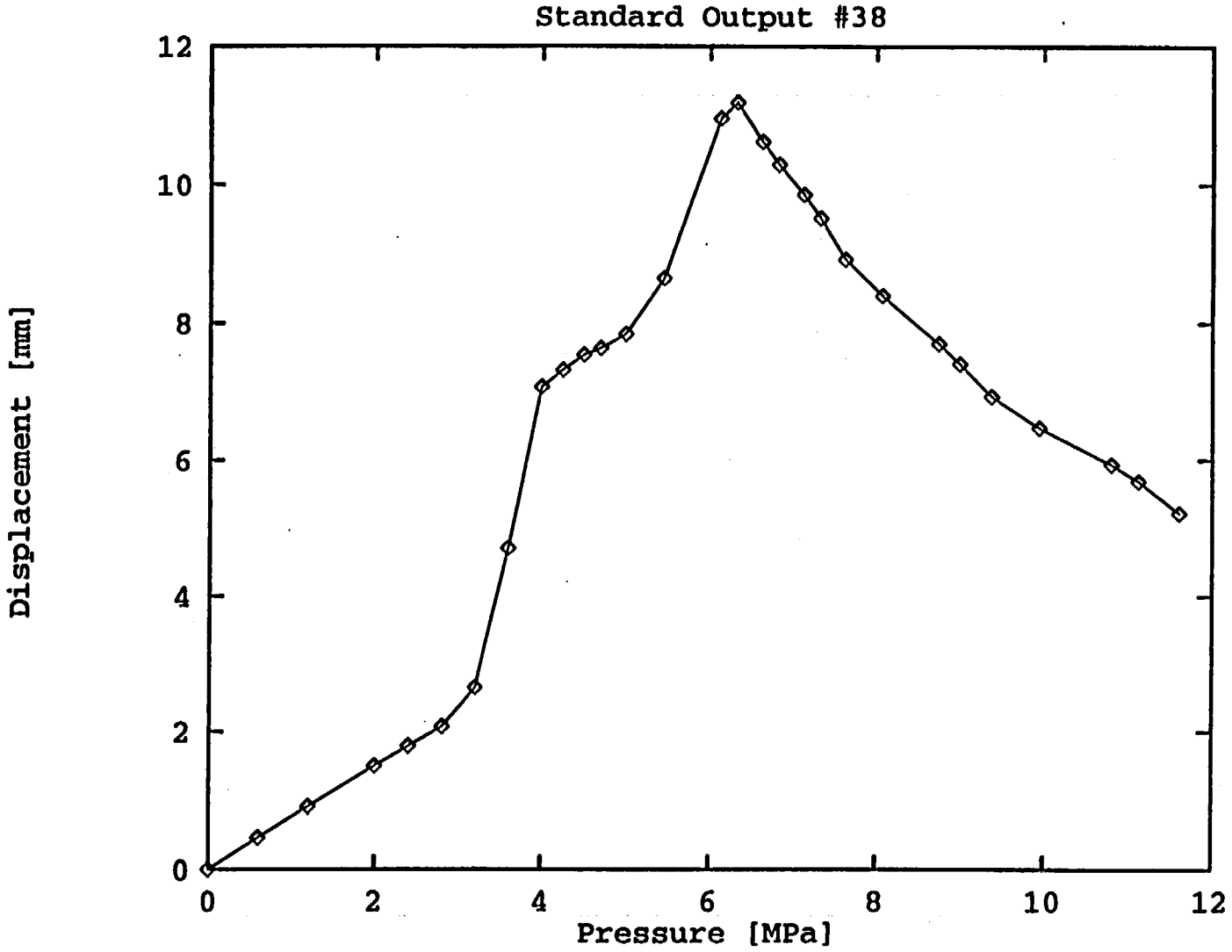
Standard Output #38
Displacement [mm]
Pressure [MPa]
0
2
4
6
8
10
12

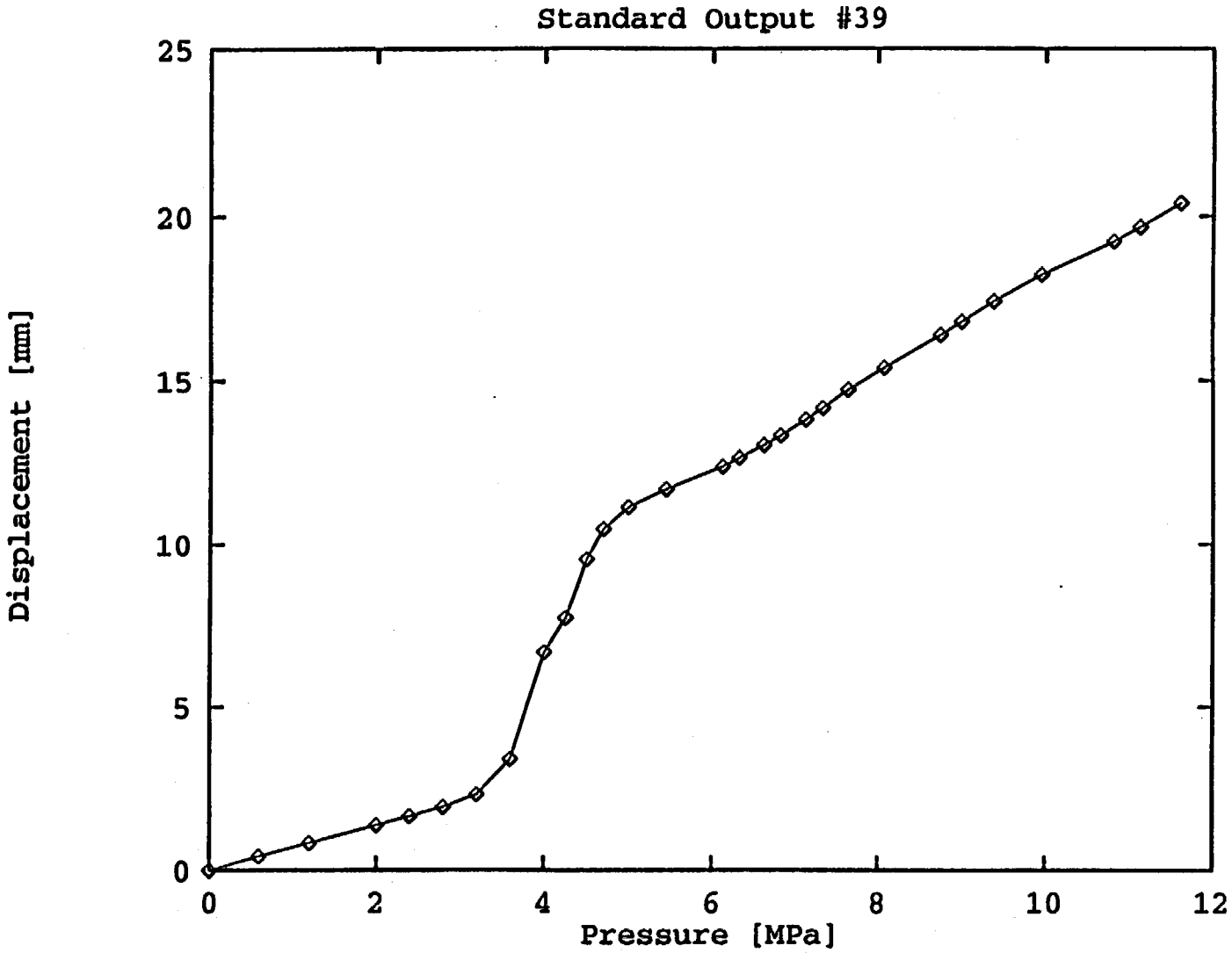
Standard Output #39
Displacement [mm]
25
20
15
10
5
0
0
2
4
6
8
10
12
Pressure [MPa]

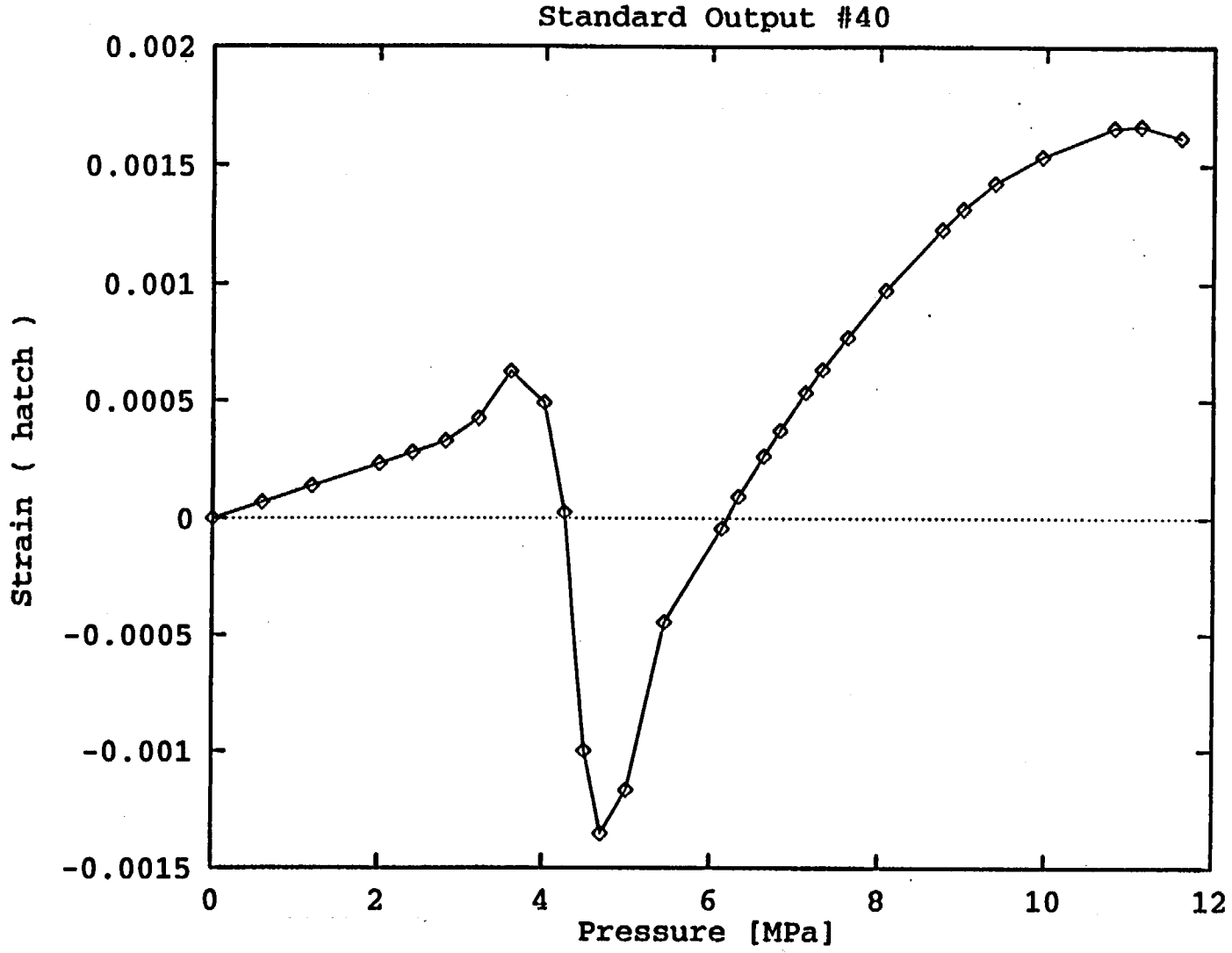
Standard Output #40
Strain (hatch)
0.002
0.0015
0.001
0.0005
0
-0.0005
-0.001
-0.0015
0
2
4
6
8
10
12
Pressure [MPa]

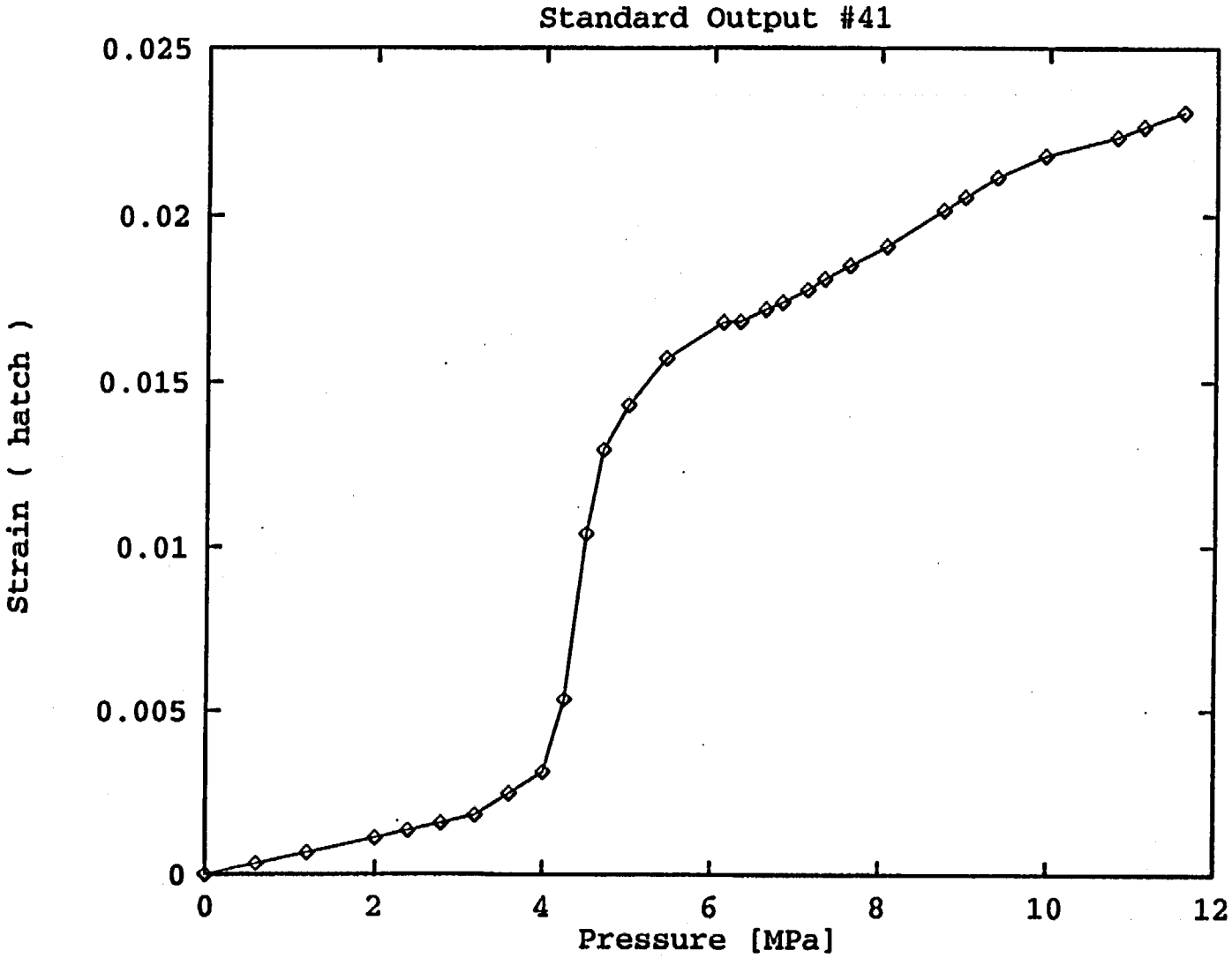
Standard Output #41
0.025
0.02
0.015
0.01
0.005
0
Strain (hatch)
0
2
4
6
8
10
12
Pressure [MPa]

Appendix E-6

Nuclear Power Engineering Corporation

Japan

Pretest Analysis of a 1:10-Scale Steel Containment Model Subject to Static Internal Pressurization

July ,1996

Nuclear Power Engineering Corporation

Contents

Pretest Analysis of a 1:10-Scale Steel Containment Model Subject to Static Internal Pressurization

K. Komine*, M. Konno** and T. Matsumoto*

*Nuclear Power Engineering Corporation
Fujita Kanko Toranomon Bldg.5F
17-1, 3-Chome Toranomon, Minato-ku,
Tokyo 105 Japan

**Hitachi Engineering Corporation
2-1, Saiwai-cho 3-Chome, Hitachi-shi,
Ibaraki-ken, 317 Japan

Abstract

This report summarizes the results of a review, on the basis of pretest analysis, about deformation behavior, failure pressure and failure mode of Steel Containment Vessel (SCV) test model, which is 1/10 scale model (1/4 thickness) of actual SCV, under pressure beyond design conditions.
The reviewed items and evaluation method are as follows :

(1) Global behavior, failure pressure and failure mode of the SCV test model 2-D axisymmetric elasto - plastic/large displacement/contact analysis.
   a. parameter study
   b. global behavior prediction of SCV test model based on the results of the parameter study.
(2) Global and local behavior, failure pressure and failure mode of the SCV test model 3-D elasto-plastic /large displacement/contact analysis.
   a. global behavior evaluation of SCV test model
   b. top head submodel
   c. equipment hatch submodel
   d. top head buckling model

Based on the above results, a predictive study of the pressure test on SCV test model was conducted.

1. Introduction

The nuclear reactor containment vessel is an important equipment which prevents release of radioactive materials outside of the system at accidents. Since Chernobyl accident, many research programs on the containment vessel under severe accident conditions, especially in the U.S. and European countries, have been conducted. Relating such research programs, the NUPEC and the USNRC are carrying out a cooperative research program on structural integrity of various containments. One of the cooperative research programs is a pneumatic pressurization test for the SCV test model. This test will be done at Sandia National Laboratories (SNL), Albuquerque, New Mexico, USA. Regarding this test, a multi-national analysis effort in the evaluation of the SCV model test, Round-Robin activity, is sponsored by the NUPEC and the USNRC and is coordinated by the SNL.

We NUPEC conducted a pretest analysis of the SCV model test for the Round-Robin activity. This paper describes the results of the pretest analysis.

2. Analysis Method and Outline of Analysis Series

During pressurization, SCV test model is predicted to show non-linear behavior, due to material yield and contact with CS, as well as large displacement effects as deformation progresses.
ABAQUS (version 5.4 and 5.5) has been used to perform the analysis, because this general structural analysis program with finite element method possesses good non-linear analytic capabilities for such materials, geometry (structure) and boundaries, and is also widely used for a number of analyses. [8.1][8.2]
Table 2-1 shows the list of calculations conducted in this analysis.
This analysis program consists of two parts, i.e. 2-D analysis to grasp the global behavior of SCV test model and 3-D analysis to grasp local behaviors.
For the 2-D analysis concerning the global behavior of SCV test model, analysis performed a study on 5 cases, case-AX1 to 5, from which the most appropriate case is to be selected, after having performed elasto-plastic/large displacement/contact analysis with such parameters as gap and friction coefficient, to realize the effects of the parameters on deformation behavior of SCV test model.
For the 3-D analysis, case-3D1 has been performed elasto-plastic/large displacement/contact analysis, aiming at the deformation of the equipment hatch and its vicinity, which can not be modeled in 2-D analysis. Case-3D2 and case-3D3 study top head, knuckle and equipment hatch regions which are expected to be under the most severe conditions in terms of strength. These regions are separated from the whole model to create a submodel with fine meshes, which has been examined meticulously. Case-3D4 has been conducted on an analytical model to study buckling of top head region and linear buckling eigenvalue analysis has also been performed.

Table 2-1 Outline of Analysis Series

Case	description
AX1	Parameter study using Global Axisymmetric Shell Model Analysis. SCV-CS Gap size = 18.0 mm (Friction Coefficient = 0.2)
AX2	Parameter study using Global Axisymmetric Shell Model Analysis. SCV-CS Gap size = 14.4 mm (Friction Coefficient = 0.2)
AX3	Parameter study using Global Axisymmetric Shell Model Analysis. SCV-CS Gap size = 21.6 mm (Friction Coefficient = 0.2)
AX4	Parameter study using Global Axisymmetric Shell Model Analysis. SCV-CS Friction Coefficient = 0.0 mm (Gap Size = 18.0 mm)
AX5	Parameter study using Global Axisymmetric Shell Model Analysis. SCV-CS Friction Coefficient = 0.4 mm (Gap Size = 18.0 mm)
3D1	Global 3-D Shell Model Analysis. Gap Size = 18.0 mm / SCV - CS Friction Coefficient = 0.2
3D2	Local Top Head 3-D Shell Submodel Analysis. Gap Size = 18.0 mm / SCV - CS Friction Coefficient = 0.2
3D3	Local E/H 3-D Shell Submodel Analysis. Gap Size = 18.0 mm / SCV - CS Friction Coefficient = 0.2
3D4	Local Top Head 3-D Shell model Buckling Eigenvalue Analysis.

3. Analytical Conditions

3.1 Adopted Analysis Options

ABAQUS (version 5.4 and 5.5) has been used for the pretest analysis. The adopted analysis options are as follows.

As for material model, an isotropic elasto-plastic material model has been selected with *ELASTIC and *PLASTIC, which are options about materials provided by ABAQUS. Then, TYPE, optional parameter of *ELASTIC, has been determined as TYPE= ISOTROPIC and HARDENING, that of *ELASTIC, as HARDENING= ISOTROPIC. And large deformation effects have been introduced by declaring NLGEOM parameter for *STEP option of ABAQUS.

Contacts have been determined by such options like *SURFACE DEFINITION, *CONTACT PAIR and *SURFACE INTERACTION, and friction coefficients by *FRICTION, which is *SURFACE INTERACTION's option. Coulomb friction has been adopted for friction model with stiffness method for the treatment. Also, analysis has been used for automatic incrementation scheme.

3.2 Material Properties

Material properties figure on Table 3.2-1, Table 3.2-2 and Table 3.2-3 shows the typical cases for SGV480 and SPV490 of stress-strain curves applied on each parts of analytic model at elasto-plastic analysis.

These stress-strain curves have been drawn based on the stress-strain curves provided by SNL from the tensile test results. That is, stress-strain curves obtained by the material tensile test have been classified according material and thickness, then is represented, for each of SGV480 and SPV490, by 2 theoretical hardening curves, namely inverse hyperbolic sine hardening and power law hardening.

- Inverse hyperbolic sine hardening : $\sigma_e - \sigma_{ys} = A \left[\text{asinh} \left\{B \left(\varepsilon^P - \varepsilon^L\right)\right\}\right]$
- Power law hardening : $\sigma_e - \sigma_{ys} = A \left(\varepsilon^P - \varepsilon^L\right)^n$

For each part of the model the stress-strain curves have been applied to each corresponding component tested, and for the parts where no experimental results are available, such as lower spherical shell and support ring, substitution has been made with values of the same material and the most approximate thickness.

Table 3.2-1 Material Properties

ITEM	SGV480	SPV490
Young's Modulus	209800 MPa (21400 kg/mm^2)	216000 MPa (22000 kg/mm^2)
Poisson's Ratio	0.3	0.3
Density	7.7×10^4 N/m^3 (7.9×10^{-6} kg/mm^3)	7.7×10^4 N/m^3 (7.9×10^{-6} kg/mm^3)

Table 3.2-2

Material Properties for Upper Cylindrical Shell (SGV480)

True Stress (MPa)	True Plastic Strain (mm/mm)	True Stress (MPa)	True Plastic Strain (mm/mm)
404.9	0.00	680.4	0.20
404.9	0.01	714.7	0.25
428.4	0.02	742.9	0.30
473.4	0.04	766.9	0.35
513.6	0.06	787.6	0.40
548.4	0.08	806.0	0.45
578.2	0.10	822.3	0.50
636.8	0.15		

Young's modulus = 209800 MPa (21400 kg/mm^2)
Poisson's ratio = 0.3
Yield Strength = 404.92 MPa (41.3 kg/mm^2)
thickness = 6.0 (mm)

Table 3.2-3

Material Properties for Lower Conical Shell and Lower Cylindrical Shell (SPV490)

True Stress (MPa)	True Plastic Strain (mm/mm)	True Stress (MPa)	True Plastic Strain (mm/mm)
656.0	0.00	756.6	0.06
656.0	0.015	774.0	0.08
672.8	0.0155	788.6	0.10
688.6	0.018	818.4	0.15
695.1	0.02	842.5	0.20
709.1	0.025	863.3	0.25
727.1	0.035	881.7	0.30
734.2	0.40		

Young's modulus = 216000 MPa (22000 kg/mm^2)
Poisson's ratio = 0.3
Yield Strength = 656.0MPa (67.3 kg/mm^2)
thickness = 9.0 (mm)

4. Global Shell Model Analyses

4.1 Analysis Model and Analytical Conditions

(1) Global 2-D Shell Model

Most of SCV test model are symmetrical to the axis. Except for the equipment hatch and its surrounding areas, 2-D model (axisymmetric) elasto-plastic/large displacement/contact analyses were performed to review the deformation behavior of SCV test model effect from friction coefficient and a gap size between the SCV test model and the CS.

Figure 4.1-1 shows the 2-D analysis model created.

This analysis model simulated the shell wall of the SCV test model, reinforcement ring, support girder and CS in axisymmetric shell element (SAX1) from each part shape and dimensions, the top head flange in axisymmetric solid element (CAX4), and ribs of the ring support girder in plane stress element (CPS4R). This model has 914 nodes and 857 elements.

As shown on Figure 4.1-1, the analysis model was given gravity acceleration in the vertical downward direction so that internal pressure as well as weight of the test model and CS may apply to the model. For the boundary condition, the node of the top head apex and symmetrical axis of the lower spherical shell has been given the symmetrical condition and the vertical displacement of the node the bottom surface of the ring support girder has been fixed.

The internal pressure applied to the model is 14.7 MPa (150kg/cm^2). This pressure gives allowance for the estimated pressure analyzed from ABAQUS due to excessive strain on the SCV test model.

Three models with gaps of 18.0 mm, 14.4 mm and 21.6 mm are available for 2-D analysis model to review the effect of the gap size between the SCV test model and the CS.

(2) Global 3-D Shell Model

Most of SCV test model are symmetrical to the axis. However, the equipment hatch is non-axisymmetric. To review the deformation behavior of the SCV test model, elasto-plastic/large displacement/contact analysis have been performed for 3-D model. Displacement or amount of rotation obtained from the 3-D model is used as the load for elasto-plastic/large displacement/contact analysis for the top head submodel and equipment hatch submodel separately analyzed.

Figure 4.1-2 shows 3-D analysis model created.

This analysis model has simulated all components in 3-D shell element (S4R) for one side of symmetric surface (180 deg.) through the center of SCV test model, CS and equipment hatch.

This model has 7812 nodes and 7640 elements.

Similar to the 2-D model, the analysis model was given gravity acceleration in the vertical downward direction so that internal pressure as well as weight of the test model and CS may apply to the model. For the boundary condition, the node on symmetrical surface of the SCV test model and CS has been given the symmetrical condition and the vertical displacement of the joint of the bottom surface of the ring support girder has been fixed. The gap between SCV test model and the CS is 18.0 mm and the friction coefficient is 0.2.

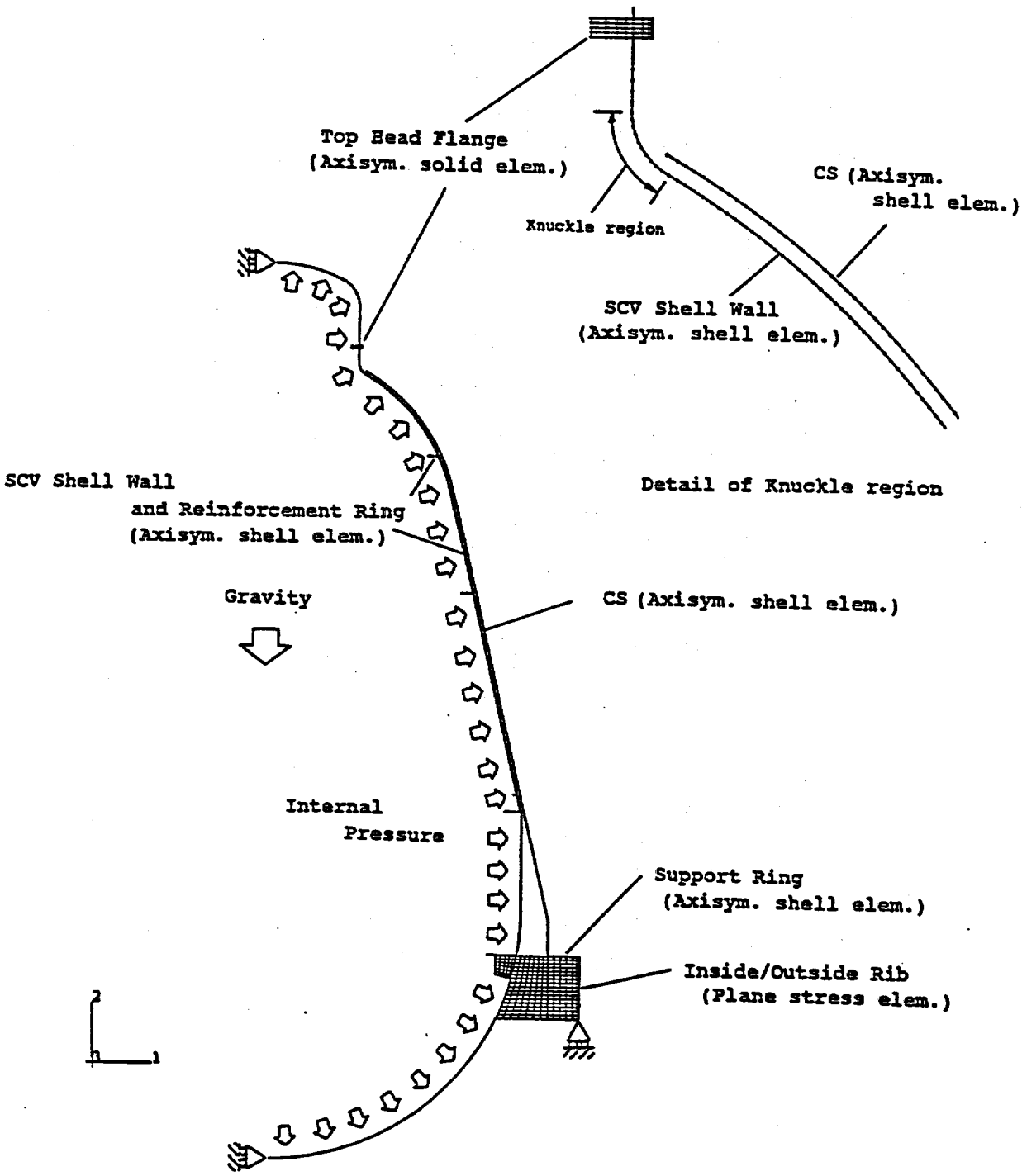

Figure 4.1-1 Global 2-D Shell Model and Analytical Conditions

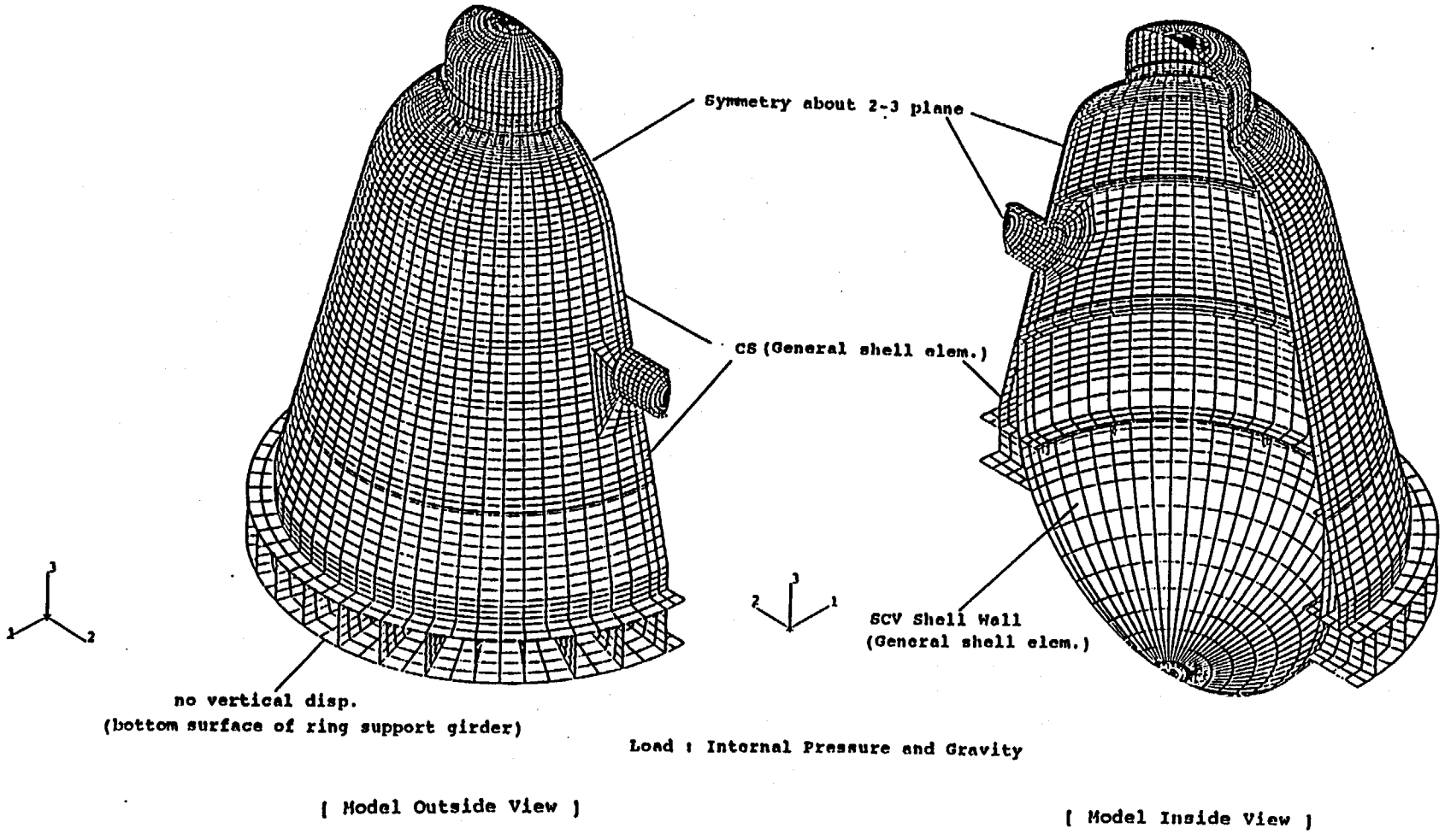

Figure 4.1-2 Global 3-D Half Shell Model and Analytical Conditions

4.2 Parameter Study Analysis

While the gap between SCV test model and CS is not constant as some allowable tolerance occurs during fabrication of the actual SCV test model and CS, the friction coefficients between SCV test model and CS are not constant either and can not be determined easily. Therefore, prior to perform the analysis on SCV test model, an analytical study has been conducted with such parameters as gap quantity and friction coefficient, in order to identify their effects on deformation behavior of SCV test model.

4.2.1 Effect of Gap Size

To understand the effect of gap size between SCV test model and CS, analyses were performed for three gap size of 18.0 mm, 14.4 mm and 21.6 mm (cases-AX1 to AX3) respectively with a constant friction coefficient of 0.2. Typical points of SCV test model and CS were checked for history of deformation, stress, and plastic strain for comparison.

(1) Radial displacement

Figure 4.2.1-1 shows the history of radial displacement at the knuckle region and middle conical shell section which are typical points on the SCV test model. The relation between displacements of these points and the internal pressure indicates that each part of the SCV test model initially expands slowly due to its elastic deformation, followed by a rapid increase of displacement due to yielding, then again expands slowly once it comes in contact with CS.

Considering the relation between the gap size and the radial displacement of SCV test model the initial contact pressure between the CS and SCV test model that has been expanded by internal pressure becomes smaller for smaller gap size, and further deformation is restrained by CS. Therefore, once in contact, the radial displacement of the SCV test model becomes smaller for smaller gap size.

(2) Vertical displacement

Figure 4.2.1-2 shows the history of vertical displacement at top head apex and knuckle region.

The vertical displacement of knuckle region at the pressure level in contact with CS tends to be smaller for smaller gap sizes due to similar reasons to that of the radial displacement . On the other hand, vertical displacement at top head apex seems to differ among gap sizes at the initial contact between SCV test model and CS, but the final displacement are almost identical in all cases. This is considered that because the top head region is not covered with CS and because the vertical displacement of the top head region is effected by the deformation of the lower part, the vertical displacement fluctuates under the effect of the contact between SCV test model and CS, but then displacement increases rapidly due to plastic deformation of the top head region itself resulting in relatively smaller displacement caused by the gap size at the initial contact.

(3) Plastic strain

Figure 4.2.1-3 shows the history of plastic strain at top head apex and knuckle region of the SCV test model. The histories of plastic strain at these typical positions on the SCV test model shows similar characteristics as the above description on displacement. The plastic deformation below the knuckle region differ among the amount of expansion before the SCV test model contacts CS. However, at top head apex where the largest plastic strain occurs, the amount of plastic strain is almost identical to any gap size because it is not covered with CS.

Based on the above (1) ~ (3) results, the difference in gap between SCV test model and CS gives an effect in such a behavior that, below the knuckle region where the SCV test model is covered with CS, the smaller the gap, the lower is the pressure at which it starts contacting with CS, slightly reducing plastic strain. The amount of plastic strain there is, however, extremely small when compared with that at the top head where such strain becomes the largest and, therefore, from an ultimate plastic strain's point of view, the effect of the difference in gap on the SCV test model's deformation behavior is negligible.

4.2.2 Effect of Friction Coefficient

To understand the effect due to the difference in friction coefficient between SCV test model and CS, three cases (case-AX1, AX4, AX5)were analyzed with friction coefficient of 0.2, 0.0 and 0.4 respectively, while setting the gap at 18.0 mm for all cases, for the comparison among noticeably representative SCV test model and CS points in terms of history in displacement, stress, and plastic strain.

(1) Radial displacement

Figure 4.2.2-1 shows the history of radial displacements at the knuckle region and lower cylindrical shell section as representative points of the SCV test model.

The radial displacement with friction coefficient of 0.2 and 0.4 are almost the same but only the case with the friction coefficient of 0.0 tends to give a larger amount of displacement than in other cases.

(2) Vertical displacement

Figure 4.2.2-2 shows the history of vertical displacements at the knuckle region and lower cylindrical shell section as representative points of the SCV test model.

The vertical displacement with friction coefficient of 0.2 and 0.4 are almost the same like in radial displacement however, when the friction coefficient is 0.0, the deformation tends to move downward after developing to a certain extent.

For the above different behavior due to the difference in friction coefficient, it is important to take notice of the lower cylindrical shell section of SCV test model. This section swells due to the internal pressure by an extremely large amount, as shown in Figure 4.2.2-1, since the gap with CS is greater than at the upper section. Possibly the section draws the upper parts downward, when it swells.

On the other hand, the difference in friction coefficient affects the friction force acting on the SCV test model when it slides over the CS. A smaller friction coefficient, therefore, allows the parts above the lower cylindrical shell section to be drawn downward due to a smaller friction force the test model receives from CS. While, if the friction coefficient and, therefore, friction force are larger, the behavior to draw the parts above the lower cylindrical shell section downward seems to be restricted, justifying the judgment that this appeared as the above difference in deformation behavior observed.

(3) Plastic strain

Figure 4.2.2-3 shows the history of plastic strains at top head apex and knuckle region of the SCV test model. It is clear from the plastic strain history at knuckle region of CS that the strain is a little larger for the friction coefficient of 0.0 than the case for 0.2 or 0.4, because of the above different deformation behavior resulting from the difference in friction coefficient. On the other hand, at top head apex causing the large plastic strain throughout the SCV test model, which is almost the regardless of the difference in friction coefficient as top head region is not covered with CS.

Based on the mentioned (1) ~ (3) results, the difference in friction coefficient between SCV test model and CS affects the deformation (sliding) behavior of the SCV test model against CS, causing a larger amount of plastic strain at the knuckle region and upper spherical shell section for the friction coefficient of 0.0 than in other cases. The amount of plastic strain is, however, extremely small when compared with that at top head apex having the largest plastic strain and, from an ultimate plastic strain's point of view, the effect of the difference in friction coefficient on the SCV test model's deformation behavior is negligible.

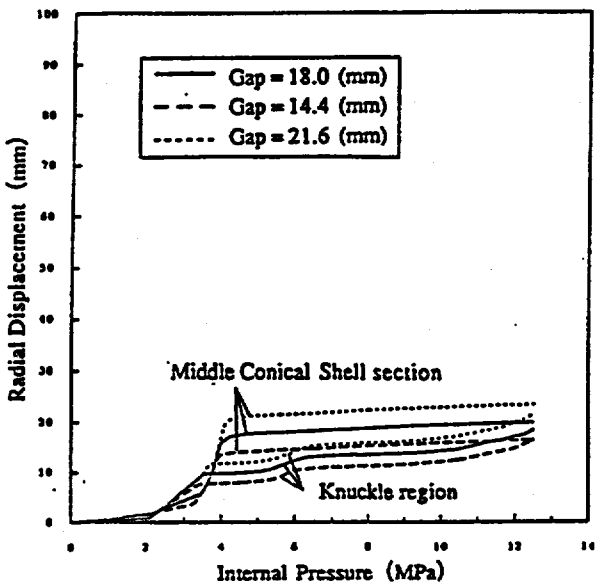

Figure 4.2.1-1 Effect of Gap size for Radial Displacement

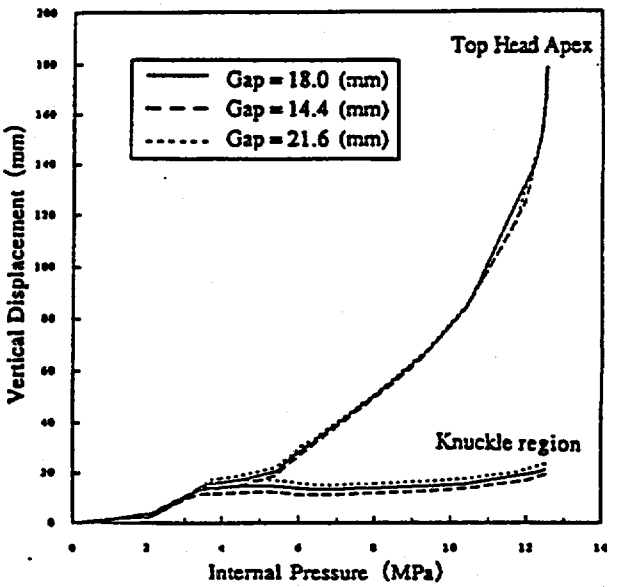

Figure 4.2.1-2 Effect of Gap size for Vertical Displacement

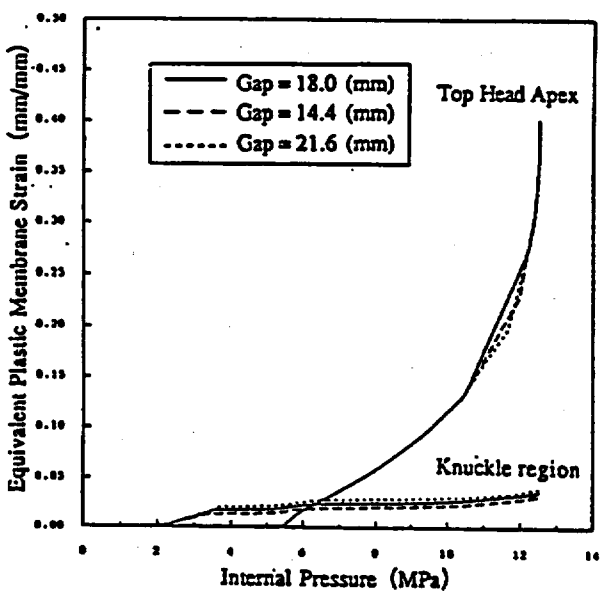

Figure 4.2.1-3 Effect of Gap size for Plastic Strain

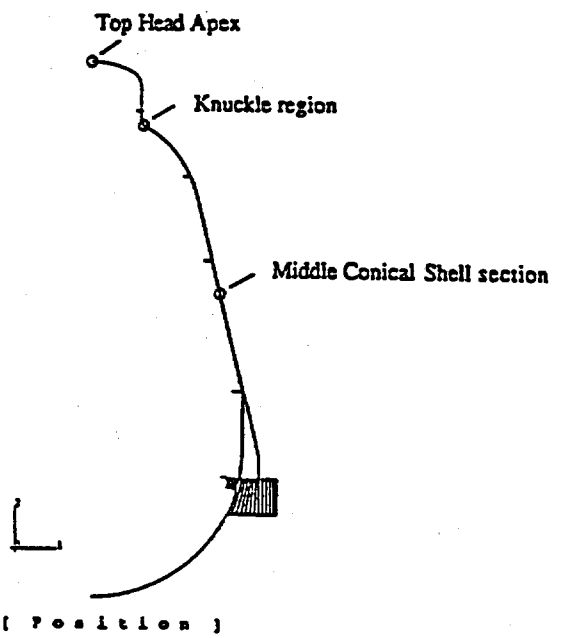

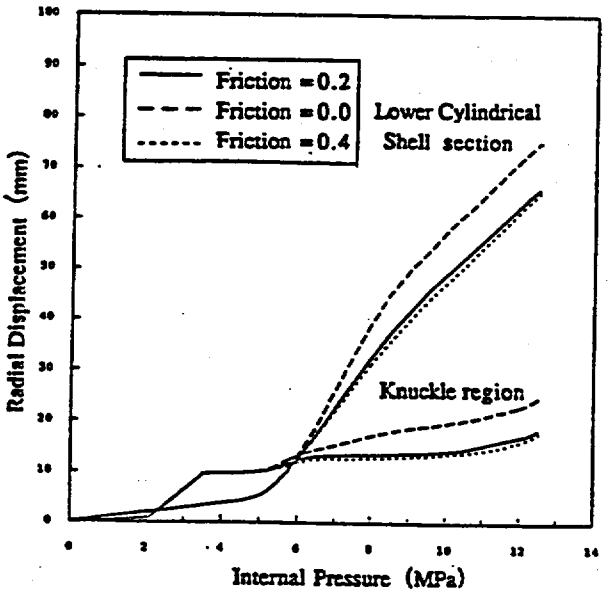

Figure 4.2.2-1 Effect of Friction for Radial Displacement

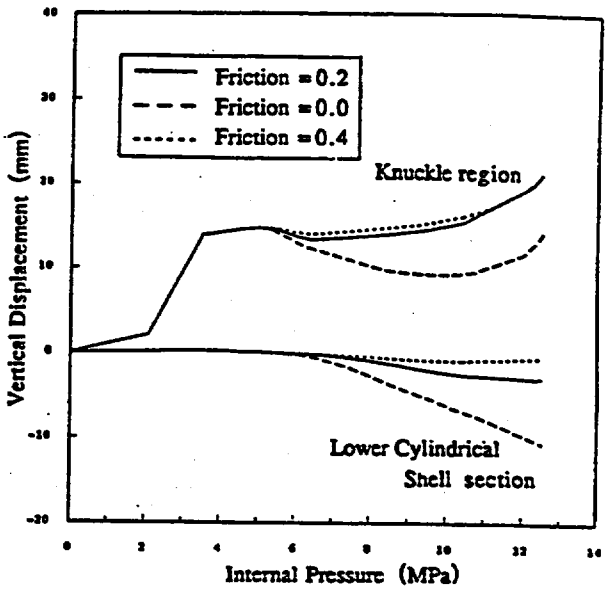

Figure 4.2.2-2 Effect of Friction for Vertical Displacement

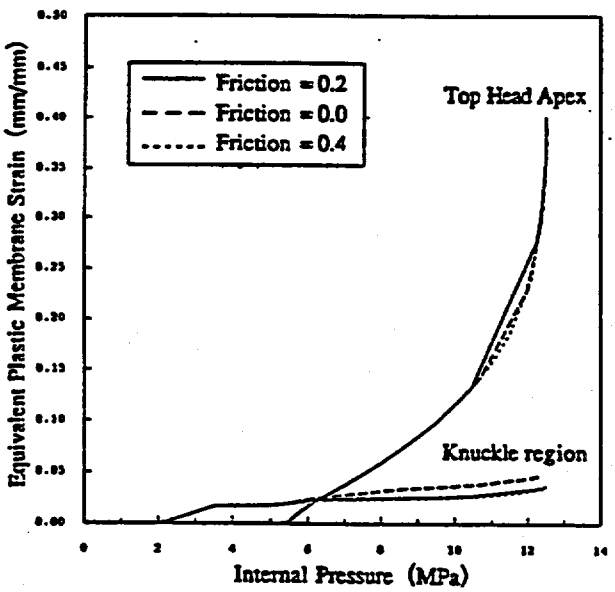

Figure 4.2.2-3 Effect of Friction for Plastic Strain

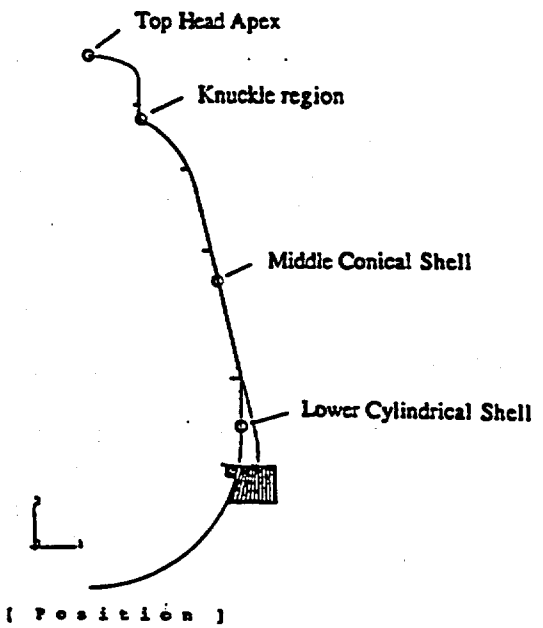

4.3 Global 2-D Shell Model Analysis

As an achievement of parameter studies in the preceding 4.2, it has been confirmed that the effect of the differences in the gap between SCV test model and CS and in friction coefficient on the SCV test model's deformation behavior is negligible. It was, therefore, decided that case-AX1 with the nominal gap of 18.0 mm and the friction coefficient of 0.2 be adopted as a case for the analysis to predict the SCV test model's behavior under pressure using a 2-D model. Followings are the detailed results of this analysis.

Figure 4.3-1 shows the deformed shape of the SCV test model at representative pressure obtained through analysis. And, Figure 4.3-2 ~ Figure 4.3-5 shows the histories of displacement, equivalent stresses and plastic strains at each section of the SCV test model.

Figure 4.3-6 shows the profile of plastic membrane strains and inside/outside surface plastic strain along the meridional direction from top head apex to the around of the ring support guarder of the SCV test model at representative levels of pressure.

From these figures concerning the deformed shape, history and profile, the SCV test model's behavior is judged as follows:

(1) Deformation due to gravity (before pressure loaded)

As seen from the deformed shape of Figure 4.3-1, the SCV test model sinks downward due to its gravity, allowing the gap between SCV test model and CS to increase only slightly at knuckle region.

The displacement due to the gravity of SCV test model is, however, as smaller 0.015 mm or less at best (occurring to top head apex). It can, therefore, be judged that the gravity gives almost no effect on the deformation behavior of SCV test model.

(2) First yielding (at the internal pressure of 2.09MPa=21.3kg/cm^2)

As seen from the plastic strain history of Figure 4.3-5, when the internal pressure is 2.09MPa (21.3kg/cm^2), the first plastic strain occurred at the knuckle region of SCV test model. The history of radial displacement shows the identical pressure at which displacement sharply increases and plastic strain occurred.

(3) First contacting (at the internal pressure of 3.52MPa=35.9 kg/cm^2)

The SCV test model caused its first contact with CS at the knuckle region when the internal pressure was about 3.52MPa (35.9 kg/cm^2). At this pressure, the gap at the upper conical shell section also decreases. This justifies the judgment that this section is expected to make contact next and the upper and middle conical sections also is started to yield allowing the radial displacement to sharply increase.

(4) After contacting (at the internal pressure of 3.52MPa~7.59MPa)

After the SCV test model and CS contacting for the first time at the knuckle region, it is shown by the history of radial displacement that, between the internal pressures of 3.52MPa to 7.59MPa, the upper conical, middle conical, lower conical and upper spherical shell section contacted in that order.

(5) After contacting (at the internal pressure of 7.59MPa=77.4 kg/cm^2)

The internal pressure of 7.59MPa (77.4 kg/cm^2) is a pressure almost equal to the middle of the pressures at which the knuckle region of SCV test model makes its first contact with CS and that reaches the final increment. At the pressure of around 7.59MPa, almost all the CS covered section of SCV test model comes to contact with CS. Deformation, however, still continues to develop at the large gap lower cylindrical shell section and top head section not covered with CS, which causes the largest plastic strain of about 4.9 % to occur near top head apex.

(6) Final increment (at the internal pressure of 12.5MPa=127.5 kg/cm^2)

At this pressure, the SCV test model comes to contact with CS at its knuckle region through lower cylindrical section except for knuckle and upper spherical shell section junction.

The junction between knuckle and upper spherical shell section did not contact even at this pressure because the knuckle region, with its plate thickness of as much as 16.5 mm, still deformed so that it fitted the shape of CS.
The largest plastic membrane strain at the SCV test model was about 40 %, causing at top head apex. Figure 4.3-6 of plastic strain profile shows that the SCV test model has a largest value at the knuckle region at lower pressure. As the pressure rises, the plastic strain of top head without CS cover and lower cylindrical shell, which has large gap between SCV test model and CS, gets larger. Therefore, top head section without CS cover needs a detailed investigation.

4.4 Global 3-D Shell Model Analysis

3-D model analysis (case-3D1) is performed under the condition that gap is nominal 18.0 mm and friction coefficient is 0.2. This condition is same as last analysis on 2-D model (case-AX1).
Followings are the detailed results of this analysis.
Figure4.4-1 shows deformed shape under representative pressure for global SCV test model.
Figure4.4-2 ~Figure4.4-4 show history of displacement at SCV shell wall and plastic membrane strain. The above mentioned result of 2-D model analysis, deformed shape obtained from above 3-D model analysis, and various history of free field, values are almost same. Therefore, from standpoint of global deformation behavior of SCV test model, 3-D model with harsh mesh is as effective as 2-D model with more fine mesh.
Figure4.4-5 show history of horizontal displacement at representative points near equipment hatch area, obtained from 3-D model analysis. Figure4.4-6 and Figure4.4-7 show plastic strain history at each point equipment hatch area of SCV test model and inside/outside surface.
Judging from history of horizontal displacement at each region near equipment hatch area and plastic strain, the point farthest from equipment hatch contacts with CS at about 4.1 MPa pressure.
The points near equipment hatch contacts with CS at about 5.2 MPa pressure.
The equipment hatch area is surrounded by thick insert plate with high material intensity (SPV490/t17.5mm), thinner lower conical shell section of same material (SPV490/t9.0mm) and thinner middle conical shell section with relatively low material intensity (SGV480/t8.5mm). Therefore, the different expansion rate of each material against internal pressure brings about large plastic at region near to material change interface (MCI) between upper and lower conical shell section and insert plate joint region.
Comparison of plastic strain history between equipment hatch area and SCV shell wall shows that the plastic strain at equipment hatch area is the largest when the internal pressure is between 4 ~ 8MPa. Therefore, equipment hatch area needs a detailed investigation.

4.5 Comparison of 2-D and 3-D Analyses

Figure4.5-1~Figure4.5-3 show comparison of history of radial displacement, vertical displacement and plastic membrane strain at representative points, obtained from above mentioned global 2-D and 3-D analyses.
From these figures, contact starting pressure of SCV test model and CS and deformation behavior are almost same in 2-D and 3-D analyses.
The history of radial displacement of 2-D and 3-D analyses may seem to show difference, but this difference is brought about because the range of vertical axis is narrow.

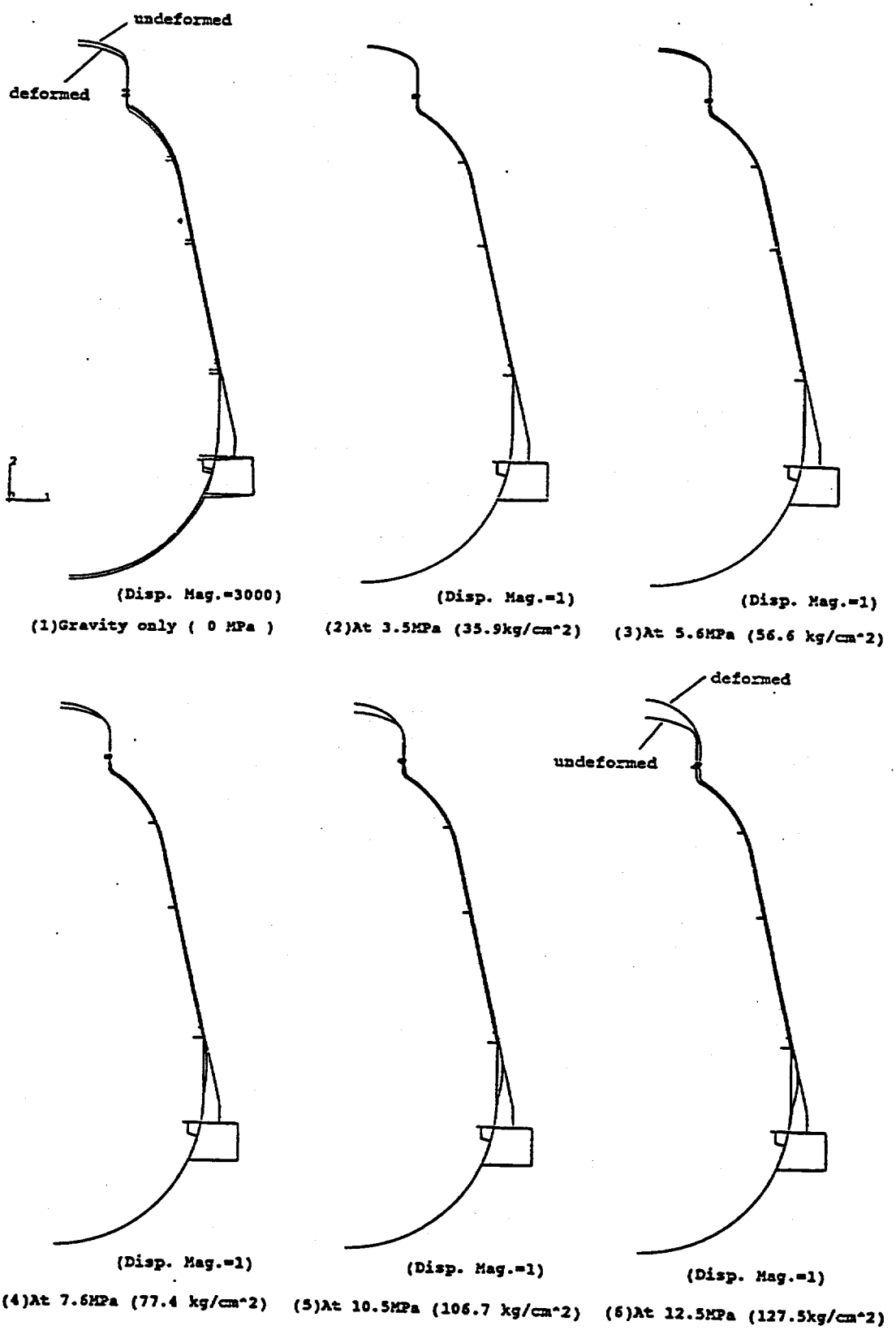

Figure 4.3-1 Deformed Shape of Global Axisymmetric Shell Model

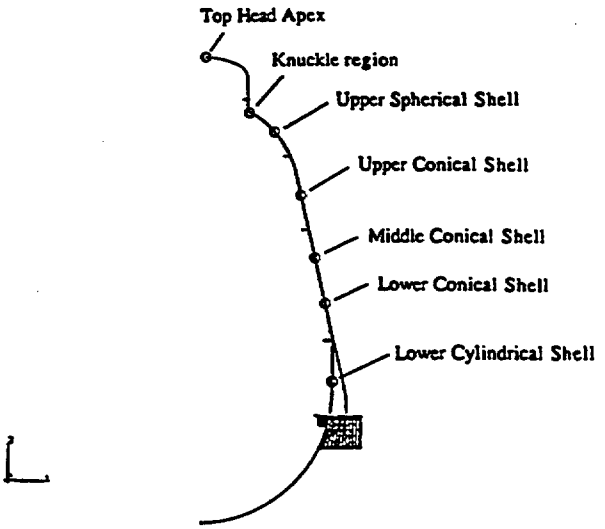

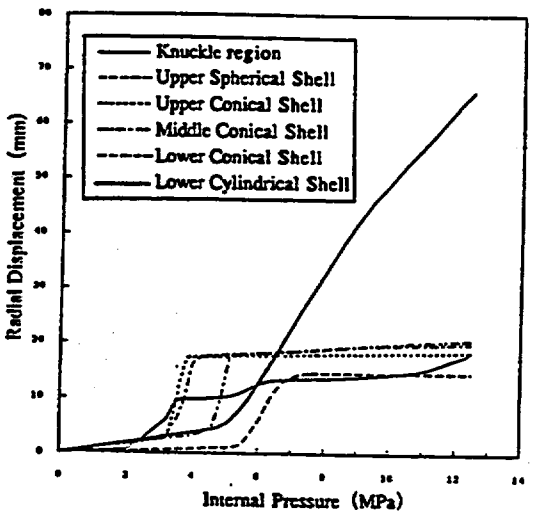

Figure 4.3-2 Radial Displacement of SCV Shell Wall

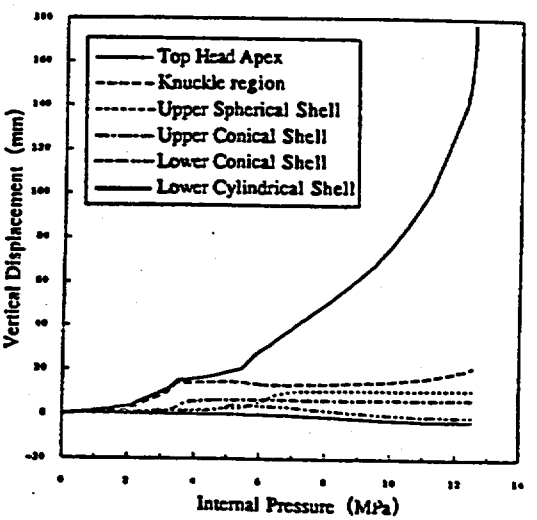

Figure 4.3-3 Vertical Displacement of SCV Shell Wall

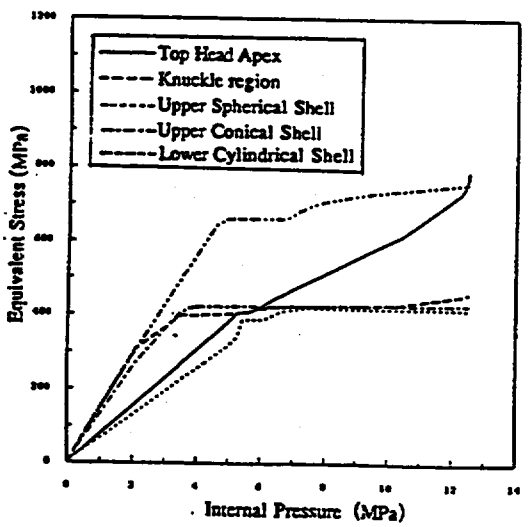

Figure 4.3-4 Equivalent Stress of SCV Shell Wall

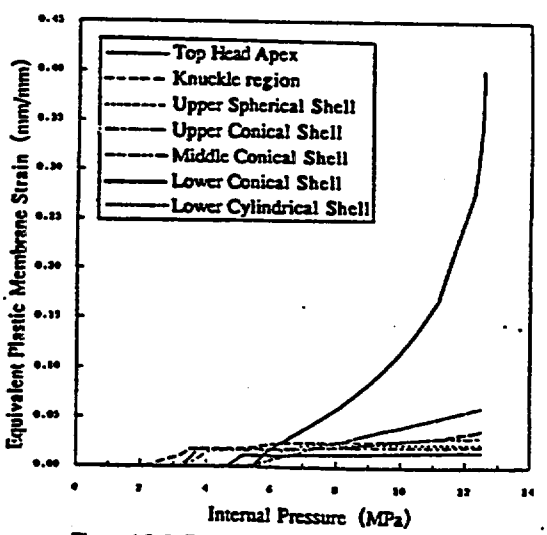

Figure 4.3-5 Equivalent Plastic Strain of SCV Shell Wall

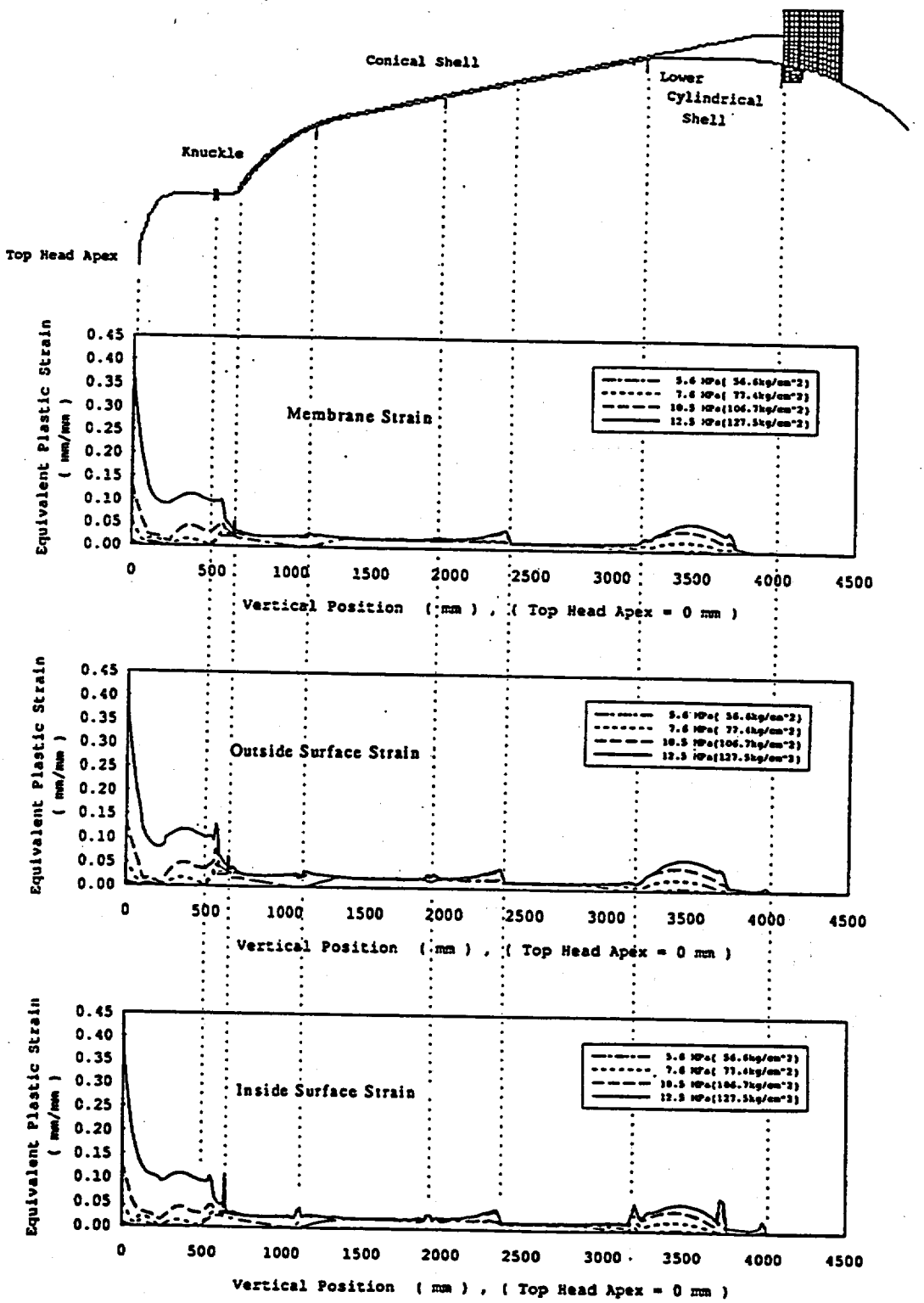

Figure 4.3-6 Equivalent Plastic Strain Profile

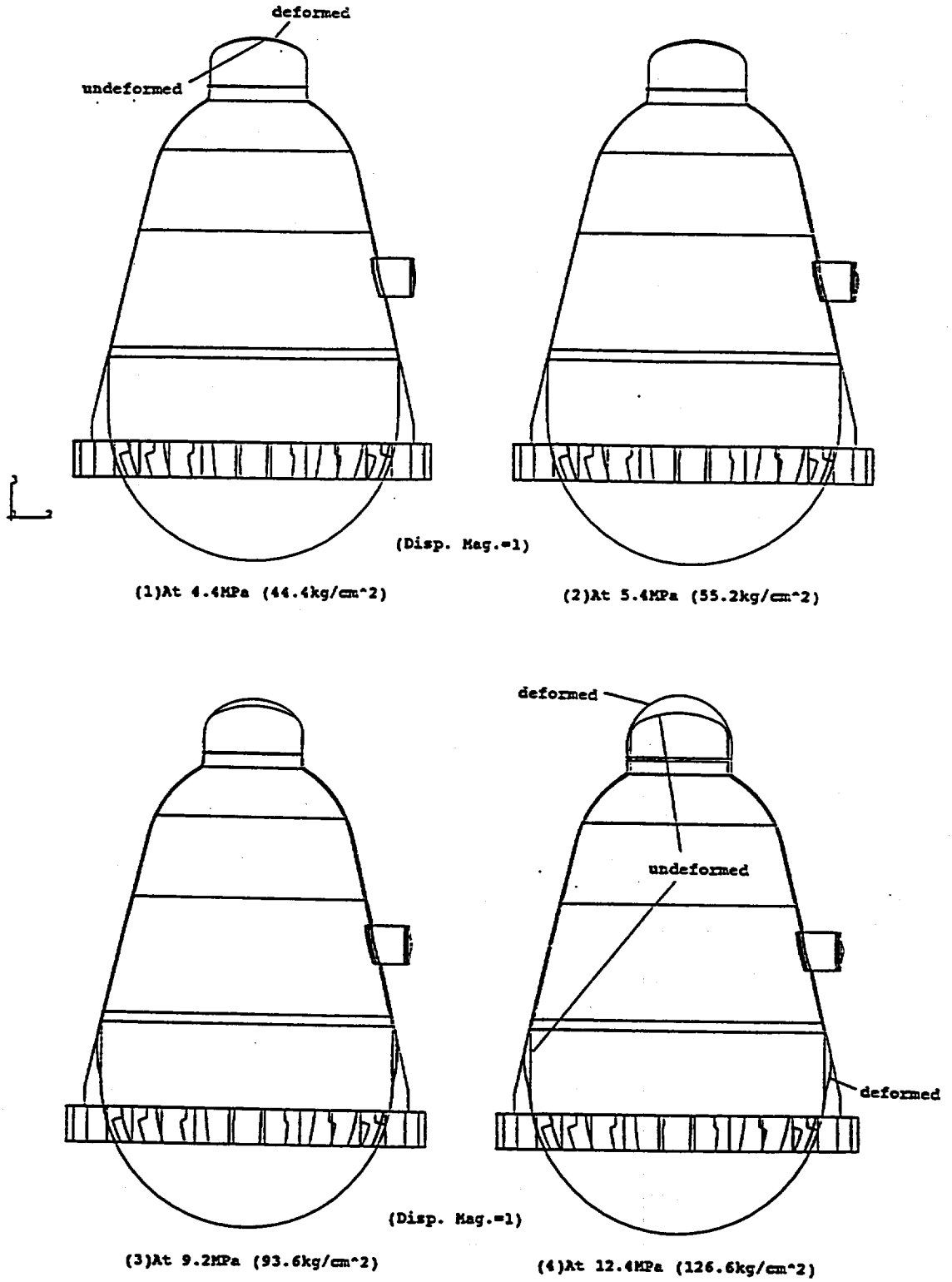

Figure 4.4-1 Deformed Shape of Global 3-D Half Shell Model

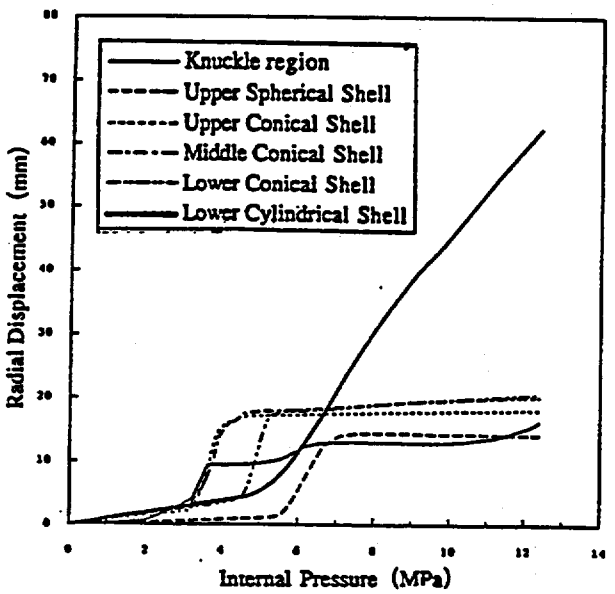

Figure 4.4-2 Radial Displacement of SCV Shell Wall

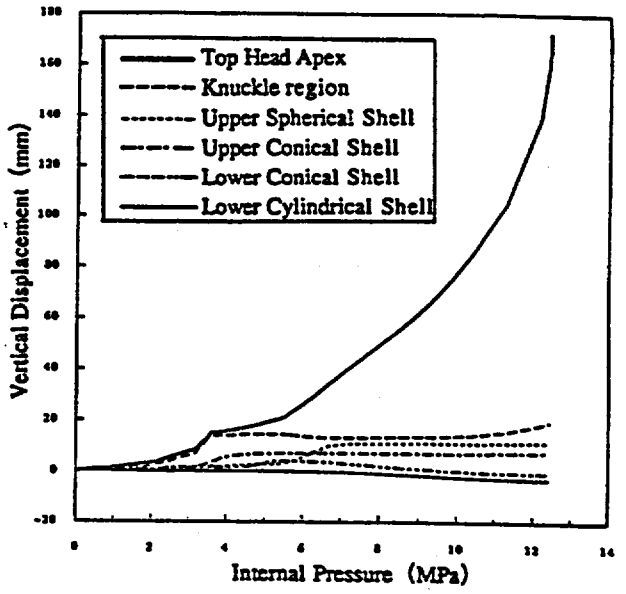

Figure 4.4-3 Vertical Displacement of SCV Shell Wall

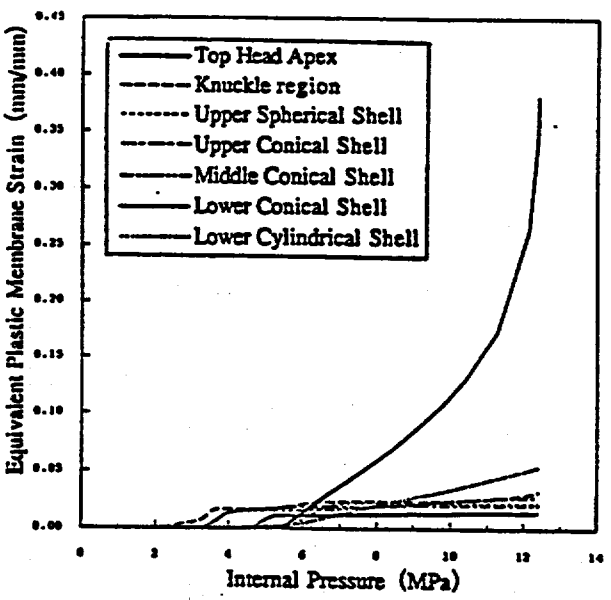

Figure 4.4-4 Equivalent Plastic Strain of SCV Shell Wall

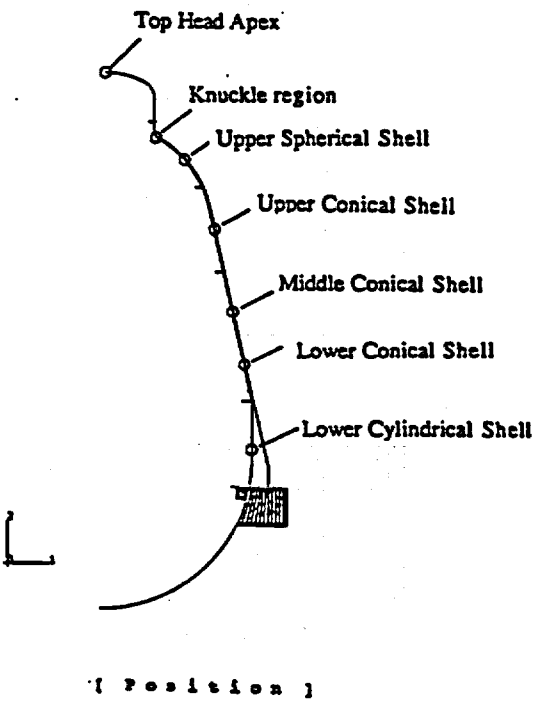

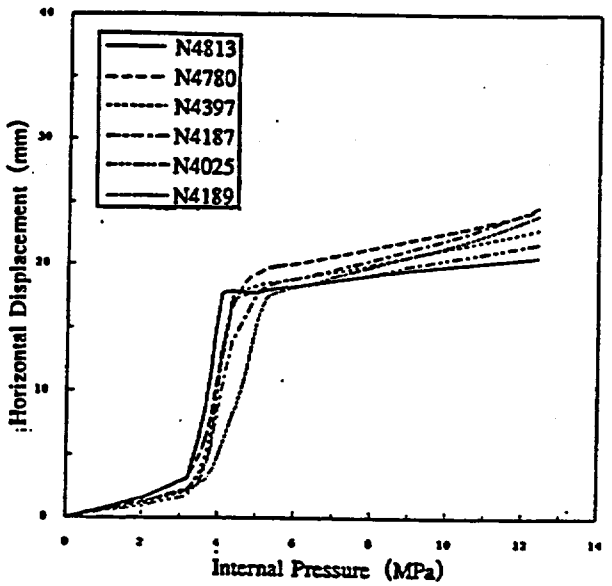

Figure 4.4-5 3-D Global Horizontal Displacement (near E/H)

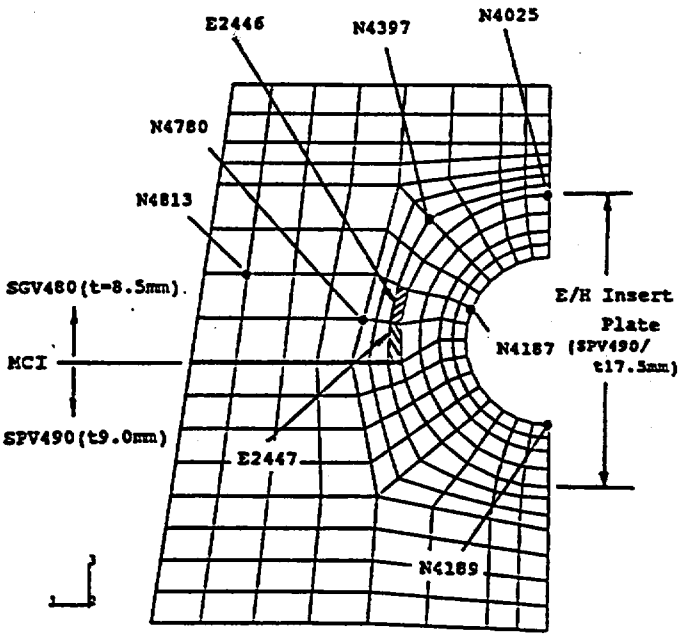

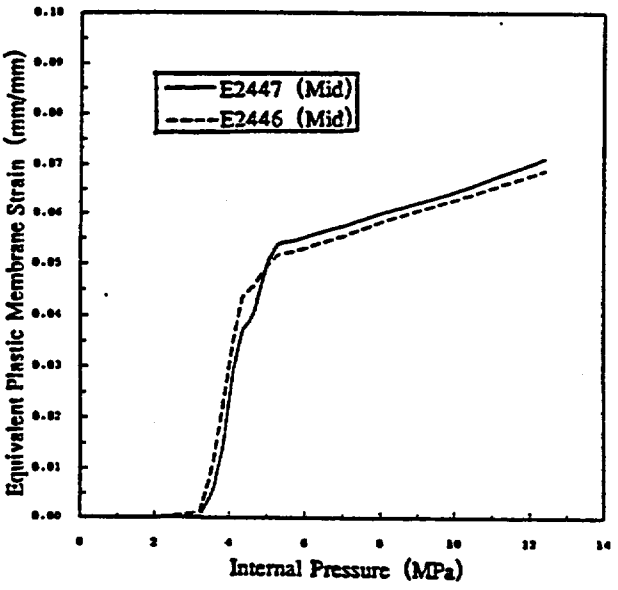

Figure 4.4-6 Equivalent Plastic Membrane Strain (near E/H)

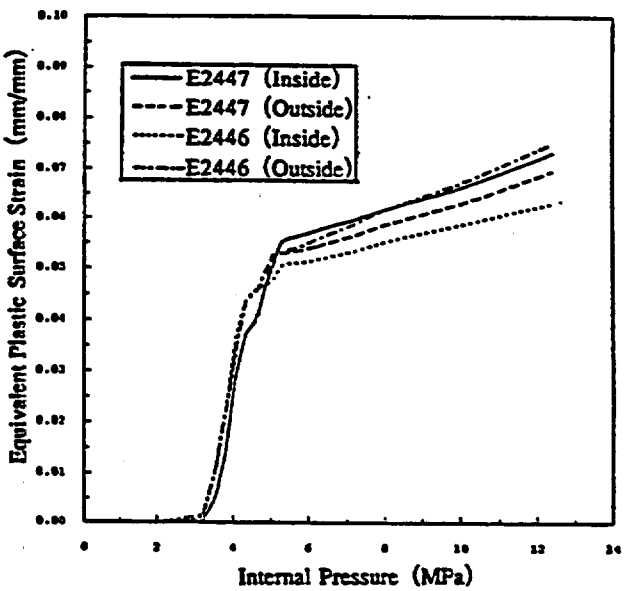

Figure 4.4-7 Equivalent Plastic Surface Strain (near E/H)

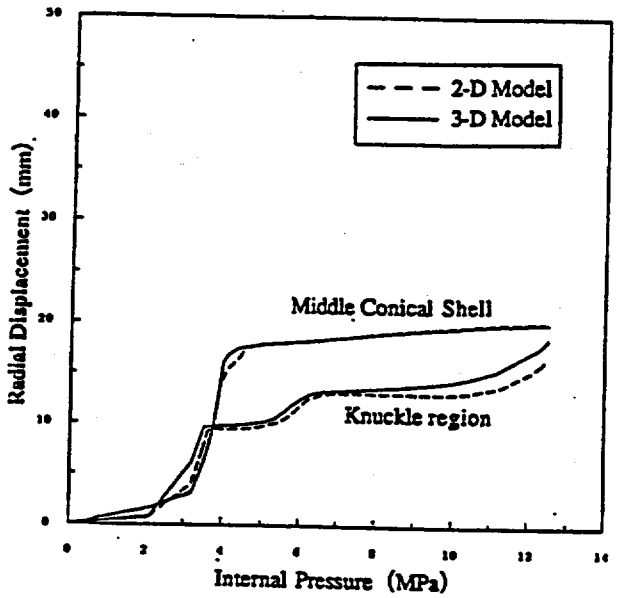

Figure 4.5-1 2-D/3-D Comparison (Radial Displacement)

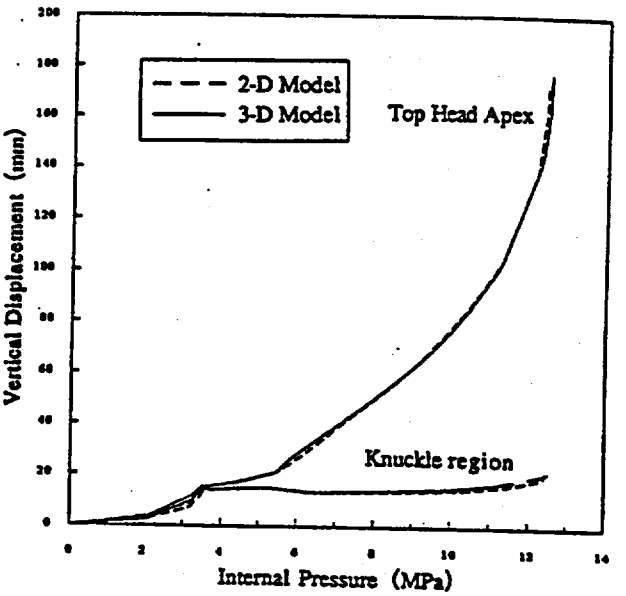

Figure 4.5-2 2-D/3-D Comparison (Vertical Displacement)

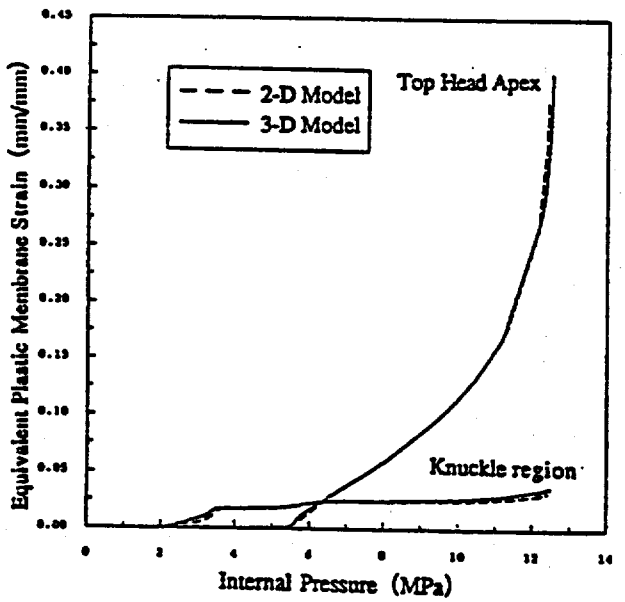

Figure 4.5-3 2-D/3-D Comparison (Equivalent Plastic Strain)

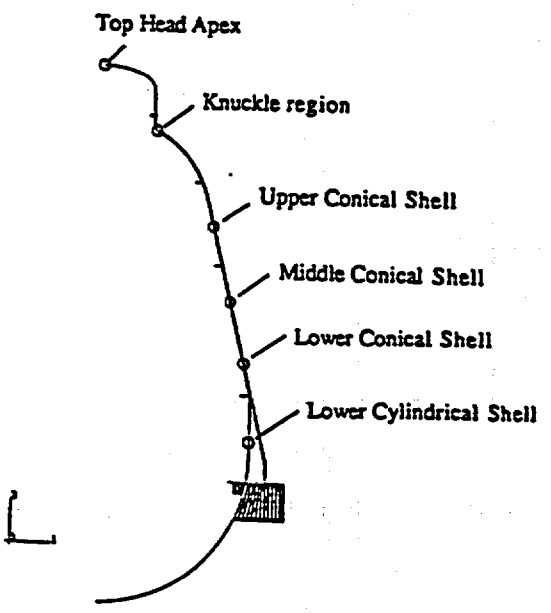

5. Local 3-D Submodel Analyses

5.1 Submodel Analysis of Local 3-D Top Head section

The results of prior analysis of 2-D model and 3-D model show that the plastic strain at pressurization on SCV test model is larger at top head region and knuckle region. Thus to perform detailed investigation on these regions, top head region submodel was prepared.

Figure5.1-1 shows the prepared top head region submodel. This analysis model is to simulate the circumference of 30 deg. for each direction from top head region to upper spherical shell section and CS. This model consists of 3-D shell element (S4R) and has 4545 nodes and 4290 elements.

This analysis model uses internal pressure, displacement and rotation obtained from prior 3-D global shell model analysis. The boundary condition is given to the SCV test model and CS nodes on symmetric surface. The internal pressure applied to the model is same as the pressure applied to the 3-D global model analysis which has been conducted in previous section.

Figure5.1-2 ~Figure5.1-5 show history of plastic membrane strain and plastic surface strain at top head apex, above and below of top head flange joint, and above and below of knuckle joint.

The plastic membrane strain history at each point shows that the largest plastic strain occurs at above or below of knuckle joint when the internal pressure is below about 7.3MPa. When internal pressure rises, the larger plastic strain occurs at top head apex. Also, plastic strain at the below of top head flange joint is larger than that at knuckle joint, when the internal pressure rises above about 10.8 MPa. This is because the deformation of knuckle region is controlled when the region contact with CS, while other parts are free from such control.

On the other hand, history of plastic surface strain shows that the plastic strain of inside surface below of top head flange joint or below of knuckle joint is the largest when the pressure is below about 11.8MPa. When the pressure rises, the plastic strain of top head apex becomes larger.

The plastic surface strain at below of top head flange joint or below of knuckle joint is larger than the plastic membrane strain up to higher pressure. This is because these regions are effected by bending deformation, but top head apex is free from such deformation.

Therefore, top head apex and below of top head flange joint and below of knuckle joint are the place that attention should be paid on the strength of these parts.

5.2 Submodel Analysis of Local 3-D E/H area

The analysis results from the previously performed 3-D analysis model show that the ultimate plastic strain of SCV test model under the higher level pressure occurs at top head apex, but the largest plastic strain occurs near equipment hatch under the lower pressure level. For further review on this part, a 3-D submodel for the equipment hatch and the adjacent areas has been prepared.

Figure5.2-1 shows a submodel of the prepared equipment hatch area. This analysis model is to simulate the equipment hatch insert plate, its surrounding conical shell and reinforcement ring, and CS which covers them 3-D shell elements (S4R). This model has 4816 nodes and 4572 elements.

This analysis model uses internal pressure, displacement and rotation obtained from prior 3-D global shell model analysis. The boundary condition is given to the SCV test model and CS nodes on symmetric surface. The internal pressure applied to the model is same as the pressure applied to the 3-D global model analysis which has been conducted in previous section.

Figure5.2-2 shows the horizontal displacement history of the representative points near equipment hatch given from analysis. Figure5.2-3 and Figure5.2-4 also show the plastic membrane strain history and plastic surface strain near equipment hatch.

Judging from the history of the horizontal displacement and plastic strain of the parts near the equipment hatch, contact is made with CS at approximate 4.1MPa on the points distant from the equipment hatch and contact is made at approximate 5.2MPa near the equipment hatch points. Therefore, the contact pressure with CS near equipment hatch proves to be close to the former 3-D global model. However, for the horizontal displacement at the point near the contact part of the

material change interface (MCI) of the upper and lower conical shell and the insert plate, which gives the largest plastic strain near the equipment hatch by the former 3-D global analysis, the detailed submodel clearly gives lager values compared to the global model. Similar result is obtained also on the plastic strain near the contact part. The strain of the submodel is higher than that of the global model by approximate13% on the plastic membrane strain and approximate 28% on the plastic surface strain at 11MPa.
Though the strain of the equipment hatch does not rise higher compared to those of the top head apex and joint of top head flange and knuckle because the contact with CS control the deformation, attention should be paid on the strength of this part.

5.3 Buckling Analysis of Local 3-D Top Head section

As the top head region of the SCV test model consists of two spherical shells with different curvatures, the rigidity difference could cause buckling under pressure. Thus, a 3-D model for the top head region of SCV test model was prepared to perform a linear buckling eigenvalue analysis.
Figure5.3-1 shows a model for the buckling eigenvalue analysis on the top head region.
This analysis model is to simulate the half side (180deg.) of the SCV test model symmetric section from the top head to the upper spherical shell, with 3-D shell elements (S4R) completely. This model has 2233 nodes and 2150 elements.
For analysis model, 9.8MPa (100kg/cm^2) internal pressure was given, and the bottom end of the upper spherical shell was completely fixed. The analysis is a linear buckling eigenvalue analysis, and the buckling eigenvalue and their buckling modes were found from 1st to 10th modes.
Figure5.3-2 shows the original model and a representative buckling mode given by the analysis.
Table5.3 shows the buckling eigenvalue given by the analysis.
It has been proven that the buckling near top head of the SCV test model occurs at the upper cylindrical shell from 1st to 6th modes, and near the top head apex from 7th to 10th modes.
Table5.3 shows the buckling load calculated from the corresponding buckling eigenvalues, and the buckling eigenvalues were all negative. An internal pressure was given to the model, so the top head of the SCV test model could buckle under external pressure. However, the model is unlikely to buckle under internal pressure in this test.
This analysis is linear buckling eigenvalue analysis and one of evaluations for the buckling of the top head section. Furthermore, we will investigate the potential of nonlinear buckling too.

Table 5.3 Buckling Analysis Result (Eigenvalue)

Mode No.	Eigenvalue	Buckling Load MPa	(kg/cm^2)
1	-0.9344	-9.2	(-93.4)
2	-0.9606	-9.4	(-96.1)
3	-0.9661	-9.5	(-96.6)
4	-1.0377	-10.2	(-103.8)
5	-1.0730	-10.5	(-107.3)
6	-1.1515	-11.3	(-115.2)
7	-1.1697	-11.5	(-117.0)
8	-1.2778	-12.5	(-127.8)
9	-1.2911	-12.7	(-129.1)
10	-1.2966	-12.7	(-129.7)

Note1; "LIVE"LOAD = 9.8 MPa (100kg/cm2)
Note2; Negative value means buckling by external pressure.

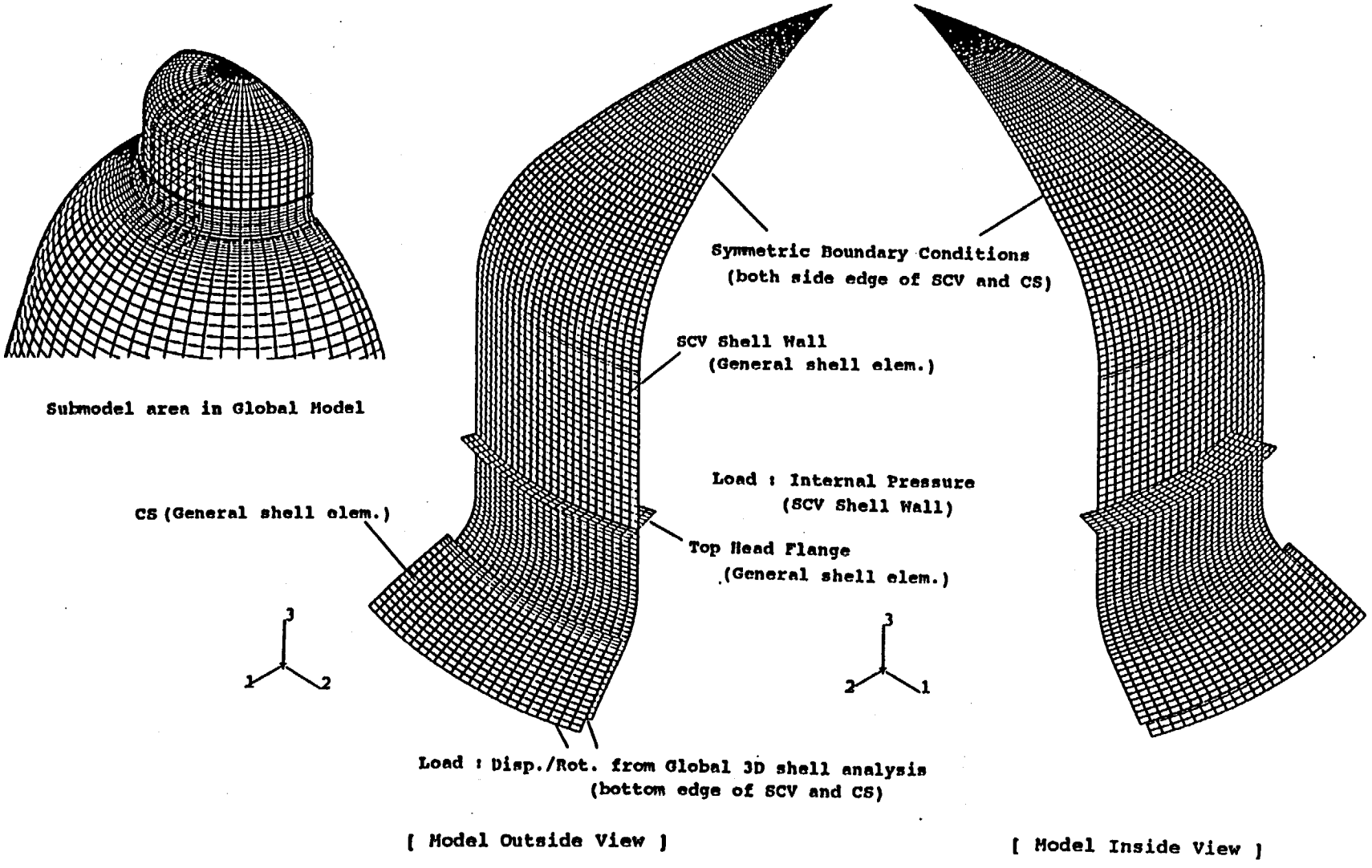

Figure 5.1-1 Local 3-D Top Head section Submodel and Analytical Conditions

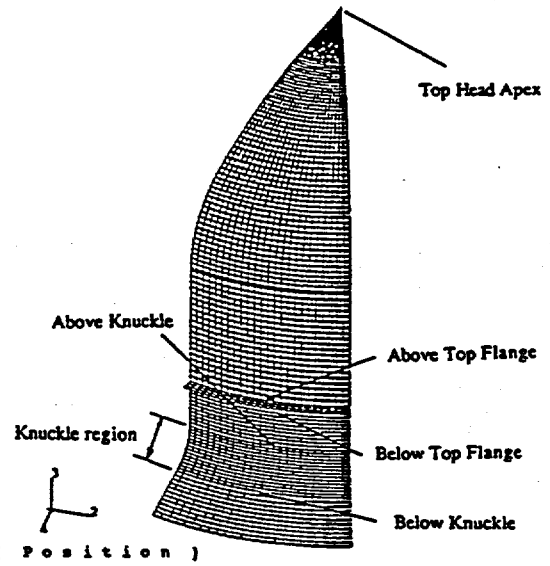

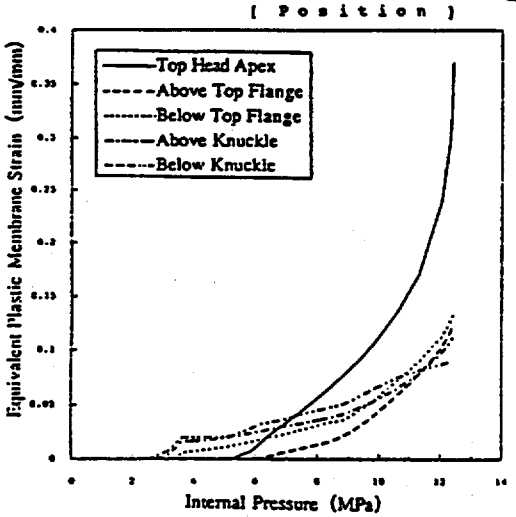

Figure 5.1-2 3-D Top Head Submodel Equivalent Plastic Membrane Strain

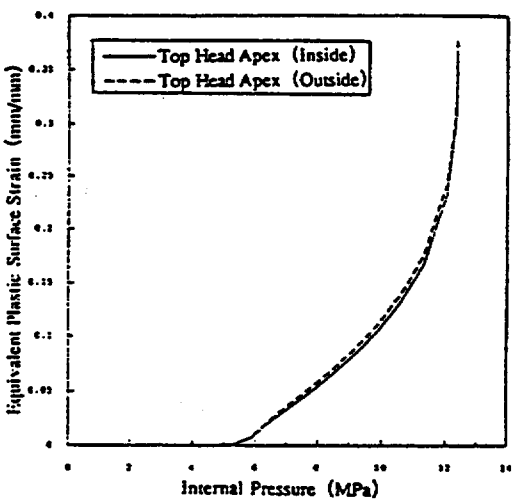

Figure 5.1-3 3-D Top Head Submodel Equivalent Plastic Strain (Top Head Apex)

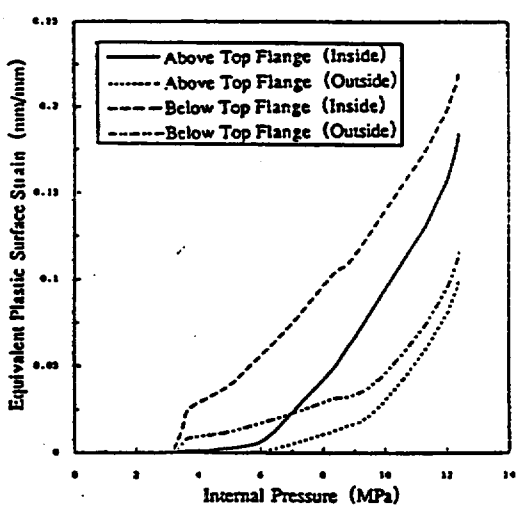

Figure 5.1-4 3-D Top Head Submodel Equivalent Plastic Strain (Top Head Flange)

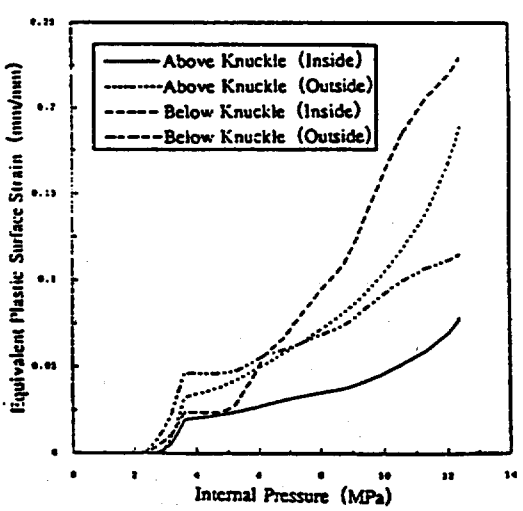

Figure 5.1-5 3-D Top Head Submodel Equivalent Plastic Strain (Knuckle Region)

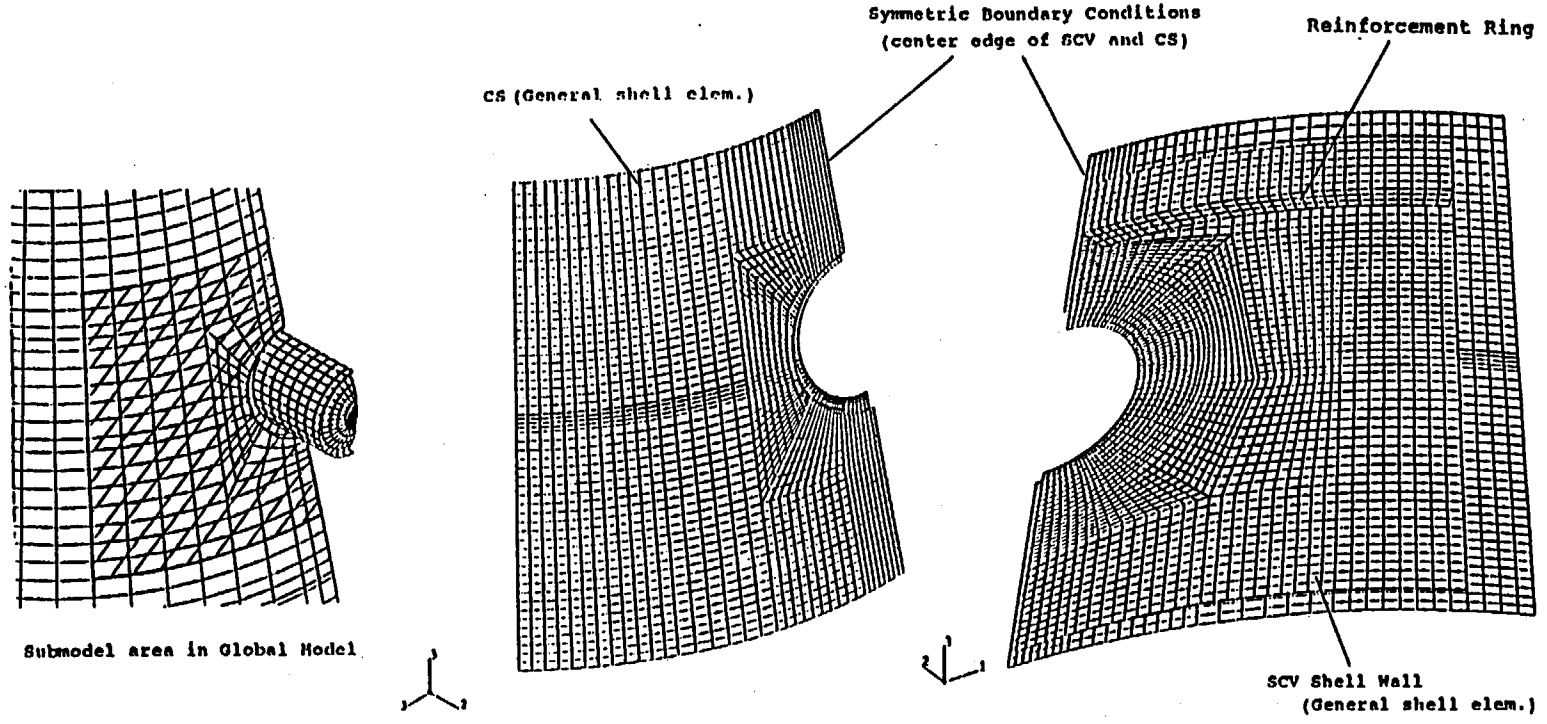

Figure 5.2-1 Local 3-D E/H area Submodel and Analytical Conditions

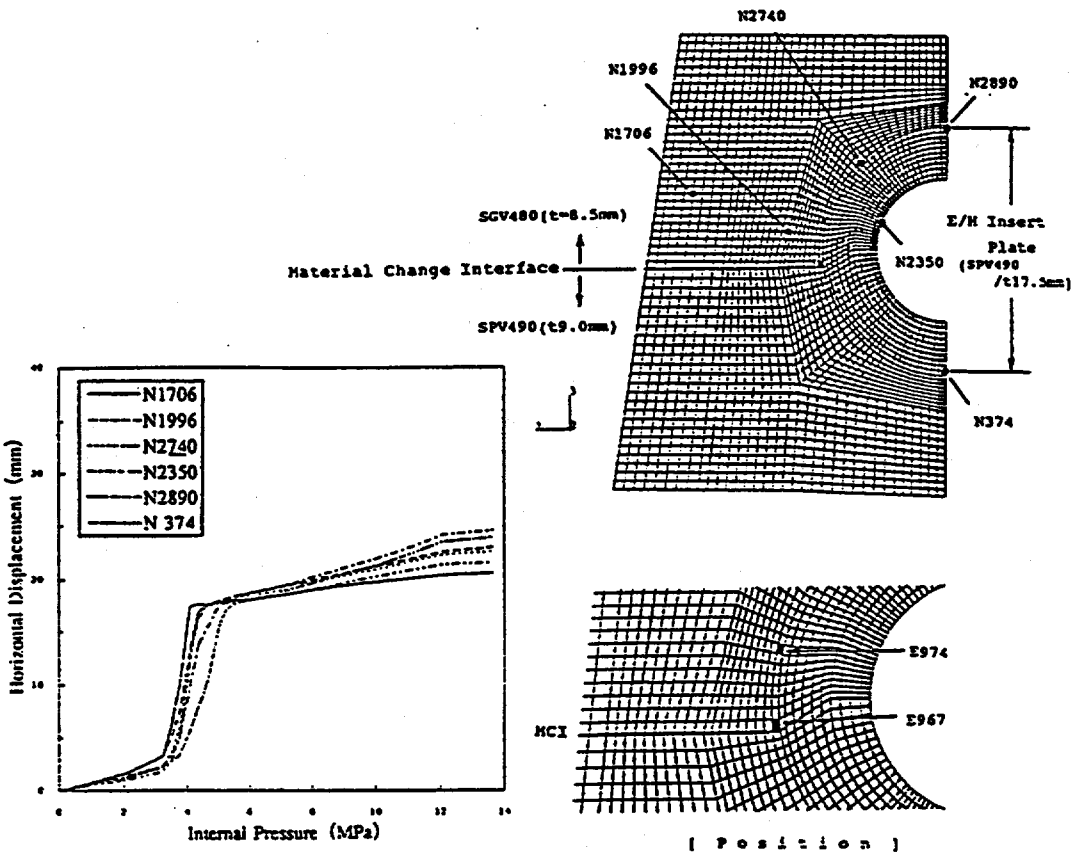

Figure 5.2-2 3-D Submodel Horizontal Displacement (near E/H)

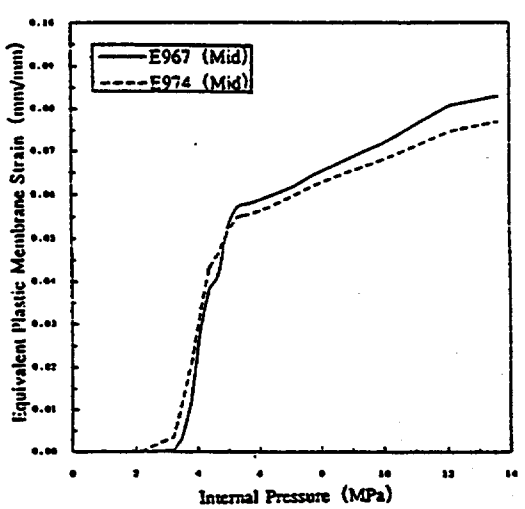

Figure 5.2-3 3-D Submodel Equivalent Plastic Membrane Strain (near E/H)

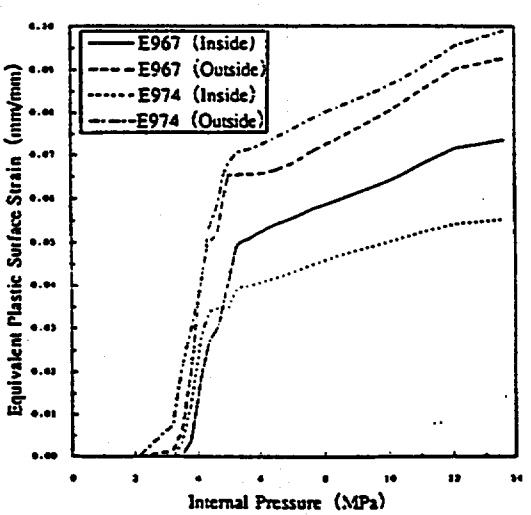

Figure 5.2-4 3-D Submodel Equivalent Plastic Surface Strain (near E/H)

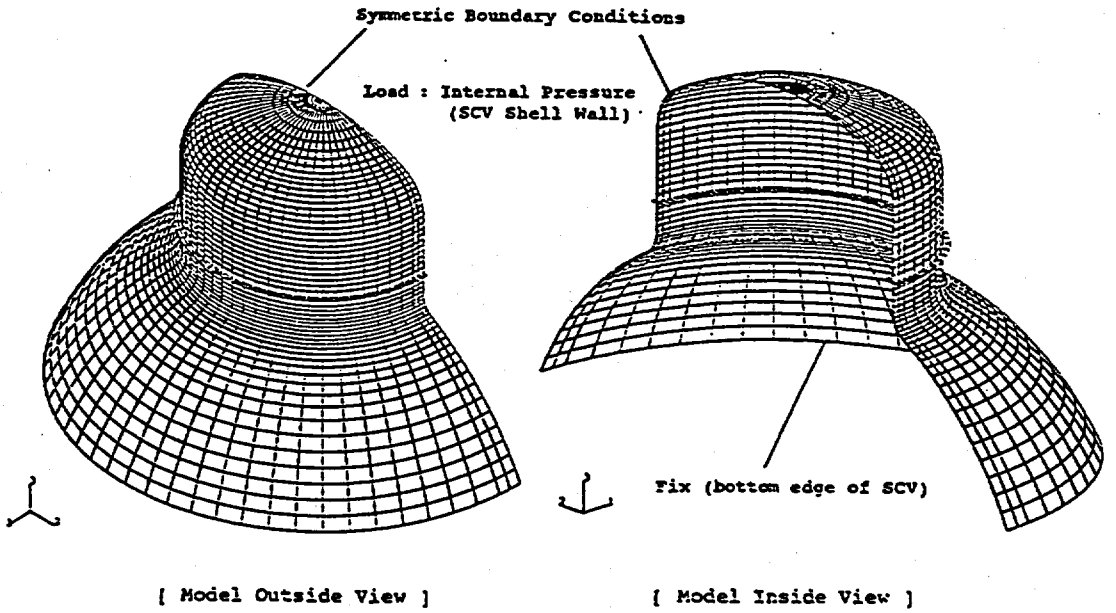

Figure 5.3-1 Local 3-D Top Head section Buckling Model and Analytical Conditions

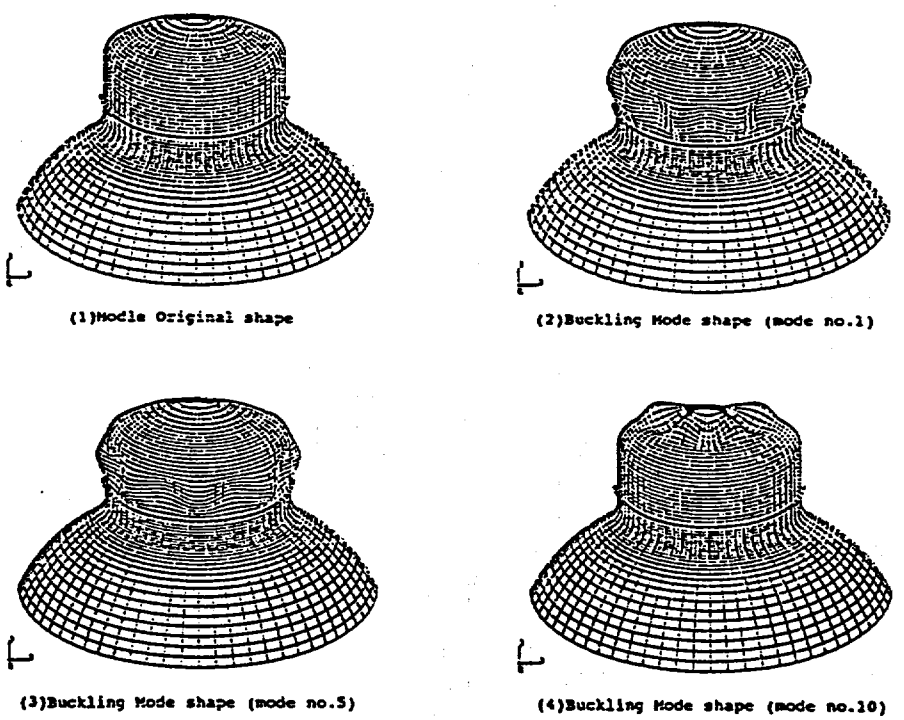

Figure 5.3-2 Buckling Mode Shape of Local 3-D Top Head section Buckling Model

6. Investigation of Critical Area

The failure place of the test model is termed of critical area. From the results of the previous two submodel analyses, the critical area of the test model is investigated.

Figure 6-1 shows the plastic membrane strains vs. the internal pressure at the typical points from the two submodel analyses. And, Figure 6-2 shows the maximum plastic surface strains at the same points. Until the internal pressure reaches to 7.3 MPa, the outside surface plastic strain near the E/H insert plate describes the maximum value. However, beyond the 7.3 MPa and until about 11.8 MPa, the inside surface plastic strains at the below of the knuckle joint and at the below of the top head flange joint describe the maximum value. Beyond the 11.8 MPa, the outside surface plastic strain at the top head apex of the model describes the maximum value.

Generally speaking, the larger the surface strain value, the larger the failure probability of the model. Therefore, it seems that these points are those in the critical area of the model for the failure initiation. However, such a behavior as in the Figure 6-2, the point that gives the maximum surface plastic strain moves depend on the internal pressure level. Therefore, it is possible to say that the critical area is one of these areas, however, it is difficult to prescribe the exact critical area. In other words, attenstion shoud be peyed to these areas in the test and have to be measured the strains at some points in those areas.

According to the references [8.3] and [8.4] concerning 1:8-scale steel containment model test like this SCV model test, the strain at failure position is expected 15%. Hence, an attempt to operate this failure criteria as a preliminary evaluation allows the occurrence of failure on the inside surface below of knuckle joint at the pressure of about 10MPa to be expected. It is, however, not physical to apply the failure mode in the references [8.3] and [8.4] to the failure position expected here. This should, therefore, be taken into account for any future post-test analysis.

7. Pretest Prediction Summary and Conclusions

As a pretest analysis, elasto-plastic/large displacement/contact analyses were conducted using global 2-D and 3-D models for the purpose of understanding the deformation behavior and failure position / pressure of SCV test model at the tests under pressure. Similar analysis was also made using separate submodel to review in detail the top head and equipment hatch area expected to cause high strain through the analysis of the global shell model. A linear buckling eigenvalue analysis was further applied on the top head region to confirm whether or not such a part is likely to suffer from buckling when pressurized.

Table 7-1 summarizes the results of the above analyses and the main phenomena involved at each pressure level of SCV test model given by the above analyses. The deformation behavior of SCV test model when pressurized starts with the initial yield occurring at the SCV test model knuckle region around 2.1MPa and then allows the deformation there to rapidly develop. As a result, when the internal pressure becomes around 3.5MPa, the first contact with CS occurs to the knuckle region. On the other hand, the strain at each region of the SCV test model becomes maximum near the equipment hatch until the internal pressure reaches around 7.3MPa. At higher pressure, the knuckle region's lower joint yields the maximum value and, when the internal pressure exceeds around 11.8MPa, the largest value is reached at the top head apex. Based on the parameter study concerning the effect of friction coefficient and/or gap distance between SCV and CS, these parameters will not be significant.

And little probability of top head buckling has been found from our study. But, this analysis is linear buckling eigenvalue analysis and one of evaluations for the buckling of top head section. Futhermore, we will investigate the potential of nonlinear buckling too.

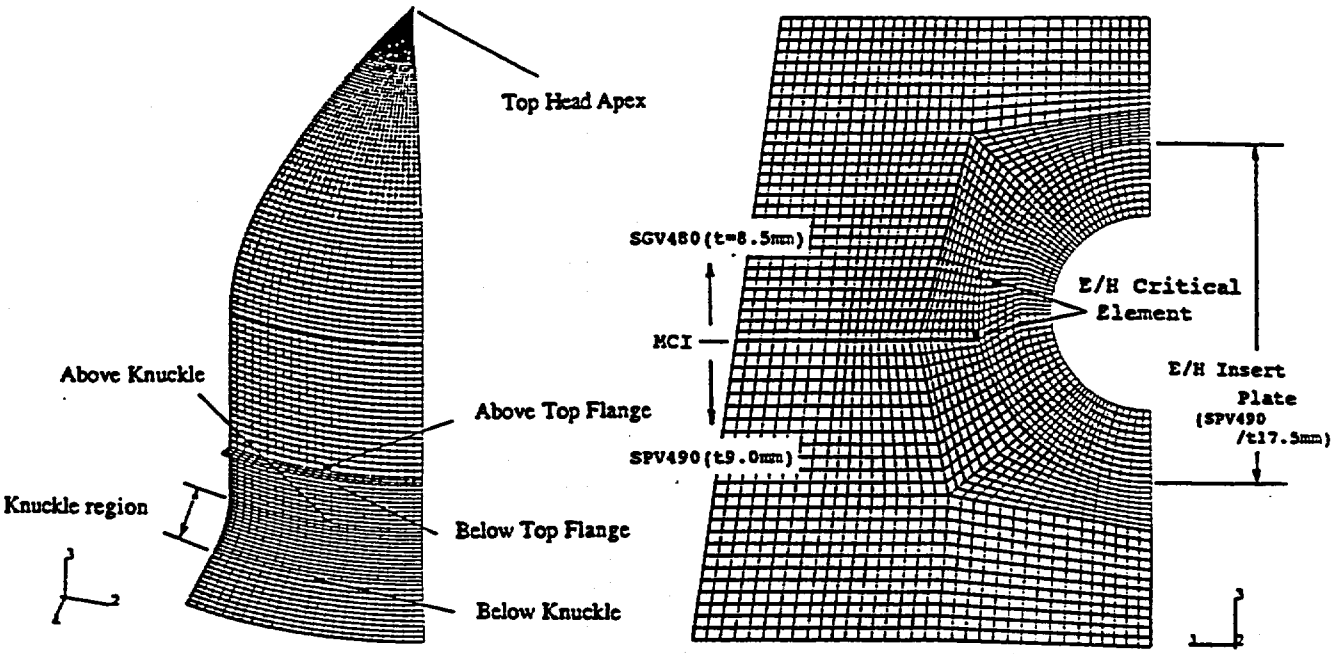

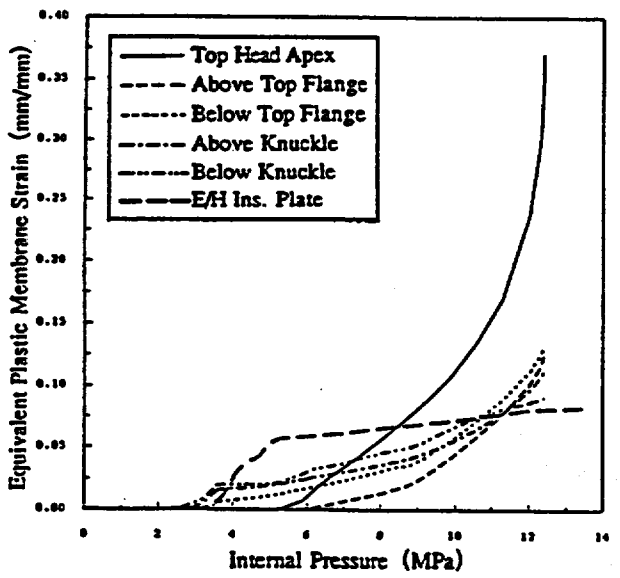

Figure 6-1 3-D Shell Submodel Membrane Plastic Strain

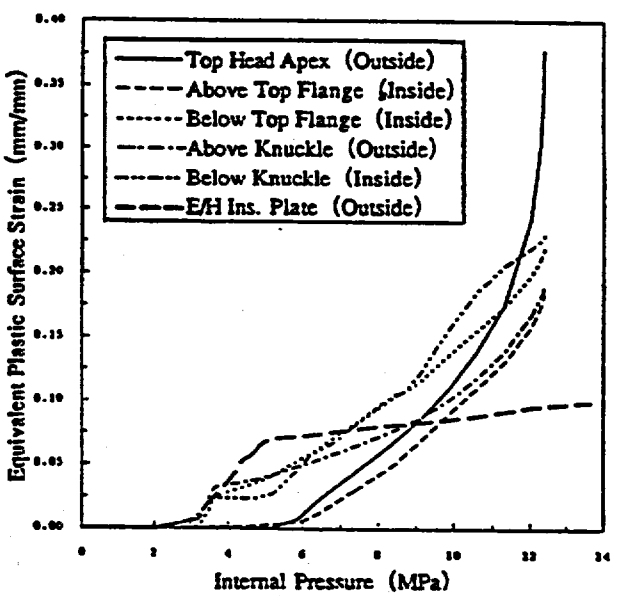

Figure 6-2 3-D Shell Submodel Surface Plastic Strain

Table 7-1 Analysis Results Summary

Analytical Methods	nonlinear axisymmetric finite element shell and general shell models; plastic, large displacement and contact analysis. [8.1][8.2]
Constitutive Models	ABAQUS nonlinear isotropic material with stress-strain curves as provided by SNL. [8.2]
Model Geometries	Global 2-D model : axisymmetric shell, axisymmetric solid and plane stress element Global 3-D model and Local 3-D submodel: general shell element

Pressure	Event
~ 2.1 MPa	First yield occurs at below of knuckle
~ 2.2 MPa	Yield occurs at near equipment hatch insert plate
~ 3.2 MPa	Yields occur at upper and middle conical shell section
~ 3.5 MPa	First contact initiates at knuckle region
~ 3.9 MPa	Contact initiates at upper conical shell section
~ 4.2 MPa	Contact initiates at middle conical shell section
~ 4.4 MPa	Yields occur at lower conical shell section and contact initiates at near equipment hatch
~ 4.8 MPa	Yields occur at lower cylindrical shell section
~ 5.2 MPa	Contact initiates at lower conical shell section
~ 5.3 MPa	Yields occur at upper spherical shell section
~ 7.6 MPa	Contact initiates at upper spherical shell section
~ 4 MPa	Maximum equivalent plastic surface strain occurs at knuckle region
4 ~ 7.3 MPa	Maximum equivalent plastic surface strain occurs at near equipment hatch insert plate
7.3 ~ 11.8 MPa	Maximum equivalent plastic surface strain occurs at below of knuckle region
11.8~ MPa	Maximum equivalent plastic surface strain occurs at top head apex

8. References

[8.1] "ABAQUS/Standard User's Manual Volume I", HIBBITT, KARLSON & SORENSEN, Inc.

[8.2] "ABAQUS/Standard User's Manual Volume II", HIBBITT, KARLSON & SORENSEN, Inc.

[8.3] "Pretest Predictions for the Response of a 1:8-Scale Steel LWR Containment Building Model to Static Overpressurization", D.B.Clauss, 1985, NUREG/CR-4137, SAND85-0175

[8.4] "Comparison of Analytical Predictions and Experimental Results for a 1:8-Scale Steel Containment Model Pressurized to Failure", D.B. Clauss, 1985, NUREG/CR-4209, SAND85-0679

Appendix

Pretest Analysis of a 1:10-Scale Steel Containment Model Subject to Static Internal Pressurization

Standard Output

July ,1996

Nuclear Power Engineering Corporation

Figures and Tables

Table

Figure

Tab. 1-1 Standard Output (Plot ID 1 - 6)

Results of Local 3-D Shell E/H Submodel Analysis

Internal Pressure			Strain					
			Plot ID 1	Plot ID 2	Plot ID 3	Plot ID 4	Plot ID 5	Plot ID 6
(kg/cm^2)	(MPa)	(Pd)	(-)	(-)	(-)	(-)	(-)	(-)
1.5	0.14710209	0.18859242	1.21E-04	1.00E-04	6.46E-05	3.81E-05	6.47E-05	1.05E-04
3	0.29420418	0.37718484	2.41E-04	2.00E-04	1.28E-04	7.68E-05	1.30E-04	2.09E-04
5.25	0.51485731	0.66007348	4.19E-04	3.48E-04	2.24E-04	1.35E-04	2.28E-04	3.65E-04
8.625	0.84583701	1.08440642	6.84E-04	5.69E-04	3.67E-04	2.23E-04	3.77E-04	5.97E-04
13.6875	1.34230656	1.72090585	1.08E-03	8.96E-04	5.79E-04	3.57E-04	6.02E-04	9.44E-04
21.282	2.08708444	2.67574928	1.66E-03	1.38E-03	8.95E-04	5.62E-04	9.43E-04	1.46E-03
32.673	3.2041777	4.10792013	6.85E-03	3.32E-03	1.38E-03	8.32E-04	1.05E-03	6.17E-03
35.52	3.48337746	4.46586854	1.30E-02	6.43E-03	1.79E-03	6.66E-04	1.41E-03	8.03E-03
38.367	3.76257723	4.82381696	2.30E-02	1.30E-02	3.80E-03	6.93E-04	4.66E-03	1.32E-02
41.214	4.04177699	5.18176538	3.39E-02	2.19E-02	8.17E-03	3.49E-03	1.49E-02	2.43E-02
41.35205	4.05923801	5.2061513	3.47E-02	2.25E-02	8.50E-03	3.72E-03	1.56E-02	2.49E-02
41.5701	4.07669903	5.22653722	3.55E-02	2.32E-02	8.83E-03	3.96E-03	1.62E-02	2.55E-02
41.74815	4.09416005	5.24892314	3.62E-02	2.38E-02	9.15E-03	4.20E-03	1.68E-02	2.60E-02
42.01515	4.12034422	5.28249259	3.71E-02	2.45E-02	9.60E-03	4.55E-03	1.76E-02	2.68E-02
42.41565	4.15962048	5.33284676	3.83E-02	2.56E-02	1.03E-02	5.11E-03	1.87E-02	2.78E-02
43.0164	4.21853486	5.40837803	4.00E-02	2.72E-02	1.14E-02	5.98E-03	2.02E-02	2.93E-02
43.2417	4.2406296	5.43670461	4.06E-02	2.77E-02	1.18E-02	6.32E-03	2.08E-02	2.98E-02
43.57965	4.2737717	5.47919448	4.15E-02	2.86E-02	1.24E-02	6.85E-03	2.16E-02	3.06E-02
43.706355	4.28619741	5.49512489	4.18E-02	2.89E-02	1.27E-02	7.05E-03	2.19E-02	3.08E-02
43.896405	4.30483525	5.51901955	4.22E-02	2.93E-02	1.31E-02	7.36E-03	2.23E-02	3.13E-02
44.181555	4.33279935	5.55487097	4.30E-02	2.97E-02	1.37E-02	7.85E-03	2.30E-02	3.19E-02
44.466705	4.36076346	5.59072238	4.36E-02	2.98E-02	1.42E-02	8.25E-03	2.36E-02	3.24E-02
44.53797	4.36775228	5.59968241	4.37E-02	2.98E-02	1.43E-02	8.33E-03	2.37E-02	3.25E-02
44.5647	4.37037364	5.60304313	4.37E-02	2.99E-02	1.43E-02	8.35E-03	2.37E-02	3.26E-02
44.604795	4.37430568	5.6080842	4.38E-02	2.99E-02	1.43E-02	8.38E-03	2.38E-02	3.26E-02
44.66493	4.380203	5.61564487	4.38E-02	2.98E-02	1.43E-02	8.41E-03	2.39E-02	3.27E-02
44.75514	4.38904972	5.62698682	4.38E-02	2.98E-02	1.43E-02	8.44E-03	2.40E-02	3.28E-02
44.89044	4.40231833	5.64399786	4.39E-02	2.98E-02	1.42E-02	8.47E-03	2.41E-02	3.29E-02
45.09339	4.42222124	5.66951441	4.40E-02	2.98E-02	1.42E-02	8.51E-03	2.43E-02	3.30E-02
45.39789	4.45208297	5.70779867	4.41E-02	2.98E-02	1.42E-02	8.56E-03	2.46E-02	3.32E-02
45.85449	4.49686084	5.76520621	4.42E-02	2.98E-02	1.41E-02	8.60E-03	2.50E-02	3.36E-02
46.53954	4.56404237	5.85133637	4.44E-02	2.98E-02	1.41E-02	8.65E-03	2.57E-02	3.41E-02
47.56704	4.6648673	5.98052217	4.43E-02	2.99E-02	1.40E-02	8.70E-03	2.69E-02	3.50E-02
47.95239	4.70259782	6.02897157	4.43E-02	2.99E-02	1.39E-02	8.71E-03	2.75E-02	3.54E-02
48.53034	4.75937626	6.10163623	4.48E-02	2.98E-02	1.39E-02	8.72E-03	2.85E-02	3.63E-02
49.39734	4.84430127	6.21064265	4.71E-02	2.97E-02	1.38E-02	8.74E-03	3.02E-02	3.78E-02
50.69769	4.97182407	6.37413342	4.70E-02	2.96E-02	1.36E-02	8.75E-03	3.23E-02	3.99E-02
51.02274	5.00370109	6.4150014	4.70E-02	2.96E-02	1.36E-02	8.76E-03	3.26E-02	4.05E-02
51.34779	5.03557811	6.45586937	4.70E-02	2.95E-02	1.36E-02	8.76E-03	3.28E-02	4.08E-02
51.83544	5.083401	6.51718077	4.71E-02	2.95E-02	1.35E-02	8.76E-03	3.36E-02	4.09E-02
52.56684	5.15512798	6.60913843	4.71E-02	2.95E-02	1.34E-02	8.77E-03	3.44E-02	4.12E-02
53.66409	5.26273316	6.74709379	4.73E-02	2.94E-02	1.33E-02	8.80E-03	3.53E-02	4.16E-02
54.76134	5.37033833	6.885049151	4.73E-02	2.94E-02	1.33E-02	8.83E-03	3.56E-02	4.17E-02
55.85859	5.47794351	7.0230045	4.74E-02	2.94E-02	1.33E-02	8.90E-03	3.58E-02	4.17E-02
56.95584	5.58554869	7.16095986	4.74E-02	2.94E-02	1.33E-02	8.93E-03	3.60E-02	4.17E-02
58.05309	5.69315387	7.29891522	4.74E-02	2.94E-02	1.33E-02	8.98E-03	3.62E-02	4.18E-02
59.15034	5.80075905	7.43687057	4.75E-02	2.94E-02	1.32E-02	9.20E-03	3.64E-02	4.18E-02
60.24759	5.90836422	7.57482593	4.75E-02	2.93E-02	1.31E-02	9.44E-03	3.66E-02	4.18E-02
61.89309	6.06973522	7.78171182	4.77E-02	2.93E-02	1.27E-02	1.11E-02	3.68E-02	4.20E-02
64.36209	6.31186525	8.09213494	4.78E-02	2.93E-02	1.22E-02	1.35E-02	3.70E-02	4.23E-02
66.83109	6.55399529	8.40255807	4.79E-02	2.93E-02	1.23E-02	1.35E-02	3.72E-02	4.26E-02
69.30009	6.79612533	8.71298119	4.81E-02	2.93E-02	1.24E-02	1.37E-02	3.74E-02	4.29E-02
73.00359	7.15932039	9.178615881	4.84E-02	2.95E-02	1.30E-02	1.43E-02	3.78E-02	4.33E-02
78.55809	7.70403942	9.87697362	4.90E-02	3.00E-02	1.43E-02	1.68E-02	3.83E-02	4.41E-02
84.11259	8.24875846	10.5753314	4.96E-02	3.06E-02	2.09E-02	2.14E-02	3.88E-02	4.49E-02
89.66709	8.79347749	11.2736891	5.02E-02	3.14E-02	2.53E-02	2.55E-02	3.93E-02	4.56E-02
97.99959	9.6106296	12.32132	5.09E-02	3.28E-02	3.04E-02	3.16E-02	4.03E-02	4.65E-02
101.12409	9.91704325	12.714158	5.12E-02	3.34E-02	3.19E-02	3.33E-02	4.07E-02	4.68E-02
105.81009	10.3765902	13.3033207	5.17E-02	3.46E-02	3.43E-02	3.61E-02	4.13E-02	4.73E-02
112.84059	11.0660577	14.1872534	5.24E-02	3.64E-02	3.84E-02	4.02E-02	4.24E-02	4.82E-02
123.38559	12.1001853	15.5130582	5.35E-02	3.88E-02	4.27E-02	4.42E-02	4.40E-02	4.94E-02
139.21059	13.6521124	17.5027082	5.37E-02	3.99E-02	4.39E-02	4.57E-02	4.51E-02	4.98E-02
Remarks			int.max. prin.strain	int.max. prin.strain	ext. merid. strain	int. merid. strain	ext. hoop strain	int. hoop strain

1 (MPa) = 10.197 (kg/cm^2)

1 (Pd) = 0.78 (MPa)

Tab. 1-2 Standard Output (Plot ID 7 - 14)

Results of Global Axisymmetric Shell Model Analysis

Internal Pressure			Strain							
			Plot ID 7	Plot ID 8	Plot ID 9	Plot ID 10	Plot ID 11	Plot ID 12	Plot ID 13	Plot ID 14
(kg/cm^2)	(MPa)	(Pd)	(-)	(-)	(-)	(-)	(-)	(-)	(-)	(-)
0	0	0	0.000	3.35E-07	-1.20E-07	-2.97E-07	0.000	-1.24E-07	-1.40E-07	-6.04E-07
1.5	0.14710209	0.18859242	4.89E-05	-6.56E-05	2.20E-05	7.86E-05	2.56E-05	-6.94E-06	9.58E-06	3.35E-05
3	0.29420418	0.37718484	9.76E-05	-1.31E-04	4.43E-05	1.57E-04	5.12E-05	-1.36E-05	1.93E-05	6.76E-05
5.25	0.51485731	0.66007348	1.70E-04	-2.28E-04	7.79E-05	2.74E-04	8.94E-05	-2.31E-05	3.37E-05	1.19E-04
8.625	0.84583701	1.08449642	2.77E-04	-3.71E-04	1.29E-04	4.47E-04	1.46E-04	-3.67E-05	5.52E-05	1.95E-04
13.6875	1.34230656	1.72090585	4.35E-04	-5.80E-04	2.06E-04	7.02E-04	2.29E-04	-5.55E-05	8.72E-05	3.09E-04
21.282	2.08708444	2.67574928	6.65E-04	-8.83E-04	3.23E-04	1.08E-03	3.51E-04	-7.93E-05	1.33E-04	4.81E-04
32.673	3.2041777	4.10792013	1.00E-03	-1.33E-03	5.20E-04	1.62E-03	-1.74E-03	-1.76E-04	-2.58E-03	2.77E-03
35.52	3.48337746	4.46586854	1.09E-03	-1.47E-03	5.86E-04	1.79E-03	-2.61E-03	-5.91E-04	-3.50E-03	3.48E-03
35.69805	3.50083848	4.48825446	1.09E-03	-1.48E-03	5.89E-04	1.81E-03	-2.66E-03	-6.13E-04	-3.56E-03	3.52E-03
35.8761	3.5182995	4.51064038	1.10E-03	-1.49E-03	5.93E-04	1.83E-03	-2.71E-03	-6.34E-04	-3.60E-03	3.55E-03
36.1431	3.54448367	4.54420984	1.10E-03	-1.51E-03	5.98E-04	1.86E-03	-2.70E-03	-6.52E-04	-3.60E-03	3.56E-03
36.5436	3.58375993	4.59456401	1.12E-03	-1.53E-03	6.06E-04	1.89E-03	-2.69E-03	-6.81E-04	-3.60E-03	3.56E-03
37.14435	3.64267432	4.67009528	1.13E-03	-1.57E-03	6.18E-04	1.96E-03	-2.67E-03	-7.23E-04	-3.59E-03	3.57E-03
38.0454	3.73103854	4.78338274	1.16E-03	-1.63E-03	6.41E-04	2.07E-03	-2.64E-03	-7.85E-04	-3.58E-03	3.57E-03
39.3969	3.86357752	4.95330452	1.20E-03	-1.72E-03	6.78E-04	2.23E-03	-2.58E-03	-8.64E-04	-3.56E-03	3.58E-03
40.7484	3.9961165	5.12322629	1.24E-03	-1.83E-03	7.45E-04	2.44E-03	-2.51E-03	-9.14E-04	-3.53E-03	3.54E-03
42.0999	4.12865549	5.29314806	1.28E-03	-1.96E-03	8.36E-04	2.68E-03	-2.44E-03	-9.70E-04	-3.51E-03	3.51E-03
43.4514	4.26119447	5.46306983	1.32E-03	-2.16E-03	9.59E-04	3.03E-03	-2.38E-03	-1.03E-03	-3.48E-03	3.48E-03
44.8029	4.39373345	5.6329916	1.35E-03	-2.42E-03	1.10E-03	3.49E-03	-2.31E-03	-1.09E-03	-3.45E-03	3.46E-03
46.8309	4.59261548	5.88796856	1.41E-03	-2.89E-03	1.36E-03	4.33E-03	-2.20E-03	-1.17E-03	-3.38E-03	3.41E-03
48.8589	4.7914975	6.14294551	1.47E-03	-3.45E-03	1.69E-03	5.31E-03	-2.08E-03	-1.24E-03	-3.29E-03	3.38E-03
50.8869	4.99037952	6.39792247	1.53E-03	-4.16E-03	2.15E-03	6.51E-03	-1.95E-03	-1.33E-03	-3.14E-03	3.37E-03
51.6471	5.06493086	6.49350111	1.55E-03	-4.45E-03	2.34E-03	7.00E-03	-1.89E-03	-1.36E-03	-3.07E-03	3.38E-03
52.4073	5.1394822	6.58907974	1.58E-03	-4.74E-03	2.55E-03	7.49E-03	-1.85E-03	-1.38E-03	-2.99E-03	3.36E-03
53.1675	5.21403354	6.68465838	1.62E-03	-5.03E-03	2.75E-03	7.98E-03	-1.82E-03	-1.40E-03	-2.90E-03	3.34E-03
53.9277	5.28858488	6.78023702	1.67E-03	-5.32E-03	2.95E-03	8.46E-03	-1.77E-03	-1.42E-03	-2.80E-03	3.32E-03
54.6879	5.36313622	6.87581566	1.78E-03	-5.60E-03	3.17E-03	8.95E-03	-1.73E-03	-1.44E-03	-2.68E-03	3.31E-03
55.4481	5.43768756	6.9713943	1.98E-03	-5.88E-03	3.38E-03	9.43E-03	-1.68E-03	-1.47E-03	-2.54E-03	3.29E-03
56.5884	5.54951456	7.11476226	3.56E-03	-6.31E-03	3.71E-03	1.02E-02	-1.59E-03	-1.51E-03	-2.27E-03	3.24E-03
58.2984	5.71721094	7.32975762	6.98E-03	-6.99E-03	4.28E-03	1.13E-02	-1.44E-03	-1.57E-03	-1.72E-03	3.12E-03
60.0084	5.88490733	7.54475298	9.62E-03	-7.66E-03	4.86E-03	1.25E-02	-1.26E-03	-1.64E-03	-1.13E-03	3.02E-03
61.7184	6.05260371	7.75974834	1.16E-02	-8.32E-03	5.47E-03	1.36E-02	-1.08E-03	-1.70E-03	-5.07E-04	2.93E-03
64.2849	6.30429538	8.08242998	1.43E-02	-9.29E-03	6.46E-03	1.52E-02	-7.17E-04	-1.82E-03	4.39E-04	2.82E-03
64.9263	6.36719623	8.1630721	1.50E-02	-9.55E-03	6.73E-03	1.56E-02	-6.01E-04	-1.88E-03	5.50E-04	2.79E-03
65.5677	6.43009709	8.24371421	1.56E-02	-9.79E-03	7.00E-03	1.60E-02	-4.83E-04	-1.93E-03	6.61E-04	2.76E-03
66.5298	6.52444837	8.36467739	1.66E-02	-1.01E-02	7.37E-03	1.66E-02	-3.02E-04	-2.00E-03	8.20E-04	2.71E-03
67.9731	6.66599	8.54614102	1.81E-02	-1.06E-02	7.90E-03	1.74E-02	-1.09E-05	-2.11E-03	1.05E-03	2.64E-03
69.4164	6.80753163	8.72760465	1.96E-02	-1.11E-02	8.44E-03	1.82E-02	2.97E-04	-2.21E-03	1.27E-03	2.56E-03
70.8597	6.94907326	8.90906828	2.11E-02	-1.15E-02	8.99E-03	1.90E-02	6.29E-04	-2.32E-03	1.48E-03	2.49E-03
73.0242	7.16134157	9.18120714	2.33E-02	-1.22E-02	9.79E-03	2.01E-02	1.16E-03	-2.45E-03	1.80E-03	2.37E-03
75.1887	7.37360989	9.45334601	2.55E-02	-1.28E-02	1.06E-02	2.11E-02	1.69E-03	-2.56E-03	2.14E-03	2.24E-03
77.3532	7.5858782	9.72548487	2.79E-02	-1.33E-02	1.14E-02	2.21E-02	2.23E-03	-2.64E-03	2.50E-03	2.09E-03
79.5177	7.79814651	9.99762374	3.02E-02	-1.38E-02	1.21E-02	2.30E-02	2.77E-03	-2.68E-03	2.86E-03	1.94E-03
81.6822	8.01041483	10.2697626	3.26E-02	-1.42E-02	1.28E-02	2.39E-02	3.31E-03	-2.70E-03	3.21E-03	1.80E-03
83.8467	8.22268314	10.5419015	3.52E-02	-1.46E-02	1.33E-02	2.46E-02	3.86E-03	-2.69E-03	3.52E-03	1.67E-03
87.0942	8.54115914	10.9502841	3.94E-02	-1.50E-02	1.40E-02	2.56E-02	4.70E-03	-2.60E-03	4.04E-03	1.47E-03
91.9647	9.01879965	11.5625636	4.58E-02	-1.54E-02	1.50E-02	2.70E-02	6.01E-03	-2.28E-03	4.84E-03	1.18E-03
96.8352	9.49644013	12.1749232	5.30E-02	-1.56E-02	1.55E-02	2.81E-02	7.44E-03	-1.65E-03	5.52E-03	9.31E-04
101.7057	9.97408061	12.7872828	6.11E-02	-1.57E-02	1.57E-02	2.95E-02	1.01E-02	9.87E-04	6.36E-03	6.03E-04
106.5762	10.4517211	13.3996424	7.05E-02	-1.55E-02	1.58E-02	2.96E-02	1.44E-02	5.22E-03	7.32E-03	2.29E-04
113.8827	11.1682554	14.3182761	8.75E-02	-1.43E-02	1.56E-02	3.32E-02	2.24E-02	1.20E-02	8.51E-03	2.93E-05
124.8417	12.2429832	15.6961323	1.43E-01	2.74E-04	4.06E-02	5.98E-02	3.94E-02	2.69E-02	9.73E-03	6.86E-04
125.52675	12.3101648	15.7822625	1.50E-01	2.30E-03	4.39E-02	6.32E-02	4.09E-02	2.83E-02	9.77E-03	7.95E-04
126.2118	12.3773463	15.8683927	1.59E-01	4.97E-03	4.79E-02	6.73E-02	4.26E-02	2.98E-02	9.82E-03	9.16E-04
127.2393	12.4781112	15.9975785	1.81E-01	1.14E-02	5.61E-02	7.59E-02	4.55E-02	3.26E-02	9.92E-03	1.13E-03
127.33563	12.4875581	16.0096899	1.85E-01	1.26E-02	5.75E-02	7.74E-02	4.59E-02	3.30E-02	9.93E-03	1.15E-03
127.480125	12.5017284	16.027857	1.99E-01	1.61E-02	6.16E-02	8.16E-02	4.67E-02	3.37E-02	9.96E-03	1.19E-03
127.493672	12.5030569	16.0295602	2.02E-01	1.70E-02	6.25E-02	8.26E-02	4.68E-02	3.39E-02	9.97E-03	1.19E-03
127.497059	12.5033891	16.029986	2.03E-01	1.72E-02	6.28E-02	8.29E-02	4.69E-02	3.39E-02	9.97E-03	1.20E-03
127.500446	12.5037212	16.0304118	2.04E-01	1.75E-02	6.31E-02	8.33E-02	4.69E-02	3.40E-02	9.97E-03	1.20E-03
127.501946	12.5038683	16.0306004	2.05E-01	1.77E-02	6.33E-02	8.35E-02	4.69E-02	3.40E-02	9.97E-03	1.20E-03
127.503446	12.5040154	16.030789	2.06E-01	1.80E-02	6.37E-02	8.38E-02	4.70E-02	3.41E-02	9.97E-03	1.20E-03
127.505696	12.5042361	16.0310719	2.06E-01	1.80E-02	6.37E-02	8.38E-02	4.70E-02	3.41E-02	9.97E-03	1.20E-03
Remarks			ext.max. prin.strain	ext. hoop strain	ext. merid. strain	int. merid. strain	ext. merid. strain	int. merid. strain	ext. merid. strain	int. merid. strain

1 (MPa) = 10.197 (kg/cm^2)

1 (Pd) = 0.78 (MPa)

Tab. 1-3 Standard Output (Plot ID 15 - 22)

Results of Global Axisymmetric Shell Model Analysis

Internal Pressure			Strain							
			Plot ID 15	Plot ID 16	Plot ID 17	Plot ID 18	Plot ID 19	Plot ID 20	Plot ID 21	Plot ID 22
(kg/cm^2)	(MPa)	(Pd)	(-)	(-)	(-)	(-)	(-)	(-)	(-)	(-)
0	0	0	-1.07E-06	5.42E-08	0.000	-7.28E-07	5.39E-07	-2.17E-06	0.000	-5.08E-07
1.5	0.14710209	0.18859242	-9.04E-06	7.19E-05	2.31E-05	2.17E-05	-7.27E-05	1.75E-04	2.03E-05	2.07E-05
3	0.29420418	0.37718484	-1.67E-05	1.43E-04	4.69E-05	4.41E-05	-1.45E-04	3.51E-04	4.12E-05	4.19E-05
5.25	0.51485731	0.66007348	-2.74E-05	2.50E-04	8.27E-05	7.77E-05	-2.51E-04	6.12E-04	7.28E-05	7.36E-05
8.625	0.84583701	1.08440642	-4.22E-05	4.07E-04	1.36E-04	1.28E-04	-4.05E-04	9.97E-04	1.21E-04	1.21E-04
13.6875	1.34230656	1.72090585	-6.13E-05	6.39E-04	2.17E-04	2.04E-04	-6.27E-04	1.56E-03	1.93E-04	1.91E-04
21.282	2.08708444	2.67574928	-8.34E-05	9.78E-04	3.39E-04	3.17E-04	-9.38E-04	2.38E-03	3.04E-04	2.96E-04
32.673	3.2041777	4.10792013	-1.12E-04	1.48E-03	5.66E-04	5.07E-04	-1.41E-03	3.68E-03	5.38E-04	4.11E-04
35.52	3.483337746	4.46586854	-7.69E-04	2.32E-03	6.28E-04	8.99E-04	-1.54E-03	4.06E-03	1.65E-03	3.23E-04
35.69805	3.50083848	4.48825446	-8.31E-04	2.44E-03	6.28E-04	9.30E-04	-1.55E-03	4.08E-03	1.74E-03	3.30E-04
35.8761	3.5182995	4.51064038	-8.75E-04	2.54E-03	6.28E-04	9.63E-04	-1.55E-03	4.10E-03	1.83E-03	3.41E-04
36.1431	3.54448367	4.54470984	-9.37E-04	2.67E-03	6.26E-04	1.01E-03	-1.57E-03	4.13E-03	1.97E-03	3.64E-04
36.5436	3.58375993	4.59456401	-1.02E-03	2.83E-03	6.38E-04	1.09E-03	-1.58E-03	4.18E-03	2.18E-03	4.17E-04
37.14435	3.64267432	4.67009528	-1.11E-03	3.04E-03	6.85E-04	1.19E-03	-1.61E-03	4.25E-03	2.43E-03	5.15E-04
38.0454	3.73103854	4.78338274	-1.27E-03	3.46E-03	8.31E-04	1.34E-03	-1.65E-03	4.36E-03	2.78E-03	6.89E-04
39.3969	3.86357752	4.95330452	-1.82E-03	4.78E-03	1.31E-03	1.59E-03	-1.71E-03	4.51E-03	3.13E-03	9.20E-04
40.7484	3.99611565	5.12322629	-1.99E-03	5.72E-03	2.13E-03	1.78E-03	-1.77E-03	4.63E-03	3.15E-03	1.04E-03
42.0999	4.12865549	5.29314806	-1.83E-03	5.98E-03	2.68E-03	1.71E-03	-1.83E-03	4.74E-03	3.08E-03	1.24E-03
43.4514	4.26119447	5.46306983	-1.60E-03	6.05E-03	3.22E-03	1.58E-03	-1.91E-03	4.94E-03	2.88E-03	1.57E-03
44.8029	4.39373365	5.6329916	-1.34E-03	6.07E-03	3.80E-03	1.44E-03	-2.01E-03	5.23E-03	2.53E-03	2.12E-03
46.8309	4.59261548	5.88796856	-8.31E-04	6.00E-03	4.65E-03	1.30E-03	-2.17E-03	5.76E-03	2.42E-03	2.42E-03
48.8589	4.7914875	6.14294551	-3.56E-04	5.87E-03	5.29E-03	1.41E-03	-2.37E-03	6.40E-03	2.50E-03	2.47E-03
50.8869	4.99037952	6.39792247	1.63E-04	5.73E-03	5.19E-03	2.15E-03	-2.82E-03	7.82E-03	2.57E-03	2.56E-03
51.6471	5.066930986	6.49350111	3.77E-04	5.67E-03	4.88E-03	2.68E-03	-3.05E-03	8.51E-03	2.60E-03	2.61E-03
52.4073	5.1394822	6.58907974	6.08E-04	5.62E-03	4.41E-03	3.55E-03	-3.39E-03	9.39E-03	2.64E-03	2.63E-03
53.1675	5.21403354	6.68465838	7.85E-04	5.58E-03	4.39E-03	3.69E-03	-3.75E-03	1.05E-02	2.68E-03	2.65E-03
53.9277	5.288258488	6.78023702	9.61E-04	5.53E-03	4.35E-03	3.87E-03	-4.15E-03	1.18E-02	2.72E-03	2.67E-03
54.6879	5.36313622	6.87581566	1.14E-03	5.48E-03	4.33E-03	4.00E-03	-4.53E-03	1.31E-02	2.74E-03	2.70E-03
55.4481	5.43768756	6.9713943	1.31E-03	5.43E-03	4.32E-03	4.12E-03	-4.94E-03	1.45E-02	2.77E-03	2.73E-03
56.5084	5.541951456	7.11476226	1.56E-03	5.36E-03	4.32E-03	4.26E-03	-5.50E-03	1.64E-02	2.80E-03	2.77E-03
58.2984	5.71721094	7.32975762	2.05E-03	5.25E-03	4.37E-03	4.40E-03	-6.30E-03	1.90E-02	2.89E-03	2.85E-03
60.0884	5.88490733	7.54475298	2.49E-03	5.15E-03	4.44E-03	4.49E-03	-7.19E-03	2.20E-02	2.96E-03	2.92E-03
61.7184	6.05260371	7.75974834	2.88E-03	5.07E-03	4.54E-03	4.60E-03	-7.96E-03	2.45E-02	3.05E-03	3.00E-03
64.2849	6.30429538	8.08242998	3.64E-03	4.96E-03	4.76E-03	4.80E-03	-8.92E-03	2.74E-02	3.16E-03	3.12E-03
64.9263	6.36719623	8.1638721	3.81E-03	4.92E-03	4.74E-03	4.84E-03	-9.14E-03	2.81E-02	3.19E-03	3.14E-03
65.5677	6.43009709	8.24371421	3.98E-03	4.89E-03	4.78E-03	4.89E-03	-9.36E-03	2.89E-02	3.20E-03	3.15E-03
66.5298	6.52444837	8.36467739	4.22E-03	4.86E-03	4.84E-03	4.97E-03	-9.64E-03	2.99E-02	3.23E-03	3.18E-03
67.9731	6.66599	8.54616102	4.67E-03	4.83E-03	4.99E-03	5.14E-03	-1.01E-02	3.13E-02	3.29E-03	3.24E-03
69.4164	6.807531163	8.72760465	5.18E-03	4.79E-03	5.14E-03	5.31E-03	-1.03E-02	3.23E-02	3.34E-03	3.29E-03
70.8597	6.949073296	8.90906828	5.72E-03	4.75E-03	5.31E-03	5.51E-03	-1.06E-02	3.32E-02	3.39E-03	3.34E-03
73.0242	7.16134157	9.18120716	6.51E-03	4.76E-03	5.63E-03	5.87E-03	-1.08E-02	3.45E-02	3.50E-03	3.45E-03
75.1887	7.37360989	9.45334601	7.35E-03	4.75E-03	6.04E-03	6.34E-03	-1.09E-02	3.57E-02	3.60E-03	3.54E-03
77.3532	7.5858782	9.72548487	8.08E-03	4.75E-03	6.54E-03	6.91E-03	-1.09E-02	3.69E-02	3.68E-03	3.62E-03
79.5177	7.79814651	9.99762374	8.77E-03	4.79E-03	7.21E-03	7.59E-03	-1.09E-02	3.79E-02	3.77E-03	3.70E-03
81.6822	8.01041483	10.2697626	9.38E-03	4.80E-03	8.15E-03	8.47E-03	-1.09E-02	3.88E-02	3.84E-03	3.77E-03
83.8467	8.22268314	10.5419015	9.99E-03	4.80E-03	9.37E-03	9.61E-03	-1.08E-02	3.96E-02	3.90E-03	3.82E-03
87.0942	8.541159916	10.9502041	1.08E-02	4.81E-03	1.16E-02	1.17E-02	-1.07E-02	4.06E-02	3.98E-03	3.90E-03
91.9647	9.01079965	11.5625636	1.14E-02	4.87E-03	1.46E-02	1.46E-02	-1.04E-02	4.19E-02	4.05E-03	3.97E-03
96.8352	9.49644013	12.1749232	1.22E-02	4.88E-03	1.72E-02	1.71E-02	-1.06E-02	4.33E-02	4.10E-03	4.01E-03
101.7057	9.97408061	12.7872828	1.27E-02	4.83E-03	1.88E-02	1.87E-02	-1.14E-02	4.56E-02	4.11E-03	4.02E-03
106.5762	10.4517211	13.3996424	1.33E-02	4.76E-03	2.08E-02	2.06E-02	-1.24E-02	4.91E-02	4.13E-03	4.03E-03
113.8827	11.1682556	14.3182761	1.42E-02	4.64E-03	2.30E-02	2.28E-02	-1.24E-02	5.03E-02	4.16E-03	4.05E-03
124.8417	12.2429832	15.6961323	1.44E-02	4.59E-03	2.47E-02	2.44E-02	-1.20E-02	5.12E-02	4.19E-03	4.08E-03
125.52675	12.3101648	15.7822625	1.44E-02	4.59E-03	2.48E-02	2.45E-02	-1.20E-02	5.13E-02	4.19E-03	4.08E-03
126.2118	12.3773463	15.8683927	1.44E-02	4.59E-03	2.49E-02	2.45E-02	-1.20E-02	5.14E-02	4.20E-03	4.08E-03
127.2393	12.4781112	15.9975785	1.44E-02	4.59E-03	2.50E-02	2.46E-02	-1.20E-02	5.16E-02	4.20E-03	4.09E-03
127.33563	12.4875581	16.0096899	1.44E-02	4.59E-03	2.50E-02	2.46E-02	-1.20E-02	5.16E-02	4.20E-03	4.09E-03
127.480125	12.5017284	16.027857	1.44E-02	4.59E-03	2.50E-02	2.46E-02	-1.20E-02	5.16E-02	4.20E-03	4.09E-03
127.493672	12.5030569	16.0295602	1.44E-02	4.59E-03	2.50E-02	2.46E-02	-1.20E-02	5.16E-02	4.20E-03	4.09E-03
127.497059	12.5033891	16.029986	1.44E-02	4.59E-03	2.50E-02	2.46E-02	-1.20E-02	5.16E-02	4.20E-03	4.09E-03
127.500446	12.5037212	16.0304118	1.44E-02	4.59E-03	2.50E-02	2.46E-02	-1.20E-02	5.16E-02	4.20E-03	4.09E-03
127.501946	12.5038683	16.0306004	1.44E-02	4.59E-03	2.50E-02	2.46E-02	-1.20E-02	5.16E-02	4.20E-03	4.09E-03
127.503446	12.5040154	16.030789	1.44E-02	4.59E-03	2.50E-02	2.46E-02	-1.20E-02	5.16E-02	4.20E-03	4.09E-03
127.505696	12.5042361	16.0310719	1.44E-02	4.59E-03	2.50E-02	2.46E-02	-1.20E-02	5.16E-02	4.20E-03	4.09E-03
Remarks			ext. merid. strain	int. merid. strain	ext. merid. strain	int. merid. strain	ext. merid. strain	int. merid. strain	ext. merid. strain	int. merid. strain

1 (MPa) = 10.197 (kg/cm^2)

1 (Pd) = 0.78 (MPa)

Tab. 1-4 Standard Output (Plot ID 23 - 30)

Results of Global Axisymmetric Shell Model Analysis

Internal Pressure			Strain							
			Plot ID 23	Plot ID 24	Plot ID 25	Plot ID 26	Plot ID 27	Plot ID 28	Plot ID 29	Plot ID 30
(kg/cm^2)	(MPa)	(Pd)	(-)	(-)	(-)	(-)	(-)	(-)	(-)	(-)
0	0	0	5.65E-08	5.71E-08	0.000	-6.94E-07	1.97E-07	1.97E-07	0.000	2.65E-07
1.5	0.14710209	0.18859242	8.87E-05	8.87E-05	1.93E-05	2.16E-05	8.60E-05	8.61E-05	3.15E-05	3.30E-05
3	0.29420418	0.37718484	1.77E-04	1.77E-04	3.92E-05	4.38E-05	1.72E-04	1.72E-04	6.35E-05	6.58E-05
5.25	0.51485731	0.66007348	3.10E-04	3.10E-04	6.92E-05	7.72E-05	3.01E-04	3.01E-04	1.11E-04	1.15E-04
8.625	0.84583701	1.08440642	5.10E-04	5.10E-04	1.14E-04	1.27E-04	4.95E-04	4.95E-04	1.84E-04	1.88E-04
13.6875	1.34230656	1.72090585	8.08E-04	8.09E-04	1.82E-04	2.02E-04	7.86E-04	7.86E-04	2.92E-04	2.98E-04
21.282	2.08708444	2.67574928	1.26E-03	1.26E-03	2.83E-04	3.14E-04	1.22E-03	1.22E-03	4.55E-04	4.63E-04
32.673	3.20417777	4.10792013	2.24E-03	2.25E-03	3.74E-04	5.37E-04	1.90E-03	1.90E-03	7.02E-04	6.81E-04
35.52	3.48337746	4.46586854	7.24E-03	7.26E-03	1.98E-04	7.69E-04	2.11E-03	2.10E-03	8.01E-04	7.28E-04
35.69805	3.50083848	4.48825446	7.72E-03	7.74E-03	1.86E-04	7.85E-04	2.12E-03	2.12E-03	8.07E-04	7.31E-04
35.8761	3.5182995	4.51064038	8.21E-03	8.24E-03	1.72E-04	8.01E-04	2.13E-03	2.13E-03	8.14E-04	7.35E-04
36.1431	3.54448367	4.54420984	8.99E-03	9.02E-03	1.50E-04	8.25E-04	2.16E-03	2.15E-03	8.16E-04	7.45E-04
36.5436	3.58375993	4.59456401	1.01E-02	1.01E-02	1.09E-04	8.66E-04	2.19E-03	2.19E-03	8.21E-04	7.60E-04
37.14435	3.64267432	4.67009528	1.15E-02	1.16E-02	3.32E-05	9.37E-04	2.26E-03	2.25E-03	8.29E-04	7.82E-04
38.0454	3.73103854	4.78338274	1.35E-02	1.36E-02	-1.15E-04	1.06E-03	2.39E-03	2.38E-03	8.40E-04	8.15E-04
39.3969	3.86357752	4.95330452	1.54E-02	1.54E-02	-4.52E-04	1.25E-03	2.76E-03	2.74E-03	8.54E-04	8.66E-04
40.7486	3.9961165	5.12322629	1.57E-02	1.57E-02	-8.32E-04	1.43E-03	3.41E-03	3.37E-03	8.52E-04	9.34E-04
42.0999	4.12865569	5.29314806	1.59E-02	1.59E-02	-8.92E-04	1.41E-03	3.85E-03	3.81E-03	8.55E-04	1.00E-03
43.4514	4.26119447	5.46306983	1.59E-02	1.60E-02	-8.92E-04	1.31E-03	4.32E-03	4.28E-03	8.64E-04	1.06E-03
44.8029	4.39373345	5.6329916	1.60E-02	1.60E-02	-8.80E-04	1.15E-03	4.93E-03	4.88E-03	8.81E-04	1.12E-03
46.8309	4.59261548	5.88796856	1.60E-02	1.60E-02	-7.95E-04	7.94E-04	6.18E-03	6.13E-03	9.14E-04	1.22E-03
48.8589	4.7914975	6.14294551	1.60E-02	1.60E-02	-7.28E-04	2.01E-04	8.68E-03	8.64E-03	9.76E-04	1.32E-03
50.8869	4.99037952	6.39792247	1.60E-02	1.60E-02	-5.99E-04	-3.94E-04	1.18E-02	1.17E-02	1.06E-03	1.45E-03
51.6471	5.06493086	6.49350111	1.60E-02	1.60E-02	-5.37E-04	-5.64E-04	1.27E-02	1.27E-02	1.10E-03	1.51E-03
52.4073	5.1394822	6.58907974	1.60E-02	1.60E-02	-4.86E-04	-6.74E-04	1.35E-02	1.35E-02	1.16E-03	1.64E-03
53.1675	5.21403354	6.68465838	1.60E-02	1.61E-02	-4.89E-04	-6.38E-04	1.35E-02	1.35E-02	1.29E-03	1.83E-03
53.9277	5.28858488	6.78023702	1.61E-02	1.61E-02	-4.68E-04	-6.31E-04	1.36E-02	1.36E-02	1.39E-03	2.15E-03
54.6879	5.36313622	6.87581566	1.61E-02	1.61E-02	-4.71E-04	-6.04E-04	1.36E-02	1.36E-02	1.50E-03	2.63E-03
55.4481	5.43768756	6.9713943	1.61E-02	1.61E-02	-4.97E-04	-5.55E-04	1.36E-02	1.36E-02	1.66E-03	3.32E-03
56.5884	5.54951456	7.11476226	1.61E-02	1.61E-02	-5.19E-04	-4.98E-04	1.36E-02	1.36E-02	1.98E-03	4.75E-03
58.2984	5.71721094	7.32975762	1.61E-02	1.61E-02	-5.31E-04	-4.26E-04	1.37E-02	1.37E-02	2.69E-03	7.48E-03
60.0084	5.88490733	7.54475298	1.61E-02	1.61E-02	-4.99E-04	-3.97E-04	1.37E-02	1.37E-02	3.45E-03	9.85E-03
61.7184	6.05260371	7.75974834	1.62E-02	1.62E-02	-4.62E-04	-3.58E-04	1.38E-02	1.38E-02	4.20E-03	1.19E-02
64.2849	6.30429538	8.08242998	1.62E-02	1.62E-02	-4.04E-04	-2.98E-04	1.38E-02	1.38E-02	5.47E-03	1.53E-02
64.9263	6.36719623	8.1630721	1.62E-02	1.62E-02	-3.90E-04	-2.84E-04	1.39E-02	1.39E-02	5.62E-03	1.58E-02
65.5677	6.43009709	8.24371421	1.62E-02	1.62E-02	-3.77E-04	-2.71E-04	1.39E-02	1.39E-02	5.75E-03	1.61E-02
66.5298	6.52444837	8.36467739	1.62E-02	1.63E-02	-3.56E-04	-2.48E-04	1.39E-02	1.39E-02	5.91E-03	1.66E-02
67.9731	6.66599	8.54614102	1.63E-02	1.63E-02	-3.10E-04	-2.01E-04	1.39E-02	1.39E-02	6.21E-03	1.69E-02
69.4164	6.80753163	8.72760465	1.63E-02	1.63E-02	-2.69E-04	-1.58E-04	1.40E-02	1.40E-02	6.78E-03	1.70E-02
70.8597	6.94907326	8.90906828	1.63E-02	1.63E-02	-2.27E-04	-1.15E-04	1.40E-02	1.40E-02	6.89E-03	1.70E-02
73.0242	7.16134157	9.18120714	1.64E-02	1.64E-02	-1.59E-04	-4.48E-05	1.41E-02	1.41E-02	6.94E-03	1.70E-02
75.1887	7.37360989	9.45334601	1.64E-02	1.64E-02	-9.03E-05	2.68E-05	1.42E-02	1.42E-02	6.97E-03	1.70E-02
77.3532	7.5858782	9.72548487	1.64E-02	1.64E-02	-2.63E-05	9.30E-05	1.43E-02	1.43E-02	6.98E-03	1.70E-02
79.5177	7.79814651	9.99762374	1.65E-02	1.65E-02	3.30E-05	1.54E-04	1.44E-02	1.44E-02	7.00E-03	1.70E-02
81.6822	8.01041483	10.2697626	1.65E-02	1.65E-02	9.07E-05	2.13E-04	1.44E-02	1.44E-02	7.00E-03	1.70E-02
83.8467	8.22268314	10.5419015	1.65E-02	1.65E-02	1.43E-04	2.66E-04	1.45E-02	1.45E-02	7.01E-03	1.70E-02
87.0942	8.54115916	10.9502041	1.66E-02	1.66E-02	2.16E-04	3.39E-04	1.47E-02	1.47E-02	7.02E-03	1.70E-02
91.9647	9.01879965	11.5625636	1.66E-02	1.66E-02	3.10E-04	4.38E-04	1.48E-02	1.48E-02	7.02E-03	1.70E-02
96.8352	9.49644013	12.1749232	1.67E-02	1.67E-02	4.00E-04	5.30E-04	1.50E-02	1.50E-02	7.03E-03	1.70E-02
101.7057	9.97408061	12.7872828	1.67E-02	1.67E-02	4.65E-04	5.98E-04	1.51E-02	1.51E-02	7.04E-03	1.70E-02
106.5762	10.4517211	13.3996424	1.68E-02	1.68E-02	5.43E-04	6.78E-04	1.53E-02	1.53E-02	7.05E-03	1.70E-02
113.8827	11.1682554	14.3182761	1.68E-02	1.68E-02	6.48E-04	7.85E-04	1.54E-02	1.54E-02	7.10E-03	1.70E-02
124.8417	12.2429832	15.6961323	1.70E-02	1.70E-02	7.54E-04	8.97E-04	1.56E-02	1.56E-02	7.24E-03	1.70E-02
125.52675	12.3101648	15.7822625	1.70E-02	1.70E-02	7.60E-04	9.04E-04	1.56E-02	1.56E-02	7.25E-03	1.70E-02
126.2118	12.3773463	15.8683927	1.70E-02	1.70E-02	7.66E-04	9.10E-04	1.56E-02	1.56E-02	7.26E-03	1.70E-02
127.2393	12.4781112	15.9975785	1.70E-02	1.70E-02	7.72E-04	9.17E-04	1.57E-02	1.57E-02	7.27E-03	1.70E-02
127.33563	12.4875581	16.0096899	1.70E-02	1.70E-02	7.73E-04	9.18E-04	1.57E-02	1.57E-02	7.27E-03	1.70E-02
127.480125	12.5017284	16.027857	1.70E-02	1.70E-02	7.75E-04	9.20E-04	1.57E-02	1.57E-02	7.28E-03	1.70E-02
127.493672	12.5030569	16.0295602	1.70E-02	1.70E-02	7.75E-04	9.20E-04	1.57E-02	1.57E-02	7.28E-03	1.70E-02
127.497059	12.5033891	16.029986	1.70E-02	1.70E-02	7.75E-04	9.20E-04	1.57E-02	1.57E-02	7.28E-03	1.70E-02
127.500446	12.5037212	16.0304118	1.70E-02	1.70E-02	7.75E-04	9.20E-04	1.57E-02	1.57E-02	7.28E-03	1.70E-02
127.501946	12.5038683	16.0306004	1.70E-02	1.70E-02	7.75E-04	9.20E-04	1.57E-02	1.57E-02	7.28E-03	1.70E-02
127.503446	12.5040154	16.030789	1.70E-02	1.70E-02	7.75E-04	9.20E-04	1.57E-02	1.57E-02	7.28E-03	1.70E-02
127.505696	12.5042361	16.0310719	1.70E-02	1.70E-02	7.75E-04	9.20E-04	1.57E-02	1.57E-02	7.28E-03	1.70E-02
Remarks			ext. hoop strain	int. hoop strain	ext. merid. strain	int. merid. strain	ext. hoop strain	int. hoop strain	int. merid. strain	int. hoop strain

1 (MPa) = 10.197 (kg/cm^2)
1 (Pd) = 0.78 (MPa)

Tab. 1-5 Standard Output (Plot ID 31 - 38)

Results of Global Axisymmetric Shell Model Analysis

Internal Pressure			Strain				Displacement			
			Plot ID 31	Plot ID 32	Plot ID 33	Plot ID 34	Plot ID 35	Plot ID 36	Plot ID 37	Plot ID 38
(kg/cm^2)	(MPa)	(Pd)	(-)	(-)	(-)	(-)	(mm)	(mm)	(mm)	(mm)
0	0	0	-5.08E-07	5.71E-08	-6.56E-07	1.94E-07	0.0	-5.047E-05	-9.478E-05	-1.304E-02
1.5	0.14710209	0.18859242	2.07E-05	8.87E-05	2.25E-05	9.04E-05	2.469E-01	1.578E-02	3.629E-02	1.103E-01
3	0.29420418	0.37718484	4.19E-05	1.77E-04	4.55E-05	1.81E-04	4.944E-01	3.158E-02	7.270E-02	2.330E-01
5.25	0.51485731	0.66007348	7.36E-05	3.10E-04	7.99E-05	3.16E-04	8.717E-01	5.520E-02	1.274E-01	4.159E-01
8.625	0.84583701	1.08440642	1.21E-04	5.10E-04	1.31E-04	5.20E-04	1.431E+00	9.047E-02	2.096E-01	6.880E-01
13.6875	1.34230656	1.72090585	1.91E-04	8.09E-04	2.07E-04	8.26E-04	2.258E+00	1.430E-01	3.332E-01	1.091E+00
21.282	2.08708444	2.67574928	2.96E-04	1.26E-03	3.19E-04	1.28E-03	3.473E+00	2.212E-01	5.192E-01	1.686E+00
32.673	3.2041777	4.10792013	4.11E-04	2.25E-03	4.84E-04	1.97E-03	1.126E+01	3.434E-01	2.845E+00	5.150E+00
35.52	3.48337746	4.46586854	3.23E-04	7.26E-03	5.21E-04	2.14E-03	1.487E+01	3.649E-01	4.465E+00	7.181E+00
35.69805	3.50083848	4.48825446	3.30E-04	7.74E-03	5.23E-04	2.15E-03	1.507E+01	3.663E-01	4.567E+00	7.294E+00
35.8761	3.5182995	4.51066038	3.41E-04	8.24E-03	5.26E-04	2.16E-03	1.524E+01	3.677E-01	4.659E+00	7.396E+00
36.1431	3.54448367	4.54420984	3.64E-04	9.02E-03	5.28E-04	2.18E-03	1.527E+01	3.700E-01	4.674E+00	7.392E+00
36.5436	3.58375993	4.59456401	4.17E-04	1.01E-02	5.31E-04	2.20E-03	1.530E+01	3.735E-01	4.697E+00	7.386E+00
37.14435	3.64267432	4.67009528	5.15E-04	1.16E-02	5.37E-04	2.24E-03	1.536E+01	3.787E-01	4.730E+00	7.379E+00
38.0454	3.73103854	4.78338274	6.89E-04	1.36E-02	5.45E-04	2.29E-03	1.545E+01	3.866E-01	4.786E+00	7.361E+00
39.3969	3.86357752	4.95330452	9.20E-04	1.54E-02	5.59E-04	2.37E-03	1.565E+01	3.986E-01	4.838E+00	7.434E+00
40.7484	3.9961165	5.12322629	1.04E-03	1.57E-02	5.73E-04	2.45E-03	1.593E+01	4.109E-01	4.881E+00	7.629E+00
42.0999	4.12865549	5.29314806	1.24E-03	1.59E-02	5.88E-04	2.54E-03	1.620E+01	4.232E-01	4.938E+00	7.788E+00
43.4514	4.26119147	5.46306983	1.57E-03	1.60E-02	6.86E-04	2.63E-03	1.650E+01	4.353E-01	5.012E+00	7.924E+00
44.8029	4.39373345	5.6329916	2.12E-03	1.60E-02	6.37E-04	2.73E-03	1.684E+01	4.475E-01	5.102E+00	8.054E+00
46.8309	4.59261548	5.88796856	2.42E-03	1.60E-02	7.41E-04	3.00E-03	1.743E+01	4.659E-01	5.274E+00	8.294E+00
48.8589	4.7914975	6.14294551	2.47E-03	1.60E-02	4.45E-04	5.02E-03	1.809E+01	4.842E-01	5.505E+00	8.557E+00
50.8869	4.99037952	6.39792247	2.56E-03	1.60E-02	-8.81E-05	8.91E-03	1.885E+01	5.023E-01	5.810E+00	8.859E+00
51.6471	5.06493086	6.49350111	2.61E-03	1.60E-02	-2.64E-04	1.04E-02	1.915E+01	5.089E-01	5.943E+00	8.980E+00
52.4073	5.1394822	6.58907974	2.63E-03	1.60E-02	-4.14E-04	1.17E-02	1.942E+01	5.157E-01	6.172E+00	9.156E+00
53.1675	5.21403354	6.68465838	2.65E-03	1.61E-02	-5.05E-04	1.22E-02	1.969E+01	5.226E-01	6.445E+00	9.372E+00
53.9277	5.28858488	6.78023702	2.67E-03	1.61E-02	-5.56E-04	1.25E-02	1.994E+01	5.303E-01	6.771E+00	9.612E+00
54.6879	5.36313622	6.87581566	2.70E-03	1.61E-02	-5.50E-04	1.27E-02	2.019E+01	5.403E-01	7.154E+00	9.874E+00
55.4481	5.43768756	6.9713943	2.73E-03	1.61E-02	-4.88E-04	1.29E-02	2.046E+01	5.537E-01	7.594E+00	1.014E+01
56.5884	5.54951456	7.11476226	2.77E-03	1.61E-02	-2.77E-04	1.30E-02	2.183E+01	5.871E-01	8.336E+00	1.055E+01
58.2984	5.717211094	7.32975762	2.85E-03	1.61E-02	9.98E-05	1.30E-02	2.458E+01	6.500E-01	9.522E+00	1.111E+01
60.0084	5.88490733	7.54475298	2.92E-03	1.61E-02	8.80E-05	1.31E-02	2.690E+01	7.883E-01	1.050E+01	1.159E+01
61.7184	6.05260371	7.75974834	3.00E-03	1.62E-02	1.40E-04	1.31E-02	2.868E+01	9.733E-01	1.138E+01	1.206E+01
64.2849	6.30429538	8.08242998	3.12E-03	1.62E-02	2.07E-04	1.32E-02	3.123E+01	1.248E+00	1.243E+01	1.250E+01
64.9263	6.36719623	8.1630721	3.14E-03	1.62E-02	2.24E-04	1.32E-02	3.195E+01	1.317E+00	1.250E+01	1.251E+01
65.5677	6.43009709	8.24371421	3.15E-03	1.62E-02	2.40E-04	1.32E-02	3.268E+01	1.387E+00	1.257E+01	1.252E+01
66.5298	6.52444837	8.36467739	3.18E-03	1.63E-02	2.65E-04	1.32E-02	3.374E+01	1.501E+00	1.265E+01	1.255E+01
67.9731	6.66599	8.54614102	3.24E-03	1.63E-02	3.19E-04	1.33E-02	3.531E+01	1.673E+00	1.275E+01	1.259E+01
69.4164	6.80753163	8.72760465	3.29E-03	1.63E-02	3.69E-04	1.33E-02	3.688E+01	1.873E+00	1.282E+01	1.265E+01
70.8597	6.94907326	8.90906828	3.34E-03	1.63E-02	4.20E-04	1.34E-02	3.844E+01	2.120E+00	1.287E+01	1.271E+01
73.0242	7.16136157	9.18120714	3.45E-03	1.64E-02	5.04E-04	1.35E-02	4.077E+01	2.481E+00	1.294E+01	1.279E+01
75.1887	7.37360989	9.45334601	3.54E-03	1.64E-02	5.92E-04	1.36E-02	4.310E+01	2.808E+00	1.301E+01	1.288E+01
77.3532	7.5858782	9.72548487	3.62E-03	1.64E-02	6.74E-04	1.37E-02	4.544E+01	3.120E+00	1.308E+01	1.298E+01
79.5177	7.79814651	9.99762374	3.70E-03	1.65E-02	7.53E-04	1.37E-02	4.776E+01	3.425E+00	1.315E+01	1.308E+01
81.6822	8.01041483	10.2697626	3.77E-03	1.65E-02	8.31E-04	1.38E-02	5.007E+01	3.723E+00	1.321E+01	1.317E+01
83.8467	8.22268314	10.5419015	3.82E-03	1.65E-02	9.03E-04	1.39E-02	5.251E+01	4.013E+00	1.326E+01	1.325E+01
87.0942	8.54115916	10.9502041	3.90E-03	1.66E-02	1.01E-03	1.41E-02	5.641E+01	4.441E+00	1.334E+01	1.339E+01
91.9647	9.01879965	11.5625636	3.97E-03	1.66E-02	1.15E-03	1.42E-02	6.220E+01	5.075E+00	1.347E+01	1.361E+01
96.8352	9.49644013	12.1749232	4.01E-03	1.67E-02	1.29E-03	1.44E-02	6.840E+01	5.728E+00	1.360E+01	1.383E+01
101.7057	9.97408061	12.7872828	4.02E-03	1.67E-02	1.40E-03	1.45E-02	7.606E+01	7.782E+00	1.375E+01	1.408E+01
106.5762	10.4517211	13.3996424	4.03E-03	1.68E-02	1.54E-03	1.47E-02	8.522E+01	1.101E+01	1.395E+01	1.437E+01
113.8827	11.1682554	14.3182761	4.05E-03	1.68E-02	1.72E-03	1.49E-02	1.009E+02	1.576E+01	1.433E+01	1.497E+01
124.8417	12.2429832	15.6961323	4.08E-03	1.70E-02	1.94E-03	1.51E-02	1.414E+02	2.376E+01	1.540E+01	1.654E+01
125.52675	12.3101648	15.7822625	4.08E-03	1.70E-02	1.96E-03	1.51E-02	1.459E+02	2.448E+01	1.549E+01	1.667E+01
126.2118	12.3773463	15.8683927	4.08E-03	1.70E-02	1.97E-03	1.51E-02	1.517E+02	2.530E+01	1.560E+01	1.682E+01
127.2393	12.4781112	15.9975785	4.09E-03	1.70E-02	1.99E-03	1.51E-02	1.645E+02	2.691E+01	1.579E+01	1.707E+01
127.33563	12.4875581	16.0096899	4.09E-03	1.70E-02	1.99E-03	1.51E-02	1.668E+02	2.714E+01	1.581E+01	1.710E+01
127.480125	12.5017284	16.027857	4.09E-03	1.70E-02	1.99E-03	1.51E-02	1.737E+02	2.768E+01	1.586E+01	1.716E+01
127.493672	12.5030569	16.0295602	4.09E-03	1.70E-02	1.99E-03	1.51E-02	1.754E+02	2.779E+01	1.586E+01	1.717E+01
127.497059	12.5033891	16.029986	4.09E-03	1.70E-02	1.99E-03	1.51E-02	1.759E+02	2.782E+01	1.587E+01	1.717E+01
127.500446	12.5037212	16.0304118	4.09E-03	1.70E-02	1.99E-03	1.51E-02	1.765E+02	2.786E+01	1.587E+01	1.718E+01
127.501946	12.5038683	16.0306004	4.09E-03	1.70E-02	1.99E-03	1.51E-02	1.768E+02	2.788E+01	1.587E+01	1.718E+01
127.503446	12.5040154	16.030789	4.09E-03	1.70E-02	1.99E-03	1.51E-02	1.774E+02	2.792E+01	1.587E+01	1.718E+01
127.505696	12.5042361	16.0310719	4.09E-03	1.70E-02	1.99E-03	1.51E-02	1.774E+02	2.792E+01	1.587E+01	1.718E+01
Remarks			same as Plot ID-22	same as Plot ID-24	int. merid. strain	int. hoop strain	vertical disp.	horizontal disp.	horizontal disp.	vertical disp.

1 (MPa) = 10.197 (kg/cm^2)

1 (Pd) = 0.78 (MPa)

Tab. 1-6 Standard Output (Plot ID 39)

Results of Global 3-D Shell Model Analysis

Internal Pressure			Displacement
			Plot ID 39
(kg/cm^2)	(MPa)	(Pd)	(mm)
0	0	0	-3.00E-03
1.5	0.14710209	0.18859242	9.23E-02
3	0.29420418	0.37718484	1.86E-01
5.25	0.51485731	0.66007348	3.27E-01
8.625	0.84583701	1.08440642	5.42E-01
13.6875	1.34230656	1.72090585	8.69E-01
21.282	2.08708444	2.67574928	1.37E+00
32.673	3.2041777	4.10792813	2.31E+00
35.52	3.48337746	4.46586854	3.10E+00
36.2319	3.55319212	4.55537451	3.37E+00
36.4989	3.57937629	4.58894396	3.48E+00
36.8994	3.61865254	4.63929813	3.66E+00
37.04955	3.63337746	4.65817624	3.72E+00
37.27485	3.6554722	4.68650282	3.84E+00
37.6128	3.6886143	4.72899269	4.04E+00
38.11965	3.73832009	4.79271807	4.36E+00
38.87985	3.81287143	4.88829671	4.99E+00
40.02015	3.92469844	5.03166467	6.38E+00
41.73015	4.09239482	5.24666093	8.82E+00
44.29665	4.3440865	5.56934166	1.19E+01
44.457	4.35981171	5.58950219	1.21E+01
44.61735	4.37553692	5.60966272	1.22E+01
44.85795	4.3991321	5.63991295	1.23E+01
45.2187	4.43451015	5.68526942	1.25E+01
45.7599	4.48758458	5.75331357	1.29E+01
46.5717	4.56719623	5.85537979	1.34E+01
47.7894	4.68661371	6.00847912	1.42E+01
49.6164	4.86578405	6.23818468	1.5EE+01
50.30145	4.93296558	6.32431484	1.63E+01
50.55825	4.95814946	6.35660187	1.65E+01
50.9436	4.99593993	6.40505126	1.68E+01
51.088095	5.01011033	6.42321837	1.69E+01
51.142275	5.01542365	6.43003033	1.69E+01
51.223545	5.02339365	6.44024826	1.70E+01
51.34545	5.03534863	6.45557517	1.71E+01
51.5283	5.05328038	6.47856459	1.72E+01
51.80265	5.08018535	6.51305814	1.73E+01
52.2141	5.12053545	6.56478904	1.75E+01
52.83135	5.18106796	6.64239482	1.77E+01
53.75715	5.27185937	6.75879406	1.80E+01
55.14585	5.40804648	6.93339293	1.82E+01
56.53455	5.5442336	7.10799179	1.83E+01
57.92325	5.68042071	7.28259066	1.84E+01
60.00675	5.88474551	7.54454553	1.85E+01
63.13125	6.19115916	7.93738354	1.88E+01
67.81725	6.65070609	8.52654627	1.91E+01
72.50325	7.11025302	9.11570899	1.95E+01
77.18925	7.56979994	9.70487172	1.99E+01
81.87525	8.02934687	10.2940344	2.03E+01
86.56125	8.48889379	10.8831972	2.07E+01
93.59175	9.17836128	11.7671298	2.13E+01
96.22875	9.43696675	12.0986753	2.15E+01
100.18275	9.82472786	12.595805	2.18E+01
106.11375	10.4063695	13.3414994	2.24E+01
115.01175	11.2789791	14.4602296	2.33E+01
123.90975	12.1515887	15.5789599	2.43E+01
126.13425	12.3697411	15.8586424	2.46E+01
126.34275	12.3901883	15.8848568	2.46E+01
126.420945	12.3978567	15.8946881	2.47E+01
126.538245	12.4093601	15.909436	2.47E+01
126.539745	12.4095072	15.9096246	2.47E+01
126.541995	12.4097279	15.9099075	2.47E+01
Remarks			horizontal disp.

1 (MPa) = 10.197 (kg/cm^2)
1 (Pd) = 0.78 (MPa)

Tab. 1-7 Standard Output (Plot ID 40 - 43)

Results of Local 3-D Shell E/H Submodel Analysis

Internal Pressure			Strain			
			Plot ID 40	Plot ID 41	Plot ID 42	Plot ID 43
(kg/cm^2)	(MPa)	(Pd)	(-)	(-)	(-)	(-)
1.5	0.147102089	0.188592422	1.99E-05	1.03E-04	2.01E-05	8.45E-05
3	0.294204178	0.377184843	3.98E-05	2.05E-04	4.02E-05	1.68E-04
5.25	0.514857311	0.660073476	6.97E-05	3.57E-04	7.04E-05	2.92E-04
8.625	0.845837011	1.084406424	1.15E-04	5.83E-04	1.16E-04	4.74E-04
13.6875	1.342306561	1.720905847	1.82E-04	9.19E-04	1.85E-04	7.43E-04
21.282	2.087084437	2.675749278	2.85E-04	1.42E-03	2.90E-04	1.14E-03
32.673	3.204177699	4.107920127	3.84E-04	2.62E-03	5.23E-04	1.76E-03
35.52	3.483377464	4.465868544	3.29E-04	3.97E-03	7.32E-04	1.97E-03
38.367	3.762577229	4.82381696	-7.89E-05	1.08E-02	5.90E-04	2.31E-03
41.214	4.041776993	5.181765376	-1.14E-03	2.37E-02	1.58E-04	6.60E-03
41.39205	4.059238011	5.204151296	-1.20E-03	2.43E-02	1.43E-04	9.15E-03
41.5701	4.076699029	5.226537217	-1.28E-03	2.49E-02	1.31E-04	9.72E-03
41.74815	4.094160047	5.248923137	-1.35E-03	2.54E-02	1.17E-04	1.03E-02
42.01515	4.120344219	5.282492588	-1.45E-03	2.62E-02	8.89E-05	1.08E-02
42.41565	4.159620477	5.332846765	-1.58E-03	2.74E-02	4.61E-05	1.16E-02
43.0164	4.218534863	5.40837803	-1.75E-03	2.91E-02	-1.45E-05	1.27E-02
43.2417	4.240629597	5.436704611	-1.81E-03	2.97E-02	-3.44E-05	1.32E-02
43.57965	4.273771698	5.479194484	-1.91E-03	3.05E-02	-6.06E-05	1.38E-02
43.706355	4.286197411	5.495124886	-1.94E-03	3.08E-02	-6.94E-05	1.41E-02
43.896405	4.304835246	5.519019546	-2.00E-03	3.12E-02	-8.22E-05	1.45E-02
44.181555	4.332799353	5.554870965	-2.09E-03	3.20E-02	-1.11E-04	1.52E-02
44.466705	4.36076346	5.590722384	-2.17E-03	3.25E-02	-1.37E-04	1.58E-02
44.53797	4.36775228	5.59968241	-2.19E-03	3.26E-02	-1.44E-04	1.59E-02
44.5647	4.3703736339	5.603043127	-2.20E-03	3.27E-02	-1.47E-04	1.59E-02
44.604795	4.374305678	5.608084203	-2.21E-03	3.28E-02	-1.51E-04	1.60E-02
44.66493	4.380203001	5.615644873	-2.23E-03	3.28E-02	-1.58E-04	1.61E-02
44.75514	4.389049721	5.626986821	-2.25E-03	3.29E-02	-1.67E-04	1.61E-02
44.89044	4.402318329	5.643997858	-2.27E-03	3.31E-02	-1.80E-04	1.62E-02
45.09339	4.422221242	5.669514412	-2.31E-03	3.33E-02	-2.01E-04	1.64E-02
45.39789	4.452082966	5.707798674	-2.37E-03	3.37E-02	-2.32E-04	1.66E-02
45.85449	4.496860841	5.765206207	-2.46E-03	3.42E-02	-2.82E-04	1.69E-02
46.53954	4.564042365	5.851336366	-2.60E-03	3.50E-02	-3.56E-04	1.74E-02
47.56704	4.664807296	5.980522175	-2.86E-03	3.65E-02	-4.78E-04	1.87E-02
47.95239	4.702597823	6.028971568	-2.97E-03	3.75E-02	-5.22E-04	1.95E-02
48.53034	4.759276258	6.101636228	-3.20E-03	3.93E-02	-6.05E-04	2.13E-02
49.39734	4.844301265	6.210642648	-3.55E-03	4.22E-02	-7.48E-04	2.41E-02
50.69769	4.971824066	6.374133418	-4.10E-03	4.65E-02	-9.78E-04	2.74E-02
51.02274	5.003701089	6.415001396	-4.22E-03	4.76E-02	-1.03E-03	2.82E-02
51.34779	5.0355781111	6.455869373	-4.34E-03	4.87E-02	-1.07E-03	2.91E-02
51.83544	5.083401	6.51718077	-4.34E-03	4.93E-02	-1.00E-03	3.06E-02
52.56684	5.155127979	6.609138434	-4.34E-03	5.03E-02	-8.92E-04	3.25E-02
53.66409	5.262733157	6.747093791	-4.40E-03	5.13E-02	-8.24E-04	3.52E-02
54.76134	5.370338335	6.885049147	-4.40E-03	5.14E-02	-8.15E-04	3.61E-02
55.85859	5.477943513	7.023004504	-4.39E-03	5.14E-02	-7.99E-04	3.65E-02
56.95584	5.585548691	7.16095986	-4.37E-03	5.13E-02	-7.72E-04	3.67E-02
58.05309	5.693153869	7.298915216	-4.36E-03	5.13E-02	-7.52E-04	3.71E-02
59.15034	5.800759047	7.436870573	-4.35E-03	5.13E-02	-7.34E-04	3.75E-02
60.24759	5.908364225	7.574825929	-4.35E-03	5.13E-02	-7.18E-04	3.79E-02
61.89309	6.069735216	7.781711816	-4.34E-03	5.13E-02	-6.89E-04	3.85E-02
64.36209	6.311865254	8.092134942	-4.35E-03	5.13E-02	-6.55E-04	3.93E-02
66.83109	6.553995293	8.402558068	-4.35E-03	5.19E-02	-6.07E-04	3.99E-02
69.30009	6.796125331	8.712981194	-4.31E-03	5.25E-02	-5.26E-04	4.05E-02
73.00359	7.159320388	9.178615882	-4.24E-03	5.35E-02	-3.86E-04	4.14E-02
78.55809	7.704039423	9.87697362	-4.18E-03	5.52E-02	-2.00E-04	4.30E-02
84.11259	8.248758458	10.57533136	-4.08E-03	5.68E-02	-4.17E-06	4.42E-02
89.66709	8.793477493	11.27368909	-4.00E-03	5.83E-02	1.80E-04	4.54E-02
97.99959	9.610629597	12.32132	-3.91E-03	6.06E-02	4.13E-04	4.72E-02
101.12409	9.917043248	12.71415801	-3.89E-03	6.15E-02	4.92E-04	4.80E-02
105.81009	10.37659017	13.30332074	-3.87E-03	6.30E-02	6.18E-04	4.92E-02
112.84059	11.06605766	14.18725342	-3.85E-03	6.51E-02	8.03E-04	5.16E-02
123.38559	12.10018535	15.51305814	-3.83E-03	6.79E-02	1.01E-03	5.49E-02
139.21059	13.65211239	17.50270819	-3.82E-03	6.96E-02	1.08E-03	5.65E-02
Remarks			int. merid. strain	int. hoop strain	int. merid. strain	int. hoop strain

1 (MPa) = 10.197 (kg/cm^2)

1 (Pd) = 0.78 (MPa)

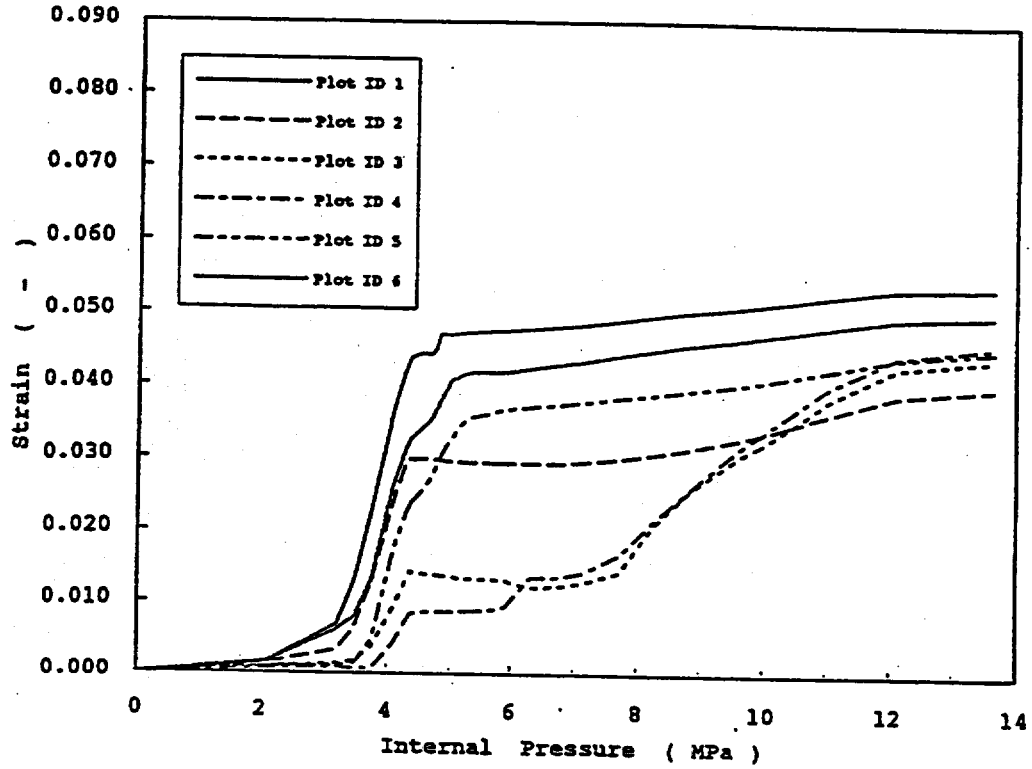

Fig. 1-1 Strain History (Plot ID 1/2/3/4/5/6)

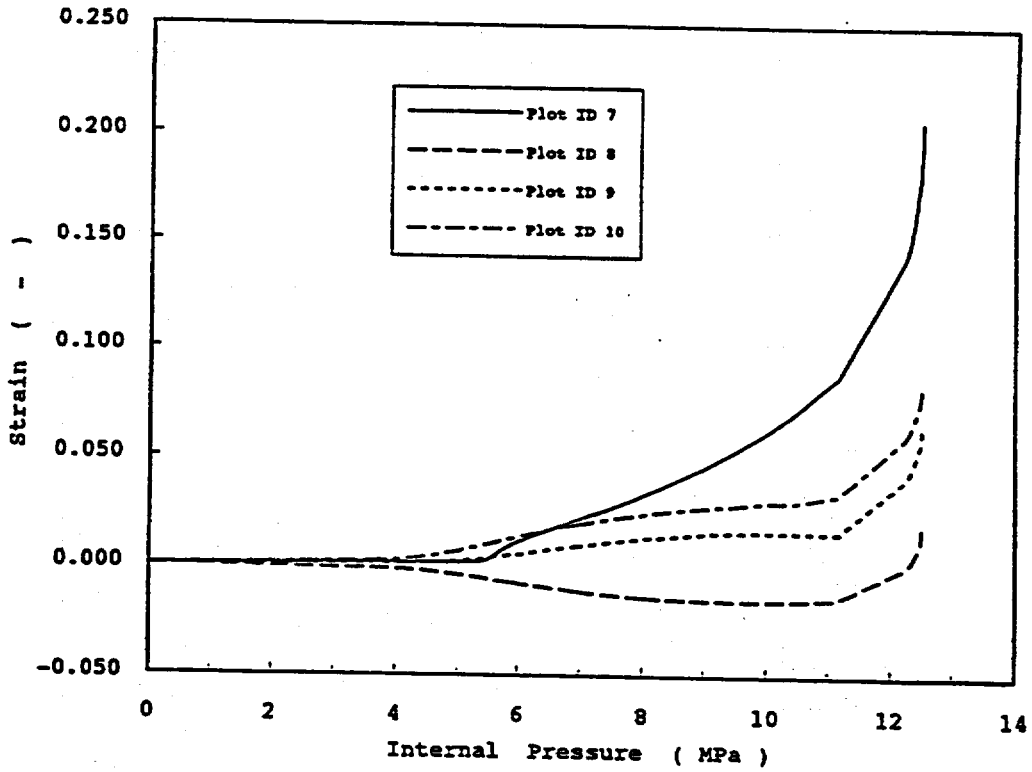

Fig. 1-2 Strain History (Plot ID 7/8/9/10)

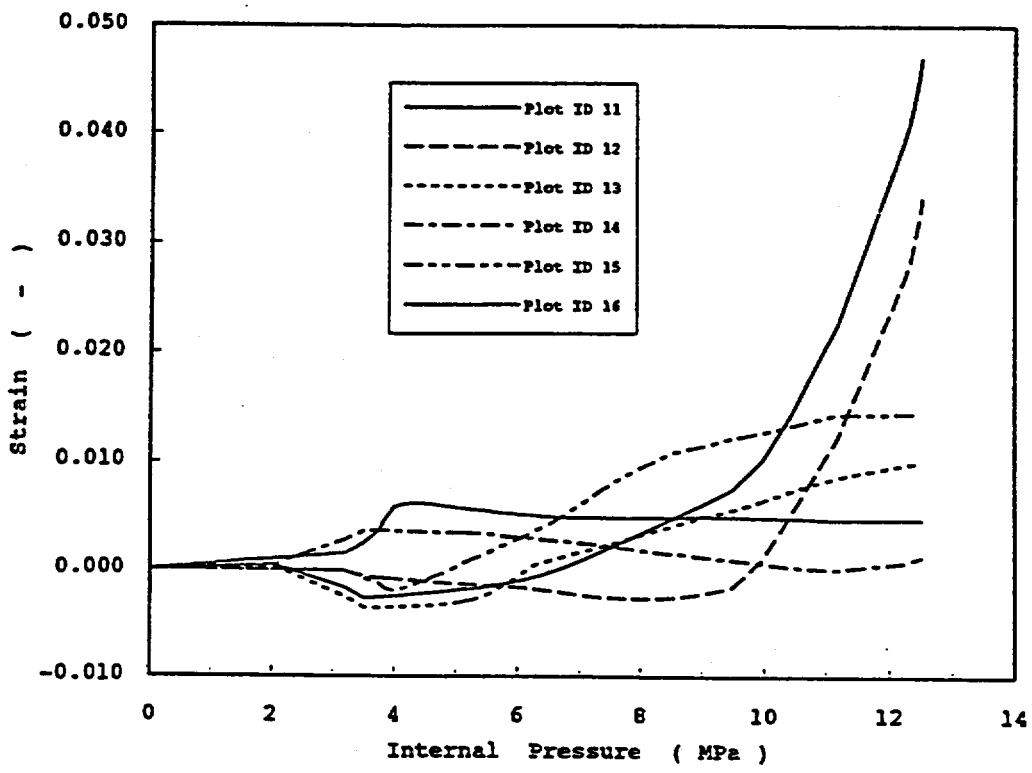

Fig. 1-3 Strain History (Plot ID 11/12/13/14/15/16)

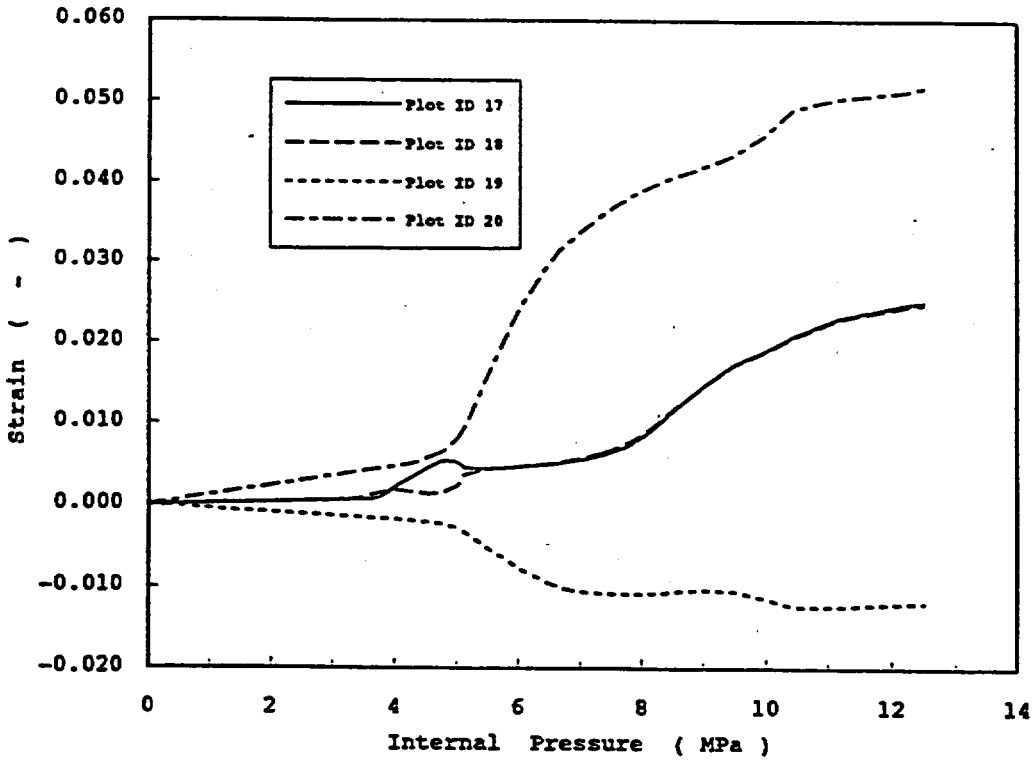

Fig. 1-4 Strain History (Plot ID 17/18/19/20)

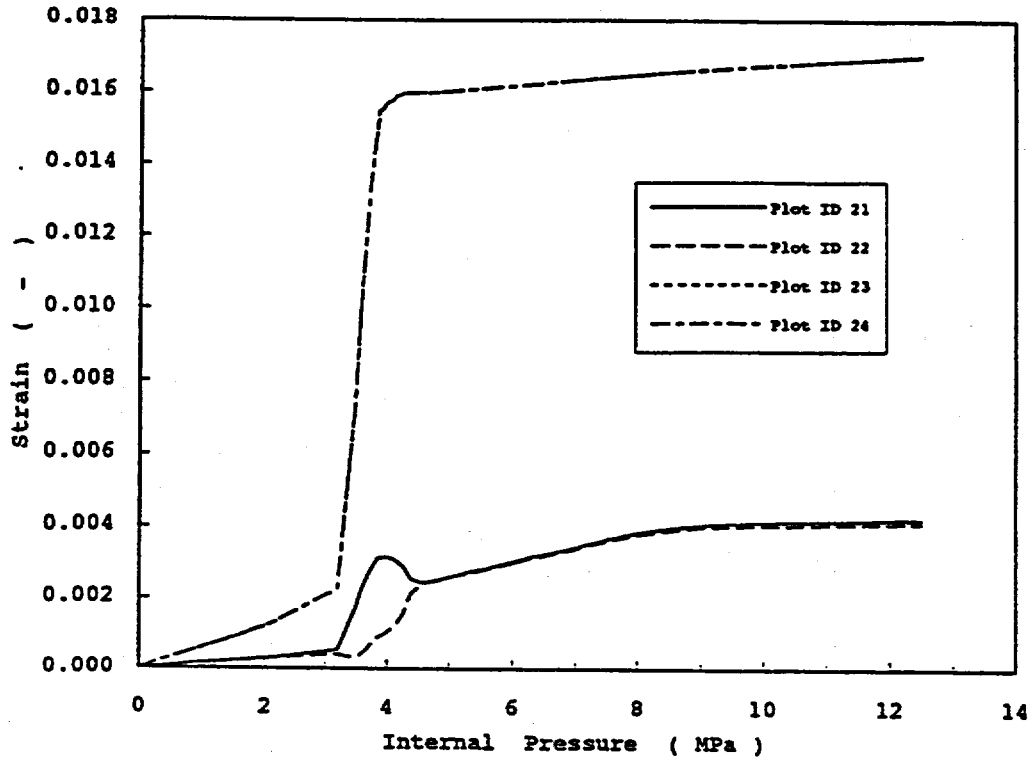

Fig. 1-5 Strain History (Plot ID 21/22/23/24)

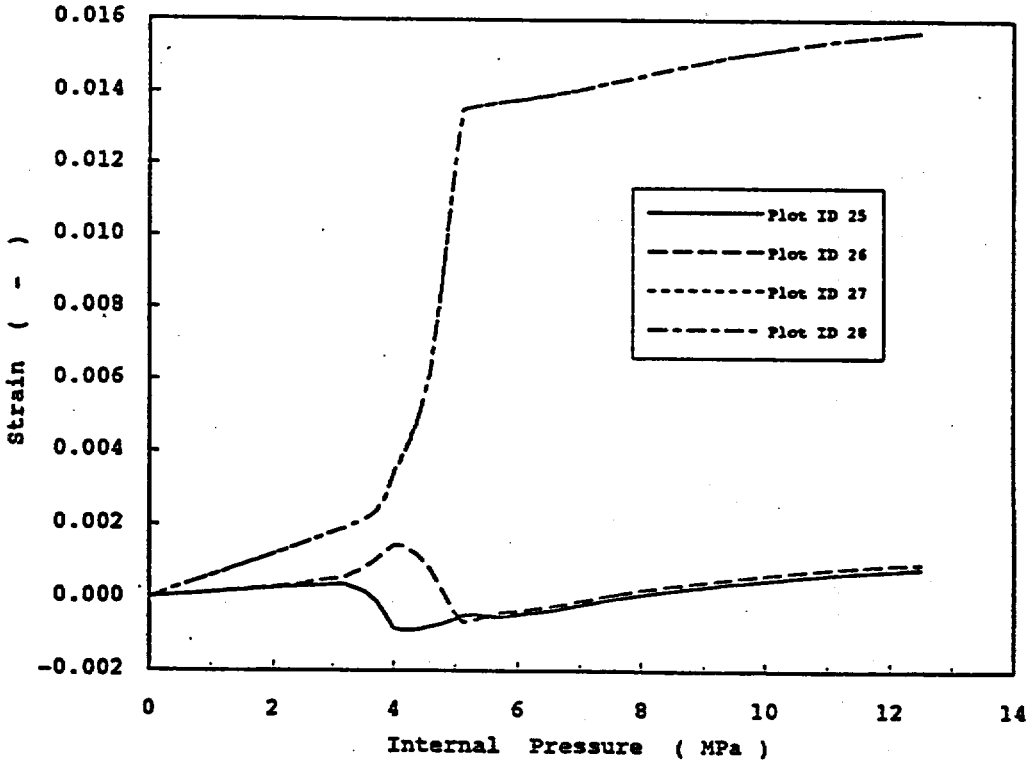

Fig. 1-6 Strain History (Plot ID 25/26/27/28)

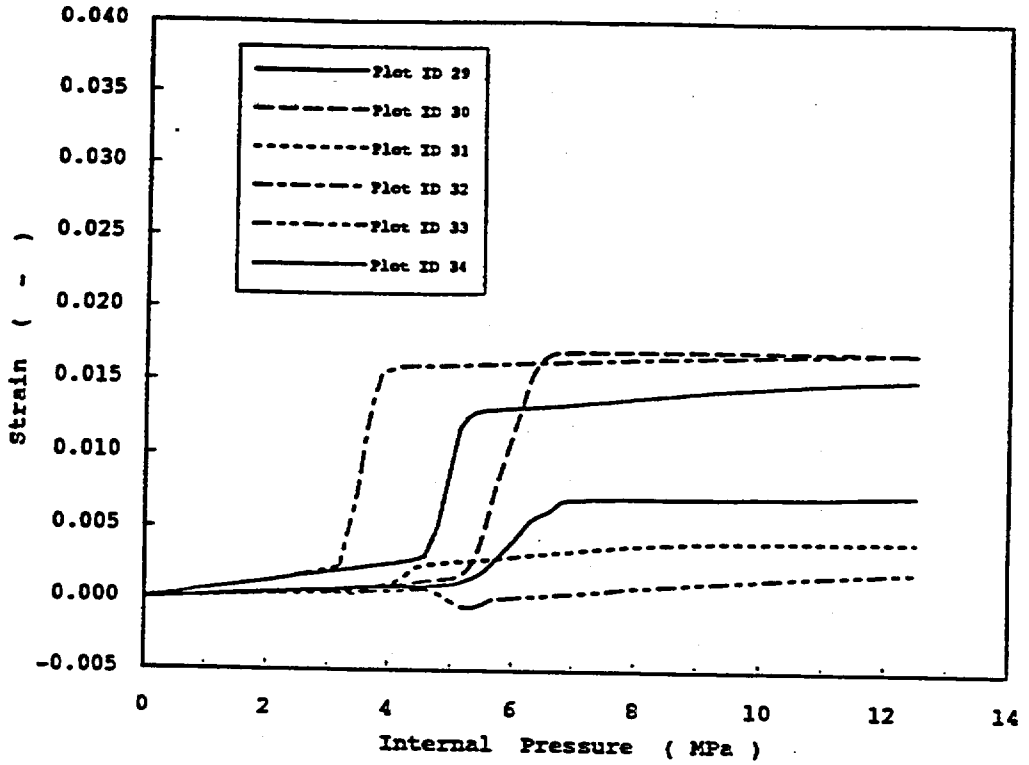

Fig. 1-7 Strain History (Plot ID 29/30/31/32/33/34)

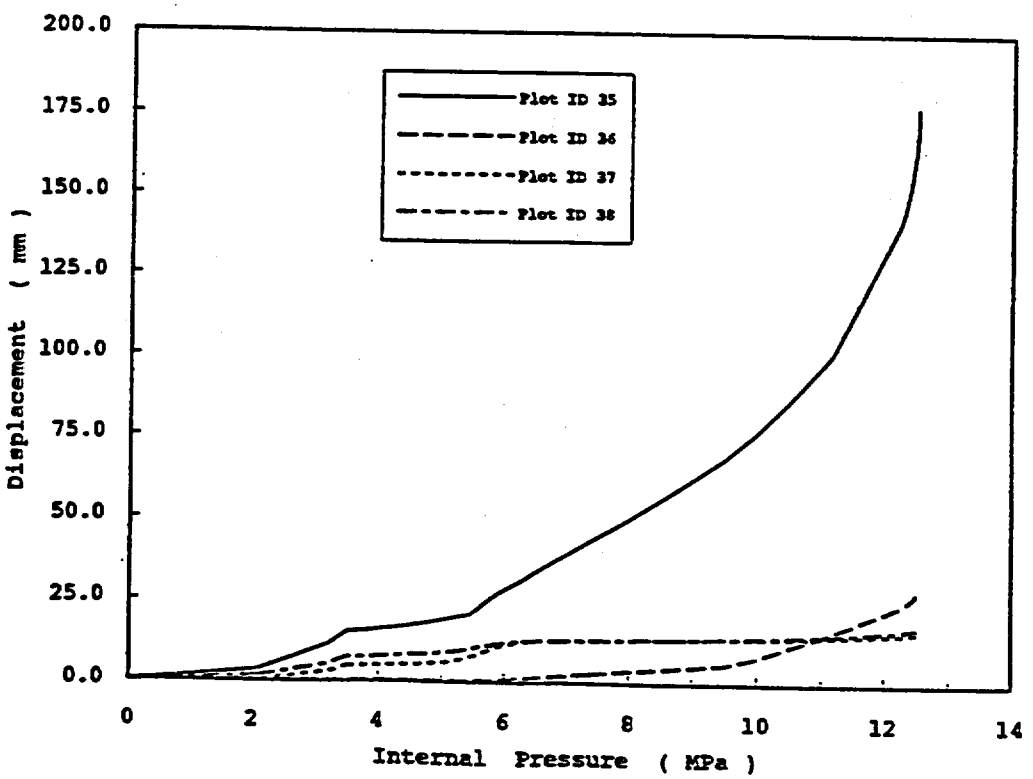

Fig. 1-8 Displacement History (Plot ID 35/36/37/38)

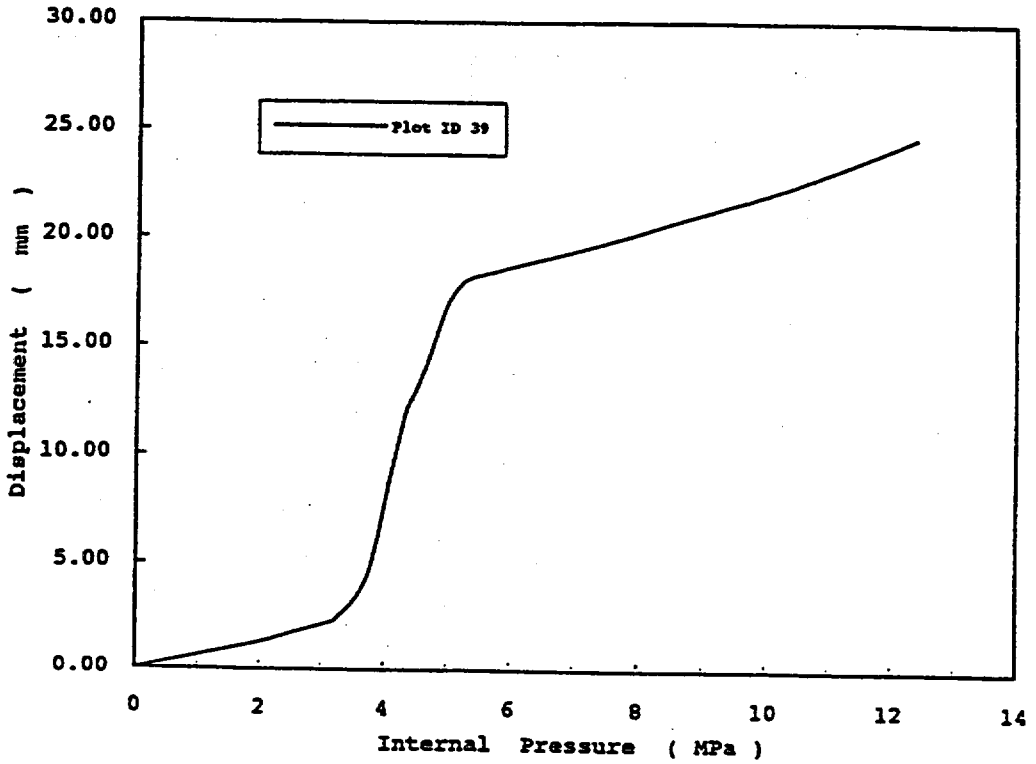

Fig. 1-9 Displacement History (Plot ID 39)

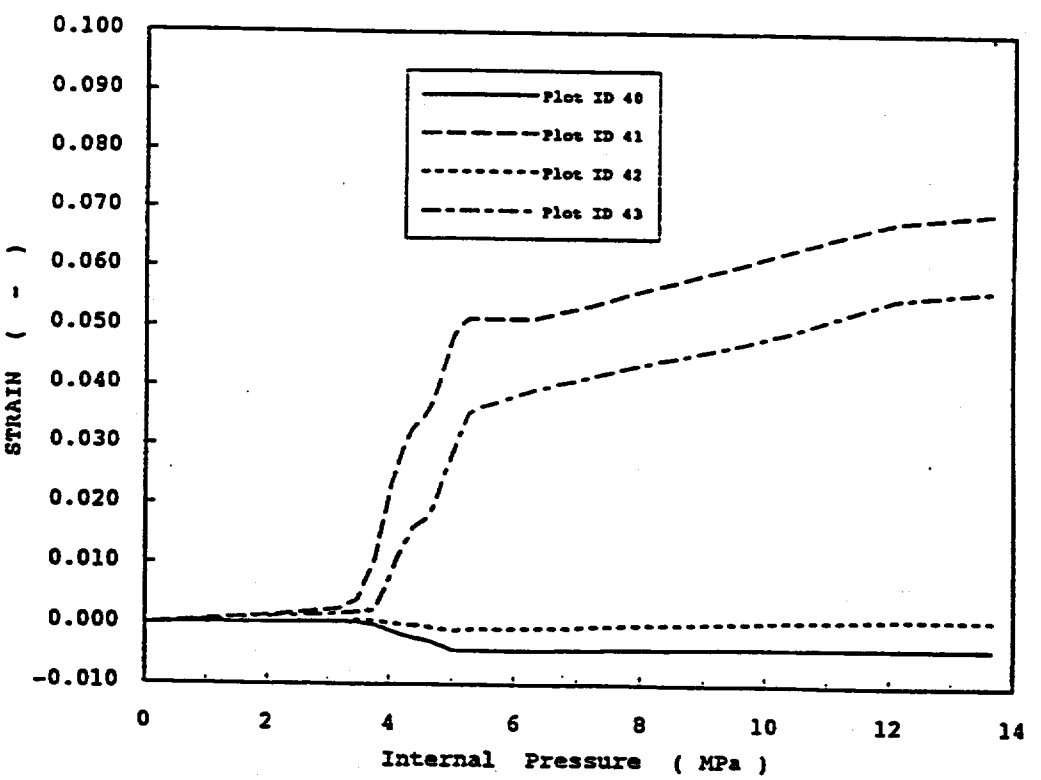

Fig. 1-10 Strain History (Plot ID 40/41/42/43)

Appendix E-7

Sandia National Laboratories

U.S.

Sandia National Laboratories

SCV Round Robin Submittal

1. INTRODUCTION

The authors of this section are Paul Carter and Samuel Key. This work was supported by the U.S. Nuclear Regulatory Commission and performed at Sandia National Laboratories, which is operated by the U.S. Department of Energy under contract number DE-AC04-94-AL85000.

This section summarizes the pretest structural analyses of a scale model of a Steel Containment Vessel (SCV) to be tested at Sandia National Laboratories. A complete description of the test is provided elsewhere. This section includes a summary of material modeling details, finite element model descriptions, results, and a failure prediction.

The structural analysis effort consisted of four basic finite element models with some analyses repeated with slight modifications. The ABAQUS general purpose finite element code was used for all structural analyses [1]. The first finite element model was a global axisymmetric shell element model. This model was run with two different gap dimensions (the nominal distance between the SCV and contact structure): 18 mm (the as-designed gap), designated the GAX18 model, and 34 mm (a worst case scenario gap), model GAX34. All remaining analyses used the as-designed 18 mm gap dimension. The second model was a 3-dimensional global shell element model, designated G3DS, whose only non-axisymmetric detail was the addition of the equipment hatch. Results from this model called for further study in two areas: 1) the area near the junction of the material change interface and the equipment hatch insert plate; 2) the top head including the knuckle. The third model was a locally refined shell element submodel of a cut-out of the material change interface/equipment hatch insert plate junction from the 3-dimensional shell element model. This model, referred to as the LEHS model, was also rerun later with some as-built shell thicknesses incorporated into the model, the LEHSTh model. The last model was a local axisymmetric continuum element model of the top head area, model LTHAXC, including the contact structure from the apex extending down to the upper 19 mm stiffener.

2. MATERIAL MODELS

2.1 Introduction

Each of the analyses used material models based on tensile test data provided by Hitachi [2]. The true stress-true strain data were used to fit a theoretical hardening curve such as a power law or inverse hyperbolic sine law. In addition to capturing the measured behavior up to maximum load, prediction of the behavior of the SCV up to failure requires reasonable extrapolations of the true stress-true strain data beyond maximum load. The tensile test were recreated using a finite element model to verify the behavior after maximum load. This section describes the procedure used to fit the material models to the tensile test data and to obtain reasonable extrapolations beyond maximum load.

2.2 Background

In a tensile test, the engineering strain, e, is written in Equation 2.1:

$$e = \frac{l - l_o}{l_o} \qquad \text{(EQ 2.1)}$$

where l_0 represents the initial gage length of the test specimen and l represents the current gage length of the test specimen. The engineering stress, s, is calculated from Equation 2.2:

$$s = \frac{F}{A_o} \qquad \text{(EQ 2.2)}$$

where F is the axial load on the tensile test specimen and A_0 is the original cross-sectional area. The true strain, ε, is defined as

$$\varepsilon = \ln\frac{l}{l_o} \qquad \text{(EQ 2.3)}$$

which is only valid for a homogeneous deformation, and the true stress, σ, is defined as

$$\sigma = \frac{F}{A} \qquad \text{(EQ 2.4)}$$

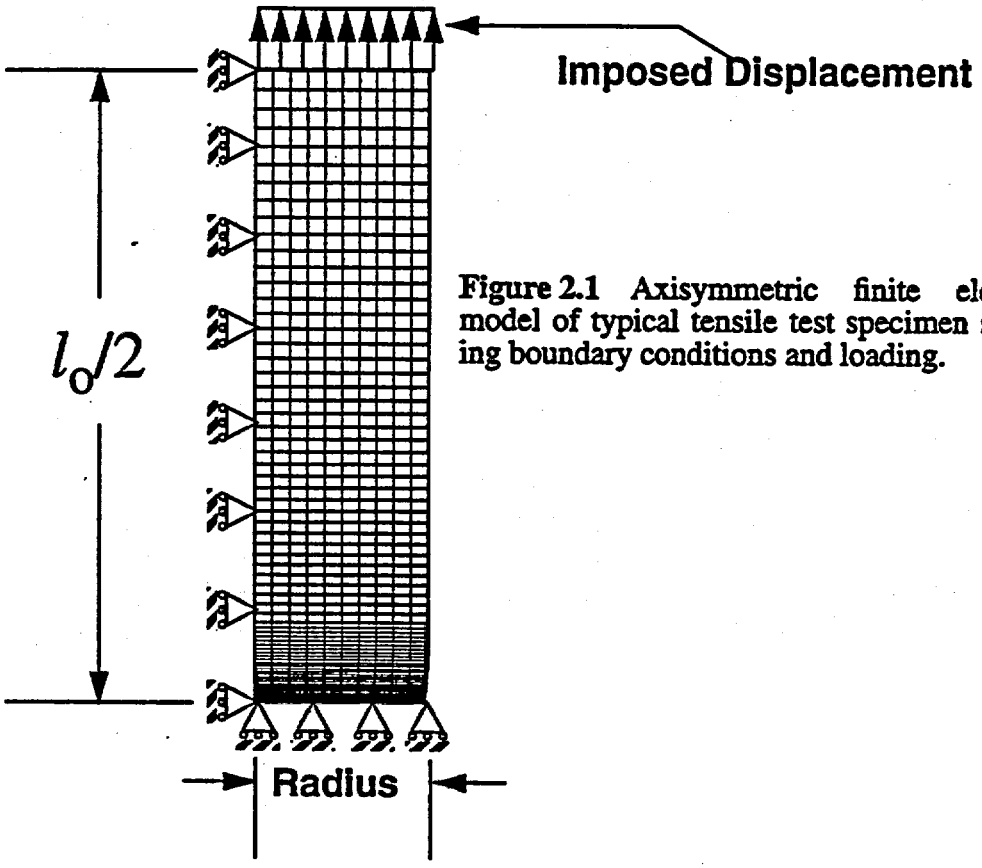

Figure 2.1 Axisymmetric finite element model of typical tensile test specimen showing boundary conditions and loading.

where A is the instantaneous cross-sectional area. By rearranging Equation 2.1 and combining with Equation 2.3, the true strain may be written in terms of the engineering strain:

$$\varepsilon = \ln(1+e)\,. \qquad \text{(EQ 2.5)}$$

By using the constant volume relationship, $A_o L_o = AL$, and combining Equation 2.2 and Equation 2.4, the true stress may be written in terms of the engineering stress:

$$\sigma = s(1+e)\,. \qquad \text{(EQ 2.6)}$$

Equation 2.5 and Equation 2.6 assume that the volume is constant, the stress is uniform through the cross-section, and the deformation is homogeneous throughout the gage length. However, at the point of maximum load, defined as the load corresponding to the highest stress on the engineering stress-strain curve, the deformation localizes and necking occurs. Thus, the assumption of homogeneous deformation throughout the gage length is violated and the stress distribution is no longer uniform through the cross-section. So, Equation 2.5 and Equation 2.6 are not valid beyond maximum load. Although the engineering stress decreases after necking because less load is carried, the true stress continues to increase [3].

In geometries which are more complex than that of a tensile test specimen, local stresses may reach values higher than the true stress in a tensile test specimen at maximum load. Also, true stress-true strain data will be required beyond maximum load to assess localized material failure. Therefore, it is necessary to extrapolate the true stress-true strain data supplied by Hitachi beyond maximum load.

2.3 Procedure

The following procedure was used to obtain the necessary data. First, two different hardening plasticity models were fit to the experimental true stress-true strain data, which is only available up to maximum load, using a MATLAB [4] curve fitting routine. These two models were chosen for their ability to accurately capture the hardening behavior of most steels. The first model is the power law hardening model shown in Equation 2.7 [5]:

$$\sigma_e - \sigma_{ys} = A\langle \bar{\varepsilon}^p - \varepsilon^L \rangle^n, \qquad \text{(EQ 2.7)}$$

where A and n are the constants calculated from the curve fit, σ_e is the effective stress, σ_{ys} is the yield stress, $\bar{\varepsilon}_p$ is the equivalent plastic strain, and ε_L is the Luder's strain or yield plateau. The use of the brackets, $\langle\rangle$, denotes the Heaviside function where the expression enclosed in the brackets takes the value of the enclosed expression when positive and is zero when the enclosed expression is negative. The second model uses the inverse hyperbolic sine function and is shown in Equation 2.8:

$$\sigma_e - \sigma_{ys} = A\sinh^{-1}(B\langle \bar{\varepsilon}^p - \varepsilon^L \rangle) \qquad \text{(EQ 2.8)}$$

where A and B are the constants calculated from the curve fit.

After determining which of the two hardening models provided the best fit to the data from each set of tensile tests, the next step was to simulate each set of tensile tests computationally using the appropriate constitutive relation in the SANTOS finite element program [6]. Figure 2.1 shows the axisymmetric finite element model used. Only half of the length of the round bar was modeled since it is symmetric about the plane normal to the axis of the specimen. To ensure that the localized deformation occurs at the center of the gage length, the diameter was reduced by 0.5-1.0% at the plane of symmetry to provide an initial geometric imperfection. The specimen is restrained in the y-direction at the plane of symmetry, and displacements were imposed in the y-direction at the free end.

As shown above in Equation 2.1, the engineering strain is obtained by dividing the change in the gage length or displacement by the original gage length. The load on the specimen can be converted to engineering stress by dividing by the original cross-sectional area as in Equation 2.2. The load-displacement data from the finite element analysis was converted to engineering stress-

Table 2.1: Summary of Material Parameters - SGV480

Batch Designation	Location	Material	Thickness (mm)	σ_{ys}, Yield Strength (MPa)	A, Hardening Constant, (MPa)	B, Strain Constant	ε_L, Luder's Strain
RT12/ RT34	Top Head, Top Head Shell	SGV480	6.0	404.9	153.7	15.36	0.01
RT56	Upper Conical Shell	SGV480	7.5	404.2	147.5	15.36	0.01
RT78	Upper Spherical Shell	SGV480	8.0	386.5	148.0	16.70	0.01
RT910	Middle Conical Shell	SGV480	8.5	399.8	145.0	17.03	0.01
RT1112	Stiffening Ring	SGV480	9.5	409.6	139.2	17.71	0.01
RT1314	Stiffening Ring	SGV480	12.5	383.6	142.1	18.25	0.01
RT1516	Stiffening Rings (2)	SGV480	19.0	378.7	126.0	23.83	0.01
RT1718	Top Flange, Hatch Covers(2), Hatch Sleeve	SGV480	20.0	379.8	122.0	25.43	0.02
RT1920	Knuckle	SGV480	28.0	371.6	110.9	33.20	0.01

strain data and compared to the engineering stress-strain data supplied by Hitachi in an attempt to verify the post-peak behavior. If the data from the finite element analysis did not correlate well with the Hitachi data, a new curve fit was tried and a new finite element analysis performed. This iterative process was repeated until reasonable post-peak behavior was obtained.

Hitachi performed a set of four tensile tests for each of the 11 different material/thickness combinations (two in the rolling direction and two in the transverse direction) for a total of 48 tests (one batch of tests was repeated). Table 2.1 summarizes the results of the curve fitting for the 9 different SGV480 thicknesses; Table 2.2 summarizes the results of the curve fitting for the SPV490 thicknesses. For the SGV480 materials, the inverse hyperbolic sine law model worked best, while the power law worked best for the SPV490 materials. Figure 2.2 shows a typical true stress-true strain tensile test data set with a typical corresponding curve fit. Figure 2.3 shows the engineering stress-engineering strain data with the output of the finite element analysis of the tensile test. These material models do not address material failure.

2.4 Implementation into ABAQUS

The ABAQUS input deck requires two options to specify an elastic-plastic material model: `*ELASTIC`, where the user specifies the elastic modulus and Poisson's ratio; and `*PLASTIC`, which specifies a metal plasticity model with a von Mises or Hill yield surface. For this option, the user must specify the yield stress as a function of plastic strain, using true stress and log plastic strain values. The above data was converted by a simple FORTRAN program to a format compatible with ABAQUS.

Table 2.2: Summary of Material Parameters - SGV 490

Batch Designation	Location	Material	Thickness (mm)	σ_{ys}, Yield Strength (MPa)	A, Hardening Constant, (MPa)	n, Strain Exponent	ε_L, Luder's Strain
RT2122	Cylindrical Wet Well, Lower Conical Shell	SPV490	9.0	660.0	390.0	0.45	0.015
RT2324	Bottom Flange, Bottom Head, Stiffening Ring, Ring Support Girder, Gusset Plates	SPV490	17.5	598.9	450.0	0.48	0.01

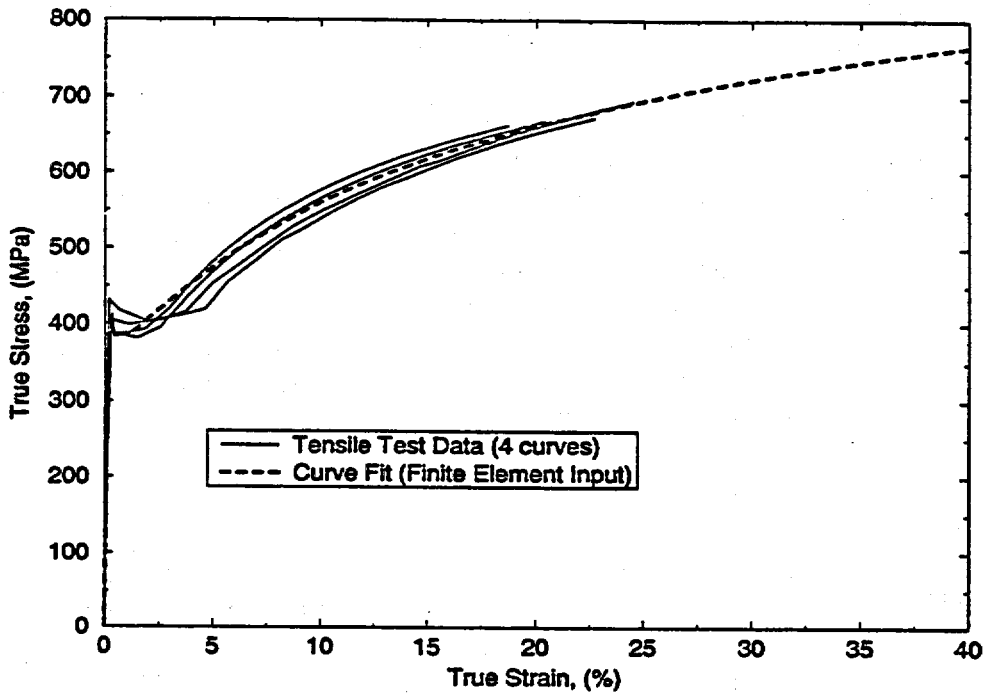

Figure 2.2 True Stress - True Strain curves for RT78; Material - SGV480; Thickness - 8.0 mm; Location - Upper Spherical Shell

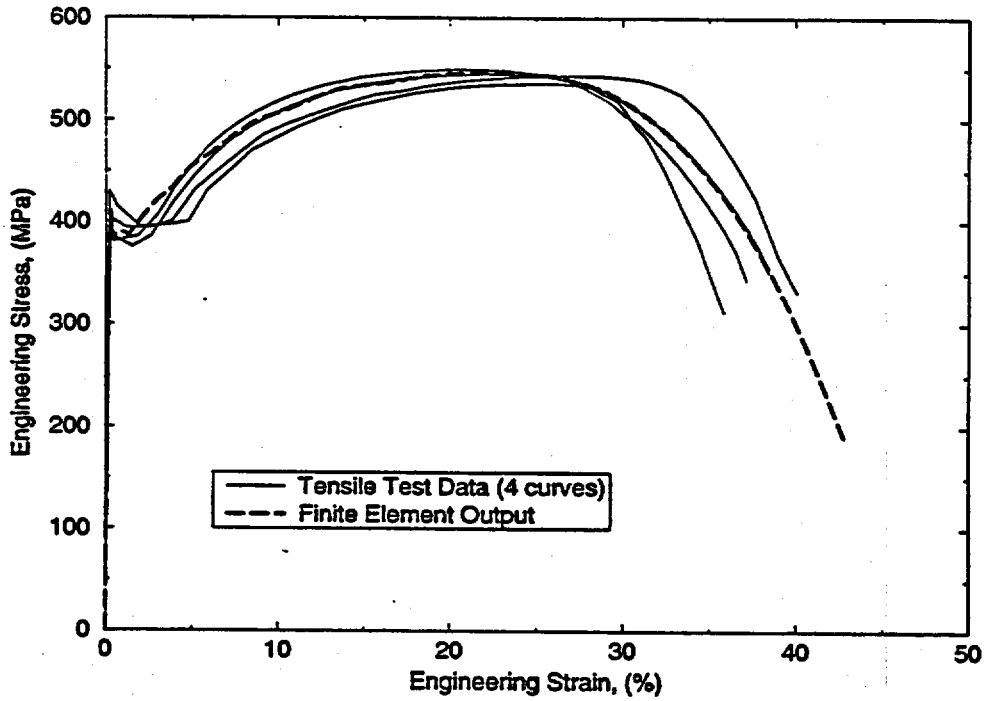

Figure 2.3 Engineering Stress - Engineering Strain curves for RT78; Material - SGV480; Thickness - 8.0 mm; Location - Upper Spherical Shell

3. GLOBAL AXISYMMETRIC ANALYSES (GAX18 / GAX34)

The first part of the analysis effort assumed the containment was axisymmetric. The effects of the non-axisymmetric features such as the equipment hatch were ignored since the primary purpose of these analyses was to study the global behavior of the SCV and its interaction with the contact structure. Two analyses were performed with different gap dimensions. The first model (GAX18) used the as-designed gap of 18 mm between the SCV and the contact structure. Table 3.1 summarizes the yielding and contact events for the 18 mm case. The second model (GAX34) used a worst-case scenario gap of 34 mm. The results for this case are presented briefly in Section 3.3.

3.1 Finite Element Model Description

The basic finite element model of the SCV and contact structure for the axisymmetric analyses appears in Figure 3.1. Two-node axisymmetric shell elements were used for the shell walls, ring stiffeners, and rings of the support girder. Four node axisymmetric quadrilaterals were used for the flanges, gusset plates, and the contact structure. Two-node axisymmetric contact elements were superimposed on the shell elements on the wall of the SCV to model the contact between the SCV and the contact structure. The total number of elements used was approximately 1600 for both the 18 mm case and the 34 mm case. Axisymmetric boundary conditions were imposed on the node at the top of the hemispherical dome of the SCV as well as at the bottom hatch cover. The model is also constrained in the vertical direction at the bottom outside corner of the ring support girder. The loading consisted of pressure on the interior of the SCV and self-weight of the entire structure and the analysis was arbitrarily terminated at 8 MPa internal pressure or roughly 10 times the scaled design pressure (1 P_d = 0.78 MPa = 113 psi). All computations for these two models were performed with the commercial finite element code ABAQUS/Standard, Version 5.3.

Table 3.1: Summary of Yielding/Contact Events for GAX18

Internal Pressure	Event
0 - 2.2 MPa	Elastic behavior
2.2 MPa	Yielding in knuckle (see Figure 3.1)
2.5 MPa	Yielding in wet well/lower conical section
2.8 MPa	Yielding in torus of top head
2.8 MPa	Yielding in spherical section
3.1 MPa	Yielding in middle/upper conical sections
4.0 MPa	Contact initiates in knuckle/upper conical section
4.1 MPa	Contact initiates in middle conical section
5.5 MPa	Contact initiates in lower conical section
5.6 MPa	Yielding in hemispherical dome in top head
6.0 MPa	Yielding in contact structure
6.7 MPa	Contact initiates in spherical section
6.7 MPa	Yielding in top flange
8.0 MPa	Analysis arbitrarily terminated

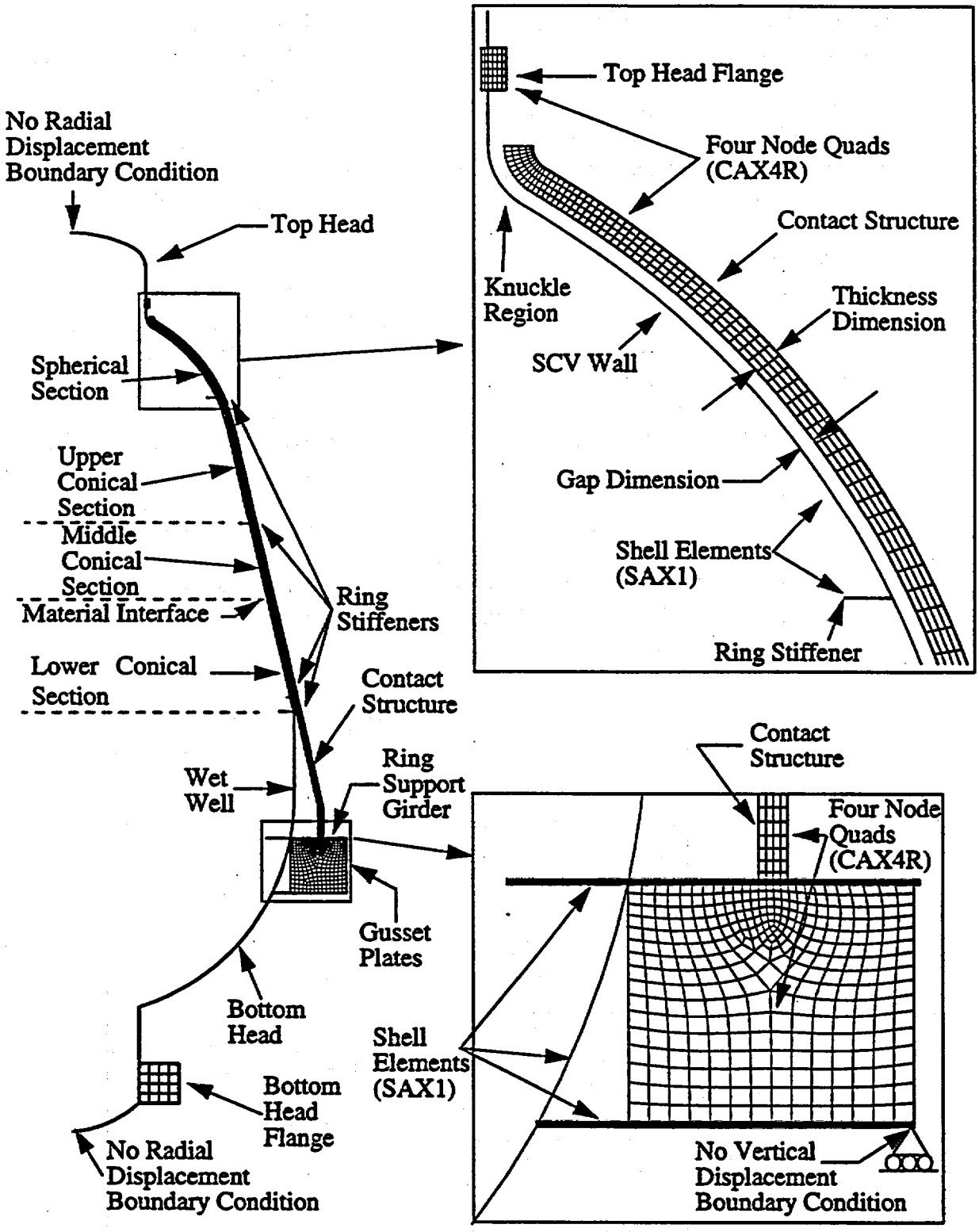

Figure 3.1 Axisymmetric finite element model (GAX18/GAX34) showing knuckle and ring support girder details.

Gusset plates are welded between the upper and lower rings of the ring support girder to provide it with significant shear and bending resistance. In order to include the effect of the 32 gusset plates in the axisymmetric finite element model, they were modeled as a solid ring with an orthotropic material model and a reduced Young's modulus. The ring representing the gusset plate is assumed to have no stiffness in the hoop direction. The reduced stiffness in the axial and radial directions is obtained by multiplying Young's modulus of the actual material by the ratio of the actual area of the gusset plates to the area of the solid ring in the axisymmetric finite element analyses.

ABAQUS/Standard Version 5.3, unlike newer versions of ABAQUS, requires the user to explicitly input contact elements. For both axisymmetric models two-node axisymmetric contact elements (ABAQUS type ISL21A) were superimposed on the wall of the SCV to model the contact between the SCV and the contact structure. These elements are capable of modeling finite sliding between two deformable bodies. Contact interaction takes place along a "slide line" which the user defines as a collection of nodes on the opposite surface of the contact elements. Based on an earlier parametric study, the coefficient of friction used for these analyses was μ=0.2 (see Section 5.2 for a discussion of the friction coefficient).

Because of recent changes in the design of the contact structure, there are two important differences between the as-modeled contact structure and the as-designed contact structure. The first design change is that the contact structure will be composed of SA516 Grade 70 steel rather than A36 steel. The SA516 has a slightly higher yield (258 MPa (38 ksi) compared to 245 MPa (36 ksi) for the A36) and also a slightly higher ultimate strength (476 MPa (70 ksi) compared to 408 MPa (60 ksi) for A36) [7]. Since the contact structure is expected to remain elastic until sometime after 10 multiples of the design pressure, it is unlikely that this difference will significantly affect the results. The other important difference lies in the geometry of the contact structure near the knuckle of the SCV. Figure 3.2 details the differences between the as-modeled and the as-designed geometry for the part of the contact structure adjacent to the knuckle. Note the gap at the top of the

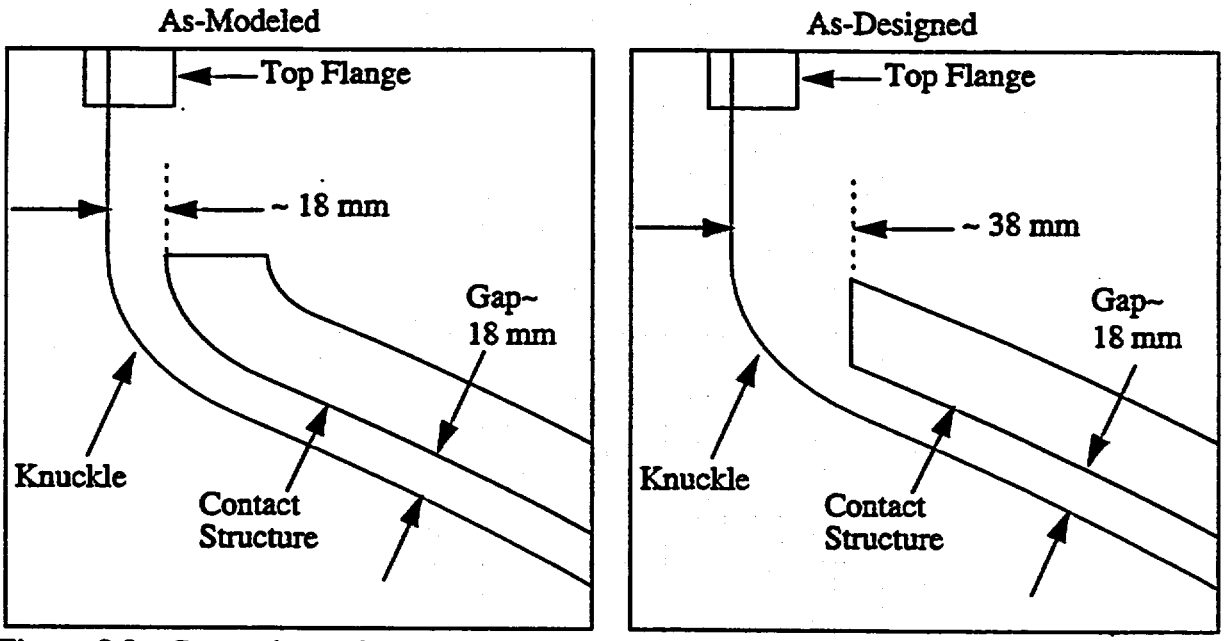

Figure 3.2 Comparison of as-modeled and as-designed details in contact structure near the SCV knuckle.

knuckle in the as-designed structure is nearly twice that of the as-modeled: 38 mm compared to 18 mm. The last finite element model, which covers the top head and knuckle region, includes the latest design information discussed above. It appears in Section 4.3.

3.2 Results - 18 mm case (GAX18)

For the 18 mm case, yielding is observed first in the knuckle at 2.2 MPa. The wet well, lower, middle and upper conical sections, as well as the transition in the top head all yield prior to contact. Contact initiates in the knuckle and upper conical section first at 4.0 MPa. By 6.7 MPa, the spherical section, the hemispherical dome, the top flange, and the contact structure have all yielded.

3.3 Results - 34 mm case (GAX34)

The axisymmetric model with a 34 mm gap was performed as a check on the worst case, as-built condition of the contact structure. With a larger gap, the contact structure will not be effective in slowing plastic flow until a higher internal pressure and may even be useless if the SCV accumulates too much plastic strain prior to contact. Since this analysis was only intended as a worst case scenario, it will only be presented as a tabulated summary. Yielding and contact events are shown in Table 3.2.

Table 3.2: Summary of Yielding/Contact Events for GAX34

Internal Pressure	Event
0 - 2.2 MPa	Elastic behavior
2.2 MPa	Yielding in knuckle (see Figure 3.1)
2.5 MPa	Yielding in wet well/lower conical section
2.8 MPa	Yielding in torus of top head
2.8 MPa	Yielding in spherical section
3.1 MPa	Yielding in middle/upper conical sections
4.3 MPa	Contact initiates in upper conical section
4.4 MPa	Contact initiates in middle conical section
4.5 MPa	Yielding in top flange
4.8 MPa	Contact initiates in knuckle
5.6 MPa	Yielding in hemispherical dome in top head
5.8 MPa	Contact initiates in lower conical section
6.3 MPa	Yielding in contact structure
7.1 MPa	Contact initiates in spherical section
8.0 MPa	Analysis arbitrarily terminated

4. 3D ANALYSES

4.1 Global 3-D Shell Model (G3DS)

The next analysis performed to characterize the global behavior of the SCV and its interaction with the contact structure used a 3-dimensional shell element model. Table 4.1 summarizes the yielding and contact events.

4.1.1 Finite Element Model Description

The finite element model of the SCV and contact structure for the G3DS Model appears in Figure 4.1. The half-symmetry model used approximately 4800 four-node reduced integration shell elements with finite membrane strain capability (ABAQUS S4R elements). The only non-axisymmetric detail included in this model is the equipment hatch. Symmetric boundary conditions were imposed on all nodes lying in the vertical (*x-y*) plane passing through the centerline of the equipment hatch, and vertical displacements were constrained at the support locations on the underside of the ring support girder. The loading consisted of gravity and internal pressure and the analysis ran until it failed to converge at approximately 12.7 MPa internal pressure or slightly over 16.3 P_d. The nominal gap between the SCV and the contact structure was 18 mm. Computations for this model were performed with the ABAQUS/Standard, Version 5.4.

Table 4.1: Summary of Yielding/Contact Events for Global 3-D Shell Model

Internal Pressure	Event
0 - 2.3 MPa	Elastic behavior
2.3 MPa	Local yielding in top/bottom of E/H sleeve at attachment to insert plate
2.3 MPa	Local yielding at middle conical section attachment to E/H insert plate
2.7 MPa	Yielding in knuckle
2.8 MPa	Local yielding at bottom of E/H insert plate
3.0 MPa	Local yielding in upper conical section above E/H
3.1 MPa	Yielding in middle conical section around circumference
3.4 MPa	Yielding in upper conical section around circumference
3.7 MPa	Yielding in lower conical section near insert plate
3.9 MPa	Yielding in lower conical section around circumference
4.1 MPa	Contact initiates in the SCV in the upper conical section and knuckle
4.1 MPa	Circumferential contact in upper conical section
4.3 MPa	Circumferential contact in middle conical section
4.7 MPa	Yielding in cylindrical wet well around circumference
5.1 MPa	Yielding in dome of top head
5.3 MPa	Circumferential contact in lower conical section
5.5 MPa	Yielding in spherical section (away from knuckle)
6.6 MPa	Contact initiates in spherical section
11.3 MPa	Circumferential contact in wet well

The contact definition in versions of ABAQUS after Version 5.3 is much simpler. The newer versions use the contact pair approach in which the user can simply specify two element sets that are candidates for eventual contact. One additional specification required for structural elements, such as the shell elements used for this model, is that the surface be specified. For this model, a small sliding formulation was used since the relative sliding of the SCV and contact structure was assumed to be small. The friction coefficient, discussed previously in Section 3.1, was μ=0.2.

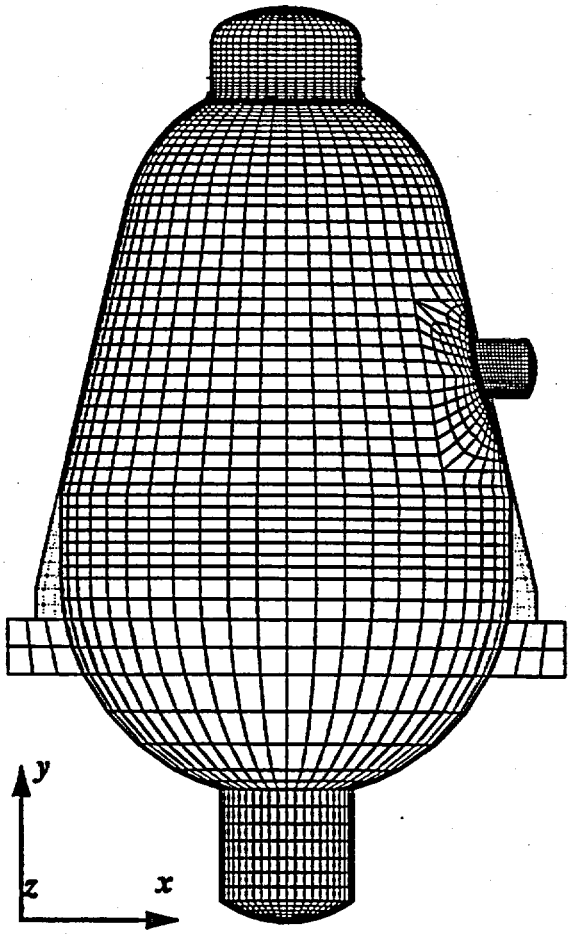

Figure 4.1 Global 3-D Shell (G3DS) model mesh. Note: contact structure appears behind SCV.

The thickened equipment hatch insert plate was constructed such that it is flush with the inside surface of the SCV. The thickness eccentricity poses a problem when using shell elements in ABAQUS since there are no means of explicitly modeling a shell with uneven material distribution about a reference line. A simple elastic test case showed that using the `*SHELL SECTION, COMPOSITE` option in ABAQUS is an accurate way of implicitly modeling the eccentricity at the equipment hatch insert plate [8]. The equipment hatch insert plate was modeled as a composite shell with 3 layers. The eccentricity was introduced by making the middle layer the same thickness as the adjacent material and then placing two shells with the same thickness on either side. The middle and outside layers were given the modulus of elasticity for the equipment hatch insert plate (measured from the Hitachi tensile tests), $E_{plate} \sim 216 \times 10^9$ Pa, while the inner composite layer was given a dummy modulus of $E_{dummy} \sim 1$ Pa. This formulation makes the stiffness of the inner layer of the composite shell negligible with respect to the outer layer.

Because of the eccentricity at the insert plate shown in Figure 4.2, the gap between the insert plate and the contact structure is reduced considerably to approximately 9 mm. The eccentricity formulation described above does not account for the smaller gap since the contact algorithm uses the centerline of both the composite shells in the SCV insert plate and the regular shells in the contact structure as the reference. So, the gap between the insert plate and the SCV in the finite element model is 18 mm.

As with the axisymmetric model described in Section 3.1, there were two important changes in the design of the contact structure which were also not incorporated into this model. The contact structure material and its geometry near the knuckle of the SCV were the same as in the axisymmetric model (see Figure 3.2 for knuckle details). It is unlikely that the difference in materials will significantly affect the results. However, the geometry near the knuckle is especially important and is modeled more accurately and completely in the LTHAXC model in Section 4.3.

4.1.2 Results

Results presented for this model include deformed shape plots, contact history plots, and a brief discussion of the high strain or critical areas.

4.1.2.1 Deformed Shape

Figure 4.3 shows the deformed shape of the SCV at 8 different pressure levels. The contact structure, ring support girders, and gusset plates are not shown for clarity. At 3 MPa, when only localized yielding has occurred, very little deformation is discernible. At 4.1 MPa, when contact first occurs, there is noticeable deformation in the upper and middle conical sections. The effect of the stiffeners is evident in the upper conical section as it tries to expand outward but is restrained by two 19 mm stiffeners. The knuckle shows deformation in both the outward (radial) and vertical directions, while the top head and top head flange appear to be deforming exclusively in the vertical direction. The equipment hatch also appears to be rotating outward and downward at this pressure. By 6 MPa, most of the upper and middle conical sections are contacting the SCV. The outward expansion of the cylindrical wet well is now apparent. At 8 MPa it is clear that the contact structure is arresting further radial expansion of most of the SCV. The apex of the top head and the cylindrical portion of the top head, which are not shielded by the contact structure, are showing excessive amounts of deformation. At 10 MPa, which is nearly 13 multiples of the design pressure, the only locations where further deformations are clear are the top head and the cylindrical wet well.

4.1.2.2 Contact History

Figure 4.4 shows the progression of contact. Only that part of the SCV which is shielded by the contact structure is displayed. Dark areas indicate contact while light areas indicate no contact. The first plot shows contact initiating in the upper conical section and the knuckle. The area of contact has increased considerably at 5 MPa to include the middle conical section and by 6 MPa includes the lower conical section. By 8 MPa, the spherical section, the last area to make contact not including the cylindrical wet well where the gap is considerably larger, has made uniform

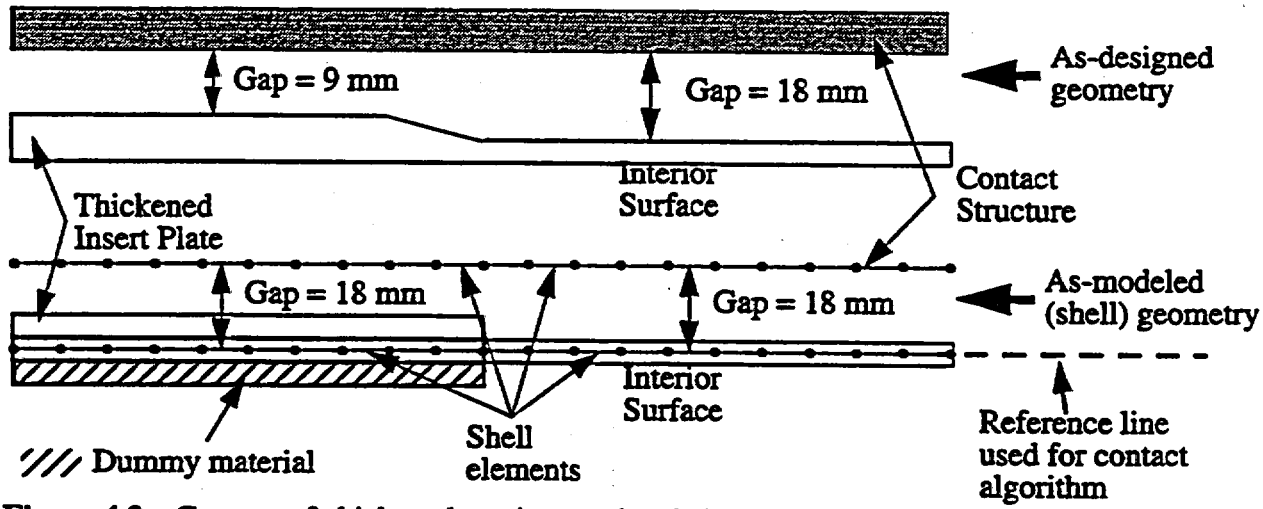

Figure 4.2 Cut-out of thickened equipment hatch insert plate and attached conical section showing as-designed geometry (top) and as-modeled geometry (bottom) using shell elements. Reference line shown at lower right is used for contact algorithm which makes the gap a uniform 18 mm even over insert plate

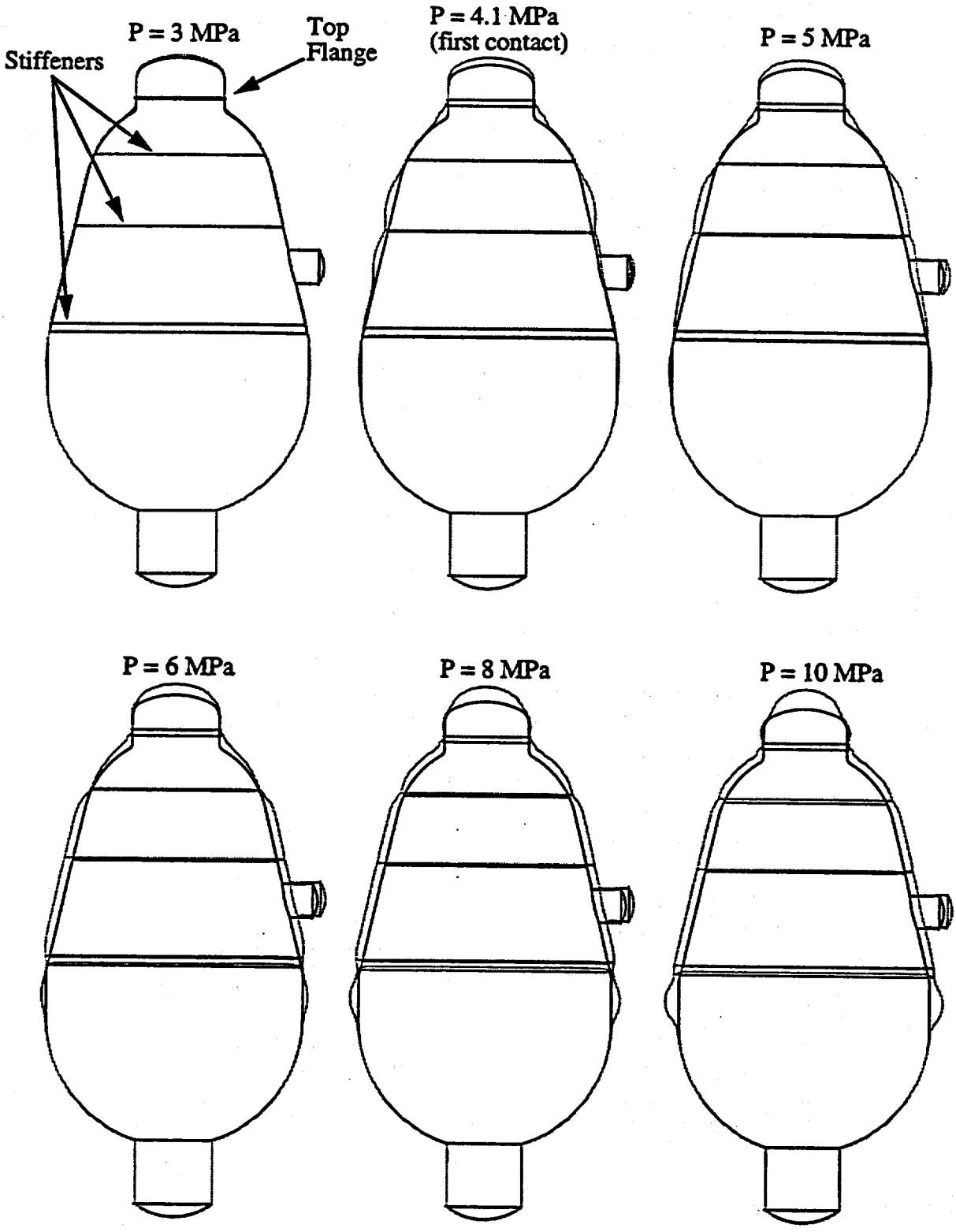

Figure 4.3 Deformed shape of G3DS at 6 pressure levels. Contact structure, ring support girders, and gusset plates are not shown. Displacements are magnified by a factor of 5.

circumferential contact except near the upper 19 mm stiffener, which is still arresting the radial growth of the SCV. At 10 MPa, the only area of the SCV that has not contacted the contact structure yet is the cylindrical wet well where the initial gap is well over 100 mm.

4.1.2.3 Critical Areas

Contour plots of equivalent plastic strain indicated three locations with high strains that dictated further study. Figure 4.5 compares the three locations which consistently displayed the highest plastic strains throughout the history: 1)the junction of the equipment hatch insert plate and the material change interface; 2) the apex of the top head; 3)the knuckle region. The element at the knuckle and at the material change interface near the insert plate both yield at roughly the same time but the element at the knuckle contacts first and so the plastic strain for this element levels out

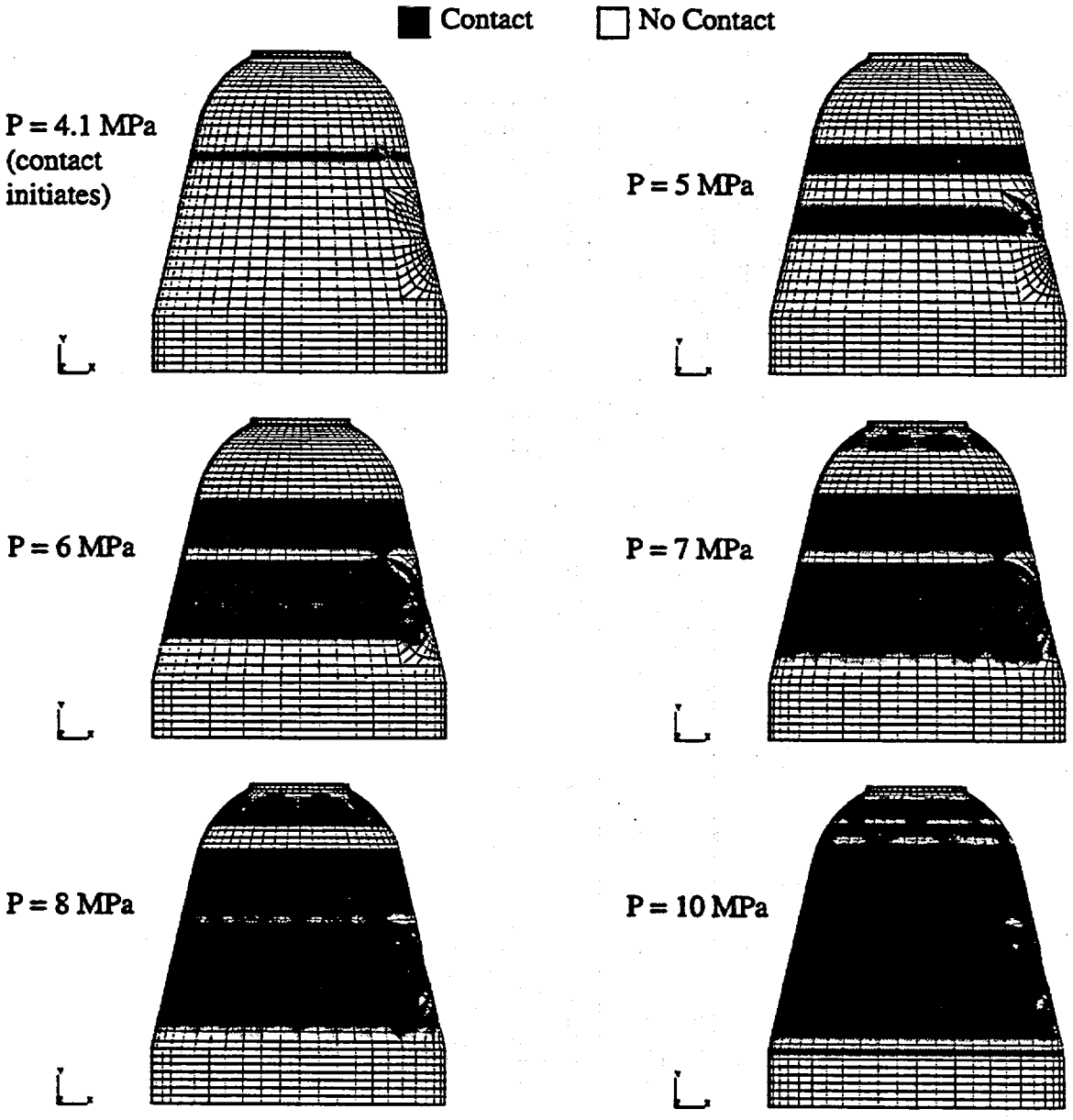

Figure 4.4 Plots showing contact evolution

earlier in the loading. Both elements are eventually shielded by the contact structure and so do not accumulate nearly as much plastic strain as the apex of the top head. The apex yields at 5.1 MPa, compared to 2.5 MPa for the other two locations, but the amount of plastic strain quickly surpasses that accumulated at the other two locations and reaches a value of nearly 40% before the analysis fails to converge at just over 12.7 MPa. To assess the importance of these critical areas, refined models for both the top head, including the knuckle, and the area near the equipment hatch insert plate were created and are discussed in Section 4.2, Section 4.3, and Section 4.4.

4.2 Local Equipment Hatch Submodel (LEHS)

This section covers the model created to study the junction of the equipment hatch insert plate and the material interface.

4.2.1 Finite Element Model Description

Shown in Figure 4.6, the model used 4800 four-node reduced integration shell elements with finite membrane strain capability (ABAQUS S4R elements). The boundary conditions were imposed using the *SUBMODEL option. Submodeling in ABAQUS is used to study a local part of a model with a refined mesh based on interpolation of the solution from an initial, global model, onto the nodes on the appropriate parts of the boundary of the submodel. Figure 4.7 compares the G3DS model mesh and the LEHS model mesh. For this particular analysis all nodes on the boundary of the submodel were "driven" by the results from the G3DS model as indicated in Figure 4.6. The loading consisted of gravity and internal pressure. The coefficient of friction used for this model is the same as in previous models, μ=0.2. The eccentricity of the equipment hatch insert plate was also modeled as described in Section 4.1.1. Since this model uses results from the previous G3DS model, the model was only allowed to run up to 12.7 MPa, the point where the global model failed to converge. Computations for this model were performed with ABAQUS, Version 5.4.

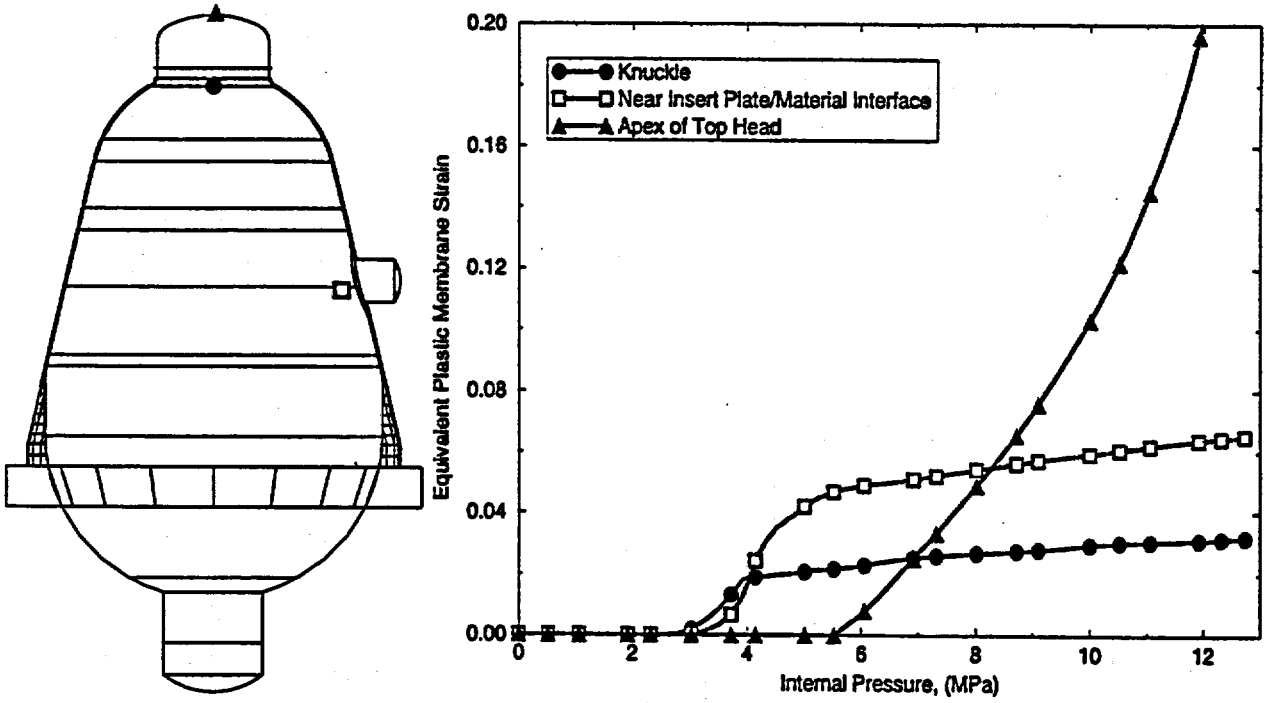

Figure 4.5 Equivalent plastic membrane strain for three critical locations in the Global 3-D Shell Model as a function of internal pressure. Locations of strains are shown at left.

4.2.2 Results

The contact history is presented for this model with a comparison of critical areas between this model and the G3DS model.

4.2.2.1 Contact History

Figure 4.8 shows the evolution of contact for the Equipment Hatch Submodel. As before, black areas indicate contact, white areas indicate no contact. The elements on the border of the model are gray because they are "driven" nodes and so are not included in the contact algorithm. Contact first

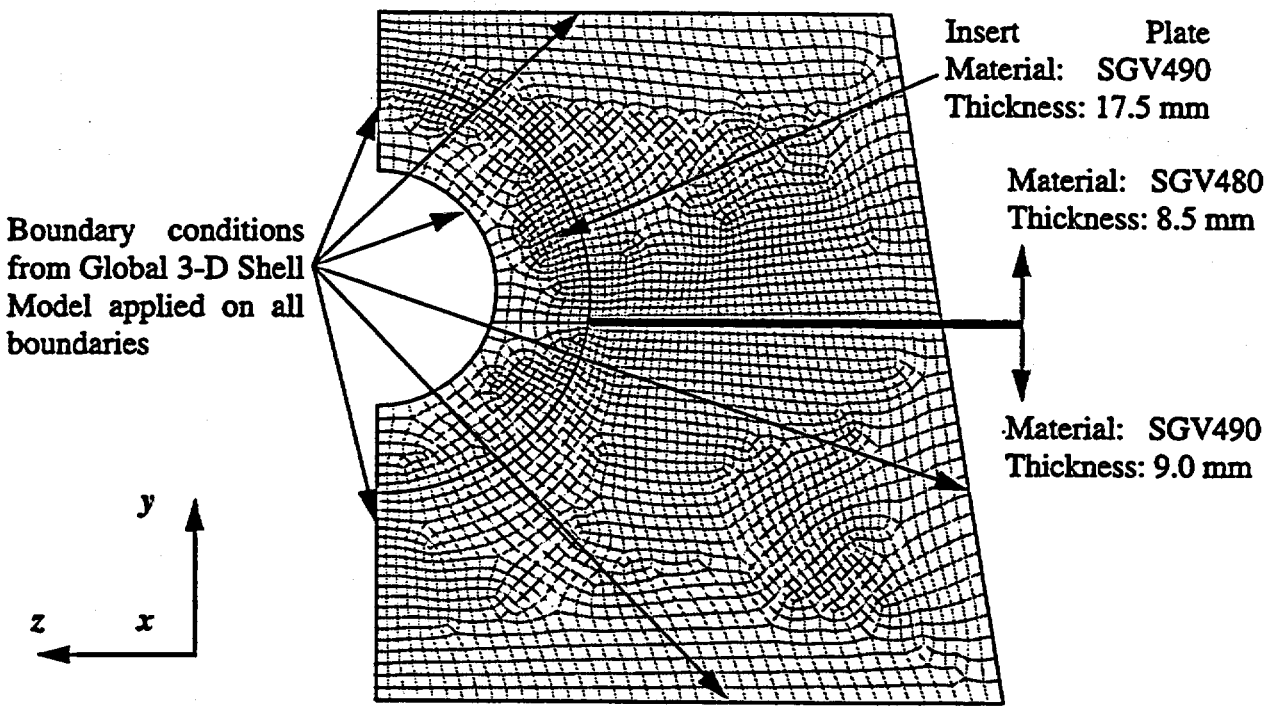

Figure 4.6 LEHS model mesh (contact structure not shown).

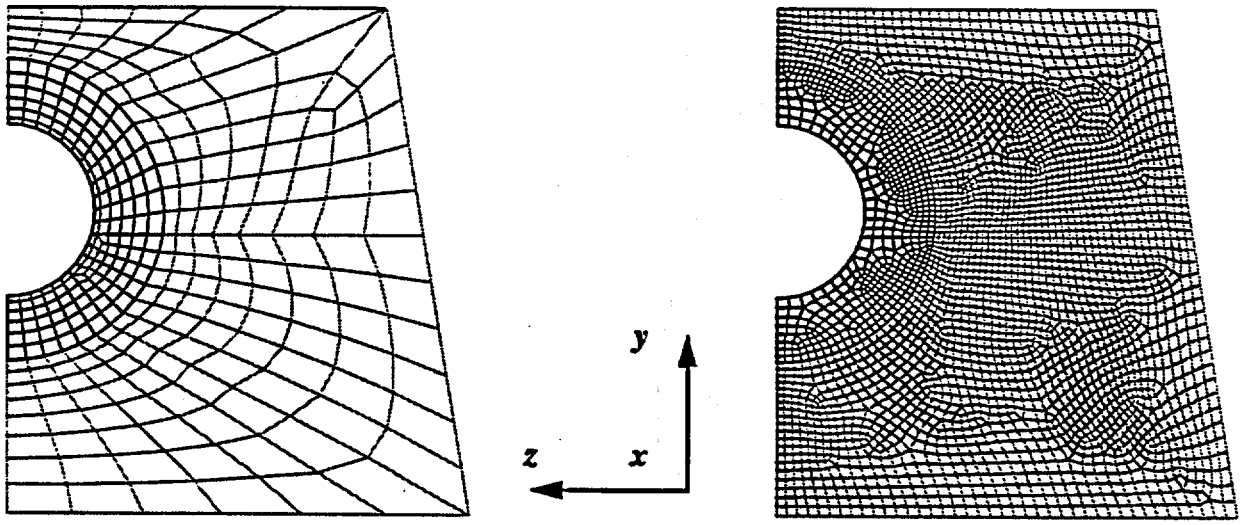

Figure 4.7 Comparison of Global 3-D mesh at left and Equipment Hatch Submodel at right. The increase in mesh density between the two models roughly a factor of 10.

occurs at 4.2 MPa in the middle conical section. It propagates towards the insert plate at 5 MPa and by 6 MPa has contacted a large part of the insert plate and has spread to the lower conical section (below the material interface). At 8 MPa the contact is widespread throughout the model.

4.2.2.2 Critical Area

This model was intended to study the junction of the equipment hatch insert plate and the material interface subsequent to the G3DS model which indicated potentially high strains in this area. Figure 4.9 compares the equivalent plastic membrane strains from the two models at the same location: the element in the 8.5 mm wall (middle conical section) that is adjacent to the equipment hatch insert plate *and* adjacent to the 9.0 mm wall (lower conical section). These elements are indicated in the figure. In the G3DS model this element is approximately 60 mm by 30 mm in size while in the LEHS model the element in the corresponding location is 11 mm by 11 mm. Qualitatively the behavior of the two elements is similar. Quantitatively the element in the LEHS

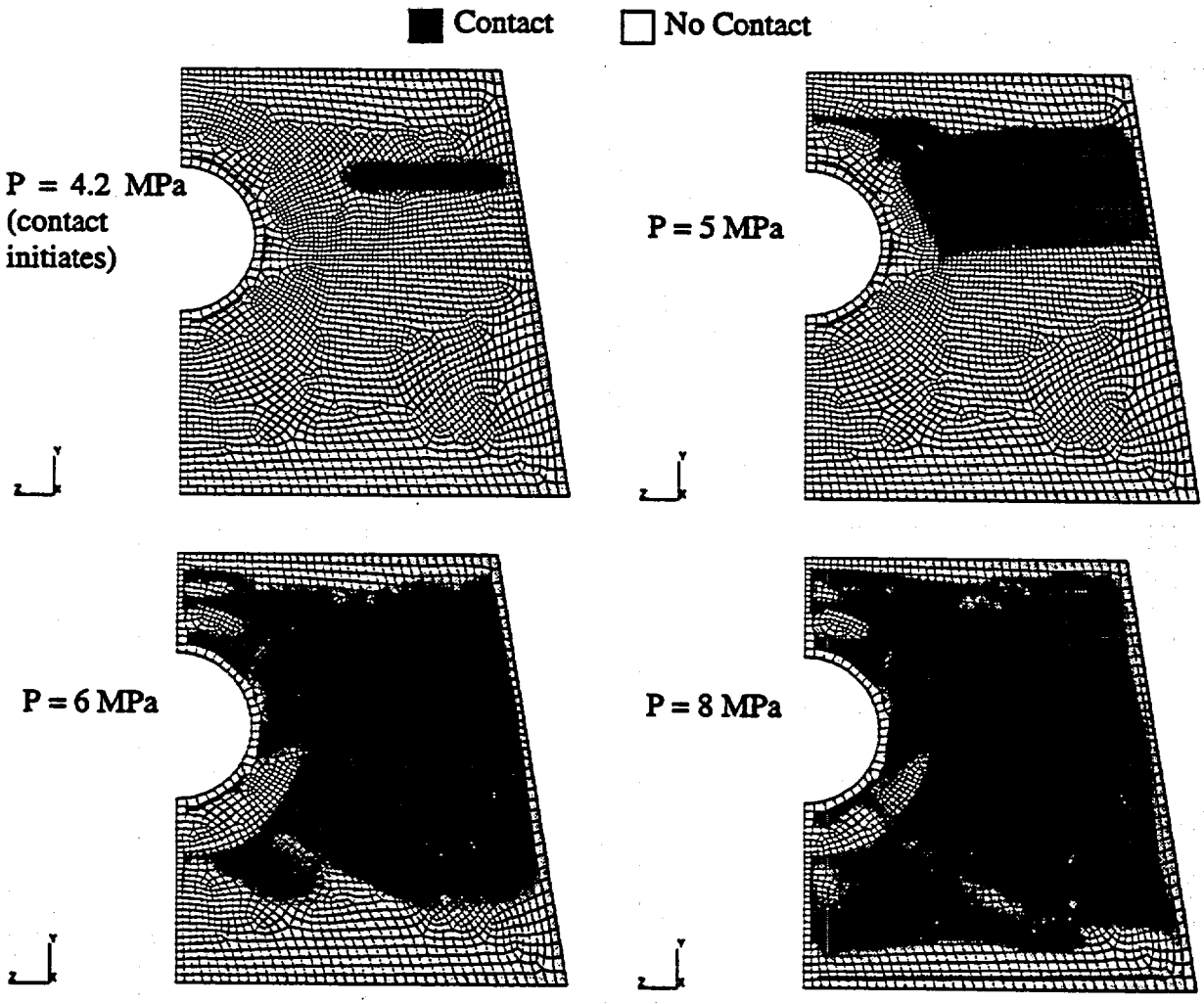

Figure 4.8 Evolution of contact for Equipment Hatch Submodel. Black areas indicate contact, white areas indicate no contact.

submodel reaches strains nearly 50% higher than the G3DS model: 9% in the submodel compared to approximately 6.5% in the global model. The difference is best explained by the submodel's ability to more accurately measure the strain concentration due to its finer mesh.

4.3 Top Head Submodel (LTHAXC)

The second critical area requiring further study as indicated by the G3DS model was the top head region including the knuckle. For this area a local axisymmetric continuum model was created which includes the most recent as-designed geometry of both the SCV and the contact structure from the top head apex down to the upper 19 mm stiffener.

4.3.1 Finite Element Model Description

Figure 4.10 shows the finite element model for the Top Head Submodel. The model used 7200 four-node reduced integration, axisymmetric continuum elements (ABAQUS CAX4R elements) and 5 two-node thin or thick linear shell elements (ABAQUS SAX1 elements). Axisymmetric boundary conditions were imposed at the apex of the top head. At the lower bound of the model, rotations and displacements from the G3DS model were applied to the shell nodes in a manner similar to the *SUBMODEL option in ABAQUS. However, ABAQUS does not allow the submodel option to be used when changing from a 3-dimensional model to an axisymmetric model, so the same process was carried out manually. The displacement and rotation histories from the appropriate nodes on the G3DS model were applied "manually" with the *USER SUBROUTINE option, which provides the user with a means of prescribing the magnitude of any degree of freedom using FORTRAN code. Multi-point constraints were used to transition from the shell elements to the continuum elements. As with the other models, the loading consisted of internal

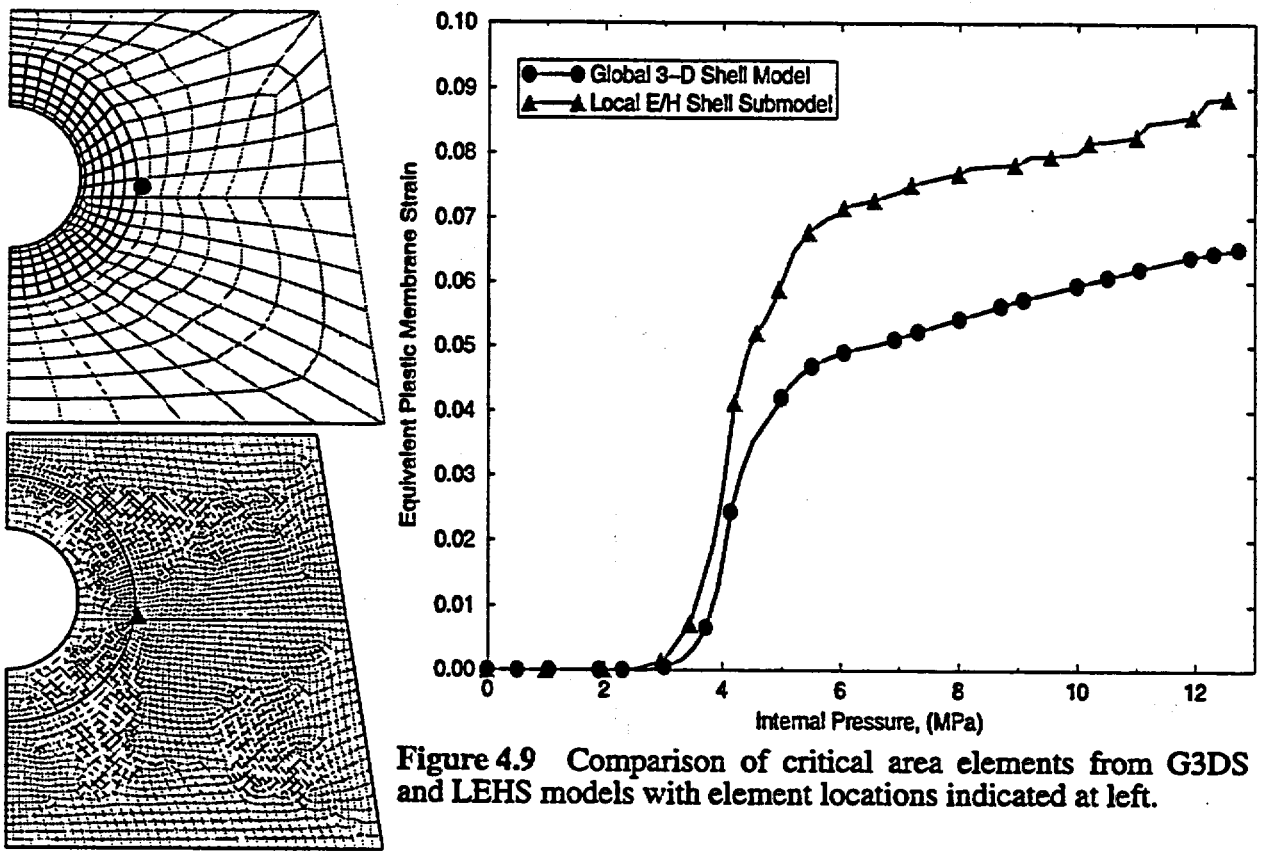

Figure 4.9 Comparison of critical area elements from G3DS and LEHS models with element locations indicated at left.

pressure and gravity. The contact definition for this model was basically the same as the previous models (the coefficient of friction was $\mu = 0.2$) except that the small sliding formulation was not specified. For this case, ABAQUS defaults to a finite sliding formulation, which allows for arbitrary separation, sliding, and rotation of the surfaces.

As mentioned in Section 3.1 and shown in Figure 3.2, the design of the contact structure was changed considerably after the GAX18/GAX34 and G3DS models were completed. This model includes those design modifications. Since continuum elements were used throughout the model, this model also more accurately models the geometry, especially near the top head flange and the knuckle.

4.3.2 Results

Results presented for this model consist of deformed shape plots and a discussion of the critical areas.

4.3.2.1 Deformed Shape

Figure 4.11 shows the deformed shape plots for the Top Head Submodel. The first three plots are the deformed shape of the entire model at 3 different internal pressures, while the last six are a close-up of the knuckle/top head flange region as in Figure 4.10 with some additional pressure steps included. The displacements are *not* magnified. First contact occurs at 3.2 MPa at the knuckle as it expands radially outward to meet the corner of the contact structure. At 6 MPa, the bending of the cylindrical section of the top head from the bottom of the top head flange is apparent and at 8 MPa bending around the top of the top head flange is now beginning. The vertical growth of the dome is also significant at 8 MPa. Note that the top head flange shows almost no radial expansion

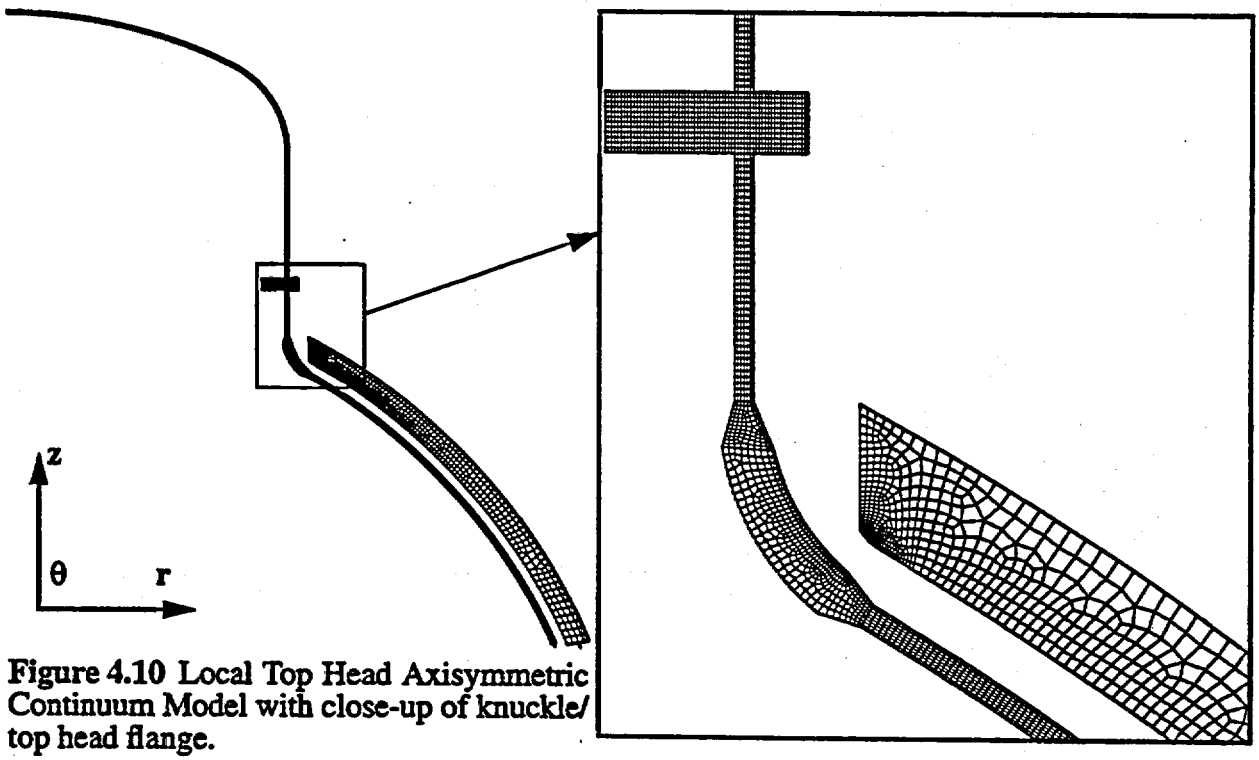

Figure 4.10 Local Top Head Axisymmetric Continuum Model with close-up of knuckle/ top head flange.

at 8 MPa. The overly stiff behavior of the top head flange and the rapid radial expansion of the knuckle create bending locations with significant plastic strains as will be shown in the next section.

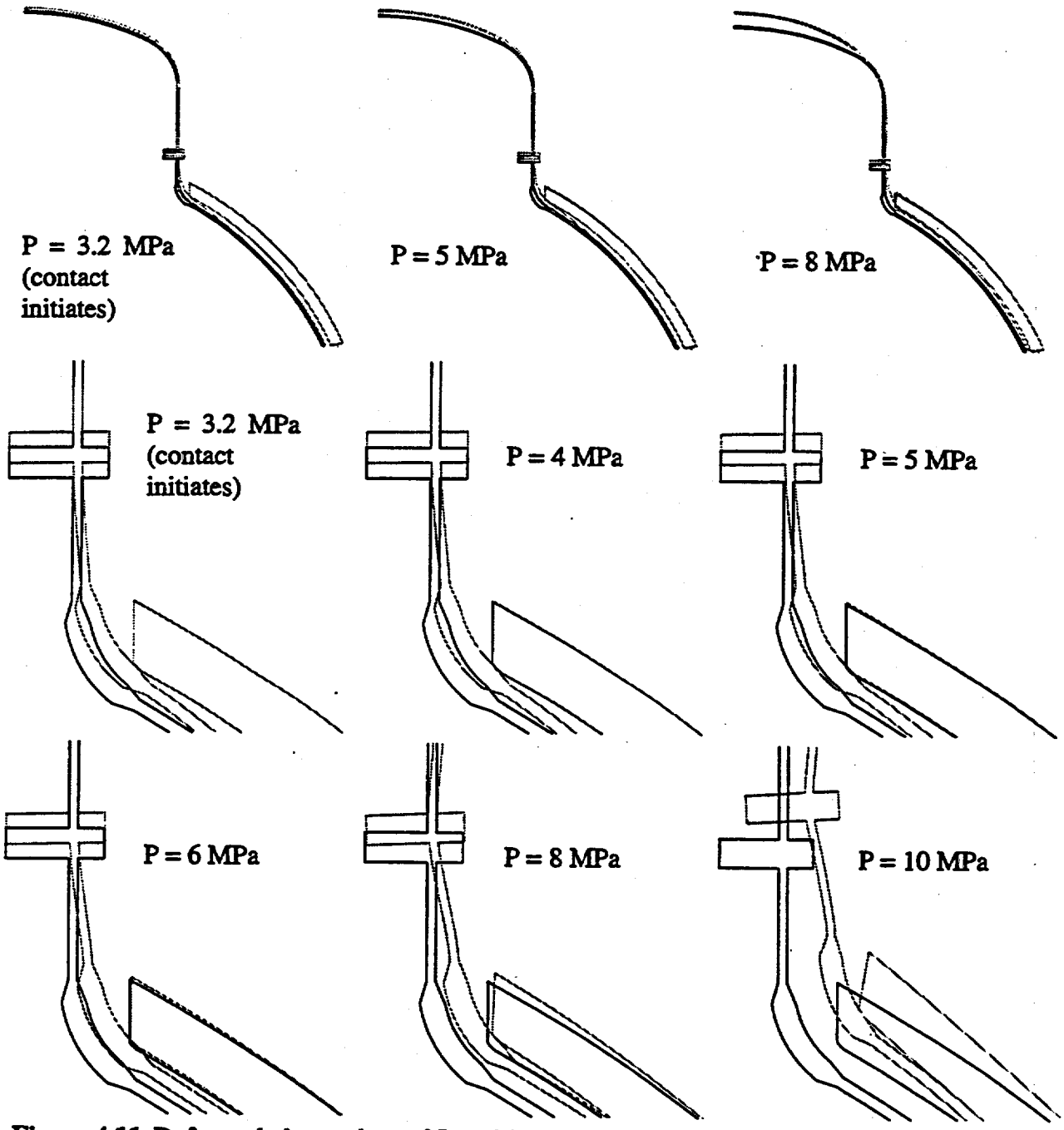

Figure 4.11 Deformed shape plots of Local Top Head Axisymmetric Continuum Model with close-up of knuckle/top head flange. The displacements are not magnified.

4.3.2.2 Critical Areas

Figure 4.12 plots the strains from the critical locations from the top head submodel as a function of internal pressure. The 5 locations can be broken down into 3 areas: the apex of the top head, the top head flange, and the knuckle. After 8 MPa, all of the locations show very similar strain histories except for the element below the knuckle. The main differences in the strain histories appear early in the loading.

The exterior surface of the apex of the top head yields late in the history compared to the other elements at about 5 MPa. Since this location is not protected by the contact structure, the growth of plastic strain is rapid up to a maximum of over 34% at an internal pressure of over 12 MPa.

The overly stiff behavior of the top head flange can probably be attributed to the mixed scaling of the SCV: 1:4 ratio thickness; 1:10 ratio on size. This causes large bending strains in the elements just below and just above the top flange on the interior surface, since they are both in tension due to bending. The element just above the top flange behaves similarly to the apex of the top head except that it yields sooner. The element just below the top flange accumulates more plastic strain early in the loading but otherwise behaves similarly to the first two elements.

The element at the interface between the top of the knuckle and the cylindrical section of the top head on the exterior surface accumulates still more plastic strain early in the loading but then appears to be temporarily affected by the contact structure at just over 3 MPa. The last location under consideration is the element at the interface between the bottom of the knuckle and the spherical section on the exterior surface. It accumulates more plastic strain than all of the other elements until it contacts the contact structure at just over 3 MPa. The effect of the contact structure on this element is much more apparent as this element reaches a maximum strain of only 12% compared to nearly 34% for the apex and 24% for the other elements.

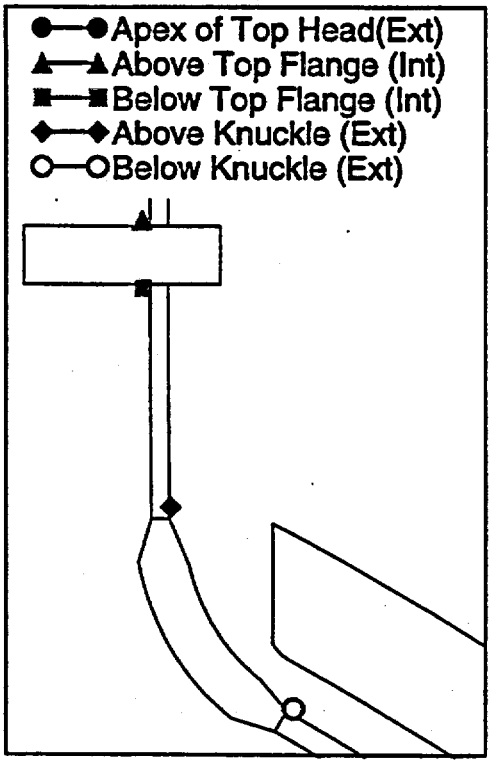

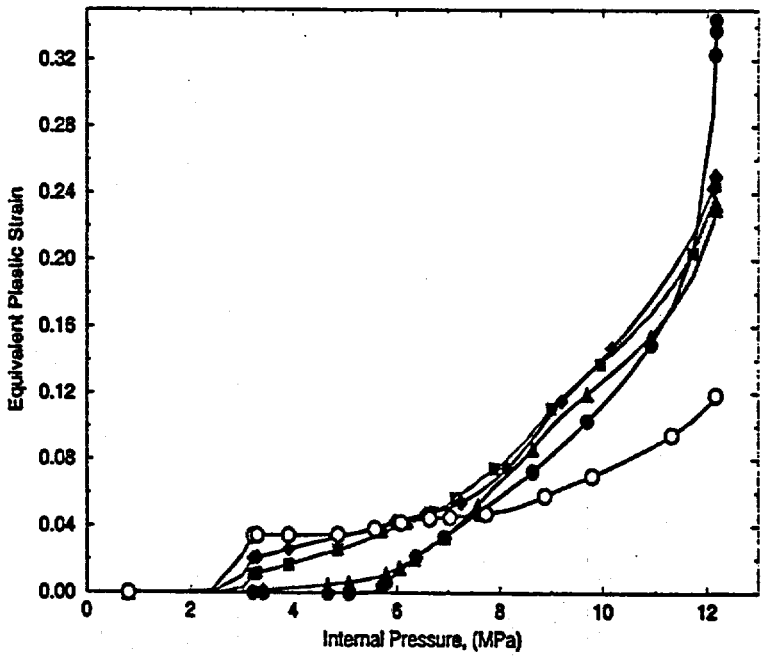

Figure 4.12 Comparison of critical high strain areas from the LTHAXC model. Four of the locations are indicated at left; the other one is the apex of the top head.

4.4 Equipment Hatch Submodel with Thinned area (LEHSTh)

The last analysis performed to characterize the global behavior of the SCV and its interaction with the contact structure was used to study the effects of thinned areas near the junction of the equipment hatch insert plate and material change interface.

4.4.1 Finite Element Model Description

Figure 4.13 shows the basic finite element model used to study the effects of thinning. The model is essentially the same as the previous Equipment Hatch Submodel except that the measured thicknesses near the junction of the equipment hatch insert plate and the material interface were input explicitly using the *NODAL THICKNESS option in ABAQUS, Version 5.5. *This model is only intended to study the thinned area near the equipment hatch insert plate and so does not include any other as-built information.*

The input data for the thinned area appeared in the February 20, 1996 memorandum from Sandia [9] regarding as-built properties of the SCV model and contact structure. The as-built measurements indicate that the nominal thicknesses of the as-built SCV are 5-10% thicker than the designed configuration of the SCV, while two locations on either side of the equipment hatch insert plate are up to 22% *thinner* than the designed configuration, on which all of the finite element models are based. To accommodate for this in the finite element model, the measured thickness

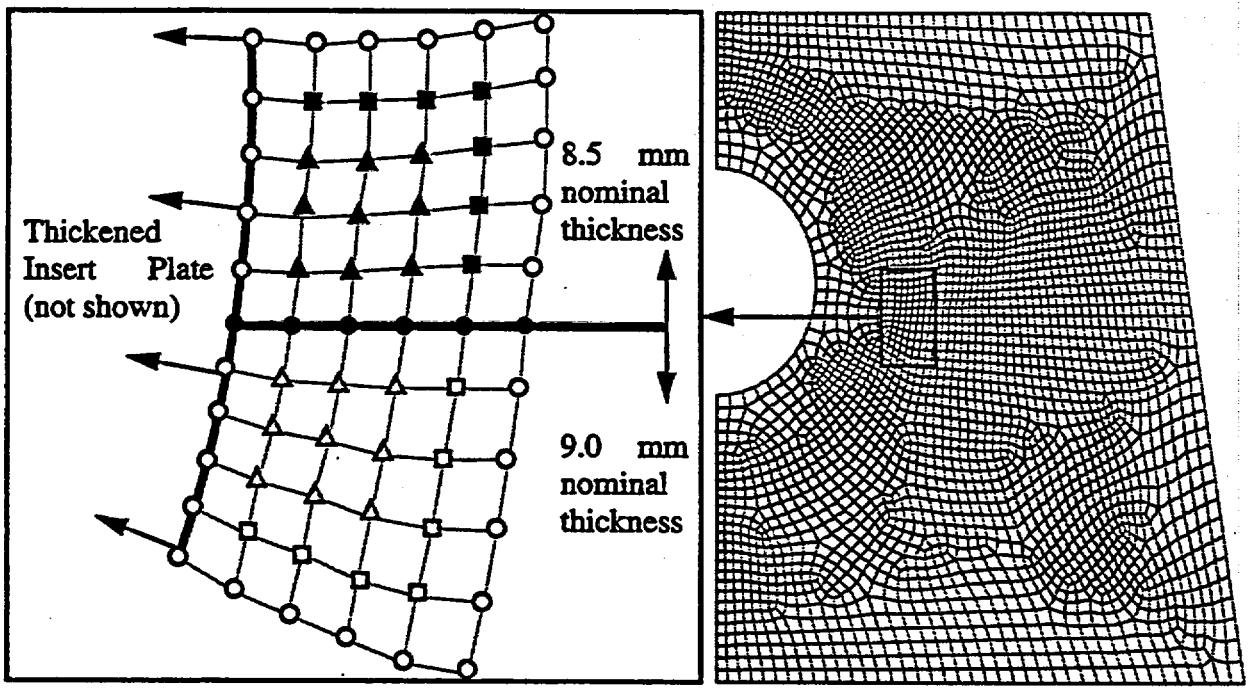

Figure 4.13 Diagram showing the equipment hatch submodel at right (contact structure not shown) with a detail of the thinned area at left. Values for thickness reduction are shown as percentages and superimposed on the appropriate nodes.

from the thinned areas from the SCV were converted to a percentage of the nominal measured thickness. Then, these percentages were used to calculate the input thicknesses for the thinned locations in the finite element model. Simply changing the nominal thickness in the finite element model was not an option since that model uses boundary conditions from a global model (G3DS) which uses the original, as-designed thicknesses.

4.4.2 Contact History

The contact behavior for this model is nearly the same as for the LEHS model (see Figure 4.8).

4.4.3 Critical Areas

Figure 4.14 compares the critical strain area from this model to the G3DS and the LEHS model with the locations indicated in the diagram at the left. This is the same figure as Figure 4.9 with the data from the LEHSTh model added. Qualitatively each curve represents the same behavior: the element yields at between 3 and 4 MPa, accumulates plastic strain very quickly until it reaches the contact structure between 5 and 6 MPa. The main difference between each curve is the amount of plastic strain accumulated prior to contact. The effect of the thinned section is apparent, as the slightly thicker and higher yield SPV490 material now shows the greatest accumulation of plastic strain. This issue will be discussed in more detail later.

5. MISCELLANEOUS CALCULATIONS

This section covers additional calculations which supported the finite element analyses presented above. Buckling is presented in Section 5.1 while a discussion of the determination of the friction coefficient is presented in Section 5.2.

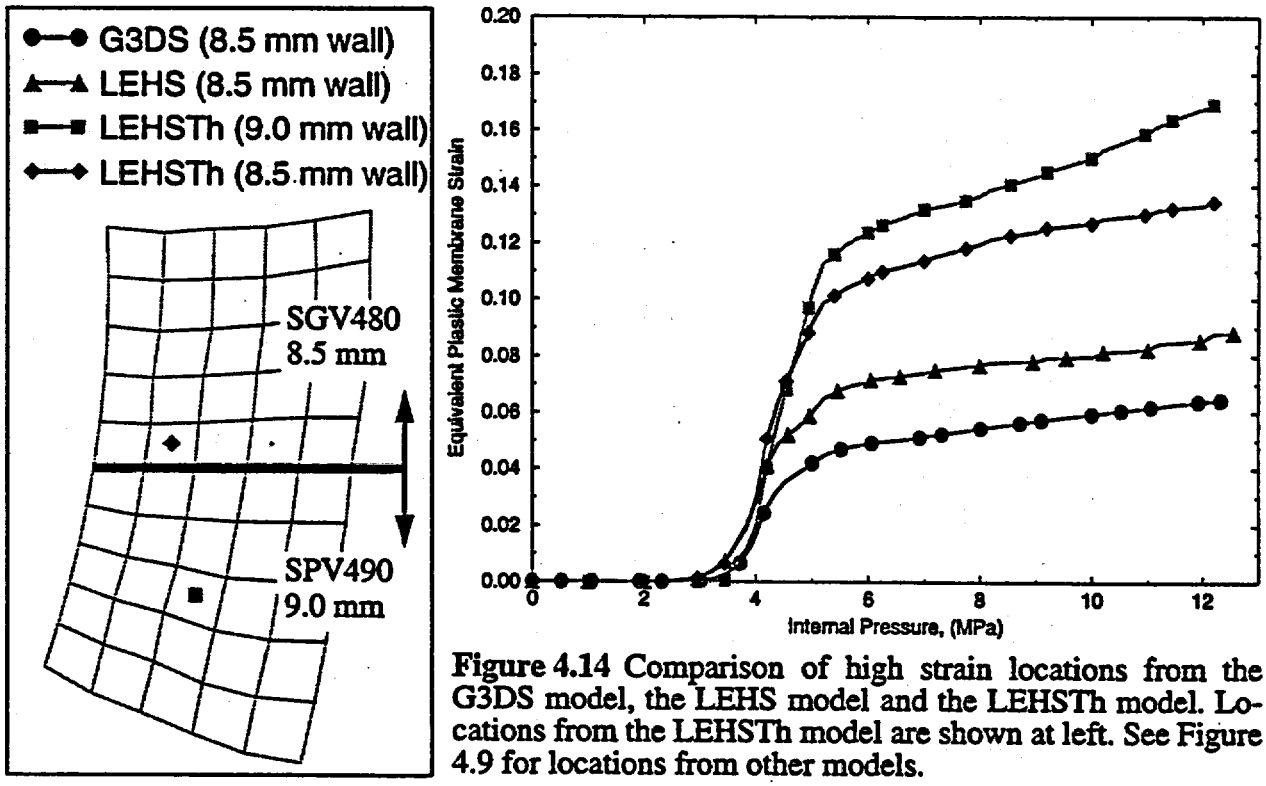

Figure 4.14 Comparison of high strain locations from the G3DS model, the LEHS model and the LEHSTh model. Locations from the LEHSTh model are shown at left. See Figure 4.9 for locations from other models.

5.1 Buckling

The G3DS model did show compressive strains in the torispherical head but they were not sufficient to cause buckling. To further investigate the potential for buckling simple closed-form solutions were used [10]. Equation 5.1 may be used to estimate the elastic buckling pressure of a torispherical head subjected to internal pressure,

$$\frac{P_B}{Y} = 285\left(1 - 125\frac{Y}{E}\right)\left(\frac{r}{D}\right)^{0.84}\left(\frac{t}{D}\right)^{1.53}\left(\frac{D}{L}\right)^{1.1} \quad \text{(EQ 5.1)}$$

while the plastic collapse pressure can be estimated by Equation 5.2:

$$\frac{P_C}{Y} = 12.6\left(1 + 240\frac{Y}{E}\right)\left(\frac{r}{D}\right)^{1.04}\left(\frac{t}{D}\right)^{1.09}\left(\frac{D}{L}\right)^{1.1}. \quad \text{(EQ 5.2)}$$

For these equations,

P_B = elastic buckling pressure,
P_C = plastic collapse pressure,
Y = yield strength (SGV480, 6 mm) = 405 MPa
E = elastic modulus (SGV480, 6mm) = 210 GPa,
D = inner diameter of adjoining cylinder = 965 mm,
L = inside radius at crown = 873 mm,
r = inside radius of knuckle = 166.7 mm,
t = thickness of head = 6 mm.

Both of these equations are valid in the ranges:

$.000667 < t/D < .002$,
$.06 < r/D < .018$, and
$.75 < L/D < 1.0$.

For the SCV scale model:

$t/D = .0062$ (out of the range),
$r/D = 0.17$ (near the upper limit), and
$L/D = 0.9$.

The t/D ratio is out of the specified range, but values for P_B and P_C can be calculated by using a thickness that falls within the range:

$$t/D = .002;\ t = .002D = 1.93 \text{ mm}.$$

Now,

$$P_B = 1.65 \text{ MPa}$$
$$P_C = 1.46 \text{ MPa}.$$

Since the actual thickness of the top head in the SCV scale model is more than three times the thickness used for these calculations it is reasonable to assume that the buckling pressure for the SCV will be significantly higher. Also, should buckling occur, it will most likely be a cosmetic failure only, since torispherical heads subjected to internal pressure can typically carry loads significantly higher than their critical buckling load.

5.2 Parameter Study - Coefficient of Friction

A parameter study was performed in which the frictional coefficient between the SCV and a rigid contact structure was varied from 0.0 (frictionless) to 0.5 in 0.1 increments [11]. Several axisymmetric finite element models were run and the displacements at the apex of the top head and at the elevation of the equipment hatch were studied. It was found that for all of the different cases with non-zero friction, the vertical displacement at the apex of the SCV did not vary significantly. The vertical displacement at the equipment hatch elevation also did not vary significantly with different values of μ. The only significant differences in vertical displacement at either location were evident when comparing the frictionless case to a non-frictionless case. For this reason, the nominal value of the friction coefficient used for all finite element analyses described here was taken to be $\mu = 0.2$.

6. CRITICAL LOCATIONS / FAILURE PREDICTIONS

Figure 6.1 shows a comparison of the critical areas from the finite element analyses. Only the results from two local models, the LEHSTh and LTHAXC models are shown. Also, in order to compare locations with differing material properties, the strains for each location were normalized by their true strain at maximum load from the Hitachi tensile tests. Therefore, a y-value of 1.0 corresponds to the strain at necking from that material's uniaxial tensile test. The raw data appeared (unnormalized) in Figure 4.12 and Figure 4.14.

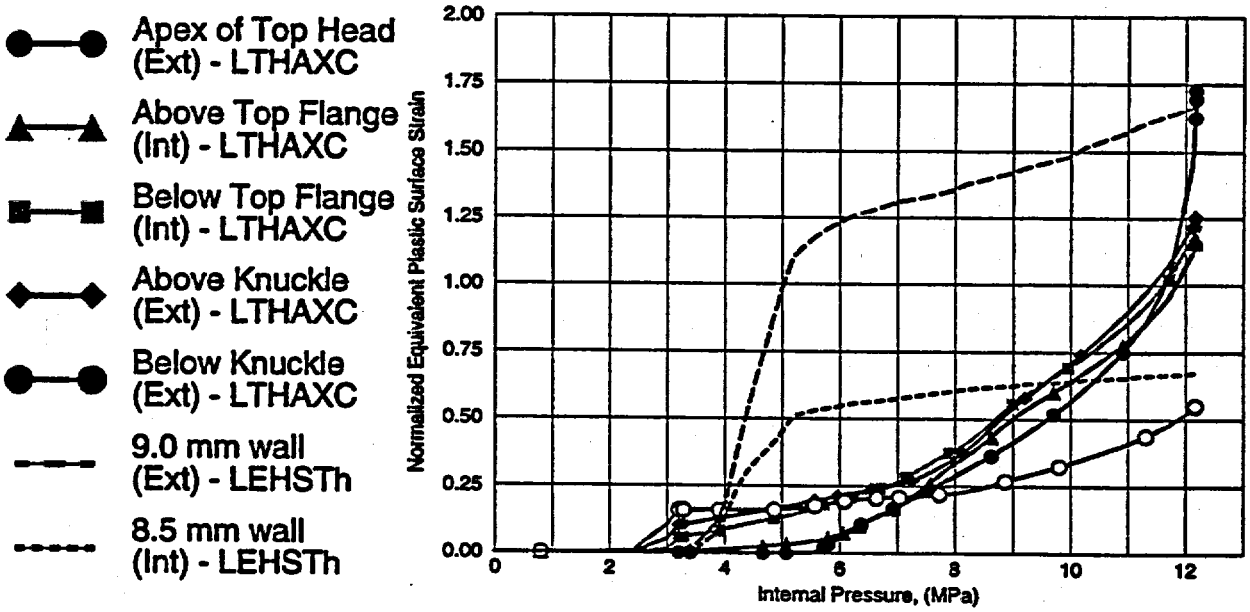

Figure 6.1 Normalized equivalent plastic strain from critical areas. Only critical areas from the local models are included since they are the most accurate. Strains have been normalized by each material's true strain at maximum load.

When the strains are normalized the primary candidate for failure location becomes clear: the 9.0 mm wall section just below the material interface and near the equipment hatch insert plate shown by the long dashes in Figure 6.1. The main reason that this particular location stands out is the difference in the ductility between the SPV490 steel and the SGV480 steel. The true strain at maximum load for the SPV490 material is approximately 10%; the true strain at maximum load for the SGV480 material is approximately 20%. Thus, the SPV490 material in the thinned section (9.0 mm nominal thickness, lower conical section) at an internal pressure of 5 MPa has reached a plastic strain that in the uniaxial-stress tensile test led to necking.

Continued deformation in the thinned section is "displacement controlled." That is, the boundary around the plastic domain in the thinned section appears to the adjacent thicker stiffer elastic sections as a "cut out" or opening with a nominally fixed membrane load. Further increases in internal pressure cause the boundary around the thin section to expand similarly to the way an unreinforced cut out or opening in a pressure vessel expands. The expansion of the opening imposes additional strain on the yielding thinned section.

While the shell element mesh used in the LEHSTh model has some ability to represent locally accelerated thinning, it does not have the refinement necessary to track the strain localization on the length scale exhibited in the tensile test. The nature of the strain state, biaxial tension, is also important for failure prediction. The analysis indicates that the total strain in the thinned section is very nearly equal in two directions (circumferential and radial directions with respect to the edge of the equipment hatch insert plate edge). Although a forming limit diagram for this material is not available, examination of a typical forming limit diagram in Figure 6.2 shows the differences between the load path for a tensile test and the load path for the area under consideration (equal biaxial strain). In a typical tensile test, necking occurs at "2n", where n is the strain-hardening exponent, while equal biaxial extension produces a neck at "1.3n". Thus, one can expect that

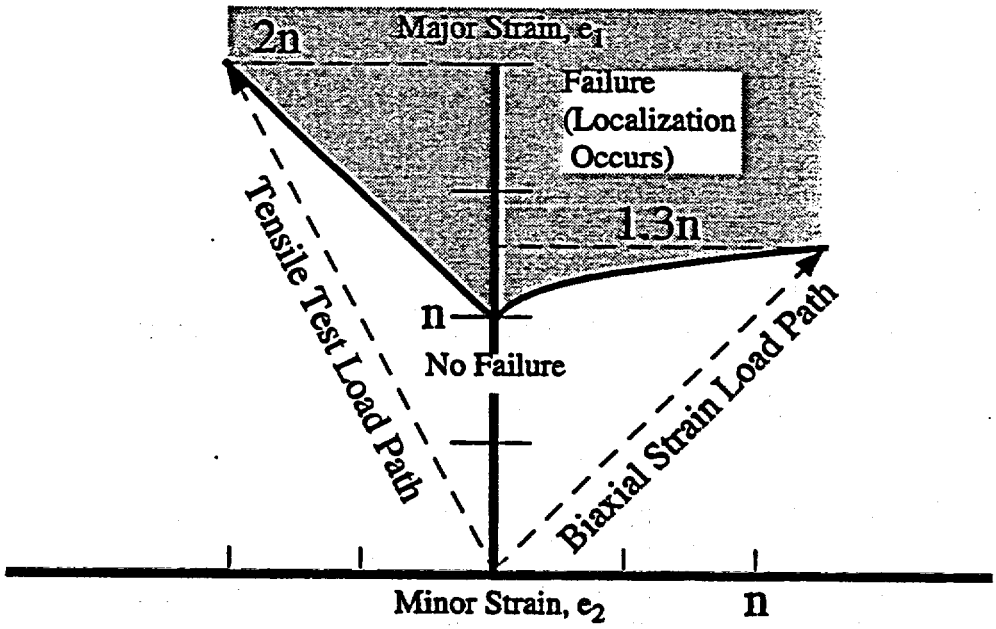

Figure 6.2 Typical forming limit diagram for low carbon steels. The strains below the curve are acceptable while those above the curve correspond to regions affected by local necking. Note the differences in major strain values between a tensile test load path and a biaxial strain load path [12].

significant localization of plastic flow with attendant tearing will occur in the thinned section when the normalized value of effective plastic strain in reaches (1.3/2.0) = 0.65 or 65% of the necking strain from the tensile test. In Figure 6.1 this corresponds to approximately 4.5 MPa internal pressure.

6.1 FAILURE LOCATION

Given the early and rapid occurrence of plastic flow compared to other locations within the pressure vessel, and the strains attained relative to the material's ductility, it is expected that failure of the pressure vessel will occur in the thinned section next to the equipment hatch insert plate.

6.2 FAILURE PRESSURE

Given the biaxial tension strain state , the strain localization characteristics exhibited by the plate material, and the involvement of weld and heat affected zone (HAZ) material, it is expected that ductile rupture of the pressure vessel will occur at or shortly after reaching an internal pressure of 4.5 MPa.

An early failure at this or another location due to the presence of welding flaws or inclusions cannot be ruled out since there are at the same time states of stress producing plastic flow in at least 4 other locations in the pressure vessel (primarily the top head and knuckle regions). The weld metal and HAZ near the thinned areas introduce additional uncertainty. The yield strength and ductility of the weld metal is typically higher than the parent material, while the same properties in the HAZ are typically lower than the parent material. Brittle failure modes have not been considered in this analysis effort.

7. ANALYSIS SUMMARY & CONCLUSIONS

Five different finite element analyses have been performed in an effort to characterize the structural behavior of a steel containment model subjected to static overpressurization. The models are summarized in Table 7.1.

7.1 First Yield / First Contact Prediction

Comparing the results of all analyses indicates that first yield will occur at 2.0 MPa in the knuckle. The analyses results also show that first contact will occur at 3.2 MPa in the knuckle.

7.2 Failure Prediction

The G3DS model, a global model which included the equipment hatch, showed two areas which dictated further study: 1) the area near the equipment hatch insert plate/material change interface junction; 2) the top head region, including the knuckle. Two additional local models were created to study these locations.

The first model, a local model which takes advantage of the new *SUBMODEL option in ABAQUS, modeled only the equipment hatch insert plate, parts of the middle and lower conical sections, and the contact structure. The results of this model, which are shown with the results of the G3DS model for the same location in Figure 4.9, indicate an increase in strain as much as 50% from the G3DS model to the LEHS model. The element shown for both models is in the middle conical section (8.5 mm thick nominally) adjacent to both the equipment hatch insert plate and the lower conical section (9.0 mm thick nominally).

The second model, an axisymmetric continuum model, included the top head from the apex down the upper 19 mm stiffener. This model, which was originally intended to study the behavior of the knuckle and the apex of the top head, also suggested other potential failure areas immediately above and below the top head flange. The results for this model, shown in Figure 4.12, indicate 5 competing areas for failure: the apex of the top head; the interior surface of the top head immediately above and below the top head flange; and at the exterior surface immediately above and below the knuckle.

After reviewing thickness measurements of the SCV in the area near the equipment hatch insert plate/material change interface, it was decided that one additional analysis would be performed. This analysis was a modification of the LEHS model where the measured thicknesses, which

Table 7.1: Summary of Pre-test Analyses

			First Yield		First Contact	
Model	Purpose	Analysis type/ Elements	Location	Pressure	Location	Pressure
GAX18	Study global behavior	Axisymmetric/ 1500 shell/continuum elements	Knuckle	2.2 MPa	Knuckle/ upper conical section	4.0 MPa
GAX34	Study global behavior with worst case gap dimension of 34 mm	Axisymmetric/ 1500 shell / continuum elements	Knuckle	2.2 MPa	Knuckle/ upper conical section	4.0 MPa
G3DS	Study global behavior with equipment hatch	3-Dimensional/ 4800 shell elements	E/H sleeve at attachment to insert plate	2.3 MPa	Knuckle/ upper conical section	4.1 MPa
LEHS	Study local behavior near equipment hatch insert plate and material change interface	3-Dimensional/ 4800 shell elements	MCS adjacent to insert plate	2.6 MPa	Middle Conical Section	4.2 MPa
LTHAXC	Study local behavior at top head and knuckle; include latest contact structure design	Axisymmetric/ 7200 continuum elements	Knuckle	2.0 MPa	Knuckle	3.2 MPa
LEHSTh	Study effect of thinned area near equipment hatch insert plate and material change interface	3-Dimensional/ 4800 shell elements	Above thinned section adjacent to insert plate	2.2 MPa	Middle Conical Section	4.2 MPa

ranged from 5% increase in the nominal thickness to 22% thinner near the weld at the material change interface near the insert plate, were incorporated into the finite element model using the ABAQUS *NODAL THICKNESS option.

Results of this analysis, when compared with the previous submodel for this area (LEHS) and the global model (G3DS) indicate a significant increase in strain and also suggest that the critical location has shifted from the 8.5 mm nominal thickness middle conical section to the 9.0 mm nominal thickness lower conical section. In Figure 6.1, the ductility of each different material is taken into account by normalizing each material's equivalent plastic strain by the true strain at maximum load from its corresponding tensile test. The forming limit diagram in Figure 6.2 indicates that the material under consideration may neck prior to the strain at which necking occurred in the uniaxial tensile test. When taking all of this into consideration, it is expected that ductile rupture of the pressure vessel will occur at or shortly after reaching an internal pressure of 4.5 MPa in the area just below the weld line in the lower conical section at the material change interface adjacent to the equipment hatch insert plate (the location is indicated by the small square in the SPV490/9.0 mm material in Figure 4.14).

8. ACKNOWLEDGMENT

The authors would like to thank Vicki Porter, Gerald Wellman, and Harold Morgan for their technical assistance.

9. REFERENCES

[1] ABAQUS, Version 5.5, Hibbitt, Karlsson, and Sorenson, Inc., Pawtucket, RI, 1994.

[2] Branstetter, L. J., Attachment to Round Robin Letter, July 10, 1995.

[3] Dieter, G. E., *Mechanical Metallurgy*, Third Edition, McGraw-Hill Book Co., New York, N.Y., 1986.

[4] *MATLAB Reference Guide*, Version 4.2, The Mathworks, Inc., Natick, MA, 1992.

[5] Stone, C. M., Wellman, G. W., Krieg, R. D., *A Vectorized Elastic/Plastic Power Law Hardening Material Model Including Luders Strain*, SAND90-0153, 1990.

[6] Stone, C. M., *SANTOS: A Two Dimensional Finite Element Program for the Quasistatic, Large Deformation, Inelastic Response of Solids*, SAND90-0543, 1997.

[7] Structural Alloys Handbook, ed. by Hucek, H. J., Volume I, Batelle's Columbus Laboratories, Columbus, OH, 1985.

[8] Carter, P. A., "Eccentricity Test Case", Sandia memorandum to V. K. Luk and M. F. Hessheimer, July 17, 1995.

[9] Hessheimer, M. F., Letter to Round Robin Participants dated February 20, 1996.

[10] Kalnins, A., Updike D. P., "New Design Curves for Torispherical Heads," Welding Research Council Bulletin, Bulletin 364, New York, June 1991.

[11] Porter, V. L., "Further Investigation of Friction Effects for Shielded SCV Model," Sandia memorandum to V. K. Luk, May 4, 1994.

[12] Hosford, W. F., Caddell, R. M., *METAL FORMING: Mechanics and Metallurgy*, Prentice-Hall, Inc. Englewood Cliffs, N. J., 1983.

10. APPENDIX OF STANDARD PLOTS

These plots are provided for comparison to results obtained by other investigators. The prescribed analysis parameters and locations are described in the original Round Robin package dated July 10, 1995 issued by the International Nuclear Safety Department at Sandia National Laboratories. Some output locations were updated later in a memorandum dated May 9, 1996. The results presented here were obtained from three models: the G3DS model, the LEHSTh model, and the LTHAXC model. Results from the local models, LEHSTh and LTHAXC, were used for locations that were contained within the domain of these models since the local models provided the most accurate results in these areas. For requested output locations outside the boundaries of the local models, the global G3DS model was used.

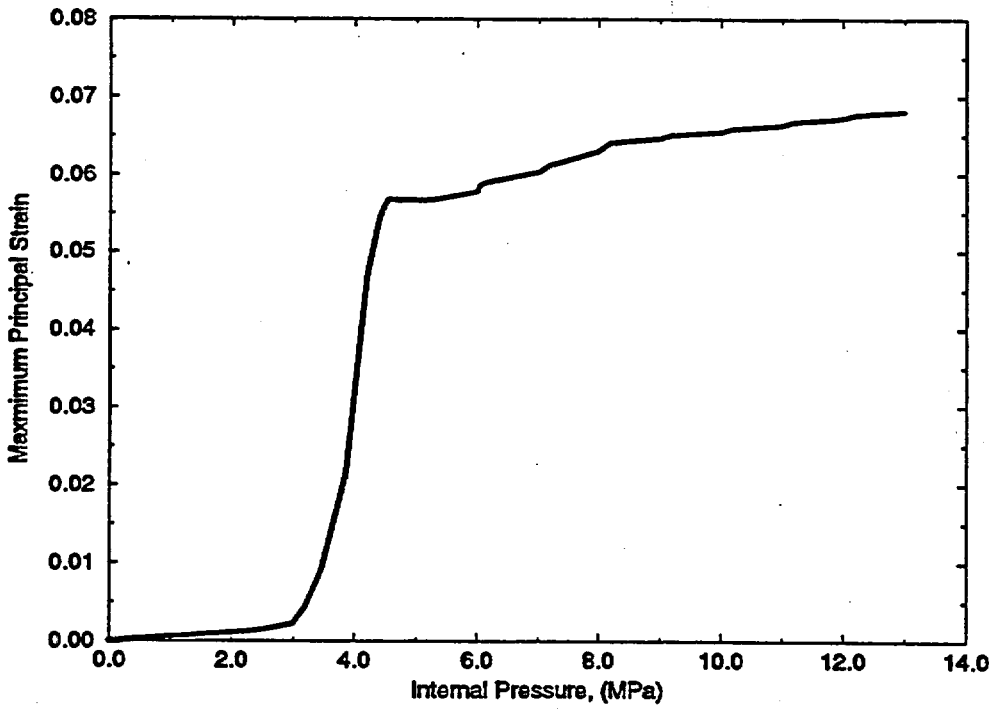

Plot 1: Maximum principal strain versus internal pressure for an element located near the equipment hatch insert plate at (67.5 degrees, 0.36 m) in the equipment hatch coordinate system (Model: LEHSTh).

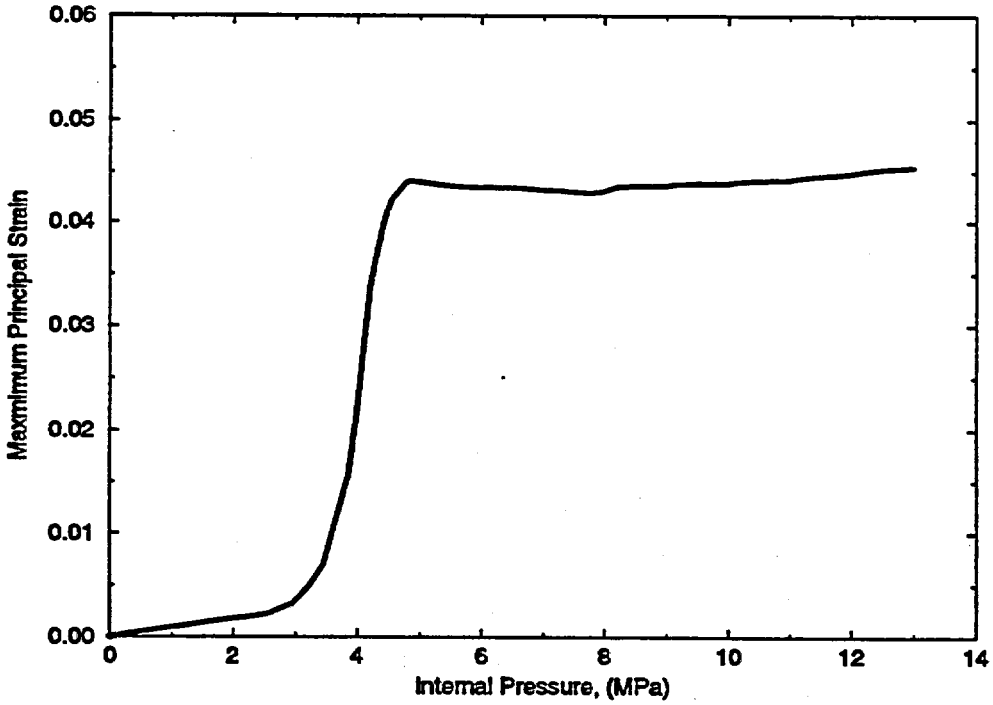

Plot 2: Maximum principal strain versus internal pressure for an element located near the equipment hatch insert plate at (45 degrees, 0.36 m) in the equipment hatch coordinate system (Model: LEHSTh).

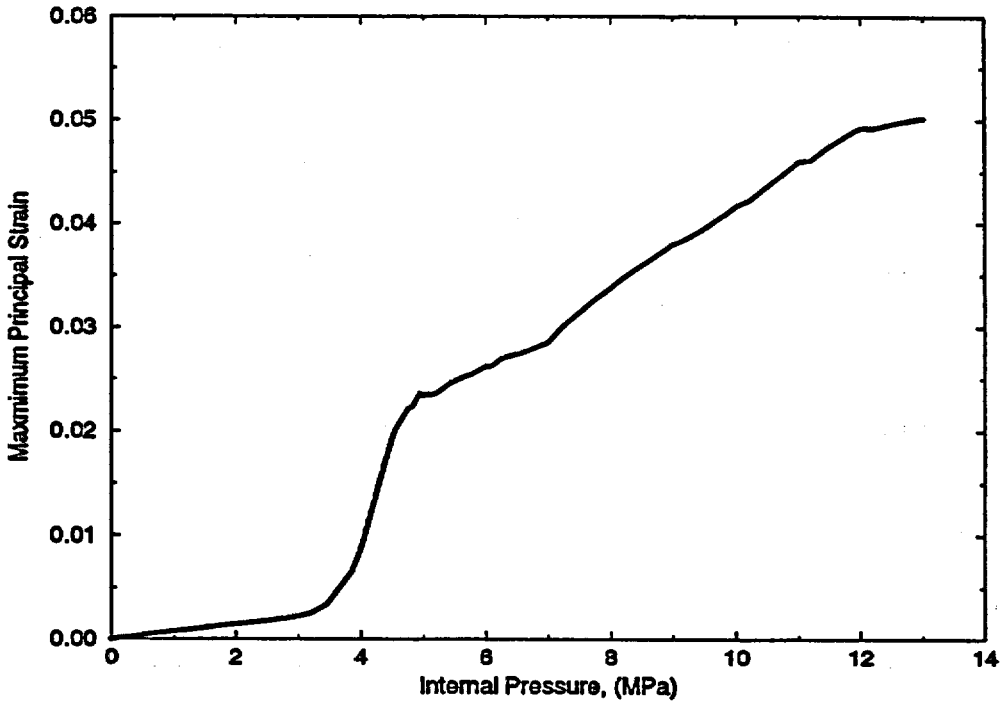

Plot 1: Maximum principal strain versus internal pressure for an element located near the equipment hatch insert plate at (67.5 degrees, 0.36 m) in the equipment hatch coordinate system (Model: LEHSTh).

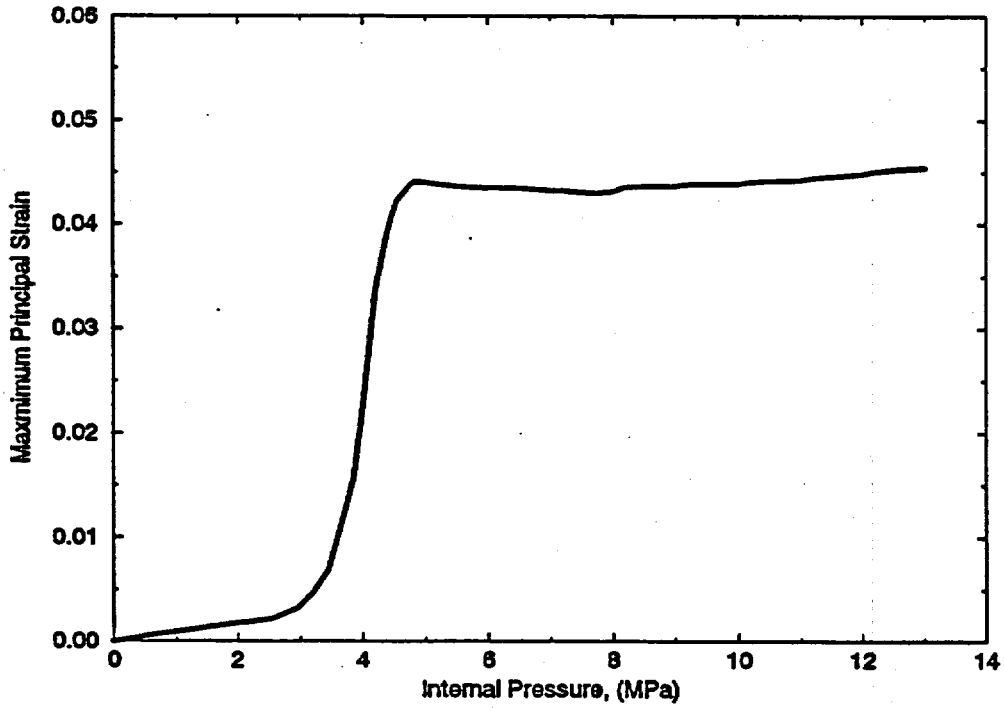

Plot 2: Maximum principal strain versus internal pressure for an element located near the equipment hatch insert plate at (45 degrees, 0.36 m) in the equipment hatch coordinate system (Model: LEHSTh).

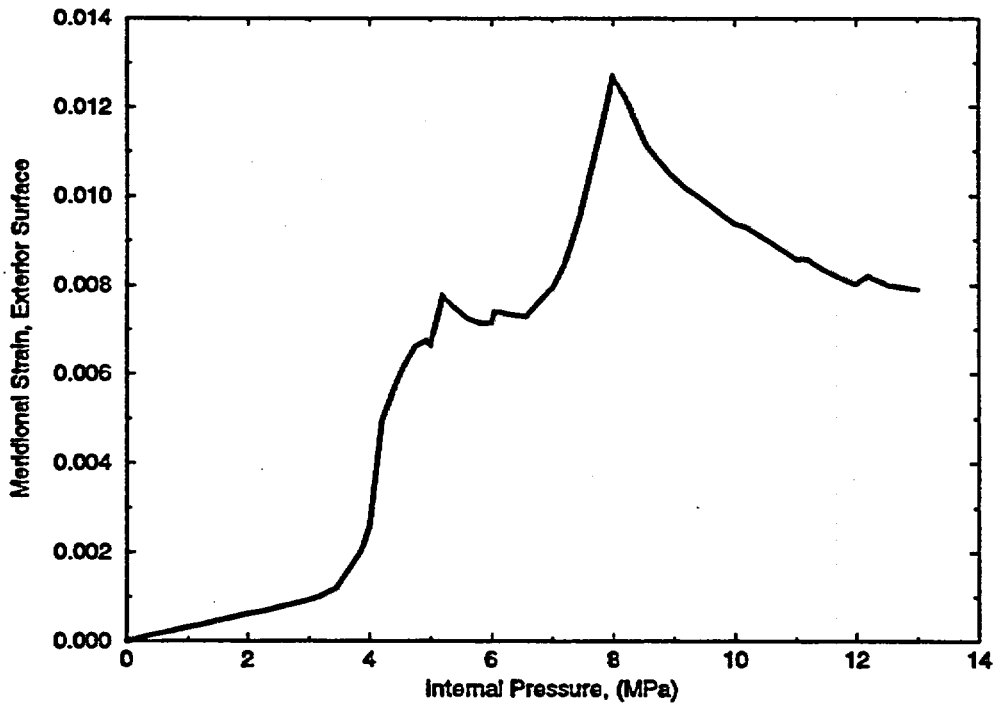

Plot 3: Exterior surface meridional strain versus internal pressure for an element located near the equipment hatch insert plate at (0 degrees, 0.36 m) in the equipment hatch coordinate system (Model: LEHSTh).

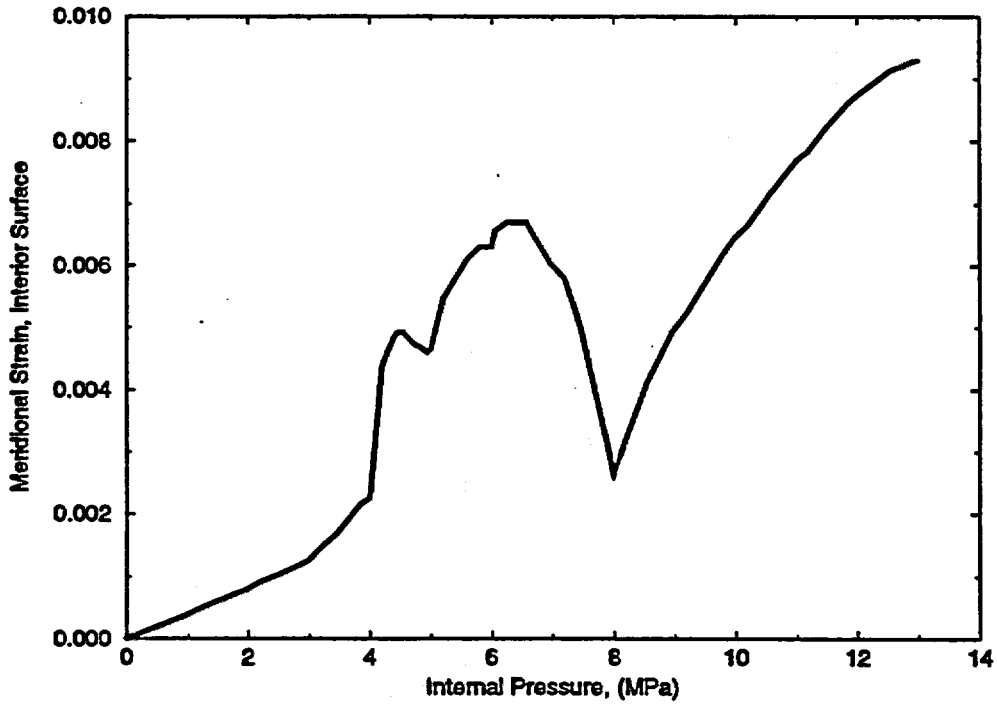

Plot 4: Interior surface meridional strain versus internal pressure for an element located near the equipment hatch insert plate at (0 degrees, 0.36 m) in the equipment hatch coordinate system (Model: LEHSTh).

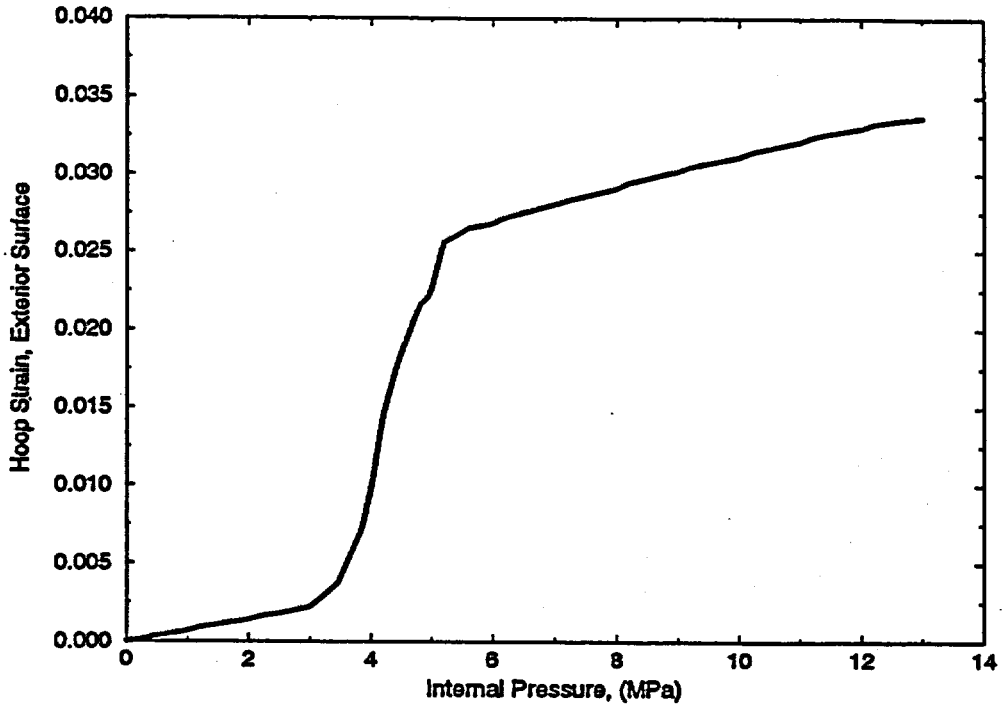

Plot 5: Exterior surface hoop strain versus internal pressure for an element located near the equipment hatch insert plate at (90 degrees, 0.36 m) in the equipment hatch coordinate system (Model: LEHSTh).

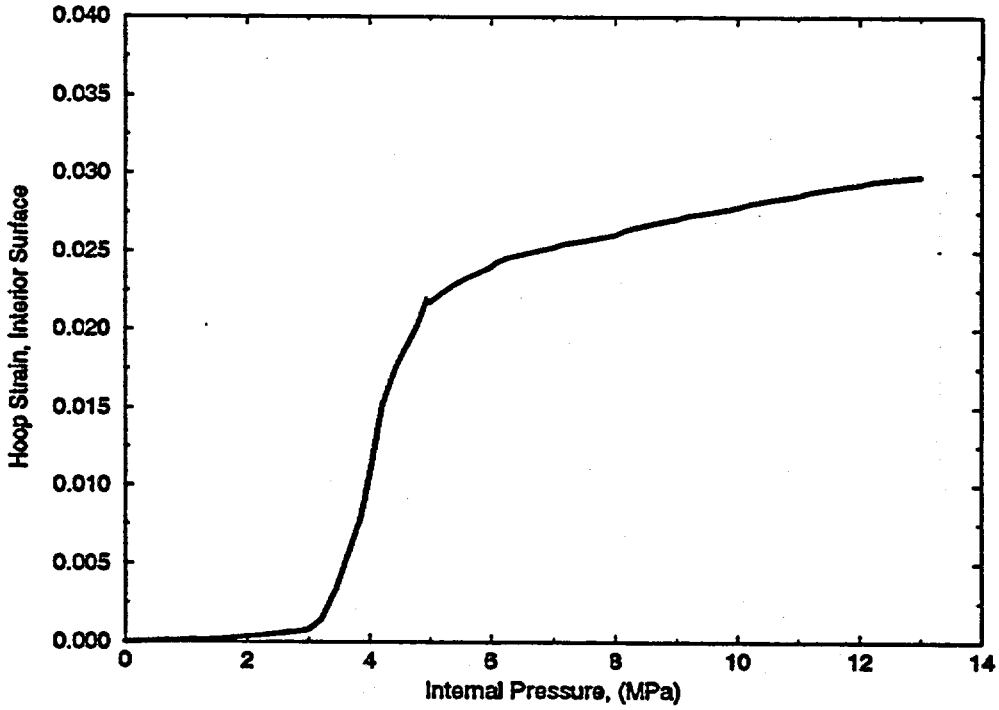

Plot 6: Interior surface hoop strain versus internal pressure for an element located near the equipment hatch insert plate at (90 degrees, 0.36 m) in the equipment hatch coordinate system (Model: LEHSTh).

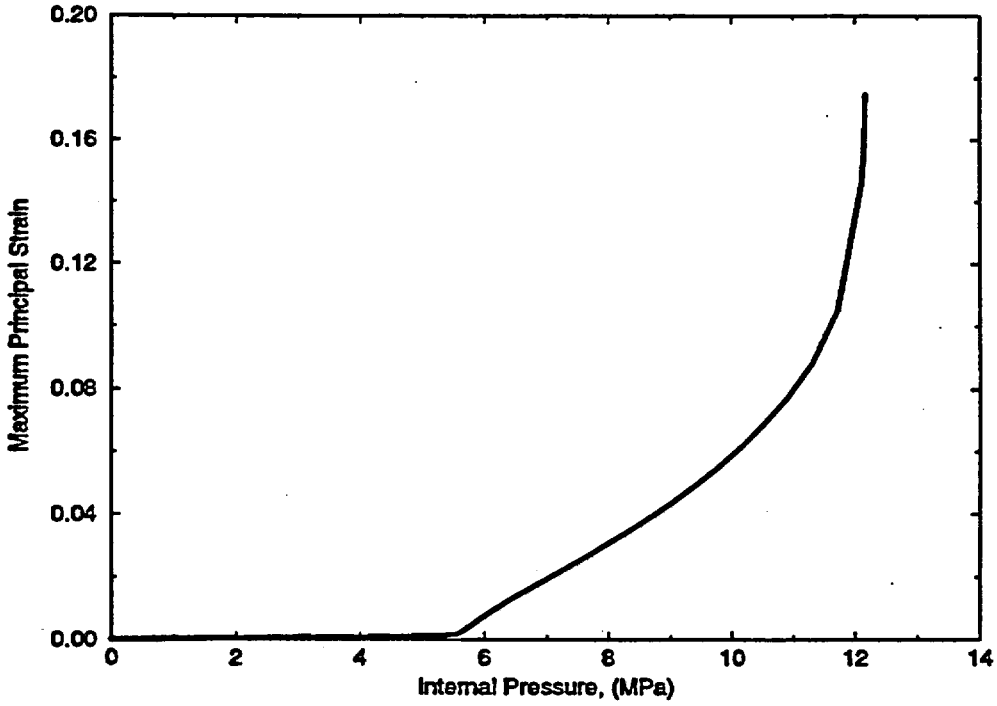

Plot 7: Maximum principal strain versus internal pressure for an element located at top head apex (Model: LTHAXC).

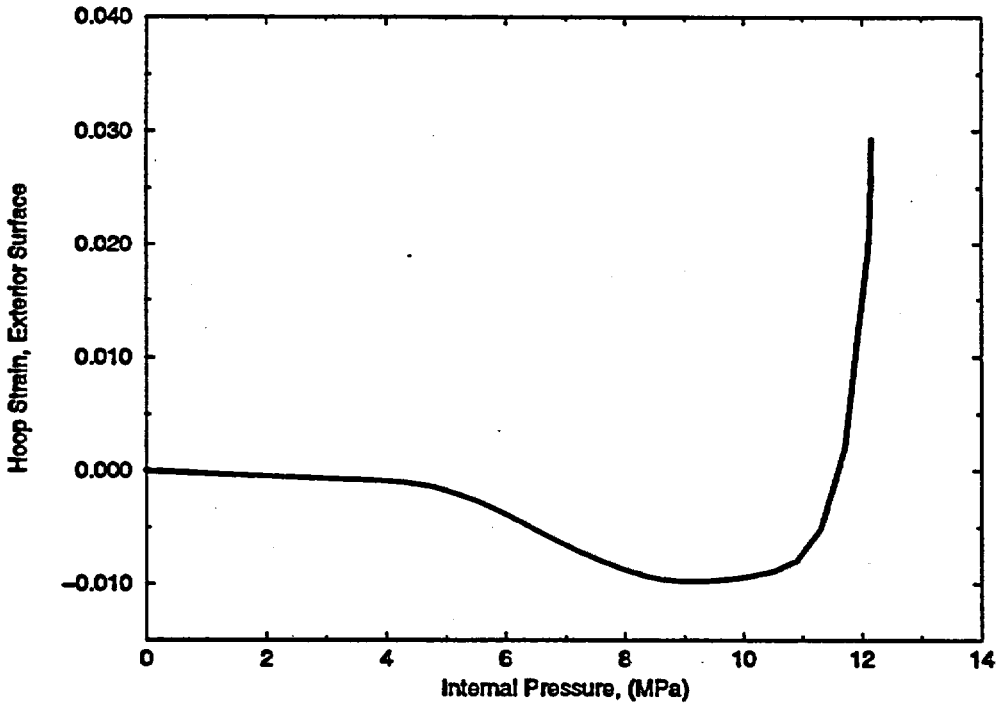

Plot 8: Exterior surface hoop strain versus internal pressure for an element located at (270 degrees, 0.48 m) in the top head coordinate system (Model: LTHAXC).

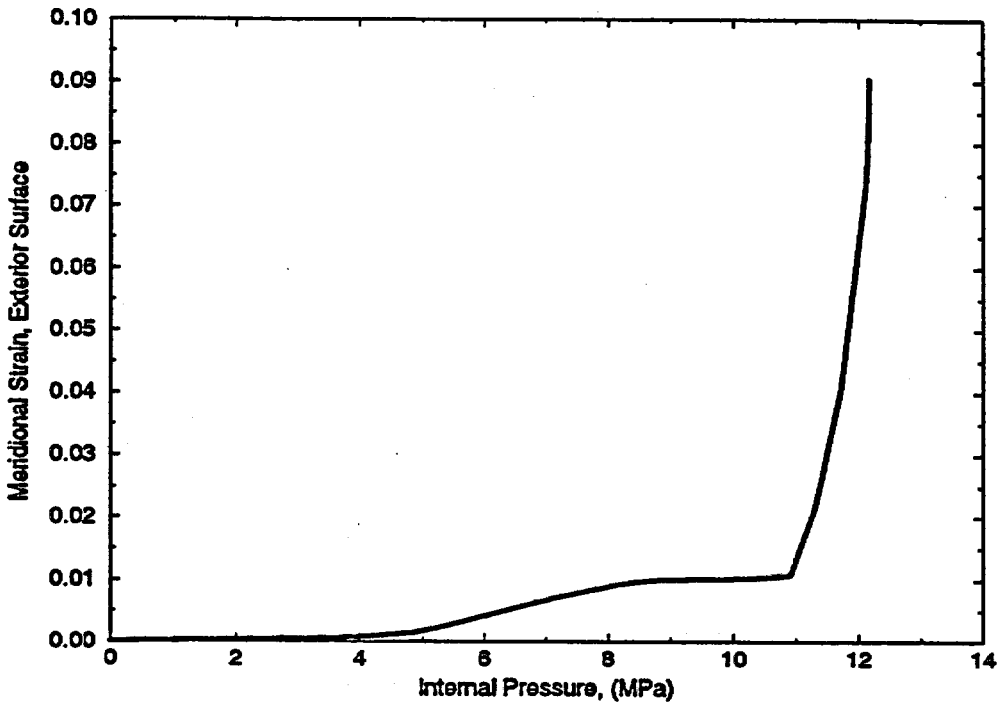

Plot 9: Exterior surface meridional strain versus internal pressure for an element located at (270 degrees, 0.48 m) in the top head coordinate system (Model: LTHAXC).

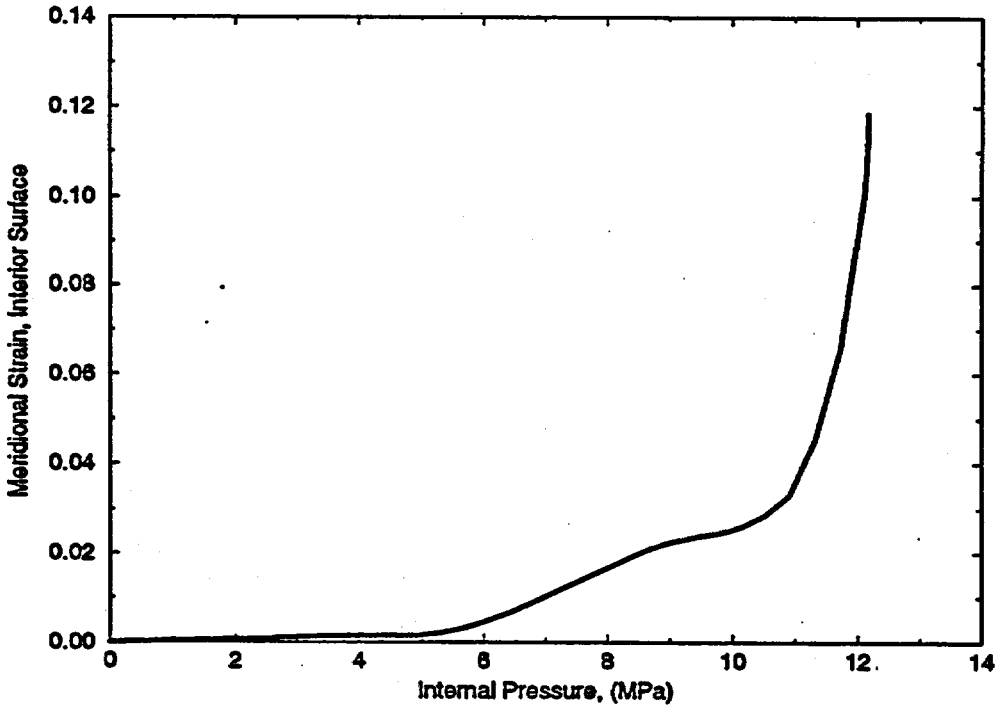

Plot 10: Interior surface meridional strain versus internal pressure for an element located at (270 degrees, 0.48 m) in the top head coordinate system (Model: LTHAXC).

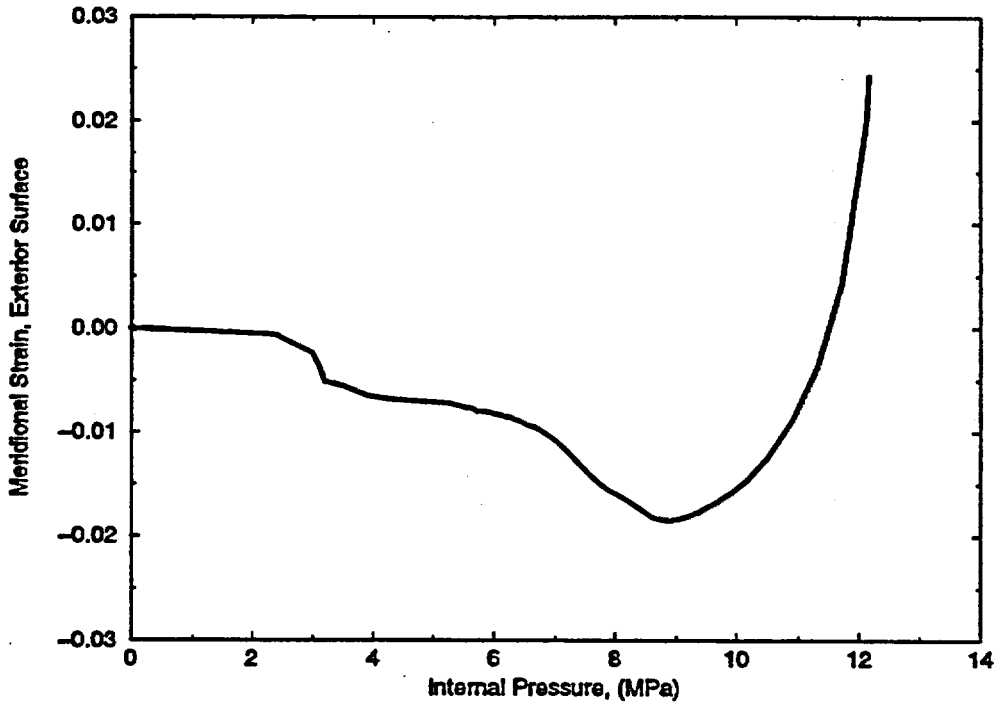

Plot 11: Exterior surface meridional strain versus internal pressure for an element located just below the top flange at (0 degrees, 3.47 m) in the global coordinate system (Model: LTHAXC).

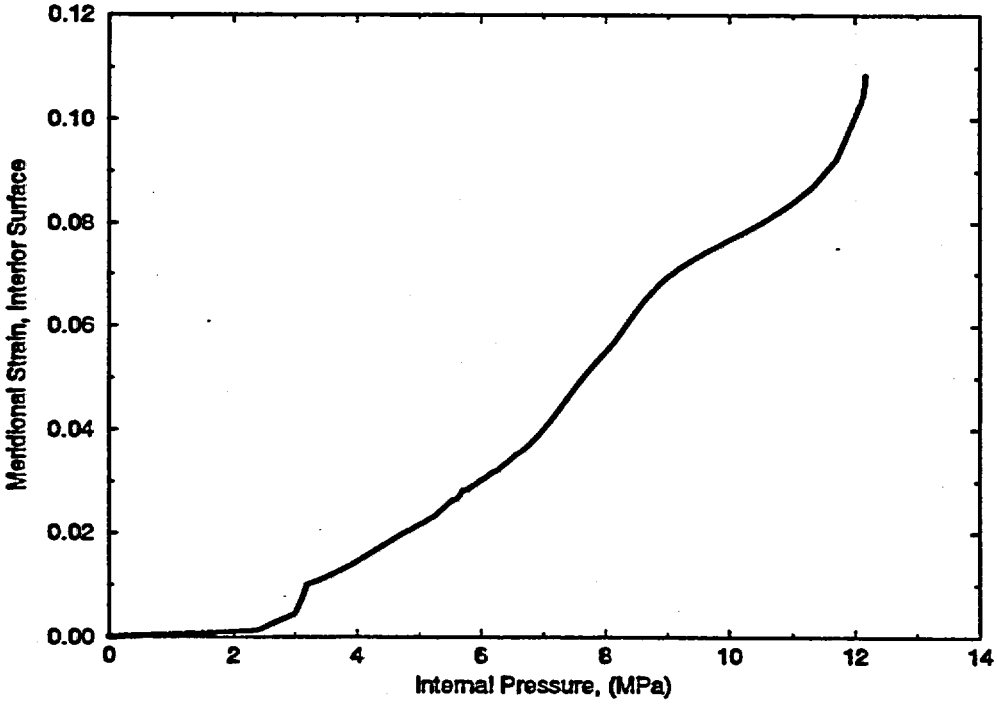

Plot 12: Interior surface meridional strain versus internal pressure for an element located just below the top flange at (0 degrees, 3.47 m) in the global coordinate system (Model: LTHAXC).

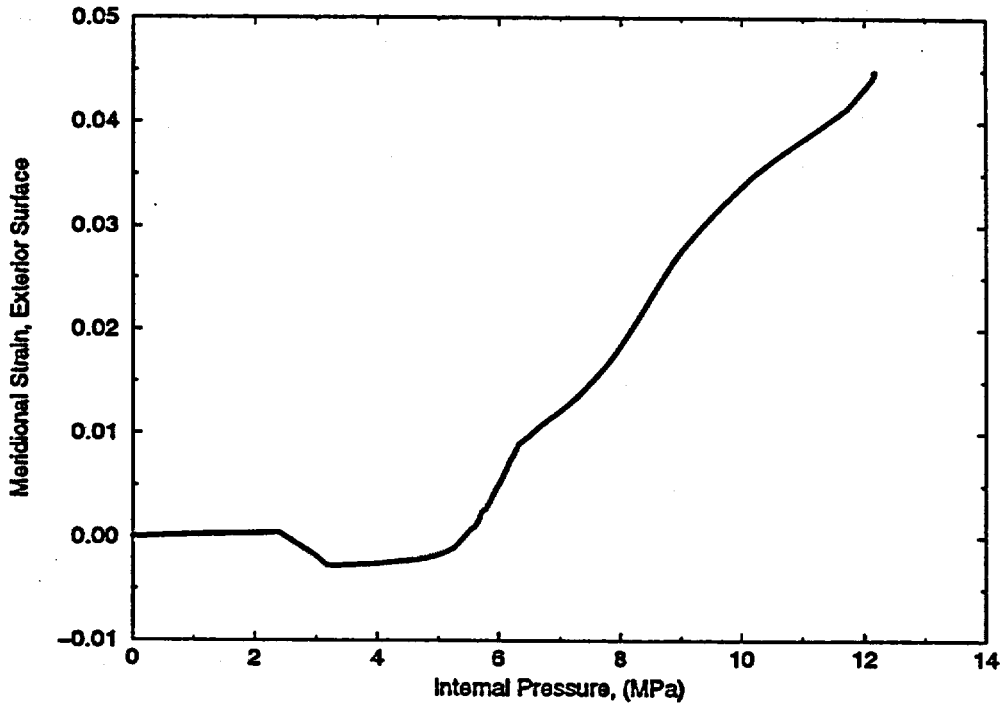

Plot 13: Exterior surface meridional strain versus internal pressure for an element located just below the knuckle at (0 degrees, 3.32 m) in the global coordinate system (Model: LTHAXC).

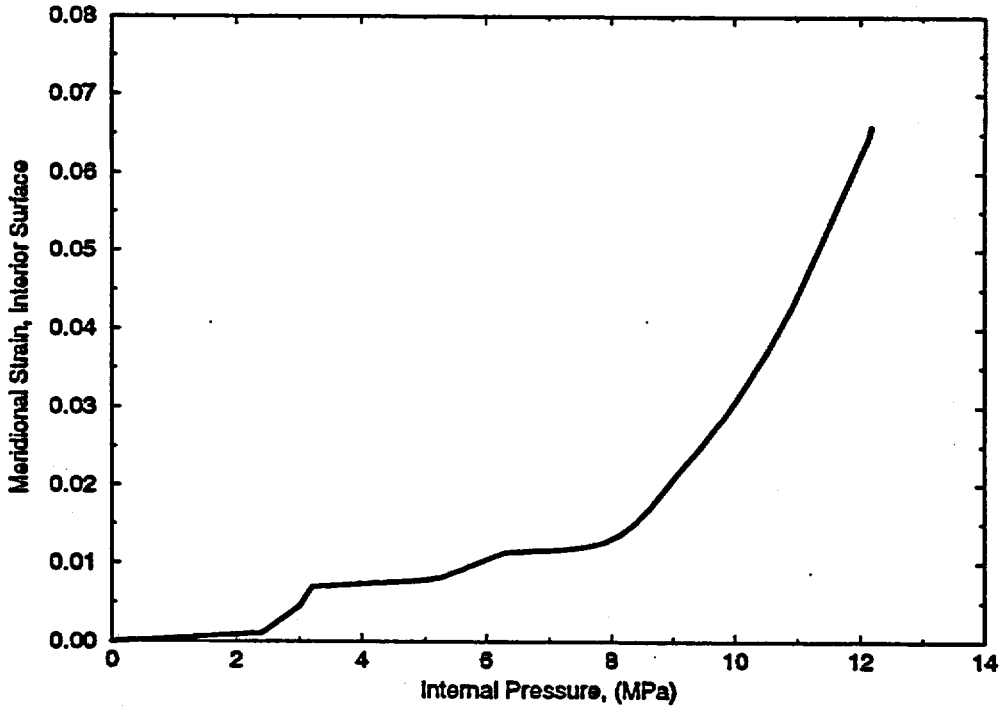

Plot 14: Interior surface meridional strain versus internal pressure for an element located just below the knuckle at (0 degrees, 3.32 m) in the global coordinate system (Model: LTHAXC).

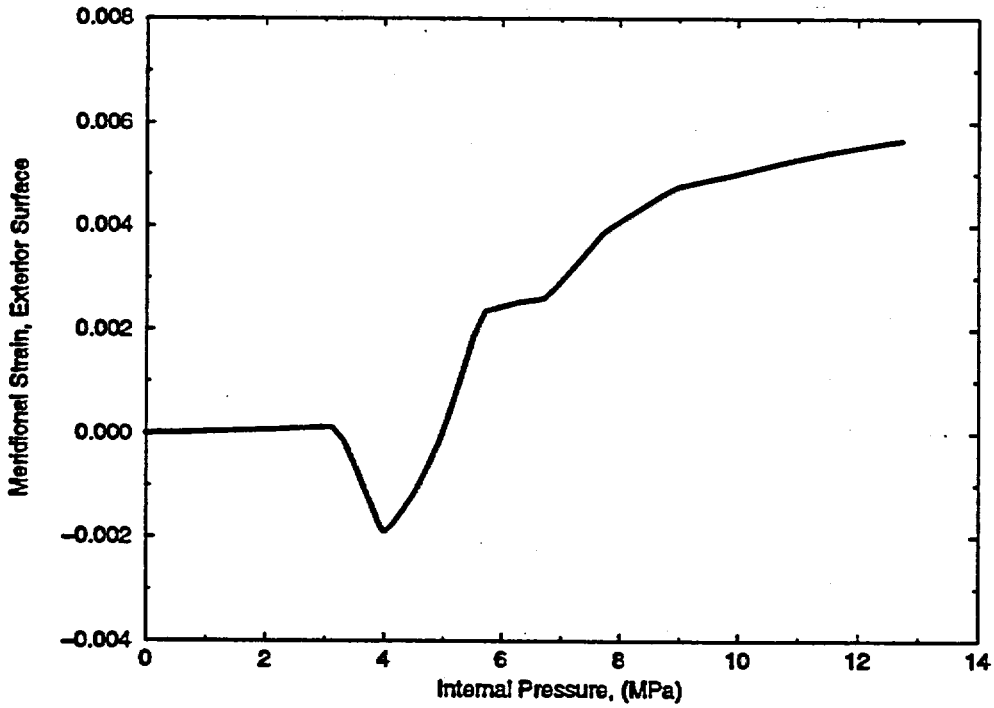

Plot 15: Exterior surface meridional strain versus internal pressure for an element located just above the middle stiffener at (0 degrees, 2.10 m) in the global coordinate system (Model: G3DS).

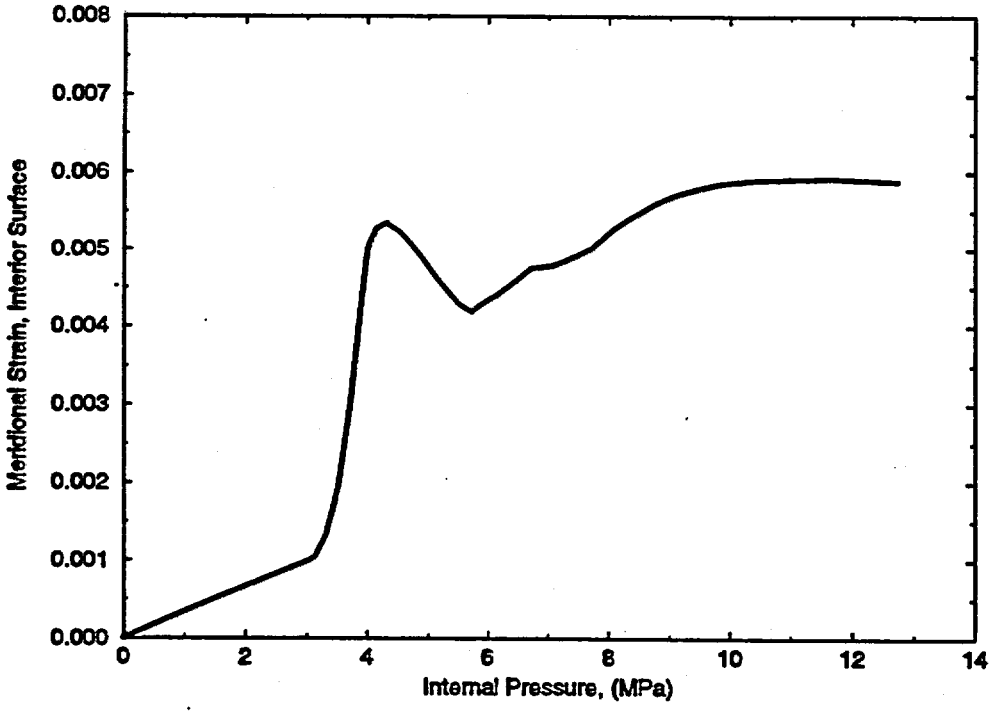

Plot 16: Interior surface meridional strain versus internal pressure for an element located just above the middle stiffener at (0 degrees, 2.10 m) in the global coordinate system (Model: G3DS).

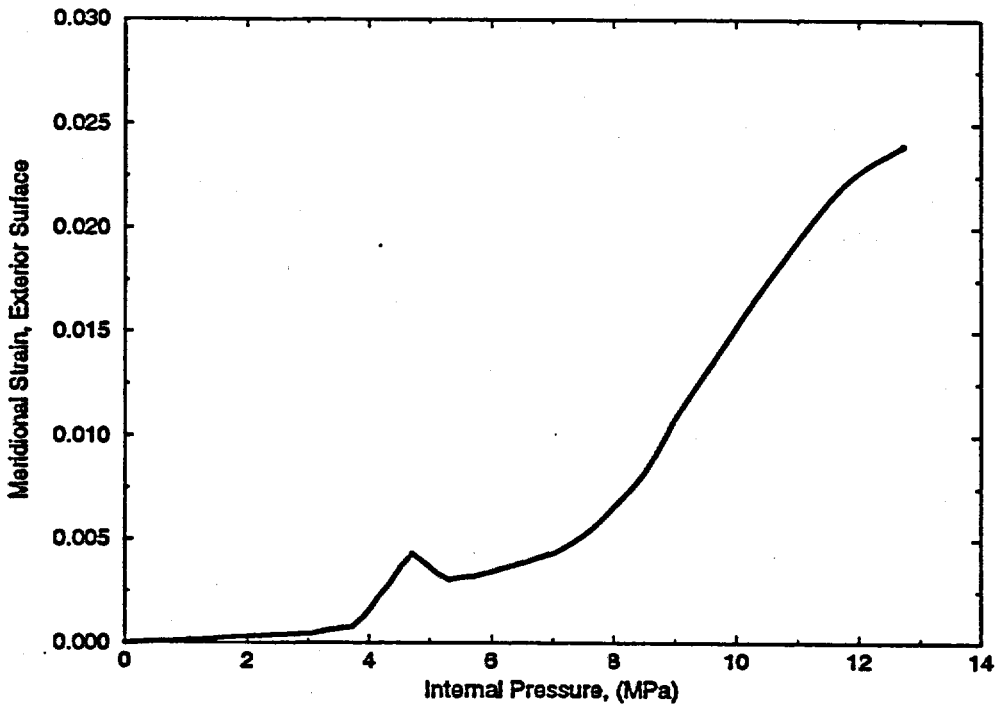

Plot 17: Exterior surface meridional strain versus internal pressure for an element located just above the material change interface at (0 degrees, 1.60 m) in the global coordinate system (Model: G3DS).

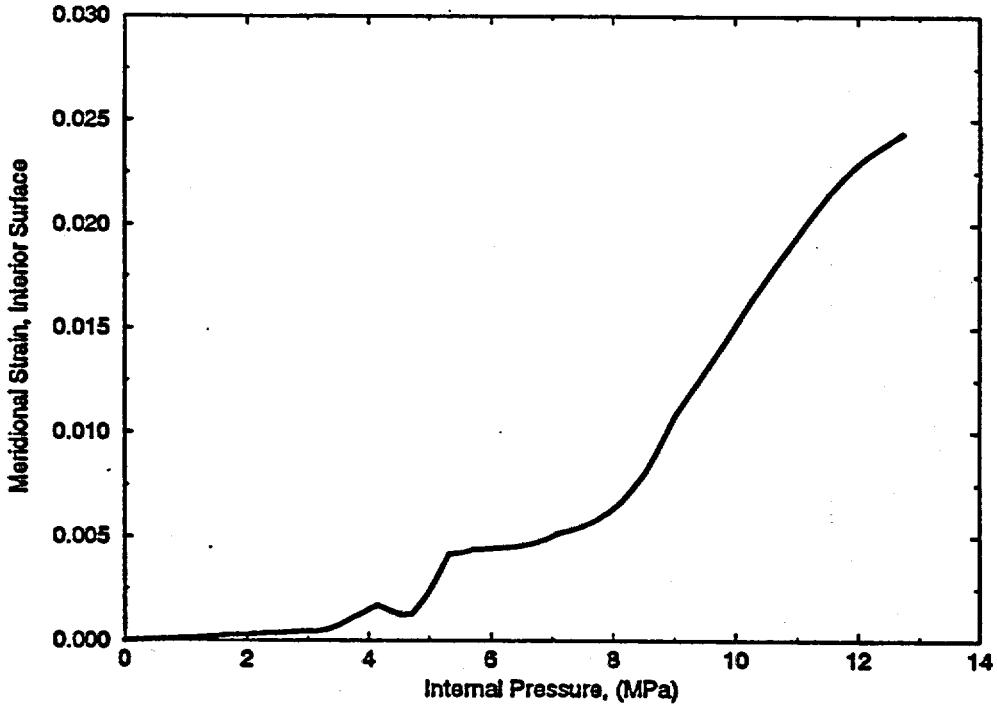

Plot 18: Interior surface meridional strain versus internal pressure for an element located just above the material change interface at (0 degrees, 1.60 m) in the global coordinate system (Model: G3DS).

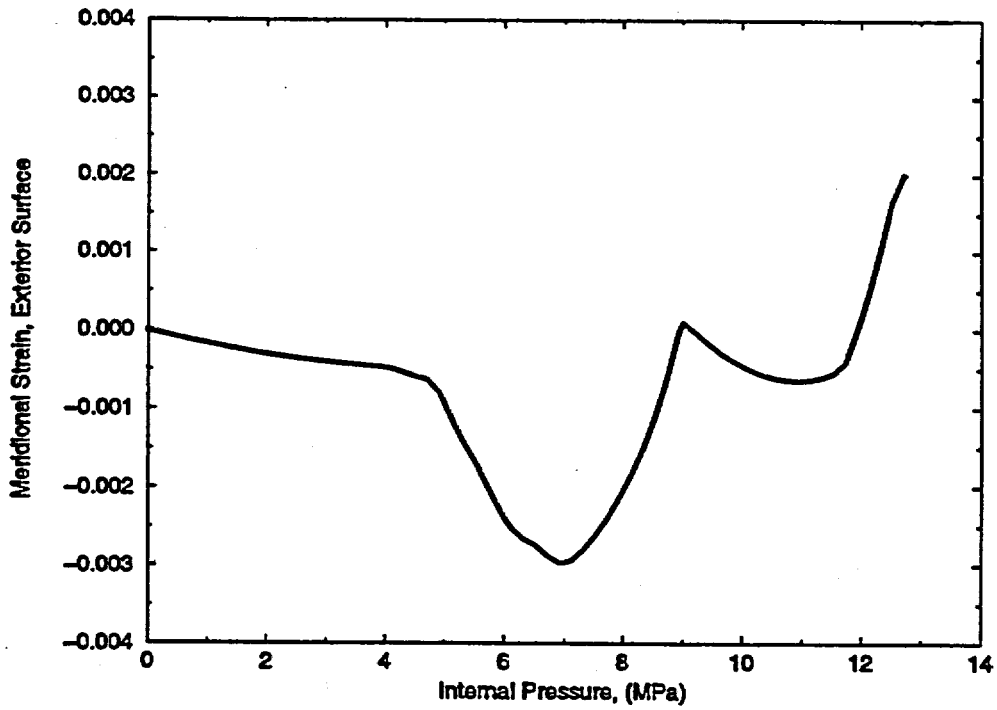

Plot 19: Exterior surface meridional strain versus internal pressure for an element located just below the lower pair of stiffeners at (0 degrees, 0.80 m) in the global coordinate system (Model: G3DS).

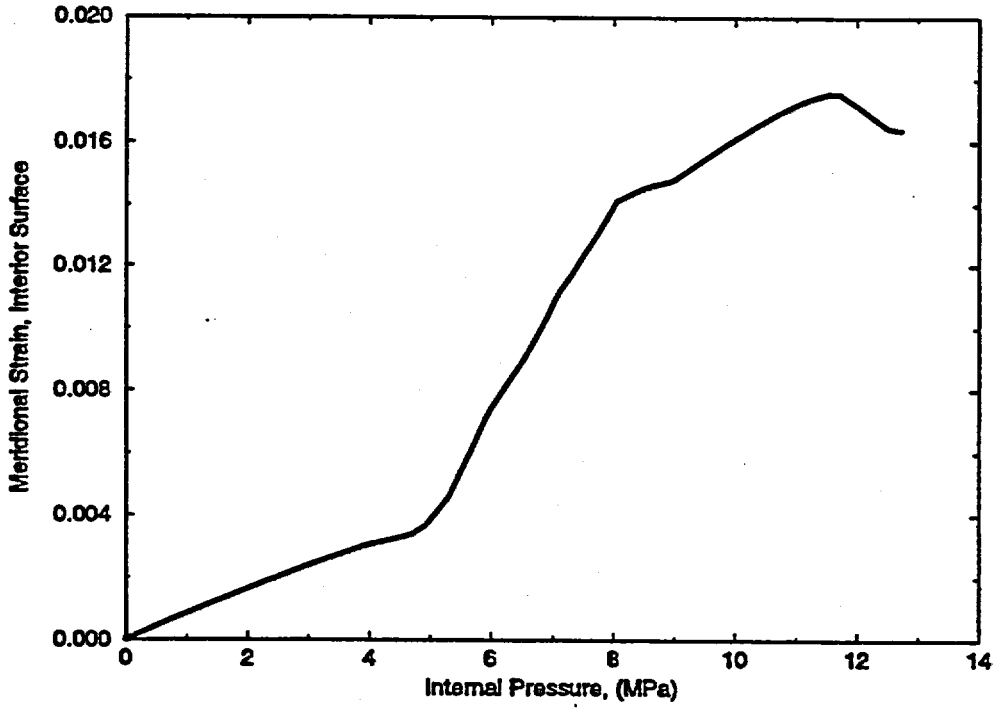

Plot 20: Interior surface meridional strain versus internal pressure for an element located just below the lower pair of stiffeners at (0 degrees, 0.80 m) in the global coordinate system (Model: G3DS).

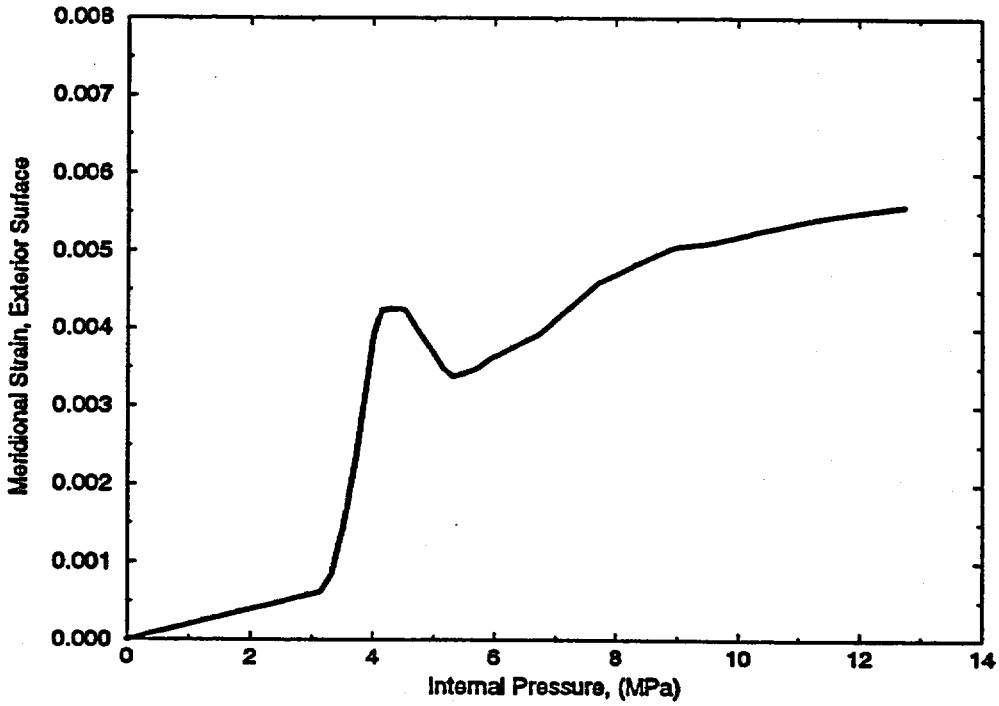

Plot 21: Exterior surface meridional strain versus internal pressure for an element located at the mid-height of the upper conical shell at (45 degrees, 2.49 m) in the global coordinate system (Model: G3DS).

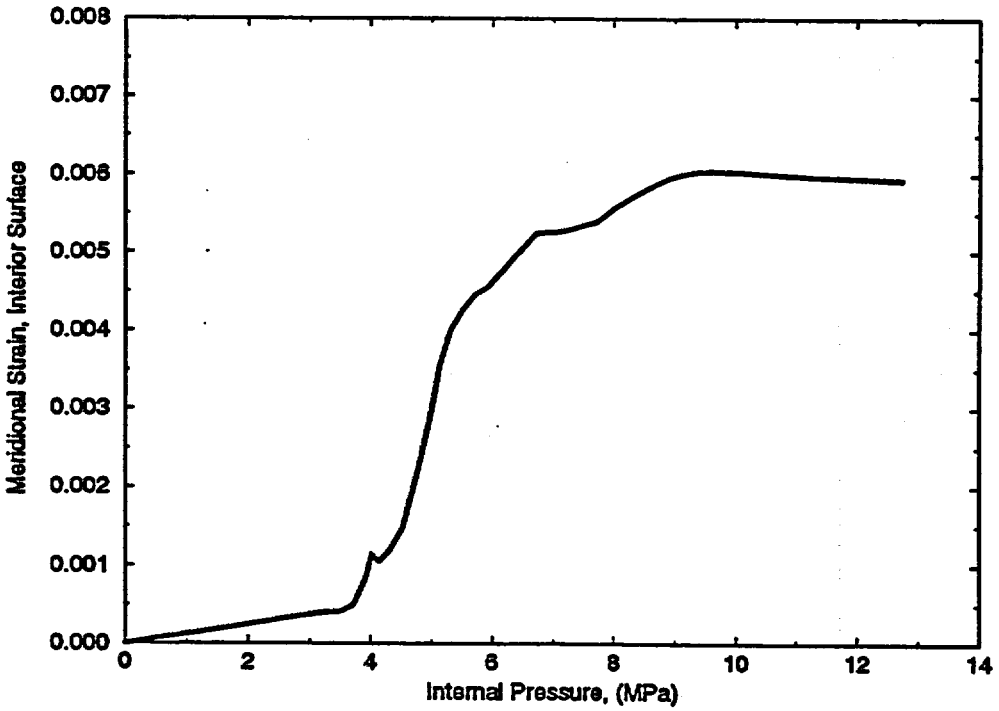

Plot 22: Interior surface meridional strain versus internal pressure for an element located at the mid-height of the upper conical shell at (45 degrees, 2.49 m) in the global coordinate system (Model: G3DS).

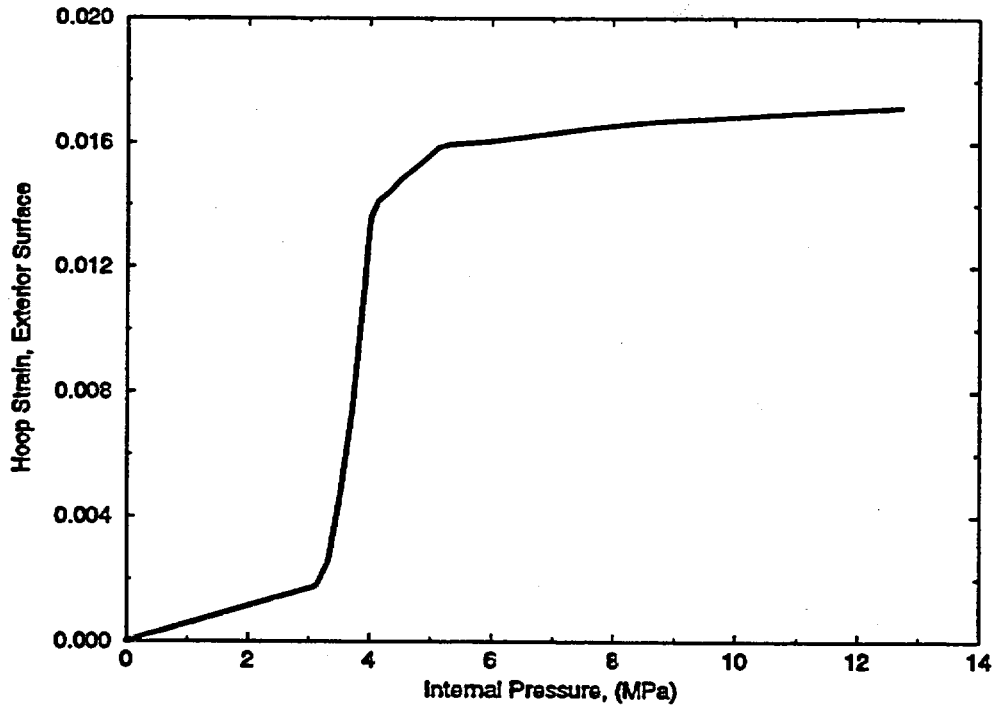

Plot 23: Exterior surface hoop strain versus internal pressure for an element located at the mid-height of the upper conical shell at (45 degrees, 2.49 m) in the global coordinate system (Model: G3DS).

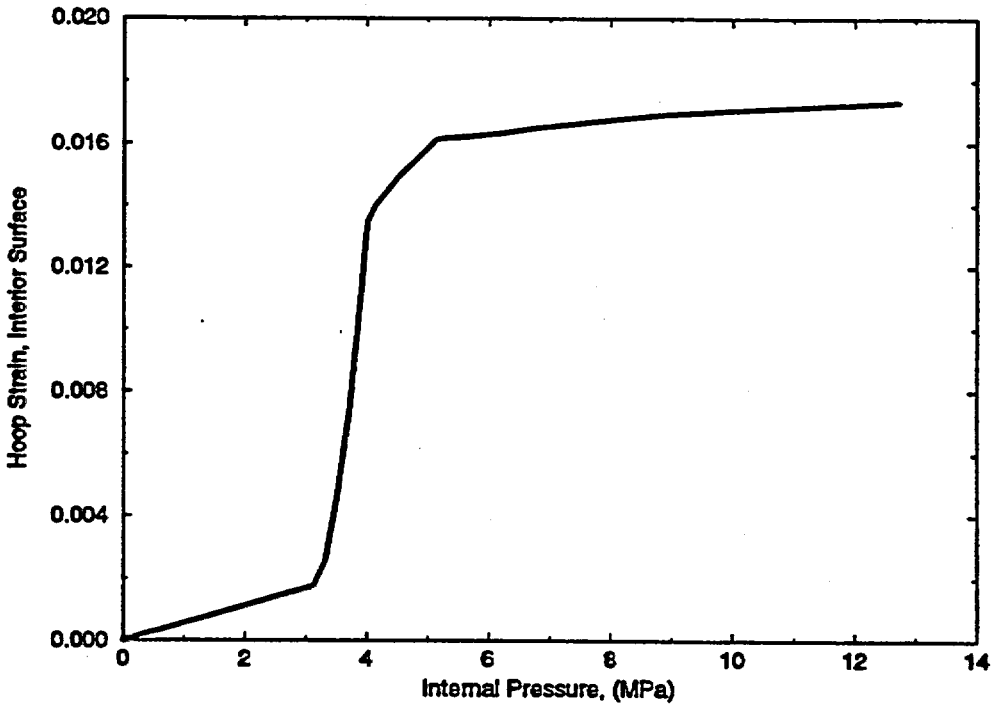

Plot 24: Interior surface hoop strain versus internal pressure for an element located at the mid-height of the upper conical shell at (45 degrees, 2.49 m) in the global coordinate system (Model: G3DS).

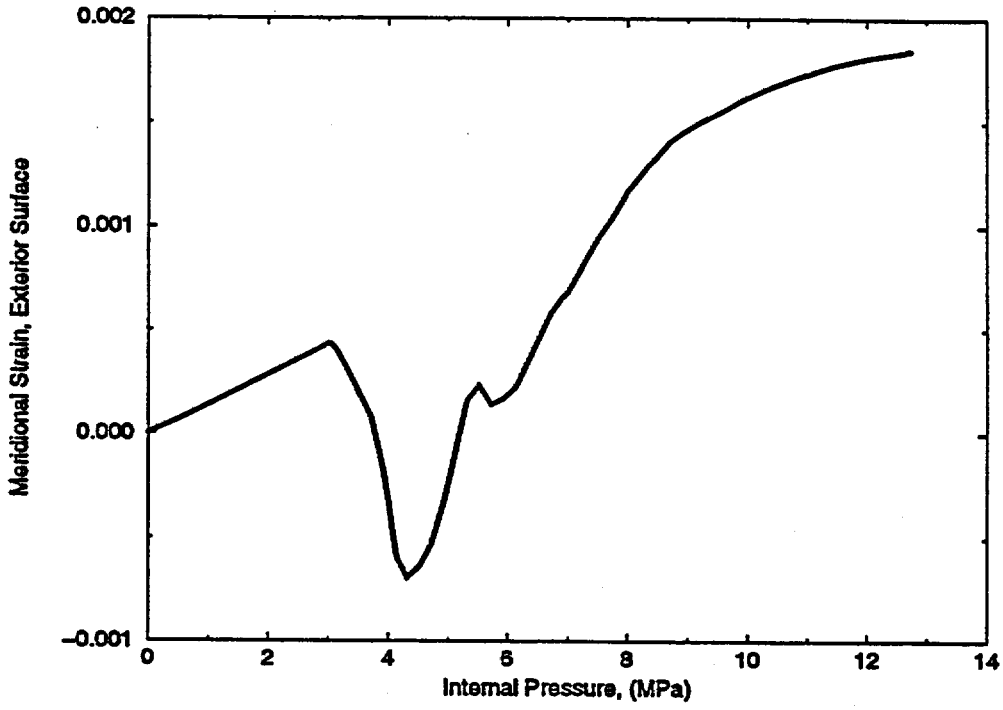

Plot 25: Exterior surface meridional strain versus internal pressure for an element located 0.126 meters below the material change interface at (45 degrees, 1.45 m) in the global coordinate system (Model: G3DS).

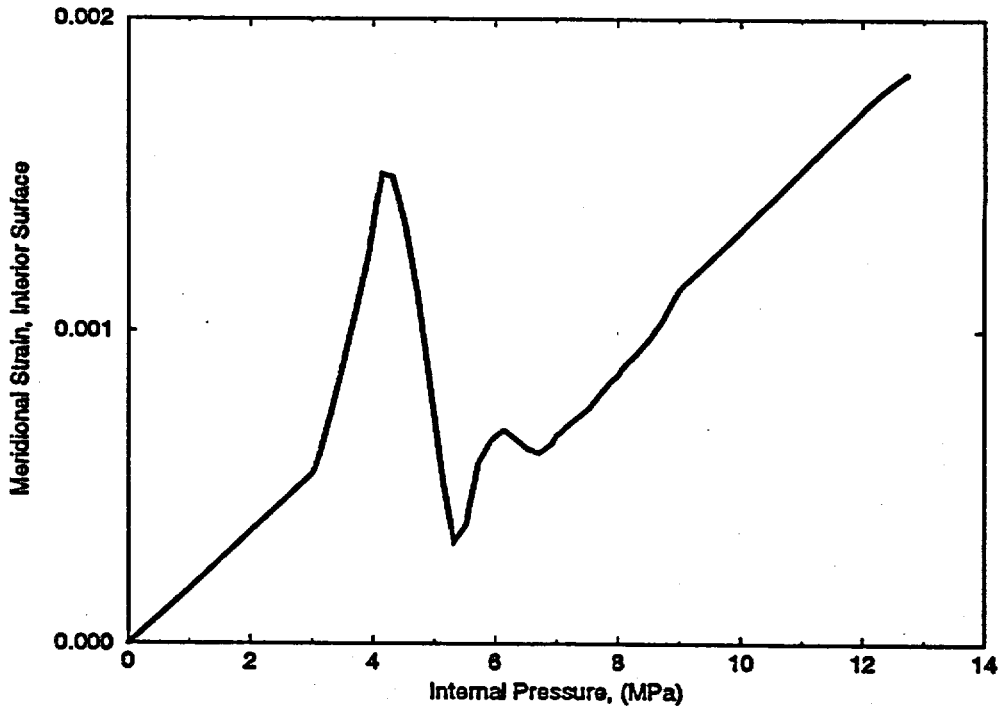

Plot 26: Interior surface meridional strain versus internal pressure for an element located 0.126 meters below the material change interface at (45 degrees, 1.45 m) in the global coordinate system (Model: G3DS).

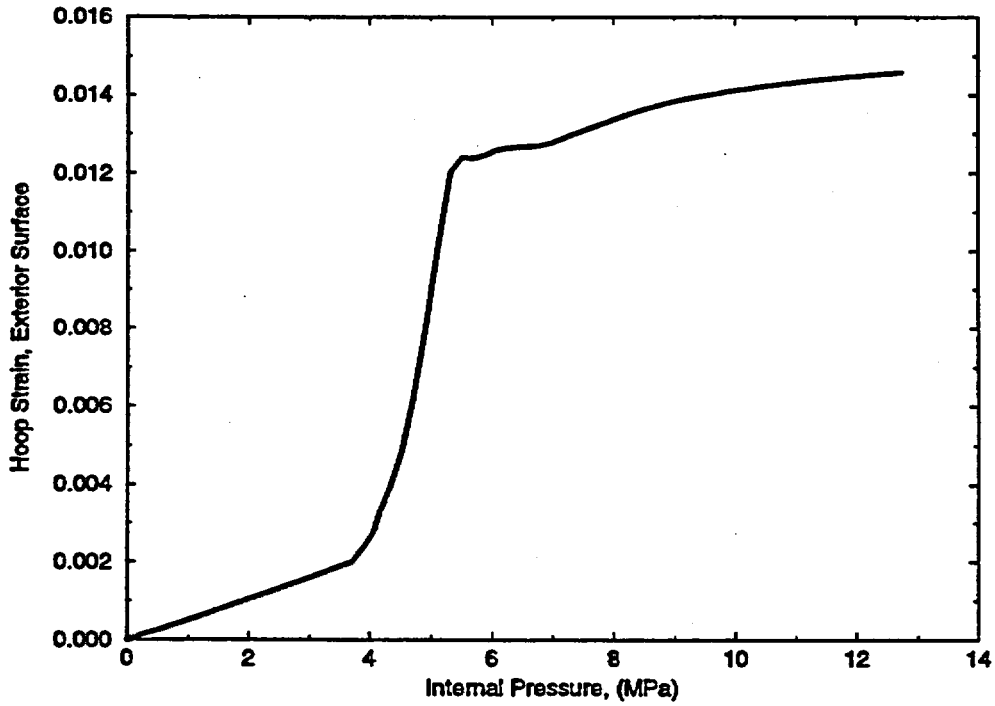

Plot 27: Exterior surface hoop strain versus internal pressure for an element located 0.126 meters below the material change interface at (45 degrees, 1.45 m) in the global coordinate system (Model: G3DS).

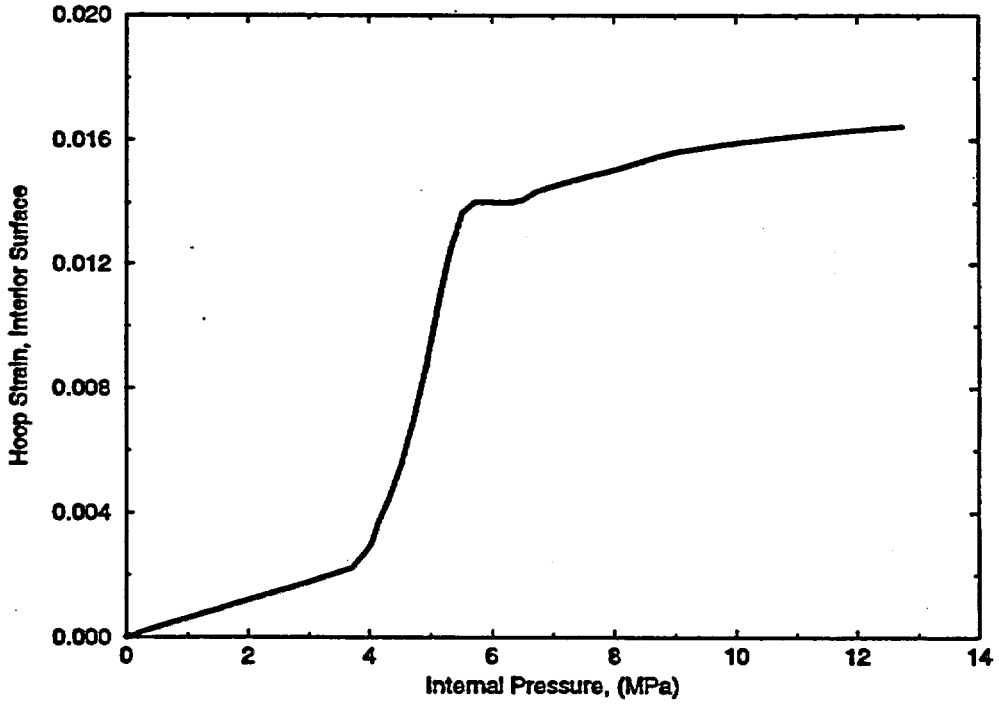

Plot 28: Interior surface hoop strain versus internal pressure for an element located 0.126 meters below the material change interface at (45 degrees, 1.45 m) in the global coordinate system (Model: G3DS).

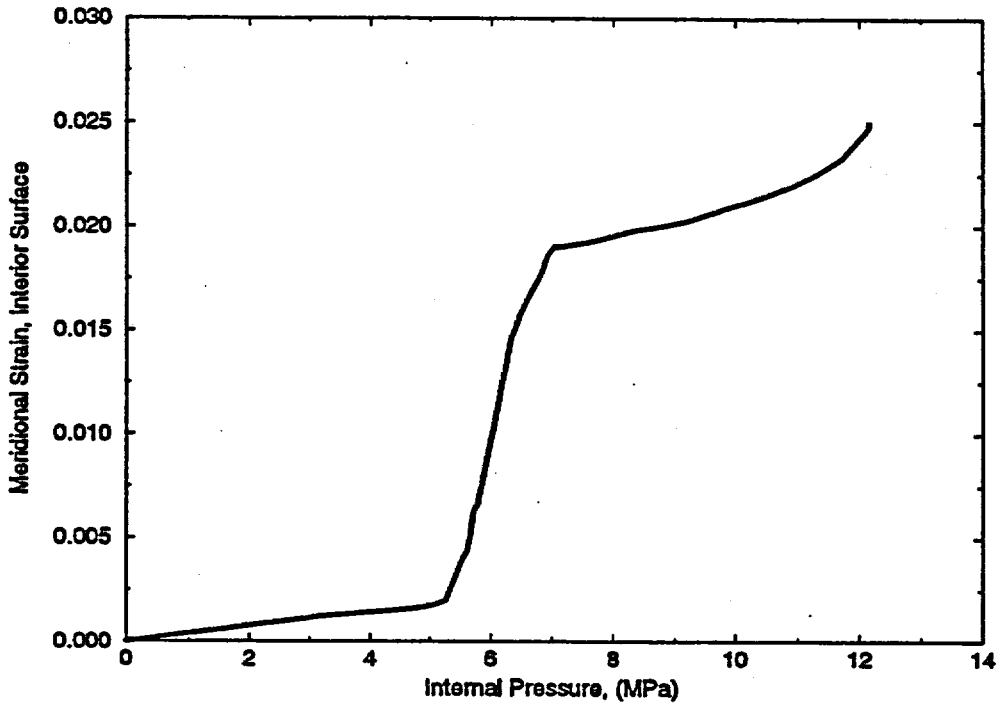

Plot 29: Interior surface meridional strain versus internal pressure for an element located at the mid-height of the spherical shell at (45 degrees, 3.13 m) in the global coordinate system (Model: LTHAXC).

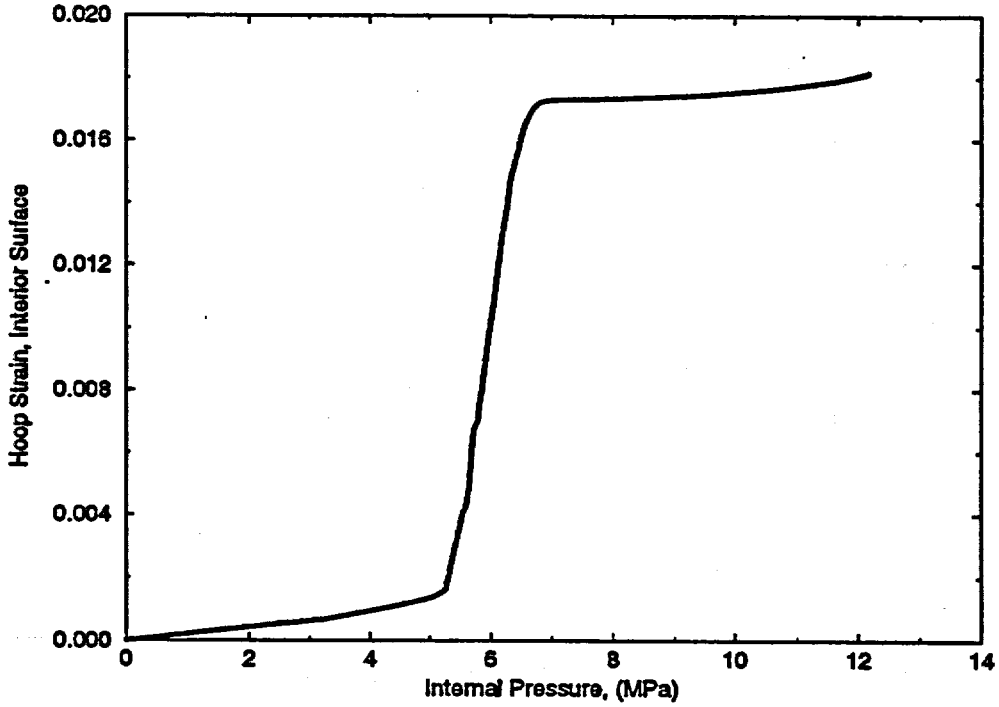

Plot 30: Interior surface hoop strain versus internal pressure for an element located at the mid-height of the spherical shell at (45 degrees, 3.13 m) in the global coordinate system (Model: LTHAXC).

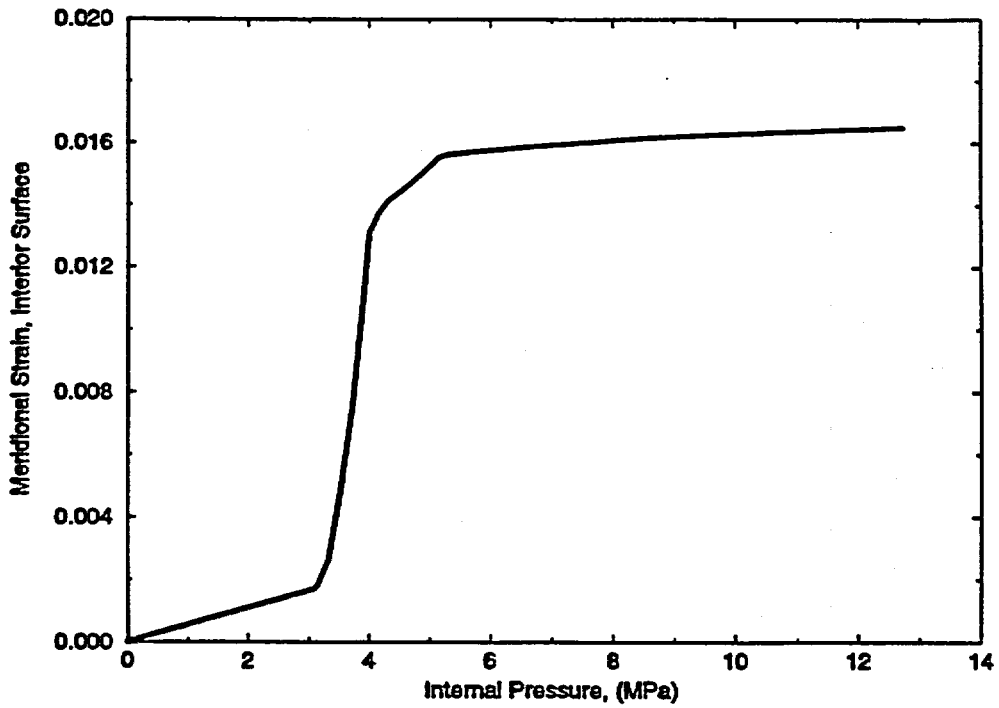

Plot 31: Interior surface meridional strain versus internal pressure for an element located at the mid-height of the upper conical shell at (270 degrees, 2.49 m) in the global coordinate system (Model: G3DS).

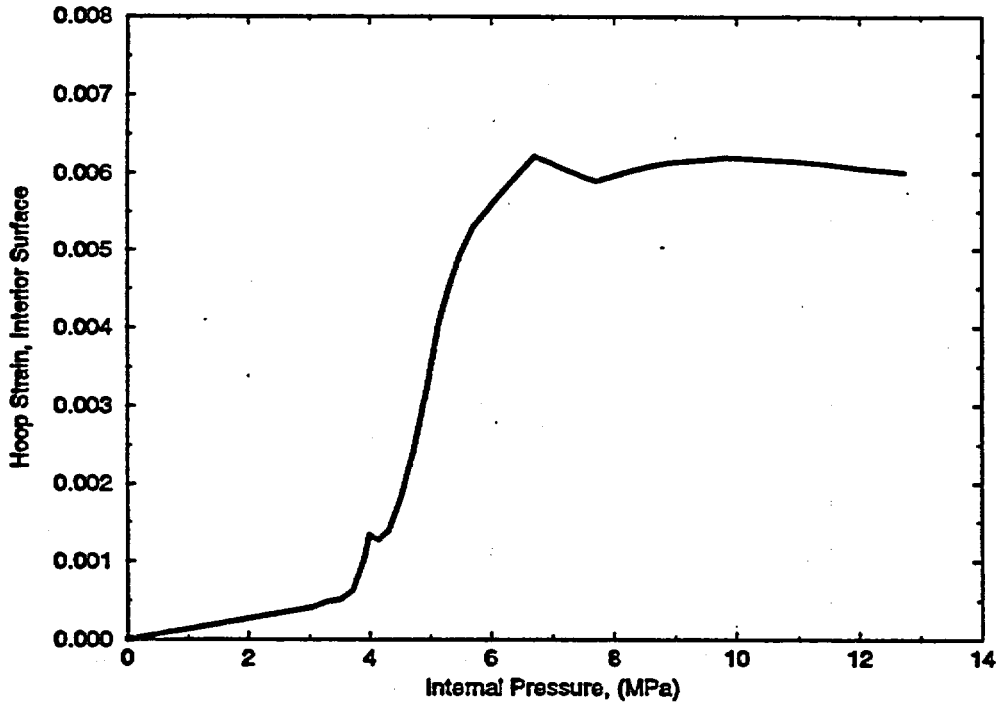

Plot 32: Interior surface hoop strain versus internal pressure for an element located at the mid-height of the upper conical shell at (270 degrees, 2.49 m) in the global coordinate system (Model: G3DS).

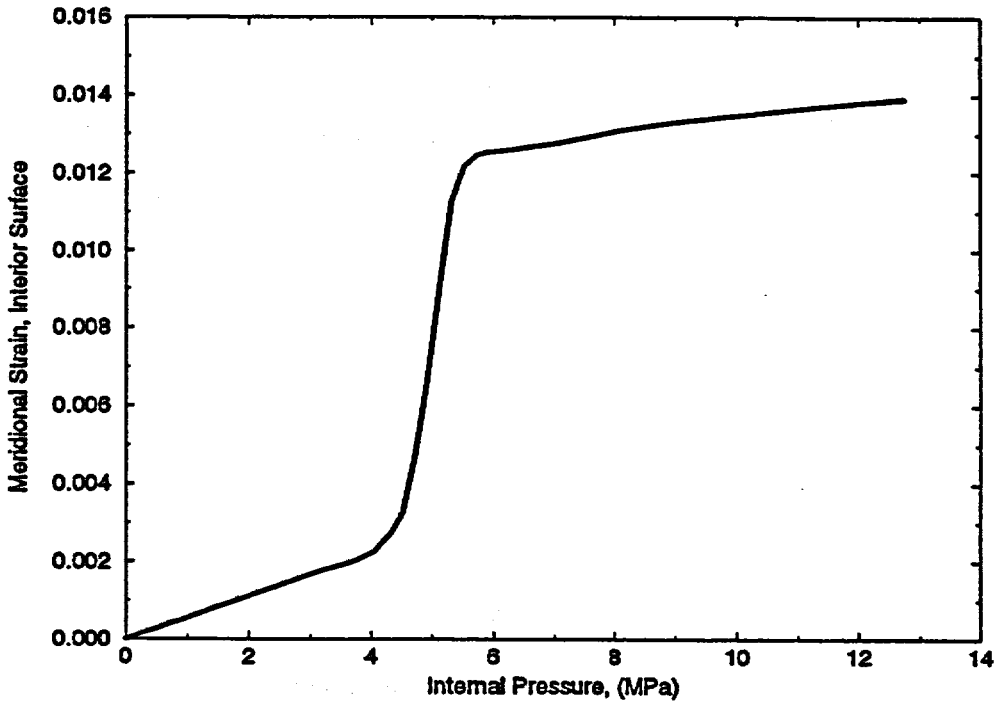

Plot 33: Interior surface meridional strain versus internal pressure for an element located midway between the material change interface and the top of the lower pair of stiffeners at (270 degrees, 1.25 m) in the global coordinate system (Model: G3DS).

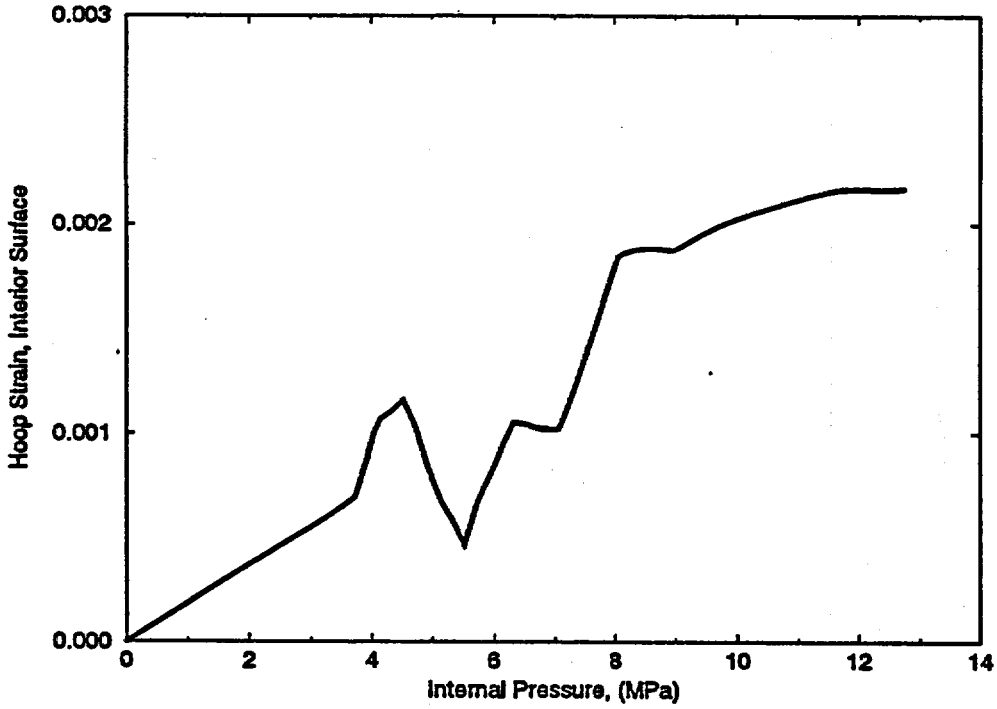

Plot 34: Interior surface hoop strain versus internal pressure for an element located midway between the material change interface and the top of the lower pair of stiffeners at (270 degrees, 1.25 m) in the global coordinate system (Model: G3DS).

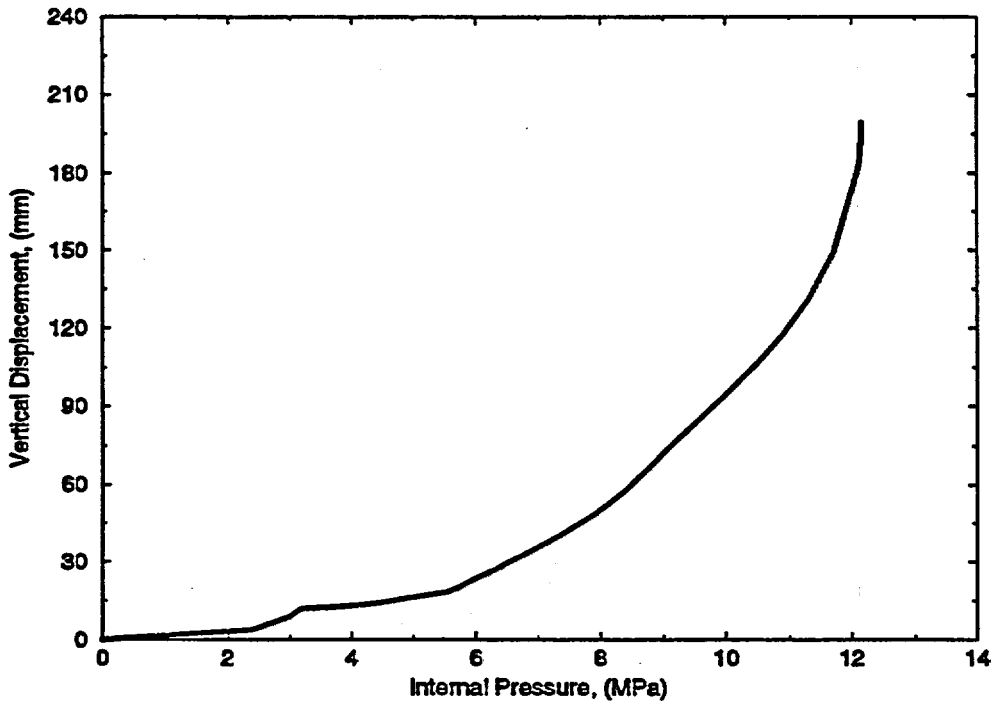

Plot 35: Vertical displacement versus internal pressure for the apex of the top head at (- degrees, 0 m) in the top head coordinate system (Model: LTHAXC).

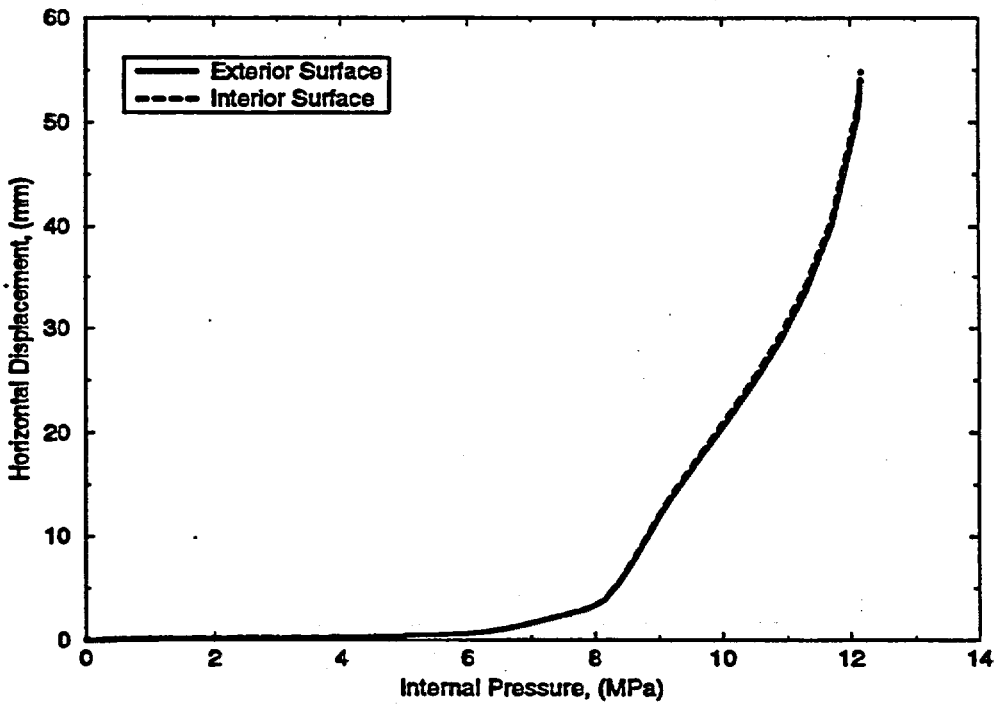

Plot 36: Horizontal displacements versus internal pressure for the interior and exterior surface 4 cm above the top surface of the top flange at (45 degrees, 3.57 m) in the global coordinate system (Model: LTHAXC).

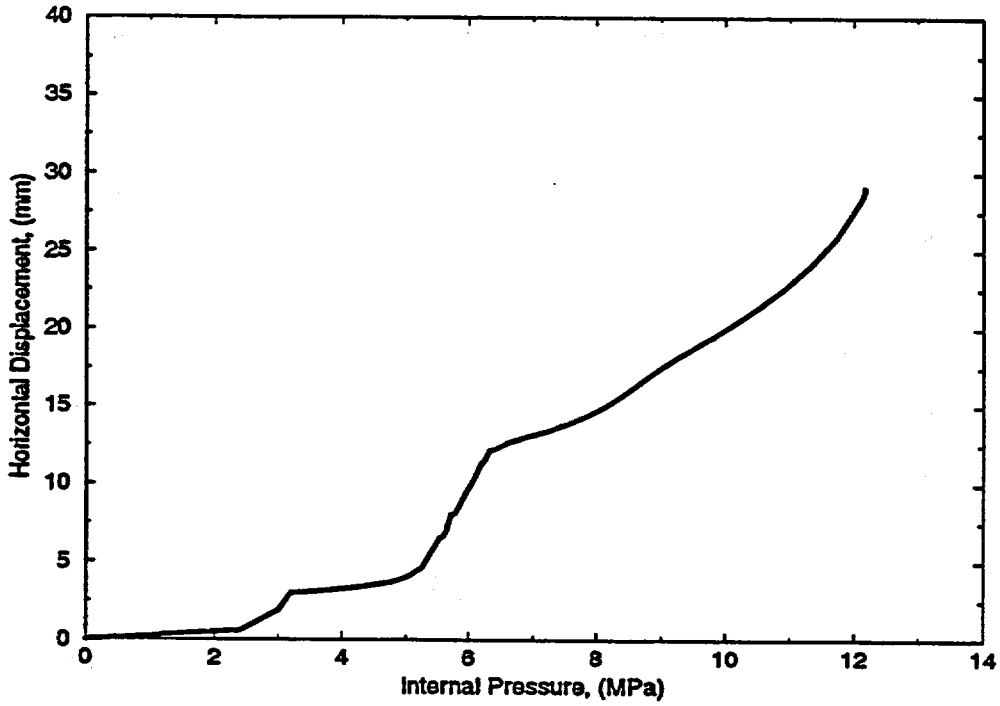

Plot 37: Horizontal displacement versus internal pressure for a location 4 cm below the bottom of the knuckle at (0 degrees, 3.32 m) in the global coordinate system (Model: LTHAXC).

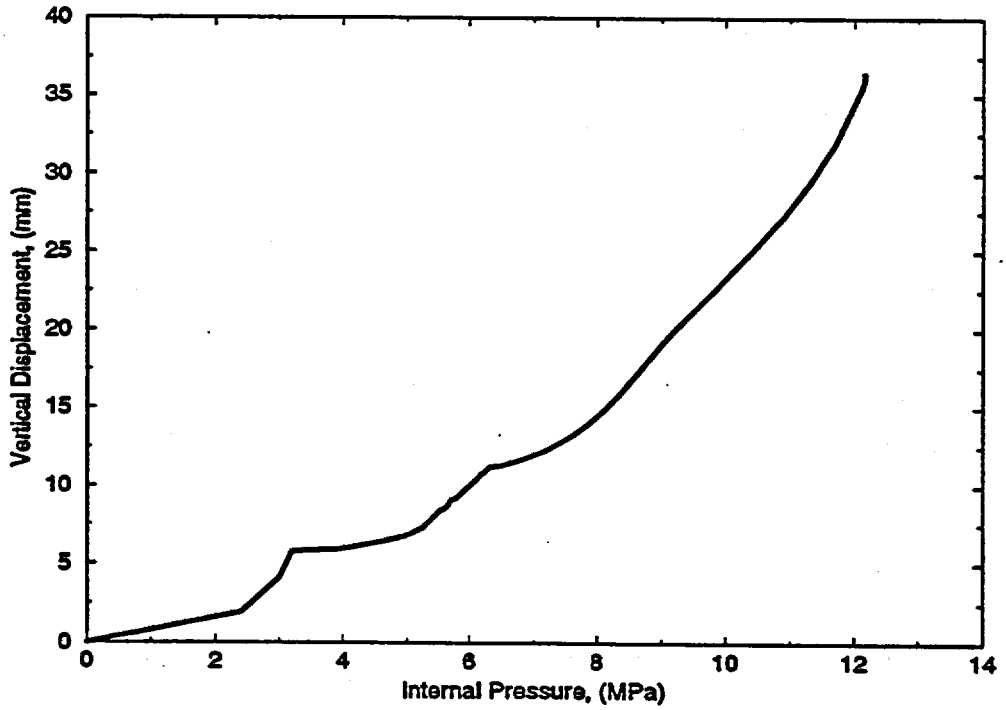

Plot 38: Vertical displacement versus internal pressure for a location 4 cm below the bottom of the knuckle at (0 degrees, 3.32 m) in the global coordinate system (Model: LTHAXC).

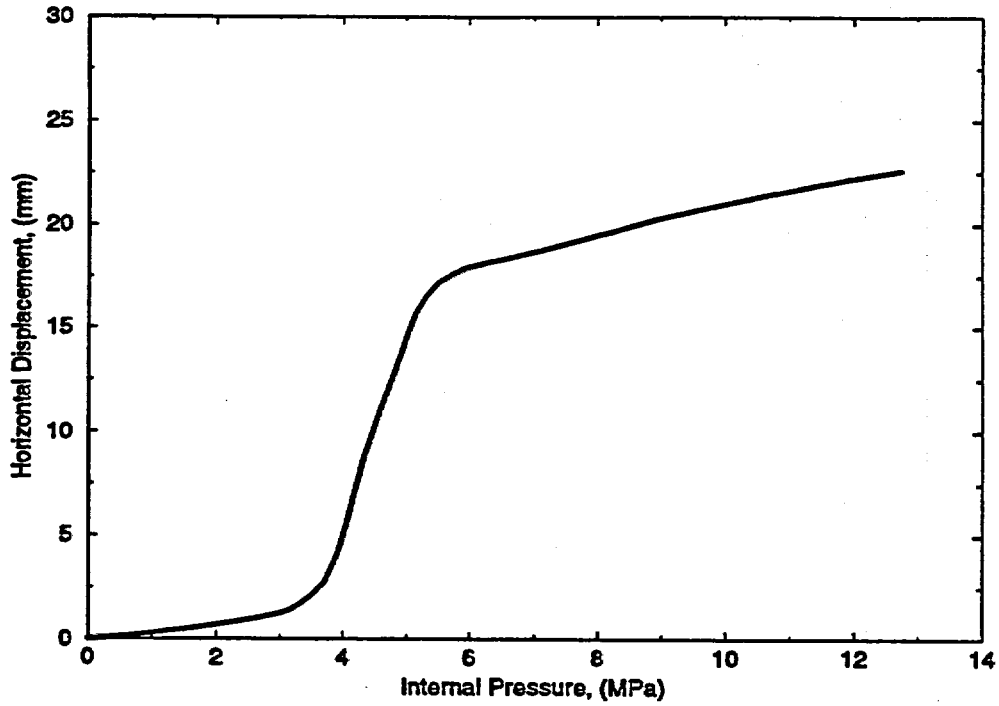

Plot 39: Horizontal displacement versus internal pressure at the apex of the equipment hatch at (- degrees, 0.0 m) in the global coordinate system (Model: G3DS).

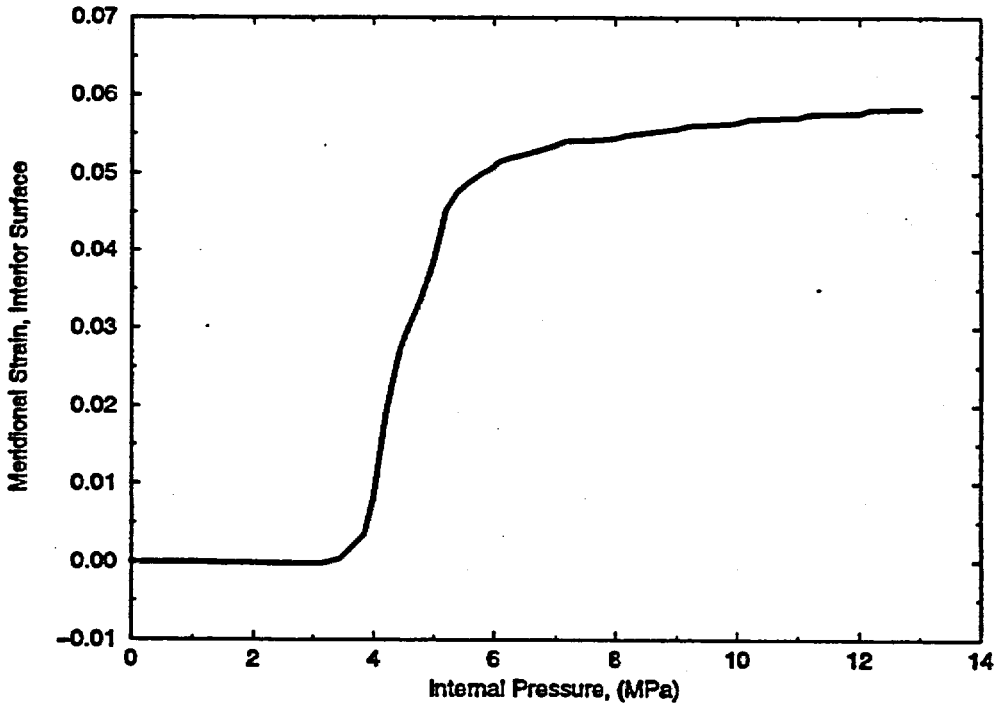

Plot 40: Interior surface meridional strain versus internal pressure for an element located at the thinned area near the equipment hatch insert plate at (74.8 degrees, 1.569 m) in the equipment hatch coordinate system (Model: LEHSTh).

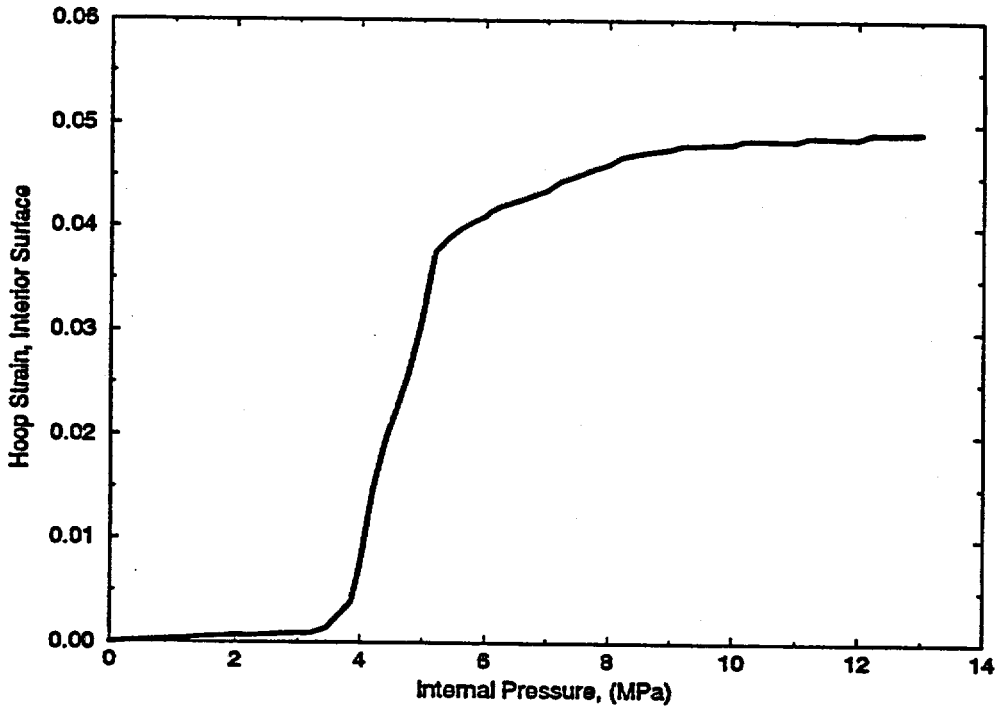

Plot 41: Interior surface hoop strain versus internal pressure for an element located at the thinned area near the equipment hatch insert plate at (74.8 degrees, 1.569 m) in the equipment hatch coordinate system (Model: LEHSTh).

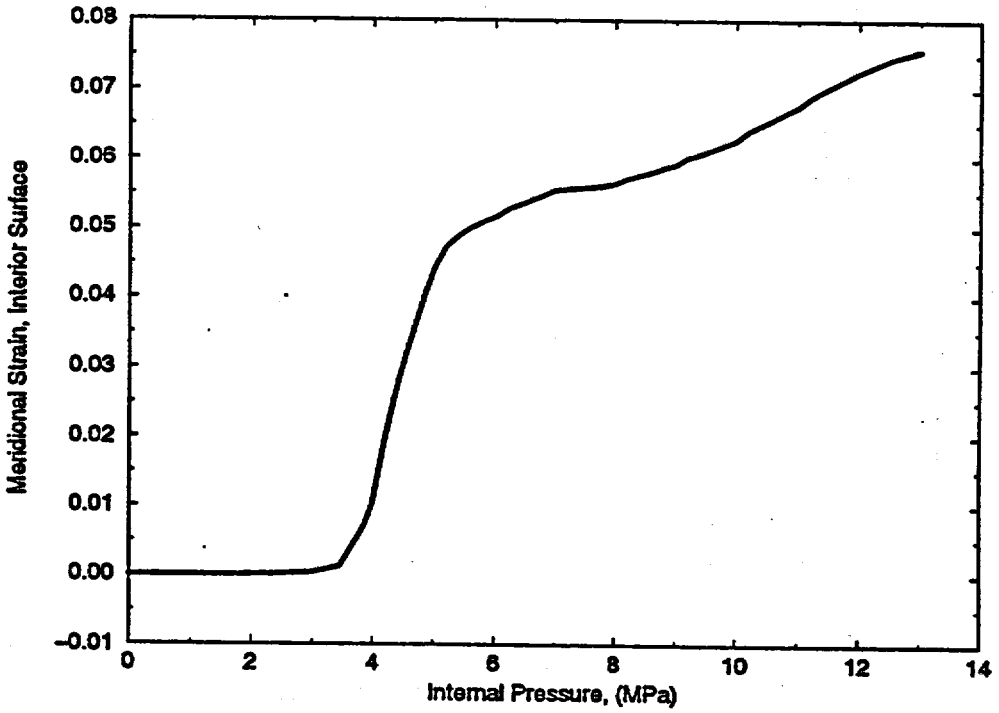

Plot 42: Interior surface meridional strain versus internal pressure for an element located at the thinned area near the equipment hatch insert plate at (105.4 degrees, 1.569 m) in the equipment hatch coordinate system (Model: LEHSTh).

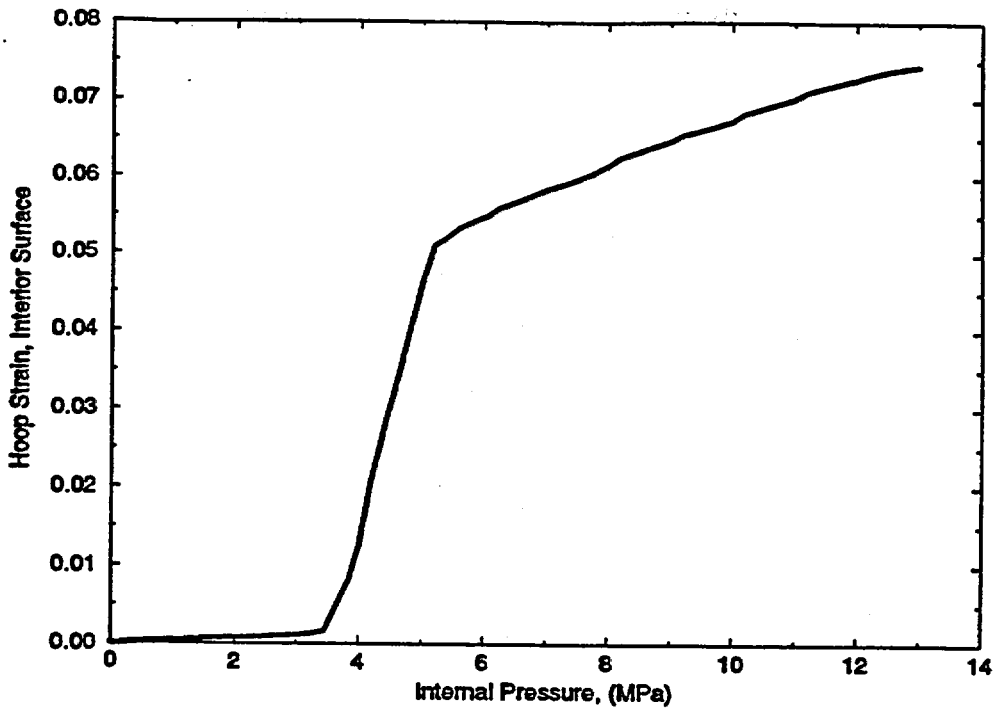

Plot 43: Interior surface hoop strain versus internal pressure for an element located at the thinned area near the equipment hatch insert plate at (74.8 degrees, 1.569 m) in the equipment hatch coordinate system (Model: LEHSTh).

Page intentionally left blank.

Appendix E-8

Staatliche Material prüfungsanstalt, Universität Stuttgart

Germany

**Staatliche
Materialprüfungsanstalt**

Universität Stuttgart

**MPA
STUTTGART**

Staatl. Materialprüfungsanstalt
Universität Stuttgart · Postfach 801140 · D-70511 Stuttgart

Dr. Vincent Luk
Sandia National Laboratories
Department 6403, Mail Stop 0744
1515 Eubank SE

Albuquerque, NM 87123
USA

Ihre Zeichen, Ihre Nachricht vom	Unsere Zeichen, unsere Nachricht vom	Durchwahl 685-	Stuttgart Vaihingen
	Dr.Stk/Ef	3041	October 16, 1996

Subject: **Steel Containment Vessel Round Robin**

Dear Dr. Luk,

Enclosed please find the pretest report of our round robin analysis in printed form. Also enclosed are the plots # 1 to # 43 in printed form and on diskette.

Sincerely yours

MPA STUTTGART

i. A.

Encl.: Pre test report
Plot # 1 to # 43
Diskette

Hausanschrift:
D-70569 Stuttgart (Vaihingen)
Pfaffenwaldring 32

Telefon (07 11) 6 85 - 1
Telefax (07 11) 6 85-26 35

Telegramm-Kurzanschrift:
MPA STUTTGART

Gütersendungen
Stuttgart-Vaihingen
Stiz. 1293

Bankverbindung:
BW-Bank Stuttgart, Klo-Nr. 1 054 611 700
(BLZ 600 200 30)

MPA STUTTGART

STEEL CONTAINMAENT VESSEL (SCV) ROUND ROBIN

Section 4 Pre-Test Analysis Report

4.1 Idealization

The analyses within the SCV round robin were performed using the finite element program ABAQUS, release 5.5 /HKS 1995/. Pre- and postprocessing of the finite element data was done with CAE-software MSC/PATRAN, release 1.4.2 /MSC 1995/.

For the geometric idealization of the steel containment vessel we used shell elements from the ABAQUS element library with 5 degrees of freedom per node and reduced integration scheme. Usually 8-noded quadrilateral elements with quadratic interpolation of geometry and displacements, called S8R5, were used. Some triangular elements with six nodes, called STRI65, were inserted for mesh refinement. The missing sixth degree of freedom, which designates the "torsion" of the shell, is essential for boundary conditions only and will be introduced automatically if necessary. The stiffeners are also idealized with shell elements and directly connected with the nodes of the vessel. A look on the total model is given in figure 4.1.

A failure criterion does not exist within ABAQUS for this kind of analysis. Therefore no failure analysis can be performed. Also no buckling analysis was done, because a combination of eigenvalue determination together with unilateral boundary conditions is not possible.

The coordinates of the nodes, which give the location of the mid surface of a shell were chosen so that the inner surface of the vessel was continuous. Therefore at the transition between the different regions of the vessel additional geometric constraints have to be applied to make sure continuity of the unknown displacements and rotations. This is done with the multiple point constraint option (MPC) of ABAQUS. In our case the type BEAM was chosen.

The symmetry of the vessel can be used to mesh only one half of the vessel. The symmetry plane is located at $\theta = 90°$ in the global coordinate system. The mesh starts just above the ring support girder, i.e. z=0 in the global coordinate system. The forces resulting from internal pressure on the lower head of the vessel are applied as external tensile forces acting tangential to the wall. Axial displacement and bending is suppressed there via boundary conditions. In the symmetry plane, displacements perpendicular to this plane are suppressed, as well as rotations around the global r- and z-axis. The loading is applied as surface loading on the inner surface of all shell elements. The maximum loading applied is 50 bar or 5 MPa.

The contact between the vessel and the contact shell is simulated with the ABAQUS surface interaction option. There one have to define two surfaces, which may contact. ABAQUS automatically calculates the initial distance of relevant nodes

before loading and subsquently for every load increment which is applied. The contact shell was defined as rigid spherical shell and as rigid conical shell for 0.816 m< z < 3.359 m. Our first analysis of the vessel without contact shell showed, that only in the region around the equipment hatch relevant displacements may occur. The initial gap size was 18 mm /SNL 1995/.

4.2 Material properties

Based on the provided tensile test data we defined three stress-strain curves. The first one describes the behaviour of the SGV480 material, the second one describes the behaviour of the SPV490 material with wall thickness of 9 mm and the third one describes the behaviour of the SPV490 material with wall thickness of 17.5 mm. The different yield strength of these materials is given in table 4.1.

Material/wall thickness	Yield strength [MPa]
SGV480/-	400
SPV490/9 mm	680
SPV490/17.5 mm	610

Table 4.1: Yield strength of the SCV materials used for FE analysis

The strength of specimens from the 9 mm blanks is quite higher than from the 17.5 mm blanks. The input stress-strain curves are given in figure 4.2. Isotropic kinematic harding model due to von Mises is used.

Young's modulus is kept constant to 200 000 MPa.

4.3 Description of the analysis

The internal pressure is applied up to a maximum load of 50 bar, i.e. 5 MPa. The automatic time incrementation algorithm of ABAQUS is used. Beginning with an initial load increment, ABAQUS enlarges the load increment with a factor of 1.5, if convergence seems to be good. For bad convergence, the load increment is reduced to a factor of 0.25 of the previous increment. The first and second load increment of the present analysis are 15 bar, each. The next increment is 3.75 bar. Subsequent increments are again smaller. It can be easily seen, that for special points in the time history, the convergence becomes much worse, and the load increments decrease rapidly. Subsequent the load increment is again increased. These events coincide with beginning of contact or with beginning of yielding of the material.

4.4 Discussion of selected results

As it can be seen from different evaluation points, first yield appears for different pressure loads.

Near the equipment hatch, yielding starts for a pressure load of about 25 bar, see figure 4.3, where the meridional strain on the inner surface is given. In the same figure, one may see that full contact between vessel and contact shell is readched for about 35 bar, for beyond this pressure load, the strains decrease (plot id # 4).

Looking at the max principal strain on the apex of the vessel, we can see that yield starts for a preesure load of about 35 bar, together with contact between vessel and contact shell. Only for higher pressure loading, the strain inrease again, figure 4.4 (plot id # 7).

In the upper conical shell, first yield is reached for a pressure load of about 33 bar and full contact in this region is reached for a slightly higher pressure load of about 35 bar, see figure 4.5 (plot id # 21). Due to the contact the meridional strains are reduced for higher pressur loads.

The performance ot the strains near the material interface are quite different. Looking on the meridional strain component, we find a strong unloading on the outer surface for pressure loads higher than 35 bar, while on the inner surface the meridional strains are increasing rather monotonic, with some steps at 35 bar and at 43 bar. These steps may be observed also on the outer surface, see figure 4.6 and 4.7 (plot id # 25 and 26).

Looking on the vertical displacement of the upper head, we find that there is a rather linear elastic behaviour up to about 33 bar, followed by a region of nearly constant displacement from 35 to 40 bar and a subsequent strong increase, see figure 4.8 (plot id # 35). This is due to a missing contact shell in our model around the upper head of the vessel.

From these evaluations we can estimate the pressure load for starting of yield near the equipment hatch to about 25 bar.

The location of first contact between vessel and contact shell is given in figure 4.9.

For simulation of friction we used a friction coefficient of 0.3. No sticking as assumed. An analysis without friction was not performed. We think that friction will reduce th stresses and strains in the vessel, due to the induced friction forces, which act again the relative motion due to the internal pressure.

Summary

The vessel was analyzed with the ABAQUS finite element code using release 5.4.1. The idealization of the vessel started just above the ring support girder. Using symmetry properties of the vessel, one half of thestructure has been modelled We used standard shell elements with 8 nodes per element and 5 degrees of freedom

per node with reduced integration scheme. The different wall thicknesses have been taken into account. The contact shell was simulated as rigid body with a prescribed initial gap of 18 mm between SCV and CS. For the material description we used best fit stress-strain-curves based on the supplied tensile test data. The loading was applied as internal pressure on all shell elements. To simulate the influence of the lower head of the vessel, forces acting in the wall are applied at the ring support girder. Friction was assumed to be constant with a friction coefficient of 0.3.

The load was raised from 0 to 50 bar using the automatic time incrementation schem of ABAQUS.

First yield will occur for a pressure load of about 25 bar near equipment hatch.

First contact between SCV and CS will occur for a pressure of about 35 bar.

References

HKS 1995: Hibbitt, Karlsson ans Sorensen, ABAQUS Users manual, Rel 5.5, 1995.
MSC 1995: McNeal-SchwendlerCorp.: MSC/PATRAN Users manual Rel 1.4.2,1995.
SNL 1995: Sandia National Laboratories, SCV Design Package, July 10,1995.

List of figures

List of tables:

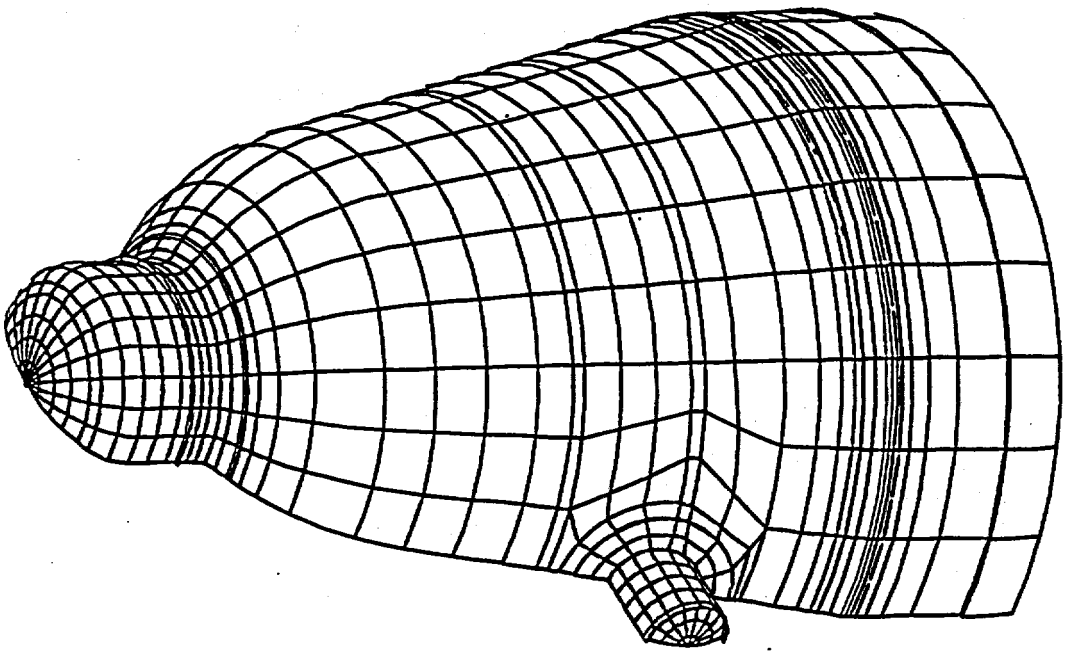

Figure 4.1: Finite element mesh of SCV

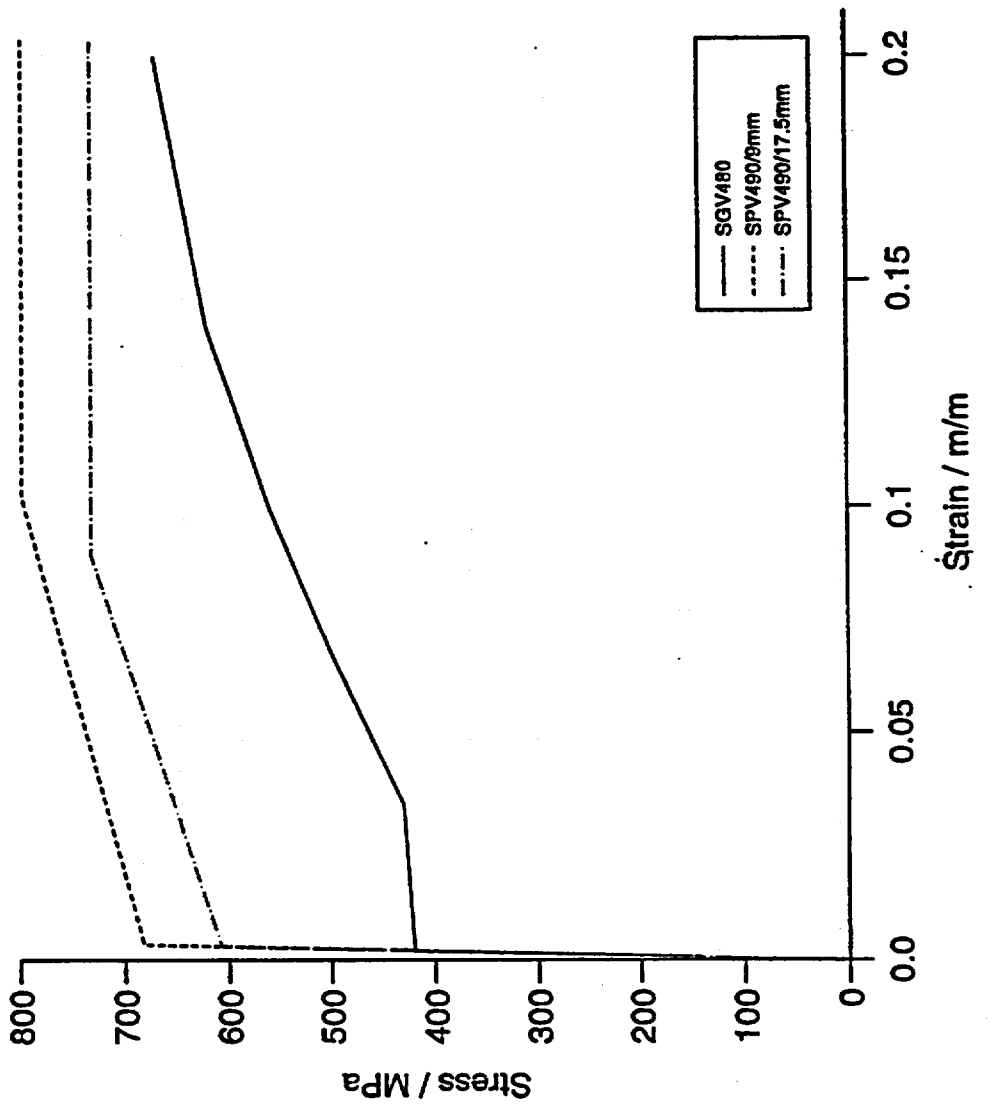

Figure 4.2: Stress strain curves used in FEM analysis

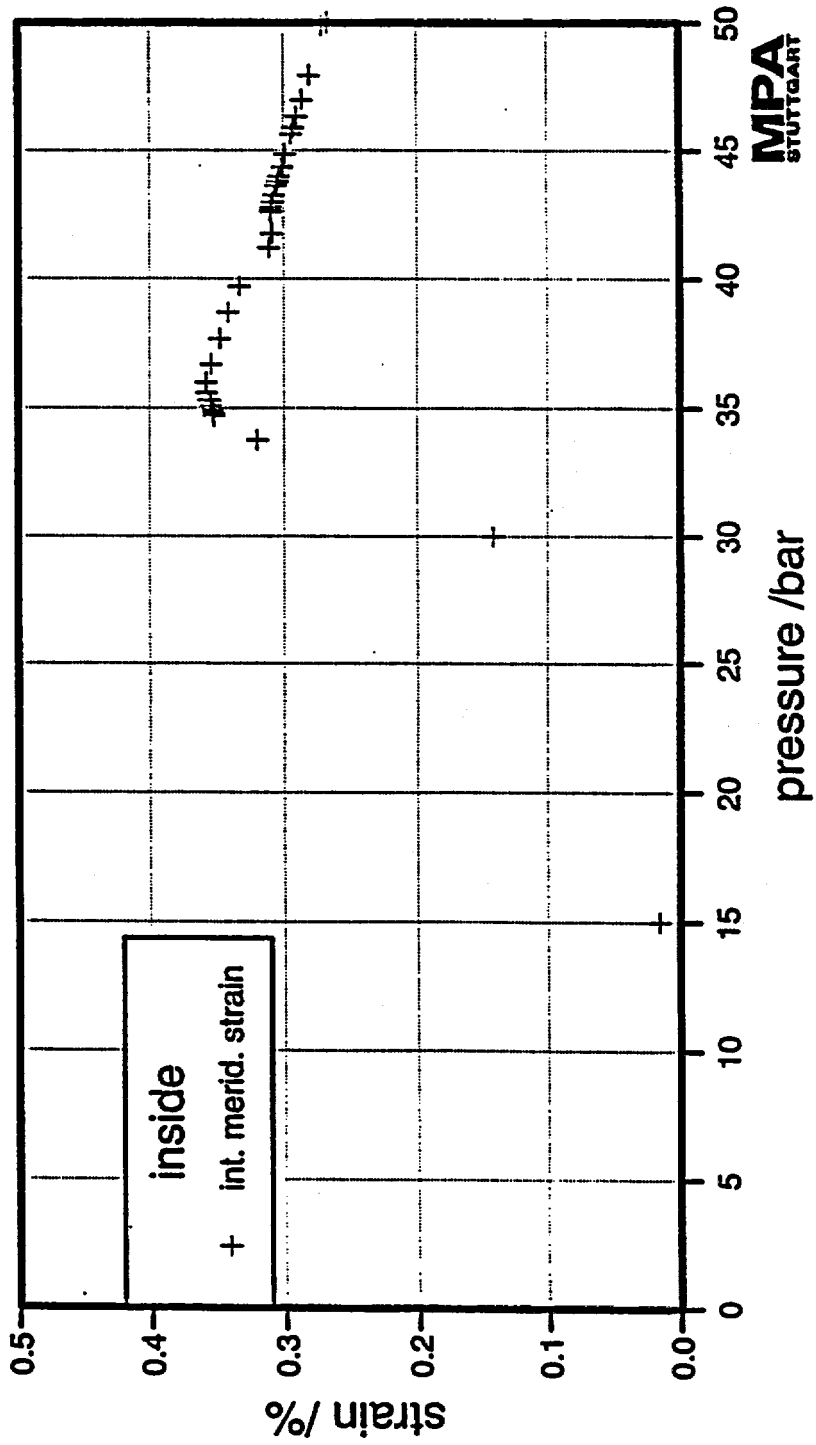

Figure 4.3: Meridional strain on the inner surface near equipment hatch

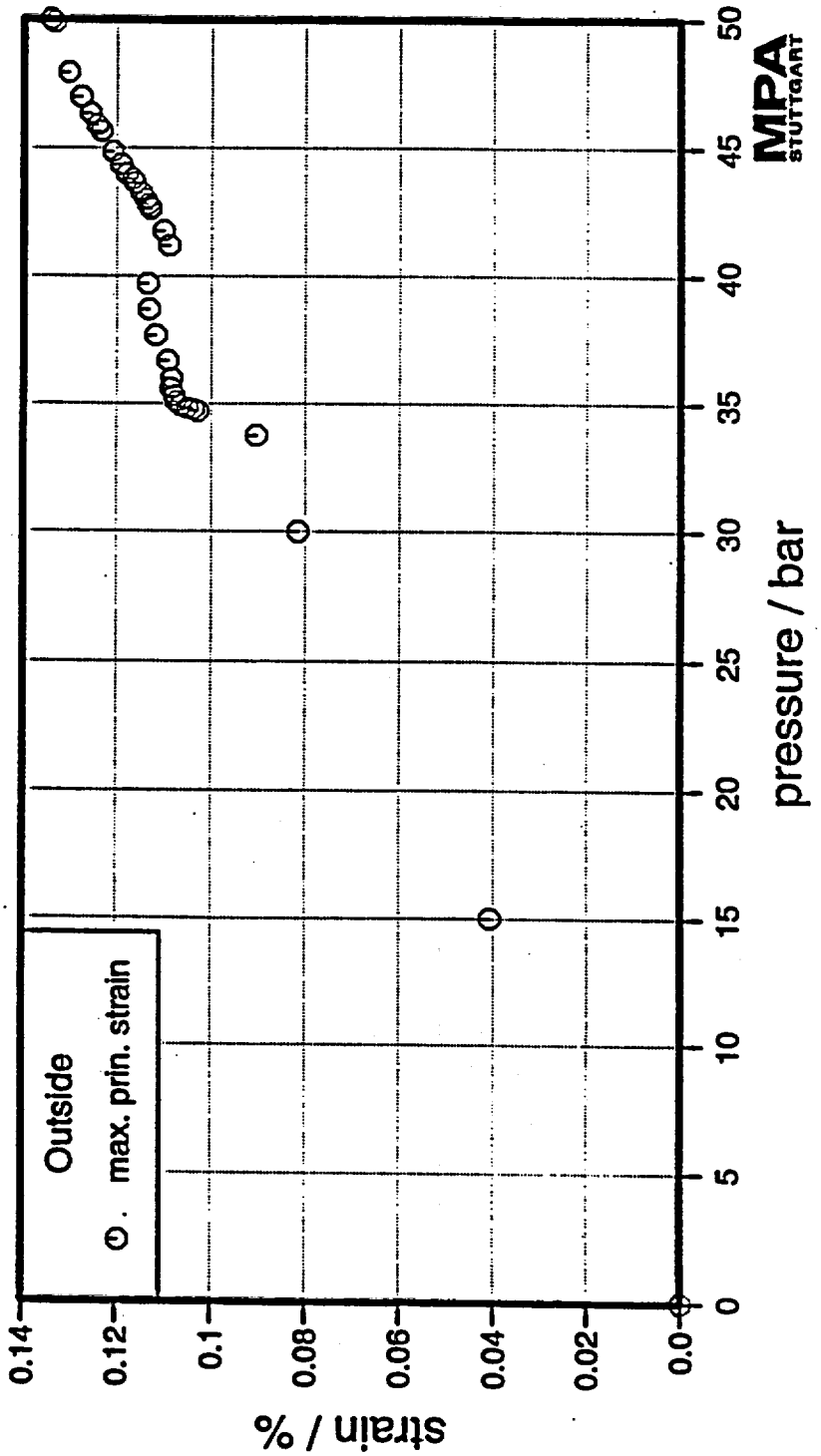

Figure 4.4: First principal strain on the apex, outside

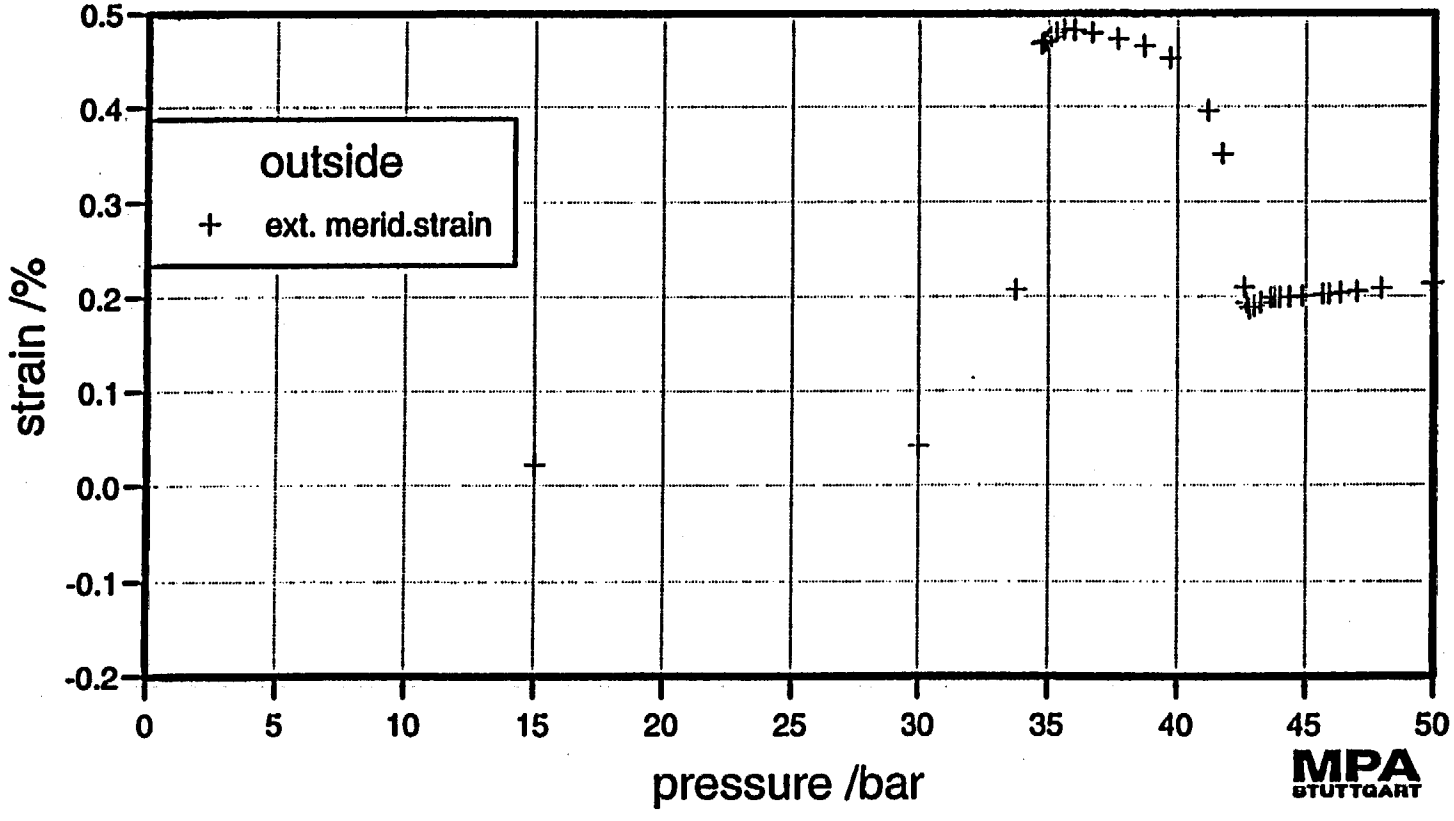

Figure 4.5: Meridional strain on the outer surface in midheight of upper conical shell

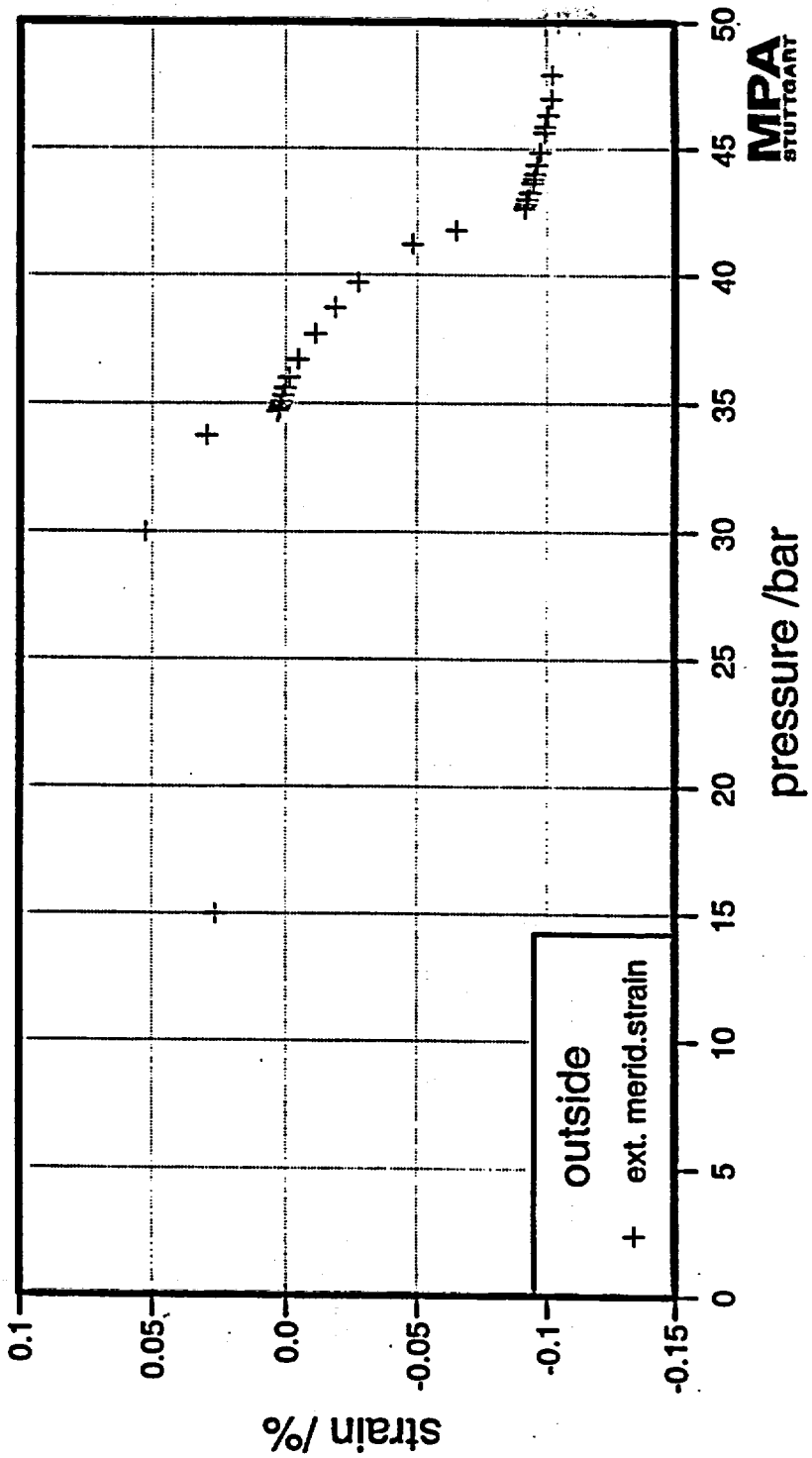

Figure 4.6: Meridional strain on the outer surface below material change interface

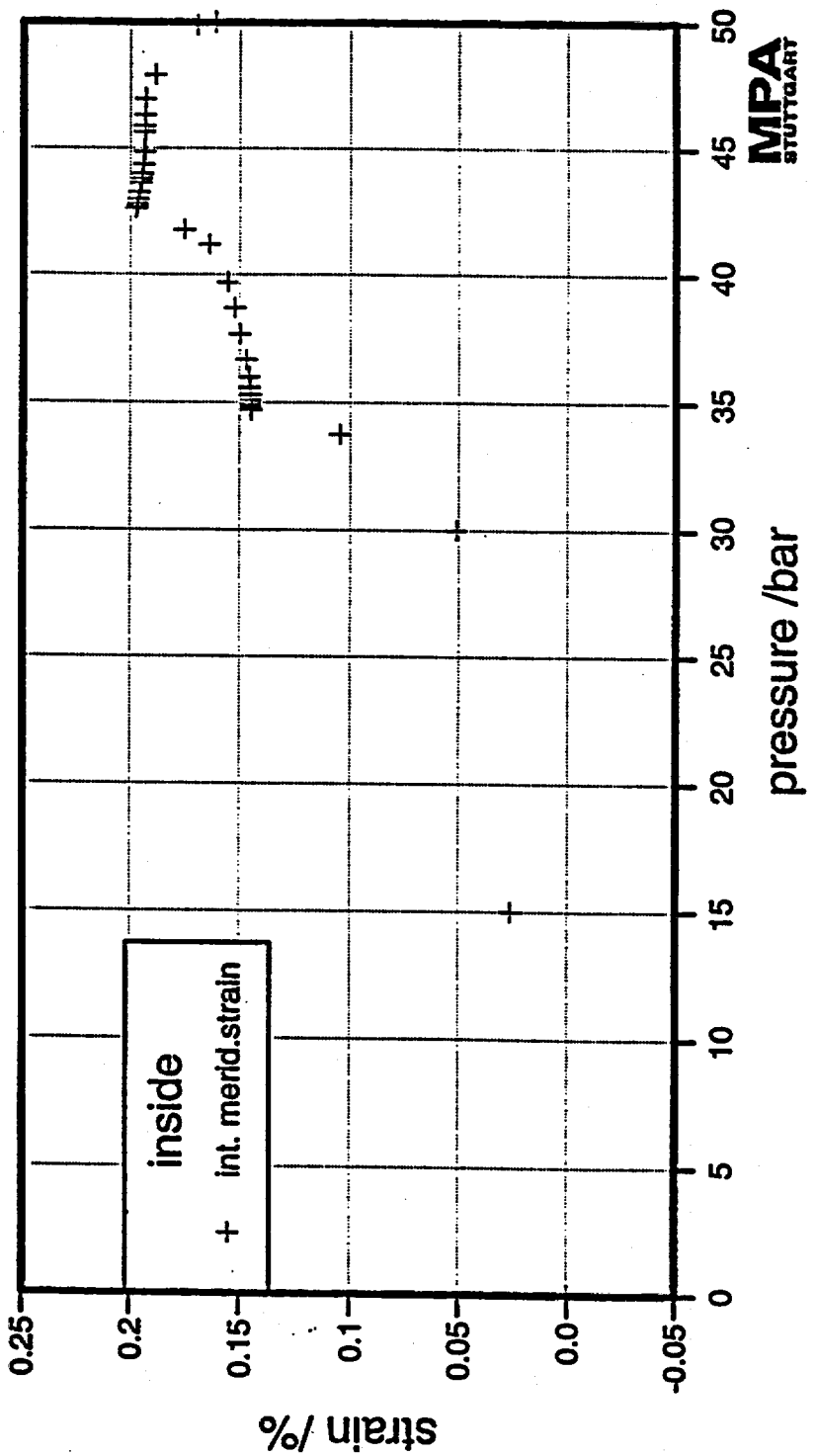

Figure 4.7: Meridional strain on the inner surface below material change interface

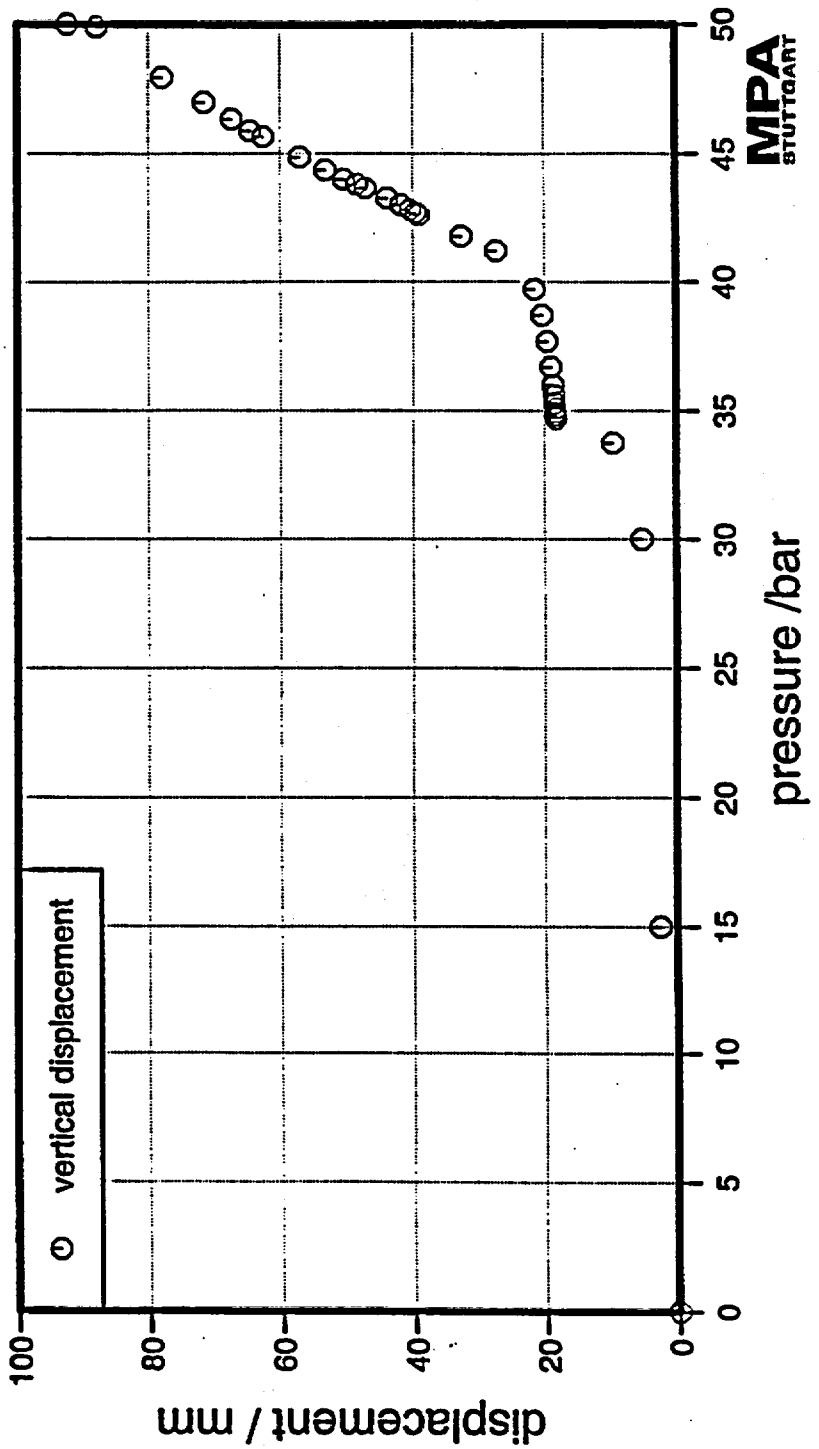

Figure 4.8: Vertical displacement of upper head

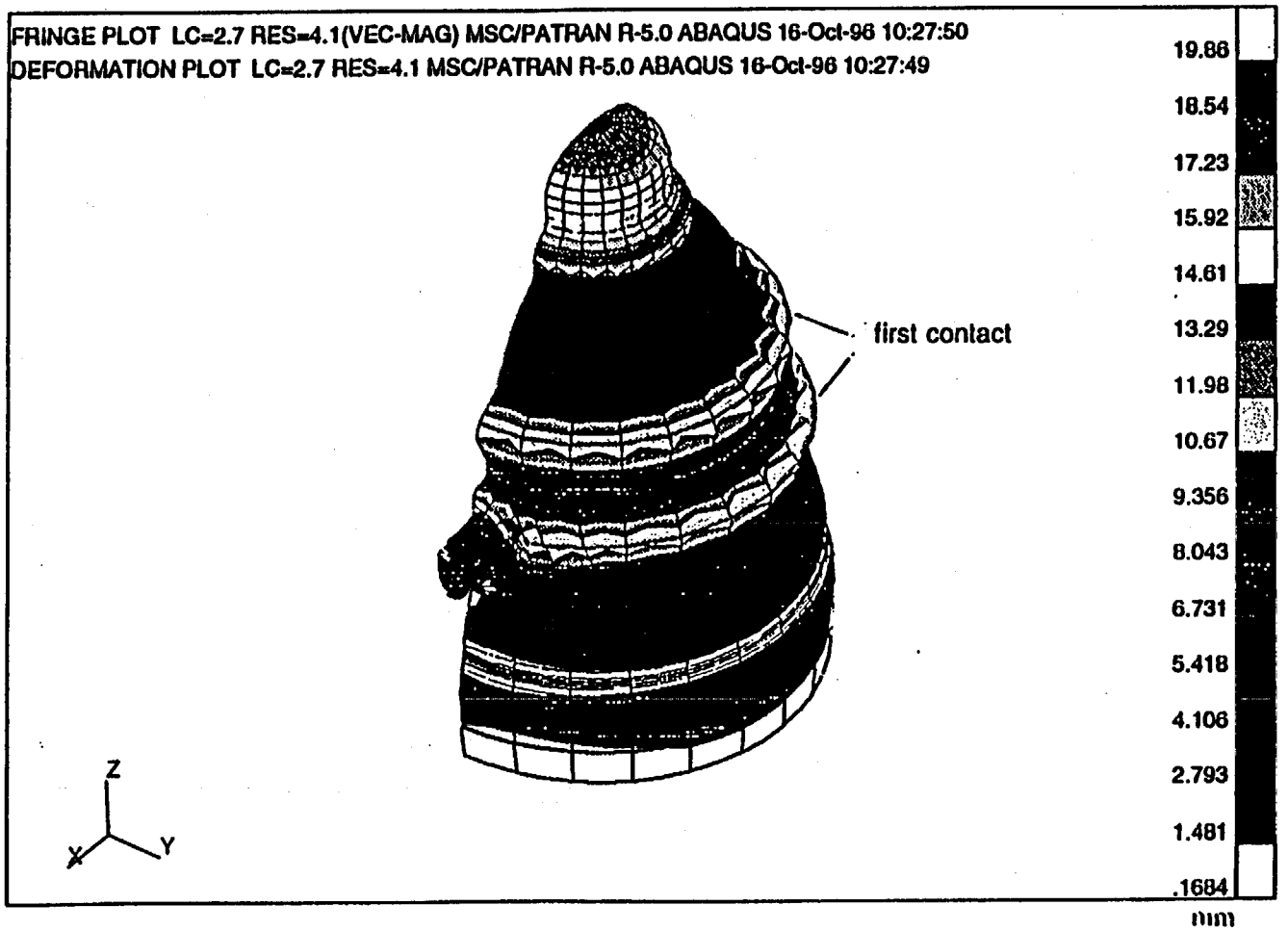

Figure 4.9: Location of first contact between SCV and CS

Notes:

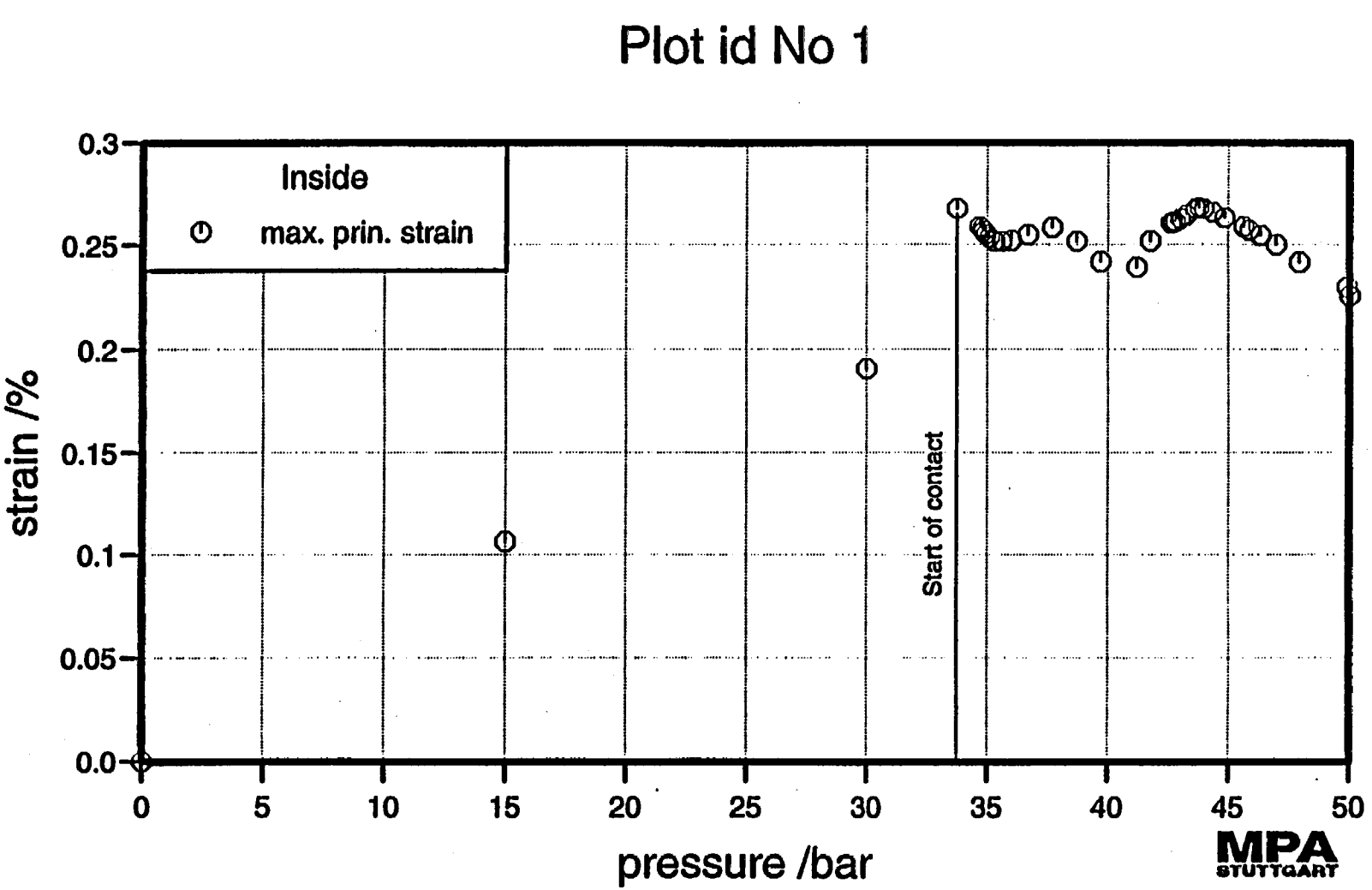
Plot id No 1
Inside
max. prin. strain
strain /%
0.3
0.25
0.2
0.15
0.1
0.05
0.0
0
5
10
15
20
25
30
35
40
45
50
pressure /bar
Start of contact
MPA
STUTTGART

Plot id No 2

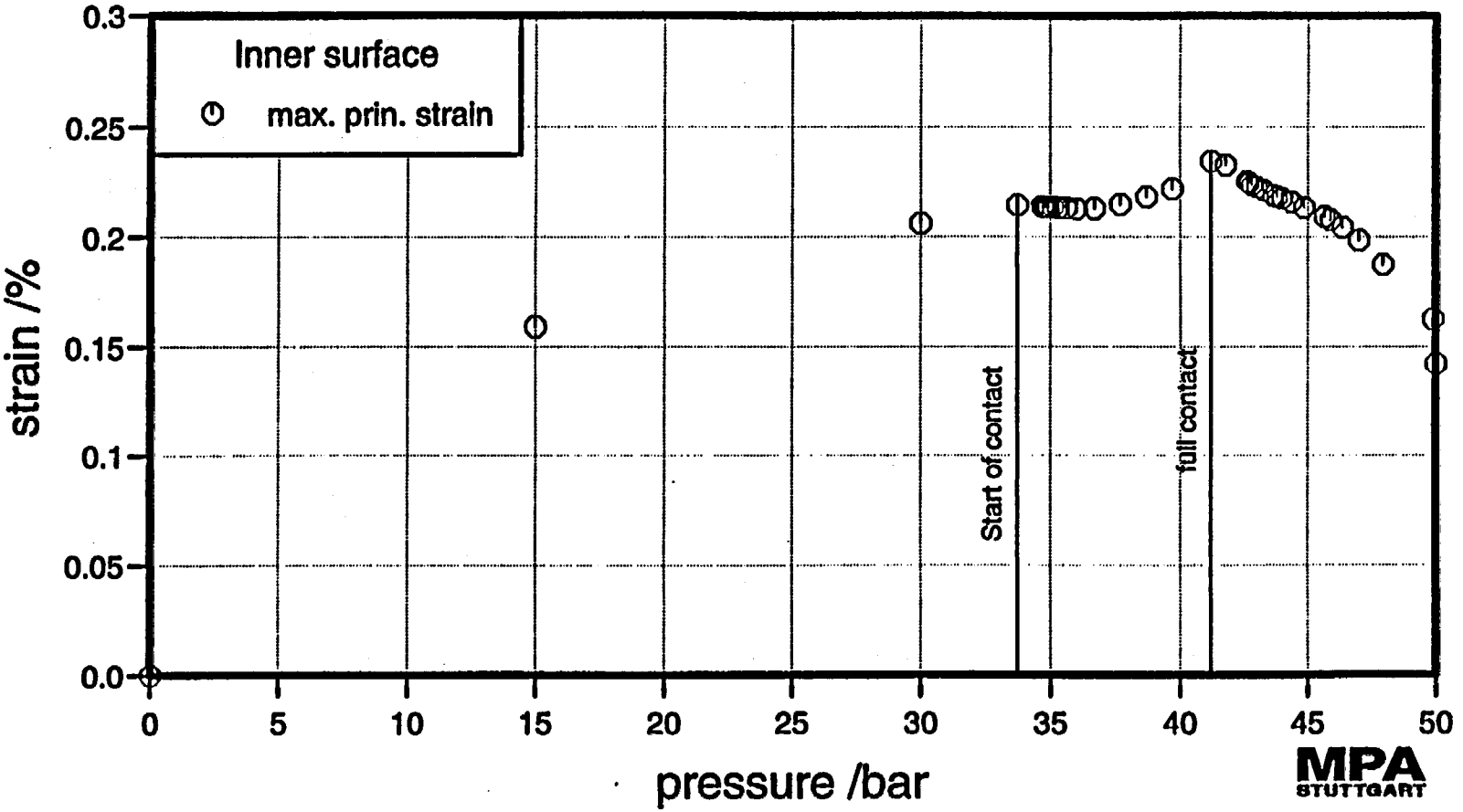
Inner surface
max. prin. strain
strain /%
0.3
0.25
0.2
0.15
0.1
0.05
0.0
0
5
10
15
20
25
30
35
40
45
50
pressure /bar
Start of contact
full contact
MPA
STUTTGART

Plot id No 3

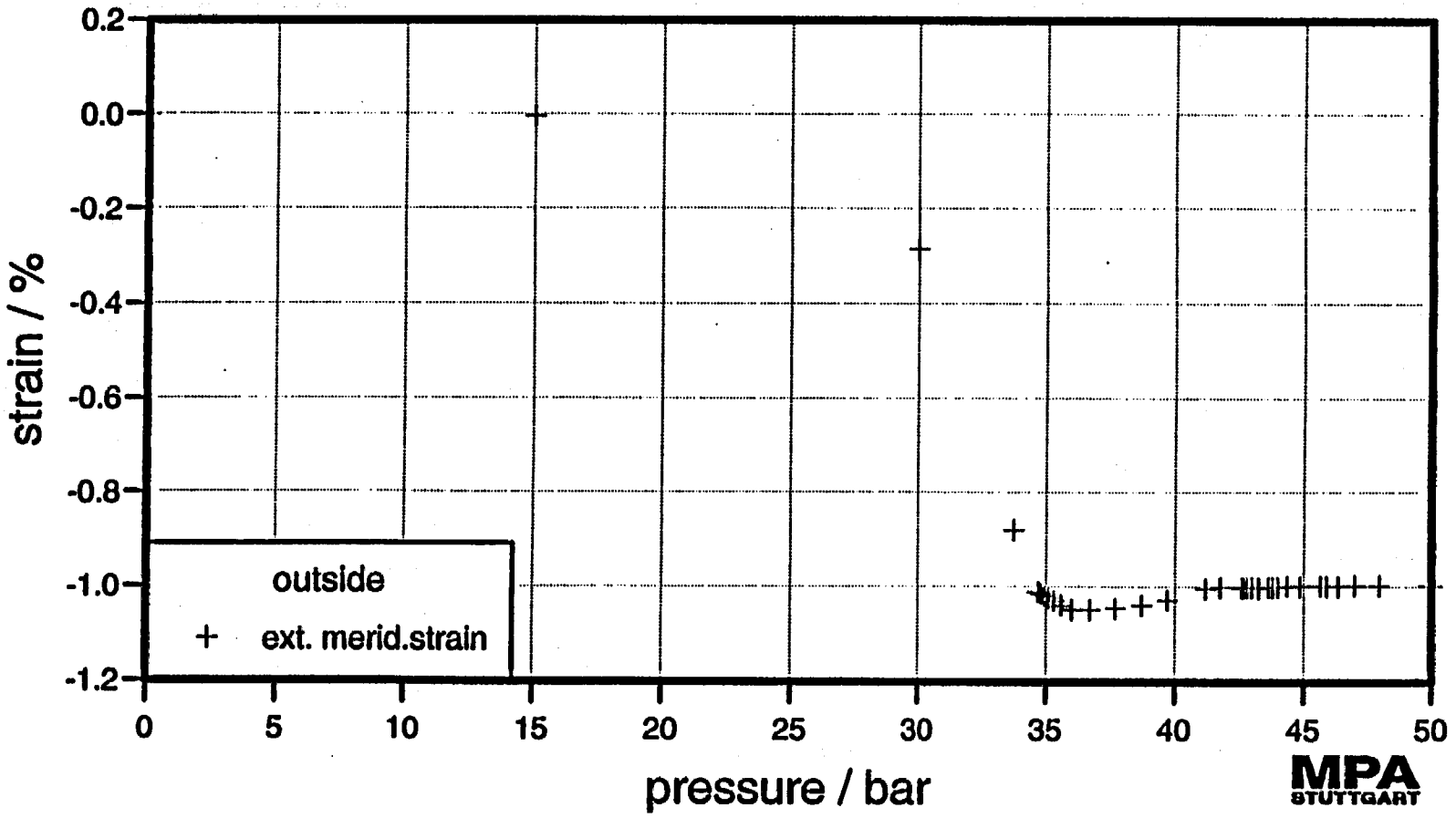
0.2
0.0
-0.2
-0.4
-0.6
-0.8
-1.0
-1.2
strain / %
outside
ext. merid.strain
0
5
10
15
20
25
30
35
40
45
50
pressure / bar
MPA
STUTTGART

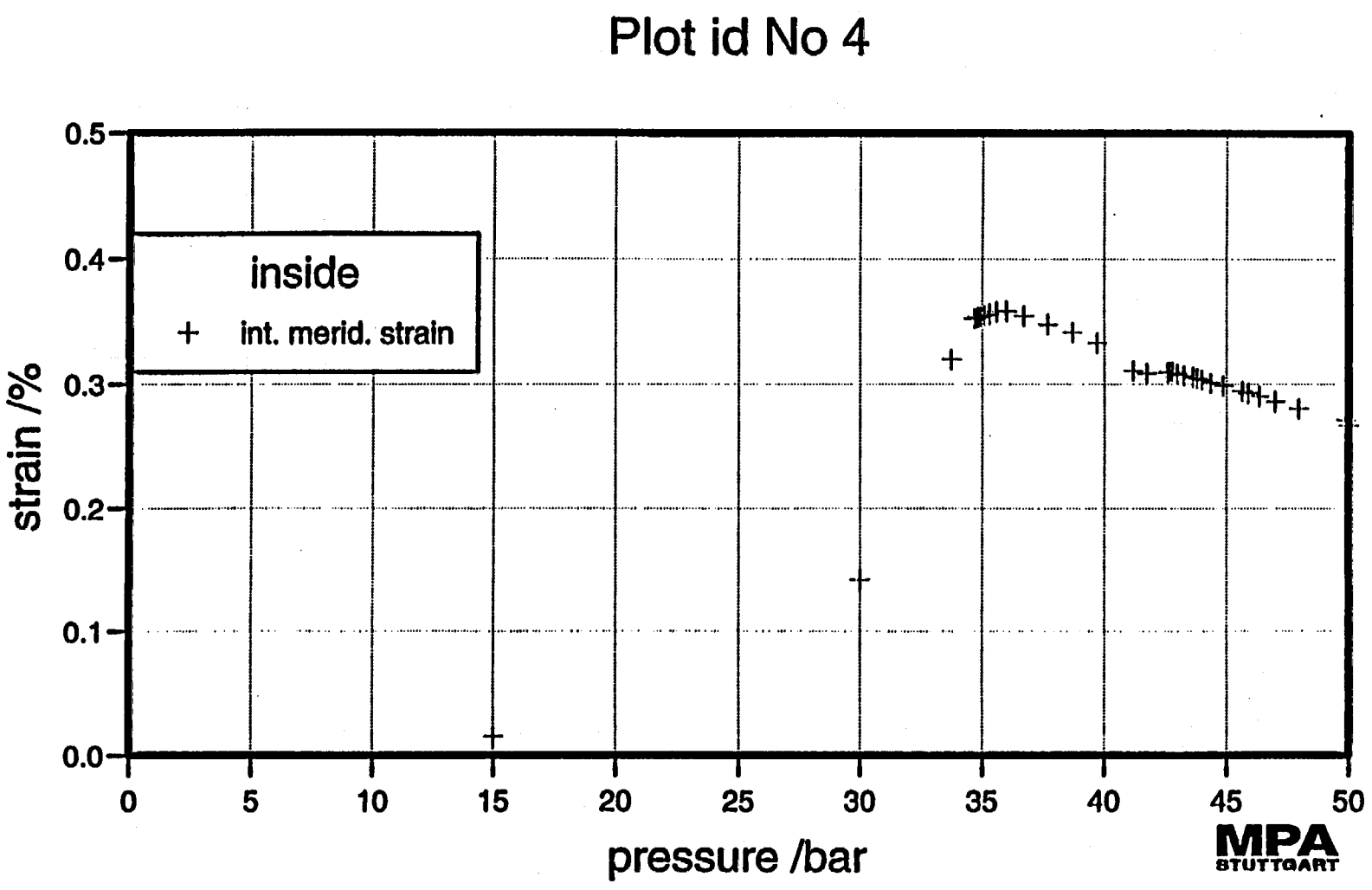
Plot id No 4
inside
int. merid. strain
strain /%
0.5
0.4
0.3
0.2
0.1
0.0
0
5
10
15
20
25
30
35
40
45
50
pressure /bar
MPA
STUTTGART

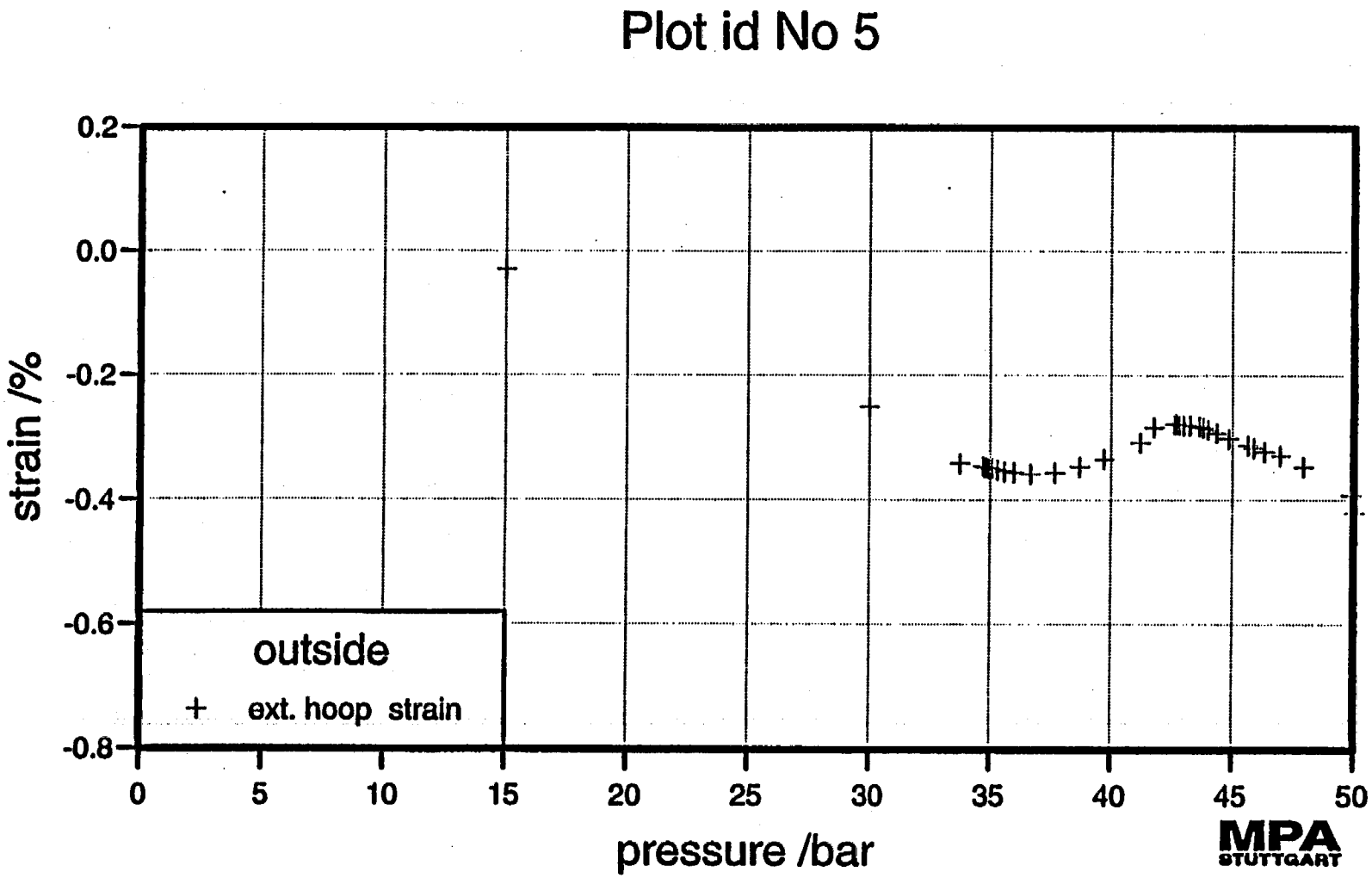
Plot id No 5
0.2
0.0
-0.2
-0.4
-0.6
-0.8
strain /%
outside
+ ext. hoop strain
0
5
10
15
20
25
30
35
40
45
50
pressure /bar
MPA
STUTTGART

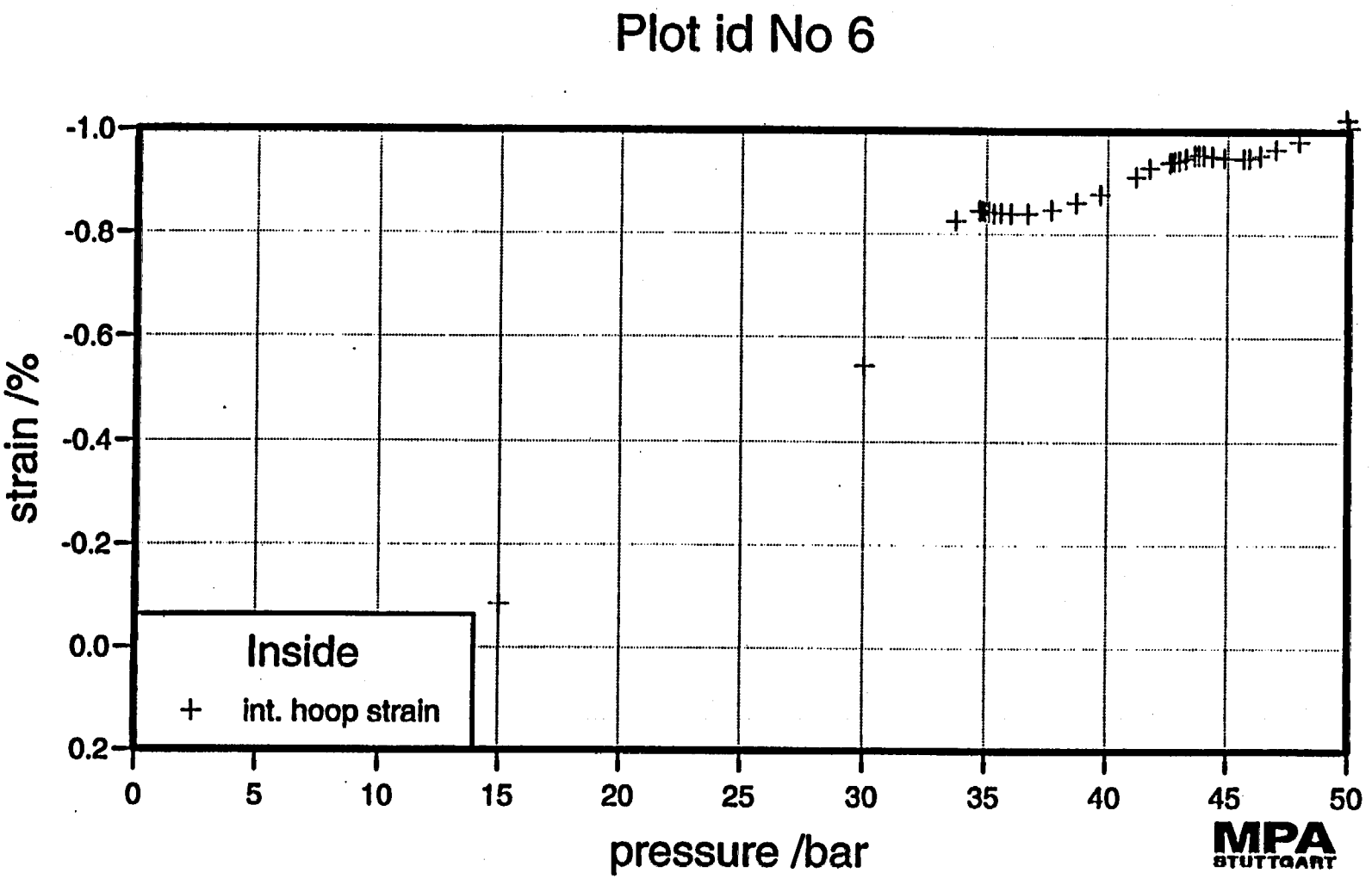
Plot id No 6
-1.0
-0.8
-0.6
-0.4
-0.2
0.0
0.2
strain /%
Inside
+ int. hoop strain
0
5
10
15
20
25
30
35
40
45
50
pressure /bar
MPA
STUTTGART

Plot id No 7

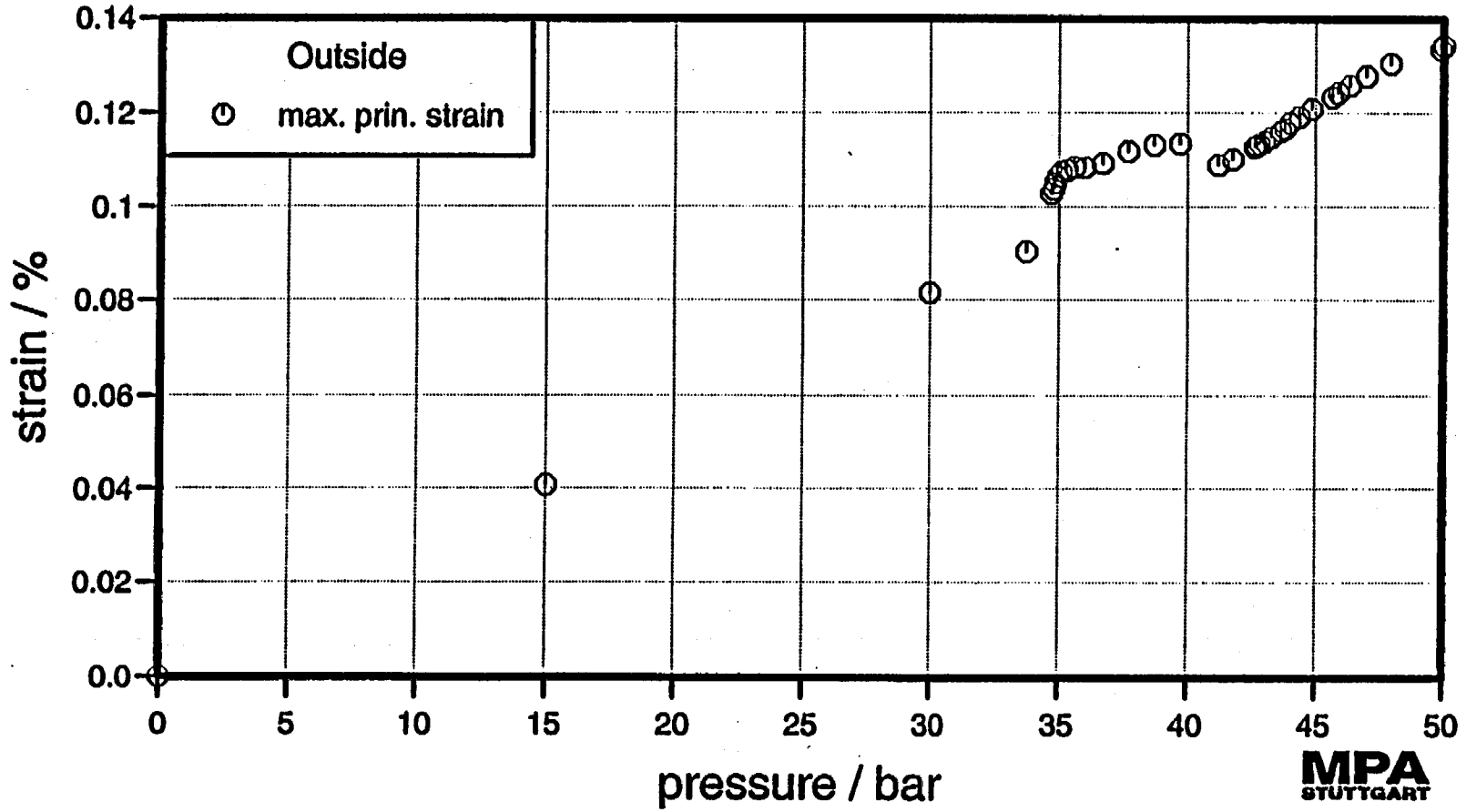
Outside
max. prin. strain
strain / %
0.14
0.12
0.1
0.08
0.06
0.04
0.02
0.0
0
5
10
15
20
25
30
35
40
45
50
pressure / bar
MPA
STUTTGART

Plot id No 8

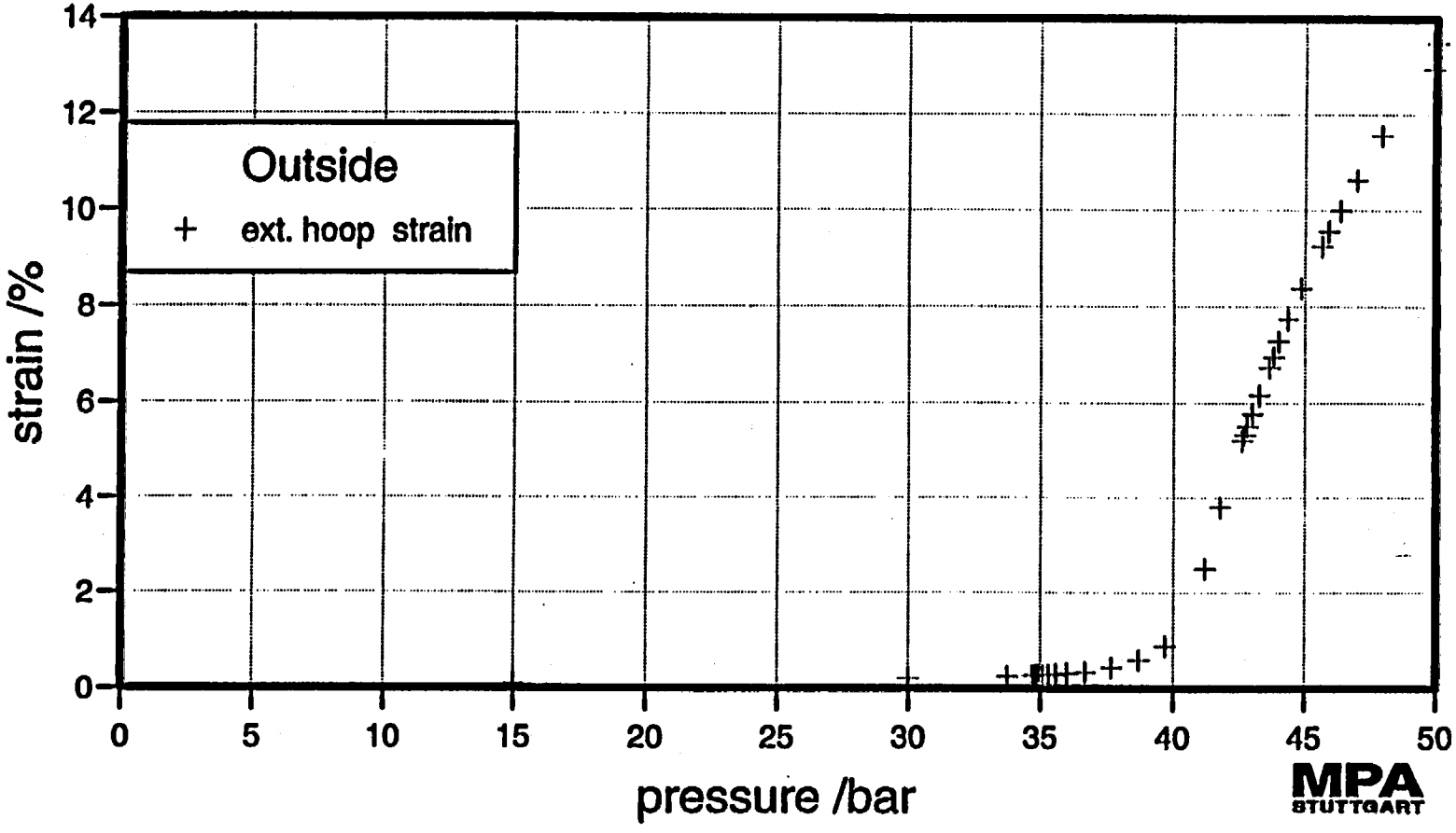
Outside
+ ext. hoop strain
strain /%
pressure /bar
0
2
4
6
8
10
12
14
0
5
10
15
20
25
30
35
40
45
50
MPA
STUTTGART

Plot id No 9

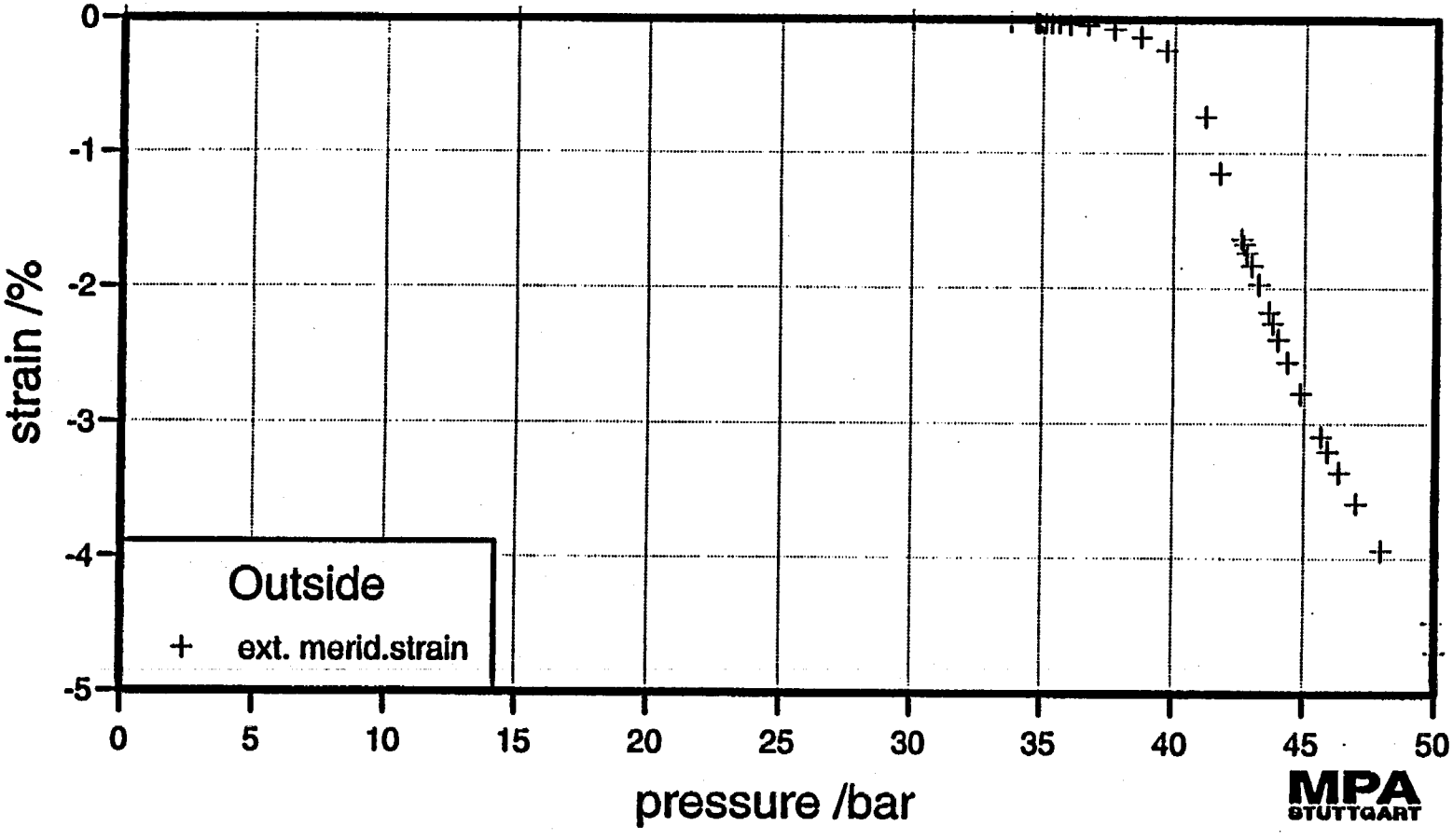
strain /%
0
-1
-2
-3
-4
-5
0
5
10
15
20
25
30
35
40
45
50
pressure /bar
Outside
ext. merid.strain
MPA
STUTTGART

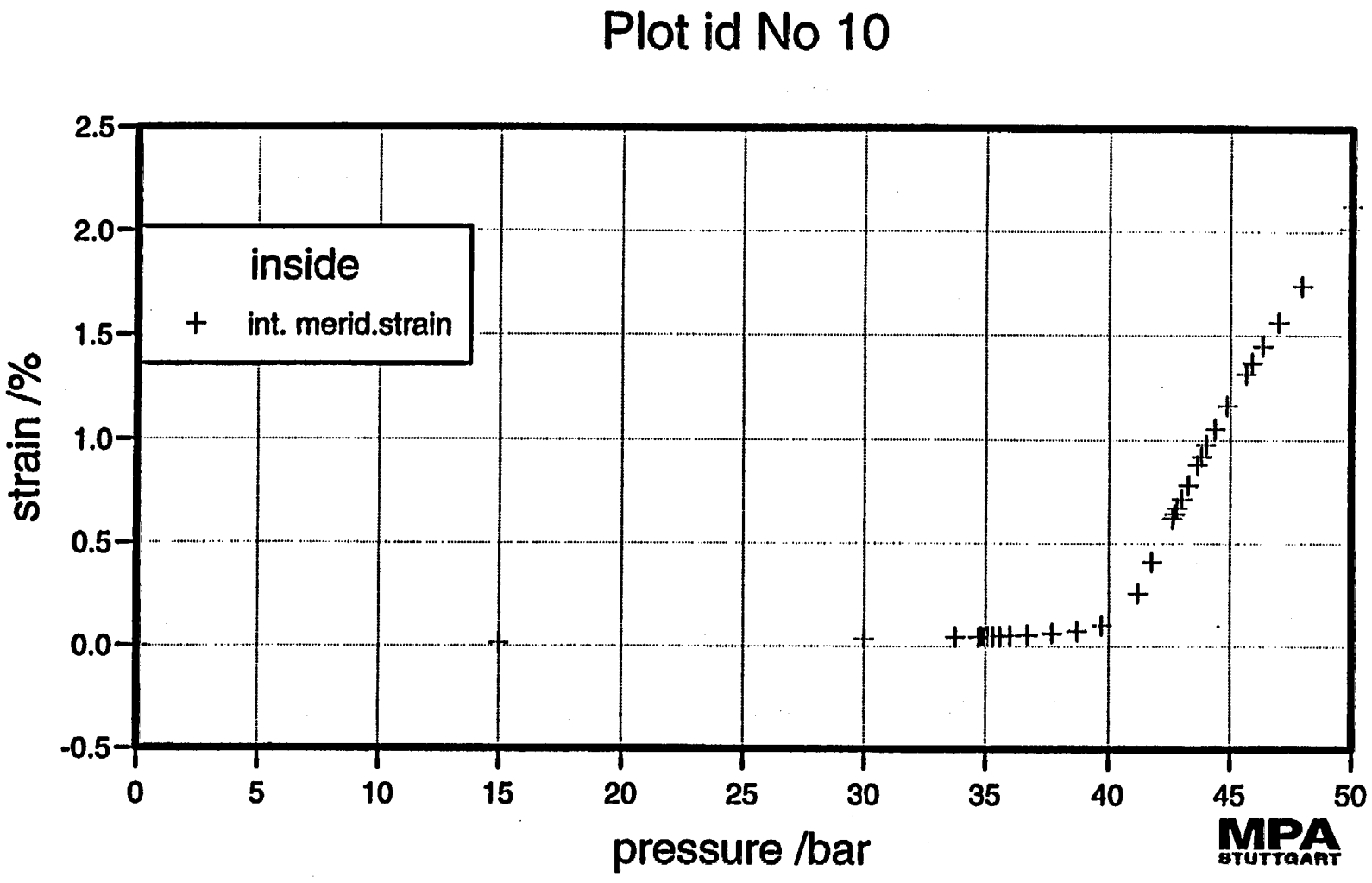
Plot id No 10
inside
int. merid.strain
strain /%
pressure /bar
2.5
2.0
1.5
1.0
0.5
0.0
-0.5
0
5
10
15
20
25
30
35
40
45
50
MPA
STUTTGART

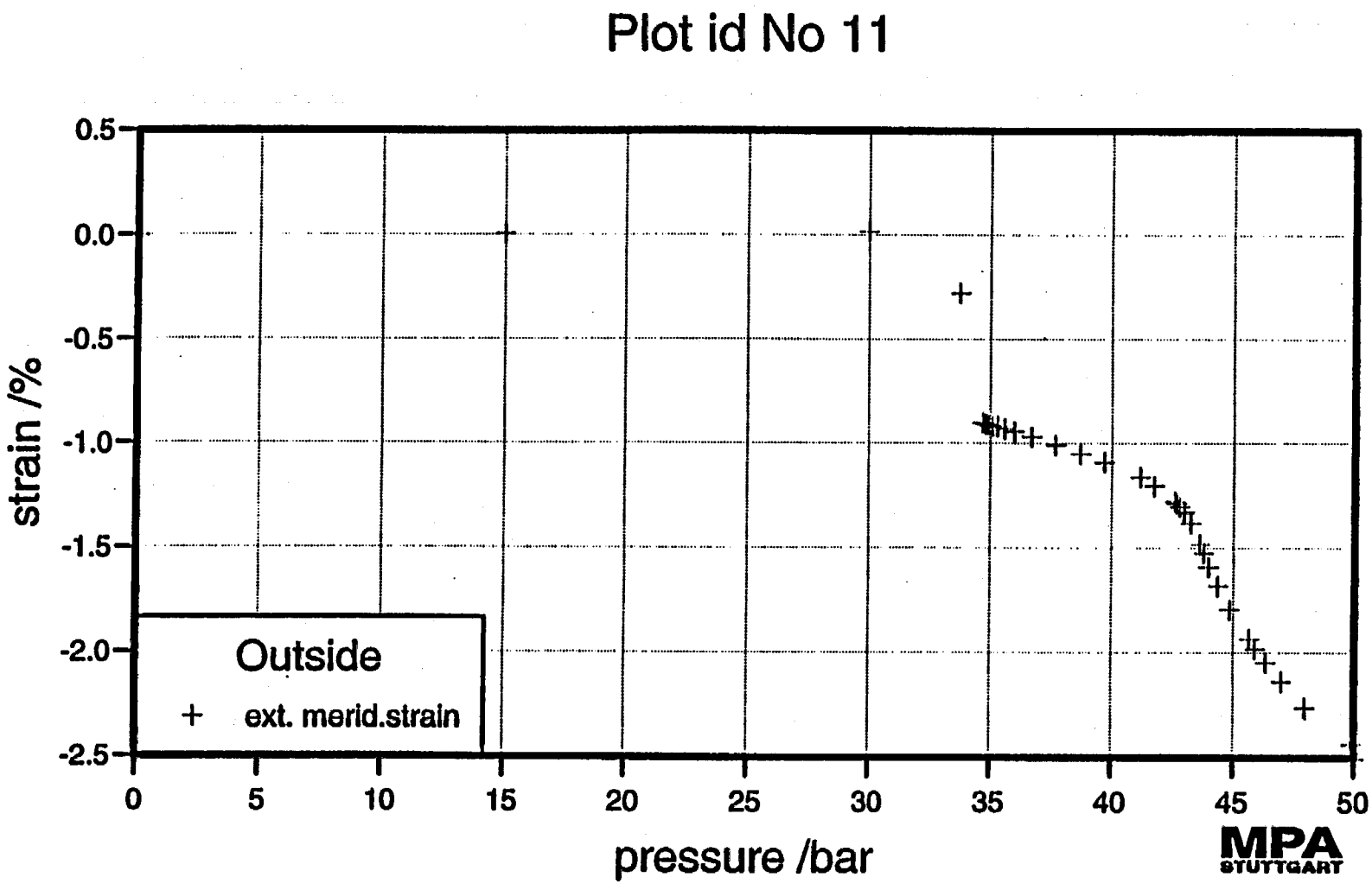
Plot id No 11
0.5
0.0
-0.5
-1.0
-1.5
-2.0
-2.5
strain /%
Outside
ext. merid.strain
0
5
10
15
20
25
30
35
40
45
50
pressure /bar
MPA
STUTTGART

Plot id No 12

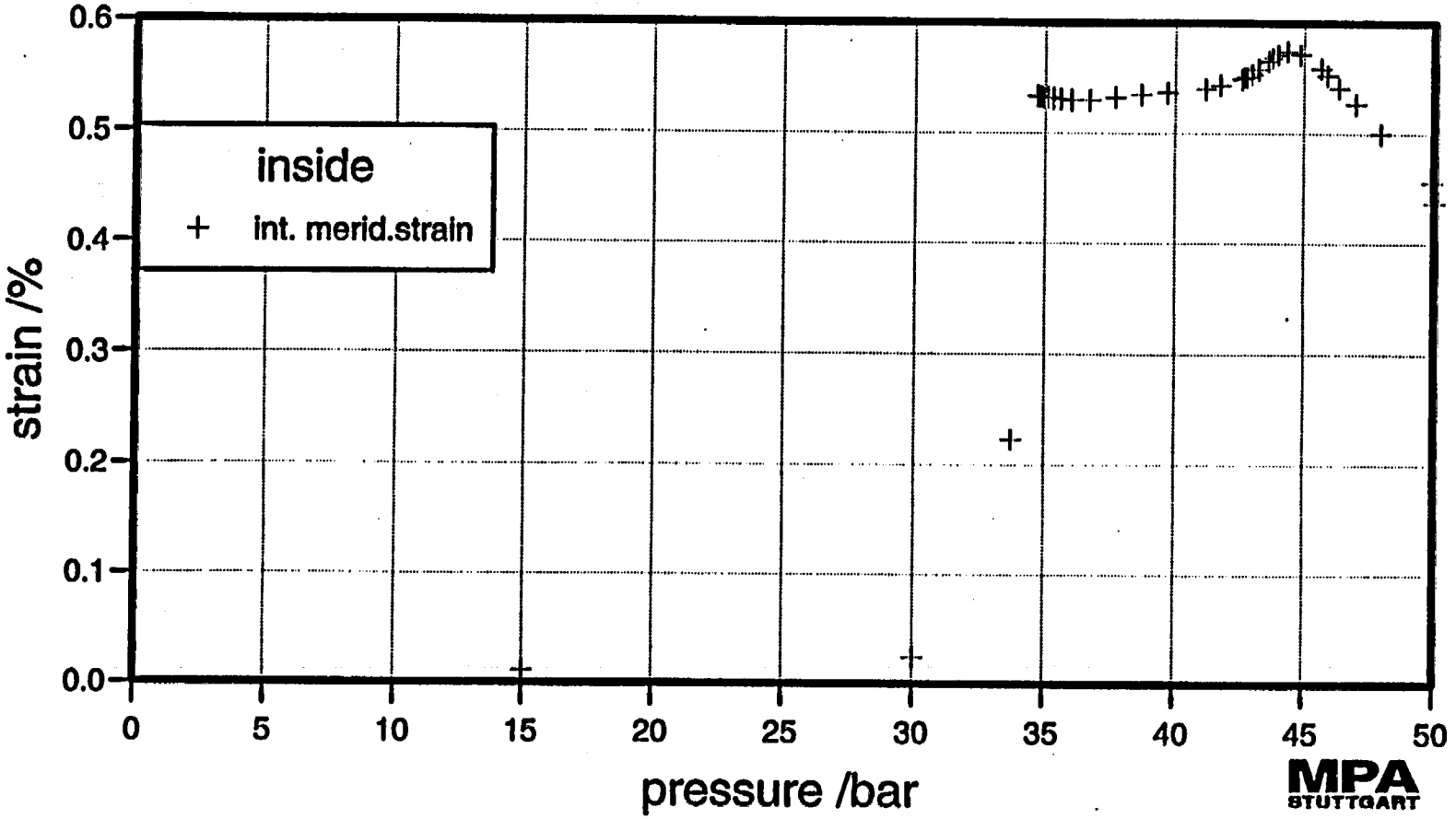
inside
+ int. merid.strain
strain /%
0.6
0.5
0.4
0.3
0.2
0.1
0.0
0
5
10
15
20
25
30
35
40
45
50
pressure /bar
MPA
STUTTGART

Plot id No 13

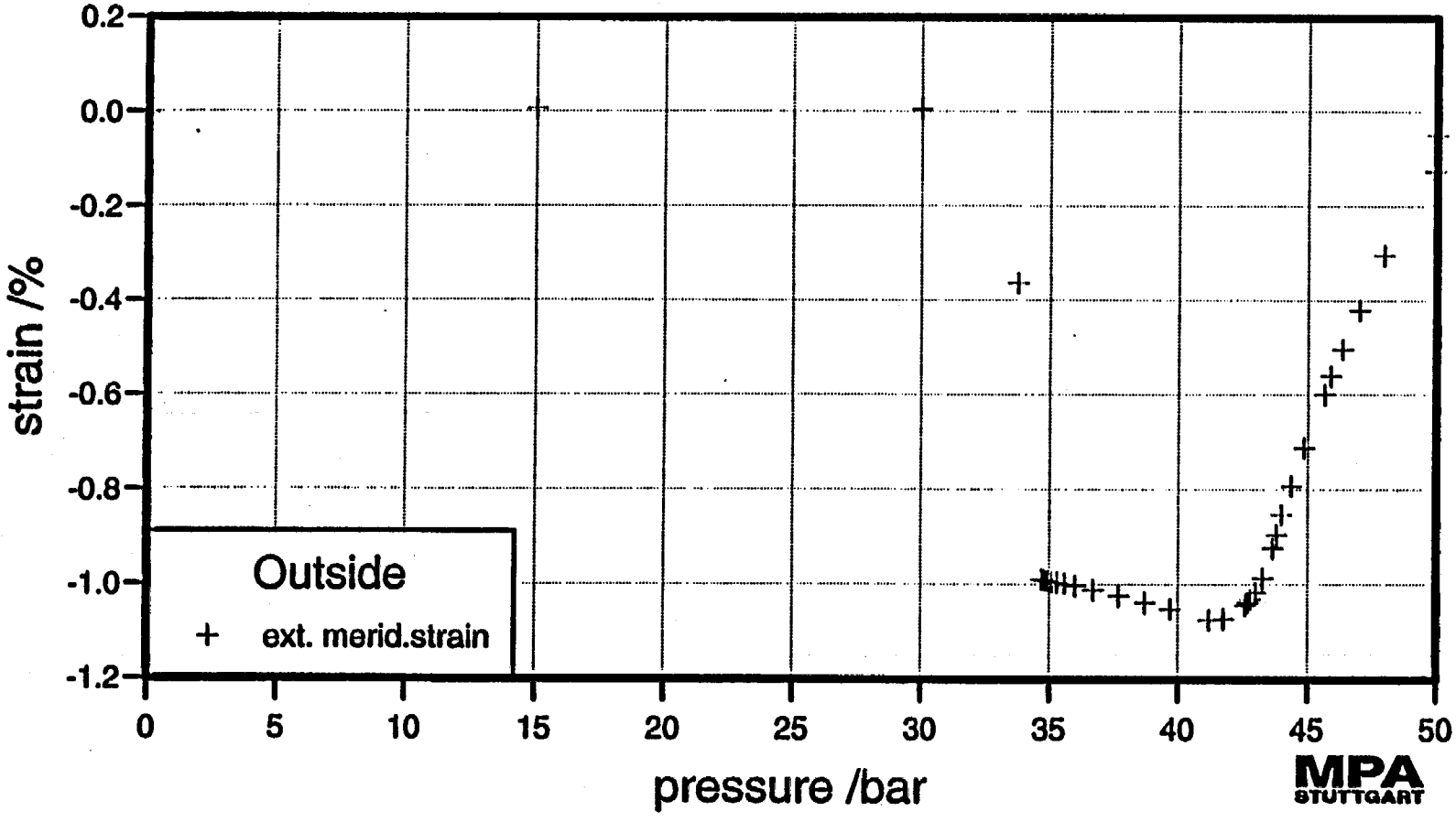
0.2
0.0
-0.2
-0.4
-0.6
-0.8
-1.0
-1.2
strain /%
0
5
10
15
20
25
30
35
40
45
50
pressure /bar
Outside
ext. merid.strain
MPA
STUTTGART

Plot id No 14

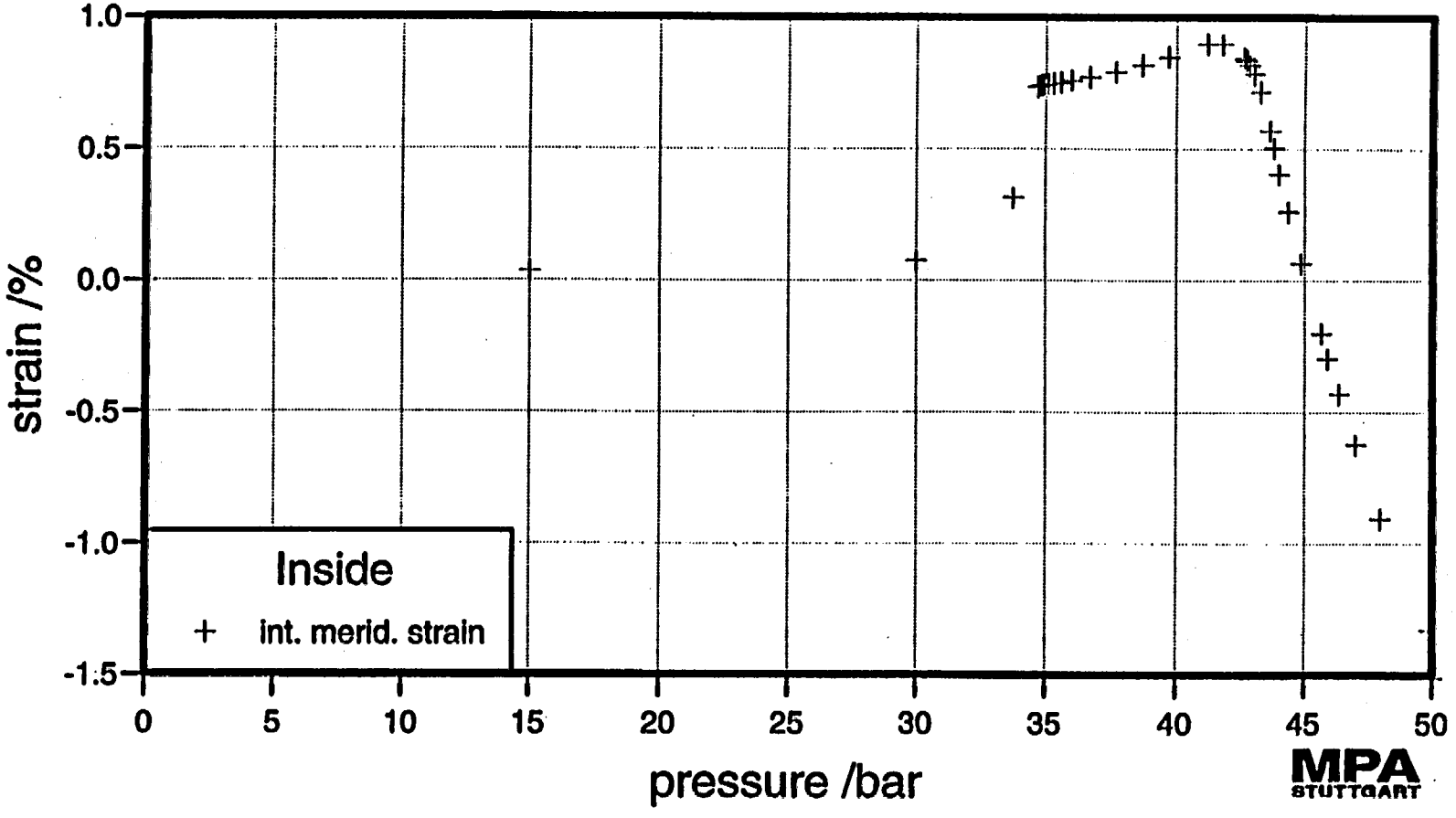
1.0
0.5
0.0
-0.5
-1.0
-1.5
strain /%
0
5
10
15
20
25
30
35
40
45
50
pressure /bar
Inside
+ int. merid. strain
MPA
STUTTGART

Plot id No 15

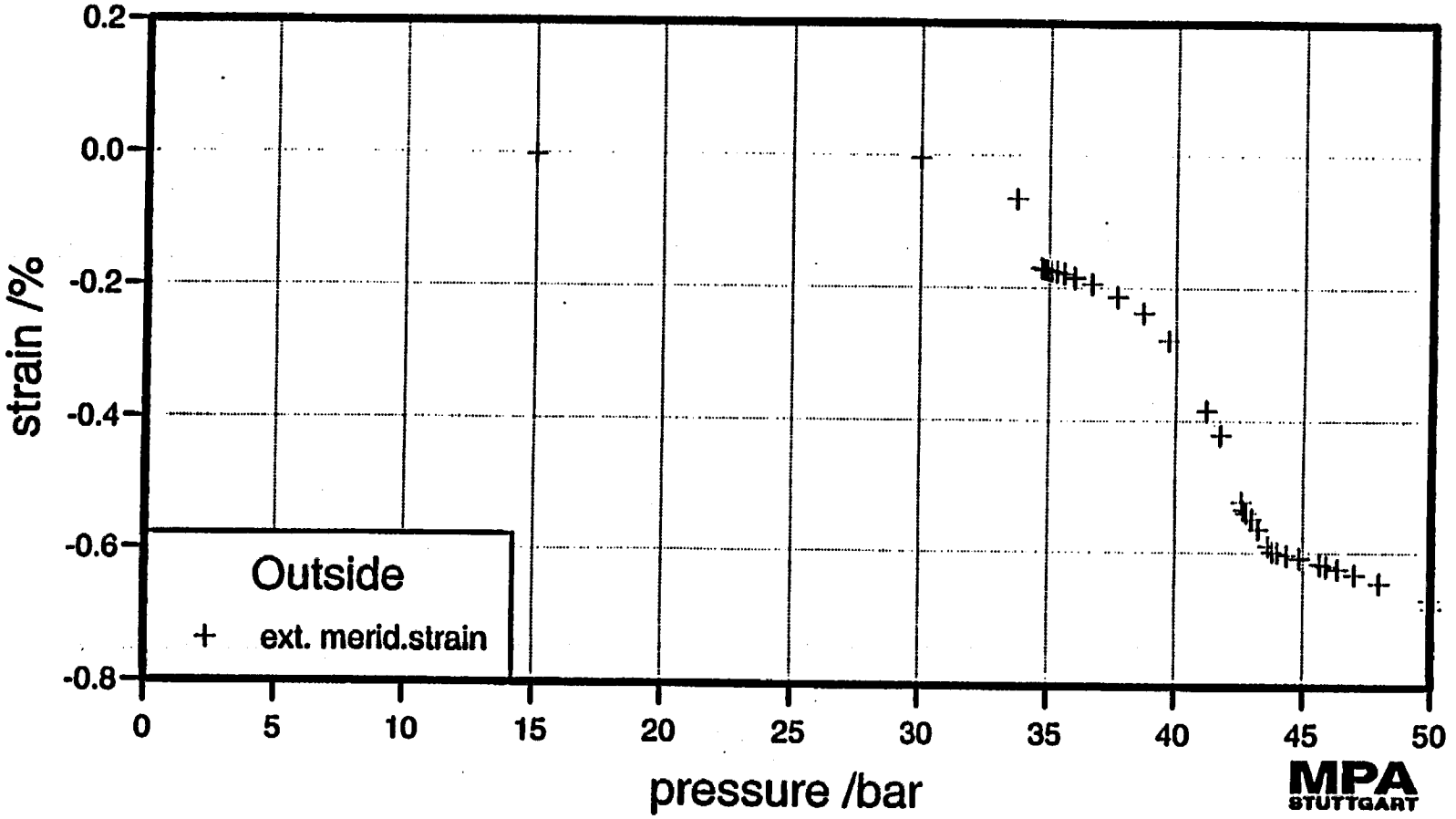
0.2
0.0
-0.2
-0.4
-0.6
-0.8
strain /%
Outside
ext. merid.strain
0
5
10
15
20
25
30
35
40
45
50
pressure /bar
MPA
STUTTGART

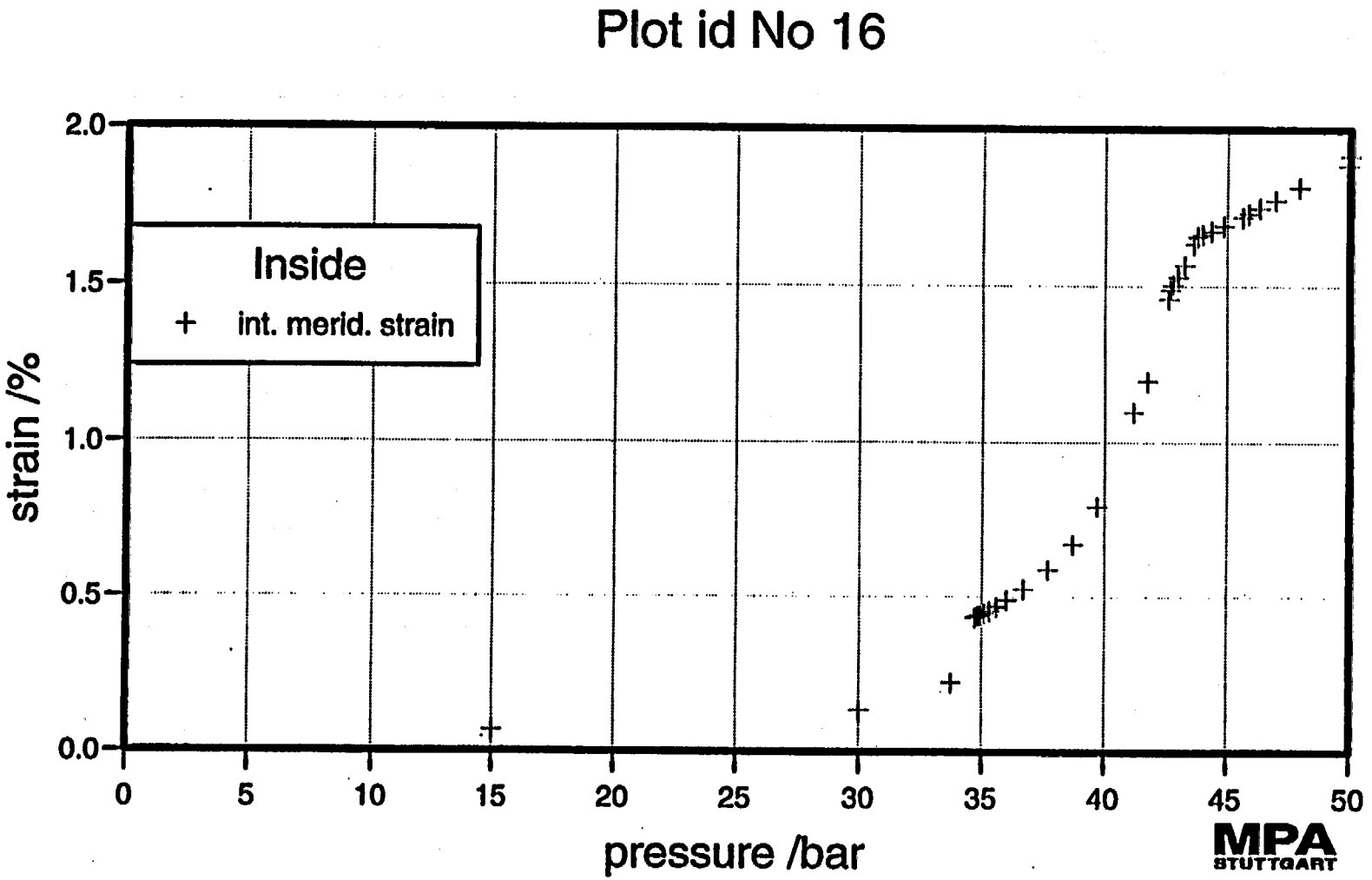
Plot id No 16
Inside
+ int. merid. strain
strain /%
2.0
1.5
1.0
0.5
0.0
0
5
10
15
20
25
30
35
40
45
50
pressure /bar
MPA
STUTTGART

Plot id No 17

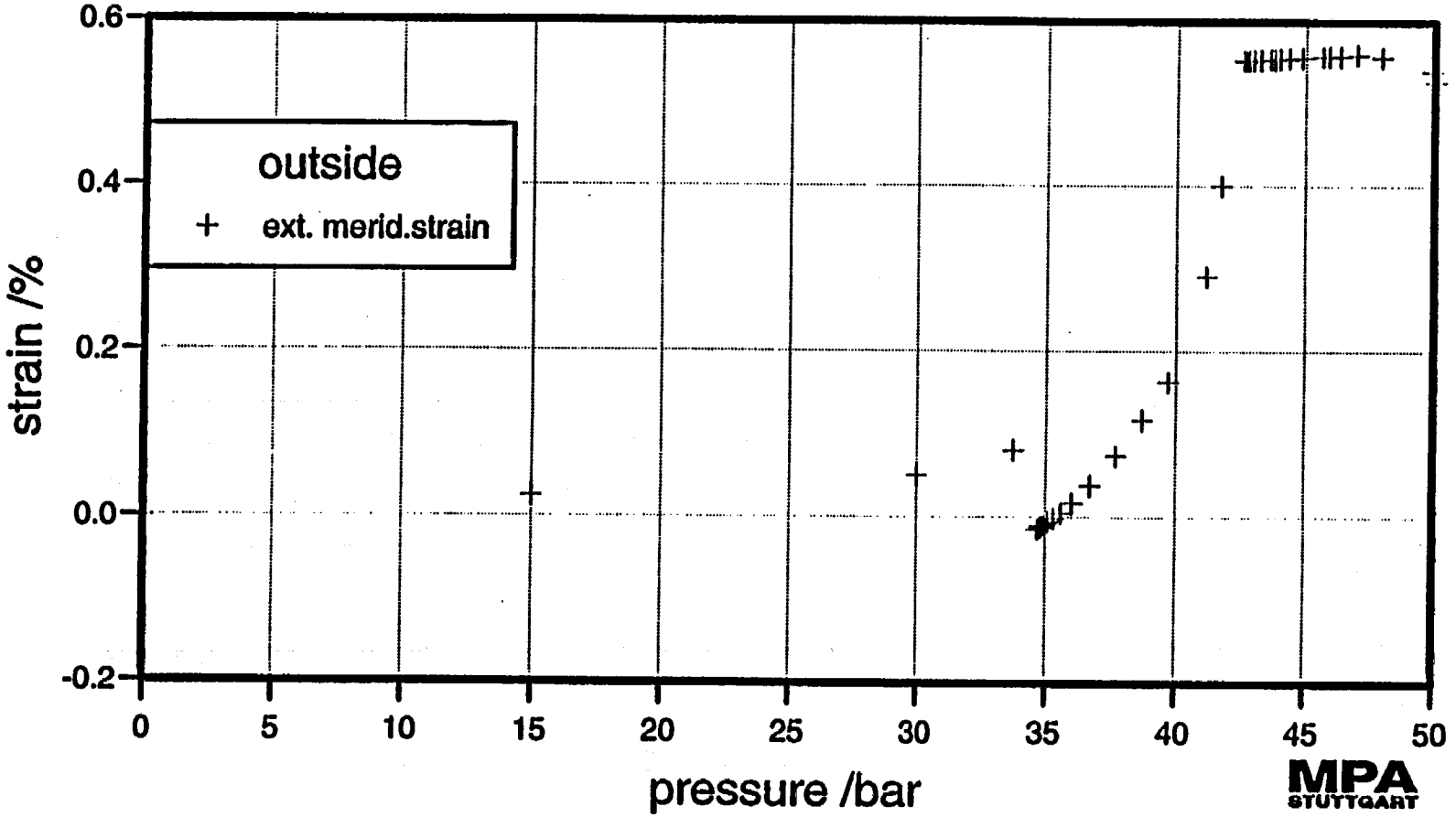
outside
ext. merid.strain
strain /%
0.6
0.4
0.2
0.0
-0.2
0
5
10
15
20
25
30
35
40
45
50
pressure /bar
MPA
STUTTGART

Plot id No 18

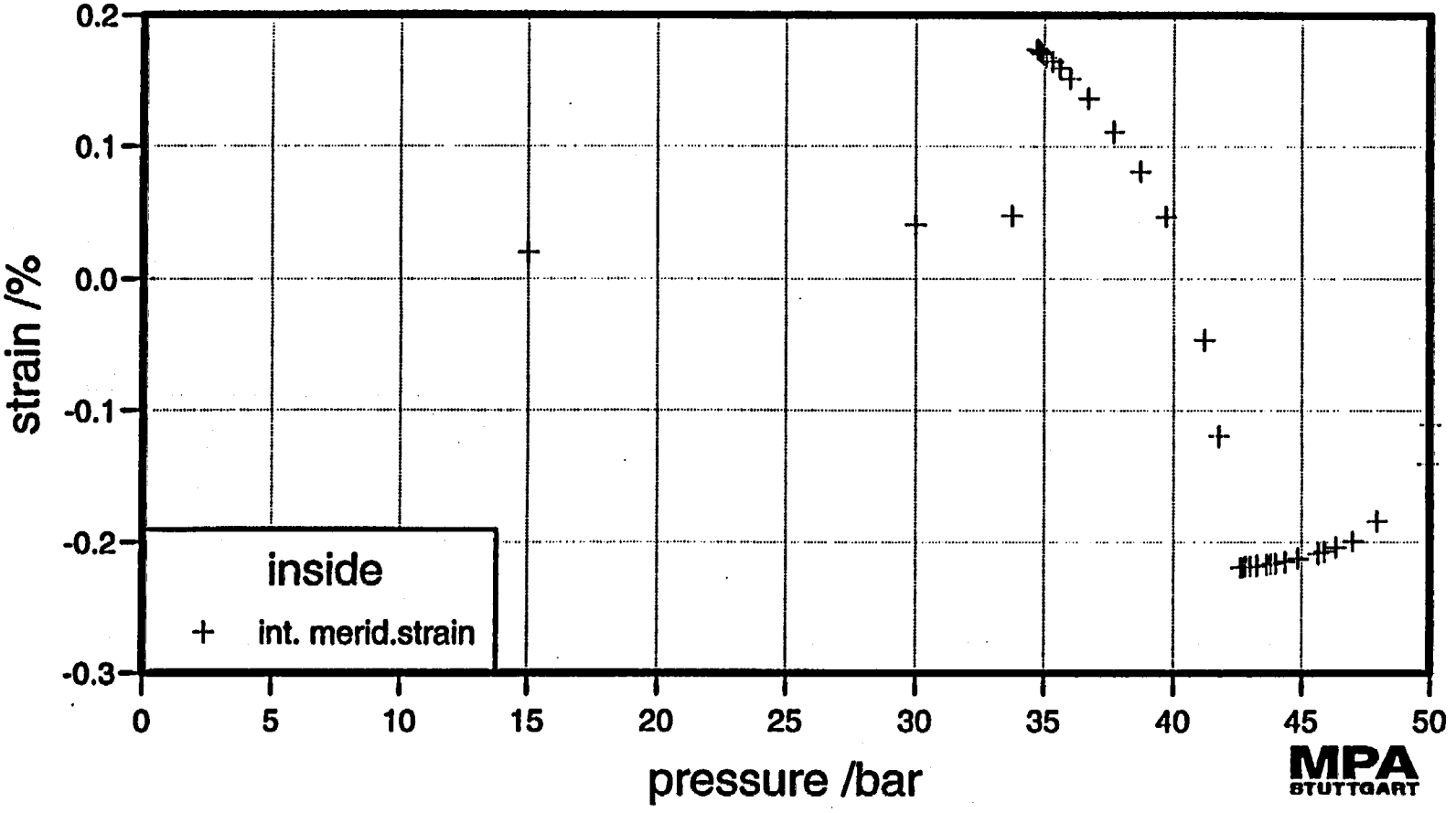
0.2
0.1
0.0
-0.1
-0.2
-0.3
strain /%
0
5
10
15
20
25
30
35
40
45
50
pressure /bar
inside
int. merid.strain
MPA
STUTTGART

Plot id No 19

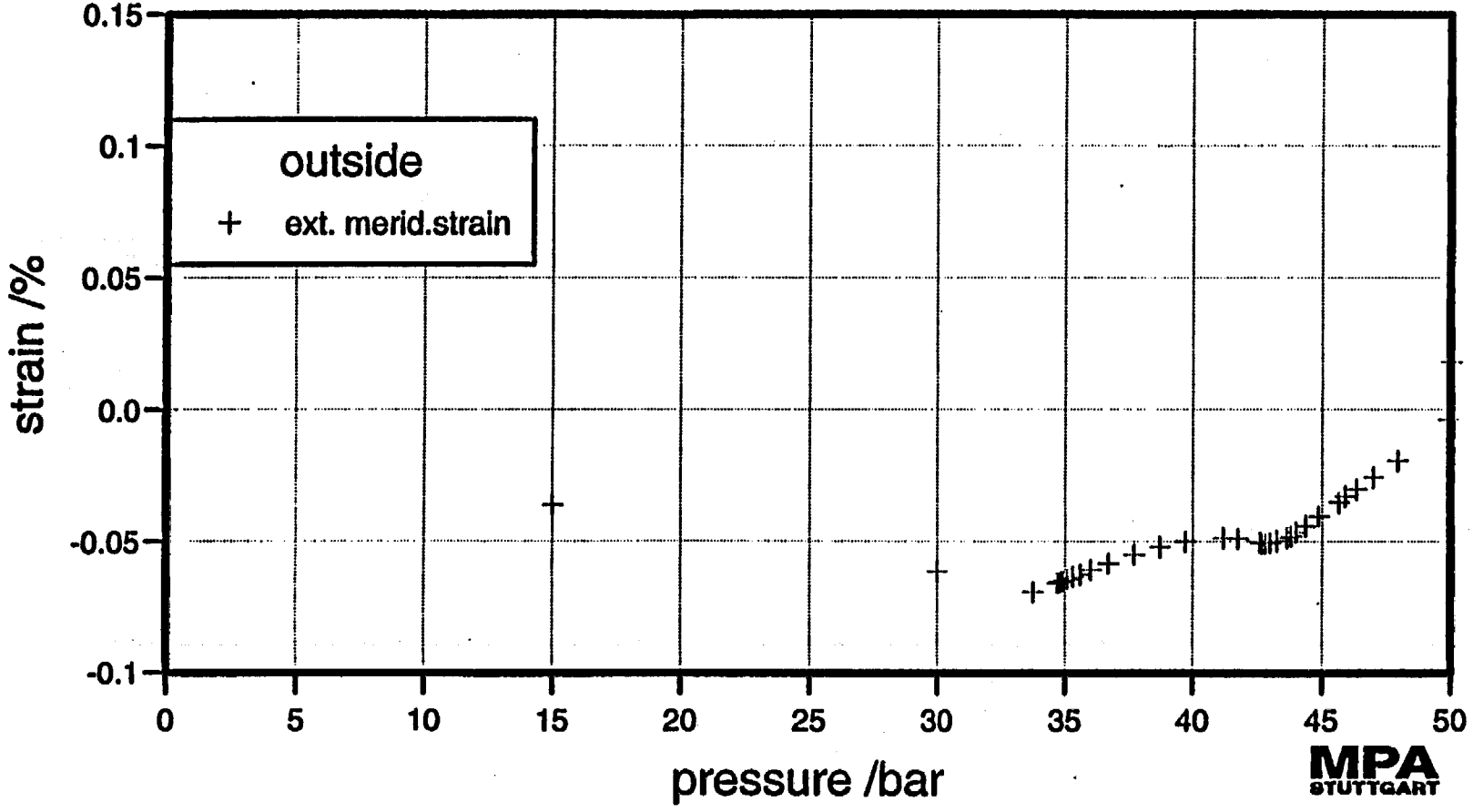
outside
+ ext. merid.strain
strain /%
0.15
0.1
0.05
0.0
-0.05
-0.1
0
5
10
15
20
25
30
35
40
45
50
pressure /bar
MPA
STUTTGART

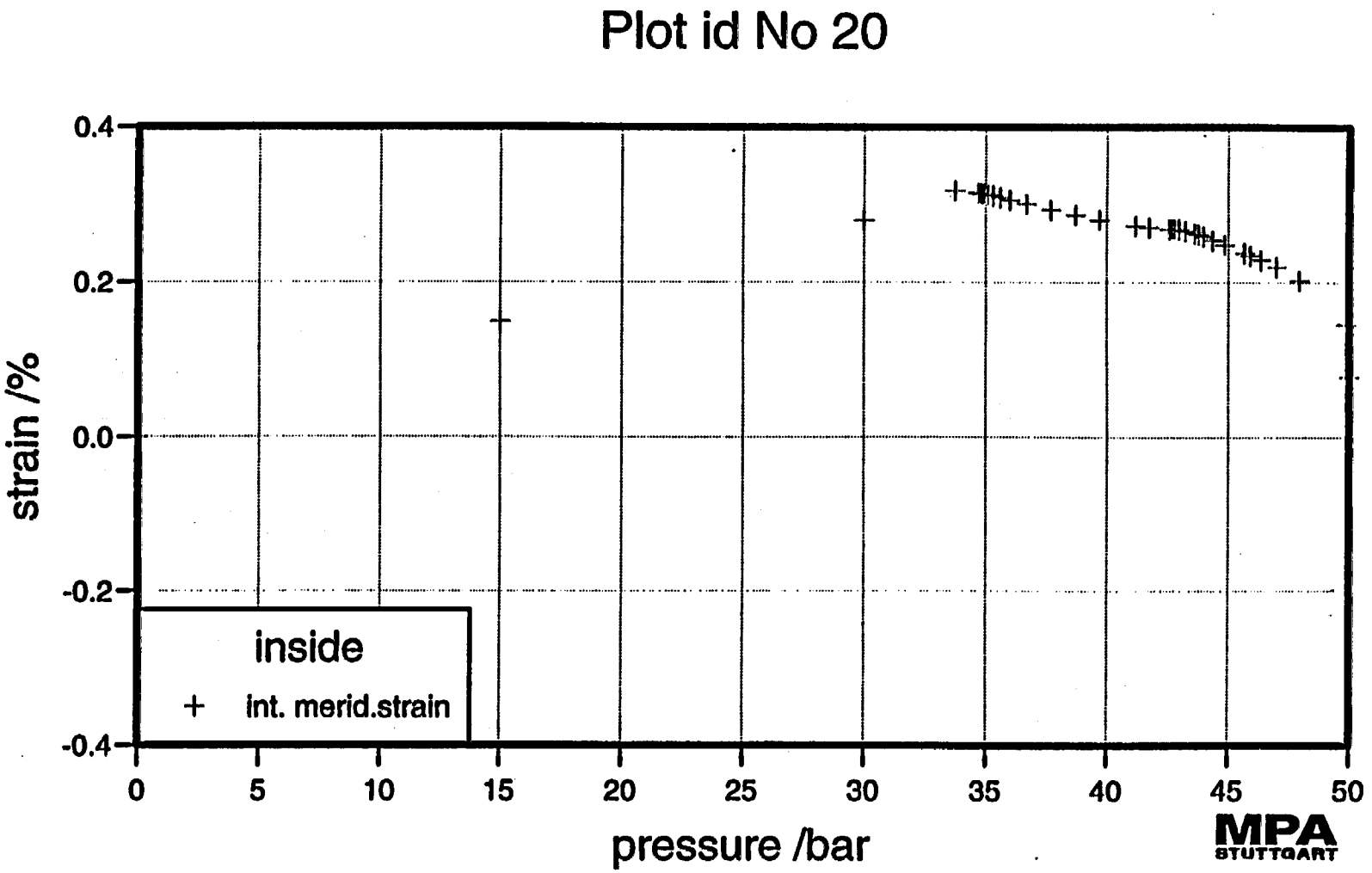
Plot id No 20
0.4
0.2
0.0
-0.2
-0.4
strain /%
inside
int. merid.strain
0
5
10
15
20
25
30
35
40
45
50
pressure /bar
MPA
STUTTGART

Plot id No 21

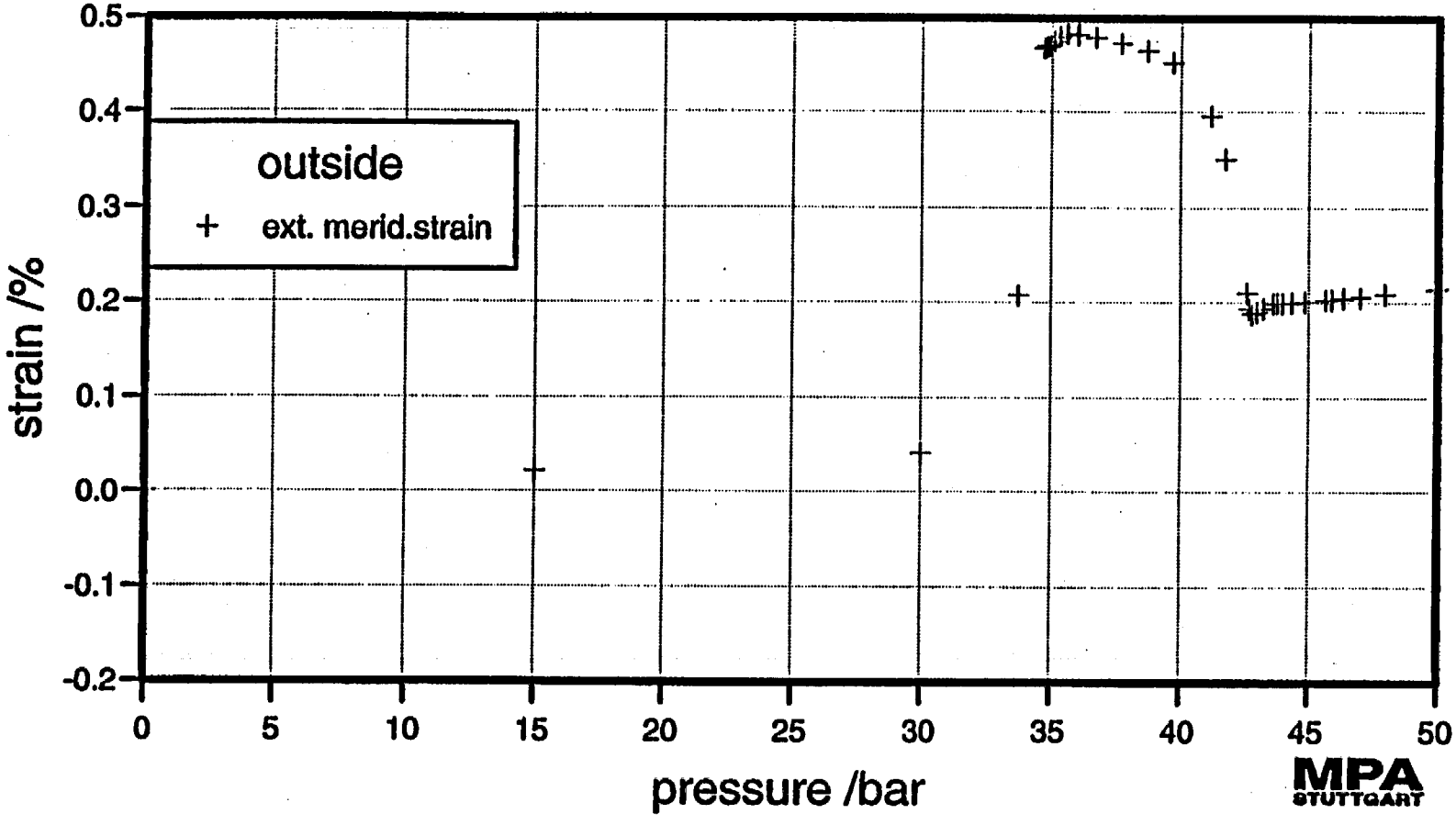
outside
+ ext. merid.strain
strain /%
0.5
0.4
0.3
0.2
0.1
0.0
-0.1
-0.2
0
5
10
15
20
25
30
35
40
45
50
pressure /bar
MPA
STUTTGART

Plot id No 22

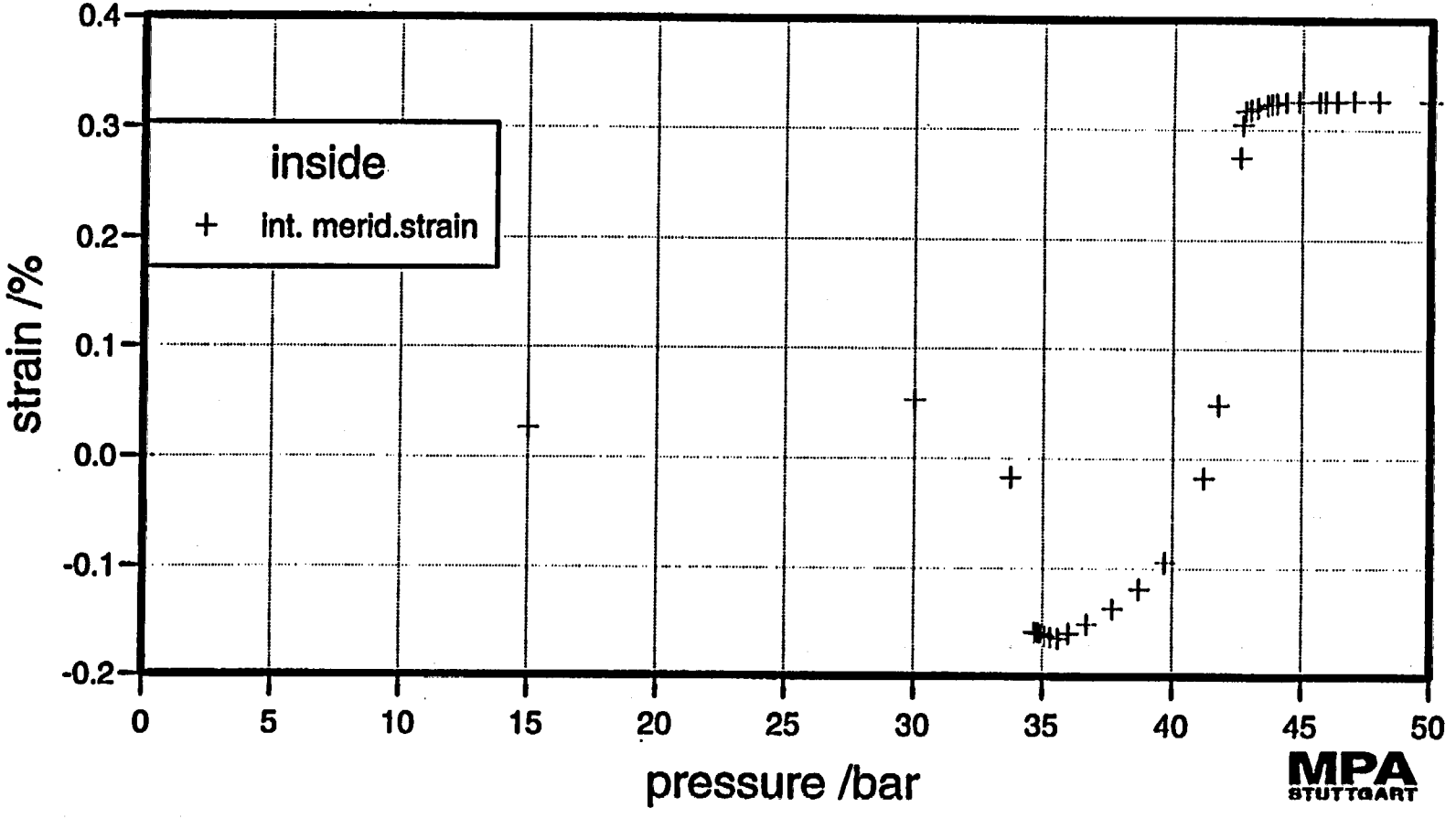
inside
int. merid.strain
strain /%
0.4
0.3
0.2
0.1
0.0
-0.1
-0.2
0
5
10
15
20
25
30
35
40
45
50
pressure /bar
MPA
STUTTGART

Plot id No 23

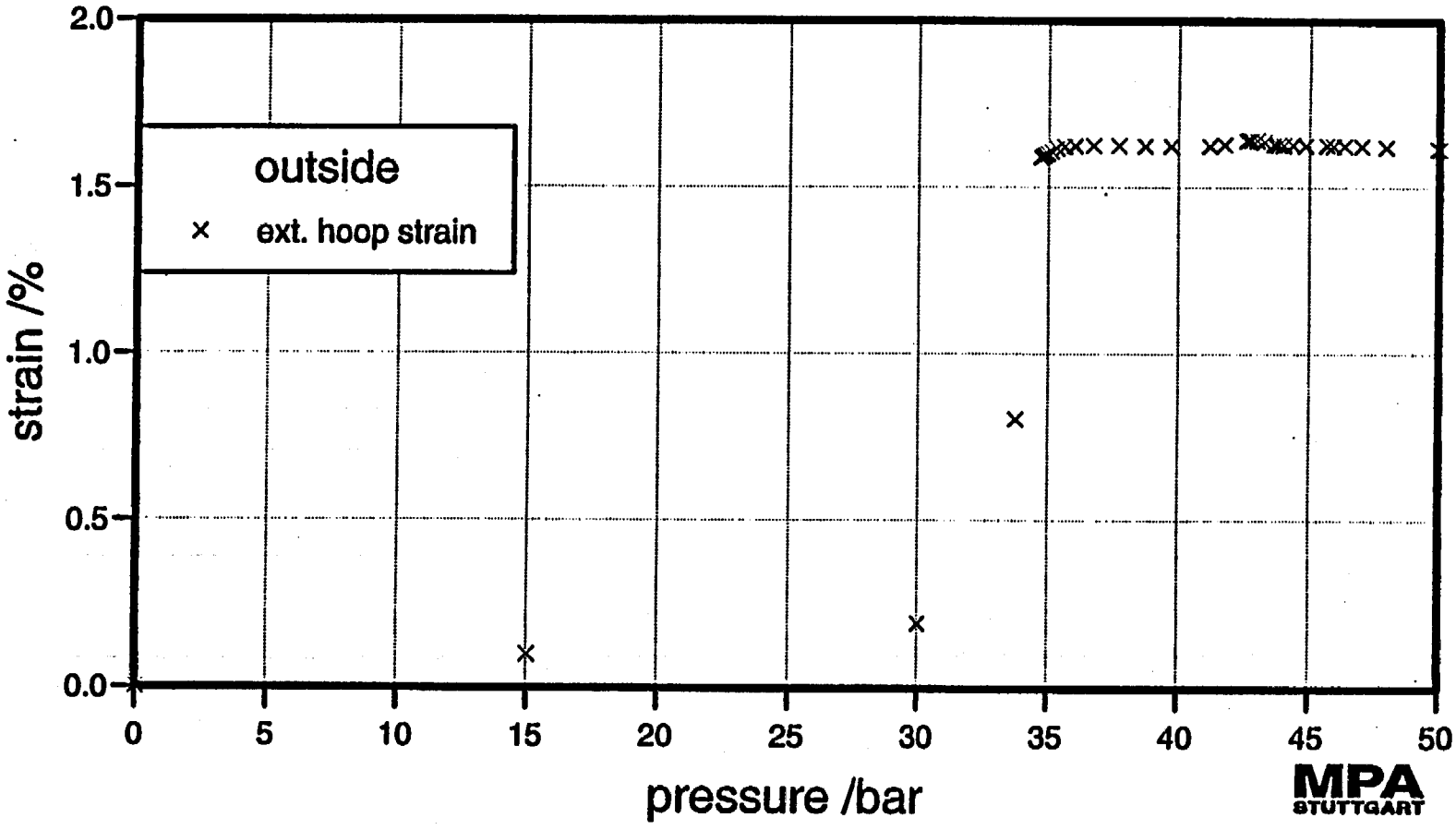
outside
ext. hoop strain
strain /%
2.0
1.5
1.0
0.5
0.0
0
5
10
15
20
25
30
35
40
45
50
pressure /bar
MPA
STUTTGART

Plot id No 24

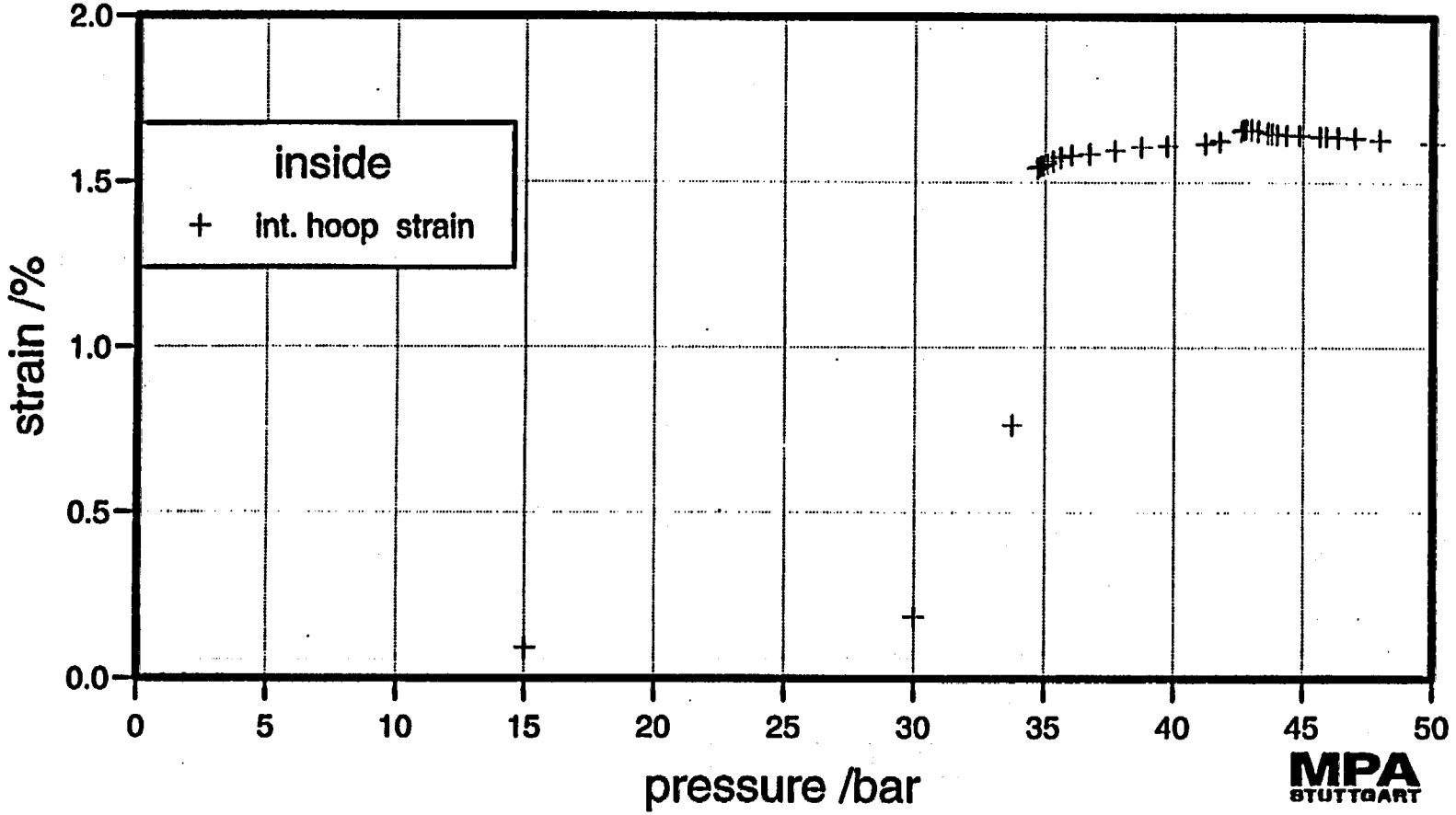
inside
+ int. hoop strain
strain /%
2.0
1.5
1.0
0.5
0.0
0
5
10
15
20
25
30
35
40
45
50
pressure /bar
MPA
STUTTGART

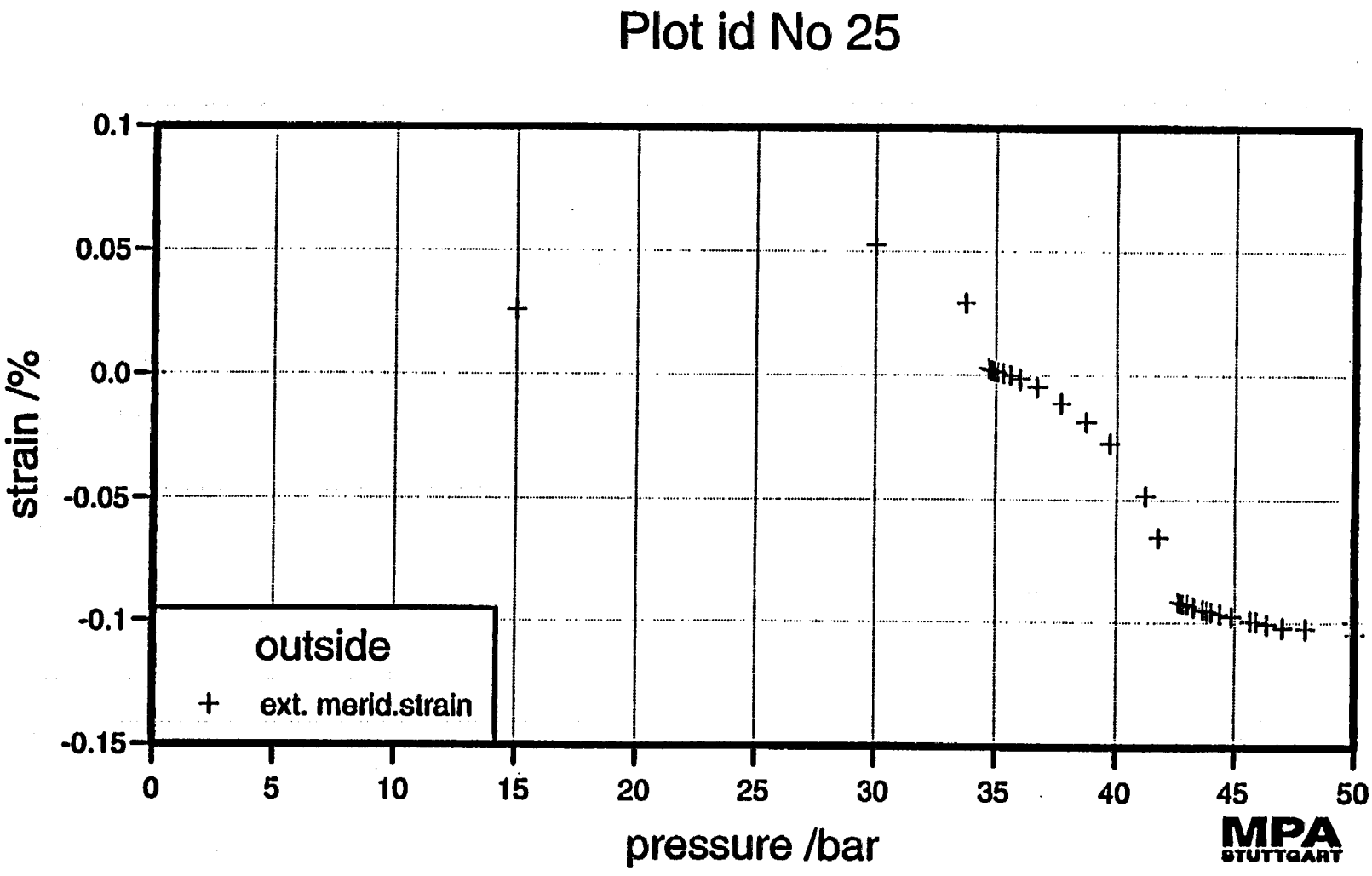
Plot id No 25
0.1
0.05
0.0
-0.05
-0.1
-0.15
strain /%
outside
ext. merid.strain
0
5
10
15
20
25
30
35
40
45
50
pressure /bar
MPA
STUTTGART

Plot id No 26

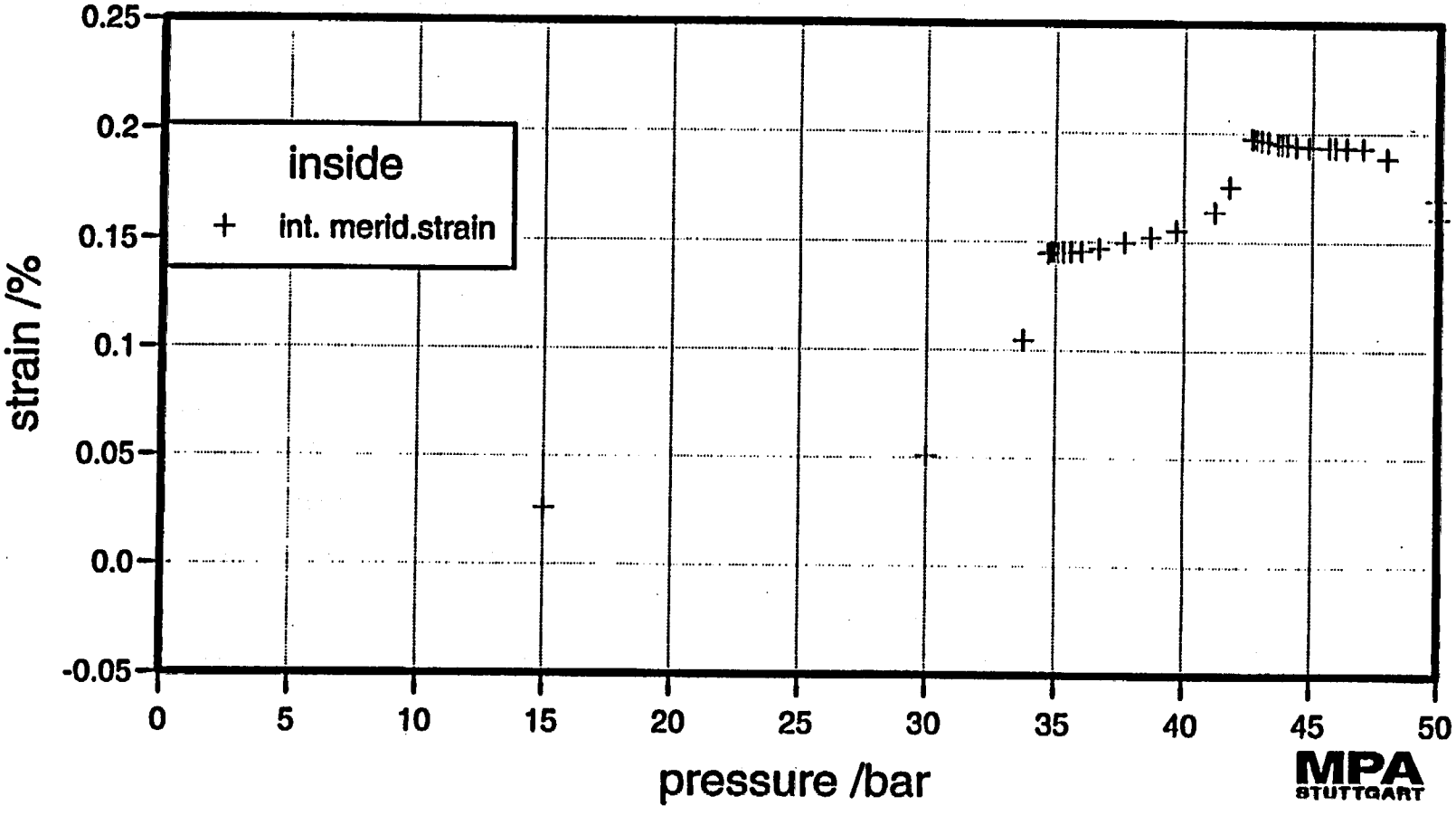
inside
int. merid.strain
strain /%
0.25
0.2
0.15
0.1
0.05
0.0
-0.05
0
5
10
15
20
25
30
35
40
45
50
pressure /bar
MPA
STUTTGART

Plot id No 27

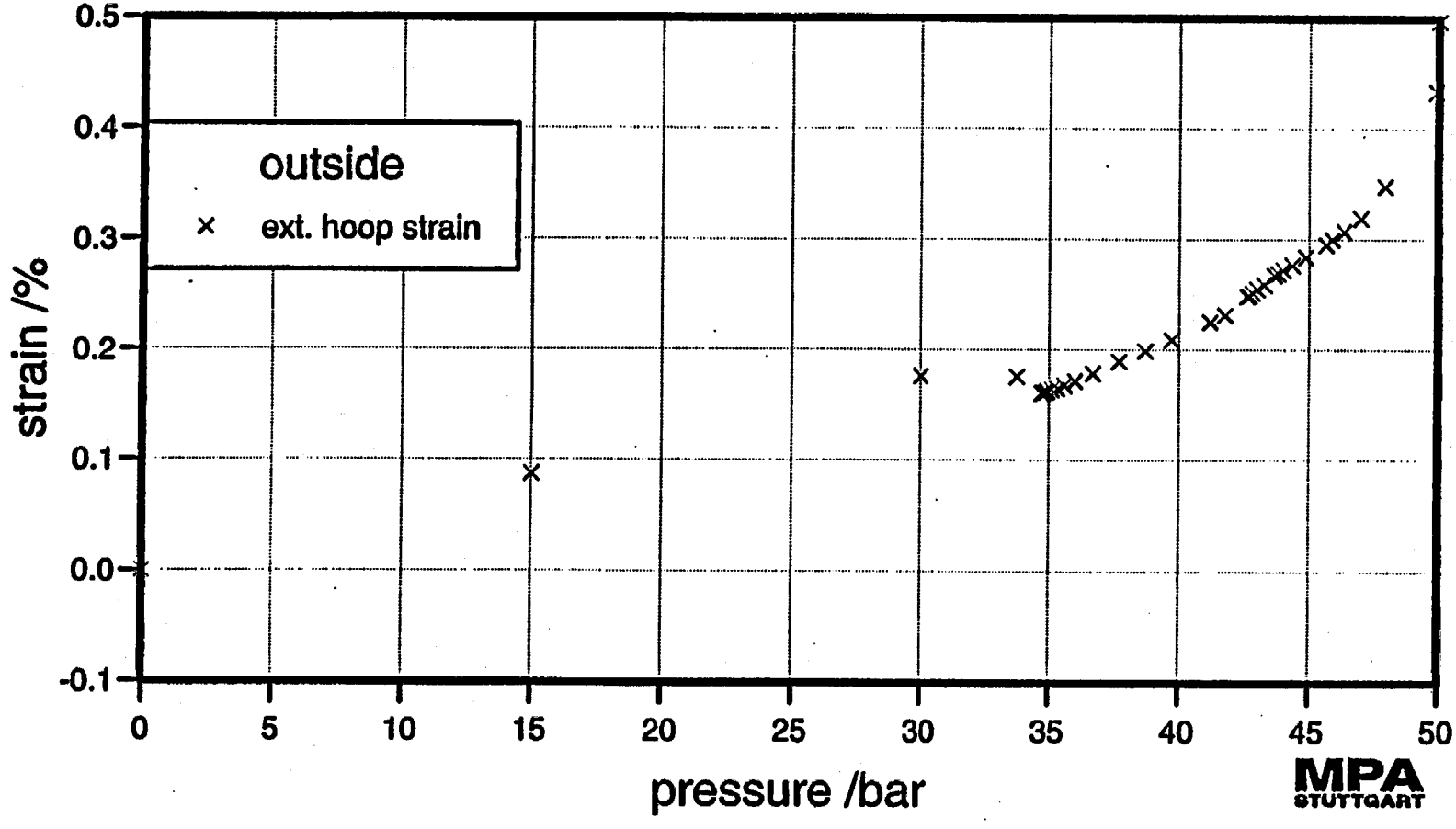
outside
ext. hoop strain
strain /%
0.5
0.4
0.3
0.2
0.1
0.0
-0.1
0
5
10
15
20
25
30
35
40
45
50
pressure /bar
MPA
STUTTGART

Plot id No 28

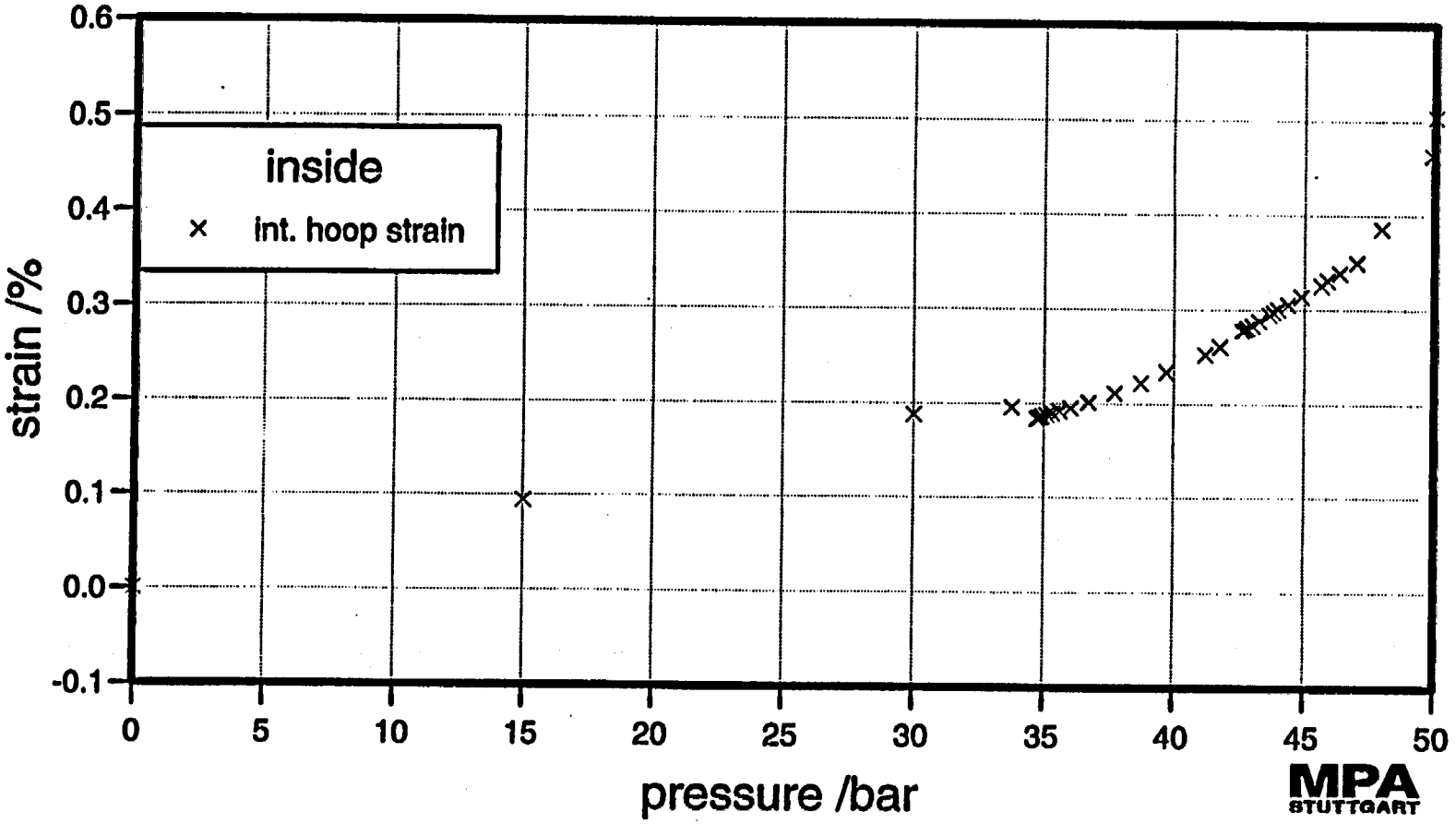
inside
int. hoop strain
strain /%
pressure /bar
0.6
0.5
0.4
0.3
0.2
0.1
0.0
-0.1
0
5
10
15
20
25
30
35
40
45
50
MPA
STUTTGART

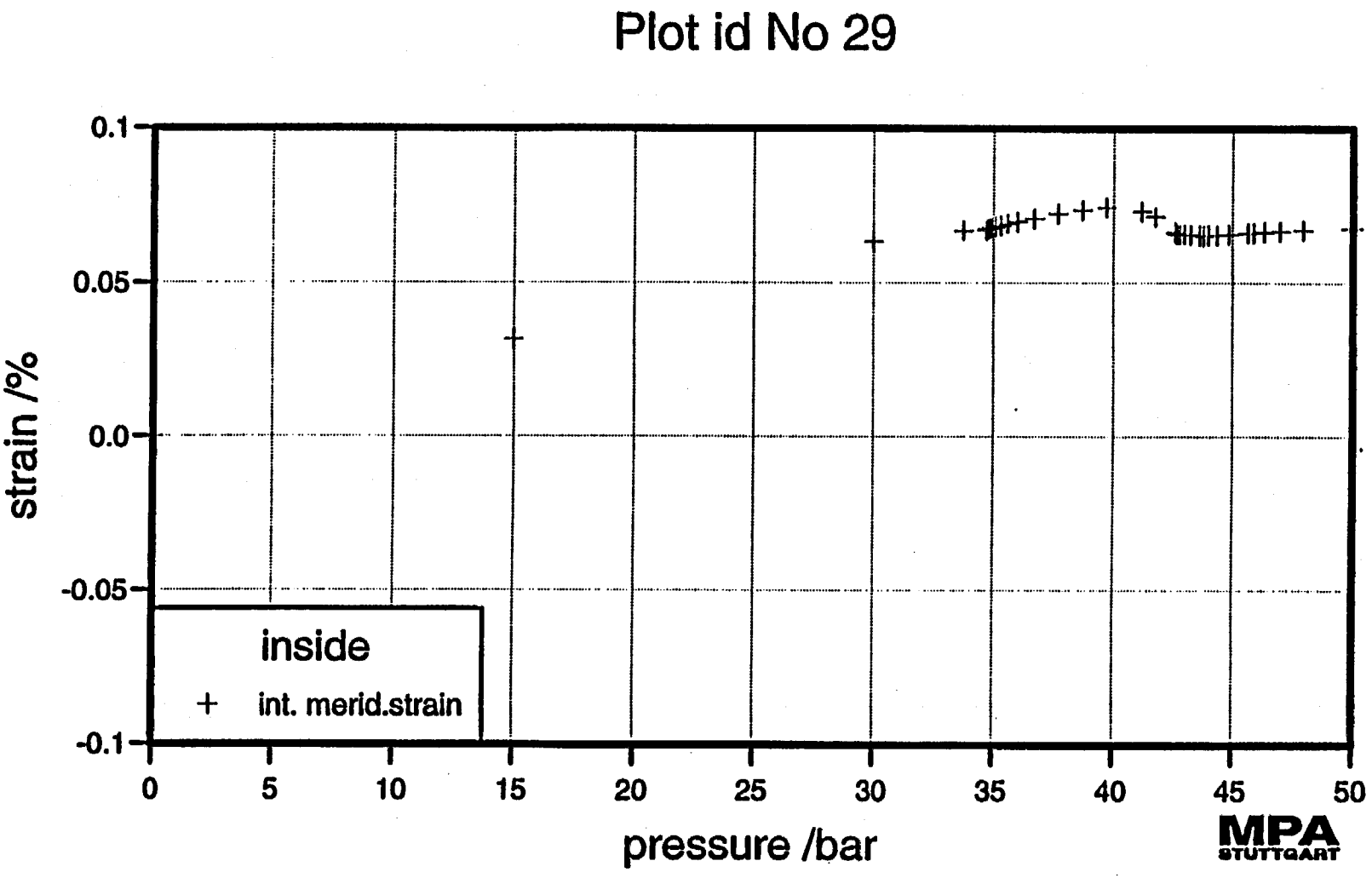
Plot id No 29
0.1
0.05
0.0
-0.05
-0.1
strain /%
inside
int. merid.strain
0
5
10
15
20
25
30
35
40
45
50
pressure /bar
MPA
STUTTGART

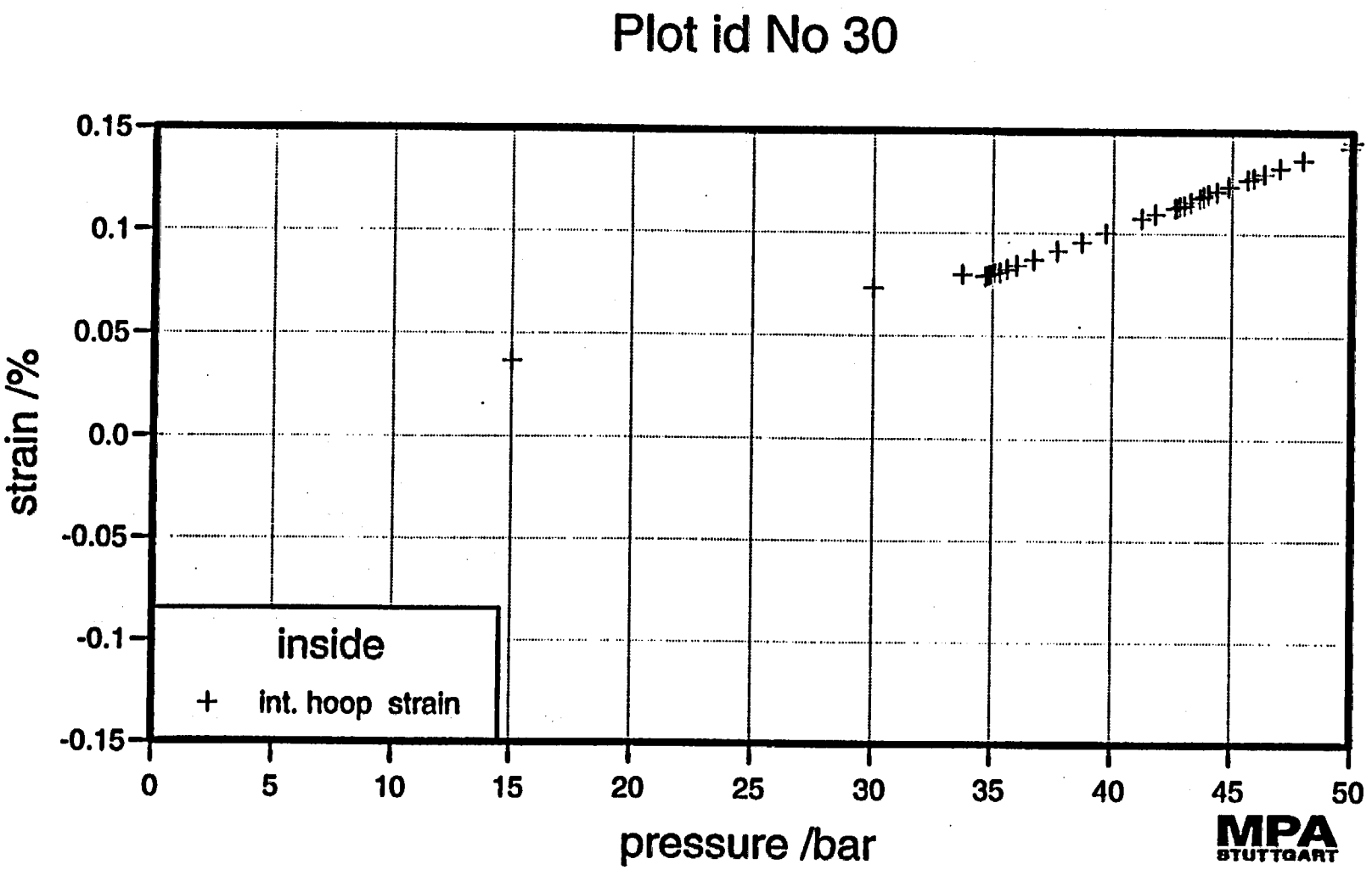
Plot id No 30
0.15
0.1
0.05
0.0
-0.05
-0.1
-0.15
strain /%
inside
+ int. hoop strain
0
5
10
15
20
25
30
35
40
45
50
pressure /bar
MPA
STUTTGART

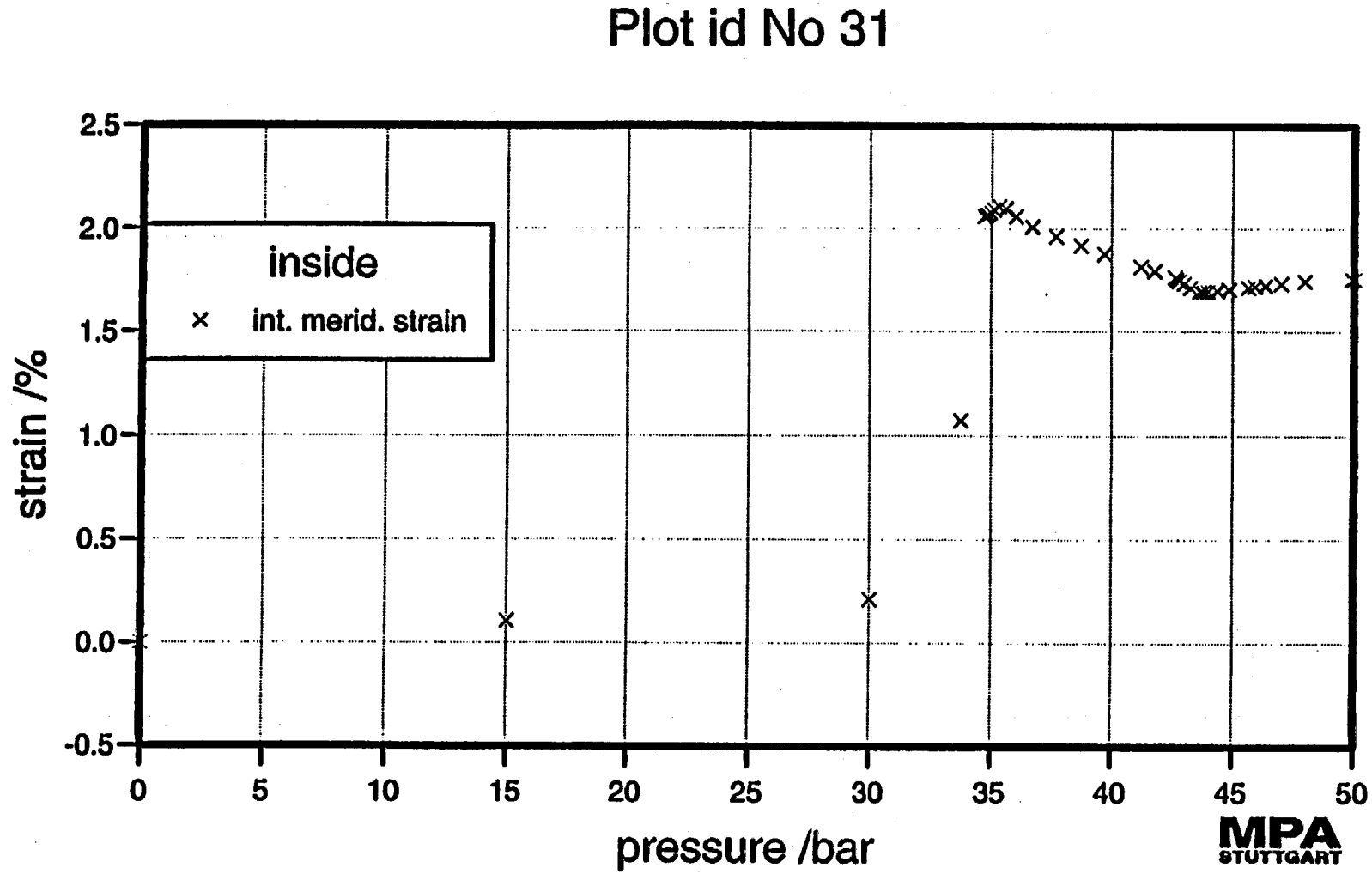
Plot id No 31
inside
int. merid. strain
strain /%
pressure /bar
2.5
2.0
1.5
1.0
0.5
0.0
-0.5
0
5
10
15
20
25
30
35
40
45
50
MPA
STUTTGART

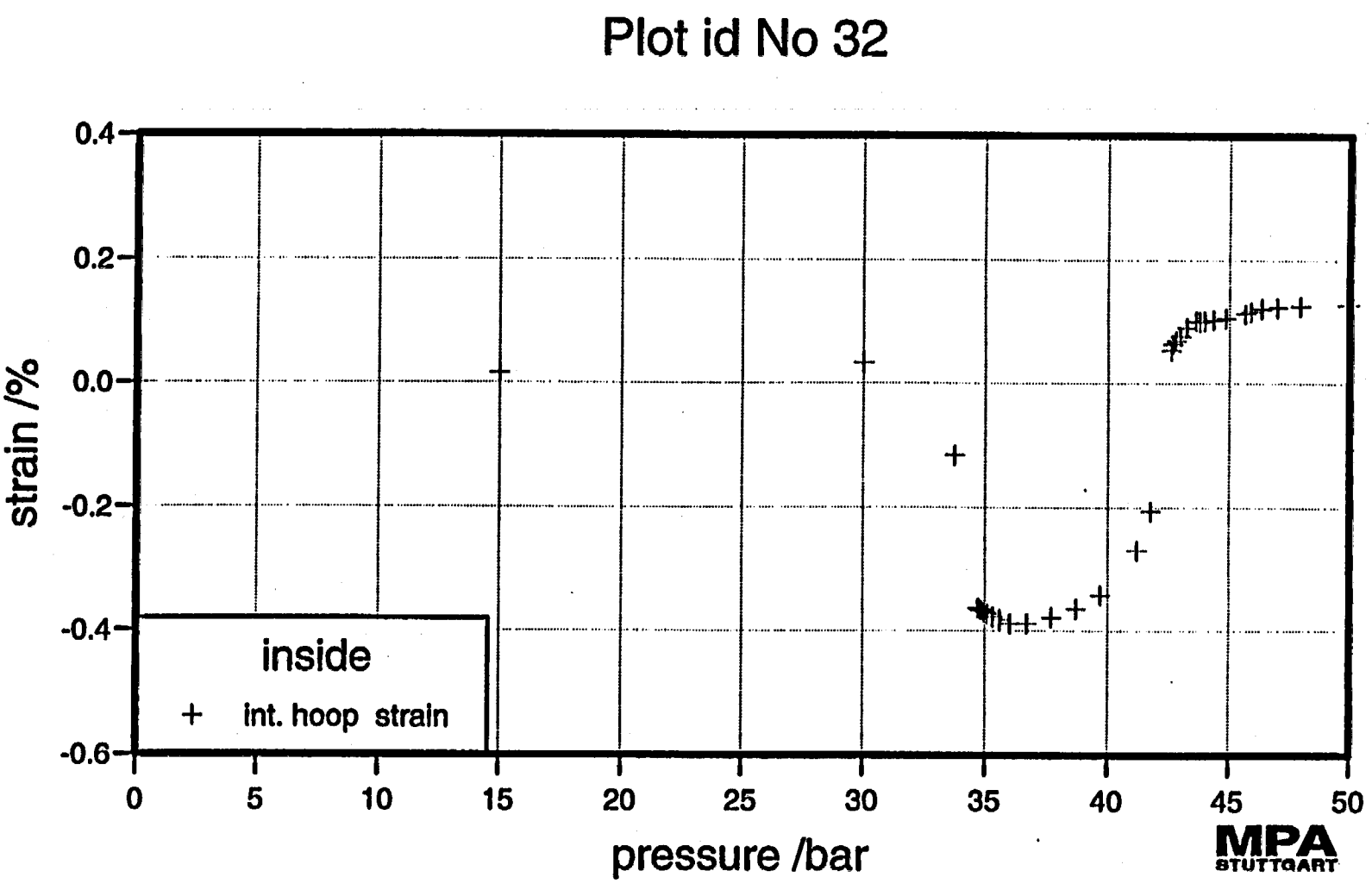
Plot id No 32
0.4
0.2
0.0
-0.2
-0.4
-0.6
strain /%
inside
int. hoop strain
0
5
10
15
20
25
30
35
40
45
50
pressure /bar
MPA
STUTTGART

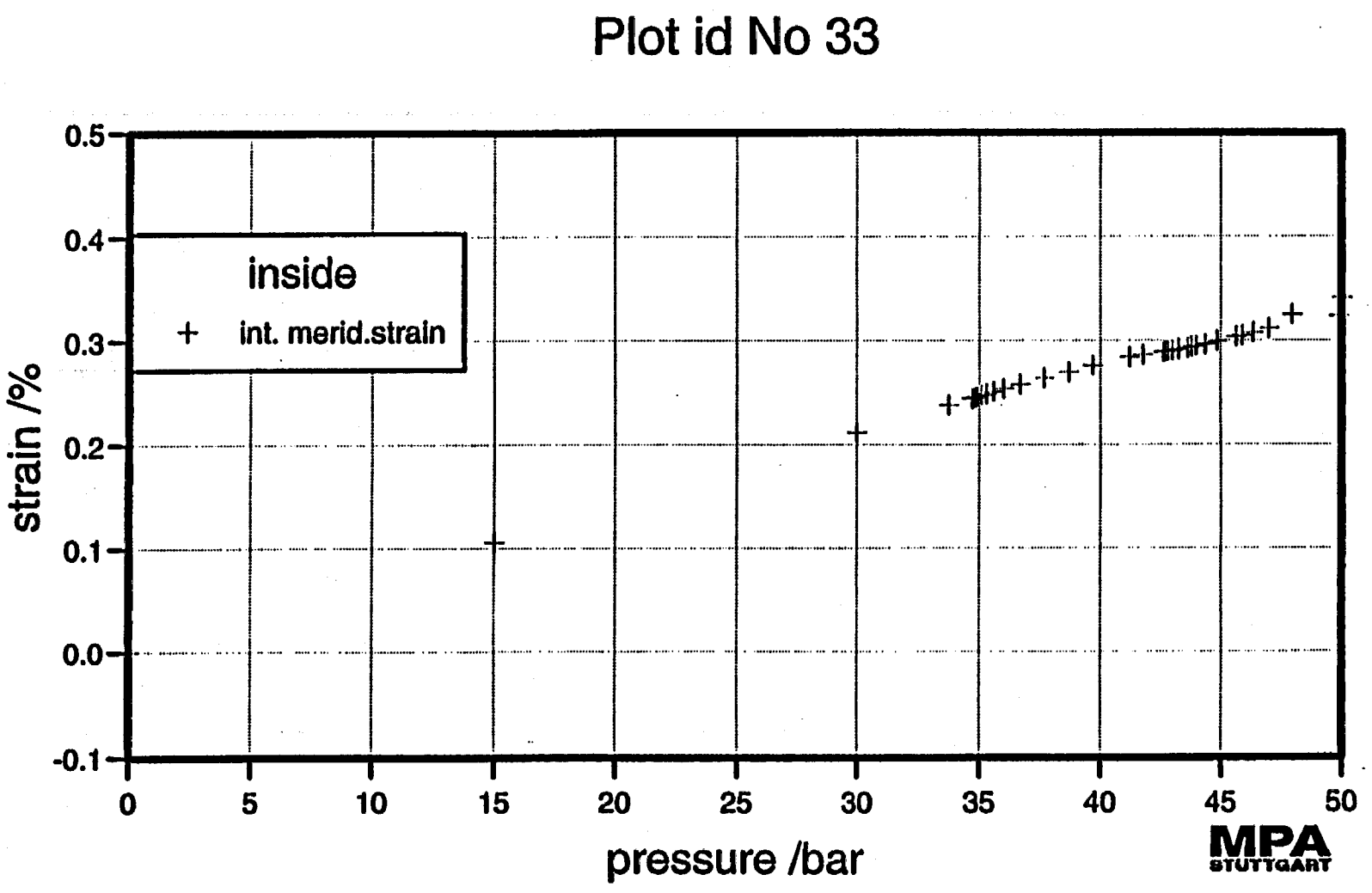
Plot id No 33
inside
int. merid.strain
strain /%
pressure /bar
0.5
0.4
0.3
0.2
0.1
0.0
-0.1
0
5
10
15
20
25
30
35
40
45
50
MPA
STUTTGART

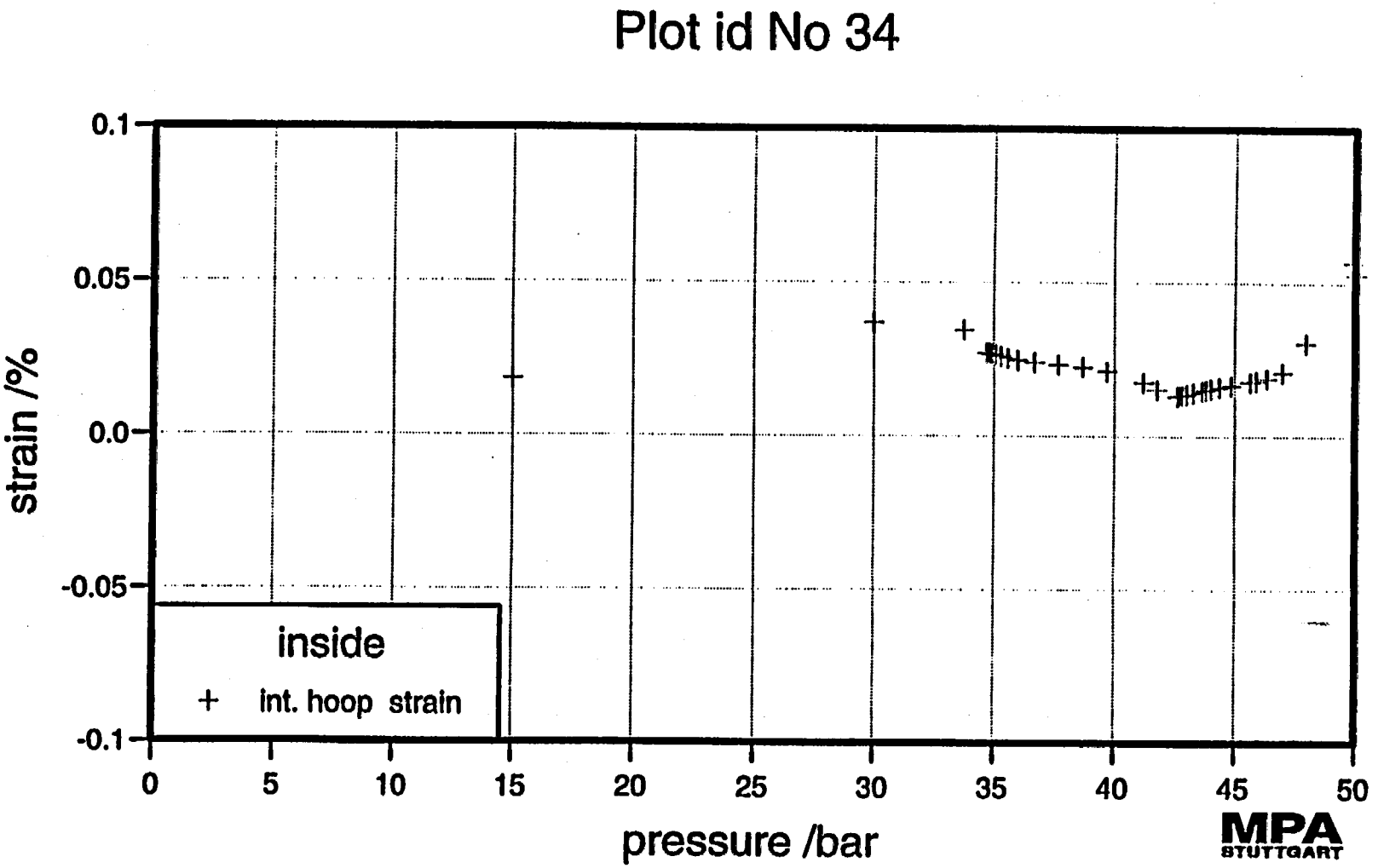
Plot id No 34
0.1
0.05
0.0
-0.05
-0.1
strain /%
inside
+ int. hoop strain
0
5
10
15
20
25
30
35
40
45
50
pressure /bar
MPA
STUTTGART

Plot id No 35

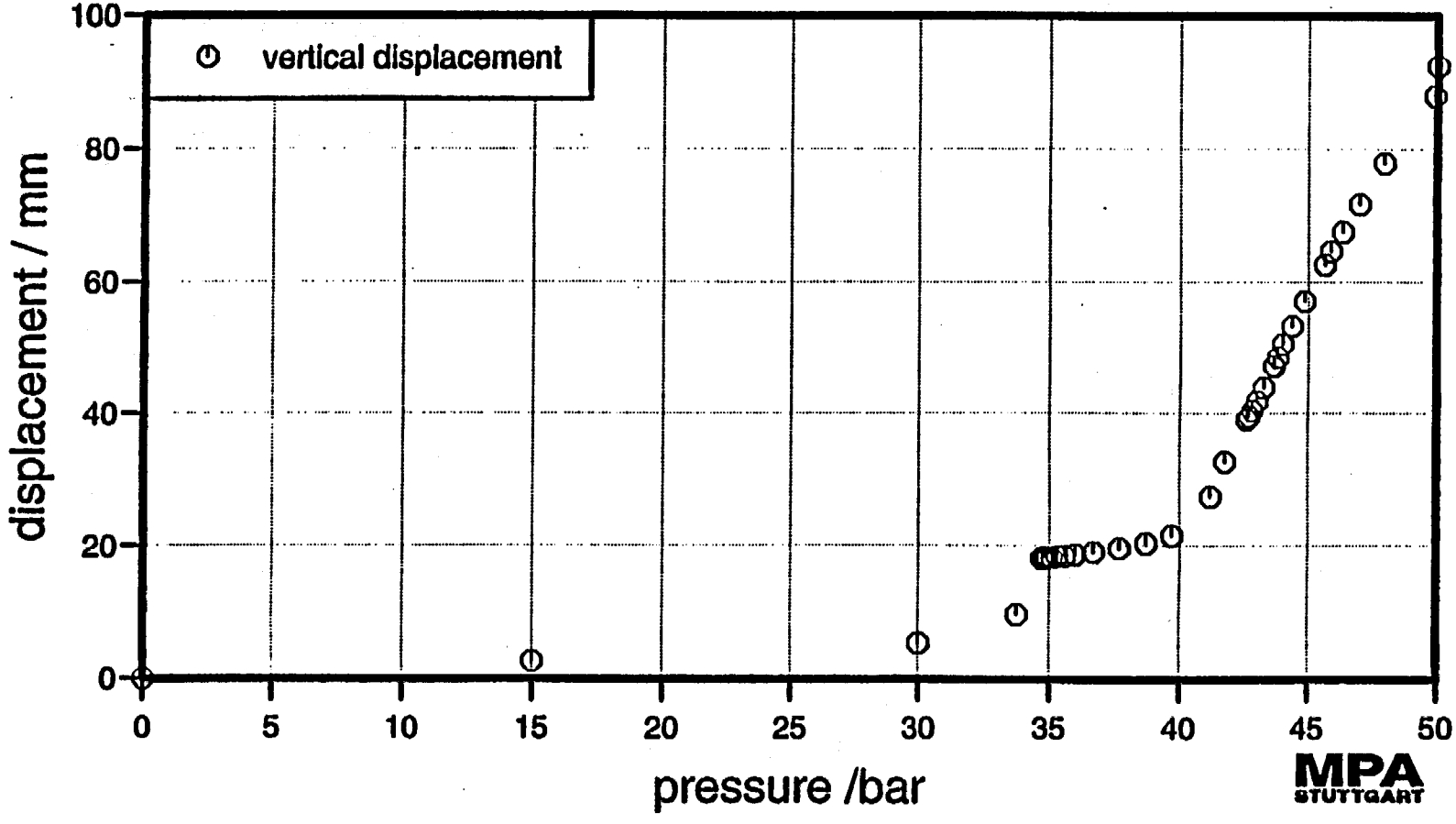
vertical displacement
displacement / mm
100
80
60
40
20
0
0
5
10
15
20
25
30
35
40
45
50
pressure /bar
MPA
STUTTGART

Plot id No 36

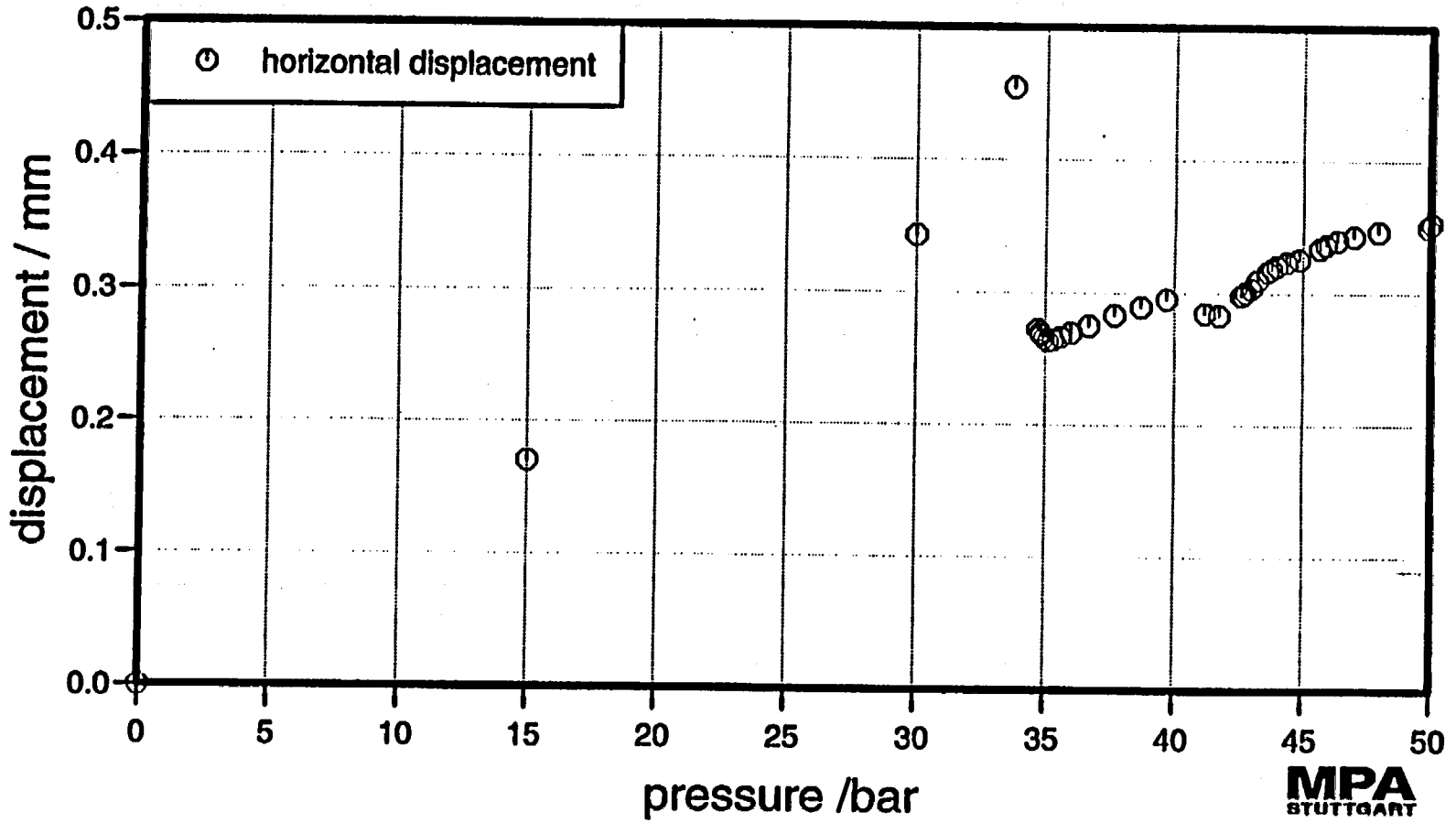
horizontal displacement
displacement / mm
0.5
0.4
0.3
0.2
0.1
0.0
0
5
10
15
20
25
30
35
40
45
50
pressure /bar
MPA
STUTTGART

Plot id No 37

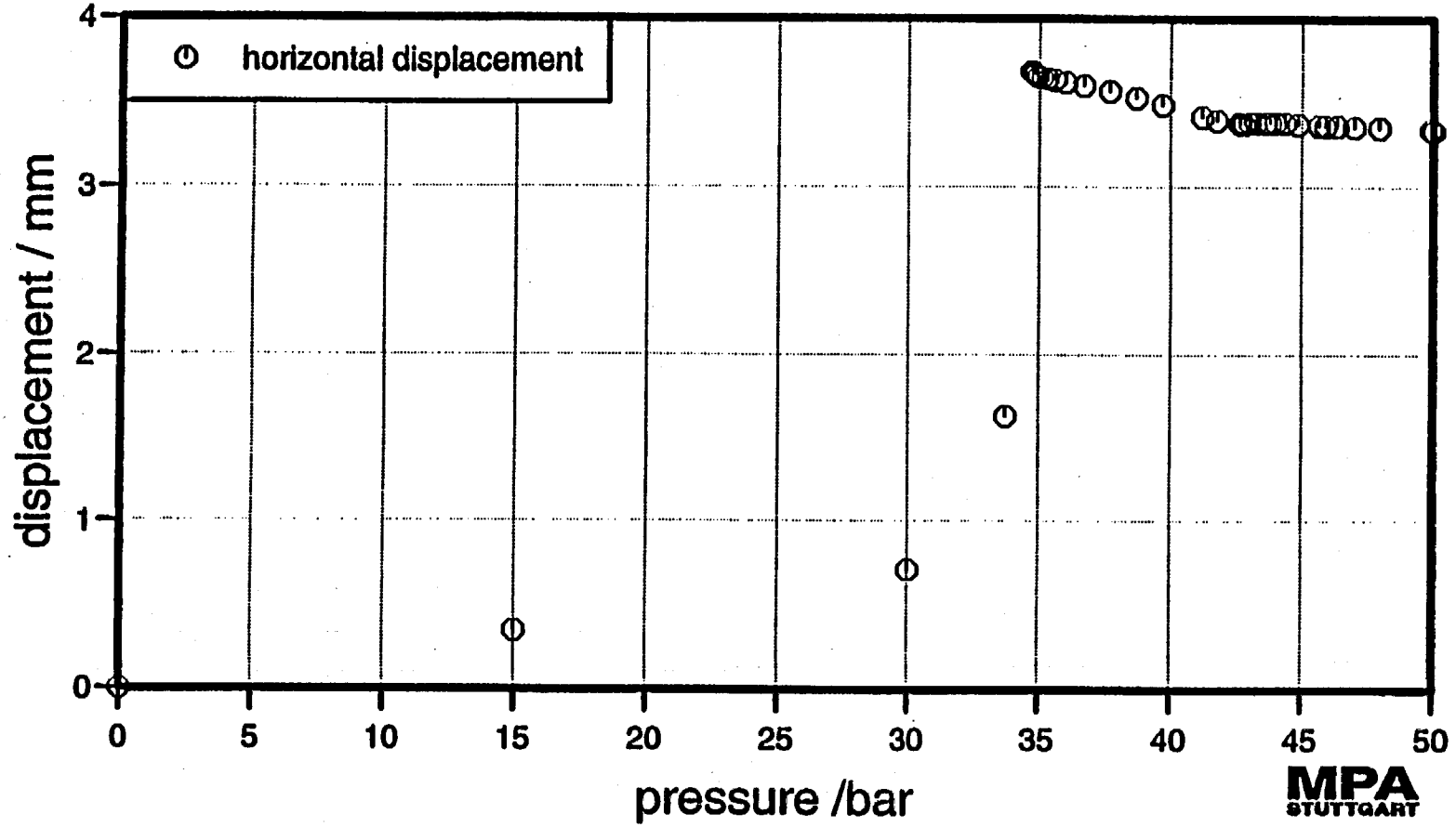
horizontal displacement
displacement / mm
0
1
2
3
4
0
5
10
15
20
25
30
35
40
45
50
pressure /bar
MPA
STUTTGART

Plot id No 38

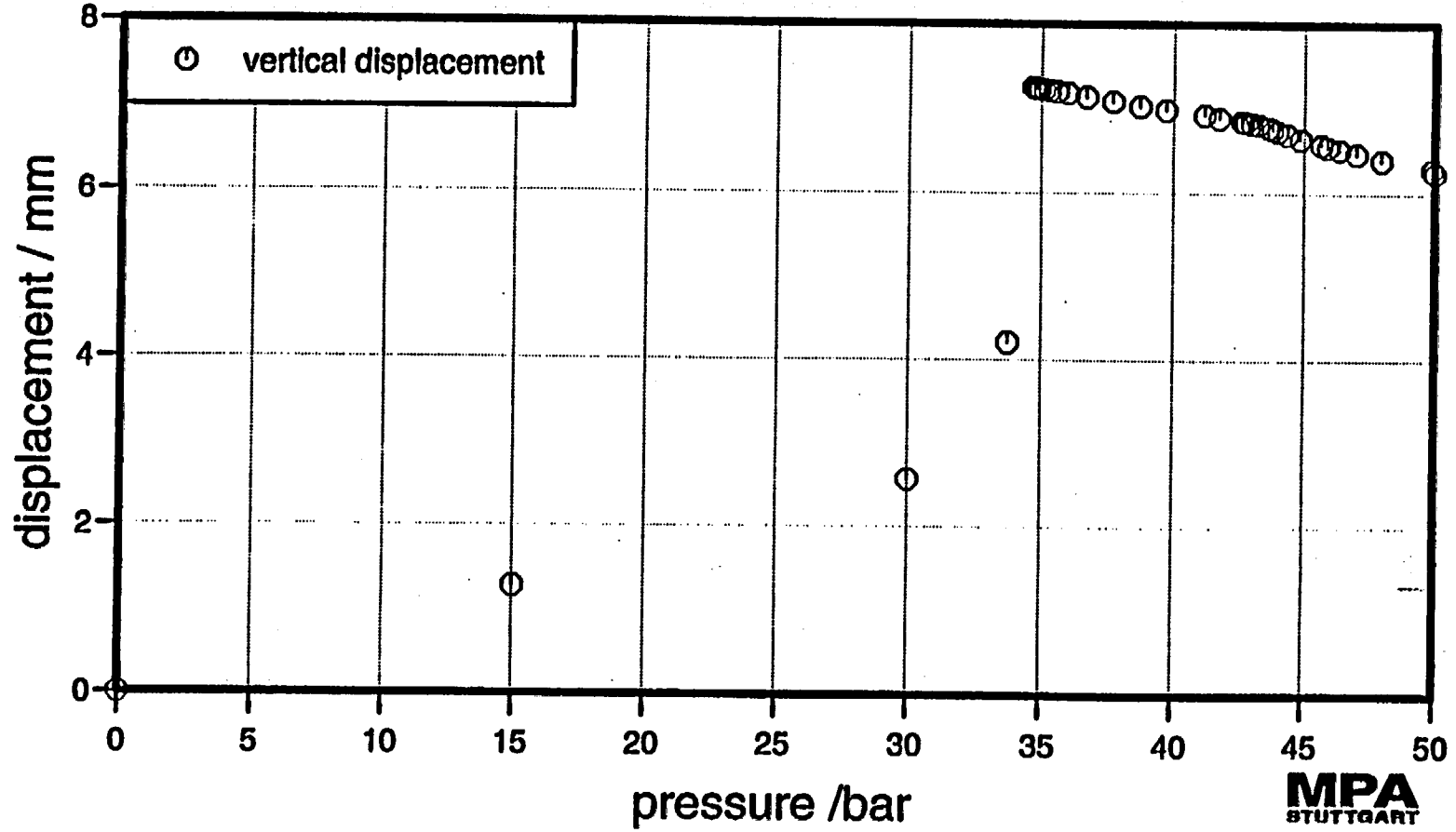
vertical displacement
displacement / mm
0
2
4
6
8
0
5
10
15
20
25
30
35
40
45
50
pressure /bar
MPA
STUTTGART

Plot id No 39

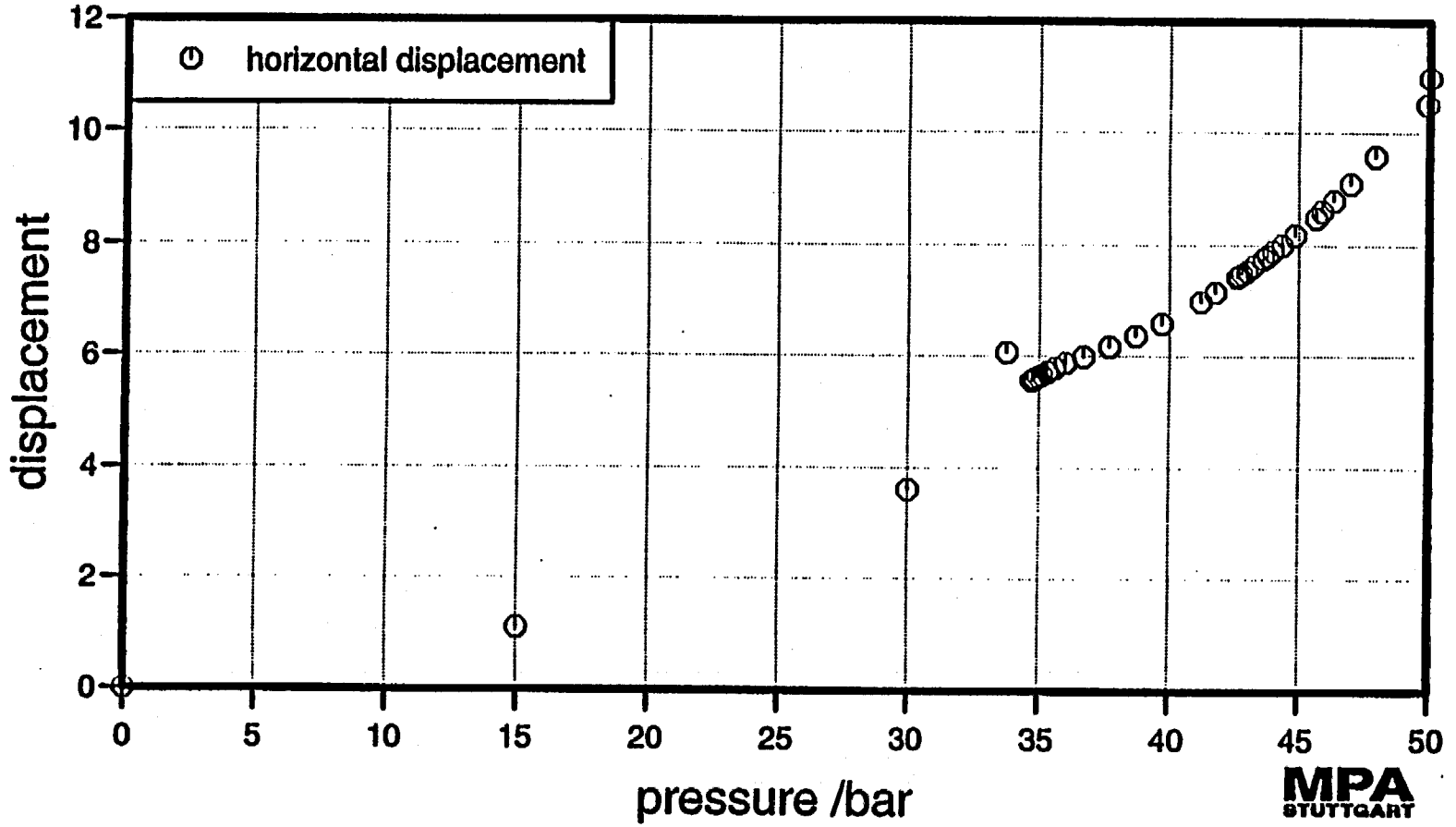
horizontal displacement
displacement
pressure /bar
0
2
4
6
8
10
12
0
5
10
15
20
25
30
35
40
45
50
MPA
STUTTGART

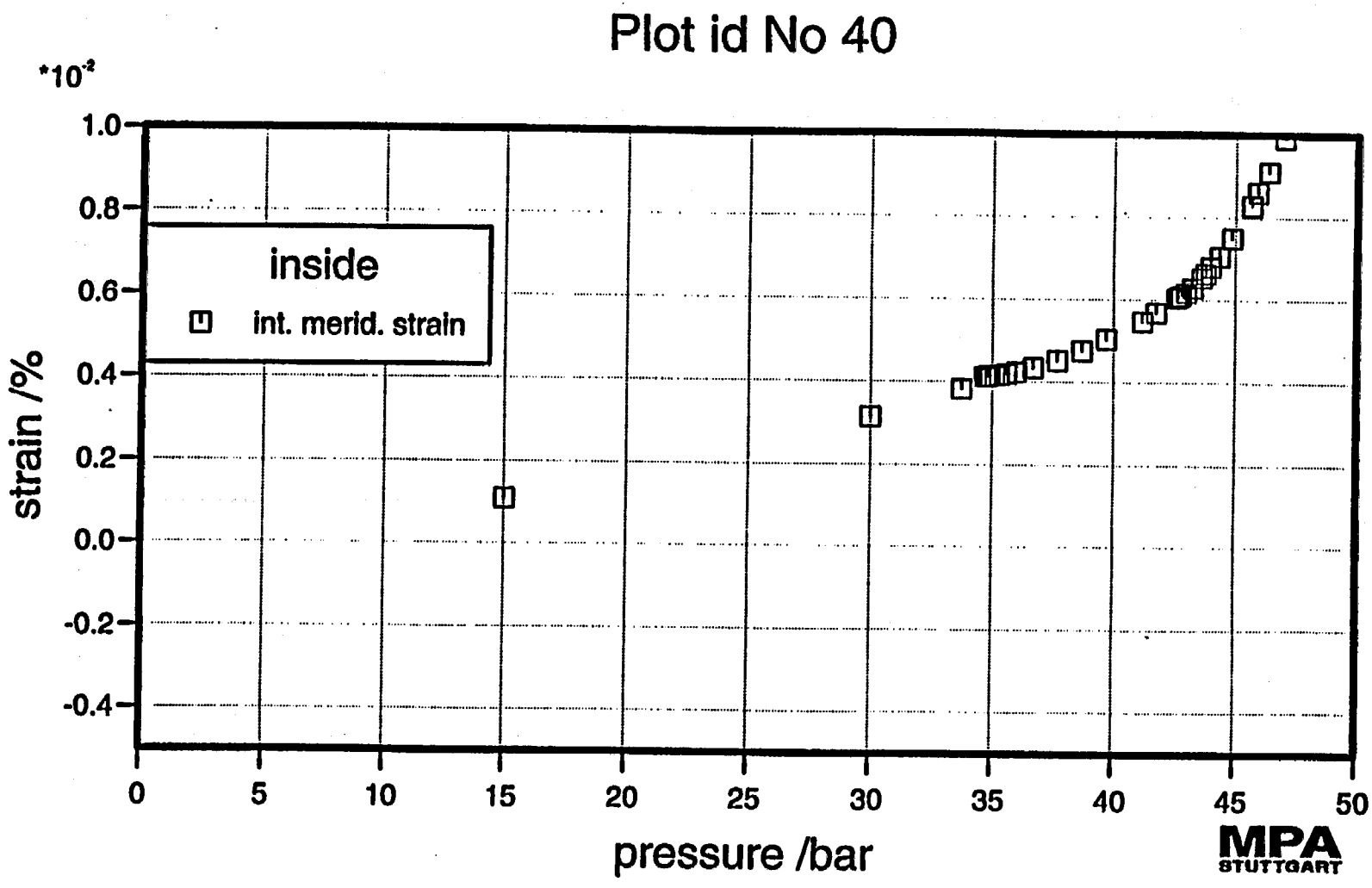
Plot id No 40
*10⁻²
1.0
0.8
0.6
0.4
0.2
0.0
-0.2
-0.4
strain /%
inside
int. merid. strain
0
5
10
15
20
25
30
35
40
45
50
pressure /bar
MPA
STUTTGART

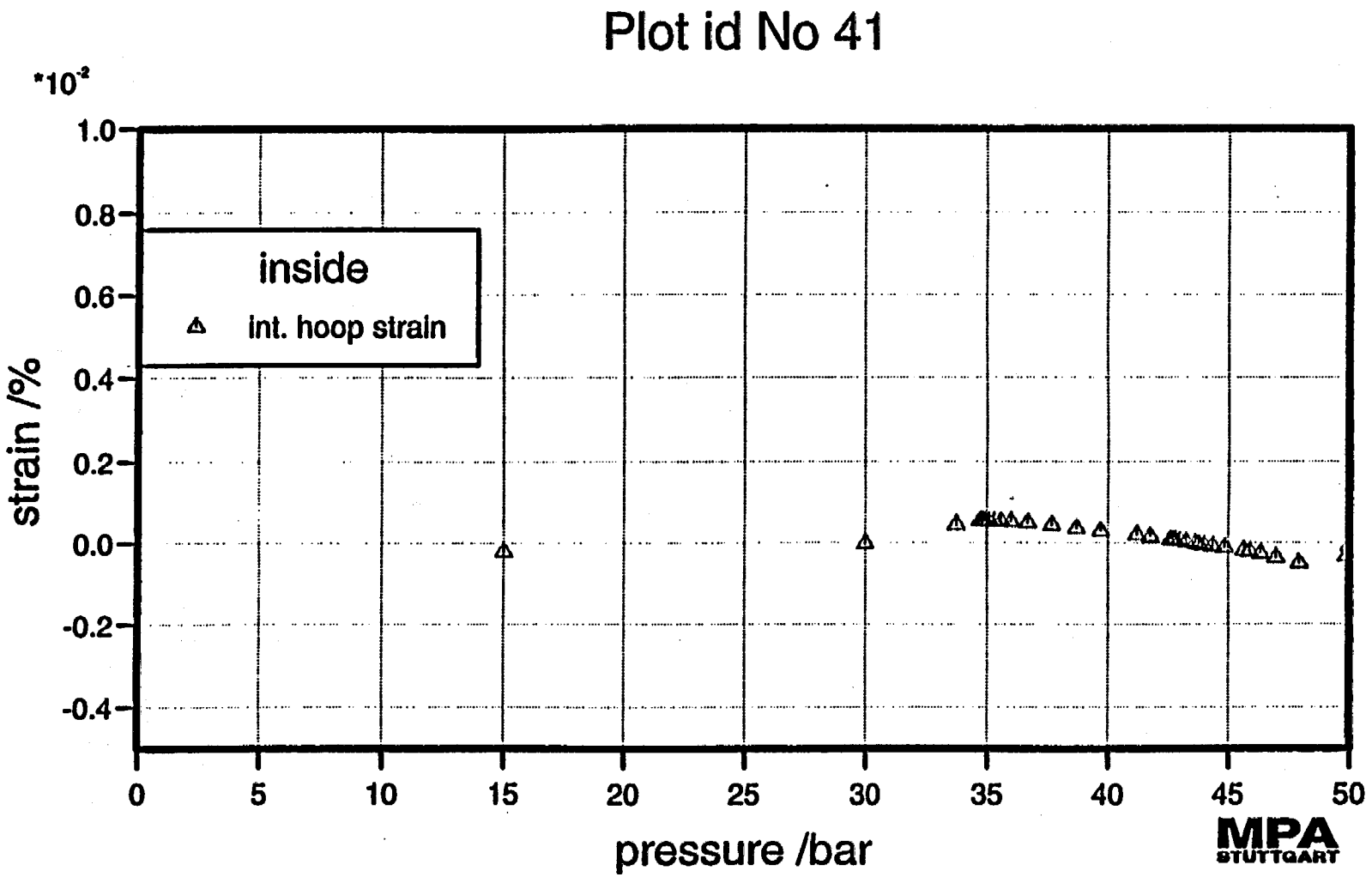
Plot id No 41
*10-2
1.0
0.8
0.6
0.4
0.2
0.0
-0.2
-0.4
strain /%
inside
int. hoop strain
0
5
10
15
20
25
30
35
40
45
50
pressure /bar
MPA
STUTTGART

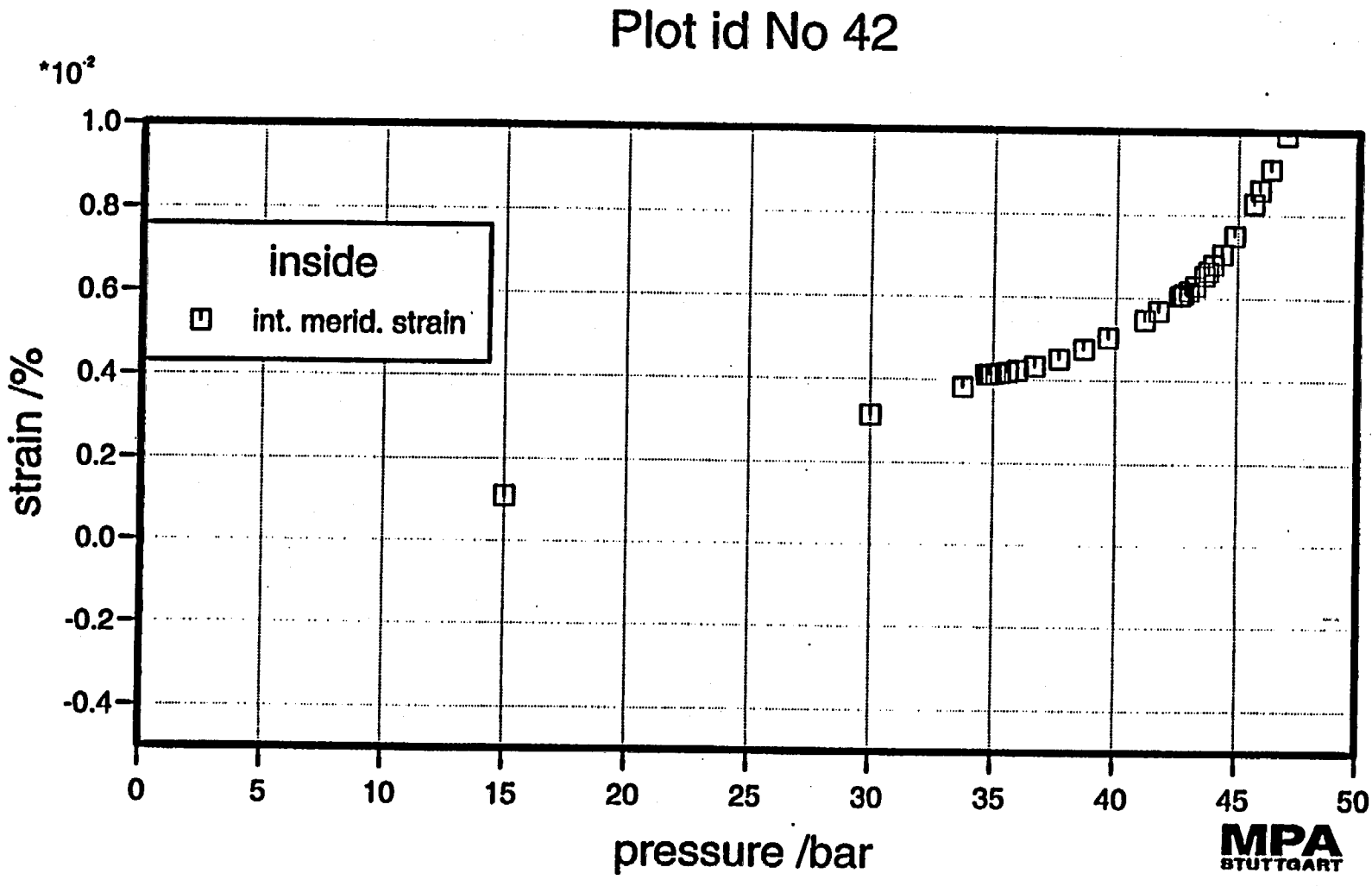
Plot id No 42
*10⁻²
1.0
0.8
0.6
0.4
0.2
0.0
-0.2
-0.4
strain /%
inside
int. merid. strain
0
5
10
15
20
25
30
35
40
45
50
pressure /bar
MPA
STUTTGART

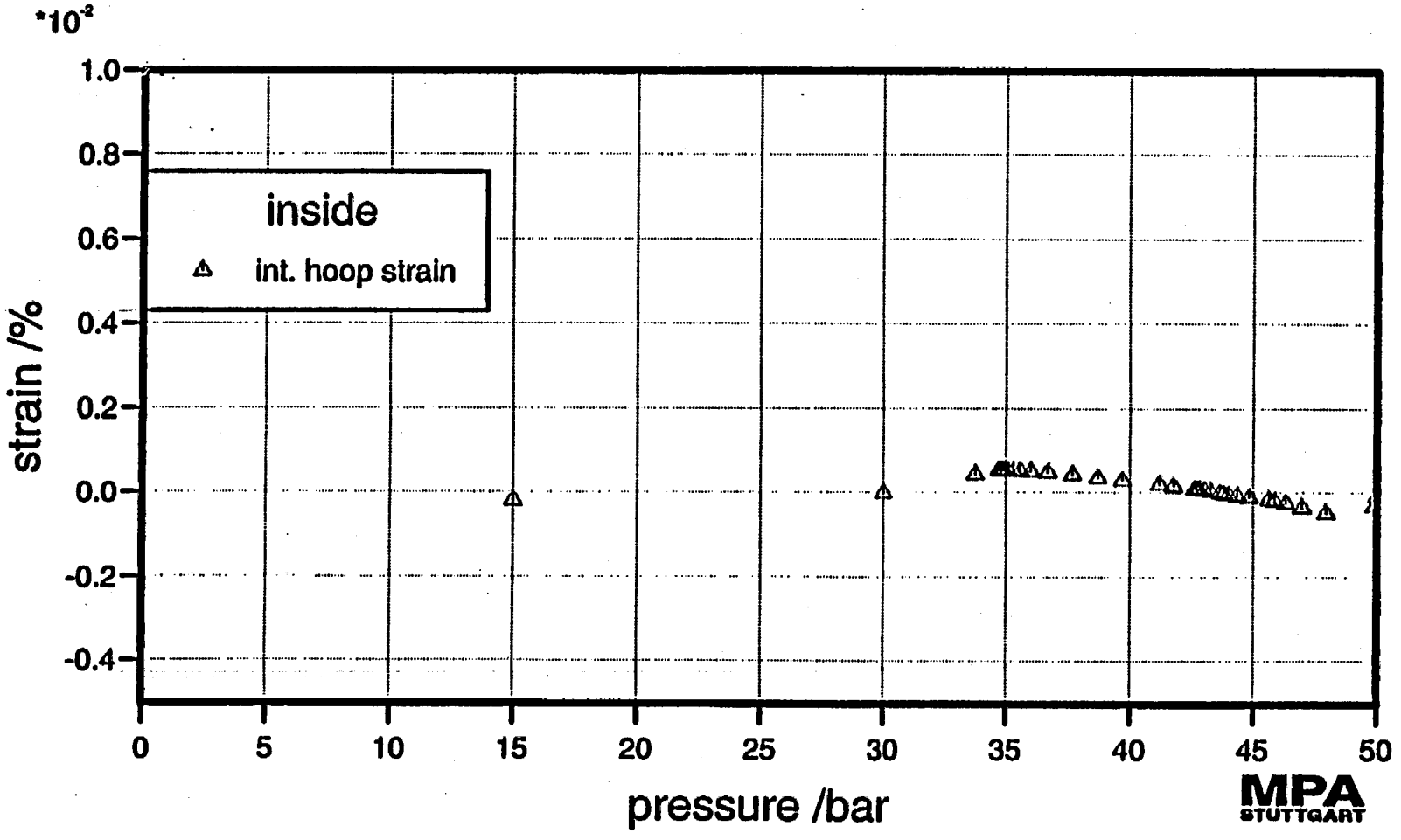
Plot id No 43
*10⁻²
1.0
0.8
0.6
0.4
0.2
0.0
-0.2
-0.4
strain /%
inside
int. hoop strain
0
5
10
15
20
25
30
35
40
45
50
pressure /bar
MPA
STUTTGART

NRC FORM 335 (2-89) NRCM 1102, 3201, 3202

U.S. NUCLEAR REGULATORY COMMISSION

BIBLIOGRAPHIC DATA SHEET

(See instructions on the reverse)

1. REPORT NUMBER (Assigned by NRC, Add Vol., Supp., Rev., and Addendum Numbers, if any.)
NUREG/CR-6517
SAND96-2899

2. TITLE AND SUBTITLE
Round Robin Pretest Analyses of a Steel Containment Vessel Model and Contact Structure Assembly Subject to Static Internal Pressurization

3. DATE REPORT PUBLISHED
MONTH: August
YEAR: 1998

4. FIN OR GRANT NUMBER
A1401

5. AUTHOR(S)
Vincent K. Luk/SNL
Eric W. Klamerus/SNL

6. TYPE OF REPORT

7. PERIOD COVERED (Inclusive Dates)
June 1994 to November 1996

8. PERFORMING ORGANIZATION – NAME AND ADDRESS (If NRC, provide Division, Office or Region, U.S. Nuclear Regulatory Commission, and mailing address; if contractor, provide name and mailing address.)
Sandia National Laboratories
P.O. Box 5800
Albuquerque, NM 87185-0744

9. SPONSORING ORGANIZATION – NAME AND ADDRESS (If NRC, type "Same as above"; if contractor, provide NRC Division, Office or Region, U.S. Nuclear Regulatory Commission, and mailing address.)
Division of Engineering Technology
Office of Nuclear Regulatory Research
U.S. Nuclear Regulatory Commission
Washington, D. C. 20555

Systems Safety Department
Nuclear Power Engineering Corporation
Fujita-Kanko Building
17-1, 3-Chome, Toranomon, Minato-ku
Tokyo 105, Japan

10. SUPPLEMENTARY NOTES
J. F. Costello, NRC Project Manager

11. ABSTRACT (200 words or less)

The Nuclear Power Engineering Corporation (NUPEC) and the U.S. Nuclear Regulatory Commission (NRC) are co-sponsoring and jointly funding a research project at Sandia National Laboratories (SNL) to conduct a failure test of a steel containment vessel (SCV) model and contact structure assembly. The SCV model, representative of an improved Mark-II Boiling Water Reactor (BWR) containment vessel, is scaled 1: 10 in geometry and 1:4 in shell thicknesses. The contact structure, a thick bell-shaped steel shell, provides a simplified representation of a concrete reactor shield building in the actual plant. The failure test will be conducted in December 1996 to provide data on the response of the composite structure up to its failure in order to validate analytical modeling, to find the pressure capacity of the model, and to observe the failure mechanisms.

Eight international organizations performed model analyses and provided predictions of the model behavior at 43 specified locations and the failure pressure and mechanisms. This report describes the analysis models and tabulates the pretest predictions submitted by each organization. A pretest meeting of all participants will be held on October 1-2, 1996, to discuss modeling approaches and analysis results.

12. KEY WORDS/DESCRIPTORS (List words or phrases that will assist researchers in locating the report.)
Steel Containment Vessel, Failure Test, Model Analysis, International Participants, Failure Pressure and Mechanisms.

13. AVAILABILITY STATEMENT
Unlimited

14. SECURITY CLASSIFICATION
(This Page) Unclassified
(This Report) Unclassified

15. NUMBER OF PAGES

16. PRICE

NRC FORM 335 (2-89)

Federal Recycling Program

UNITED STATES
NUCLEAR REGULATORY COMMISSION
WASHINGTON, DC 20555-0001

OFFICIAL BUSINESS
PENALTY FOR PRIVATE USE, $300

SPECIAL STANDARD MAIL
POSTAGE AND FEES PAID
USNRC
PERMIT NO. G-67